

به نام خدا



# مرکز دانلود رایگان مهندسی متالورژی و مواد

[www.Iran-mavad.com](http://www.Iran-mavad.com)



*Multilayer Thin Films*. Edited by Gero Decher, Joseph B. Schlenoff  
Copyright © 2002 Wiley-VCH Verlag GmbH & Co. KGaA  
ISBNs: 3-527-30440-1 (Hardback); 3-527-60057-4 (Electronic)

**Multilayer Thin Films**

Sequential Assembly of Nanocomposite Materials

*Edited by G. Decher, J. B. Schlenoff*

# Multilayer Thin Films

Sequential Assembly of Nanocomposite Materials

*Edited by*

*Gero Decher, Joseph B. Schlenoff*

**Gero Decher**

Institut Charles Sadron  
6, rue Boussingault  
F-67083 Strasbourg Cedex  
France

**Joseph B. Schlenoff**

Florida State University  
Dept. of Chemistry and Biochemistry  
Tallahassee, Florida 32306-4390  
USA

This book was carefully produced. Nevertheless, editors, authors and publisher do not warrant the information contained therein to be free of errors. Readers are advised to keep in mind that statements, data, illustrations, procedural details or other items may inadvertently be inaccurate.

**Library of Congress Card No.:** applied for

**British Library Cataloguing-in-Publication Data**

A catalogue record for this book is available from the British Library.

**Bibliographic information published by Die Deutsche Bibliothek**

Die Deutsche Bibliothek lists this publication in the Deutsche Nationalbibliografie; detailed bibliographic data is available in the Internet at <http://dnb.ddb.de>

© 2003 WILEY-VCH Verlag GmbH & Co. KGaA, Weinheim

All rights reserved (including those of translation in other languages). No part of this book may be reproduced in any form – by photoprinting, microfilm, or any other means – nor transmitted or translated into machine language without written permission from the publishers. Registered names, trademarks, etc. used in this book, even when not specifically marked as such, are not to be considered unprotected by law.

Printed in the Federal Republic of Germany  
Printed on acid-free paper

**Typesetting** K+V Fotosatz GmbH, Beerfelden  
**Printing** Strauss Offsetdruck GmbH,  
Mörlenbach

**Bookbinding** J. Schäffer GmbH & Co. KG,  
Grünstadt

**ISBN** 3-527-30440-1



## Foreword

Over the last ten years, scientists from varying backgrounds have rallied around a versatile new method for the synthesis of thin films. Because the layer-by-layer assembly method provides opportunities for creative design and application of function-specific films, the field has experienced an initial period of exponential growth. This book, the first on the topic, contains many insightful contributions from leaders in the field that will enable novices and experts to understand the promises and premises of multilayers.

Readers will instantly identify with a particular aspect of the technology, whether it is the design and synthesis of new polymeric or nanoparticulate building blocks, understanding the polymer physical chemistry of multilayers, or characterizing their optical, electrical or biological activities. The reasons for the intense interest in the field are also clearly evident: multilayers bridge the gap between monolayers and spun-on or dip-coated films, and they provide many of the aspects of control found in classical Langmuir-Blodgett (LB) films, yet multilayers are more versatile, in many respects, and easier to create.

This book is an essential and welcome addition to the literature on thin films. Readers with interests in self-assembled systems, supramolecular chemistry, nanocomposites or polymers will find themselves fascinated by the diversity of topics herein. The message that multilayers are making significant inroads into numerous aspects of chemistry, physics and biology is made clear. The editors and authors are to be commended for creating a comprehensive yet readable volume.

Jean-Marie LEHN

## Contents

	<b>Foreword</b>	V
	<b>Preface</b>	XV
	<b>List of Contributors</b>	XVII
<b>1</b>	<b>Polyelectrolyte Multilayers, an Overview</b>	<b>1</b>
	<i>G. Decher</i>	
1.1	Why is the Nanoscale so Interesting	1
1.2	From Self-Assembly to Directed Assembly	1
1.3	The Layer-by-Layer Deposition Technique	3
1.3.1	LbL Deposition is the Synthesis of Polydisperse Supramolecular Objects	4
1.3.2	Reproducibility and Deposition Conditions	6
1.3.3	Monitoring Multilayer Buildup	7
1.3.3.1	Ex-situ Characterisation	7
1.3.3.2	In-situ Characterisation	9
1.3.4	Multilayers by Solution Dipping, Spraying or Spin Coating	12
1.3.5	Post-preparation Treatment of Multilayer Films	12
1.3.5.1	Annealing	12
1.3.5.2	Photopatterning	15
1.4	Multilayer Structure	16
1.4.1	The Zone Model for Polyelectrolyte Films	17
1.4.2	Layered or Amorphous: What Makes Multilayers Unique Supramolecular Species?	20
1.4.3	Soft and Rigid Materials	23
1.4.4	Deviation from Linear Growth Behaviour	24
1.5	Multimaterial Films	24
1.6	Toward Compartmentalized Films: Barrier Layers and Nanoreactors	26
1.7	Commercial Applications	30
1.8	References	31

<b>2</b>	<b>Fundamentals of Polyelectrolyte Complexes in Solution and the Bulk</b>	<b>47</b>
	<i>V. Kabanov</i>	
2.1	Introduction	47
2.2	Interpolyelectrolyte Reactions and Solution Behavior of Interpolyelectrolyte Complexes	48
2.2.1	Kinetics and Mechanism of Polyelectrolyte Coupling and Interchange Reactions	52
2.2.2	Solution Properties of Equilibrated Nonstoichiometric Interpolyelectrolyte Complexes	61
2.2.3	Transformation of Interpolyelectrolyte Complexes in External Salt Solutions	66
2.3	Complexation of Polyelectrolytes with Oppositely Charged Hydrogels	74
2.4	Structural and Mechanical Properties of Interpolyelectrolyte Complexes in the Bulk	76
2.5	Conclusion	82
2.6	References	83
<b>3</b>	<b>Polyelectrolyte Adsorption and Multilayer Formation</b>	<b>87</b>
	<i>J.-F. Joanny and M. Castelnovo</i>	
3.1	Introduction	87
3.2	Polyelectrolytes in Solution	89
3.3	Polyelectrolytes at Interfaces	90
3.4	Polyelectrolyte Complexes	92
3.5	Multilayer Formation	94
3.6	Concluding Remarks	96
3.7	References	97
<b>4</b>	<b>Charge Balance and Transport in Polyelectrolyte Multilayers</b>	<b>99</b>
	<i>J. B. Schlenoff</i>	
4.1	Introduction	99
4.2	Interactions	101
4.2.1	Mechanism: Competitive Ion Pairing	101
4.2.2	Intrinsic vs. Extrinsic Charge Compensation	103
4.2.2.1	Key Equilibria	103
4.2.2.2	Swelling and Smoothing: Estimating Interaction Energies	105
4.2.2.3	Multilayer Decomposition	108
4.3	Excess Charge	109
4.3.1	Surface vs. Bulk Polymer Charge	109
4.3.2	Distribution of Surface Charge in Layer-by-Layer Buildup: Mechanism	113
4.3.3	Equilibrium vs. non-Equilibrium Conditions for Salt and Polymer Sorption	117
4.4	Equilibria and Transport	118
4.4.1	Ion Transport through Multilayers: the “Reluctant” Exchange Mechanism	118
4.4.2	Practical Consequences: Trapping and Self-Trapping	126

4.5	Conclusions	127
4.6	References	130
<b>5</b>	<b>pH-Controlled Fabrication of Polyelectrolyte Multilayers: Assembly and Applications</b>	<b>133</b>
	<i>M. F. Rubner</i>	
5.1	Introduction	133
5.2	Layer-by-Layer Assembly of Weak Polyelectrolyte Multilayers	134
5.3	Light Emitting Thin Film Devices	137
5.4	Microporous Thin Films	139
5.5	Nanoreactors, Electroless Plating and Ink-jet Printing	141
5.6	Surface Modification via Selective Adsorption of Block Copolymers	144
5.7	Patterning of Weak Polyelectrolyte Multilayers	145
5.7.1	Micro-Contact Printing	146
5.7.2	Ink-jet Printing of Hydrogen-Bonded Multilayers	148
5.8	Conclusions and Future Prospects	152
5.9	References	153
<b>6</b>	<b>Recent Progress in the Surface Sol–Gel Process and Protein Multilayers</b>	<b>155</b>
	<i>I. Ichinose, K. Kuroiwa, Y. Lvov, and T. Kunitake</i>	
6.1	Alternating Adsorption	155
6.1.1	Surface Sol–Gel Process	155
6.1.2	Adsorption of Cationic Compounds on Metal Oxide Gels	157
6.1.3	Multilayer Assembly of Metal Oxides and Proteins	162
6.1.4	Protein/Polyelectrolyte Multilayer Assembly	166
6.2	Recent Topics in Biological Applications	167
6.2.1	Biosensors	168
6.2.2	Nano-filtration	169
6.2.3	Bioreactors	171
6.2.4	Protein Capsule and Protein Shell	173
6.3	References	174
<b>7</b>	<b>Internally Structured Polyelectrolyte Multilayers</b>	<b>177</b>
	<i>K. Glinel, A. M. Jonas, A. Laschwesky, and P. Y. Vuillaume</i>	
7.1	Introduction	177
7.2	Experimental Considerations	179
7.3	Stratified Binary (A/B) <sub>n</sub> Organic Multilayers	182
7.4	Stratified Binary (A/B) <sub>n</sub> Hybrid Organic/Inorganic Multilayers	188
7.4.1	Initial Studies on Hybrid Assemblies	189
7.4.2	Layered Assemblies from Analogous Poly(diallyl ammonium) Salt Derivatives and Hectorite Platelets	190
7.4.2.1	General Structural Observations	190
7.4.2.2	Detailed Analysis of the Structure of Laponite-Based Hybrid LBL Films	192
7.4.3	Ordering in Hybrid Assemblies Employing Functional Polyions	194
7.4.3.1	Photocrosslinkable Polyelectrolytes	194

7.4.3.2	The Use of Mesomorphic Polyions	195
7.5	Hybrid Superlattices of the $\{(A/B)_m/(C/D)_p\}_n$ Type	196
7.5.1	Literature Survey	197
7.5.2	Hybrid Organic/Inorganic Compartmentalized Multilayers from Clay Platelets	198
7.6	Conclusions	201
7.7	References	202
<b>8</b>	<b>Layer-by-Layer Assembly of Nanoparticles and Nanocolloids: Intermolecular Interactions, Structure and Materials Perspectives</b>	<b>207</b>
	<i>N. A. Kotov</i>	
8.1	Introduction	207
8.2	Layer-by-Layer Assembly of Nanoparticles and Nanocolloids	208
8.3	Structural Factors of Individual Adsorption Layers	217
8.3.1	Intermolecular Interactions in the LBL Process	217
8.3.2	Ionic Conditions	222
8.3.3	Effect of Particle Shape on the Density of the Adsorption Layer	224
8.4	Stratified LBL Assemblies of Nanoparticles and Nanocolloids	225
8.4.1	Self-standing LBL Films	227
8.4.2	Magnetic Properties of the Stratified LBL Assemblies of Nanoparticles	229
8.4.3	Nanorainbows: Graded Semiconductor Films from Nanoparticles	231
8.5	Conclusion	235
8.6	References	236
<b>9</b>	<b>Layer-by-Layer Self-assembled Polyelectrolytes and Nanoplatelets</b>	<b>245</b>
	<i>J. H. Fendler</i>	
9.1	Introduction	245
9.2	Self-assembled Polyelectrolytes and Clay Nanoplatelets	246
9.3	Self-assembled Polyelectrolytes and Graphite Oxide Nanoplatelets	250
9.4	Potential Applications	256
9.4.1	Pollutant Photodestruction	256
9.4.2	Electronic Applications	259
9.4.3	Charge Storage	263
9.5	References	268
<b>10</b>	<b>Chemistry Directed Deposition via Electrostatic and Secondary Interactions: A Nonlithographic Approach to Patterned Polyelectrolyte Multilayer Systems</b>	<b>271</b>
	<i>P. T. Hammond</i>	
10.1	Introduction and Overview	272
10.2	Selective Deposition of Polyelectrolyte Multilayer Systems	273
10.2.1	Selective Deposition of Strong Polyelectrolytes	273
10.2.1.1	Basis of Selective Adsorption and Ionic Strength Effects	273
10.2.1.2	Formation of Complex Multilayer Structures	276
10.2.2	Understanding and Utilizing Secondary Interactions in Selective Deposition	277

10.2.2.1	Establishing the Rules for Weak Polyamine Deposition	277
10.2.2.2	Confirming the Rules of Selective Adsorption: SFM Investigations	279
10.2.2.3	Using the Rules: Side-by-Side Structures	280
10.2.2.4	The Next Steps: Surface Sorting of Multilayers and Other Elements	281
10.3	Polymer-on-Polymer Stamping	282
10.3.1	Fundamental Studies of Polymer-on-Polymer Stamping	284
10.3.1.1	Stamping of Ionic Polymers	285
10.3.1.2	Stamping of Block Copolymers	285
10.3.2	POPS as a Template for Other Materials Deposition	287
10.4	Directed Assembly of Colloidal Particles	289
10.4.1	Selective Deposition and Controlled Cluster Size on Multilayer Templates	290
10.4.2	Surface Sorting with Particles on Multilayer Surfaces	292
10.4.3	Selective Electroless Plating of Colloidal Particle Arrays	293
10.5	Functional Polymer Thin Films for Electrochemical Device and Systems Applications	294
10.5.1	Electrochromic Polyelectrolyte Multilayer Device Constructon	295
10.5.2	Ionically Conducting Multilayers for Electrochemical Device Applications	296
10.6	Summary	297
10.7	References	298

## 11 Layered Nanoarchitectures Based on Electro- and Photo-active Building Blocks 301

*X. Zhang, J. Sun, and J. Shen*

11.1	Introduction	301
11.2	Multilayer Assemblies of Electroactive Species of Chemically Modified Electrodes	304
11.2.1	Controlled Fabrication of Multilayers with a Single Active Component	305
11.2.2	Controlled “Cascade” Modification with Binary Active Components	309
11.2.2.1	Bienzyme Assemblies of Glucose Oxidase and Glucoamylase	310
11.2.2.2	Alternating Assemblies of Glucose Oxidase and Polycationic Electron Transfer	313
11.2.3	The Incorporation of Conductive Species to Improve the Performance of the Modified Electrodes	314
11.3	Ionic Self-assembly of Photoactive Materials and the Fabrication of “Robust” Multilayer	318
11.3.1	Ways to Fabricate Covalently Attached Multilayer Assemblies	319
11.3.2	Stable Entrapment of Oligo-charged Molecules Bearing Sulfonate Groups in Multilayer Assemblies	323
11.3.3	Covalently Attached Multilayer Assemblies of Polycationic Diazo-resins and Polymeric Poly(Acrylic Acid)	324

11.3.4	Robust Nanoassemblies with Complex and Hybrid Structures	326
11.4	Summary and Outlook	328
11.5	References	328
<b>12</b>	<b>Coated Colloids: Preparation, Characterization, Assembly and Utilization</b>	<b>331</b>
	<i>F. Caruso and G. Sukhorukov</i>	
12.1	Introduction	331
12.2	Preparation and Characterization of Coated Colloids	333
12.2.1	Layer-by-Layer Adsorption	334
12.2.1.1	Multilayered Coatings	337
12.2.1.2	Coating of Specific Cores	344
12.2.2	Colloid Precipitation	349
12.3	Assembly and Utilization of Coated Colloids	351
12.3.1	Mesoscopic Arrangement	351
12.3.1.1	Colloidal Crystals	351
12.3.1.2	Macro- and Mesoporous Materials	351
12.3.2	Enzymatic Catalysis	354
12.3.2.1	Dispersions	354
12.3.2.2	Thin Films	355
12.3.3	Optical Properties	356
12.3.4	Further Applications	357
12.4	Summary and Outlook	358
12.5	References	359
<b>13</b>	<b>Smart Capsules</b>	<b>363</b>
	<i>H. Möhwald, E. Donath, and G. Sukhorukov</i>	
13.1	Preparation and Structure	364
13.1.1	General Aspects	364
13.1.1.1	Core Materials	364
13.1.1.2	Wall Materials	365
13.1.1.3	Molecular Dynamics	368
13.1.2	Physics and Chemistry of Core Removal	369
13.1.2.1	Core Destruction	369
13.1.2.2	Core Material Release	372
13.1.2	Modification of Walls	375
13.2	Properties and Utilization	376
13.2.1	Permeability Control	376
13.2.1.1	Permeation Mechanisms	377
13.2.1.2	Controlled Release Profiles	378
13.2.1.3	Switchable Release	379
13.2.2	Stability and Mechanical Properties	380
13.2.2.1	Temperature Dependent Structures	381
13.2.2.2	Capsule Elasticity	382
13.2.2.3	Plasticity, Viscosity and Rupture Strength	385
13.2.3	Chemistry and Physics in Nanovolumes	385

13.2.3.1	Chemical Gradients from Inside to Outside	386
13.2.3.2	Precipitation and Dissolution	387
13.1.3.3	Chemistry in Capsules	389
13.3	Summary and Outlook	390
13.4	References	391
<b>14</b>	<b>Multilayers on Solid Planar Substrates: From Structure to Function</b>	<b>393</b>
	<i>D. G. Kurth, D. Volkmer, and R. v. Klitzing</i>	
14.1	Introduction	393
14.2	Formation and Structure of LbL Multilayers	395
14.2.1	Adsorption Kinetics of Polyelectrolytes	395
14.2.2	LbL Multilayer Formation	397
14.2.3	$\zeta$ -potential	398
14.2.4	Effect of Polymer Charge	398
14.2.5	Influence of Ionic Strength	400
14.2.6	Permeability of Polyelectrolyte Multilayer	401
14.2.7	Internal Structure	403
14.3	Implementing Metallsupramolecular Devices in Thin Layered Films	405
14.3.1	Introduction	405
14.3.2	Metallosupramolecular Coordination Polyelectrolytes	408
14.3.3	Polyoxometalate Clusters	415
14.4	Conclusions	421
14.5	References	423
<b>15</b>	<b>Functional Layer-by-Layer Assemblies with Photo- and Electrochemical Response and Selective Transport of Small Molecules and Ions</b>	<b>427</b>
	<i>B. Tieke, M. Pyrasch, and A. Toutianoush</i>	
15.1	Introduction	427
15.2	Photoreactive Assemblies	428
15.2.1	Diacetylene Derivatives	429
15.2.2	Azobenzene Derivatives	434
15.3	Diphenyldiketopyrrolopyrrole Derivatives	438
15.4	Electroactive Assemblies	441
15.4.1	Poly(metal tetrathiooxalates)	441
15.4.2	Prussian Blue and Analogues	442
15.5	Transport of Small Molecules and Ions Across Polyelectrolyte Multilayers	446
15.5.1	Transport of Small Molecules	446
15.5.1.1	Gas Permeation	446
15.5.1.2	Pervaporation Separation of Alcohol/Water Mixtures	447
15.5.2	Transport of Ions	451
15.5.2.1	Uptake of Ions	454
15.6	Summary and Conclusions	456
15.7	References	458



<b>16</b>	<b>Self-assembly and Characterization of Electro-optic Materials</b>	<b>461</b>
	<i>R. Claus, Y.-X. Wang, L. Zhang, and K. Cooper</i>	
16.1	Nonlinear Optical Polymers	462
16.1.1	Design, Synthesis and Characterization of Polydyes	462
16.1.2	ESA Fabrication of NLO Thin Films and Their Characterization	464
16.1.3	Nonlinear Optical Measurements	467
16.2	Electrostatic Self-assembly of CLD-1 Thin Films	471
16.2.1	Modification of CLD-1 and Fabrication of CLD-1 Thin Films	471
16.2.2	Measurements of Electro-optic Properties	472
16.3	Electrostatic Self-assembly of CdSe/PDDA Thin Films	474
16.3.1	Fabrication and Characterization	475
16.3.2	Electro-optic Modulation Measurements	477
16.3.2.1	Linear Electro-optic Modulation Measurement	477
16.3.2.2	Quadratic Electro-optic Modulation	481
16.4	Summary	484
16.5	References	485
<b>17</b>	<b>Controlling the Ion-Permeability of Layered Polyelectrolyte Films and Membranes</b>	<b>487</b>
	<i>M. Bruening</i>	
17.1	Introduction	487
17.2	Electrochemical Studies of the Permeability of MPFs	488
17.2.1	As-deposited MPFs	488
17.2.2	Cross-linked PAA/PAH Films	490
17.2.3	Derivatized Polyelectrolyte Films	493
17.3	MPFs as Ion-Separation Membranes	495
17.3.1	Membrane Formation	495
17.3.2	Permeability of PAH/PSS and PAH/PAA Membranes	496
17.3.3	Cross-linked PAA/PAH Membranes	499
17.3.4	Hybrid PSS/PAH + PAA/PAH Membranes	500
17.3.5	Controlling the Charge Density in MPMs	503
17.3.5.1	Use of Cu <sup>2+</sup> Complexes to Imprint Charged Sites into PAA/PAH Films	503
17.3.5.2	Control of Intrinsically Compensated Charge Through Derivatization and Photocleavage	504
17.3.6	Highly Selective Ultrathin Polyimide Membranes Formed from Layered Polyelectrolytes	505
17.3.7	Modeling of Selective Transport Through Layered Polyelectrolyte Membranes	506
17.4	Conclusions	508
17.5	References	509
	<b>Index</b>	<b>511</b>

## Preface

When a new field is growing exponentially, as judged by the number of publications, presentations and patents, when is the “right” time to assemble a volume of contributed chapters from some of the acknowledged leaders in the field? What if every potential contributor is incredibly busy, following up an ever-expanding plethora of ideas and experiments? It was in this harried atmosphere that our colleagues carved out the time to write their contributions. We are extremely grateful to them for gathering their thoughts and accomplishments into chapters.

The idea for this book came together following a very successful symposium at the ACS in San Francisco 2000, which we organized. No volume on the topic had yet been published, but there was already a large store of knowledge that had been created as groups had responded enthusiastically to the promise of the first few papers appearing in the early 90’s. Multilayers had gathered a great deal of momentum, flourishing in the more “informal” space of papers, preprints, talks and word-of-mouth. By 2000, the field had simply outgrown informality.

We had been riding the wave of this activity, enjoying a growing number of colleagues. We were fully aware of the infectious nature of multilayers research, which is like a good mystery novel – hard to put down once you start. We are honored to have been in the thick of things during the early years. Every experiment was significant and the results suggested several more experiments. This dizzying atmosphere pervades even today: ask any multilayerer!

We are pleased to have edited this book. Our object was not only to document what is known about multilayers, but also to promote the potential of these versatile thin films and to facilitate the adoption of the technology by others. The field is new. We are proud of its ability to catalyze interdisciplinary thought and action. In this regard, multilayers represent a model platform for promoting modern research. Also, the intellectual distance between concept and application is minimal. Commercial applications have already been realized.

We hope the message of abundant research opportunities is made loud and clear. It is easy to get started. Easy to get “hooked.” This book is essential in showing you how. We look forward to more elegant and complex multilayered architectures and functionalities, as well as significant expansion at the biological/biomedical interface.

Finally, we would like to express our thanks to Jean-Marie Lehn for his support in writing the forward. His “big-picture” viewpoint is sincerely appreciated.

August 2002

Gero DECHER  
Joe SCHLENOFF

## List of Contributors

M. L. BRUENING

Department of Chemistry  
Michigan State University  
East Lansing, MI 48824  
bruening@cem.msu.edu  
USA

F. CARUSO,

Max Planck Institute of Colloids and  
Interfaces  
D-14424 Potsdam  
caruso@servg.mpikg-golm.mpg.de  
Germany

M. CASTELNOVO

Institut Charles Sadron  
6, rue Boussingault  
F-67083 Strasbourg Cedex  
France

R. O. CLAUS,

Fiber & Electro-Optics Research Center  
Virginia Tech  
106 Plantation Road  
Blacksburg, VA 24061-0356  
roclaus@vatech.edu  
USA

K. L. COOPER

NanoSonic Inc.  
1485 South Main Street  
Blacksburg, VA 24060  
USA

G. DECHER

Institut Charles Sadron  
6, rue Boussingault  
F-67083 Strasbourg Cedex  
decher@cerbere.u-strasbg.fr  
France

E. DONATH,

Max Planck Institute of Colloids  
and Interfaces  
D-14424 Potsdam  
edwin.donath@mpikg-golm.mpg.de  
Germany

J. H. FENDLER

Center for Advanced Materials  
Processing  
Clarkson University  
Potsdam, NY 13699-5814  
fendler@clarkson.edu  
USA

K. GLINEL,

Unite de Physique et de Chimie des  
hauts polymères (POLY)  
Université Catholique de Louvain  
Place Croix du Sud, 1  
B-1348 Louvain-la-Neuve  
glinel@poly.ucl.ac.be  
Belgium

P. T. HAMMOND  
 Department of Chemical Engineering  
 Massachusetts Institute of Technology  
 Cambridge, MA 02139  
 hammond@mit.edu  
 USA

I. ICHINOSE,  
 Topochemical Design Laboratory  
 Frontier Research System  
 Institute of Physical  
 and Chemical Research (RIKEN)  
 2-1 Hirosawa, Wako  
 Saitama  
 351-0198 Japan  
 izumi@postman.riken.go.jp

J. F. JOANNY  
 Physicochimie Curie  
 Institut Curie Section Recherche  
 26, Rue d'Ulm  
 F-75248 Paris Cedex 05  
 joanny@ics.u-strasbg.fr  
 France

A. JONAS  
 Unite de Physique et de Chimie  
 des hauts polymères (POLY)  
 Université Catholique de Louvain  
 Place Croix du Sud, 1  
 B-1348 Louvain-la-Neuve  
 jonas@poly.ucl.ac.be  
 Belgium

V. KABANOV  
 Chemistry Department  
 Moscow State University  
 119899 Moscow  
 kabanov@libro.genebee.msu.su  
 Russia

R. KLITZING  
 Iwan-N.-Stranski-Institut (Sekt. ER 1)  
 TU Berlin  
 Straße des 17. Juni 112  
 D-10623 Berlin  
 klitzing@chem.zu-berlin.de  
 Germany

N. A. KOTOV  
 Department of Chemistry  
 Oklahoma State University  
 Stillwater, OK 74078  
 kotov@okstate.edu  
 USA

T. KUNITAKE  
 Topochemical Design Laboratory  
 Frontier Research System  
 Institute of Physical  
 and Chemical Research (RIKEN)  
 2-1 Hirosawa, Wako  
 Saitama  
 351-0198 Japan  
 kunitake@ruby.ocn.ne.jp

K. KUROIWA  
 Department of Chemistry  
 and Biochemistry  
 Graduate School of Engineering  
 Kyushu University  
 Japan

D. KURTH,  
 Max Planck Institute of Colloids and  
 Interfaces  
 D-14424 Potsdam  
 kurth@mpikg-golm.mpg.de  
 Germany

A. LASCHEWSKY,  
 Fraunhofer Institute  
 Geiselbergstraße 69  
 14476 Golm  
 andre.laschewsky@iap.fraunhofer.de  
 Germany

Y. Lvov  
 Institute for Micromanufacturing and  
 Chemistry Department  
 Louisiana Tech University  
 P.O. Box 10137  
 Ruston, LA 71272  
 ylvov@coes.latech.edu  
 USA

H. MÖHWALD,  
Max Planck Institute of Colloids and  
Interfaces  
D-14424 Potsdam  
moehwald@mpikg-golm.mpg.de  
Germany

H. RIEGLER,  
Max Planck Institute of Colloids and  
Interfaces  
D-14424 Potsdam  
hans.riegler@mpikg-golm.mpg.de  
Germany

M. F. RUBNER  
Department of Materials Science and  
Engineering  
Massachusetts Institute of Technology  
Cambridge, MA 02139  
rubner@mit.edu  
USA

J. SCHLENOFF  
Chemistry Department  
Florida State University  
Tallahassee, FL 32306-4390  
schlen@chem.fsu.edu  
USA

J. SHEN,  
Key Laboratory for Supramolecular  
Structure and Spectroscopy,  
Department of Chemistry,  
Jilin University  
Changchun  
130023 People's Republic of China  
sjc@mail.jlu.edu.cn

G. SUKHORUKOV  
Max Planck Institute of Colloids and  
Interfaces  
D-14424 Potsdam  
Germany

B. TIEKE  
Institut für Physikalische Chemie  
Universität zu Köln  
Luxemburger Straße 116  
D-50939 Köln  
tieke@uni-koeln.de  
Germany

P. Y. VUILLAUME  
Unite de Chimie des materiaux  
(CMAT)  
Université Catholique de Louvain  
Place Louis Pasteur 1  
B-1348 Louvain-la-Neuve  
vuillaume@chim.ucl.ac.be  
Belgium

Y.-X. WANG,  
Fiber & Electro-Optics Research Center  
Virginia Tech  
106 Plantation Road  
Blacksburg, VA 24061-0356  
USA

L. ZHANG,  
Fiber & Electro-Optics Research Center  
Virginia Tech  
106 Plantation Road  
Blacksburg, VA 24061-0356  
USA

X. ZHANG  
Key Laboratory for Supramolecular  
Structure and Spectroscopy,  
Department of Chemistry,  
Jilin University  
Changchun  
130023 People's Republic of China  
xi@mail.jlu.edu.cn

# 1

## **Polyelectrolyte Multilayers, an Overview**

G. DECHER

### 1.1

#### **Why is the Nanoscale so Interesting?**

In our research team, we strongly believe that the functionality of any object (on any length scale) arises from the intricate interplay of its constituents. In complex systems, new properties appear that are not observed for each individual component. While it is trivial that electrons and nuclei form atoms (sub-ångstrom scale), that atoms form molecules (ångstrom scale) or that monomers can be transformed into polymers (early nanometer scale), we are just beginning to explore the potential of supramolecular assemblies or of large multifunctional objects (e.g. copolymers of complex architecture). While nature plays with the full range of objects on the length scale from femtometers to parsecs, mankind is somewhat limited to the length scale between subatomic particles and the size of our planet. Although the range accessible to man is already reduced, we hardly master more than a fraction of what is available to us. A particularly interesting length scale is, of course, the nanoscopic organization of matter. Taking life as the most fascinating and complex property of matter, nature clearly shows that the minimum size of a lifeform (in the definition of life as we know it) is of nanoscopic to microscopic dimension. It is exactly this length scale that is just being touched but not mastered by either bottom up (chemical synthesis) or top down (miniaturization) approaches. Fig. 1.1 summarizes our philosophy and motivation for working on the synthesis, properties and fabrication of complex nanoorganized and nanocomposite materials.

### 1.2

#### **From Self-Assembly to Directed Assembly**

Suppose you do not like the way materials end up being arranged after carrying out a self-assembly experiment and obtaining equilibrium. The obvious pathway for improvements seems to be to re-engineer the chemical structure of the molecules involved and to hope to obtain a more suitable structure with the new molecules. This is often time-consuming as several optimization cycles are frequently required.

## LENGTH SCALES OF COMPLEXITY IN MATTER

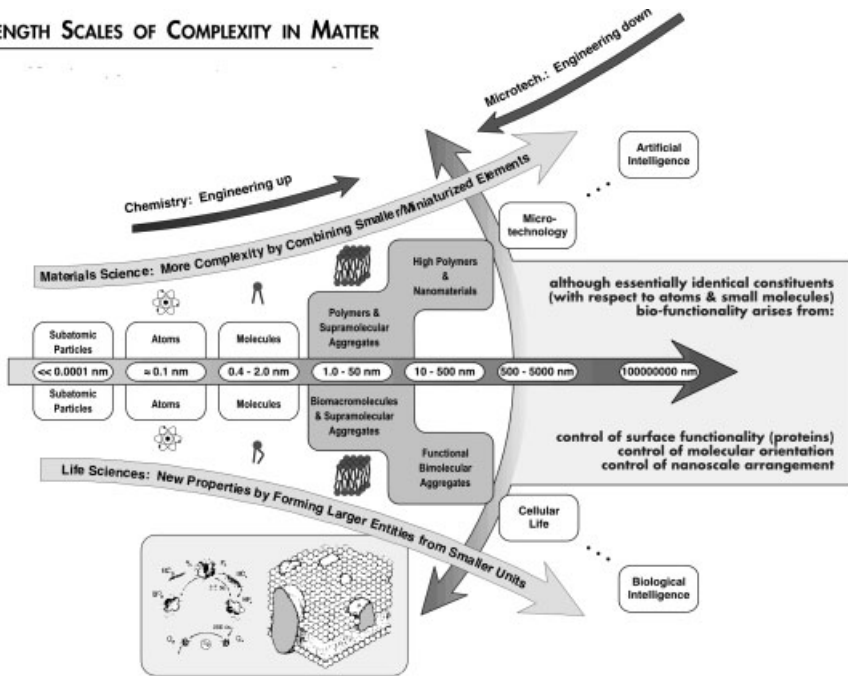


Fig. 1.1 Complexity as a function of length scale. Materials Science is not yet as far advanced as the evolutionary developments present everywhere in nature. The photosystem

is just one example of the precise spatial assembly of a functional molecular machine. The drawing is adapted from [1].

Another possible route to a desired target structure is to use an assembly procedure that prevents equilibrium by trapping every compound kinetically in a predetermined spatial arrangement. At present there are only very few approaches in this direction. Most of the work has been carried out for the simplest case, in which different materials are put in one-dimensional order in a multilayer film. For about 65 years the molecularly controlled fabrication of nanostructured films has been dominated by the conceptually elegant Langmuir-Blodgett (LB) technique, in which monolayers are formed on a water surface and subsequently transferred onto a solid support [2, 3]. The pioneering work on synthetic nanoscale multicomposites of organic molecules was carried out by Kuhn and colleagues in the late 1960s using the LB technique [4]. His experiments with donor and acceptor dyes in different layers of LB films provided direct proof of distance-dependent Förster energy transfer on the nanoscale. These were also the first true nanomanipulations as they allowed for mechanical handling of individual molecular layers such as separation and contact formation with ångström precision [5]. Unfortunately the LB technique is rather limited with respect to the set of molecular components suitable for LB deposition, and molecules are often not firmly trapped and frequently rearrange after or even during deposition.



### 1.3

#### The Layer-by-Layer Deposition Technique

The so-called layer-by-layer (LbL) deposition technique [6–14] (Fig. 1.2) also falls into the category of template assisted assembly. Template assisted assembly is much faster than self-assembly/chemical modification cycles whose outcome is often uncertain or difficult to predict. For the case of LbL-deposition, it can be tailored to even allow multimaterial assembly of several compounds without special chemical modifications [15–19], thus giving access to multilayer films whose complex functionality can fall into the two following categories:

1. Tailoring of surface interactions: Every object interacts with its environment via its surface. Thus all properties depending on this interaction are dictated by surface functionality which can be tailored for many needs (e.g. corrosion protection [20], antireflective coatings [21], antistatic coatings, stickiness or non-stickiness [22], surface induced nucleation [23–26], antifouling [27–29], hydrophilicity or hydrophobicity, biocompatibility [30, 31], antibacterial properties, molecular recognition, chemical sensing or biosensing [32–46], microchannel flow control [47, 48]...).

2. Fabrication of surface based devices: The sequence of deposition of different materials defines the multilayer architecture and thus the device properties. One may call this knowledge based (or programmed, or directed, or controlled, or template assisted) assembly, in contrast to self-assembly. It leads to property engineering by controlling the mostly one-dimensional spatial arrangement of functionality in multimaterial layered nanocomposites (membrane reactors [49–51], photonic devices such as light emitting diodes [52–75] or complex waveguides, compartmentalized films with barrier layers or separation membranes [34, 44, 75–83],...).

The fabrication of multicomposite films by the LbL procedure means literally the nanoscopic assembly of hundreds of different materials in a single device using environmentally friendly, ultra-low-cost techniques. The materials can be small organic molecules or inorganic compounds [7, 61, 84–99], macromolecules [12, 39, 53, 55, 76, 86, 100–116, 117–125], biomacromolecules such as proteins or DNA [15–18, 30, 32, 49, 50, 126–151] or even colloids (metallic or oxidic colloids or latex particles) [18, 21, 75, 79, 98, 108, 121, 142, 152–198]. The technique can be applied to solvent accessible surfaces of almost any kind and any shape, the more exotic ones being microcapsules, colloids or biological cells [104, 122, 199–206].

Note that the list of references above is intended to give some introductory information on some recent developments of layer-by-layer assembly. Since many groups have provided reviews of their excellent work for this book, a complete reference list to all of their work is not needed in this overview chapter. A more detailed history of LbL deposition, the principle of which was apparently first described by Iler [207], is found in a recent review [208]. In the last eight years the field has been reviewed on several occasions outlining the concepts behind and the potential of the LbL technology [208–215]. The approach has spread from our laboratory to the international community and kindled research of physicists, che-

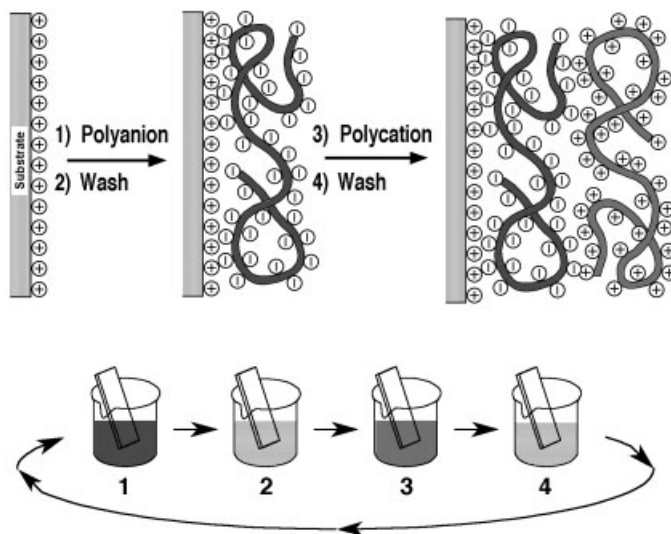


**Fig. 1.2** Top: Simplified molecular concept of the first two adsorption steps depicting film deposition starting with a positively charged substrate. The polyanion conformation and layer interpenetration are an idealization of the surface charge reversal with each adsorption step which is the basis of the electrostatically driven multilayer buildup depicted here. Counterions are omitted for clarity. Bottom: Schematic of the film deposition process

using glass slides and beakers. Steps 1 and 3 represent the adsorption of a polyanion and polycation respectively, and steps 2 and 4 are washing steps. The four steps are the basic buildup sequence for the simplest film architecture  $(A/B)_n$  where  $n$  is the number of deposition cycles. The construction of more complex film architectures requires additional beakers and an extended deposition sequence.

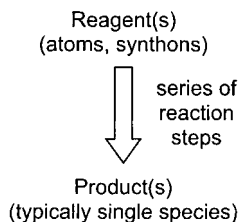
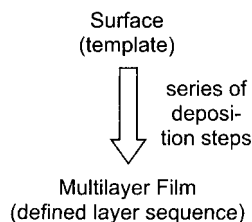
mists and of scientists in the biomedical field, because it is extremely powerful yet simple to use and because it challenges theory at the level of polyelectrolyte adsorption.

### 1.3.1

#### LbL Deposition is the Synthesis of Polydisperse Supramolecular Objects

For most cases an LbL film has a unique layer sequence that depends strictly on the deposition sequence. This points to the fact that LbL deposition should be considered as an analogue to a chemical reaction sequence (Fig. 1.3). While a chemical reaction takes place between different synthons and typically yields a unique molecule after each synthetic step, layer-by-layer deposition involves the adsorption of a single species in each adsorption step and yields a multilayer film with a defined layer sequence. While molecules are synthesized in several consecutive reaction steps, a multicomposite film is fabricated in several adsorption steps.

The reagents in classic synthesis are typically molecules, in layer-by-layer deposition they can be chosen from a wide range of materials. This is represented schematically in Fig. 1.4. While today most of the multilayer films have been fabri-

**Classic Synthesis****LbL - Deposition**

**Fig. 1.3** Analogy of chemical multistep synthesis and multilayer deposition, both leading to a unique molecular and supramolecular species (multilayer film).

cated using mainly electrostatic attraction as the driving force for multilayer build-up, this is by no means a prerequisite. There are many other interactions that have been used successfully for multilayer deposition including: donor/acceptor interactions [216-218], hydrogen bonding [173, 219-224], adsorption/drying cycles [225, 226], covalent bonds [11, 14, 45, 227-238], stereocomplex formation [239-241] or specific recognition [6, 17, 126, 128, 132, 139, 242-246].

In general one needs just any interaction (this may be one or several different interactions) between two species “reagents” in order to incorporate them into a multilayer film. The interaction can easily be tested in solution prior to carrying out the deposition if both film constituents are soluble in the same solvent. When

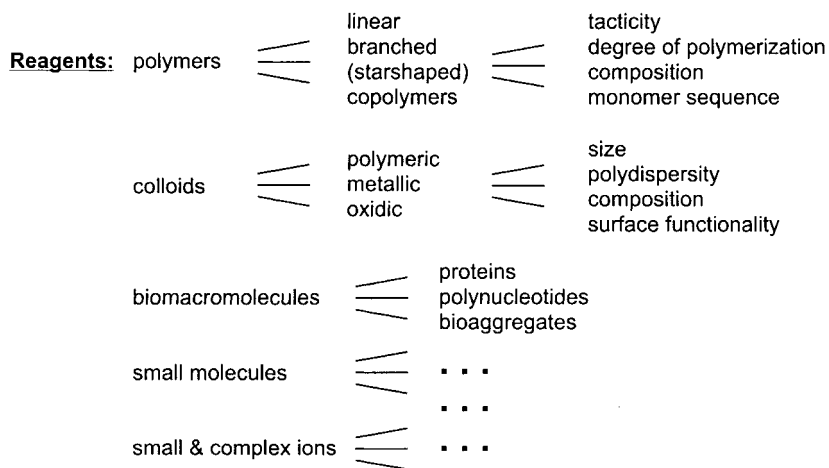


**Fig. 1.4** Reagents for layer-by-layer deposition. Some details on composition and structural properties are shown for polymers and colloids. To keep the schematic simple, this level of detail is not carried through for the last three types of reagents. One should also note that small molecules and complex ions are sometimes more difficult to incorporate into multilayer films in a regular way than, for example, charged macromolecules.

<b>Advantages:</b>	deposition on surfaces of almost any kind and any shape
	broad processing window
many control parameters:	concentration
	adsorption time
	ionic strength
	solvent composition
	temperature
	...

**Fig. 1.5** Summary of some of the advantages of layer-by-layer deposition. While the structure and properties of each layer depend on certain control parameters as mentioned above, the deposition is highly reproducible if these parameters are maintained strictly constant.

both solutions are mixed and flocculation occurs it is a good sign that multilayer fabrication will be possible. This is only a very crude test: multilayer formation may also be possible in the absence of flocculation.

Given the large set of materials which are easily incorporated into multilayer films, layer-by-layer deposition is a rather general approach for the fabrication of complex surface coatings. It combines several advantages as shown in Fig. 1.5. It is possible to coat almost any solvent-accessible surface starting with sub-micron objects [104, 122, 199–202, 204–206] up to the inside of tubings or even objects with a surface of several square meters. Like a chemical reaction, the precise structure of each layer depends on a set of control parameters such as concentration, adsorption times, ionic strength (e.g. [9]), pH (e.g. [247]), or temperature (e.g. [248]), but in general the processing window is rather broad.

### 1.3.2

#### Reproducibility and Deposition Conditions

The question of reproducibility arises immediately when we draw the analogy between a chemical reaction and layer-by-layer adsorption. At first sight one may say that molecules are unique species and multilayer films are “only” ill-defined supramolecular objects. This is essentially the same argument that has downgraded macromolecular chemistry for years in comparison to organic chemistry. Today it is generally accepted that “ill-defined” macromolecules are also unique species that can indeed be well described by distributions and average properties like polydispersity or degree of polymerisation. The situation is similar for multilayer films as they are characterised by a sequence of layers in which each layer has its individual structure and properties. While the sequence of layers is as strict as the arrangement of atoms in a molecule, the properties of each layer can only be described as an average over a certain area. The most obvious property of an individual layer is its thickness, which is dependent on the nature of the underlying surface and on the deposition conditions. Parameters presumed to be important with respect to the underlying surface are, for example, the nature and density of charged groups, their local mobility (in the case of a polymeric surface) and the

surface roughness. The most important reaction parameters or deposition conditions are mentioned in Fig. 1.5. However, the list is somewhat longer including: solvent, concentration of adsorbing species, adsorption time, temperature, nature and concentration of added salt, rinsing time, humidity of the surrounding air, drying, agitation during adsorption or rinsing, dipping speed and so forth. While the LbL technique generally works very well due to the fact that the processing window is rather large, it is highly recommended to keep the deposition conditions as constant as possible in order to get highly reproducible results. If this is done rigorously, one obtains films composed of tens of layers whose thickness for example, differs by about one percent. When comparing data, one should not overlook that it is not sufficient only to maintain the deposition conditions exactly, but also the conditions under which the measurements were taken. Fig. 1.6 shows an example of how the film thickness of a (PSS/PAH)<sub>8</sub> multilayer film, for which both polyions were deposited from solutions containing 2 M sodium chloride, depends on the temperature and on the relative humidity at the time of the measurement.

Often it is said that polyelectrolyte multilayer films are independent of the underlying substrate. This is an oversimplified statement, of course there is a dependence on the underlying surface as stated above. However, since polyanion and polycation adsorption is repeated consecutively, each polyanion adsorbs onto a polycation-covered surface and vice versa. This means that, after a few layers, the structure and properties of each layer are governed by the choice of polyanion/polycation pair and by the deposition conditions and that the influence of the substrate is typically lost after a few deposition cycles. The issue of the substrate is examined again when discussing soft and rigid materials later.

### 1.3.3

#### Monitoring Multilayer Buildup

##### 1.3.3.1 Ex-situ Characterisation

The easiest way to follow multilayer buildup is probably by UV/Vis spectroscopy, which works for all colored materials. Fig. 1.7 is an example for poly(styrene sulfonate)/poly(allyl amine) (PSS/PAH) films which constitute probably the best characterised system at present.

Equivalent to measuring the optical absorbance, one can also determine the film thickness by ellipsometry or X-ray reflectometry as shown in Fig. 1.8. The reflectivity traces on the left were taken on a dry specimen at various stages of multilayer buildup. Each trace corresponds to a single data point in the diagram on the right. In this case PSS was deposited from aqueous solutions containing different amounts of salt, while PAH was deposited from pure water. One clearly sees that the film thickness is slightly, but very precisely, increased with increasing salt concentrations [9]. This effect would be much stronger if both polyions were deposited from solutions containing salt. The fact that only interference fringes resulting from the total film thickness are observed in such samples will be discussed in the section on the structure of multilayer films. The salt concen-

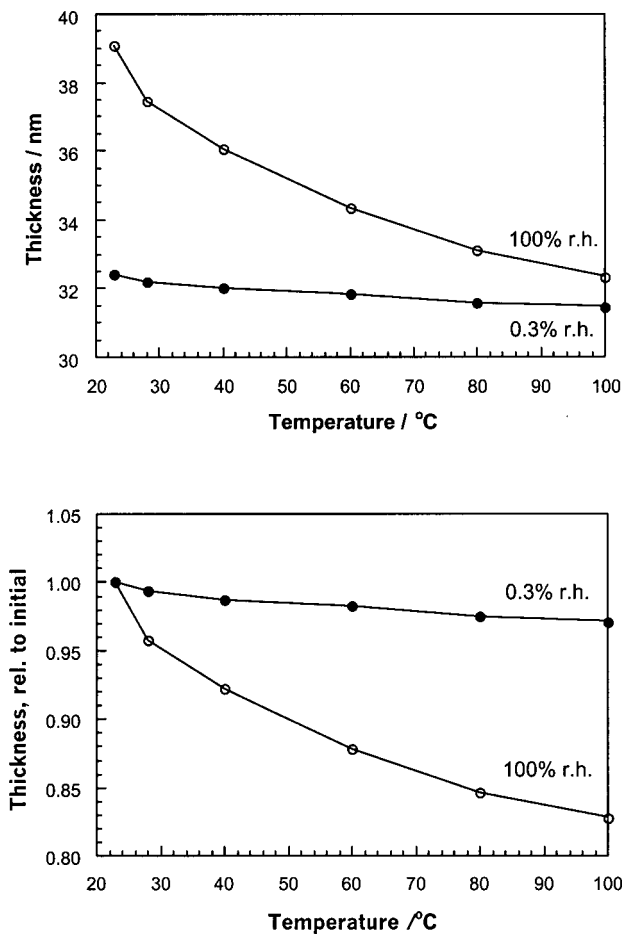


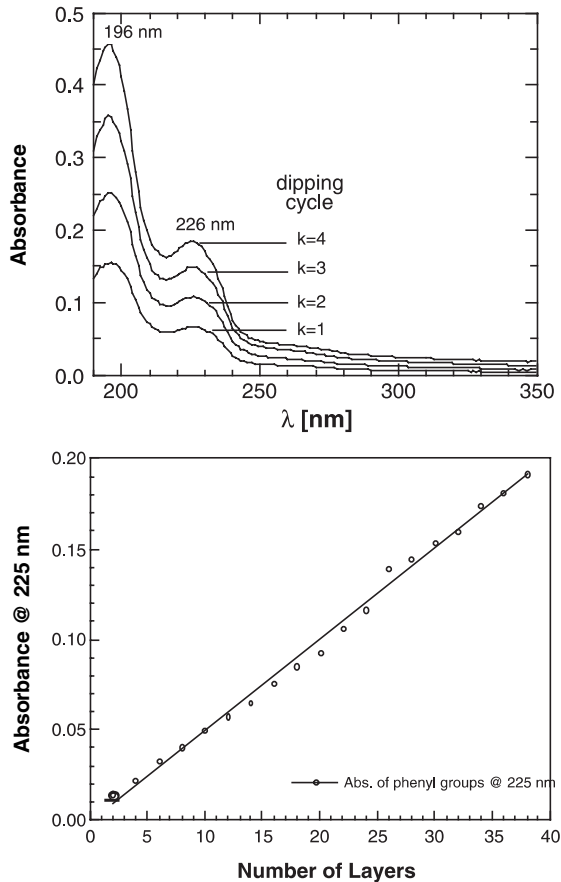
**Fig. 1.6** Top: Film thickness of the same multilayer specimen as a function of temperature and of relative humidity (r.h.). The differences in thickness at identical temperatures are entirely due to a difference in water content within the film and not due to a negative thermal expansion coefficient. This difference becomes less pronounced at elevated temperature, when the water is driven out of the

film. Bottom: The same data as above, but normalised with respect to the initial film thickness. It becomes obvious that even small differences in temperature or humidity can easily account for changes in film thickness of the order of 5–10% depending on the swellability of the film. (G. Sukhorukov, J. Schmitt and G. Decher, unpublished results.)

tration is not the only parameter that allows one to control the thickness of individual layers. Rubner has shown that, for the case of weak polyelectrolytes, layer thickness can be precisely controlled by pH [247].

While the two methods above are simple but sufficient to get some preliminary ideas on the deposition behaviour, there are numerous additional characterization methods described in the other chapters of this book. Very recently, nuclear mag-

**Fig. 1.7** Upper: UV/Vis spectra taken after different adsorption cycles ( $k$ ) during the preparation of a PSS/PAH multilayer. The bands at 195 nm and 226 nm originate from the aromatic chromophore of the styrene monomer unit of PSS. The absorbance increases regularly with the number of PSS layers. Lower: Plot of the absorbance of the PSS band at 225 nm versus the number of layers deposited. The numerical fit to the data (solid line) shows that the increase of absorbance per layer is constant. The absorbance per layer is less than in the case on the left because the salt concentration in the deposition solutions was different. The slight deviation from a straight increase after 26 layers is due to the interruption of the deposition overnight. A change in the deposition protocol such as standing overnight is quantitatively described in Fig. 1.17.



netic resonance (NMR) was added to the “toolbox” of multilayer research [249, 250], and this deserves special attention as it gives access to important new data.

### 1.3.3.2 In-situ Characterisation

The characterisation methods described above are straightforward and widely available, but they require one to interrupt the deposition process to take the measurement. Not only are the measurements an interruption, they also have to be taken in the dry, which may not be desirable in some cases. An obvious consequence of different deposition regimes is, for example, that the film thicknesses are different for identical numbers of layers. Of course it is to be expected, and it is observed, that films deposited from identical solutions with identical adsorption times for identical temperature show a different film thickness for the same number of layers depending on whether they have intermittently been dried and characterized or not. Depending on the dose of X-rays we have even observed an effect

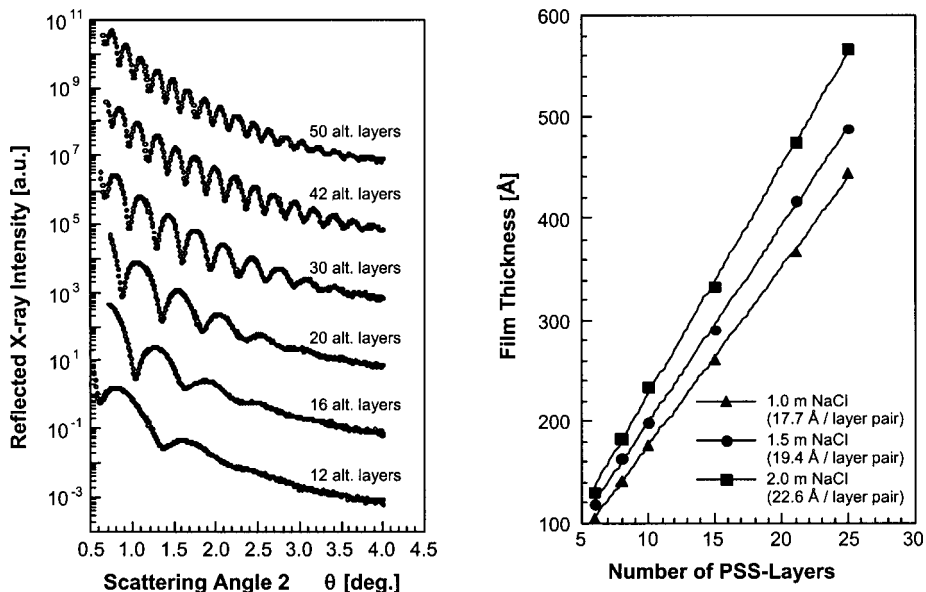


Fig. 1.8 X-ray reflectometry of multilayer films of the architecture  $(\text{PSS}/\text{PAH})_n$ ,  $n$  ranging from 6 to 25. Left: raw data obtained from a single specimen at different  $n$  in the dry

state. Right: plot of film thickness versus number of layers for three sets of curves as the one on the left.

of the irradiation on film growth (J. Schmitt and G. Decher, unpublished data). In-situ methods are thus necessary in order to compare results for samples that cannot be dried. Depending on their time resolution, such methods also allow one to follow the kinetics of adsorption and/or multilayer reorganisation. Besides measurements of the zeta potential and results obtained by quartz crystal microbalance (both of which are shown below), typical in-situ methods include surface plasmon spectroscopy [113, 251, 252], optical waveguide lightmode spectroscopy (OWLS) [149, 253, 254], optical reflectometry in stagnation point flow cells [109], scanning angle reflectometry (SAR) [23, 143, 255], ellipsometry [78, 256–258], in-situ atomic force microscopy (AFM) [254, 259], attenuated total reflection Fourier transform infrared spectroscopy (ATR-FTIR) [148, 260], surface forces measurements [261, 262], X-ray and neutron reflectometry [263–265] or second harmonic generation (SHG) [266], but the latter are not widely available. The quartz crystal microbalance is ideally suited for screening the adsorption kinetics for new components and for optimizing the adsorption conditions (see, for example, [43, 46, 120, 149, 267–269]). A prerequisite, however, is that the multilayer being deposited should be rather rigid in order to evaluate frequency displacements as adsorbed mass using the Sauerbrey equation. If the multilayer has to be treated as a viscous film, a more sophisticated QCM instrument and data evaluation are needed. The data in Fig. 1.9 on the consecutive deposition of poly(styrene sulfonate) and poly(allyl amine) were taken with a so-called QCM-D instrument, that



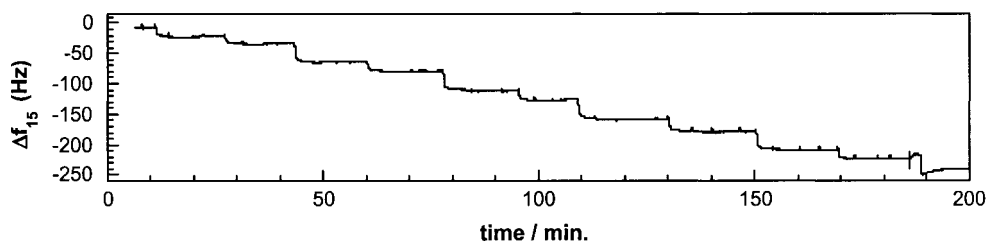
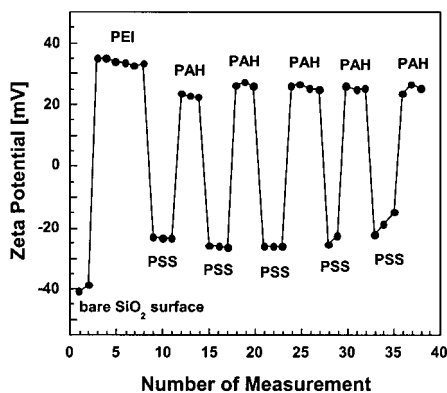


Fig. 1.9 Continuous QCM-trace of the third harmonic at 15 MHz (raw data) during the deposition of PSS (large displacements) and PAH (small displacements) during 11 adsorption steps.

also registers viscoelastic components of adsorbed films (data not shown). It is seen nicely that adsorption kinetics are rather fast (about one minute per layer), that the thickness of each monolayer is autolimited (plateau) and that there is no visible desorption after rinsing (plateau). In this plateau region the QCM cell was rinsed three times for each adsorption step, once with the solution containing the polyion and twice with the buffer in which the polyions were dissolved. The small frequency displacements at about 30, 60, 95, 130 and 170 min correspond to the adsorption of PAH, the large frequency shifts correspond to the adsorption of PSS. The diagram shows that the film buildup is very regular.

When we started layer-by-layer deposition around 1990, there was just the idea of layer buildup driven by electrostatics, the surface potential of polyelectrolyte covered surfaces was only discussed to some extent, mostly in colloid science. Since then, several Zeta potential measurements have been published (for example [109, 122, 270–274]). The diagram shown in Fig. 1.10 results from a measurement using a quartz capillary that was carried out in collaboration with the groups of Schaaf and Voegel [255]. It demonstrates nicely that the adsorption of each polyelectrolyte layer leads to an overcompensation of the previous surface charge, just as we had assumed earlier on and drawn schematically in illustrations such as Fig. 1.2.

Today the theoretical description of the charge overcompensation process has progressed considerably [275–279], Chapter 3 by Joanny is devoted to theoretical approaches concerning this problem. However, measurements such as shown in Fig. 1.8 are not proof that multilayer buildup is entirely driven by electrostatic attraction (incoming layer) and electrostatic repulsion (autolimitation to a single layer). Such measurements only show that there is a contribution of electrostatics in the case of multilayer buildup using positively and negatively charged components. Depending on the chemical nature of the polyions and/or colloids employed for deposition, the importance of the electrostatic contribution should vary and other interactions such as van der Waals, hydrogen bonding or charge transfer may more or less be involved as well.



**Fig. 1.10** Streaming potential measurement showing the surface charge reversal during multilayer buildup in situ. The first layer was poly(ethylene imine) (PEI) followed by 5 deposition cycles PSS and PAH [255].

### 1.3.4

#### Multilayers by Solution Dipping, Spraying or Spin Coating

In a variation of the deposition by adsorption from solution, the application of layers by spraying was introduced by Schlenoff [280] and the use of spin-coaters was demonstrated by Hong [281, 282] and also by Wang [283]. Both spraying and spin coating have the advantage that only small amounts of liquids are needed to coat large surface areas. Fig. 1.11 shows the comparison of these new methods with solution dipping.

As is also evident from Fig. 1.11, the deposition conditions play an important role with respect to the final film characteristics. Spraying and spin coating extend the parameter space of LbL deposition even further. However, it is to be expected that both methods will contribute to the general acceptance of the technology.

### 1.3.5

#### Post-preparation Treatment of Multilayer Films

##### 1.3.5.1 Annealing

As already seen in Fig. 1.6, there is a strong influence of environmental conditions on the film properties. A dedicated post-preparation treatment can in fact be used to modify the film properties in a controlled way. For the case of multilayer films composed of polyelectrolytes, one could expect to open and close salt bridges between positively and negatively charged ions located on the corresponding polyanion and polycation chains by immersing a multilayer sample in solutions containing salt and in pure water respectively. A similar influence of salt on polyion complexes in bulk is already known. In Fig. 1.12 we show the consecutive swelling of a multilayer film in salt solution and the deswelling in pure water over a total of three treatment cycles [284]. The film thicknesses after each treatment were obtained by X-ray reflectometry in the dry state. Fig. 1.12 also shows the influence of the salt concentration on the swelling effect. Interestingly, the ef-

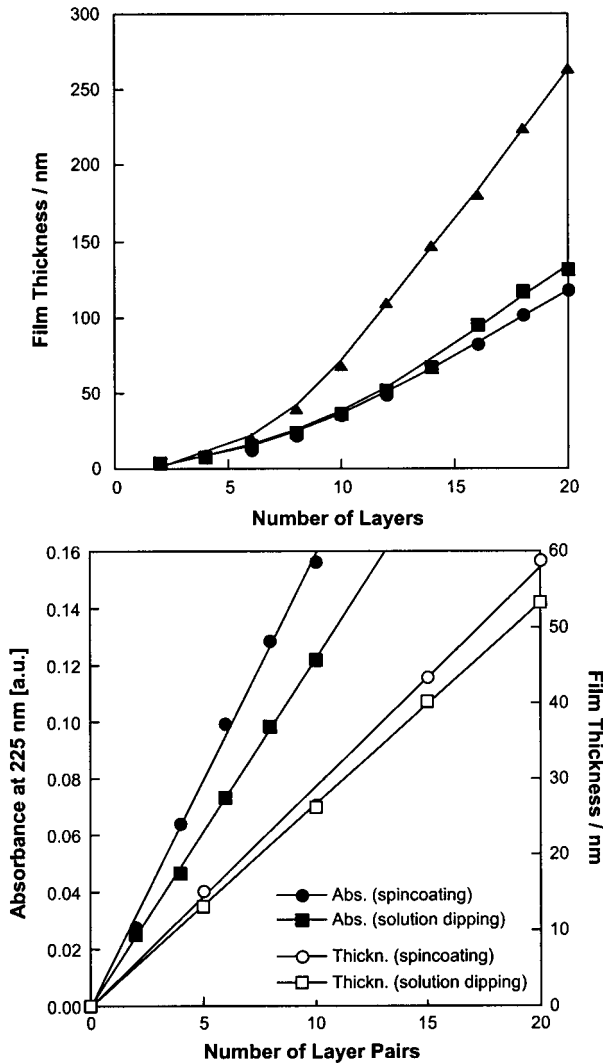
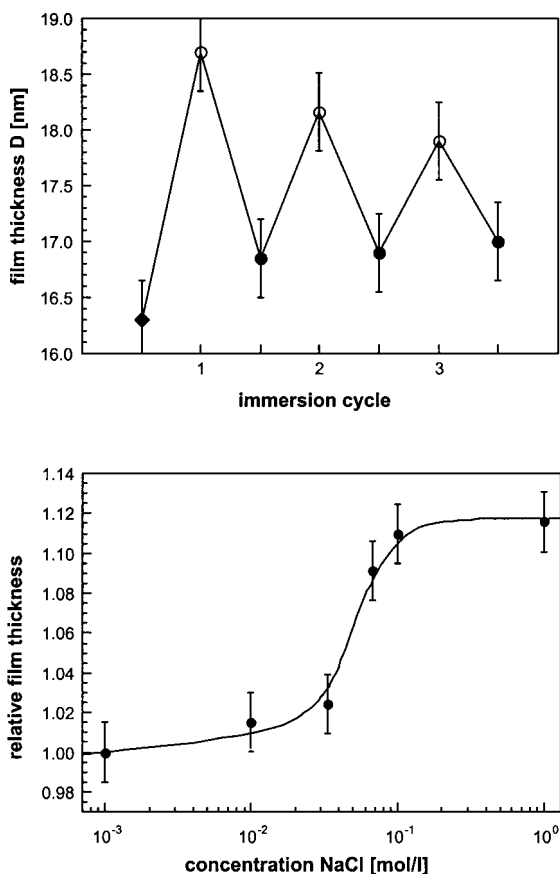


Fig. 1.11 Upper: Ellipsometric monitoring of the growth of a multilayer film composed of poly(diallyldimethylammonium chloride) and poly(styrene sulfonate), both deposited from 1.0 M NaCl. Circles represent data on a film prepared by solution dipping, squares are from spraying. In both cases the contact time was about 10 s. Triangles were also obtained by solution dipping, but with a contact time of 5 min. The solid lines are a guide to the eye. All data are taken from the original work

by Schlenoff [280]. Lower: Comparison of spin-coated and solution-dipped films with respect to optical absorbance and film thickness. The films are composed of poly(((4,4'-bis(6-dimethylammonio)hexyl)-oxy) azobenzene bromide) and *ι*-carrageenan, they were deposited on a precursor film composed of 5 layer pairs of poly(allyl amine) and *ι*-carrageenan. All data taken from the original work of Hong [282].



**Fig. 1.12** Film thicknesses of a film composed of 12 alternating layers ((PSS/PAH)<sub>6</sub>) which was adsorbed from solutions containing 0.5 M NaCl. Error bars are estimates taking into account that the films are sensitive to small changes in humidity and temperature and do not represent the actual experimental scatter, the lines connecting the data points are guides to the eye. All data were obtained by X-ray reflectivity in the dry state. Top: Film thickness over 3 treatment cycles in

solutions of 0.1 M NaCl and pure water. The filled diamond denotes the thickness of the initial film, open circles denote the thicknesses after immersion in a solution of 0.1 M NaCl and filled circles denote the thicknesses after treatment in pure water. Bottom: Film thickness as dependent on the concentration of NaCl in the solutions used for the swelling treatment. The thickness is normalized with respect to the thickness of the film in pure water.

fect of salt is negligible at small concentrations and levels off again at high concentrations. This indicates that a certain concentration of salt is required for the salt to penetrate into the film and that even high salt concentrations do not completely dissociate the polyions within the multilayer. Obviously, this depends on the chemical structure and deposition conditions as the group of Schlenoff has noted that some multilayers can actually be deconstructed at high ionic strength

[285]. The degree of swelling also depends on the fabrication conditions of the multilayer, films prepared in pure water swell considerably less than films adsorbed from solutions containing salt. In the dry state the maximum swelling of a  $(\text{PSS}/\text{PAH})_n$  film is about 5% when the polyelectrolytes are deposited from pure water and up to about 20% when the film is prepared in solutions of high ionic strength. Of course this comparison refers to films of equal total film thickness, the smaller thickness increment per layer in the case of films deposited from pure water was compensated by an appropriately higher number of layers in order to arrive at a matched film thickness.

The swelling and deswelling in solutions of salt and pure water may have an annealing effect on the film. When salt is diffusing into the film then presumably some of the interchain ionic bonds open up. These bonds would close when the salt diffuses out of the film again, but the closure may take place with different counterion partners, thus removing some strain as the polyion chains can adapt to a “more equilibrated” structure. The idea is that, in the presence of salt, the local mobility of the chains is enhanced and the “more equilibrated” structure is stabilized again after rinsing with water. There is only indirect evidence for this “annealing”, it was observed that the surface roughness of multilayer films of “poor quality” can be improved by cyclic immersion in salt and water to values typically observed with samples of “good quality” (data not shown). The smoothing of polyelectrolyte multilayer films was recently demonstrated by Schlenoff using in-situ AFM [259].

#### 1.3.5.2 Photopatterning

Of course it is attractive to create order not only along the layer normal but also within the plane of the film. Chapter 10 by Hammond, who leads these efforts at present, gives detailed insight into the possibilities of patterning [222, 286–289]. She has developed the lateral structuring of polyelectrolyte multilayer films to a remarkable degree using mostly microcontact printing, which itself originates from the laboratory of Whitesides [290], who has also used this technique to synthesise geometrically well-defined, molecularly thin polymer films [231, 234, 291]. Another patterning method is ink jet printing, adapted to multilayer patterning by Rubner [292]. It should not be forgotten, however, that classic methods like photocrosslinking [293] or photoablation can also be applied to polyelectrolyte multilayers. This is also intensively discussed in Chapter 11 by Shen and Zhang. The example shown in Fig. 1.13 is an early example from our group [17]. This fluorescence micrograph shows in the bright areas the fluorescence of FITC-labeled streptavidin that was adsorbed onto a photopatterned multilayer which terminates with a layer containing biotinylated poly(l-lysine). The pattern arises from placing a copper electron microscope grid onto a homogeneous multilayer sample and subsequently irradiating with a penray mercury lamp. The dark areas in the micrograph represent areas to which the streptavidin does not bind. These are the areas that were exposed to irradiation and where the multilayer was photodegraded. It is interesting that there is very little unspecific protein adsorption in

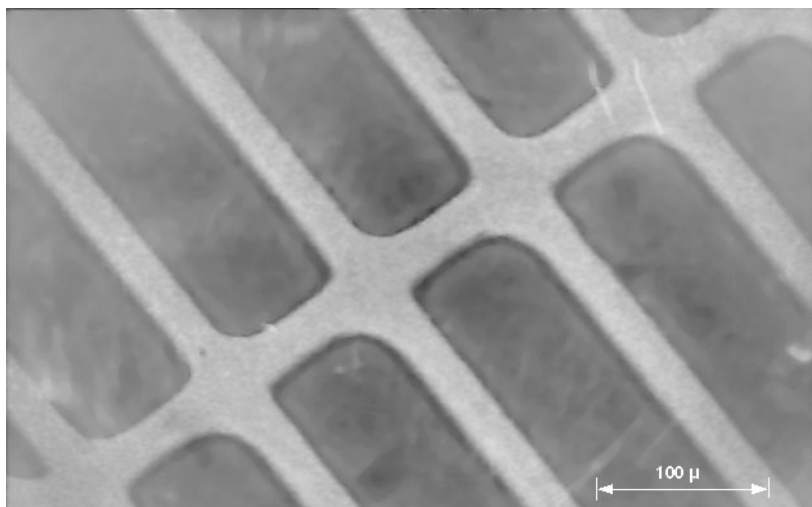


**Fig. 1.13** Fluorescence micrograph showing area-selective binding of FITC-labeled streptavidin on an in-plane photostructured precursor

film. Dark areas represent photodesorbed film, bright areas correspond to protein bound to the intact biotinylated surface.

the irradiated part of the film. The bright areas correspond to regions that were protected from irradiation by the copper grid. In these regions the biotin surface remains intact which is demonstrated by the fluorescence of the bound protein. Of course a copper grid is a rather crude mask, we have not attempted to improve the resolution further using better masks. With conventional light sources such as the mercury lamp used here, the resolution would be limited to somewhat below one micron as the shortest wavelength is 185 nm.

The effect of UV-light on a polyelectrolyte multilayer is more directly seen in a photoablation experiment using X-ray reflectometry. In Fig. 1.14 the film is exposed to the UV-light from a distance of a few cm for increasing time intervals and the X-ray reflectograms are registered after each exposition. Depending on the intensity and on the conditions of film preparation, typical photodesorption rates are in the range of about 1 nm per minute of UV-exposure [17].

#### 1.4 Multilayer Structure

A consistent picture of film growth and structure has been rather difficult to obtain. The combination of data from X-ray and neutron reflectivity, X-ray photoelectron spectroscopy (XPS) (for example [118, 251, 294, 295], radioactive labelling of counterions [116, 296], zeta potential measurements (for example [109, 297]), ellipsometry and related techniques (for example [258, 297]), quartz crystal microbalance, classic polyelectrolyte complexes in bulk and from other sources over the

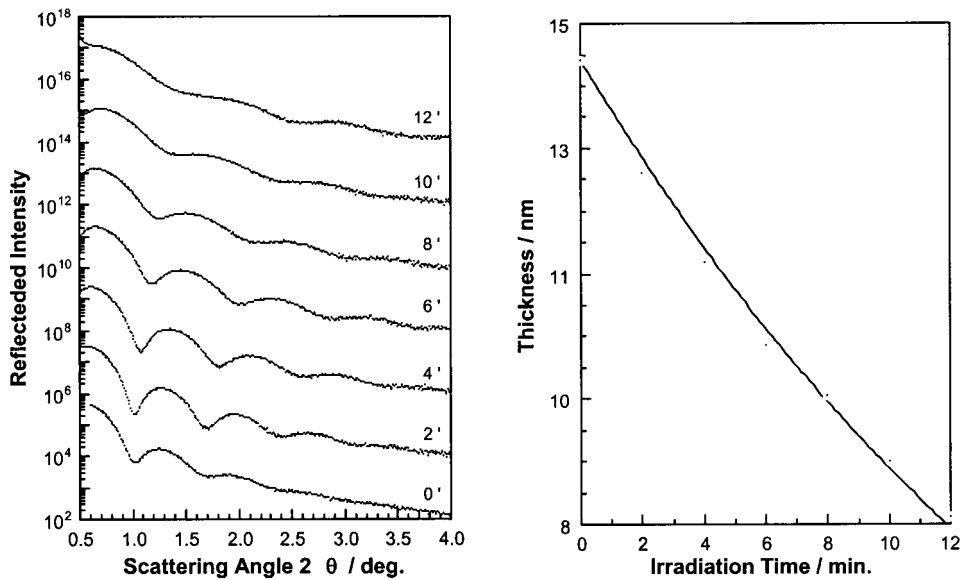


**Fig. 1.14** X-ray determination of the film thickness of a (PSS/PAH) multilayer film after different irradiation times with a mercury lamp at short distance. Left: X-ray reflectograms taken after 2 min intervals of UV-irradiation. Individual traces are displaced along the Y-axis for better viewing. The reduction in the depth of the interference minima is either

due to increasing roughness with irradiation time or to the inhomogeneous irradiation at a close distance. Right: Film thicknesses after different irradiation times (data points) as calculated from the traces on the left. The line corresponds to an exponential fit with an initial reduction of film thickness of about  $0.7 \text{ nm min}^{-1}$  of irradiation.

last years has finally led to a coherent view, which is discussed in the following section. Basically it integrates the observations of layer interpenetration, individual layer profiles, charge stoichiometry, surface charge, and counterion content in a consistent way. All this is only valid for simple, flexible, highly charged homopolyelectrolytes, other systems are not discussed at this point.

#### 1.4.1

##### The Zone Model for Polyelectrolyte Multilayer Films

Our current picture of a multilayer film composed of two simple polyelectrolytes, an anionic homopolyelectrolyte and a cationic homopolyelectrolyte, is that of a film subdivided into three distinct zones (Fig. 1.15) [297, 298]. Zone I is comprised of one or a few polyelectrolyte layers close to the substrate. In this zone the multilayer is influenced by the nature of the substrate. Zone III is comprised of one or a few polyelectrolyte layers close to the surface of the film. In this zone the multilayer is influenced by the interface to the solution or to air. Zone II is "bulk" film, in this region the multilayer is not influenced by either interface.

Zones I, II and III would normally differ in both chemical composition and in structure. In the very coarse and simple picture, Zone II is neutral and the Zones

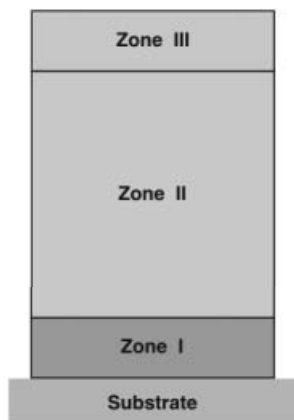


**Fig. 1.15** The zone model for polyelectrolyte multilayers. Zone I is adjacent to the substrate, Zone II forms the “bulk” of the multilayer and Zone III is adjacent to the film/solution or film/air interface [297, 298]. The interface between the zones is diffuse rather than a sharp plane which is indicated here for clarity.

I and III are charged. Depending on the charge density of the substrate and on the substrate roughness, varying amounts of small counterions may be present in Zone I. Even polyelectrolytes that form a 1:1 stoichiometric complex in Zone II might not be able to adsorb in a conformation that would allow for 1:1 charge compensation with the substrate and the next layer. There is also experimental evidence (e.g. unpublished XPS data, F. Brand and G. Decher) that some small counterions might be present in Zone I. Whereas the presence of small counterions is only optional in Zone I, they are probably ubiquitous in Zone III. This is evident from both the construction principle and from measurements of the surface potential. As the adsorption of every layer leads to an overcompensation of the original surface charge, the newly created excess charge must be accompanied by the presence of small counterions. This does not mean that the excess charge is exclusively associated with the polymer molecules deposited as the very last layer, it is well established that individual polymer layers are often strongly intermingled with neighboring layers. Thus it is to be expected that layers further away from the surface will also contribute to the surface charge excess. A more detailed description of charge compensation and layer growth was given recently by Schlenoff [279].

Note that the borders between Zones I and II and between Zones II and III are not sharp but gradual. At present it is not known how many layers actually contribute to Zones I and III, but this should be a function of the substrate, of the chemical structure of the respective polyion pair used for the deposition and of the deposition conditions. It should be understood that the situation outlined here is expected to be valid only for simple and relatively flexible polyions, it may become more complicated, especially if polymers are employed that are not capable of forming a 1:1 stoichiometric complex. Such a case will be described later.

The model of three more or less distinct zones is only valid once a sufficient number of layers has been deposited. Initially, for the first few layers, there will probably exist a situation in which Zones I and III will not have reached their final thickness and the transition between them may occur directly (without forming a Zone II). Polyion pairs that do form a 1:1 complex will form a Zone II



when Zones I and III have reached their final composition and thickness. When more layers are added to the film, Zones I and III are expected to keep their respective thicknesses and character and Zone II will increase in thickness. This should proceed in the following way: A new layer is adsorbed to the surface of Zone III, but this will not increase the number of layers in this zone as the layer closest to the (diffuse!) interface between Zones II and III will now be so far away from the surface that it will no longer be influenced by it and must be counted as belonging now to Zone II rather than Zone III. Thus new layers added to Zone III make the interface between Zones II and III move up rather than increase the thickness of Zone III itself (Fig. 1.16). A more detailed model for multilayer growth was recently proposed by Schlenoff [279].

It is also interesting to speculate on differences in the physicochemical behavior of Zones I, II and III. While details are hard to predict due to insufficient data on the exact structure and composition of the three zones, one can use the assumptions outlined above to predict certain effects. Let us assume charge neutrality (1:1 complex of polyanions and polycations) in Zone II and small gradients of excess charge (neutralized by small counterions) in Zones I and III. The gradient of increasing excess charge in Zone III will begin at the interface of Zones II and III, which represents the last plane coplanar with the surface and substrate in which charge neutrality exists, and will end at the plane of maximum charge ex-

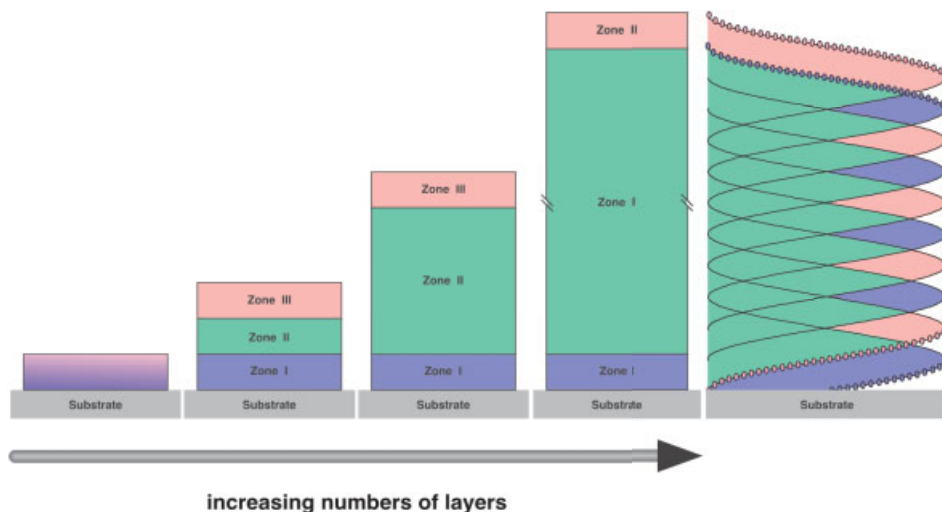


**Fig. 1.16** The zone model for polyelectrolyte multilayers. The part of the schematic above the arrow shows the development of zones during film deposition. The first layer pair is shown on the left and a film consisting of several layers is shown on the right. Note that once all three zones are established only Zone II grows with increasing numbers of

layers [298]. On the very right is depicted how the three zones can be correlated with a model consisting of individual but strongly overlapping layers. In this model layers of equal charge overlap at 50% relative chain segment concentration, a prerequisite for the formation of neutral (1:1) polyion complexes [208, 213].

cess, the surface. In this definition a plane is not infinitely sharp but somewhat fuzzy as interfaces are not discontinuous borders but rough. The gradient of increasing excess charge in Zone I will begin at the interface between Zones I and II and probably end at the surface of the substrate. This gradient is expected to be smaller than the gradient in Zone III, but might also be zero.

However, there should be pronounced differences in physicochemical behavior between the neutral Zone II and that with excess charge, namely Zone III. Zone II is essentially charge compensated and should therefore behave similarly to a polyzwitterion, while regions of the film in which there is a charge excess should behave more like a polyelectrolyte. The differences between both behaviors should depend on the number and length of polyion segments that carry small counterions. One of the most pronounced differences between both species might be their tendency to swell/deswell in the presence of salt. While polyions swell in pure water, they collapse in salt solutions due to the screening of electrostatic repulsion between the charges along the polymer backbone. The behavior of a neutral polyelectrolyte complex should be closer to that of polyzwitterions which swell in the presence of salt and deswell in pure water. However, one should not forget that there will be differences arising from the fact that in a polyzwitterion both charged groups are connected to the same polymer chain, while in a polyelectrolyte complex anionic and cationic groups are connected to different polymer chains, thus intrachain electrostatic interactions are repulsive and interchain interactions are attractive. In polyzwitterions intra- and interchain interactions should be approximately the same. The swelling behavior of polyelectrolyte multilayer films in salt solutions has already been described above.

#### 1.4.2

##### **Layered or Amorphous: What Makes Multilayers Unique Supramolecular Species?**

Simple X-ray reflectometry scans of multilayer films such as those shown in Fig. 1.8 or 1.14 can be explained by a model consisting of a single homogeneous film with a constant electron density along the layer normal. At first sight this seems to indicate that the interior of multilayer films is structureless, as in the corresponding bulk complexes. The same was suggested by the first neutron reflectivity experiments [12] in which every PSS layer of a conventional  $(\text{PSS}/\text{PAH})_n$  film was replaced by perdeuterated PSS ( $\text{PSS-d}_7$ ). Again, only interference fringes from the solid/film and film/air interfaces were observed and no signals were detected that would point to a layered structure. Only when the  $\text{PSS-d}_7$  layers were placed further apart, replacing every second or every third  $\text{PSS-h}_7$  layer, did Bragg peaks show up [12, 299]. Similar data have been reported by us and several other groups [110, 300–303]. It became immediately clear that the layer structure is only picked up in neutron reflectivity experiments if the two deuterium labeled layers do not overlap with each other. This condition is only reached for the majority of simple polyelectrolytes if the labeled layers are at least four layers apart, although other examples are known [304]. Examples of some of these reflectometry experiments are given in Fig. 1.17.

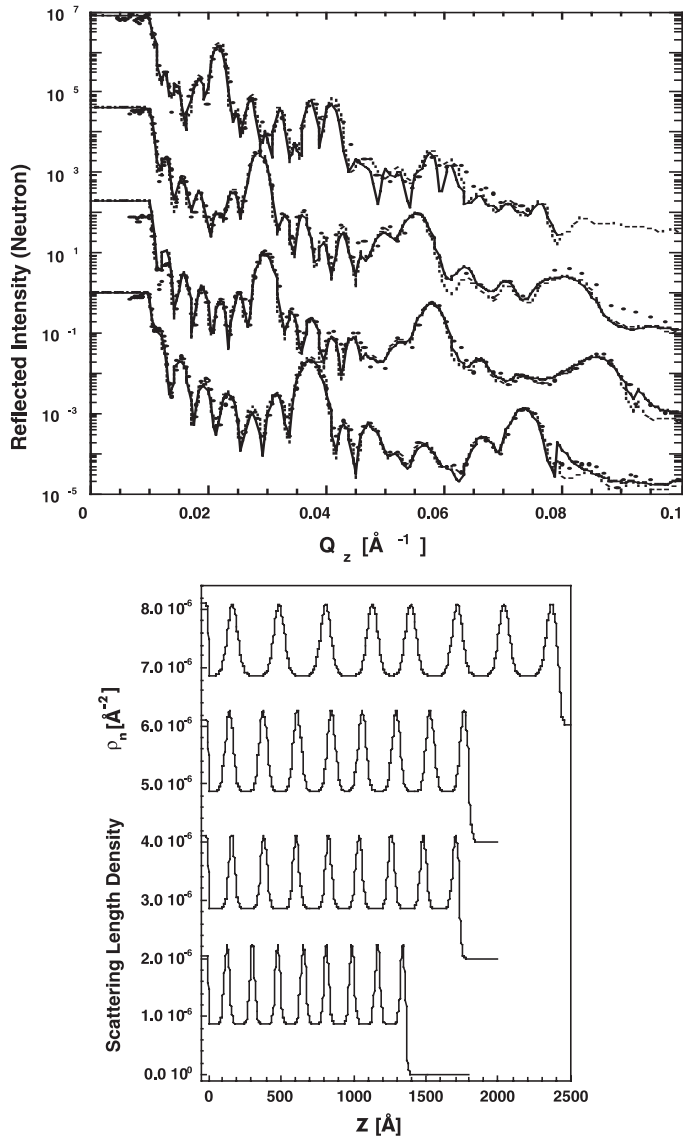


**Fig. 1.17** Neutron reflectivity scans and layer profiles of 4 multilayer samples with different film structure [299]. Individual traces are displaced along the, Y-axis for better viewing. The layer numbers are different, but all four samples contain 8 deuterated layers. The thinnest film was deposited from 0.5 M NaCl (traces at the bottom), the thickest film was deposited from 3.0 M NaCl (traces at the top). The two intermediate traces correspond to films deposited from 1.0 M NaCl and 2.0 M NaCl. The two traces at the bottom correspond to films

comprised of a total of 80 layers the film architecture being  $((\text{PSS-h}_7/\text{PAH})_4/\text{PSS-d}_7/\text{PAH})_8$ . The two traces at the top correspond to films comprised of a total of 64 layers the film architecture being  $((\text{PSS-h}_7/\text{PAH})_3/\text{PSS-d}_7/\text{PAH})_8$ . Upper: Neutron reflectivity scans and numerical fits leading to the layer profiles shown on the right. Lower: Scattering length density profiles of the 4 reflectometry scans on the left. Each of the eight deuterated layers is clearly picked up in every multilayer sample.

What results such as those reported in Fig. 1.17 suggest is that there exist multilayer films in which the components are kinetically trapped in their positions. Certainly  $(\text{PSS}/\text{PAH})_n$  films are an example of films with a layered structure, although the equilibrium structure of polyion complexes in general, which is most likely the bulk structure of such complexes, does not represent a layered structure. What this means is that polyelectrolyte multilayer films can in most cases be described as layered structures in which each layer is trapped at the position where it was originally deposited. Thus each layer is confined with a certain spread to a plane which is represented by the highest segment concentration of a given material. This plane is represented in Fig. 1.17 for the case of the deuterated layers as the maximum scattering length density in any of the 32 maxima in the multilayer profiles in the diagram on the right. The spread around the center of the plane arises from the two factors: 1. the distribution of the concentration of chain segments averaged over all existing conformations of polymers that belong to the same layer and 2. the distribution of the positions of individual polymer chains along the film normal. The combination of both distributions is observed experimentally as a segment concentration profile, whose maximum corresponds to the plane which represents the center of each layer. As clearly seen in Fig. 1.17, the position and spread of an individual layer depends strongly on the deposition conditions. If one defines the spread of an individual layer as the FWHM (full width at half maximum) of a given layer profile and the average layer thickness as the total film thickness divided by the total number of layers, one sees that both values have the same dependence on the salt concentration. For a NaCl concentration of 0.5 M the average spread is 0.41 nm, about 2.4 times the average layer thickness of 0.17 nm, for a NaCl concentration of 3.0 M the average spread is 0.84 nm, also about 2.3 times larger than the average layer thickness of 0.37 nm. However, this is only a crude estimate not taking into account that the layer profiles are not deconvoluted from the contributions of the surrounding non-deuterated layers and that the average layer thicknesses are the average of the contributions from polyanions and polycations. However, these results agree well with our measurements on streptavidin binding and with recent conductivity measurements that indicate that a single polymer layer penetrates no further down into the surrounding film than about 4–7 layers. Both of the latter types of measurements look at the farthest penetrating chain ends that represent the tailing part of the segment density distribution. Such experiments represent a minority of chain segments that cannot even be detected in conventional reflectivity experiments.

The conclusion of this discussion is that the segment concentration profiles of individual layers of identical charge in simple multilayer films with  $(\text{A}/\text{B})_n$  architecture overlap roughly at 50% relative segment concentration. This allows for a 1:1 stoichiometry between polyanions and polycations in Zone II of a film and a well defined, albeit somewhat “fuzzy”, layer structure at the same time. This is true for multilayers of any material that is kinetically trapped during deposition. The absence of reflections typical for a “layer structure” does not indicate that the layers are not confined to planes during deposition. It is in most cases due to a lack of “contrast” between layers arising either from insufficient labeling or from

insufficient spacing between labeled layers. Polyelectrolyte multilayers and related multimaterial assemblies indeed represent nanoscopically ordered species whose unique layer sequence and layer spread are characteristic for a given deposition sequence and for given deposition conditions. They are thus polydisperse supramolecular objects, similar to polymers being a polydisperse molecular species.

### 1.4.3

#### **Soft and Rigid Materials**

In multimaterial films one should pay attention to the nature of the individual components. While the above discussion focuses mostly on rather flexible homopolymers that can adapt to the surface when they are being deposited and that can adapt to the next incoming layer, this is different for more rigid materials. We have already shown that the steric demand for multilayer growth using the specific recognition between the protein streptavidin, a small globular object, and biotin bound to a polycation is much higher than in conventional multilayer films [132]. Thus film growth using non-electrostatic interactions and non-flexible objects might proceed differently or be more difficult than in the classic case. An interesting example in this respect is the comparison of the deposition of  $(\text{PSS}/\text{PAH})_n$  multilayers and of a monolayer of gold colloids on two different substrates. The substrates to be compared are silica wafers either aminofunctionalized by covalent attachment of classic aminosilanization reagents or coated with a layer of poly(ethylene imine) (PEI) a branched polymer that strongly promotes adhesion on various surfaces. In the case of  $(\text{PSS}/\text{PAH})_n$  deposition, the only difference observed on both substrates is a slightly increased amount of the first adsorbed PSS layer on the PEI coated surface (data not shown, J. Schmitt and G. Decher unpublished results). This is easily understood as the surface roughness and thus also the surface charge of the PEI coated surface is expected to be somewhat higher than the roughness and surface charge of the aminosilane coated surface. After the first PSS layer the multilayer deposition becomes independent of the original surface as for example the UV spectra or the growth increments per layer are the same for both systems. However, the situation is quite different when non-flexible objects are deposited on both kinds of substrates. It is advantageous to employ gold colloids (obtained by classic reduction with citrate) for this purpose as they are not only rigid objects, but they also act as a marker reporting colloid/colloid interactions as a color shift in the UV/Vis spectra [305]. The negatively charged gold colloids repel each other on the rather flat aminosilane surface leading to a monolayer of gold colloids whose absorbance spectrum indicates that all the colloids are well isolated [306]. In contrast, it seems that dangling chains of the branched PEI can cause bridging between individual colloids thus bringing colloids into close contact. The absorbance spectrum of a gold monolayer on the PEI surface indicates strong lateral aggregation [306]. This is only a simple case that demonstrates nicely that factors like the flexibility or rigidity of an object to be deposited in a multilayer need to be taken into account when planning target architectures of multilayer films.

## 1.4.4

**Deviation from Linear Growth Behaviour**

Many combinations of strong polyelectrolytes yield a growth behavior that becomes linear after the first few layers, typical examples are shown in Fig. 1.7 and 1.8. However, we [132, 258] and others (e.g. [30, 269, 307]) have noted that a linear regime is never reached or only after the deposition of a large number of layers. In collaboration with the groups of Schaaf and Voegel, we have very recently reported on multilayers composed of weak polyelectrolytes that show strong superlinear growth [149, 254]. In order to explain the data that were observed, we have proposed a model in which polyions are not kinetically trapped in the position where they were originally deposited, but diffuse inside the film [254].

## 1.5

**Multimaterial Films**

What is unique to layer-by-layer deposition in comparison with other film deposition techniques is the broad range of materials that is available for incorporation into polyelectrolyte multilayers. As observed throughout this book, already mentioned above and shown in Fig. 1.4, multilayer deposition can be carried out using small molecules, complex ions, polymers, proteins, DNA or various colloids.

The simple case of two monofunctional materials is depicted in Fig. 1.3 for the case of polycations and polyanions. Fig. 1.18 shows how the use of bi-functional polymers allows one to functionalize the surface of the film with groups  $-F$ . An example for  $-F$  groups could be a fluorescent label or a functional group that promotes cell adhesion. Such a surface can now adsorb molecules interacting with either  $-F$  groups or positive charges or both types of molecules at the same time. This could be useful in cases when the synthesis of a certain bi-functional material would be difficult.

In a second step these  $-F$  groups can be used to change to another interaction of deposition (for example from ionic to covalent or to donor/acceptor) or to vary the material for the next layer. An even simpler case than the one depicted is the case of conventional polyamines. The cationic nature of amino groups allows deposition with a polyanion, however, the chemical reactivity of most amino groups also allows co-deposition with poly(anhydrides) or, as shown in Fig. 1.19, the co-deposition with fullerene  $C_{60}$ .

Fig. 1.19 shows a simplified drawing in which fullerenes  $C_{60}$  and poly(ethylene imine) were used to fabricate films by covalent interaction. The fullerenes are interesting because they are chemically reactive species with a spherical shape. It is well established that  $C_{60}$  can react up to six times with nucleophiles, depending on the nature of the nucleophilic group and of the steric requirements of the nucleophile. The combination of six-fold reactivity with the spherical shape leads to a situation in which some of the reactive sites will react with a surface, exposing amino groups, in such a way that some of the reactive sites will always remain in-

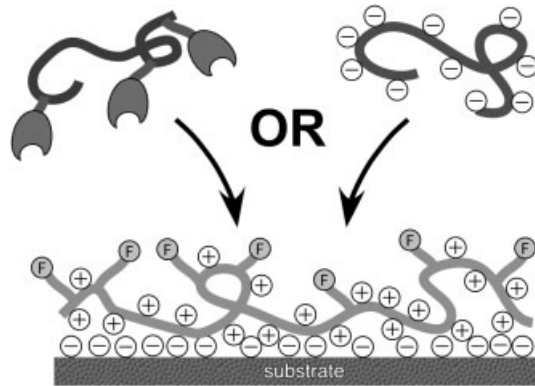


**Fig. 1.18** Schematic depicting the situation in which a polymer equipped with two different functional groups (positive charges and functional groups  $-F$ ) is deposited onto a negatively charged substrate. Thus the surface of a multilayer film can easily be functionalized depending on the chemical nature of  $-F$ . There

is another advantage of bifunctional materials: in the next layer one can either adsorb a polyanion or a polymer capable of binding to  $-F$ . Depending on the nature of  $-F$ , one can switch from electrostatic multilayer buildup to another interaction.

tact and will be oriented toward the solution. Thus  $C_{60}$  acts as a “connecting agent” for covalent multilayer deposition as seen in Fig. 1.19 [209]. The formation of  $C_{60}$  monolayers by covalent attachment of  $C_{60}$  to amino functionalized surfaces was first described by Mirkin [308].

$C_{60}$  is not only useful due to its nature as a “connecting agent”, but also because it is a molecule containing only carbon atoms. This makes fullerenes interesting as markers for X-ray or neutron reflectivity measurements. The absence of other elements in the fullerene layers creates contrast gradients for the  $C_{60}$  layers that are easily detected by either technique. However, as in the case of perdeuterated polymers, a film with  $(A/B)_n$  architecture shows too much layer interpenetration for such an experiment. If the fullerene layers are put at a larger distance with respect to each other, the reflectivity signals arising from the high concentration of a carbon rich species in a layered arrangement are easily detected. Fig. 1.20 shows unpublished data for electron and scattering length densities obtained from the same fullerene containing film with the architecture substrate( $SiO_2$ )/PEI/((PSPMA/PEI) $_3$ / $C_{60}$ /PEI) $_6$ . PSPMA is an alternating copolymer of styrene and maleic anhydride that easily reacts with PEI by forming amide bonds.

Fig. 1.20 shows the layer profiles of a multilayer sample containing 6 fullerene layers as obtained by neutron and X-ray reflectivity. With the exception of the fullerene layer at the surface of the film both traces agree very well, layer positions and spread appear identical in both techniques. The reason for the absence of the last fullerene layer in X-ray reflectivity is due to the combination of two factors, a slightly higher roughness of the film/air interface as determined by X-ray reflectivity

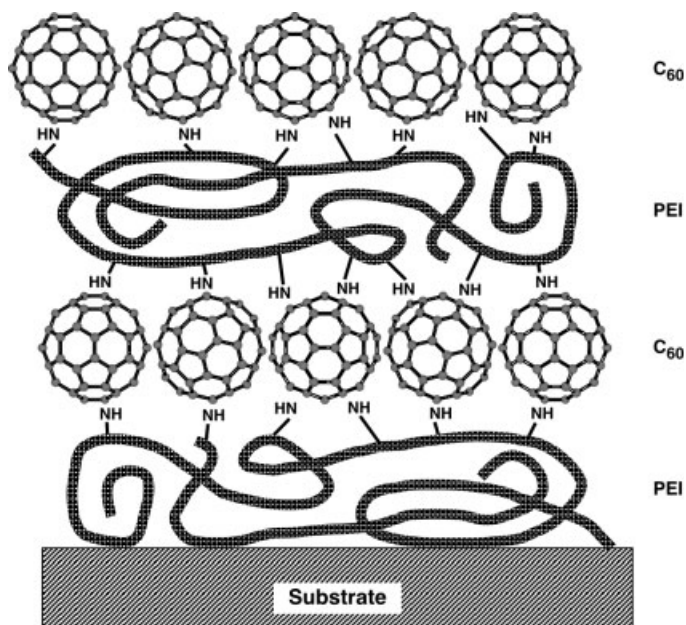


**Fig. 1.19** Schematic showing a multilayer film composed of  $C_{60}$  and poly(ethylene imine) (PEI) [209]. The PEI can be replaced by other polynucleophiles as the reaction between  $C_{60}$  and nucleophilic groups is quite general. The drawing is drastically simplified for reasons of clarity, only some of the amino groups of the PEI are drawn and the covalent bonds be-

tween the amino groups and the  $C_{60}$  are omitted. A film architecture like the one drawn here would not show layer signals in X-ray or neutron reflectivity. However, if the fullerene layers are spaced over a larger distance by depositing more polymer layers between them, signals corresponding to the  $C_{60}$ -layers appear.

ity and only a small difference in the electron densities of the fullerene layer and the crosslinked PSPMA/PEI layers.

Since  $C_{60}$  is a monodisperse sphere with a diameter of about 1.0 nm, the spread of the fullerene layer, about 3 nm as estimated from the FWHM of the layer profile, is entirely due to the displacement of the fullerene molecules from the plane representing the maximum fullerene concentration. Interestingly, the spread of a fullerene layer is about 2.5–3.0 times bigger than the layer thickness (=fullerene diameter), only slightly larger than the value obtained for deuterated poly(styrene sulfonate) layers.

## 1.6

### Toward Compartmentalized Films: Barrier Layers and Nanoreactors

In the context of this chapter compartmentalization is referred to as a temporary concentration difference between two environments which is imposed by a designed barrier. Of course there is enormous potential for compartmented systems



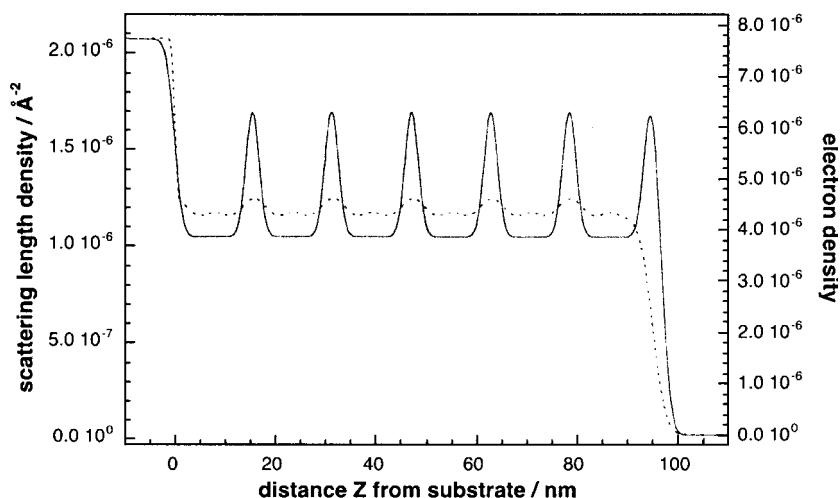


**Fig. 1.20** Layer profiles as obtained by neutron (scattering length density, solid line) and X-ray (electron density, dotted line) reflectivity (J. Schmitt, G. Decher, unpublished data). The

film contains 6 layers of fullerenes and is comprised of a total of 49 layers, the film architecture being PEI/((PSPMA/PEI)<sub>3</sub>/C<sub>60</sub>/PEI)<sub>6</sub>.

on the nanoscopic scale. This includes, for example, studying reactions involving only a few molecules or controlling the function of transport based devices. Simple transport based devices are, for example, separation membranes, more sophisticated ones are, for example, light emitting diodes.

The incorporation of materials into multilayers that can limit transport allows one to create confined environments that may be interesting for certain devices or for the creation of nanoscopic reaction spaces. Such materials include lipid bilayers, mineral platelets or two-dimensional sol-gel layers and others. Lipid bilayers would act as a barrier separating aqueous compartments, mineral platelets and sol-gel layers could have various transport limiting characteristics.

The first multistep membrane reactor based on LbL-multilayers was introduced by Kunitake [49, 50]. In this device, the separate reaction environments for the two consecutive enzymatic reactions were not separated by a barrier layer, it was the transmembrane flux which allowed this device to function as nanoreactor. It should be noted that devices of this type are very potent as such and compartmentalization would not necessarily improve their function.

It is obvious that spherically closed polyelectrolyte multilayers, also called multilayer capsules [309], are compartmentalized systems themselves in which the multilayer membrane itself acts as the barrier between the inside and the outside of these hollow spheres. One can already imagine multilayer films comprised of different layers of such capsules, each layer containing capsules with different liquid content.

In terms of compartmentalization within the multilayer film itself, we will briefly describe two examples from our own group. The first example concerns

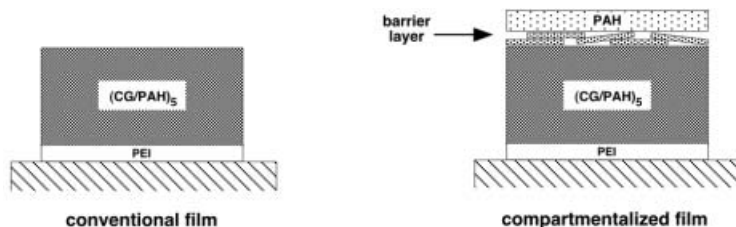


**Fig. 1.21** Schematic depicting a “classic” film of poly(allyl amine) (PAH) and Calcium Green (CG) on the left and a very simple compartmentalized form of the same film on the right. The barrier layer in the case depicted here is obviously not perfect as it is com-

posed of somewhat overlapping montmorillonite platelets. Nevertheless films of this primitive kind do already show that they are subdivided by barriers purposely put into the film [79].

compartmentalization induced by a barrier layer of montmorillonite that limits the transport of ions along the layer normal [79]. The effect was studied in two ways, by neutron reflectivity in films of PSS and PAH and by selective ion binding in films of PAH and Calcium Green. In the latter case the negatively charged chromophore Calcium Green was incorporated in a multilayer film using poly(allyl amine) as cationic partner. Onto this multilayer assembly, montmorillonite platelets were deposited from an aqueous suspension and a layer of PAH was put on as a terminal layer. When films of this type were immersed into solutions containing different concentrations of  $\text{CaCl}_2$ , the films containing the montmorillonite barrier layer showed considerably less uptake of  $\text{Ca}^{2+}$  ions as compared to films without a mineral layer. Since Calcium Green is a calcium sensitive dye, one can describe the control of the binding of  $\text{Ca}^{2+}$  to the Calcium Green as a reaction in a confined environment.

The second example concerns the control of the transport of electrons and/or holes in multilayer based light emitting diodes (LEDs) [75]. It demonstrates how powerful layer-by-layer deposition is with respect to obtaining different high precision devices just by switching beakers in the deposition sequence. The fabrication and investigation of the multilayer, LEDs based on the classic semiconducting polymer poly(*p*-phenylene-vinylene) (PPV) was pioneered by Rubner in the mid-nineties [52, 59, 62], our devices are compartmentalized variations of those he described earlier.

Our device of choice was a LED composed of 20 layers of PPV co-deposited with poly(methacrylic acid) (PMA) as anionic partner polymer, sandwiched between conventional ITO and aluminum electrodes. The photo on the left of Fig. 1.22 shows a typical device of this type with a homogeneously emitting surface of about  $2 \text{ cm}^2$  and a thickness of the active layer of 8.3 nm.

The idea is that any of the PMA layers can easily be replaced with a layer of montmorillonite by simply changing the deposition sequence. This would allow one to shift the position of the barrier layer effortlessly by substituting any of the 21 different PMA layers with a layer of the anionic montmorillonite. Given the

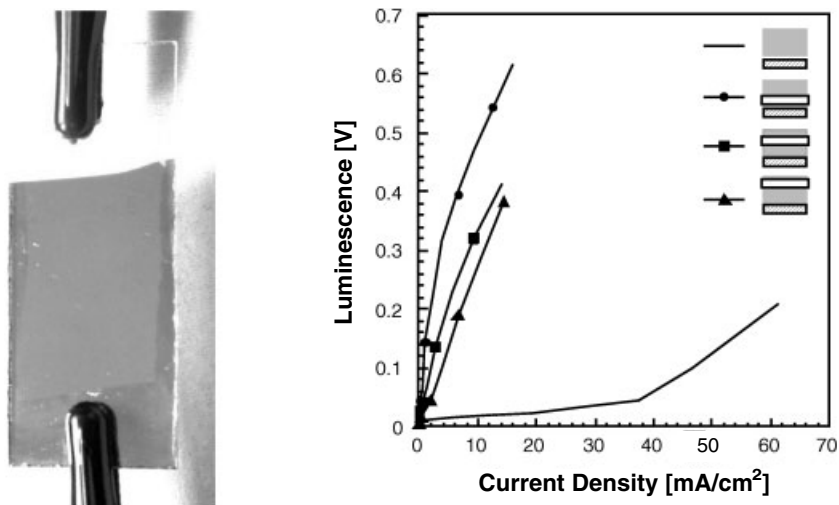


**Fig. 1.22** Left: Photograph of a LED with an active area of about  $2 \text{ cm}^2$ . Right: Luminescence vs. current density characteristics of different LEDs showing the greatly enhanced performance of LEDs containing a montmorillonite layer. The device without a clay layer (line without symbols) has a somewhat lower

relative efficiency than those with a barrier layer. Device efficiency is further increased when the isolating inorganic layer is close to the ITO anode (filled circles). The luminescence is reported as raw output of the photodiode in V. Data points and solid lines are data from different samples [75].

total thickness of the device of 8.3 nm, this means that the barrier layer could be moved through the whole device with raster steps of about 0.4 nm. The diagram on the right of Fig. 1.22 shows the effect of 3 different positions of the mineral layer on the performance of a LED device in comparison with a LED without a clay layer. The 3 positions were 1. close to the ITO electrode, 2. in the center of the device and 3. close to the aluminum electrode, all three cases showing a clear enhancement of the electroluminescence by the montmorillonite layer. If several barrier layers are put into a LED, the luminescence increases more than 50-fold with respect to the device without a clay layer (data not shown). There are several different hypotheses by which one may explain the barrier effect of a mineral layer in LEDs, but all of them suggest that shifting the position of the montmorillonite layer also shifts the position of the recombination zone within the device.

Clearly, these experiments were not intended to compete in the race for the most brilliant LED, it is evident that PPV-based devices would not even stand a chance here. These experiments are intended to underline that even LED amateurs (like us) are able to contribute interesting results to the field by putting the power of LbL-technology to work. It should be underlined that homogeneously emitting devices with large active areas such as that in Fig. 1.22 were prepared with success rates of 90% or more, completely avoiding vacuum techniques or clean rooms, with a cost for the coating of a few cents per device.

## 1.7

## Commercial Applications

As outlined in Fig. 1.1, multimaterial composites are key elements for the molecular machinery of nature herself. Layer-by-layer assembly is a low-cost, environmentally friendly, wet-bench technique that allows one to fabricate very simple, mostly one-dimensionally ordered nanocomposites. After the failure of the Langmuir-Blodgett technique to transfer its elegance and usefulness from academia into the commercial sector, the big question was whether the polyelectrolyte multilayer technology could become a “real world” industrial process.

While we have seen for quite a while that several startup companies have been created out of academic environments, it was only at the 223rd ACS National Meeting, held April 7–11, 2002 in Orlando, that an established company announced the first commercial product that is today available on the market. Fig. 1.23 shows the package of a contact lens from CIBA-Vision that has a layer-by-layer based coating on its surface. While the name of the product is likely to change in the future, we are happy that Focus<sup>®</sup> Excelens<sup>™</sup> demonstrates that a new coating process can overcome all the initial counterarguments often associated with new technologies. With respect to LbL, we often heard: 1. it cannot work, 2. the previous layer should desorb upon deposition of the next one, 3. multilayer coatings cannot be stable, 4. LB did not work out for applications so why should LbL. Luckily, CIBA-Vision did not listen to arguments of this kind or did not find them valid. This first product will encourage all the authors of this book to continue their activities and hopefully will also convince new research teams to pick up on layer-by-layer deposition to realize devices in their own field of interest.



**Fig. 1.23** After 12 years of steadily growing research in academia, all of us were happy to see CIBA-Vision announce the first commercially available product that is equipped with a multilayer coating. Photo courtesy of L. Winterton of CIBA-Vision: it was presented at the 223rd, ACS National meeting on April 7–11, 2002 in Orlando. Focus<sup>®</sup> Excelens<sup>™</sup>, a contact lens, Copyright CIBA-Vision.

## 1.8

## References

- 1 DECHER, G., Layered Nanoarchitectures via Directed Assembly of Anionic and Cationic Molecules, in *Comprehensive Supramolecular Chemistry*, Vol. 9, *Templating, Self-Assembly and Self-Organization*, (Ed. SAUVAGE J.-P., HOSSEINI M. W.), Pergamon Press, New York, pp. 507–528, 1996.
- 2 BLODGETT, K. B., Monomolecular Films of Fatty Acids on Glass, *J. Am. Chem. Soc.* 1934, 56, 495.
- 3 BLODGETT, K. B., LANGMUIR, I., Build-Up Films of Barium Stearate and Their Optical Properties, *Phys. Rev.* 1937, 51, 964–982.
- 4 KUHN, H., MÖBIUS, D., Systeme aus Monomolekularen Schichten – Zusammenbau und chemisches Verhalten, *Angew. Chem.* 1971, 83, 672–690.
- 5 INACKER, O., KUHN, H., MÖBIUS, D., DEBUCH, G., Manipulation in Molecular Dimensions, *Z. Phys. Chem. Neue Folge* 1976, 101, 337–360.
- 6 DECHER, G., HONG, J.-D., Auf Trägern angebrachte ein- oder mehrlagige Schichtelemente und ihre Herstellung, 1990, *Germ. Pat.* DE 402 6978, 1990.
- 7 DECHER, G., HONG, J.-D., Buildup of Ultrathin Multilayer Films by a Self-Assembly Process: I. Consecutive Adsorption of Anionic and Cationic Bipolar Amphiphiles, *Makromol. Chem., Macromol. Symp.* 1991, 46, 321–327.
- 8 DECHER, G., HONG, J.-D., SCHMITT, J., Buildup of Ultrathin Multilayer Films by a Self-Assembly Process: III. Consecutively Alternating Adsorption of Anionic and Cationic Polyelectrolytes on Charged Surfaces, *Thin Solid Films* 1992, 210/211, 831–835.
- 9 DECHER, G., SCHMITT, J., Fine-Tuning of the Film Thickness of Ultrathin Multilayer Films Composed of Consecutively Alternating Layers of Anionic and Cationic Polyelectrolytes, *Progr. Colloid Polym. Sci.* 1992, 89, 160–164.
- 10 DECHER, G., HONG, J.-D., One- or Multilayered Elements Applied to Supports and Their Production, *US Pat.* US 520 8111, 1993.
- 11 DECHER, G., SCHMITT, J., SIEGMUND, H.-U., HEILIGER, L., Auf Trägern angebrachte ein- oder mehrlagige Schichtelemente und ihre Herstellung, *Germ. Pat.* DE 433 3107, 1993.
- 12 SCHMITT, J., GRÜNEWALD, T., KJÆR, K., PERSHAN P, DECHER, G., LÖSCHE, M., The Internal Structure of Layer-by-Layer Adsorbed Polyelectrolyte Films: A Neutron and X-ray Reflectivity Study, *Macromolecules* 1993, 26, 7058–7063.
- 13 DECHER, G., HONG, J.-D., Mono or Multilayer Deposits on a Substrate and Process for Making Them, *Eur. Pat.* EP 472 990 B1, 1995.
- 14 DECHER, G., SCHMITT, J., SIEGMUND, H.-U., HEILIGER, L.: Layer-elements of One or More Layers Deposited on Substrates and Their Manufacture, *Eur. Pat.* EP 647 477 A1, 1995.
- 15 HONG, J.-D., LOWACK, K., SCHMITT, J., DECHER, G., Layer-by-Layer Deposited Multilayer Assemblies of Polyelectrolytes and Proteins: From Ultrathin Films to Protein Arrays, *Progr. Colloid Polym. Sci.* 1993, 93, 98–102.
- 16 LVOV, Y., DECHER, G., SUKHORUKOV, G., Assembly of Thin Films by Means of Successive Deposition of Alternate Layers of DNA and Poly(allylamine), *Macromolecules* 1993, 26, 5396–5399.
- 17 DECHER, G., LEHR, B., LOWACK, K., LVOV, Y., SCHMITT, J., New Nanocomposite Films for Biosensors: Layer-by-Layer adsorbed Films of Polyelectrolytes, Proteins or DNA, *Biosens. Bioelectron.* 1994, 9, 677–684.
- 18 LVOV, Y., HAAS, H., DECHER, G., MÖHWALD, H., MICHAÏLOV, A., MTCHEDLISHVILY, B., MORGUNOVA, E., VAINSHTAIN, B., Successive Deposition of Alternate Layers of Polyelectrolytes and a Charged Virus, *Langmuir* 1994, 10, 4232–4236.
- 19 SUKHORUKOV, G. B., MÖHWALD, H., DECHER, G., LVOV, Y.M., Assembly of Polyelectrolyte Multilayer Films by Consecutively Alternating Adsorption of Polynucleotides and Polycations, *Thin Solid Films* 1996, 284/285, 220–223.

- 20 FARHAT, T., SCHLENOFF, J., Corrosion Control using Polyelectrolyte Multilayers, *Electrochem. Solid State Lett.* **2002**, *5*, B13–B15.
- 21 HATTORI, H., Antireflection Surface with Particle Coating Deposited by Electrostatic Attraction, *Adv. Mater.* **2001**, *13*, 51.
- 22 GRAUL, T.W., SCHLENOFF, J.B., Capillaries Modified by Polyelectrolyte Multilayers for Electrophoretic Separations, *Anal. Chem.* **1999**, *71*, 4007–4013.
- 23 NGANKAM, P.A., LAVALLE, P., VOEGEL, J.C., SZYK, L., DECHER, G., SCHAAF, P., CUISINIER, F.J.G., Influence of Polyelectrolyte Multilayer Films on Calcium-Phosphate Nucleation. *J. Am. Chem. Soc.* **2000**, *122*, 8998–9004.
- 24 DUTTA, A.K., HO, T.T., ZHANG, L.Q., STROEVE, P., Nucleation and Growth of Lead Sulfide Nanocrystallites and Microcrystallites in Supramolecular Polymer Assemblies, *Chem. Mater.* **2000**, *12*, 1042–1048.
- 25 DUTTA, A.K., JARERO, G., ZHANG, L.Q., STROEVE, P., In-Situ Nucleation and Growth of Gamma-FeOOH Nanocrystallites in Polymeric Supramolecular Assemblies, *Chem. Mater.* **2000**, *12*, 176–181.
- 26 ZHANG, L.Q., DUTTA, A.K., JARERO, G., STROEVE, P., Nucleation and Growth of Cobalt Hydroxide Crystallites in Organized Polymeric Multilayers, *Langmuir* **2000**, *16*, 7095–7100.
- 27 MULLER, M., RIESER, T., LUNKWITZ, K., MEIERHAACK, J., Polyelectrolyte Complex Layers – A Promising Concept for Antifouling Coatings Verified by in-Situ ATR-FTIR Spectroscopy, *Macromol. Rapid Commun.* **1999**, *20*, 607–611.
- 28 MEIERHAACK, J., RIESER, T., LENK, W., LEHMANN, D., BERWALD, S., SCHWARZ, S., Influence of Polyelectrolyte Complex Layers on the Separation Performance of Fouling Behavior on Surface-Modified and Bulk-Modified Membranes, *Chem.-Ing.-Tech.* **1999**, *71*, 839–844.
- 29 RIESER, T., LUNKWITZ, K., BERWALD, S., MEIERHAACK, J., MULLER, M., CASSEL, F., DIOSZEGHY, Z., SIMON, F., Surface Modification of Microporous Polypropylene Membranes by Polyelectrolyte Multilayers, *ACS Symp. Ser.* **2000**, *744*, 189–204.
- 30 ELBERT, D.L., HERBERT, C.B., HUBBELL, J.A., Thin Polymer Layers Formed by Polyelectrolyte Multilayer Techniques on Biological Surfaces, *Langmuir* **1998**, *15*, 5355–5362.
- 31 HWANG, J.J., JAEGER, K., HANCOCK, J., STUPP, S.I., Organoapatite Growth on an Orthopedic Alloy Surface, *J. Biomed. Mater. Res.* **1999**, *47*, 504–515.
- 32 CARUSO, F., NIIKURA, K., FURLONG, D.N., OKAHATA, Y., 2. Assembly of Alternating Polyelectrolyte and Protein Multilayer Films for Immunosensing, *Langmuir* **1997**, *13*, 3427–3433.
- 33 SWANSON, B., JOHNSON, S., SHI, J., YANG, X., Cyclodextrin-Based Microsensors for Volatile Organic-Compounds, *ACS Symp. Ser.* **1998**, *690*, 130–138.
- 34 CHEN, T., FRIEDMAN, K.A., LEI, I., HELLER, A., In-Situ Assembled Mass-Transport Controlling Micromembranes and Their Application in Implanted Amperometric Glucose Sensors. *Anal. Chem.* **2000**, *72*, 3757–3763.
- 35 HOSHI, T., SAIKI, H., KUWAZAWA, S., KOBAYASHI, Y., ANZAI, J., Polyelectrolyte Multilayer Film-Coated Electrodes for Amperometric Determination of Hydrogen-Peroxide in the Presence of Ascorbic Acid, Uric-Acid and Acetaminophen, *Anal. Sci.* **2000**, *16*, 1009–1010.
- 36 LEE, S.H., KUMAR, J., TRIPATHY, S.K., Thin-Film Optical Sensors Employing Polyelectrolyte Assembly, *Langmuir* **2000**, *16*, 10482–10489.
- 37 LI, W.J., WANG, Z., SUN, C.Q., XIAN, M., ZHAO, M.Y., Fabrication of Multilayer Films Containing Horseradish-Peroxidase and Polycation-Bearing Os Complex by Means of Electrostatic Layer-by-Layer Adsorption and Its Application as a Hydrogen-Peroxide Sensor, *Anal. Chim. Acta* **2000**, *418*, 225–232.
- 38 NARVAEZ, A., SUAREZ, G., POPESCU, I.C., KATAKIS, I., DOMINGUEZ, E., Reagentless Biosensors Based on Self-Deposited Redox Polyelectrolyte-Oxidoreductases Architectures, *Biosens. Bioelectron.* **2000**, *15*, 43–52.
- 39 YOON, H.C., KIM, H.S.: Multilayered Assembly of Dendrimers with Enzymes on

- Gold – Thickness-Controlled Biosensing Interface, *Anal. Chem.* **2000**, *72*, 922–926.
- 40 WU, Z. Y., YAN, Y. H., SHEN, G. L., YU, R. Q., A Novel-Approach of Antibody Immobilization Based on N-Butyl Amine Plasma-Polymerized Films for Immunosensors, *Anal. Chim. Acta* **2000**, *412*, 29–35.
- 41 RUSLING, J. F., ZHOU, L. P., MUNGE, B., YANG, J., ESTAVILLO, C., SCHENKMAN, J. B., Applications of Polyion Films Containing Biomolecules to Sensing Toxicity, *Faraday Discuss.* **2000**, *116*, 77–87.
- 42 SIRKAR, K., REVZIN, A., PISHKO, M. V., Glucose and Lactate Biosensors Based on Redox Polymer/Oxidoreductase Nanocomposite Thin-Films, *Anal. Chem.* **2000**, *72*, 2930–2936.
- 43 CALVO, E. J., ETCHENIQUE, R., PIETRASANTA, L., WOLOSUK, A., DANIŁOWICZ, C., Layer-by-Layer Self-Assembly of Glucose-Oxidase and Os(bpy)<sub>2</sub>(2)Cipych<sub>2</sub>Nh-Poly(Allylamine) Bioelectrode, *Anal. Chem.* **2001**, *73*, 1161–1168.
- 44 DAI, J. H., JENSEN, A. W., MOHANTY, D. K., ERNDT, J., BRUENING, M. L. Controlling the Permeability of Multilayered Polyelectrolyte Films Through Derivatization, Cross-Linking, and Hydrolysis, *Langmuir* **2001**, *17*, 931–937.
- 45 PEARSON, C., NAGEL, J., PETTY, M. C., Metal-Ion Sensing Using Ultrathin Organic Films Prepared by the Layer-by-Layer Adsorption Technique, *J. Phys. D, Appl. Phys.* **2001**, *34*, 285–291.
- 46 ZHOU, X. C., HUANG, L. Q., LI, S. F. Y., Microgravimetric DNA Sensor-Based on Quartz-Crystal Microbalance – Comparison of Oligonucleotide Immobilization Methods and the Application in Genetic Diagnosis, *Biosens. Bioelectron.* **2001**, *16*, 85–95.
- 47 BARKER, S. L. R., ROSS, D., TARLOV, M. J., GAITAN, M., LOCASCIO, L. E., Control of Flow Direction in Microfluidic Devices with Polyelectrolyte Multilayers, *Anal. Chem.* **2000**, *72*, 5925–5929.
- 48 BARKER, S. L. R., TARLOV, M. J., CANAVAN, H., HICKMAN, J. J., LOCASCIO, L. E., Plastic Microfluidic Devices Modified with Polyelectrolyte Multilayers, *Anal. Chem.* **2000**, *72*, 4899–4903.
- 49 ONDA, M., LVOV, Y., ARIGA, K., KUNITAKE, T., Sequential Actions of Glucose Oxidase and Peroxidase in Molecular Films Assembled by Layer-by-Layer Alternate Adsorption, *Biotechnol. Bioeng.* **1996**, *51*, 163–167.
- 50 ONDA, M., LVOV, Y., ARIGA, K., KUNITAKE, T., Sequential Reaction and Product Separation on Molecular Films of Glucoamylase and Glucose Oxidase Assembled on an Ultrafilter, *J. Ferment. Bioeng.* **1996**, *82*, 502–506.
- 51 MECKING, S., THOMANN, R., Core-Shell Microspheres of a Catalytically Active Rhodium Complex Bound to a Polyelectrolyte-Coated Latex, *Adv. Mater.* **2000**, *12*, 953.
- 52 FERREIRA, M., RUBNER, M. F., HSIEH, B. R., Luminescence Behavior of Self-Assembled Multilayer Heterostructures of Poly(phenylene-vinylene), *Mater. Res. Soc. Symp. Proc.* **1994**, *328*, 119–124.
- 53 FOU, A. C., ONITSUKA, O., FERREIRA, M., RUBNER, M. F., HSIEH, B. R., Interlayer Interactions in Self-Assembled Poly(phenylene vinylene) Multilayer Heterostructures, Implications for Light-Emitting and Photorectifying Diodes, *Mater. Res. Soc. Symp. Proc.* **1995**, *369*, 575–580.
- 54 HONG, H., DAVIDOV, D., AVNY, Y., CHAYET, H., FARAGGI, E. Z., NEUMANN, R., Electroluminescence, Photoluminescence and X-Ray Reflectivity Studies of Self-Assembled Ultra-Thin Films, *Adv. Mater.* **1995**, *7*, 846–849.
- 55 ONODA, M., YOSHINO, K., Fabrication of Self-Assembled Multilayer Heterostructure of Poly(p-Phenylene Vinylene) and Its Use for an Electroluminescent Diode, *J. Appl. Phys.* **1995**, *78*, 4456–4462.
- 56 ONODA, M., YOSHINO, K., Heterostructure Electroluminescent Diodes Prepared from Self-Assembled Multilayers of Poly(p-phenylene vinylene) and Sulfonated Polyaniline, *Jpn. J. Appl. Phys.* **1995**, *34*, L260–L263.
- 57 TIAN, J., WU C-C, THOMPSON, M. E., STURM, J. C., REGISTER RA, MARSELLA, M. J., SWAGER, T. M., Electroluminescent Properties of Self-Assembled Polymer Thin Films, *Adv. Mater.* **1995**, *7*, 395–398.

- 58 TIAN, J., WU, C. C., THOMPSON, M. E., STURM, J. C., REGISTER, R. A., Photophysical Properties, Self-Assembled Thin-Films, and Light-Emitting-Diodes of Poly(p-Pyridylvinylene)s and Poly(p-Pyridinium Vinylene)s, *Chem. Mater.* **1995**, *7*, 2190–2198.
- 59 FOU, A. C., ONITSUKA, O., FERREIRA, M., RUBNER, M. F., HSIEH, B. R., Fabrication and Properties of Light-Emitting-Diodes Based on Self-Assembled Multilayers of Poly(Phenylene Vinylene), *J. Appl. Phys.* **1996**, *79*, 7501–7509.
- 60 HONG, H., TARABIA, M., CHAYET, H., DAVIDOV, S., FARAGGI, E. Z., AVNY, Y., NEUMANN, R., KIRSTEIN, S., Possible Evidence for Quantum-Size Effects in Self-Assembled Ultrathin Films Containing Conjugated Copolymers, *J. Appl. Phys.* **1996**, *79*, 3082–3088.
- 61 LEE, J. K., YOO, D. S., HANDY, E. S., RUBNER, M. F., Thin-Film Light-Emitting Devices from an Electroluminescent Ruthenium Complex, *Appl. Phys. Lett.* **1996**, *69*, 1686–1688.
- 62 ONITSUKA, O., FOU, A. C., FERREIRA, M., HSIEH, B. R., RUBNER, M. F., Enhancement of Light-Emitting-Diodes Based on Self-Assembled Heterostructures of Poly(p-Phenylene Vinylene), *J. Appl. Phys.* **1996**, *80*, 4067–4071.
- 63 ARREGUI, F. J., LIU, Y. J., MATIAS, I. R., CLAUS, R. O., Optical-Fiber Humidity Sensor Using a Nano Fabry-Perot Cavity Formed by the Ionic Self-Assembly Method, *Sens. Actuators* **1999**, *59*, 54–59.
- 64 ARREGUI, F. J., MATIAS, I. R., LIU, Y. J., LEHANAN, K. M., CLAUS, R. O., Optical-Fiber Nanometer-Scale Fabry-Perot-Interferometer Formed by the Ionic Self-Assembly Monolayer Process, *Opt. Lett.* **1999**, *24*, 596–598.
- 65 WU, A., YOO, D., LEE, J. K., RUBNER, M. F., Solid-State Light-Emitting Devices Based on the Tris-Chelated Ruthenium(II) Complex-3-High-Efficiency Devices via a Layer-by-Layer Molecular-Level Blending Approach, *J. Am. Chem. Soc.* **1999**, *121*, 4883–4891.
- 66 CASSAGNEAU, T., FENDLER, J. H., JOHNSON, S. A., MALLOW, T. E., Self-Assembled Diode Junctions Prepared from a Ruthenium Tris(Bipyridyl) Polymer, N-Type TiO<sub>2</sub> Nanoparticles, and Graphite Oxide Sheets, *Adv. Mater.* **2000**, *12*, 1363–1366.
- 67 GAO, M. Y., LESSER, C., KIRSTEIN, S., MÖHWALD, H., ROGACH, A. L., WELLER, H., Electroluminescence of Different Colors from Polycation/CdTe Nanocrystal Self-Assembled Films, *J. Appl. Phys.* **2000**, *87*, 2297–2302.
- 68 HO, P. K. H., KIM J. S., BURROUGHS, J. H., BECKER, H., LI S. F. Y., BROWN, T. M., CACIALLI, F., FRIEND, R. H., Molecular-Scale Interface Engineering for Polymer Light-Emitting-Diodes, *Nature* **2000**, *404*, 481–484.
- 69 MATTOUSSI, H., RUBNER, M. F., ZHOU F, KUMAR, J., TRIPATHY, S. K., CHIANG, L. Y., Photovoltaic Heterostructure Devices Made of Sequentially Adsorbed Poly(Phenylene Vinylene) and Functionalized C-60, *Appl. Phys. Lett.* **2000**, *77*, 1540–1542.
- 70 SONODA, T., FUJISAWA, T., FUJII, A., YOSHINO, K., Optical-Properties of Self-Assembled Thin-Film of Poly(P-Phenylene Vinylene)s and Its Application to Light-Emitting Devices with Microring Geometry, *Appl. Phys. Lett.* **2000**, *76*, 3227–3229.
- 71 FUJISAWA, T., SONODA, T., OOTAKE, R., FUJII, A., YOSHINO, K., Microring Light-Emitting Devices with Self-Assembled Multilayer Structures Based on Poly(P-Phenylene Vinylene)s, *Synth. Met.* **2001**, *121*, 1739–1740.
- 72 PIOK, T., BRANDS, C., NEYMAN, P. J., ERLACHER, A., SOMAN, C., MURRAY, M. A., SCHROEDER, R., GRAUPNER, W., HEFLIN, J. R., MARCIU, D., et al., Photovoltaic Cells Based on Ionically Self-Assembled Nanostructures, *Synth. Met.* **2001**, *116*, 343–347.
- 73 PIOK, T., SCHROEDER, R., BRANDS, C., HEFLIN, J. R., LEISING, G., GRAUPNER, W., Photocarrier Generation Quantum Yield for Ionically Self-Assembled Monolayers, *Synth. Met.* **2001**, *121*, 1589–1590.
- 74 DURSTOCK, M. F., TAYLOR, B., SPRY, R. J., CHIANG, L., REULBACH, S., HEITFELD, K., BAUR, J. W., Electrostatic Self-Assembly as a Means to Create Organic Photovoltaic Devices, *Synth. Met.* **2001**, *116*, 373–377.



- 75 ECKLE, M., DECHER, G., Tuning the Performance of Layer-by-Layer Assembled OLEDs by Controlling the Position of Isolating Clay Barrier Sheets, *Nanoletters* **2001**, *1*, 45–49.
- 76 STROEVE, P., VASQUES, V., COELHO, M. A. N., RABOLT, J. F., Gas Transfer in Supported Films Made by Molecular Self-Assembly of Ionic Polymers, *Thin Solid Films* **1996**, *284/285*, 708–712.
- 77 KRASEMANN, L., TIEKE, B., Selective Ion-Transport Across Self-Assembled Alternating Multilayers of Cationic and Anionic Polyelectrolytes, *Langmuir* **2000**, *16*, 287–290.
- 78 HARRIS, J. J., BRUENING, M. L., Electrochemical and in-Situ Ellipsometric Investigation of the Permeability and Stability of Layered Polyelectrolyte Films, *Langmuir* **2000**, *16*, 2006–2013.
- 79 STRUTH, B., ECKLE, M., DECHER, G., OESER, R., SIMON, P., SCHUBERT, D. W., SCHMITT, J., Hindered Ion Diffusion in Polyelectrolyte/Montmorillonite Multilayers: Toward Compartmentalized Films, *Eur. Phys. J. E* **2001**, *6*, 351–358.
- 80 MEIERHAACK, J., LENK, W., LEHMANN, D., LUNKWITZ, K., Pervaporation Separation of Water/Alcohol Mixtures Using Composite Membranes Based on Polyelectrolyte Multilayer Assemblies, *J. Membr. Sci.* **2001**, *184*, 233–243.
- 81 KRASEMANN, L., TOUTIANOUSH, A., TIEKE, B., Self-Assembled Polyelectrolyte Multilayer Membranes with Highly Improved Pervaporation Separation of Ethanol/Water Mixtures, *J. Membr. Sci.* **2001**, *181*, 221–228.
- 82 TIEKE, B., VANACKERN, F., KRASEMANN, L., TOUTIANOUSH, A., Ultrathin Self-Assembled Polyelectrolyte Multilayer Membranes, *Eur. Phys. J. E* **2001**, *5*, 29–39.
- 83 FARHAT, T.R., SCHLENOFF, J.B., Ion-Transport and Equilibria in Polyelectrolyte Multilayers, *Langmuir* **2001**, *17*, 1184–1192.
- 84 DECHER, G., HONG, J.-D., Buildup of Ultrathin Multilayer Films by a Self-Assembly Process: II. Consecutive Adsorption of Anionic and Cationic Bipolar Amphiphiles and Polyelectrolytes on Charged Surfaces, *Ber. Bunsen-Ges. Phys. Chem.* **1991**, *95*, 1430–1434.
- 85 MAO, G., TSAO, Y., TIRRELL, M., DAVIS, H. T., HESSEL, V., RINGSDORF, H., Self-Assembly of Photopolymerizable Bolaform Amphiphile Mono- and Multilayers, *Langmuir* **1993**, *9*, 3461–3470.
- 86 COOPER, T.M., CAMPBELL, A. L., CRANE, R. L., Formation of Polypeptide-Dye Multilayers by an Electrostatic Self-Assembly Technique, *Langmuir* **1995**, *11*, 2713–2718.
- 87 SAREMI F, MAASSEN, E., TIEKE, B., JORDAN, G., RAMMENSEE, W., Self-Assembled Alternating Multilayers Built-up from Diacetylene Bolaamphiphiles and Poly(allylamine hydrochloride): Polymerization Properties, Structure, and Morphology, *Langmuir* **1995**, *11*, 1068–1071.
- 88 SAREMI, F., TIEKE, B., Polymerization of 10,12-Docosadiyne-1,22-disulfate in Self-Assembled Multilayers, *Adv. Mater.* **1995**, *7*, 378–380.
- 89 ARAKI, K., WAGNER, M. J., WRIGHTON, M. S., Layer-by-Layer Growth of Electrostatically Assembled Multilayer Porphyrin Films, *Langmuir* **1996**, *12*, 5393–5398.
- 90 SAREMI, F., LANGE, G., TIEKE, B., Deeply Colored Self-Assembled Multilayers of Anionic DPP Bolaamphiphiles and Cationic Polyelectrolytes, *Adv. Mater.* **1996**, *8*, 923–926.
- 91 SELLERGREN, B., SWIETLOW, A., ARNEBRANDT, T., UNGER, K., Consecutive Selective Adsorption of Pentamidine and Phosphate Biomolecules on a Self-Assembled Layer: Reversible Formation of a Chemically Selective Coating, *Anal. Chem.* **1996**, *68*, 402–407.
- 92 ARIGA, K., LVOV, Y., KUNITAKE, T., Assembling Alternate Dye-Polyion Molecular Films by Electrostatic Layer-by-Layer Adsorption, *J. Am. Chem. Soc.* **1997**, *119*, 2224–2231.
- 93 AUER, F., SCHUBERT, D. W., STAMM, M., ARNEBRANDT, T., SWIETLOW, A., ZIZLSPERGER, M., SELLERGREN, B., Switchable Assembly of Stable, Ordered Molecular Layers, *Chem.-Eur. J.* **1999**, *5*, 1150–1159.
- 94 CHENG, L., NIU, L., GONG, J., DONG, S. J., Electrochemical Growth and Characterization of Polyoxometalate-Containing Monolayers and Multilayers on Alkanethiol Monolayers Self-Assembled on

- Gold Electrodes, *Chem. Mater.* **1999**, *11*, 1465–1475.
- 95 CHENG, L., DONG, S. J., Electrochemical Behavior and Electrocatalytic Properties of Ultrathin Films Containing Silicotungstic Heteropolyanion SiW<sub>12</sub>O<sub>40</sub>, *J. Electrochem. Soc.* **2000**, *147*, 606–612.
- 96 JIANG, H., SU, W., HAZEL, J., GRANT, J. T., TSUKRUK, V. V., COOPER, T. M., BUNNING, T. J., Electrostatic Self-Assembly of Sulfonated C-60-Porphyrin Complexes on Chitosan Thin-Films, *Thin Solid Films* **2000**, *372*, 85–93.
- 97 KURTH, D. G., VOLKMER, D., RUTTORF, M., RICHTER, B., MULLER, A., Ultrathin Composite Films Incorporating the Nanoporous Isopolyoxomolybdate Keplerate (NH<sub>4</sub>)<sub>42</sub>(Mo<sub>132</sub>O<sub>372</sub>(CH<sub>3</sub>COO)<sub>30</sub>)(H<sub>2</sub>O)<sub>72</sub>), *Chem. Mater.* **2000**, *12*, 2829.
- 98 VANDUFFEL, B., VERBIEST, T., VANELSHOCHT, S., PERSOONS, A., DESCHRYVER, F. C., SCHOONHEYDT, R. A., Fuzzy Assembly and 2nd-Harmonic Generation of Clay/Polymer/Dye Monolayer Films, *Langmuir* **2001**, *17*, 1243–1249.
- 99 ZOU, B., WANG, L. Y., WU, T., ZHAO X. Y., WU, L. X., ZHANG, X., GAO, S., GLEICHE, M., CHI, L. F., FUCHS, H., Ex-Situ SFM Study of 2-D Aggregate Geometry of Azobenzene Containing Bolaform Amphiphiles After Adsorption, at the Mica/Aqueous Solution Interface, *Langmuir* **2001**, *17*, 3682–3688.
- 100 LVOV, Y., DECHER, G., MÖHWALD, H., Assembly, Structural Characterization and Thermal Behavior of Layer-by-Layer Deposited Ultrathin Films of Poly(vinyl sulfate) and Poly(allylamine), *Langmuir* **1993**, *9*, 481–486.
- 101 LVOV, Y., HAAS, H., DECHER, G., MÖHWALD, H., KALACHEV, A., Assembly of Polyelectrolyte Molecular Films onto Plasma-Treated Glass, *J. Phys. Chem.* **1993**, *97*, 12835–12841.
- 102 CHEUNG, J. H., FOU, A. F., RUBNER, M. F., Molecular Self-Assembly of Conducting Polymers. *Thin Solid Films* **1994**, *244*, 985–989.
- 103 FERREIRA, M., CHEUNG, J. H., RUBNER, M. F., Molecular Self-Assembly of Conjugated Polyions: a New Process for Fabricating Multilayer Thin Film Heterostructures, *Thin Solid Films* **1994**, *244*, 806–809.
- 104 POMMERSHEIM, R., SCHRENZENMEIR, J., VOGT, W., Immobilization of Enzymes by Multilayer Microcapsules, *Macromol. Chem. Phys.* **1994**, *195*, 1557–1567.
- 105 WATANABE, S., REGEN, S. L., Dendrimers as Building Blocks for Multilayer Construction, *J. Am. Chem. Soc.* **1994**, *116*, 8855–8856.
- 106 FERREIRA, M., RUBNER, M. F., Molecular-level Processing of Conjugated Polymers. 1. Layer-by-layer Manipulation of Conjugated Polyions, *Macromolecules* **1995**, *28*, 7107–7114.
- 107 FOU, A. C., RUBNER, M. F., Molecular-level Processing of Conjugated Polymers. 2. Layer-by-layer Manipulation of in situ Polymerized p-Type Doped Conducting Polymers, *Macromolecules* **1995**, *28*, 7115–7120.
- 108 KLEINFELD, E. R., FERGUSON, G. S., Nanostructured Organic/Inorganic Films from Poly(d-Lysine Hydrobromide) or Poly(N-Methyl-4-vinyl Pyridinium Bromide) and Hectorite, *Mater. Res. Soc. Symp. Proc.* **1995**, *369*, 697–702.
- 109 HOOGEVEEN, N. G., STUART, M. A. C., FLEER, G., BÖHMER, M. R., Formation and Stability of Multilayers of Polyelectrolytes, *Langmuir* **1996**, *12*, 3675–3681.
- 110 KELLOG, G. J., MAYES, A. M., STOCKTON, W. B., FERREIRA, M., RUBNER, M. F., SATTIJA, S. K., Neutron Reflectivity Investigations of Self-Assembled Conjugated Polyion Multilayers, *Langmuir* **1996**, *12*, 5109–5113.
- 111 LASCHEWSKY, A., MAYER, B., WISCHERHOFF, E., ARYS, X., BERTRAND, P., DELCORTE, A., JONAS, A., A New Route to Thin Polymeric, Non-centrosymmetric Coatings, *Thin Solid Films* **1996**, *284/285*, 334–337.
- 112 LASCHEWSKY, A., MAYER, B., WISCHERHOFF, E., ARYS X, JONAS, A., Polyelectrolyte Complexes at Interfaces, *Ber. Bunsenges. Phys. Chem.* **1996**, *100*, 1033–1038.
- 113 ADVINCULA, R., AUST, E., MEYER, W., KNOLL, W., In-situ Investigations of Polymer Self-Assembly Solution Adsorption by Surface Plasmon Spectroscopy, *Langmuir* **1996**, *12*, 3536–3540.

- 114 LEHR, B., SEUFERT, M., WENZ, G., DECHER, G., Fabrication of Poly (p-phenylene vinylene) (PPV) Nanoheterocomposite Films via Layer-by-layer Adsorption. *Supramol. Sci.* **1996**, *2*, 199–207.
- 115 LVOV, Y., YAMADA, S., KUNITAKE, T., Non-linear Optical Effects in Layer-by-layer Alternate Films of Polycations and an Azobenzene-containing Polyanion, *Thin Solid Films* **1996**, *300*, 107–112.
- 116 SCHLENOFF, J.B, LI, M., Kinetics and Multilayering in the Adsorption of Polyelectrolytes to a Charged Surface, *Ber. Bunsen-Ges. Phys. Chem.* **1996**, *100*, 943–947.
- 117 TSUKRUK, V.V., RINDERSPACHER, F., BLIZNYUK, V.N., Self-Assembled Films From Dendrimers, *Langmuir* **1997**, *13*, 2171.
- 118 LAURENT, D., SCHLENOFF, J. B., Multi-layer Assemblies of Redox Polyelectrolytes, *Langmuir* **1997**, *13*, 1552–1557.
- 119 CHENG, Y.F., CORN, R.M., Ultrathin Polypeptide Multilayer Films for the Fabrication of Model Liquid/Liquid Electrochemical Interfaces, *J. Phys. Chem. B* **1999**, *103*, 8726–8731.
- 120 DANTE, S., ADVINCULA, R., FRANK, C.W., STROEVE, P., Photoisomerization of Polyionic Layer-by-Layer Films Containing Azobenzene, *Langmuir* **1999**, *15*, 193–201.
- 121 HE, J.A., VALLUZZI, R., YANG, K., DOLUKHANYAN, T., SUNG C.M., KUMAR, J., TRIPATHY, S.K., SAMUELSON, L., BALOGH, L., TOMALIA, D.A.: Electrostatic Multilayer Deposition of a Gold-Dendrimer Nanocomposite, *Chem. Mater.* **1999**, *11*, 3268–3274.
- 122 TRUBETSKOY, V.S., LOOMIS, A., HAGSTROM, J.E., BUDKER, V.G., WOLFF, J.A., Layer-by-Layer Deposition of Oppositely Charged Polyelectrolytes on the Surface of Condensed DNA Particles. *Nucleic Acids Res.* **1999**, *27*, 3090–3095.
- 123 CASSON, J.L., MCBRANCH, D.W., ROBINSON, J.M., WANG, H.L., ROBERTS, J.B., CHIARELLI, P.A., JOHAL, M.S., Reversal of Interfacial Dipole Orientation in Polyelectrolyte Superlattices Due to Polycationic Layers, *J. Phys. Chem. B* **2000**, *104*, 11996–12001.
- 124 CHEN, J. Y., LUO, G. B., WANG, R. X., ZHAO, X. S., CAO, W. X., Ultrathin-Film Fabricated from Pddac/DSB and Ndr/DSB, *Mater. Res. Bull.* **2000**, *35*, 1945–1954.
- 125 CHENG, L., COX, J.A., Preparation of Multilayered Nanocomposites of Polyoxometalates and Poly(Amidoamine) Dendrimers, *Electrochem. Commun.* **2001**, *3*, 285–289.
- 126 HE, P.-G., TAKAHASHI, T., HOSHI, T., ANZAI, J.-I., SUZUKI, Y., OSA, T., Preparation of Enzyme Multilayers on Electrode Surface by Use of Avidin and Biotin-labeled Enzyme for Biosensor Applications, *Mater. Sci. Eng.* **1994**, *C2*, 103–106.
- 127 LVOV, Y., ARIGA, K., KUNITAKE, T., Layer-by-Layer Assembly of Alternate Protein/Polyion Ultrathin Films, *Chem. Lett.* **1994**, 2323–2326.
- 128 LVOV, Y., ARIGA, K., ICHINOSE, I., KUNITAKE, T., Layer-by-Layer Architectures of Concanavalin A by Means of Electrostatic and Biospecific Interactions, *J. Chem. Soc., Chem. Commun.* **1995**, 2313–2314.
- 129 KAYUSHINA, R., LVOV, Y., STEPINA, N., BELYAEV, V., KHURGIN, Y., Construction and X-ray Reflectivity Study of Self-assembled Lysozyme/Polyion Multilayers, *Thin Solid Films* **1996**, *284/285*, 246–248.
- 130 SUN, C., ZHANG, X., JIANG, D., GAO, Q., XU, H., SUN, Y., ZHANG, X., SHEN, J., Electrocatalytic Oxidation of Carbohydrates at a Molecular Deposition Film Electrode Based on Water-soluble Cobalt Phthalocyanine and Its Application to Flow-through Detection, *J. Electroanal. Chem.* **1996**, *411*, 73–78.
- 131 SUN, Y., ZHANG, X., SUN, C., WANG, B., SHEN, J., Fabrication of Ultrathin Film Containing Bienenzyme of Glucose Oxidase and Glucoamylase Based on Electrostatic Interaction and Its Potential Application as a Maltose Sensor, *Macromol. Chem. Phys.* **1996**, *197*, 147–153.
- 132 CASSIER, T., LOWACK, K., DECHER, G., Layer-by-layer Assembled Protein/Polymer Hybrid Films: Nanoconstruction via Specific Recognition, *Supramol. Sci.* **1998**, *5*, 309–315.
- 133 HE, J.A., SAMUELSON, L., LI, L., KUMAR, J., TRIPATHY, S.K., Oriented Bacteriorhodopsin/Polycation Multilayers by Electrostatic Layer-by-Layer Assembly. *Langmuir* **1998**, *14*, 1674–1679.

- 134 LANG, J., LIN, M. H., Layer-by-Layer Assembly of DNA Films and Their Interactions with Dyes. *J. Phys. Chem. B* **1999**, *103*, 11393–11397.
- 135 SERIZAWA, T., GOTO, H., KISHIDA, A., ENDO, T., AKASHI, M., Improved Alternately Deposition of Biodegradable Naturally-Occurring Polymers Onto a Quartz-Crystal Microbalance. *J. Polym. Sci. A* **1999**, *37*, 801–804.
- 136 SUKHISHVILI, S. A., GRANICK, S., Adsorption of Human Serum-Albumin – Dependence on Molecular Architecture of the Oppositely Charged Surface. *J. Chem. Phys.* **1999**, *110*, 10153–10161.
- 137 BRYNDA, E., HOUSKA, M., WIKERSTAL, A., PIENKA, Z., DYR, J. E., BRANDENBURG, A., Characterization of Flexibility of Ultrathin Protein Films by Optical Sensing. *Langmuir* **2000**, *16*, 4352–4357.
- 138 CALVO, E. J., BATTAGLINI, F., DANILOWICZ, C., WOLOSUK, A., OTERO, M., Layer-by-Layer Electrostatic Deposition of Biomolecules on Surfaces for Molecular Recognition, Redox Mediation and Signal Generation. *Faraday Discuss.* **2000**, *116*, 47–65.
- 139 DELACEY, A. L., DETCHEVERRY, M., MOIROUX, J., BOURDILLON, C., Construction of Multicomponent Catalytic Films Based on Avidin- Biotin Technology for the Electroenzymatic Oxidation of Molecular-Hydrogen. *Biotechnol. Bioeng.* **2000**, *68*, 1–10.
- 140 FORZANI, E. S., SOLIS, V. M., CALVO, E. J., Electrochemical-Behavior of Polyphenol Oxidase Immobilized in Self-Assembled Structures Layer-by-Layer with Cationic Polyallylamine. *Anal. Chem.* **2000**, *72*, 5300–5307.
- 141 LU, Z. Q., LVOV, Y., JANSSON, I., SCHENKMAN, J. B., RUSLING, J. F., Electroactive Films of Alternately Layered Polycations and Iron-Sulfur Protein Putidaredoxin on Gold. *J. Colloid Interface Sci.* **2000**, *224*, 162–168.
- 142 LVOV, Y., MUNGE, B., GIRALDO, O., ICHINOSE, I., SUIB, S. L., RUSLING, J. F., Films of Manganese Oxide Nanoparticles with Polycations or Myoglobin from Alternate-Layer Adsorption. *Langmuir* **2000**, *16*, 8850–8857.
- 143 LADAM, G., GERGELY, C., SENGER, B., DECHER, G., VOEGEL, J.-C., SCHAAF, P., CUISINIER, F. J. G., Protein Interactions with Polyelectrolyte Multilayers: Interactions between Human Serum Albumin and Polystyrene Sulfonate/Polyallylamine Multilayers. *Biomacromolecules* **2000**, *1*, 674–687.
- 144 RAM, M. K., ADAMI, M., PADDEU, S., NICOLINI, C., Nano-Assembly of Glucose-Oxidase on the in-Situ Self-Assembled Films of Polypyrrole and Its Optical, Surface and Electrochemical Characterizations. *Nanotechnology* **2000**, *11*, 112–119.
- 145 TACHABOONYAKIAT, W., SERIZAWA, T., ENDO, T., AKASHI, M.: The Influence of Molecular-Weight over the Ultrathin Films of Biodegradable Polyion Complexes Between Chitosan and Poly(Gamma-Glutamic Acid). *Polym. J.* **2000**, *32*, 481–485.
- 146 HEMPENIUS, M. A., ROBINS, N. S., LAMMERTINK, R. G. H., VANCISO, G. J., Organometallic Polyelectrolytes – Synthesis, Characterization and Layer-by-Layer Deposition of Cationic Poly(Ferrocenyl(3-Ammoniumpropyl)Methylsilane). *Macromol. Rapid Commun.* **2001**, *22*, 30–33.
- 147 LADAM, G., SCHAAF, P., CUISINIER, F. J. G., DECHER, G., VOEGEL, J. C., Protein Adsorption Onto Auto-Assembled Polyelectrolyte Films. *Langmuir* **2001**, *17*, 878–882.
- 148 MULLER, M., RIESER, T., DUBIN, P. L., LUNKWITZ, K., Selective Interaction Between Proteins and the Outermost Surface of Polyelectrolyte Multilayers – Influence of the Polyanion Type, pH and Salt. *Macromol. Rapid Commun.* **2001**, *22*, 390–395.
- 149 PICART, C., LAVALLE, P., HUBERT P, CUISINIER, F. J. G., DECHER, G., SCHAAF, P., VOEGEL, J.-C., Buildup Mechanism for Poly(L-lysine)/Hyaluronic Acid Films onto a Solid Surface. *Langmuir* **2001**, *17*, 7414–7424.
- 150 SCHENKMAN, J. B., JANSSON, I., LVOV, Y., RUSLING, J. F., BOUSSAAD, S., TAO, N. J., Charge-Dependent Sidedness of Cytochrome-P450 Forms Studied by Quartz-Crystal Microbalance and Atomic-Force Microscopy. *Arch. Biochem. Biophys.* **2001**, *385*, 78–87.

- 151 WANG, L. W., HU, N. F., Direct Electrochemistry of Hemoglobin in Layer-by-Layer Films with Poly(Vinyl Sulfonate) Grown on Pyrolytic-Graphite Electrodes, *Bioelectrochemistry* **2001**, *53*, 205–212.
- 152 KELLER, S. W., KIM, H.-N., MALLOUK, T. E., Layer-by-Layer Assembly of Intercalation Compounds and Heterostructures on Surfaces: Towards Molecular “Beaker” Epitaxy, *J. Am. Chem. Soc.* **1994**, *116*, 8817–8818.
- 153 KLEINFELD, E. R., FERGUSON, G. S., Stepwise Formation of Multilayered Nanostructural Films from Macromolecular Precursors, *Science* **1994**, *265*, 370–373.
- 154 GAO, M., ZHANG, X., YANG, Y., YANG, B., SHEN, J., Constructing PbI<sub>2</sub> Nanoparticles into a Multilayer Structure using the Molecular Deposition (MD) Method, *J. Chem. Soc., Chem. Commun.* **1994**, 2777–2778.
- 155 FERGUSON, G. S., KLEINFELD, E. R., Mosaic Tiling in Molecular Dimensions, *Adv. Mater.* **1995**, *7*, 414–416.
- 156 KELLER, S. W., JOHNSON, S. A., BRIGHAM, E. S., YONEMOTO, E. H., MALLOUK, T. E., Photoinduced Charge Separation in Multilayer Thin Films Grown by Sequential Polyelectrolyte Adsorption, *J. Am. Chem. Soc.* **1995**, *117*, 12879–12880.
- 157 KLEINFELD, E. R., FERGUSON, G. S., Rapid, Reversible Sorption of Water from the Vapor by a Multilayered Composite Film: A Nanostructured Humidity Sensor, *Chem. Mater.* **1995**, *7*, 2327–2331.
- 158 FELDHEIM, D. L., GRABAR, K. C., NATAN, M. J., MALLOUK, T. E., Electron Transfer in Self-Assembled Inorganic Polyelectrolyte/Metal Nanoparticle Heterostructures, *J. Am. Chem. Soc.* **1996**, *118*, 7640–7641.
- 159 KASCHAK, D. M., MALLOUK, T. E., Interlayer and Intralayer Energy-Transfer in Zirconium-Phosphate Poly(Allylamine Hydrochloride) Multilayers – An Efficient Photon Antenna and a Spectroscopic Ruler for Self-Assembled Thin Films, *J. Am. Chem. Soc.* **1996**, *118*, 4222–4223.
- 160 KOTOV, N. A., DKNY, I., FENDLER, J. H., Ultrathin Graphite Oxide-Polyelectrolyte Composites Prepared by Self-Assembly: Transition Between Conductive and Non-Conductive States, *Adv. Mater.* **1996**, *8*, 637–641.
- 161 LVOV, Y., ARIGA, K., ICHINOSE, I., KUNITAKE, T., Formation of Ultrathin Multilayer and Hydrated Gel from Montmorillonite and Linear Polycations, *Langmuir* **1996**, *12*, 3038–3044.
- 162 ARIGA, K., LVOV, Y., ONDA, M., ICHINOSE, I., KUNITAKE, T., Alternately Assembled Ultrathin Film of Silica Nanoparticles and Linear Polycations, *Chem. Lett.* **1997**, 125–126.
- 163 GAO, M., RICHTER, B., KIRSTEIN, S., White-Light Electroluminescence from Self-Assembled Q-CdSe/PPV Multilayer Structures, *Adv. Mater.* **1997**, *9*, 802–805.
- 164 BLIZNYUK, V. N., CAMPBELL, A., TSUKRUK, V. V., Organized Multilayer Films of Charged Organic Latexes, *ACS Symp. Ser.* **1998**, *695*, 220–232.
- 165 CASSAGNEAU, T., FENDLER, J. H., High Density Rechargeable Lithium-Ion Batteries Self-Assembled from Graphite Oxide Nanoplatelets and Polyelectrolytes, *Adv. Mater.* **1998**, *10*, 877.
- 166 KOTOV, N. A., HARASZTI, T., TURI, L., ZAVALA, G., GEER, R. E., DÉKÁNY, I., FENDLER, J. H., Mechanism of and Defect Formation in the Self-assembly of Polymeric Polycation-Montmorillonite Ultrathin Films, *J. Am. Chem. Soc.* **1998**, *119*, 6821–6832.
- 167 LVOV, Y. M., RUSLING, J. F., THOMSEN, D. L., PAPADIMITRAKOPOULOS, F., KAWAKAMI, T., KUNITAKE, T., High-Speed Multilayer Film Assembly by Alternate Adsorption of Silica Nanoparticles and Linear Polycation, *Chem. Commun.* **1998**, 1229–1230.
- 168 SCHROF, W., ROZOUVAN, S., KEUREN, E. V., HORN, D., SCHMITT, J., DECHER, G., Nonlinear Optical Properties of Polyelectrolyte Thin Films Containing Gold Nanoparticles Investigated by Wavelength Dispersive Femtosecond Degenerate Four Wave Mixing (DFWM). *Adv. Mater.* **1998**, *10*, 338–341.
- 169 BOUDREAU, L. C., KUCK, J. A., TSAPATSIS, M., Deposition of Oriented Zeolite-A Films – In-Situ and Secondary Growth, *J. Membr. Sci.* **1999**, *152*, 41–59.
- 170 HE, J. A., YANG, K., KUMAR, J., TRIPATHY, S. K., SAMUELSON, L. A., OSHIKIRI, T., KATAGI, H., KASAI, H., OKADA, S., OIKAWA, H., et al., Electrostatic Self-Assembly of

- Polydiacetylene Nanocrystals – Non-linear-Optical Properties and Chain Orientation, *J. Phys. Chem. B* **1999**, *103*, 11050–11056.
- 171 CASSAGNEAU, T., GUERIN, F., FENDLER, J.H.: Preparation and Characterization of Ultrathin Films Layer-by-Layer Self-Assembled from Graphite Oxide Nanoplatelets and Polymers, *Langmuir* **2000**, *16*, 7318–7324.
- 172 GOLE, A., SAINKAR, S.R., SASTRY, M., Electrostatically Controlled Organization of Carboxylic-Acid Derivatized Colloidal Silver Particles on Amine-Terminated Self-Assembled Monolayers, *Chem. Mater.* **2000**, *12*, 1234–1239.
- 173 HAO, E.C., LIAN, T.Q., Buildup of Polymer/Au Nanoparticle Multilayer Thin-Films Based on Hydrogen-Bonding, *Chem. Mater.* **2000**, *12*, 3392–3396.
- 174 KIM, D.W., BLUMSTEIN, A., KUMAR, J., TRIPATHY, S.K., Layered Aluminosilicate/Chromophore Nanocomposites and Their Electrostatic Layer-by-Layer Assembly, *Chem. Mater.* **2001**, *13*, 243–246.
- 175 KOVTYUKHOVA, N.I., BUZANEVA, E.V., WARAKSA, C.C., MALLOUK, T.E., Ultrathin Nanoparticle ZnS and ZnS Mn Films – Surface Sol-Gel Synthesis, Morphology, Photophysical Properties, *Mater. Sci. Eng. B* **2000**, *69*, 411–417.
- 176 KOVTYUKHOVA, N.I., BUZANEVA, E.V., WARAKSA, C.C., MARTIN, B.R., MALLOUK, T.E., Surface Sol-Gel Synthesis of Ultrathin Semiconductor-Films, *Chem. Mater.* **2000**, *12*, 383–389.
- 177 KOVTYUKHOVA, N.I., GORCHINSKIY, A.D., WARAKSA, C., Self-Assembly of Nanostructured Composite ZnO/Polyaniline Films, *Mater. Sci. Eng. B* **2000**, *69*, 424–430.
- 178 KUMAR, A., MANDALE, A.B., SASTRY, M., Sequential Electrostatic Assembly of Amine-Derivatized Gold and Carboxylic Acid-Derivatized Silver Colloidal Particles on Glass Substrates, *Langmuir* **2000**, *16*, 6921–6926.
- 179 LVOV, Y.M., PRICE, R.R., SELINGER, J.V., SINGH, A., SPECTOR, M.S., SCHNUR, J.M., Imaging Nanoscale Patterns on Biologically Derived Microstructures, *Langmuir* **2000**, *16*, 5932–5935.
- 180 MA, H.Y., HU, N.F., RUSLING, J.F.: Electroactive Myoglobin Films Grown Layer-by-Layer with Poly(Styrenesulfonate) on Pyrolytic-Graphite Electrodes. *Langmuir* **2000**, *16*, 4969–4975.
- 181 MAMEDOV, A., OSTRANDER, J., ALIEV, F., KOTOV, N.A., Stratified Assemblies of Magnetite Nanoparticles and Montmorillonite Prepared by the Layer-by-Layer Assembly, *Langmuir* **2000**, *16*, 3941–3949.
- 182 MAMEDOV, A.A., KOTOV, N.A., Freestanding Layer-by-Layer Assembled Films of Magnetite Nanoparticles, *Langmuir* **2000**, *16*, 5530–5533.
- 183 MUSICK, M.D., KEATING, C.D., LYON, L.A., BOTSKO, S.L., PEÑA, D.J., HOLLISWAY, W.D., MCEVOY, T.M., RICHARDSON, J.N., NATAN, M.J., Metal-Films Prepared by Stepwise Assembly-2-Construction and Characterization of Colloidal Au and Ag Multilayers, *Chem. Mater.* **2000**, *12*, 2869–2881.
- 184 PASTORIZASANTOS, I., KOKTYSH, D.S., MAMEDOV, A.A., GIERSIG, M., KOTOV, N.A., LIZMARZAN, L.M., One-Pot Synthesis of Ag-at-TiO<sub>2</sub> Core-Shell Nanoparticles and Their Layer-by-Layer Assembly, *Langmuir* **2000**, *16*, 2731–2735.
- 185 RHODES, K.H., DAVIS, S.A., CARUSO, F., ZHANG, B.J., MANN, S., Hierarchical Assembly of Zeolite Nanoparticles into Ordered Macroporous Monoliths Using Core-Shell Building-Blocks, *Chem. Mater.* **2000**, *12*, 2832.
- 186 ROGACH, A.L., KOKTYSH, D.S., HARRISON, M., KOTOV, N.A., Layer-by-Layer Assembled Films of HgTe Nanocrystals with Strong Infrared-Emission, *Chem. Mater.* **2000**, *12*, 1526.
- 187 SASAKI, T., EBINA, Y., WATANABE, M., DECHER, G., Multilayer Ultrathin Films of Molecular Titania Nanosheets Showing Highly Efficient UV-Light Absorption, *Chem. Commun.* **2000**, 2163–2164.
- 188 SERIZAWA, T., KAMIMURA, S., AKASHI, M., Electrostatic Adsorption of Polystyrene Particles with Different Surface-Charges Onto the Surface of an Ultrathin Polymer Film, *Colloids Surf., A* **2000**, *164*, 237–245.
- 189 CARUSO, R.A., SUSHA, A., CARUSO, F., Multilayered Titania, Silica, and Laponite Nanoparticle Coatings on Polystyrene

- Colloidal Templates and Resulting Inorganic Hollow Spheres, *Chem. Mater.* **2001**, *13*, 400–409.
- 190 HAO, E. C., ZHANG, H., YANG, B., REN, H., SHEN, J. C., Preparation of Luminescent Polyelectrolyte/Cu-Doped ZnSe Nanoparticle Multilayer Composite Films, *J. Colloid Interface Sci.* **2001**, *238*, 285–290.
- 191 HATTORI, H., 2-Step Assembly Technique for Preparation of Polymer-Particle Composite Films, *Thin Solid Films* **2001**, *385*, 302–306.
- 192 KIM, D. W., BLUMSTEIN, A., TRIPATHY, S. K., Nanocomposite Films Derived from Exfoliated Functional Aluminosilicate Through Electrostatic Layer-by-Layer Assembly, *Chem. Mater.* **2001**, *13*, 1916–1922.
- 193 OSTRANDER, J. W., MAMEDOV, A. A., KOTOV, N. A., 2 Modes of Linear Layer-by-Layer Growth of Nanoparticle-Polyelectrolyte Multilayers and Different Interactions in the Layer-by-Layer Deposition, *J. Am. Chem. Soc.* **2001**, *123*, 1101–1110.
- 194 SASAKI, T., EBINA, Y., TANAKA, T., HARADA, M., WATANABE, M., DECHER, G., Layer-by-Layer Assembly of Titania Nanosheet/Polycation Composite Films, *Chem. Mater.* **2001**, *13*, 4661–4667.
- 195 Sastry, M., Kumar, A., Datar, S., Dharmadhikari, C. V., Ganesh, K. N., DNA-Mediated Electrostatic Assembly of Gold Nanoparticles into Linear Arrays by a Simple Drop-Coating Procedure, *Appl. Phys. Lett.* **2001**, *78*, 2943–2945.
- 196 TSENG, J. Y., LIN, M. H., CHAU, L. K., Preparation of Colloidal Gold Multilayers with 3-(Mercaptopropyl)-Trimethoxysilane as a Linker Molecule, *Colloids Surf., A* **2001**, *182*, 239–245.
- 197 UNG, T., LIZMARZAN, L. M., MULVANEY, P., Optical-Properties of Thin-Films of Au-at-SiO<sub>2</sub> Particles, *J. Phys. Chem. B* **2001**, *105*, 3441–3452.
- 198 WANG, M. T., ZHANG, L. D., Precipitation of Multilayered Core-Shell TiO<sub>2</sub> Composite Nanoparticles Onto Polymer Layers, *J. Mater. Res.* **2001**, *16*, 765–773.
- 199 CARUSO, F., CARUSO, R. A., MÖHWALD, H., Nanoengineering of Inorganic and Hybrid Hollow Spheres by Colloidal Templating, *Science* **1998**, *282*, 1111–1114.
- 200 CARUSO, F., LICHTENFELD, H., GIERSIG, M., MÖHWALD, H., Electrostatic Self-Assembly of Silica Nanoparticle – Polyelectrolyte Multilayers on Polystyrene Latex-Particles, *J. Am. Chem. Soc.* **1998**, *120*, 8523–8524.
- 201 DONATH, E., SUKHORUKOV, G. B., CARUSO, F., DAVIS, S. A., MÖHWALD, H., Novel Hollow Polymer Shells by Colloid-Templated Assembly of Polyelectrolytes, *Angew. Chem. Int. Ed. Engl.* **1998**, *37*, 2202–2205.
- 202 GAUMANN, A., LAUDES, M., JACOB, B., POMMERSHEIM, R., LAUE, C., VOGT, W., SCHREZENMEIR, J., Effect of Media Composition on Long-Term in-Vitro Stability of Barium Alginate and Polyacrylic-Acid Multilayer Microcapsules, *Biomaterials* **2000**, *21*, 1911–1917.
- 203 MOYA, S., DAHNE, L., VOIGT, A., LEPORATTI, S., DONATH, E., MÖHWALD, H., Polyelectrolyte Multilayer Capsules Templated on Biological Cells – Core Oxidation Influences Layer Chemistry, *Colloids Surf., A* **2001**, *183*, 27–40.
- 204 NEU, B., VOIGT, A., MITLOHNER, R., LEPORATTI, S., GAO, C. Y., DONATH, E., KIESEWETTER, H., MÖHWALD, H., MEISELMAN, H. J., BAUMLER, H., Biological Cells as Templates for Hollow Microcapsules, *J. Microencapsul.* **2001**, *18*, 385–395.
- 205 GAUMANN, A., LAUDES, M., JACOB, B., POMMERSHEIM, R., LAUE, C., VOGT, W., SCHREZENMEIR, J., Xenotransplantation of Parathyroids in Rats Using Barium-Alginate and Polyacrylic-Acid Multilayer Microcapsules, *Exp. Toxicol. Pathol.* **2001**, *53*, 35–43.
- 206 SCHNEIDER, S., FEILEN, P. J., SLOTTY, V., KAMPFNER, D., PREUSS, S., BERGER, S., BEYER, J., POMMERSHEIM, R., Multilayer Capsules – A Promising Microencapsulation System for Transplantation of Pancreatic-Islets, *Biomaterials* **2001**, *22*, 1961–1970.
- 207 ILER, R. K., Multilayers of Colloidal Particles, *J. Colloid Interface Sci.* **1966**, *21*, 569–594.
- 208 DECHER, G., Fuzzy Nanoassemblies: Toward Layered Polymeric Multicomposites. *Science* **1997**, *277*, 1232–1237.
- 209 LVOV, Y. M., DECHER, G., Assembly of Multilayer Ordered Films by Alternating Ad-

- sorption of Oppositely Charged Macromolecules, *Crystallogr. Rep.* **1994**, *39*, 628–647.
- 210 DECHER, G., Multilayer Films (Polyelectrolytes), in *The Polymeric Materials Encyclopedia: Synthesis, Properties, and Applications* (ed. SALAMONE, J. C.), CRC Press, Boca Raton, FL, **1996**, vol. 6, pp. 4540–4546.
- 211 KNOLL, W., Self-assembled Microstructures at Interfaces, *Curr. Opin. Colloid Interface Sci.* **1996**, *1*, 137–143.
- 212 LASCHEWSKY, A., Ultrathin Polymer Coatings by Self-organization Techniques, *Eur. Chem. Chronicle* **1997**, *2*, 13–24.
- 213 DECHER, G., ECKLE, M., SCHMITT, J., STRUTH, B., Layer-by-Layer Assembled Multicomposite Films, *Curr. Opin. Colloid Interface Sci.* **1998**, *3*, 32–39.
- 214 BERTRAND, P., JONAS, A., LASCHEWSKY, A., LEGRAS, R., Ultrathin Polymer-Coatings by Complexation of Polyelectrolytes at Interfaces – Suitable Materials, Structure and Properties, *Macromol. Rapid Commun.* **2000**, *21*, 319–348.
- 215 HAMMOND, P. T., Recent Explorations in Electrostatic Multilayer Thin Film Assembly. *Curr. Opin. Colloid Interface Sci.* **2000**, *4*, 430–442.
- 216 SHIMAZAKI, Y., MITSUISHI, M., ITO, S., YAMAMOTO, M., *Langmuir* **1997**, *13*, 1385–1387.
- 217 SHIMAZAKI, Y., MITSUISHI, M., ITO, S., YAMAMOTO, M., Preparation and Characterization of the Layer-by-Layer Deposited Ultrathin-Film Based on the Charge-Transfer Interaction in Organic-Solvents, *Langmuir* **1998**, *14*, 2768–2773.
- 218 SHIMAZAKI, Y., NAKAMURA, R., ITO, S., YAMAMOTO, M., Molecular-Weight Dependence of Alternate Adsorption Through Charge-Transfer Interaction, *Langmuir* **2001**, *17*, 953–956.
- 219 STOCKTON, W. B., RUBNER, M. F., Molecular-level processing of conjugated polymers. 4. Layer-by-layer manipulation of Polyaniline via Hydrogen-Bonding Interactions. *Macromolecules* **1997**, *30*, 2717–2725.
- 220 PONTES, R. S., RAPOSO, M., CAMILO, C. S., DHANABALAN, A., FERREIRA, M., OLIVEIRA, O. N., Nonequilibrium Adsorbed Polymer Layers via Hydrogen-Bonding, *Phys. Status Solidi A* **1998**, *173*, 41–50.
- 221 WANG, L. Y., CUI, S. X., WANG, Z. Q., ZHANG, X., JIANG, M., CHI, L. F., FUCHS, H., Multilayer Assemblies of Copolymer Psoh and PVP on the Basis of Hydrogen-Bonding, *Langmuir* **2000**, *16*, 10490–10494.
- 222 CLARK, S. L., HAMMOND, P. T., The Role of Secondary Interactions in Selective Electrostatic Multilayer Deposition, *Langmuir* **2000**, *16*, 10206–10214.
- 223 HAO, E. C., LIAN, T. Q., Layer-by-Layer Assembly of CdSe Nanoparticles Based on Hydrogen-Bonding, *Langmuir* **2000**, *16*, 7879–7881.
- 224 BERGBREITER, D. E., TAO, G. L., FRANCHINA, J. G., SUSSMAN, L., Polyvalent Hydrogen-Bonding Functionalization of Ultrathin Hyperbranched Films on Polyethylene and Gold. *Macromolecules* **2001**, *34*, 3018–3023.
- 225 SERIZAWA, T., HASHIGUCHI, S., AKASHI, M., Stepwise Assembly of Ultrathin Poly(Vinyl Alcohol) Films on a Gold Substrate by Repetitive Adsorption/Drying Processes, *Langmuir* **1998**, *15*, 5363–5368.
- 226 SERIZAWA, T., AKASHI, M., A Novel-Approach for Fabricating Ultrathin Polymer-Films by the Repetition of the Adsorption Drying Processes, *J. Polym. Sci. A* **1998**, *37*, 1903–1906.
- 227 FANG, M. M., KASCHAK, D. M., SUTORIK, A. C., MALLOUK, T. E., A Mix and Match Ionic-Covalent Strategy for Self-Assembly of Inorganic Multilayer Films, *J. Am. Chem. Soc.* **1997**, *119*, 12184–12191.
- 228 ICHINOSE, I., KAWAKAMI, T., KUNITAKE, T., Alternate Molecular Layers of Metal-Oxides and Hydroxyl Polymers Prepared by the Surface Sol-Gel Process, *Adv. Mater.* **1998**, *10*, 535–539.
- 229 KOETSE, M., LASCHEWSKY, A., MAYER, B., ROLLAND, O., WISCHERHOFF, E., Ultrathin Coatings by Multiple Polyelectrolyte Adsorption/Surface Activation (Compas). *Macromolecules*, **1998**, *31*, 9316–9327.
- 230 SUN, J. Q., WU, T., SUN, Y. P., WANG, Z. Q., ZHANG, X., SHEN, J. C., CAO, W. X., Fabrication of a Covalently Attached Multilayer via Photolysis of Layer-by-Layer Self-Assembled Films Containing Diazo-



- Resins, *Chem. Commun.* **1998**, 1853–1854.
- 231 HUCK, W. T. S., YAN, L., STROOCK, A., HAAG, R., WHITESIDES, G. M., Patterned Polymer Multilayers as Etch Resists, *Langmuir* **1999**, *15*, 6862–6867.
- 232 ICHINOSE, I., MUZUKI, S., OHNO, S., SHIRAIISHI, H., KUNITAKE, T., Preparation of Cross-Linked Ultrathin Films Based on Layer-by-Layer Assembly of Polymers, *Polym. J.* **1999**, *31*, 1065–1070.
- 233 KASCHAK, D. M., LEAN, J. T., WARAKSA, C. C., SAUPE, G. B., USAMI, H., MALLOUK, T. E.: Photoinduced Energy and Electron-Transfer Reactions in Lamellar Polyanion/Polycation Thin-Films – Toward an Inorganic Leaf, *J. Am. Chem. Soc.* **1999**, *121*, 3435–3445.
- 234 YAN, L., HUCK, W. T. S., ZHAO, X. M., WHITESIDES, G. M., Patterning Thin-Films of Poly(Ethylene Imine) on a Reactive SAM Using Microcontact Printing, *Langmuir* **1999**, *15*, 1208–1214.
- 235 HUCK, W. T. S., STROOCK, A. D., WHITESIDES, G. M., Synthesis of Geometrically Well-Defined, Molecularly Thin Polymer-Films, *Angew. Chem. Int. Edn. Engl.* **2000**, *39*, 1058.
- 236 KOHLI, P., BLANCHARD, G. J., Design and Demonstration of Hybrid Multilayer Structures – Layer-by-Layer Mixed Covalent and Ionic Interlayer Linking Chemistry, *Langmuir* **2000**, *16*, 8518–8524.
- 237 ROUSE, J. H., MACNEILL, B. A., FERGUSON, G. S., Sol-Gel Processing of Ordered Multilayers to Produce Composite Films of Controlled Thickness, *Chem. Mater.* **2000**, *12*, 2502–2507.
- 238 SUN, J. Q., WU, T., LIU, F., WANG, Z. Q., ZHANG, X., SHEN, J. C.: Covalently Attached Multilayer Assemblies by Sequential Adsorption of Polycationic Diazo-Resins and Polyanionic Poly(Acrylic Acid), *Langmuir* **2000**, *16*, 4620–4624.
- 239 SERIZAWA, T., HAMADA, K., KITAYAMA, T., KATSUKAWA, K., HATADA, K., AKASHI, M., Stepwise Assembly of Isotactic Poly(Methyl Methacrylate) and Syndiotactic Poly(Methacrylic Acid) on a Substrate, *Langmuir* **2000**, *16*, 7112–7115.
- 240 SERIZAWA, T., HAMADA, K., KITAYAMA, T., FUJIMOTO, N., HATADA, K., AKASHI, M., Stepwise Stereocomplex Assembly of Stereoregular Poly(Methyl Methacrylate) on a Substrate, *J. Am. Chem. Soc.* **2000**, *122*, 1891–1899.
- 241 SERIZAWA, T., YAMASHITA, H., FUJIWARA, T., KIMURA, Y., AKASHI, M.: Stepwise Assembly of Enantiomeric Poly(Lactide)s on Surfaces, *Macromolecules* **2001**, *34*, 1996–2001.
- 242 SPAETH, K., BRECHT, A., GAUGLITZ, G., Studies on the Biotin-Avidin Multilayer Adsorption by Spectroscopic Ellipsometry, *J. Colloid Interface Sci.* **1997**, *196*, 128–135.
- 243 ANZAI, J., KOBAYASHI, Y., SUZUKI, Y., TAKESHITA, H., CHEN, Q., OSA, T., HOSHI, T., DU, X. Y., Enzyme Sensors Prepared by Layer-by-Layer Deposition of Enzymes on a Platinum-Electrode Through Avidin-Biotin Interaction, *Sens. Actuators B* **1998**, *52*, 3–9.
- 244 ANZAI, J., KOBAYASHI, Y., NAKAMURA, N., NISHIMURA, M., HOSHI, T., Layer-by-Layer Construction of Multilayer Thin-Films Composed of Avidin and Biotin-Labeled Poly(Amine)s, *Langmuir* **1999**, *15*, 221–226.
- 245 ANZAI, J., KOBAYASHI, Y., Construction of Multilayer Thin-Films of Enzymes by Means of Sugar-Lectin Interactions, *Langmuir* **2000**, *16*, 2851–2856.
- 246 STEVENS, M. M., ALLEN, S., CHAN, W. C., DAVIES, M. C., ROBERTS, C. J., TENDLER, S. J. B., WILLIAMS, P. M., Probing Peptide-Protein Molecular Architecture by Atomic-Force Microscopy and Surface Plasmon Resonance, *Analyst* **2000**, *125*, 245–250.
- 247 SHIRATORI, S. S., RUBNER, M. F., PH-Dependent Thickness Behavior of Sequentially Adsorbed Layers of Weak Polyelectrolytes, *Macromolecules* **2000**, *33*, 4213–4219.
- 248 BÜSCHER, K., GRAF, K., AHRENS, H., HELM, C. A., Influence of Adsorption Conditions on the Structure of Polyelectrolyte Multilayers, *Langmuir* **2002**, *18*, 3585–3591.
- 249 RODRIGUEZ, L. N. J., DEPAUL, S. M., BARRETT, C. J., REVEN, L., SPIESS, H. W., Fast Magic-Angle-Spinning and Double-Quantum H-1 Solid-State NMR-Spectroscopy of Polyelectrolyte Multilayers, *Adv. Mater.* **2000**, *12*, 1934.

- 250 SCHWARZ, B., SCHÖNHOF, M., A 1H NMR relaxation study of hydration water in polyelectrolyte mono- and multilayers adsorbed to colloidal particles. *Colloids Surf. A* **2002**, 198–200, 293–304.
- 251 CARUSO, F., NIKURA, K., FURLONG, D. N., OKAHATA, Y., 1. Ultrathin Multilayer Polyelectrolyte Films on Gold: Construction and Thickness Determination, *Langmuir* **1997**, 13, 3422–3426.
- 252 KURTH, D. G., OSTERHOUT, R., In-Situ Analysis of Metallo-supramolecular Coordination Polyelectrolyte Films by Surface-Plasmon Resonance Spectroscopy, *Langmuir* **1999**, 15, 4842–4846.
- 253 RAMSDEN, J. J., LVOV, Y. M., DECHER, G., Determination of Optical Constants of Molecular Films Assembled via Alternate Polyelectrolyte Adsorption, *Thin Solid Films* **1995**, 254, 246–251; erratum: idem **1995**, 1261, 1343–1344.
- 254 LAVALLE, P., GERGELY, C., CUISINIER, F. J. G., DECHER, G., SCHAAF, P., VOEGEL, J.-C., PICART, C., Comparison of the Structure of Polyelectrolyte Multilayer Films Exhibiting a Linear and an Exponential Growth Regime: An in Situ Atomic Force Microscopy Study, *Macromolecules* **2002**, 35, 4458–4465.
- 255 LADAM, G., SCHAAD, P., VOEGEL, J. C., SCHAAF, P., DECHER, G., CUISINIER, F., In-situ Determination of the Structural Properties of Initially Deposited Polyelectrolyte Multilayers. *Langmuir* **2000**, 16, 1249–1255.
- 256 AUER, F., SCOTTI, M., ULMAN, A., JORDAN, R., SELLERGREN, B., GARNO, J., LIU, G. Y., Nanocomposites by Electrostatic Interactions-1-Impact of Sublayer Quality on the Organization of Functionalized Nanoparticles on Charged Self-Assembled Layers, *Langmuir* **2000**, 16, 7554–7557.
- 257 MENDELSON, J. D., BARRETT, C. J., CHAN, V. V., PAL, A. J., MAYES, A. M., RUBNER, M. F., Fabrication of Microporous Thin-Films from Polyelectrolyte Multilayers, *Langmuir* **2000**, 16, 5017–5023.
- 258 RUTHS, J., ESSLER, F., DECHER, G., RIEGLER, H., Polyelectrolytes I – Polyanion/Polycation Multilayers at the Air/Monolayer/Water Interface as Elements for Quantitative Polymer Adsorption Studies and Preparation of Hetero-Superlattices on Solid-Surfaces, *Langmuir* **2000**, 16, 8871–8878.
- 259 DUBAS, S. T., SCHLENOFF, J. B., Swelling and Smoothing of Polyelectrolyte Multilayers by Salt, *Langmuir* **2001**, 17, 7725–7727.
- 260 MULLER, M., RIESER, T., LUNKWITZ, K., MEIERHAACK, J., Polyelectrolyte Complex Layers – A Promising Concept for Anti-fouling Coatings Verified by in-Situ ATR-FTIR Spectroscopy, *Macromol. Rapid Commun.* **1999**, 20, 607–611.
- 261 LOWACK, K., HELM, C. A., Polyelectrolyte Monolayers at the Mica/Air Interface: Mechanically Induced Rearrangements and Monolayer Annealing, *Macromolecules* **1995**, 28, 2912–2921.
- 262 LOWACK, K., HELM, C. A., Molecular Mechanisms Controlling the Self-Assembly Process of Polyelectrolyte Multilayers, *Macromolecules* **1998**, 31, 823–833.
- 263 PLECH, A., SALDITT, T., MUNSTER, C., PEISL, J., Investigation of Structure and Growth of Self-Assembled Polyelectrolyte Layers by X-Ray and Neutron-Scattering Under Grazing Angles, *J. Colloid Interface Sci.* **2000**, 223, 74–82.
- 264 STEITZ, R., LEINER, V., SIEBRECHT, R., VON KLITZING, R., Influence of the Ionic-Strength on the Structure of Polyelectrolyte Films at the Solid/Liquid Interface, *Colloids Surf., A* **2000**, 163, 63–70.
- 265 TRAN, Y., AUROY, P., Complexation and Distribution of Counterions in a Grafted Polyelectrolyte Layer, *Eur. Phys. J. E* **2001**, 5, 65–79.
- 266 MCALONEY, R. A., GOH, M. C., In-Situ Investigations of Polyelectrolyte Film Formation by 2nd- Harmonic Generation, *J. Phys. Chem. B* **1999**, 103, 10729–10732.
- 267 BABA, A., KANEKO, F., ADVINCULA, R. C., Polyelectrolyte Adsorption Processes Characterized in-Situ Using the Quartz-Crystal Microbalance Technique – Alternate Adsorption Properties in Ultrathin Polymer-Films, *Colloids Surf., A* **2000**, 173, 39–49.
- 268 GINZBURG, M., GALLORO, J., JAKLE, F., POWERBILLARD, K. N., YANG, S. M., SOKOLOV, I., LAM, C. N. C., NEUMANN, A. W., MANNERS, I., OZIN, G. A., Layer-by-Layer Self-Assembly of Organic-Organometallic



- Polymer Electrostatic Superlattices Using Poly(Ferrocenylsilanes), *Langmuir* **2000**, *16*, 9609–9614.
- 269 PARDOYISSAR, V., KATZ, E., LIOUBASHEVSKI, O., WILLNER, I., Layered Polyelectrolyte Films on Au Electrodes – Characterization of Electron-Transfer Features at the Charged Polymer Interface and Application for Selective Redox Reactions, *Langmuir* **2001**, *17*, 1110–1118.
- 270 OKUBO, T., SUDA, M., Alternate Sign Reversal in the Zeta-Potential and Synchronous Expansion and Contraction in the Absorbed Multilayers of Poly(4-Vinyl-N-N-Butylpyridinium Bromide) Cations and Poly(Styrene Sulfonate) Anions on Colloidal Silica Spheres, *Colloid Polym. Sci.* **1999**, *277*, 813–817.
- 271 SCHWARZ, S., EICHHORN, K. J., WISCHERHOFF, E., LASCHEWSKY, A., Polyelectrolyte Adsorption Onto Planar Surfaces – A Study by Streaming Potential and Ellipsometry Measurements, *Colloids Surf., A* **1999**, *159*, 491–501.
- 272 CARUSO, F., FIEDLER, H., HAAGE, K., Assembly of Beta-Glucosidase Multilayers on Spherical Colloidal Particles and Their Use as Active Catalysts, *Colloids Surf., A* **2000**, *169*, 287–293.
- 273 MOYA, S., DONATH, E., SUKHORUKOV, G. B., AUCH, M., BAUMLER, H., LICHTENFELD, H., MÖHWALD, H., Lipid Coating on Polyelectrolyte Surface-Modified Colloidal Particles and Polyelectrolyte Capsules, *Macromolecules* **2000**, *33*, 4538–4544.
- 274 OKUBO, T., SUDA, M., Synchronous Alternate Multilayered Adsorption of Poly(4-Vinyl-N-N-Butylpyridinium) Cations and Poly(Styrene Sulfonate) Anions on Polystyrene Colloidal Spheres, *Colloid Polym. Sci.* **2000**, *278*, 380–384.
- 275 NETZ, R. R., JOANNY, J. F., Adsorption of Semiflexible Polyelectrolytes on Charged Planar Surfaces – Charge Compensation, Charge Reversal, and Multilayer Formation, *Macromolecules* **1998**, *32*, 9013–9025.
- 276 ANDELMAN, D., JOANNY, J. F., Polyelectrolyte Adsorption, *C. R. Acad. Sci. Ser. IV Phys. Astron.* **2000**, *1*, 1153–1162.
- 277 CASTELNOVO, M., JOANNY, J. F., Formation of Polyelectrolyte Multilayers, *Langmuir* **2000**, *16*, 7524–7532.
- 278 JOANNY, J. F., CASTELNOVO, M., NETZ, R., Adsorption of Charged Polymers, *J. Phys.: Condens. Matter* **2000**, *12*, A1–A7.
- 279 SCHLENOFF, J. B., DUBAS, S. T., Mechanism of Polyelectrolyte Multilayer Growth – Charge Overcompensation and Distribution, *Macromolecules* **2001**, *34*, 592–598.
- 280 SCHLENOFF, J. B., DUBAS, S. T., FARHAT, T., Sprayed Polyelectrolyte Multilayers, *Langmuir* **2000**, *16*, 9968–9969.
- 281 CHO, J., CHAR, K., HONG, J.-D., LEE, K.-B., Fabrication of Highly Ordered Multilayer Films Using a Spin Self-Assembly Method, *Adv. Mater.* **2001**, *13*, 1076–1078.
- 282 LEE, S.-S., HONG, J.-D., KIM, C. H., KIM, K., KOO, J. P., LEE, K.-B., Layer-by-Layer Deposited Multilayer Assemblies of Ionenene-Type Polyelectrolytes Based on the Spin-Coating Method, *Macromolecules* **2001**, *34*.
- 283 CHIARELLI, P. A., JOHAL, M. S., CASSON, J. L., ROBERTS, J. B., ROBINSON, J. M., WANG, H.-L., Controlled Fabrication of Polyelectrolyte Multilayer Thin Films Using Spin-Assembly, *Adv. Mater.* **2001**, *13*, 1167–1171.
- 284 SUKHORUKOV, G. B., SCHMITT, J., DECHER, G., Reversible Swelling of Polyanion/Polycation Multilayer Films in Solutions of Different Ionic Strength, *Ber. Bunsen-Ges. Phys. Chem.* **1996**, *100*, 948–953.
- 285 DUBAS, S. T., SCHLENOFF, J. B., Polyelectrolyte Multilayers Containing a Weak Polyacid – Construction and Deconstruction, *Macromolecules* **2001**, *34*, 3736–3740.
- 286 HAMMOND, P. T., WHITESIDES, G. M., Formation of Polymer Microstructures by Selective Deposition of Polyion Multilayers Using Patterned Self-Assembled Monolayers as a Template, *Macromolecules* **1995**, *28*, 7569–7571.
- 287 CLARK, S. L., MONTAGUE, M., HAMMOND, P. T., Selective Deposition in Multilayer Assembly: SAMs as Molecular Templates, *Supramol. Sci.* **1997**, *4*, 141–146.
- 288 CLARK, S. L., MONTAGUE, M. F., HAMMOND, P. T., The Effect of Ion Type and Ionic Content on Templating Patterned Ionic Multilayers, *ACS Symp. Ser.* **1998**, *695*, 206–219.

- 289 CHEN, K. M., JIANG, X. P., KIMERLING, L. C., HAMMOND, P. T., Selective Self-Organization of Colloids on Patterned Polyelectrolyte Templates, *Langmuir* **2000**, *16*, 7825–7834.
- 290 XIA, Y., WHITESIDES, G. M., *Angew. Chem. Int. Ed. Engl.* **1998**, *37*, 551.
- 291 HUCK, W. T. S., STROOCK, A. D., WHITESIDES, G. M., Synthesis of Geometrically Well-Defined, Molecularly Thin Polymer-Films, *Angew. Chem. Int. Ed. Engl.* **2000**, *39*, 1058.
- 292 YANG, S. Y., RUBNER, M. F., Micropatterning of Polymer Thin Films with pH-Sensitive and Cross-linkable Hydrogen-Bonded Polyelectrolyte Multilayers, *J. Am. Chem. Soc.* **2002**, *124*, 2100–2101.
- 293 CHEN, J. Y., LUO, H., YANG, B. X., CAO, W. X., Photoimaging Technique on Printing Al Plate via Self-Assembly Multilayer Films Based on Diazo-resin, *J. Appl. Polym. Sci.* **2001**, *80*, 1983–1987.
- 294 DELCORTE, A., BERTRAND, P., ARYS, X., JONAS, A., LEGRAS, R., WISCHERHOFF, E., MAYER, B., LASCHEWSKY, A., Characterisation of Alternate Polyelectrolyte Thin films by Surface Techniques. *Surf. Sci.* **1996**, *366*, 149–165.
- 295 PHUVANARTNURUKS, V., MCCARTHY, T. J., Stepwise Polymer Surface Modification – Chemistry-Layer-by-Layer Deposition, *Macromolecules* **1998**, *31*, 1906–1914.
- 296 SCHLENOFF, J. B., LY, H., LI, M., Charge and Mass-Balance in Polyelectrolyte Multilayers, *J. Am. Chem. Soc.* **1998**, *120*, 7626–7634.
- 297 LADAM, G., SCHAAD, P., VOEGEL, J. C., SCHAAF, P., DECHER, G., CUISINIER, F., In-Situ Determination of the Structural-Properties of Initially Deposited Polyelectrolyte Multilayers, *Langmuir* **2000**, *16*, 1249–1255.
- 298 POINTU, D., DECHER, G., Vers une Compréhension de la Croissance et de la Structure des Films Multicouches de Polyelectrolytes, Actualites GFP **2000**, *Bulletin No 88*, 3.
- 299 LÖSCHE, M., SCHMITT, J., DECHER, G., BOUWMAN, W. G., KJAER, K., Detailed structure of molecularly thin polyelectrolyte multilayer films on solid substrates as revealed by neutron reflectometry, *Macromolecules* **1998**, *31*, 8893–8906.
- 300 KORNEEV, D., LVOV, Y., DECHER, G., SCHMITT, J., YARADAİKIN, S., Neutron Reflectivity Analysis of Self-Assembled Film Superlattices with Alternate Layers of Deuterated and Hydrogenated Polystyrenesulfonate and Polyallylamine, *Physica B* **1995**, *213*, 214, 954–956.
- 301 HONG, H. P., STEITZ, R., KIRSTEIN, S., DAVIDOV, D., Superlattice Structures in Poly(Phenylenevinylene)-Based Self-Assembled Films, *Adv. Mater.* **1998**, *10*, 1104.
- 302 TARABIA, M., HONG, H., DAVIDOV, D., KIRSTEIN, S., STEITZ, R., NEUMANN, R., AVNY, Y., Neutron and X-Ray Reflectivity Studies of Self-Assembled Heterostructures Based on Conjugated Polymers, *J. Appl. Phys.* **1998**, *83*, 725–732.
- 303 KIRSTEIN, S., HONG, H. P., STEITZ, P., DAVIDOV, D., Super-Lattice Structure in PPV-Based Self-Assembled Films, *Synth. Met.* **1999**, *102*, 1067–1068.
- 304 ARYS, X., LASCHEWSKY, A., JONAS, A. M., Ordered Polyelectrolyte Multilayers-1-Mechanisms of Growth and Structure Formation – A Comparison with Classical Fuzzy Multilayers, *Macromolecules* **2001**, *34*, 3318–3330.
- 305 SCHMITT, J., DECHER, G., DRESSIK, W. J., BRANDOW, S. L., GEER, R. E., SHASHIDHAR, R., CALVERT, J. M., Metal Nanoparticle/Polymer Superlattice Films: Fabrication and Control of Layer Structure, *Adv. Mater.* **1997**, *9*, 61–65.
- 306 SCHMITT, J., MÄCHTLE, P., ECK, D., MÖHWALD, H., HELM, C. A., Preparation and Optical-Properties of Colloidal Gold Monolayers, *Langmuir* **1999**, *15*, 3256–3266.
- 307 KOLARIK, L., FURLONG, D. N., JOY, H., STRUIJK, C., ROWE, R., Building Assemblies from High-Molecular-Weight Polyelectrolytes, *Langmuir* **1999**, *15*, 8265–8275.
- 308 CHEN, K., CALDWELL, W. B., MIRKIN, C. A., Fullerene Self-Assembly onto (MeO)3Si(CH2)3NH2-Modified Oxide Surfaces, *J. Am. Chem. Soc.* **1993**, *115*, 1193–1194.
- 309 CARUSO, F., Hollow Capsule Processing Through Colloidal Templating and Self-Assembly, *Chem.-Eur. J.* **2000**, *6*, 413–419.

## 2

# Fundamentals of Polyelectrolyte Complexes in Solution and the Bulk

V. KABANOV

### Abstract

Interpolyelectrolyte coupling reactions resulting in the formation of insoluble stoichiometric or soluble nonstoichiometric interpolyelectrolyte complexes (IPEC)s, and IPEC interchange reactions are discussed in the light of their thermodynamics, kinetics and mechanisms. It is shown that the solution behavior of equilibrated nonstoichiometric IPECs is similar to ordinary polyelectrolytes on the one hand, and to segmented polymers on the other. Transformations of IPECs in external salt solutions include redistribution of electrostatically coupled chains and phase separation. These processes are substantially dependent not only on electrostatic interactions but also specific interactions of small ions with IPEC forming polyelectrolyte counterparts. They are important for understanding the essence of IPECs as a special family of polymeric substances. In particular, the formation of polycation–polyanion alternating layers by consecutive surface deposition of oppositely charged polyelectrolytes is dependent on the above mentioned transformations. The same is true for the complexation of polyelectrolytes with oppositely charged hydrogels. Factors controlling the interpenetration of linear polyions into highly swollen oppositely charged networks may play an important role in determining the morphology and thickness of polyelectrolyte layers. Finally, data on the conformations of polyelectrolyte chains in the bulk IPECs and the thermomechanical behavior of slightly swollen IPECs are considered.

### 2.1

#### Introduction

Interpolyelectrolyte complexes (IPECs) form a special class of polymeric compounds [1–6], consisting of oppositely charged polyions. Depending on their composition, IPECs can be either insoluble but swellable, or soluble in water solution.

Investigations of IPECs have a quite lengthy history. As early as the 1930s, the attention of colloid chemists was attracted by the fact that upon mixing aqueous solutions of oppositely charged natural polyelectrolytes, characterized by a relatively low charge density on the macromolecules (e.g. gelatin and gum arabic), un-

der certain conditions, a phase separation and the formation of liquid coacervates takes place [7–9]. These studies were later developed mainly in terms of the description of the conditions of phase separation [10, 11].

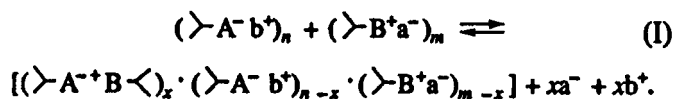
Insoluble IPECs have also been known for many years [1, 12–14] at least since the beginning of the 1960s when a number of synthetic polyelectrolytes with a high linear charge density became available. Some practical applications have been reported. In particular, insoluble IPECs show unique efficiency as hydrophilic soil binders, preventing wind and water erosion. Such an IPEC composition was used, for example, after the Chernobyl accident to suppress the formation of radioactive aerosols in contaminated dusty areas. On an industrial scale, insoluble IPECs were also demonstrated to be much more effective than the individual polyelectrolytes in coagulating colloid dispersions, particularly slag wastes in metallurgy, see for example [15]. They have been also reported as biocompatible coatings for hemosorbents and other medical items in contact with blood and other biological fluids, see for example [16]. There are also some other promising applications. One of them is the formation of ultrathin multilayer polymer coatings by complexation of polyelectrolytes at interfaces.

Finding soluble IPECs as isolated examples [17, 18] and then establishing the general conditions of soluble IPEC formation, valid for most pairs of oppositely charged polyelectrolytes [3, 5, 19, 20], marked a significant breakthrough in the field. It brought studies to a qualitatively new level, owing to the application of modern techniques commonly used for studying macromolecules in solution (light scattering, analytical ultracentrifugation, viscometry, GPC etc.). The fundamental data obtained with these methods led to a deeper understanding of the structural organization and specific behavior of IPECs, not only in solution, but also in concentrated phases. At the same time, these studies opened up a new range of prospective applications of IPECs, related primarily to biomimetics, biotechnology and medicine [21–25].

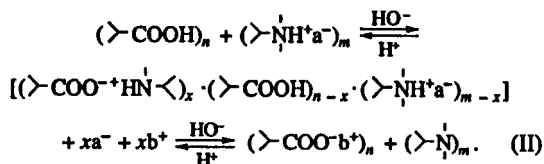
## 2.2

### Interpolyelectrolyte Reactions and Solution Behavior of Interpolyelectrolyte Complexes

The simplest way to prepare IPECs is to mix two aqueous solutions, one of which contains a polyanion and the other a polycation. The degree of conversion  $\Theta$  in Scheme I is defined as the ratio of an existing or equilibrium number of interpolyion salt bonds (ion pairs) to their maximum number ( $\Theta = x/m$ , when  $n \geq m$ , and  $\Theta = x/n$  when  $n < m$ ). Complexation of weak polyelectrolytes can be conveniently controlled by varying the pH [3, 6], see Scheme II. In these cases, IPECs can be prepared under equilibrium conditions by gradually acidifying the reaction mixture or making it more alkaline.



Scheme I



Scheme II

The value of  $\theta$  can be calculated from the data of potentiometric titration [3, 6]

$$\theta = \left( m_b/V + [\text{H}^+] - \sqrt{K_a c_0} \right) / c_0 \quad (\text{weak polyacid}), \quad (1)$$

$$\theta = \left( m_a/V + [\text{OH}^-] - \sqrt{K_b c_0} \right) / c_0 \quad (\text{weak polybase}), \quad (2)$$

where  $m_a$  or  $m_b$  is the molar amount of added acid or base,  $V$  is the volume of the reaction mixture,  $K_a$  and  $K_b$  are intrinsic dissociation constants of polyacid and polybase, and  $c_0$  is the concentration of one of the polyelectrolytes.

Fig. 2.1 shows typical  $\theta$  versus pH plots (solid lines) calculated from experimental titration curves of weak polyelectrolytes in the presence of oppositely charged polyion counterparts. The plots enclose the pH region in which IPEC can be formed in the absence of an external salt. If one of the interacting polyelectrolytes is weak while the other is strong, such a region is defined by a single plot only. The dashed lines in the same figure show the pH versus the degree of ionization  $\alpha$  of the individual polyelectrolytes. In other words, polyacids and polybases whose ionization is pH controlled show respectively either stronger acidity, or stronger basicity in the presence of oppositely charged polyions, compared to their individual behavior.

The quantity  $\Delta\text{pH}(\theta, \alpha)$  is a measure of the free energy,  $\Delta G_{\text{cs}}$ , providing the driving force for complexation and characterizing multisite interaction of the oppositely charged repeating units at a specified  $\theta = \alpha$

$$\Delta\text{pH}(\theta, \alpha) = [\Delta G(\alpha) - \Delta G(\theta)] / 2.3RT = \Delta G_{\text{cs}}(\theta, \alpha) / 2.3RT \quad (3)$$

Here,  $\Delta G(\alpha)$  and  $\Delta G(\theta)$  are the free energies of ionization of a weak polyelectrolyte in the absence and in the presence of the oppositely charged polyion respec-

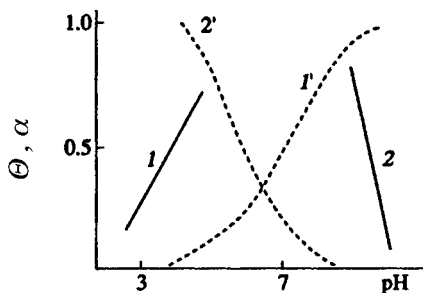


Fig. 2.1 Typical dependences of degree of conversion,  $\theta$ , in the weak polyelectrolytes coupling reaction (1, 2) and their individual degrees of ionization,  $\alpha$ , (1', 2') on pH in aqueous solution.

tively. Equation (3) was derived on the assumption that each ionized group of a titrated polyelectrolyte component forms a salt bond (ion pair) with an oppositely charged polyion. It is close to reality if the ratio between ionizable groups of the components  $Z=m/n=1$ , or at  $Z \neq 1$ , if the total number of ionizable groups of a titrated weak polyelectrolyte is smaller than the degree of polymerization (DP) of the completely ionized counterpart.

The free energy decrease responsible for shifting an equilibrium as in Schemes I or II to formation of IPECs is basically due to an entropy gain caused by release of counterions originally localized in the vicinity of the polyelectrolyte coils. However, depending on the polyelectrolyte composition and structure other attraction factors such as hydrophobic interaction, hydrogen bonding, charge-transfer etc. may also contribute.

In terms of conventional classification, Schemes I and II describing the formation of IPECs represent ionic exchange and neutralization reactions, respectively. However, with respect to polyion interaction these processes may be considered as *polyion coupling reactions*.

IPECs can also result from polymerization of ionic monomers on oppositely charged polyions, which act as templates [26]. Then the total free energy change  $\Delta G_{tp}$  may be treated as consisting of two components

$$\Delta G_{tp} = \Delta G_p + \Delta G_{cs} \quad (4)$$

where  $\Delta G_p$  is the free energy of polymerization in the absence of a template. The negative value of  $\Delta G_{cs}$  functions as a thermodynamic factor promoting formation of the polymer. This factor can be decisive when polymerization of the free monomer is thermodynamically disfavored ( $\Delta G_p > 0$ ). In this case  $\Delta G_{tp}$  is still negative, if  $|\Delta G_{cs}| > |\Delta G_p|$ . In other words, as a potential component of IPECs, a templating polyion may shift a polymerization–depolymerization equilibrium towards formation of the oppositely charged polyion counterpart.

In principle, the same factor (i.e.,  $\Delta G_{cs}$ ) is responsible for clustering of protein globules by oppositely charged polyions upon polyelectrolyte–protein complexation [27–29] and aggregation of ionic surfactants occurring in polyelectrolyte solutions and hydrogels at surfactant concentrations markedly lower than the intrinsic c.m.c. values [30–36]. Both of these processes amount to “polymerization” of protein globules or surfactant ions on oppositely charged polymer templates.

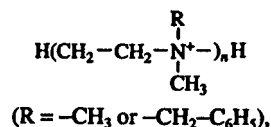
For a given structure of polyelectrolyte components the ability of IPECs to dissolve or swell in water is controlled by  $Z$ ,  $\theta$  and the ratio of DP of oppositely charged polyions, as well as by the composition of the aqueous phase (nature and concentration of external salts, pH, organic additives, etc.). If  $Z=1$ , and  $\theta$  is close to unity, stoichiometric IPECs are formed as the product of an interpolyelectrolyte reaction. Such IPECs are always insoluble, but swell to a limited extent in water.

Under certain conditions, water-soluble IPECs can be prepared using most pairs of oppositely charged polyelectrolytes [3, 5, 19, 20]. At  $Z=1$ , solubility may be achieved only at  $\theta < 1$ , that is, for the products of an incomplete Scheme II [19]. Then, free units of polyelectrolytes which have not formed interchain salt bonds act as hydrophilic fragments “holding” IPEC species in solution.



However, IPECs may be soluble in water at  $\Theta$  equal or close to 1, but only at  $Z \neq 1$  and if the DP of an excess polyion component is higher (host polyelectrolyte, HPE), than that of a deficient one (guest polyelectrolyte, GPE). Then the ratio of GPE to HPE repeating units within IPEC species is  $\varphi = [\text{GPE}]/[\text{HPE}] < \varphi_c < 1$  (at uniform distribution of GPE by HPE  $\varphi = Z$ ). The critical value  $\varphi_c$  determines the ultimate population of HPE by GPE chains above which the hydrophilicity of the excess single-stranded segments is no longer sufficient to meet the lowest free energy minimum to hold all the IPEC species in solution. For the majority of systems studied,  $\varphi_c$  is predominantly controlled by the chemical structure of polyelectrolyte components and lies between 0.6 and 0.2.

In the pH range confined by potentiometric titration curves 1 and 2 (Fig. 2.1) the cooperative character of multisite electrostatic bonding ensures very high stability of IPECs with respect to their individual components. The effective dissociation constant at  $\Theta$  close to 1 sharply decreases while the length of GPE increases and approaches close to zero even for relatively short oligomers. For example, in the case of quaternized linear ethyleneimine oligomers (Structure 1) interacting with poly(methacrylate) (PMA) polyanions, the degree of dissociation of the corresponding IPECs becomes negligible starting from about the octamer and higher [4, 37]. Similar behavior was reported for oligo(phosphate)s interacting with poly(*N*-dimethylaminoethyl methacrylate) (PDMAEMA) [38] and for oligo(2,5-ionene)s interacting with poly(acrylate) (PA) polyanions [39]. Therefore, after attaining a certain critical length of polyions, IPECs formed practically do not dissociate to initial polyion components.



Structure 1

If polyelectrolytes have one or more ordered conformations in solution, such as ionic polypeptides or DNA, oppositely charged polyelectrolyte counterparts are able either to stabilize or destabilize these conformations on complexation [6, 23]. For example, free poly(lysine) (PL) having  $\alpha$ -helical conformation in strongly alkaline media transforms into a random coil on protonation of the amine groups in water-ethanol mixed solvent even at pH 9–8.5. At the same time PL being fully protonated within PL–PMA IPEC retains its helicity over a broad pH range. The helix–coil transition occurs only at pH 4–3.5 when the IPEC is decomposed as a result of protonation of -COO<sup>-</sup> groups in PMA [6]. In other words the PL  $\alpha$ -helix is stabilized by complexation. However, this is not the case for poly(glutamic acid) (PGA). The PGA  $\alpha$ -helix being stable in acidic water solutions transforms into a random coil at pH 6.0–6.5. At the same time helix–coil transition occurs at pH 3–4 in the presence of linear poly(ethylene imine) (PEI) polycations, when PGA–PEI IPEC is formed. The conclusion is that ion pairing of the PGA  $\alpha$ -helix with PEI is less favorable thermodynamically in comparison with the PGA random coil [6]. Another example relates to DNA. It is known that free native DNA in aqueous so-

lution has the B-form of the double helix. Complexation with polycations results in transformation of the B-form into the more compact C- or A-forms [23].

### 2.2.1

#### Kinetics and Mechanism of Polyelectrolyte Coupling and Interchange Reactions

As is obvious from Scheme I the course of polyelectrolyte coupling reactions between strong polyelectrolytes may be monitored by any experimental technique capable of measuring the amount of released counterions, such as elemental analysis, conductivity, ion-specific potentiometry etc. Methods applicable to salt free polyelectrolyte solutions cannot always be used at relatively high concentrations of external salts.

If one of the polyelectrolytes is a weak polyacid or polybase, the extent of the reaction may be determined by measuring pH [6]. However, this method is valid only for the pH range where  $\Theta$  does not exceed 0.4–0.5 [23].

Luminescence quenching measurements are very useful for quantitative studies of the formation and transformations of soluble IPECs, if one of the polyelectrolytes carries a luminescence group and the counterpart is a luminescence quencher. Then the extent of oppositely charged polyion in contact with each other within IPEC species can be monitored at any pH, either in the presence or in absence of external salts, simply by measuring luminescence intensity.

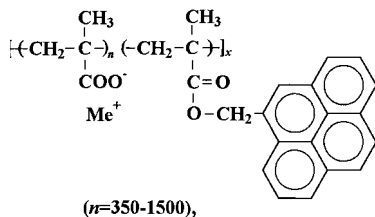
Using this technique, the kinetics of some typical polyelectrolyte coupling reactions has been studied. In parallel with this, the IPECs ability to take part in polyion interchange reactions [40–43] has been revealed. The evidence of such interchange with respect to complexation of DNA with poly(*N*-ethyl-4-vinylpyridinium-bromide) was noted earlier [17]. The general scheme of an interchange reaction can be represented as shown in Scheme III where  $n$  or  $x$  is the number of GPE chains in the IPEC species. If  $\text{HPE}_1$  is identical to  $\text{HPE}_2$ , Scheme III with respect to IPEC–polyion interaction represents the *polyion self-exchange reaction*. If  $\text{HPE}_1$  and  $\text{HPE}_2$  are chemically different Scheme III can be considered as a *polyion substitution reaction*. GPE exchange can also proceed as intra-IPEC rearrangement involving various segments of HPE within the same IPEC species. This is equivalent to migration of GPE inside the HPE coil. The fact that such a migration is possible gives an opportunity for internal rearrangements in IPEC particles and their optimization for interaction with their surroundings.



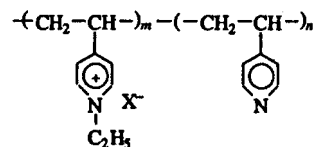
#### Scheme III

Most studies [40–47] were conducted using fluorescence tagged poly(methacrylate) (PMA\*) [48] containing one anthryl or pyrenyl tag per 350–1500 repeating units (Structure 2) and (*N*-ethyl-4-vinylpyridinium)-vinylpyridine co-polymer polycations (PVP) (Structure 3) prepared by quaternization of the fractions of poly(4-vinylpyridine) with ethyl bromide [49]. The content of quaternized units was controlled by the degree of quaternization  $\beta(\%) = [m/(m+n)]100$ . Hereafter most of the described experiments have been performed with PVP of close to 100%, except the cases

specially noted. Vinylpyridinium (VP) units are quenchers of the fluorescence of anthryl and pyrenyl groups.



Structure 2



Structure 3

The kinetics of a representative polyion coupling reaction were studied using pyrenyl tagged Na PMA\* and PVP [44, 46]. Formation of the PMA\*–PVP complex results in a decrease in the fluorescence intensity,  $I$ , of the pyrenyl tags attached to PMA\* chains due to quenching by bound PVP. The reaction mixture was prepared by quick injection of 0.02 ml of aqueous PVP solution into the cell containing 1.5 ml of Na PMA\* under continuous stirring, so that the mixing time did not exceed 2–4 s. The data of Fig. 2.2 show that mixing the reagents in the absence of an external salt is accompanied by an immediate drop of  $I$  to a constant level corresponding to a certain number of rapidly formed contacts between PMA\* and PVP (curve 1). However, the observed decrease is smaller than expected in the case of the equilibrated system containing PMA\*–PVP IPEC of the same composition (curve 1'). Moreover, mixing of the same reagent solutions but at  $[\text{NaCl}]=0.03 \text{ M}$  resulted in a much larger fall in the  $I$  value and its gradual decrease tending to the equilibrium level (cf. curves 2 and 2').

Stop-flow measurements have shown that the fast stage of the polyion coupling reaction, corresponding to the falls on the kinetic curves is actually characterized by the rate constant of the order  $10^9 \text{ l mol}^{-1} \text{ s}^{-1}$  that is close to the bimolecular rate constant expected for diffusion collisions of the polyelectrolyte coils in dilute solution [44, 46]. Such collisions between the oppositely charged polyions result in the formation of random salt bonds. Polyanion–polycation associates formed remain “frozen” in a non-equilibrium state while the concentration of a simple salt is very small (Fig. 2.2, curve 1). In contrast, in the presence of an external salt, the non-equilibrium association initially formed appears not to be frozen: intramolecular and intermolecular rearrangements of the interacting polyions are not restricted. Apparently, due to such rearrangements, the number of salt bonds between the polyions increases, so that primary associates gradually transform into the equilibrated PMA\*–PVP IPEC species (Fig. 2.2, curve 2). The above rearrangements occur via

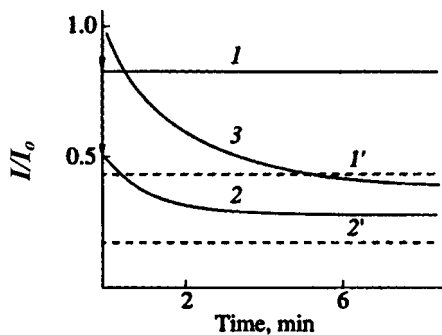


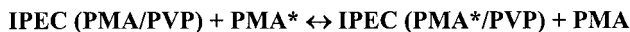
**Fig. 2.2** Typical kinetic curves of polyion coupling and exchange reactions.  $I$  and  $I_0$  are the current and initial PMA\* fluorescence intensities ( $\lambda_{\text{ex}}=342$  nm,  $\lambda_{\text{reg}}=395$  nm) (1) Na PMA\* ( $DP_w=4.4 \times 10^3$ , 1 label per 600 monomer units) + PVP ( $DP_w=2.0 \times 10^2$ ,  $\beta=95\%$ ) in the absence of an external salt;  $[\text{Na PMA}^*]=8.6 \times 10^{-8}$  mol  $\text{l}^{-1}$  (as calculated per polyion),

$Z=[\text{PVP}]/[\text{Na PMA}^*]=0.2$ . (2) The same reaction in the presence of  $[\text{NaCl}]=0.03$  mol  $\text{l}^{-1}$ .

(3) (PMA-PVP) IPEC + Na PMA\*,  $[\text{Na PMA}^*]=[\text{IPEC}]=8.6 \times 10^{-8}$  mol  $\text{l}^{-1}$ ,  $P_w=4.4 \times 10^3$ ,  $\varphi=0.2$ ,  $T=20^\circ\text{C}$ , pH 10,  $\theta \rightarrow 1$ . (1') is the equilibrium limit for curve 1, (2') is the equilibrium limit for curves 2 and 3 [46].

polyion exchange reactions involving segments of oppositely charged chains. Curve 3 in Fig. 2.2 demonstrates the pure case of a polyion exchange. Pyrenyl tags attached to PMA\* chains contribute an additional hydrophobic interaction stabilizing the PMA\*-PVP IPECs as compared to the PMA-PVP IPEC species. Therefore, PMA\* replaces PMA in the complex. Hence, curve 2 may be considered qualitatively as the superposition of kinetic curves 1 and 3. In other words, the occurrence of a single pyrenyl tag per several hundred monomer units in PMA\* is sufficient for PVP to prefer the tagged PMA chain to the ordinary PMA.

For soluble IPECs, it has been shown [45, 46] that the polyion exchange reaction involving transfer of a single GPE chain (PVP) from HPE<sub>1</sub> (PMA) to HPE<sub>2</sub> (PMA\*) in dilute solution is of second order kinetics with respect to the concentrations of interacting polymer species (IPEC and PMA\*) (Scheme III').



**Scheme III'**

The experimental kinetic curves are perfectly linearized in coordinates of Eq. (5)

$$q/(1-q) = k_2[\text{PMA}^*]_0 t \quad (5)$$

where  $q$  is the degree of conversion in Scheme III', and  $[\text{PMA}^*]_0 = [\text{PMA}]_0 = [\text{IPEC}]_0$  are initial molar concentrations of the reacting species. This makes it possible to determine the absolute rate constant,  $k_2$ , for GPE transfer from one HPE chain to another under various conditions. The data are listed in Tab. 2.1.

One can see that, in agreement with Eq. (5),  $k_2$  values are independent of the concentration of the reacting species (runs 1–3 and 6). It is also important that  $k_2$

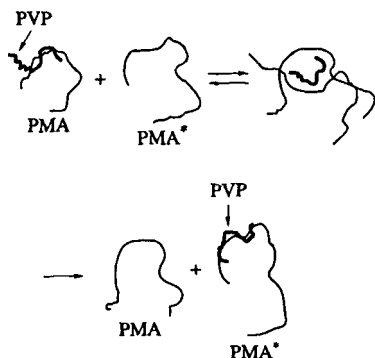
**Tab. 2.1** Rate constants of the polyion exchange reaction between (PMA–PVP) IPEC and PMA\*Na (pH 10,  $\theta \rightarrow 1$ ,  $T=20^\circ\text{C}$ )

Run No.	[PMA*Na] $10^9 / \text{mol l}^{-1}$	$P_w \times 10^3$		$\beta$ (%)	[NaCl] / $\text{mol l}^{-1}$	$k_2 \times 10^5 / \text{mol l}^{-1} \text{ s}^{-1}$
		PVP	PMA			
1	3	0.6	3.9	95	0.08	5.1
2	7	0.6	3.9	95	0.08	5.0
3	15	0.6	3.9	95	0.08	4.7
4	40	0.6	3.9	95	0.06	1.2
5	40	0.6	3.9	95	0.07	2.6
6	40	0.6	3.9	95	0.08	5.1
7	40	0.6	3.9	95	0.09	8.7
8	33	0.1	4.4	95	0.04	2.0
9	33	0.1	1.0	95	0.04	2.0
10	28	0.6	4.4	95	0.07	1.5
11	28	0.32	4.4	95	0.07	6.0
12	28	0.2	4.4	95	0.07	11.0
13	28	0.1	4.4	95	0.07	23.0
14	23	0.2	2.8	89	0.035	0.2
15	23	0.2	2.8	80	0.035	0.7
16	23	0.2	2.8	69	0.035	2.6
17	23	0.2	2.8	62	0.035	16.2
18	23	0.2	2.8	55	0.035	36.1

The  $[\text{PMA}^*]_0 = [\text{PMA}]_0$  values are given as calculated per polyion;  $P_w(\text{PMA}) = P_w(\text{PMA}^*)$ , PMA\* contains one pyrenyl label per 350 units.

is independent of HPE (PMA) degree of polymerization (runs 8 and 9) but decreases sharply with increasing degree of polymerization of GPE (PVP) (runs 10–13). Under the conditions used,  $k_2$  is of the order of  $10^4$ – $10^6$   $1 \text{ mol}^{-1} \text{ s}^{-1}$ , i.e. 3–5 orders less than the estimated value of the rate constant of diffusion collisions of the reacting species. The scope of these data suggests that the process occurs via formation of a short-lived intermediate ternary (PMA · · · PVP–PMA\*) complex resulting from interpenetration of the original IPEC and Na PMA\* coils upon their random collisions in solution. This complex acts as a “transition state” in a bimacromolecular reaction of polyion exchange as is illustrated in Scheme IV. Under the specified conditions, not every collision is productive. Approximately  $10^3$ – $10^5$  collisions are required for a single event involving transfer of PVP from PMA to PMA\*. The strong dependence of  $k_2$  on the external salt concentration (runs 4–7) and on the linear charge density of PVP chains (runs 14–18) is consistent with the suggested reaction mechanism.

Reactions of polyion exchange, which involve IPEC species incorporating more than one GPE chain, are described by more complicated polychronous kinetics. However, the general trends controlling these reactions are qualitatively similar to those discussed above [42]. For example, their rate depends strongly on the concentration of external simple salts as illustrated by the data in Tab. 2.2.



Scheme IV

**Tab. 2.2** Effect of an external salt on polyion exchange reaction, when IPEC containing more than one GPE chain is involved

$[\text{NaCl}] \times 10^3 / \text{M}$	0	35	70	100
Half-conversion time	No reaction	240	6	<1.5

$\text{DP}_w(\text{Na PMA}^*) = \text{DP}_w(\text{Na PMA}) = 3 \times 10^3$ ,  $\text{DP}_w(\text{PVP}) = 2 \times 10^2$ ;  $[\text{Na PMA}^*] = [\text{Na PMA}] = [\text{IPEC}] = 4 \times 10^{-3}$  base-mole,  $\varphi = 0.33$ ; pH 10,  $T = 20^\circ\text{C}$ .

External salts also strongly affect the rate of polyion substitution reactions [38, 39, 43, 47, 50–52]. For example, the rate of the reaction between  $\text{PMA}^*$ -PVP IPEC and poly(potassium vinylsulfate) (K PVS) shows the most dramatic dependence on concentration of a simple salt (Tab. 2.3).

It was also found that in the case of polyion substitution reactions not only the kinetics but also the position of the equilibrium depends strongly on the structure of the polyion counterparts. In particular, polyanions containing a sulfonate or sulfate group in a repeating unit such as PVC, poly(ethylenesulfonate), poly(styrenesulfonate), heparin etc. usually replace poly(carboxylate)s, such as PA or PMA in original IPECs containing a poly(amine) or poly(ammonium) component [39]. The substitution reaction is driven by the specific affinity of the sulfonate or sulfate groups to protonated or quaternized amine groups.

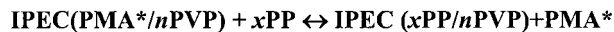
The dramatic impact of the degree of polymerization of competing polyelectrolytes and the nature of the external salt on the equilibrium degree of conversion ( $q_e$ ) in polyion substitution reactions was reported [47] for IPECs consisting of

**Tab. 2.3** Effect of an external salt on polyion substitution reaction

$[\text{NaCl}] \times 10^3 / \text{M}$	0	2	4	6	8	10
Half-conversion time	No reaction	600	60	13	5	<1.5

$\text{DP}_w(\text{Na PMA}^*) = 3 \times 10^3$ ,  $\text{DP}_w(\text{K PVS}) = 1.3 \times 10^3$ ,  $\text{DP}_w(\text{PVP}) = 2 \times 10^2$ ;  $[\text{IPEC}(\text{PMA}^* - \text{PVP})] = 4 \times 10^{-3}$  base-mole,  $\varphi = 0.2$ ;  $[\text{K PVS}] = [\text{PVP}]$ ; pH 10,  $T = 20^\circ\text{C}$ .

PMA\* (HPE) tagged with anthryl groups and PVP (GPE) when interacting with poly(phosphate) (PP) fractions with different DPs. (Scheme V.)



Scheme V

Fig. 2.3 shows  $q_e$  plots versus concentration of the external salts in the mixture of Scheme V. It is noteworthy that the patterns of the plots in Fig. 2.3 differ from each other depending on the DP of PP (Fig. 2.3 (a)) or the nature of the external salt cations (Fig. 2.3 (b)), other conditions being identical. At sufficiently high concentrations of salt, differences are significant. For example, in a 0.3 M aqueous solution of NaCl, the equilibrium of Scheme V is completely shifted to the right when PPs with the longest chains (230 repeating units) are used, whereas it is shifted to the left in the case of short PP chains (20 repeating units), with the concentration of all polymer components being fixed. For PPs of intermediate DPs,  $q_e$  in Scheme V is also intermediate. For PP of a fixed chain length (70 repeating units), the equilibrium is completely shifted to the right in a 0.3 M solution of LiCl, whereas in a 0.3 M solution of KCl it is completely shifted to the left. In 0.3 M solution of NaCl  $q_e$  acquires intermediate values. The phenomena described do not have analogs in nonpolymer systems. Moreover, they seem to mimic biologically important rearrangements in cells involving oppositely charged biological polyelectrolytes. Both IPECs involved in Scheme V virtually do not dissociate to the initial counterparts. Therefore, the transformation described by Scheme V does not affect the total excess of free nonblocked charged groups in the competing PMA\* and PP polyanions.

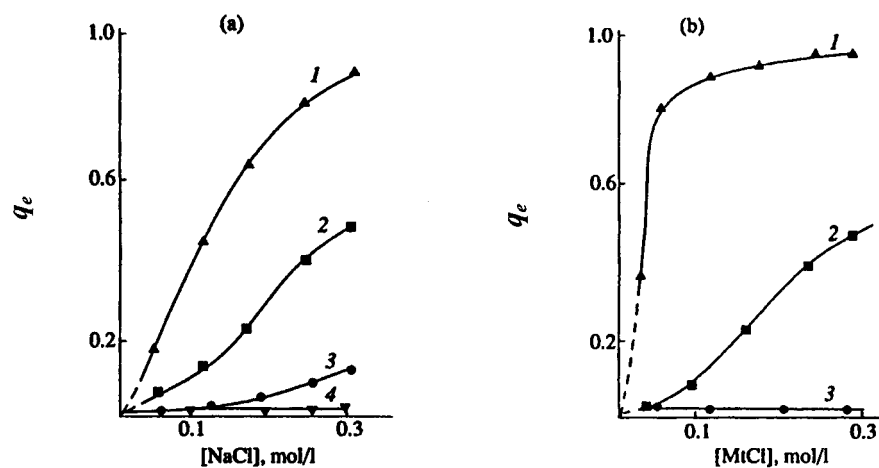


Fig. 2.3 Equilibrium conversion in polyion substitution reaction between IPEC (PMA\*–PVP) and PP as a function of concentration (a) of NaCl and (b) of other alkali metal chlorides.  $[\text{PMA}^*] = [\text{PP}] = 1.5 \times 10^{-3} \text{ mol l}^{-1}$  (as

calculated per monomer unit of polyion),  $\varphi = [\text{PVP}]/[\text{PMA}^*] = 0.33$ ,  $T = 25^\circ\text{C}$ ,  $\text{pH} 10$ . (a) The degrees of polymerization of PP are: (1) 230, (2) 70, (3) 50, (4) 20. (b) 70; (1) LiCl, (2) NaCl, (3) KCl [47].

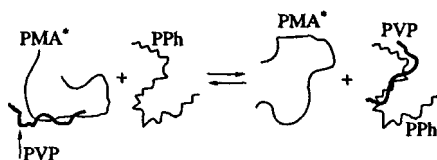
Thus, the sensitivity of the equilibrium to a concentration of external salt reveals a difference in concentration dependences of apparent binding constants for the simple salt cations involved, with respect to PMA or PP.

A qualitative thermodynamic explanation for these at first glance amazing effects was first given in [47]. The essence of the explanation is as follows: the total free energy change,  $\Delta G_t$ , in Scheme V may be written as the sum of two terms

$$\Delta G_t = \Delta G_p + \Delta G_{ci} \quad (6)$$

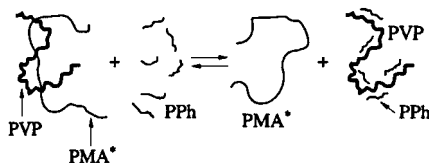
Here,  $\Delta G_p$  pertains to substitution of the contacts between PVP and PMA\* for the contacts between PVP and PP, whereas  $\Delta G_{ci}$  gives the difference in free energies of the interaction of positive counterions with PMA\* and PP.

Consider first the case of Scheme V when the DP of both polyanions (e.g. 4100 for PMA\* and 230 for PP) is greater than the degree of polymerization of PVP (e.g. 170). This is illustrated by Scheme V'. In this case, the total number of polymer species in the system is independent of the shift of the equilibrium in both directions. As follows from the above experimental data in NaCl solutions, the equilibrium in Scheme V' is shifted to the right. This means that the total free energy change  $\Delta G'_t$  in this particular case is negative ( $\Delta G'_t = \Delta G'_p + \Delta G'_{ci} < 0$ ). However, a decrease in the DP of PP shifts the equilibrium to the left.



Scheme V

This means the total free energy change in Scheme V'' becomes positive ( $\Delta G''_t = \Delta G''_p + \Delta G''_{ci} > 0$ ). Because the total number of electrostatic contacts between oppositely charged polyelectrolytes remains constant (under the experimental conditions  $\theta$  is close to 1 for both IPECs),  $\Delta G_{ci}$  does not depend on the DP of the involved polyelectrolytes, that is,  $\Delta G'_{ci} = \Delta G''_{ci}$ . Hence, the effect must be attributed to the increase in  $\Delta G_p$ , that is,  $\Delta G''_p > \Delta G'_p$ . Indeed, it is qualitatively clear that shifting of the equilibrium in Scheme V'' from left to the right, compared to that in Scheme V', results in a decrease in the number of polymer species in the system and therefore is entropically less favorable.

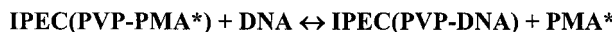


Scheme V'



Consider now the case when the DPs of the polyions are fixed, but the nature of the alkali metal counterions is varied. Then  $\Delta G_p$  is constant. Therefore the  $\Delta G_t$  sign reversal on replacing  $\text{Li}^+$  by  $\text{K}^+$  is caused by a change in the  $\Delta G_{ci}$  value associated with the free energy difference of interaction between polyanions and positive counterions. Clearly, this difference is due to specific interaction superposed on a nonspecific Coulomb attraction between opposite charges. Indeed, the critical salt concentration, at which PMA–PVP IPEC dissociates into individual polyelectrolyte components (see below), increases in the order  $\text{LiCl} < \text{NaCl} < \text{KCl}$ , whereas for the PP–PVP IPEC the order is reversed [53].

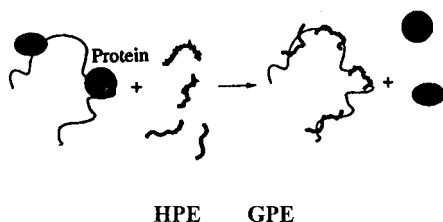
Similar phenomena were observed with IPEC incorporating DNA as a polyanion [50–52]. The substitution reaction involving IPECs formed between DNA or PMA\* and PVP was studied (Scheme VI). This reaction is fully reversible and equilibrates with any order of mixing the reagents. Here also the reaction rate and position of the equilibrium are strongly controlled by the concentration and the nature of the external salts (Fig. 2.4). For example, changing the concentration of NaCl from 0.125 to 0.25 M almost completely shifts the equilibrium to the right [from IPEC(PVP–PMA\*) to IPEC(PVP–DNA)] (Fig. 2.4(a)). Moreover, the half-conversion time of the reaction decreases from tens of minutes to several seconds. Fig. 2.4(b) shows the effect of concentration and of the nature of positive counterions on  $q_e$ . In the series  $\text{Na}^+ > \text{K}^+ > \text{Li}^+$  the equilibrium shifts more and more from the right to the left [from IPEC(PVP–DNA) to IPEC(PVP–PMA\*)]. It is noteworthy that, in contrast to  $\text{Na}^+$  and  $\text{K}^+$ , the effect of  $\text{Li}^+$  depends on whether Scheme VI involves native or denatured DNA. Indeed, in the case of native DNA, the equilibrium is completely shifted to PVP–PMA\* IPEC over the entire range of LiCl concentrations studied, whereas in the case of denatured DNA the equilibrium shifts significantly to the right with increase in LiCl concentration. This difference may be related to a higher affinity of  $\text{Li}^+$  cations to the native than to the denatured DNA revealing another example of specific interactions superposed on general electrostatic attractions.



#### Scheme VI

Not only linear but also dendritic polyelectrolytes (dendrimers) [21–23], proteins [27, 28] and other compact globular species such as poly(silicic) acid sols [54–59] may act as GPEs in forming IPECs, if their diameter is much smaller than the HPE contour length. Such IPECs are formed by coupling and are equilibrated by interchange reactions akin to those described above. The IPEC species may exist in aqueous solution as long as the occupancy of HPEs by globular guests does not exceed certain critical values. It is noteworthy that linear polyions with a relatively high charge density usually replace globular species, e.g. proteins in the initial IPEC [28] (see Scheme VII).

In addition it should be noted that polyion interchange reactions playing a critical role in equilibration of IPEC systems may be hindered or fully prohibited even in the presence of external salts. This happens if the interpolyion electrostatic attraction is



Scheme VII

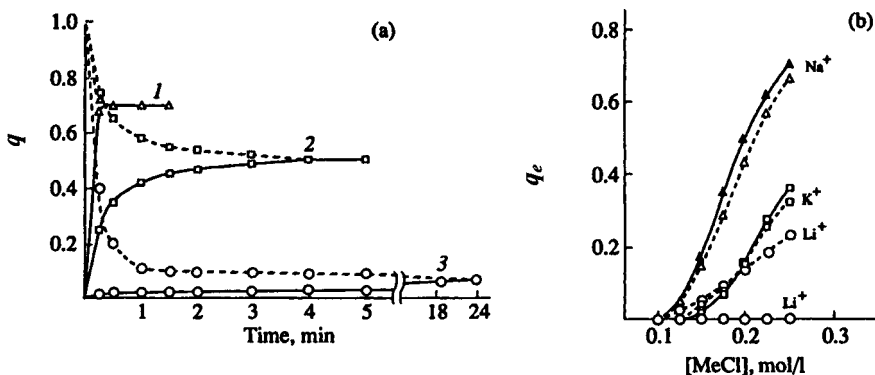
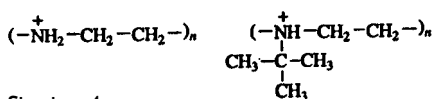


Fig. 2.4 Kinetics of substitution reaction of Scheme VI between IPEC (PVP–PMA\*) and DNA at  $[\text{NaCl}] = (1) 0.25, (2) 0.20, \text{ and } (3) 0.125 \text{ mol l}^{-1}$  (a). The effect of simple salt on

the equilibrium of the reaction of Scheme VI involving native and denatured DNA. Solid lines refer to native DNA, dashed lines to denatured DNA (b) [30].

dominated by other interactions such as hydrophobic or donor–acceptor bonding etc. A typical example is provided by the different solution behavior of two closely related nonstoichiometric IPECs. Both are based on the same polyanionic HPE component: Na PA or Na PMA, but one contains linear PEI and the other poly(*tert*-butylaziridine) (PTBA) as a cationic GPE counterpart, equal to PEI in linear charge density. (See Structure 4.) Both IPECs are able to exchange GPEs at room temperature. However, at elevated temperatures ( $40\text{--}60^\circ\text{C}$ ) when hydrophobic interactions becomes more substantial, PTBA chains, in contrast to PEI, are fixed within IPEC species and do not transfer from one species to another [60].



Structure 4

Some other examples demonstrating critical effects in interchange restriction will be given below.

## 2.2.2

**Solution Properties of Equilibrated Nonstoichiometric Interpolyelectrolyte Complexes**

A nonstoichiometric IPEC may be considered to be a block-copolymer containing free hydrophilic segments of HPE chains and relatively hydrophobic GPE–HPE domains [3, 5]. Such IPECs, if water soluble and equilibrated (see above), behave in dilute solution to some extent like ordinary polyelectrolytes. The procedures for preparing soluble equilibrated non-stoichiometric IPECs from a number of various GPE–HPE pairs were described in detail some time ago [61–63] and thoroughly reviewed in ref. [3].

It has been shown by analytical ultracentrifugation [53, 61, 62], light scattering [3, 5, 28, 63] and GPC [64], that equilibrated water soluble nonstoichiometric IPECs, prepared from rather narrow HPE and GPE fractions in dilute solutions, are actually individual polymer species, characterized with a high composition homogeneity and narrow size distribution. Characteristics of the IPEC consisting of PDMAEMA and PP prepared via different routes are tabulated in Tab. 2.4. Fig. 2.5 (a) represents a typical Zimm diagram, one of a series of those plotted to handle light scattering data. As may be seen from the values presented in the table, the preparation route has essentially no effect on either measured molecular mass ( $M_w$ ), or radius of gyration ( $R_g$ ), or second virial coefficient ( $A_2$ ), or sedimentation coefficient ( $S_c$ ). However, the above characteristics (except  $M_w$  compensated due to counterions release) are acutely sensitive to IPEC composition. The data tabulated in Tab. 2.5 show that  $R_g$  and  $A_2$  decrease, while  $S_c$  increases with increasing GPE/HPE ratio, *i.e.* the lowering of the HPEs effective charge in the range  $0 < \varphi < \varphi_c$ . It is remarkable that in dilute solution the IPECs listed in Tab. 2.5, at  $\varphi < \varphi_c$  exist in the form of “unimer” complex species: each one contains one HPE polyion carrying a certain number of GPEs. However, the situation changes drastically in the vicinity of  $\varphi_c$ . First of it is manifested by a dramatic change in the Zimm diagram, which takes on a pattern characteristic for scattering by polymers in poor solvents.  $A_2$  decreases sharply and reverses sign while the molecular mass of the dissolved species increase indicating formation of IPEC aggregates not dissociated on dilution (Fig. 2.5 (b), Tab. 2.5, run 8).

The tendency toward aggregation of nonstoichiometric IPEC species in dilute solutions naturally depends on the HPE and GPE chemical structure. In particular it builds up when the hydrophobicity of the initial polyelectrolytes increases.

**Tab. 2.4** Characteristics of the interpolyelectrolyte complex obtained using different experimental procedures

Route of IPEC preparation	$(M_w)/10^5$	$(R_g^2)/nm$	$(A_2) \times 10^4$
Titration of HPE with GPE solution	7.7	38	3.3
Titration of GPE with HPE solution	7.7	39	2.9
Titration of HPE–GPE mixture with HCl	7.2	37	2.8

HPE is PDMAEM,  $M_w = 6.3 \times 10^5$ ; GPE is PP,  $M_w = 6.6 \times 10^4$ ,  $\varphi = 0.33$ , 0.1 M NaCl. PH 4.0.

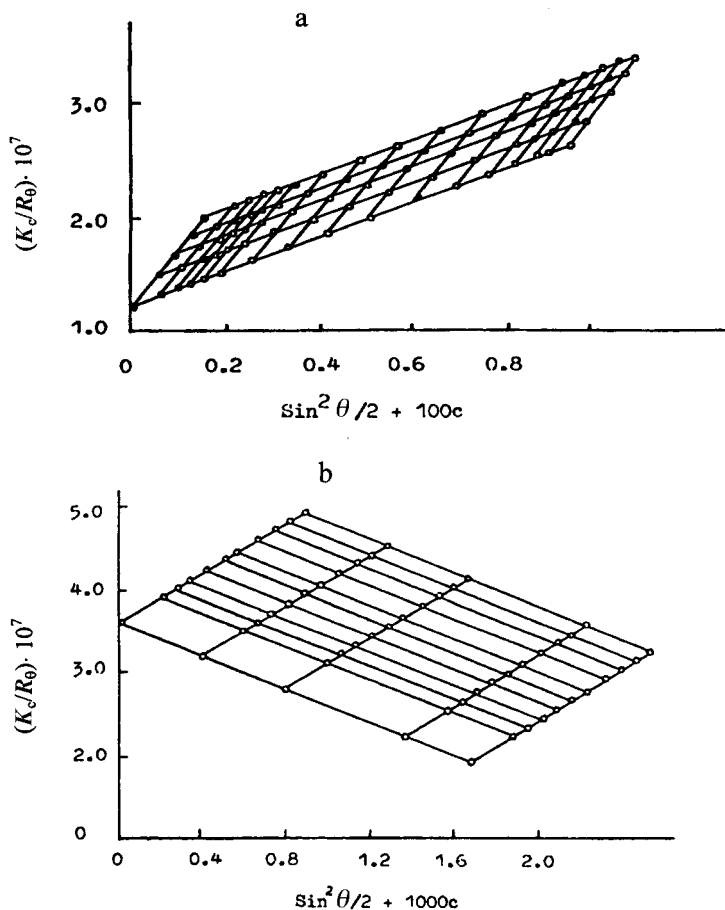


Fig. 2.5 Zimm diagrams for PDMAEMA-PP IPEC solution; (a)  $\varphi=0.33$  (see run 6 in Tab. 2.5); (b)  $\varphi=0.56$  (see run 8 in Tab. 2.5).

The behavior of IPEC formed by NaPA as HPE, and 5,6-ionene bromide (IB) as GPE may be referred to as a representative example [66]. Each repeating unit of IB polycation (Structure 5) contains 5.5 methylene and 2 methyl groups per charge. These hydrophobic groups are not sufficient to suppress the water solubility of the individual IB. However, being ion-paired with PA segments IB units apparently enhance the affinity of binary IPEC domains to each other. The data of Tab. 2.6 show that at  $\varphi \geq 0.2$ , which is still considerably lower than  $\varphi_c$ , PA-IB IPEC species aggregate, in contrast to the IPECs tabulated in Tab. 2.5. It is likely that binary domains in such aggregated IPECs segregate to form a water insoluble core while excess PA segments exposed in water form a corona providing solubility of the species as a whole.

Tab. 2.5 Characteristics of equilibrated nonstoichiometric interpolyelectrolyte complexes in dilute water-salt solutions (20 °C) [3, 5, 57]

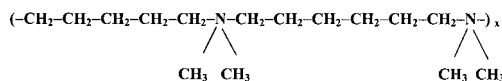
No.	HPE	GPE	$\varphi = [\text{GPE}]/[\text{HPE}]$	IPEC mol. mass		n	$(R_g^2)^{1/2}/nm$ ( $A_2$ ) $\times 10^4$		S <sub>d</sub> /S <sub>v</sub>	Other conditions
				(M <sub>w</sub> )/10 <sup>5</sup>	(M <sub>calc</sub> )/10 <sup>5</sup>		HPE	GPE		
1.	PDMAEMA	Na PP (M <sub>w</sub> = 1.7 × 10 <sup>5</sup> )	0 (no GPE)	6.3	—	1	51	8.2	2.5	PH 4.0
2.	Same	Same	0.07	7.15	6.4	1	48	6.5	2.7	0.1 M NaCl
3.	4. Same	Same	0.10	6.9	6.4	1	44	5.9	2.8	
5.	Same	Same	0.13	7.35	6.5	1	43	5.2		
6.	Same	Same	0.20	6.75	6.6	1	40	4.9	3.7	
7.	Same	Same	0.33	6.7	6.8	1	35	2.9	6.0	
8.	Same	Same	0.50	7.0	7.0	1	27	1.1	5.9	
	Same	Same	0.56	28			27	-0.45		
9.	PDMAEMA	Na PA (M <sub>w</sub> = 1.4 × 10 <sup>5</sup> )	0 (no GPE)	5.3	—	1	48.5	9.4	2.0	PH 4.5
10.	Same	Same	0.125	5.5	5.4	1	47.5	9.5	2.1	0.1 M NaCl
11.	Same	Same	0.20	6.0	5.5	1	46.0	9.0	2.3	
12.	Same	Same	0.33	5.6	5.6	1	43.5	8.6	2.6	
13.	Same	Same	0.50	5.6	5.8	1	40.0	7.6	3.3	
14.	Na PP	IB (M <sub>w</sub> = 1.4 × 10 <sup>4</sup> )	0 (no GPE)	0.66	—	1	14.3	2.2	2.2	PH 7.0
15.	Same	Same	0.125	0.61	0.73	1	4.8	2.5	2.5	0.025 M
16.	Same	Same	0.20	0.62	0.78	1	1.9	2.2	2.7	NaCl
17.	Same	Same	0.33	0.66	0.85	1	1.7	1.7	3.4	

Scattering intensity and refractive index increment were measured varying concentration of IPEC at constant activity of the simple salt.

That was achieved by dialysis against the common salt solution [65].

Molecular mass of IPECs of a given composition was calculated as  $M_{\text{calc}} = P_{\text{HPE}} [m_{\text{HPE}} + \varphi(m_{\text{GPE}} - m_{\text{s}})]$ , where  $P_{\text{HPE}}$  is the HPE degree of polymerization,  $m_{\text{HPE}}$  and  $m_{\text{GPE}}$  are molecular masses of HPE and GPE repeating units,  $m_{\text{s}}$  is molecular mass of the salt released as the result of polyelectrolyte coupling reaction. NaPA is poly(sodium acrylate), IB is 5,6-ionene bromide.

$S_c$  determined at the fixed IPEC concentration,  $c = 0.35$  wt. %



Structure 5

**Tab. 2.6** Characteristics of the interpolyelectrolyte complex formed by NaPA (HPE),  $M_w=1.2 \times 10^5$  and 5, 6-ionene bromide (GPE)  $M_w=1.4 \times 10^4$  (pH 7.2 in 0.025 M NaBr, 20°C)

N	$\varphi$	$M_w \times 10^{-5}$ of IPEC	n		$A_2 \times 10^3$
			HPE	GPE	
1	0.07	1.8	1	1.4	11.8
2	0.10	1.8	1	1.8	10.3
3	0.13	1.8	1	2.4	7.4
4	0.20	2.6	2	7.3	3.8
5	0.33	3.8	3	18	1.9

Turning back to the experimental  $A_2$  values decreasing with increasing  $\varphi$ , let us recall that according to Donnan–Guggenheim theory [67] the contribution of the electrostatic repulsion of polyion charges to the total value of  $A_2$  can be expressed as

$$A_{2,\text{el}} = 1000z_e^2\gamma^2/4M^2I \quad (7)$$

where  $z_e$  is the total charge of a polyion,  $\gamma$  is the degree of binding of counterions by free HPE segments,  $M$  is the polyion molecular mass,  $I$  is the ionic strength, equal to the concentration of a simple salt in the solution. The effective charge of nonstoichiometric IPEC species in the pH range corresponding to complete ionization of HPE depends on  $\varphi$  as follows

$$z_e/M = (1 - \varphi)/M_0 \quad (8)$$

where  $M_0$  is the molecular mass of the HPE repeating unit. From Eq. (7) and (8) we obtain

$$A_{2,\text{el}} \sim (1 - \varphi)^2/I \quad (9)$$

Fig. 2.6(a) shows the plot of the experimental  $A_2$  values at fixed  $I$ , vs.  $(1-\varphi)^2$ , which fits correlation (8) quite well. Fig. 2.6(b) shows that correlation (8) is also valid for variation of  $I$  when  $\varphi$  is fixed. On the other hand, assuming that  $R_g$  of a polyelectrolyte coil is directly proportional to the radius of the equivalent sphere, and the charge in the vicinity of a polyelectrolyte chain is mainly compensated with counterions, the excluded volume theory gives the correlation

$$A_2 \sim R_g^3/M_w^2 \quad (10)$$

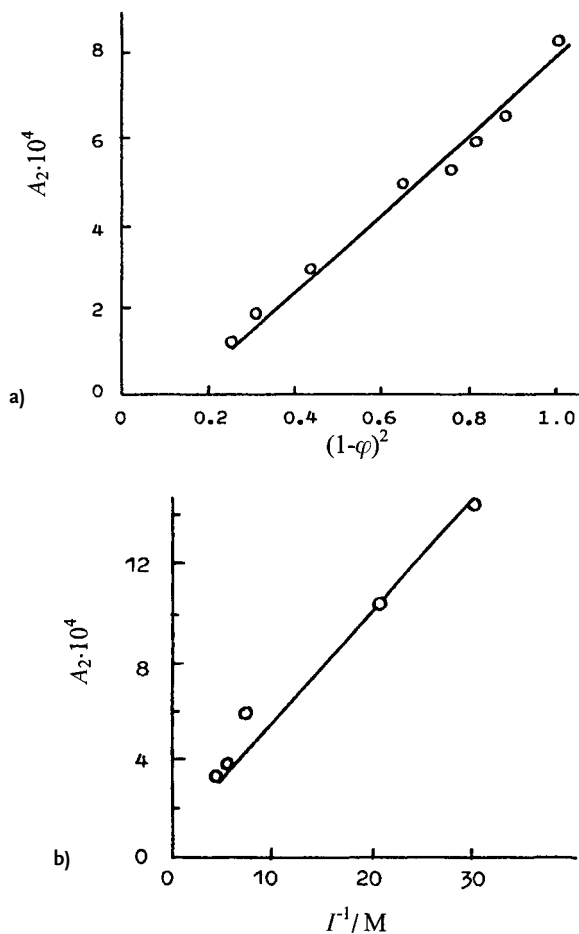


**Fig. 2.6** The second virial coefficient,  $A_2$ , of solutions of IPEC formed by PDMAEMA ( $M_w = 6.3 \times 10^5$ ) and NaPP ( $M_w = 1.7 \times 10^4$ ) as a function: (a) of its composition at fixed ion-

ic strength  $I = [\text{NaCl}] = 0.1$  M and (b) of ionic strength at fixed composition  $\varphi = 0.33$ ; pH 4.0, 20°C.

Fig. 2.7 shows that the data taken from Tab. 2.5 nearly meet this correlation.

The above correlations, experimentally observed, all contribute to the conclusion that a soluble equilibrated IPEC of composition in the range  $0 < \varphi < \varphi_c$  in dilute solution actually behaves like a series of ordinary polyelectrolytes of various charge densities.

The solution behavior of nonstoichiometric IPECs formed by complexation of linear HPE polyions with relatively small oppositely charged globular species playing the role of GPEs, is similar to IPECs made of linear polyions. This is true either for cationic dendrimers [21–23], or proteins [27–29], or negatively charged sols of poly(silicic acid) [54–59] interacting with linear polyelectrolyte partners of sufficiently high DP.

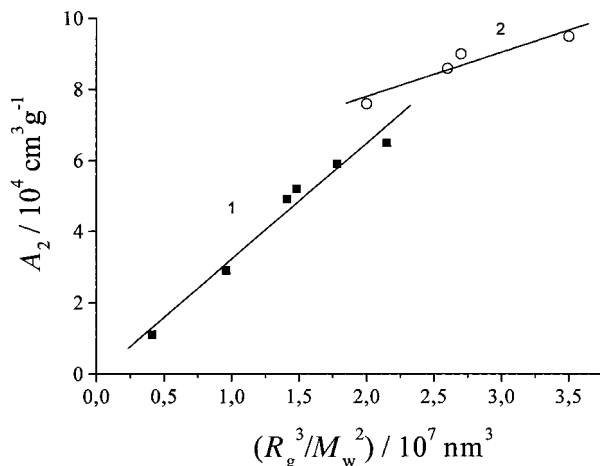


Fig. 2.7 Second virial coefficient ( $A_2$ ) plot in coordinates of Eq. (9) (see Tab. 2.5).

However, it should be emphasized that the above behavior is not typical for IPECs formed from polyelectrolyte partners which are not favorably disposed towards interchange, even if they are taken in nonstoichiometric ratio with an excess of the polyions of higher DP. Such is the case for mixing poly(amines) with poly(sulfates) or poly(sulfonates), when pairing of oppositely charged ionic groups is substantially aided by specific interactions. Then, complexation results in formation of relatively large IPEC aggregates containing a large number of complementary polyions. An example is poly(sodium styrenesulfonate) (NaPSS) interacting with poly(*N*-dimethyl-*N*-diallylammonium chloride) [68–71].

### 2.2.3

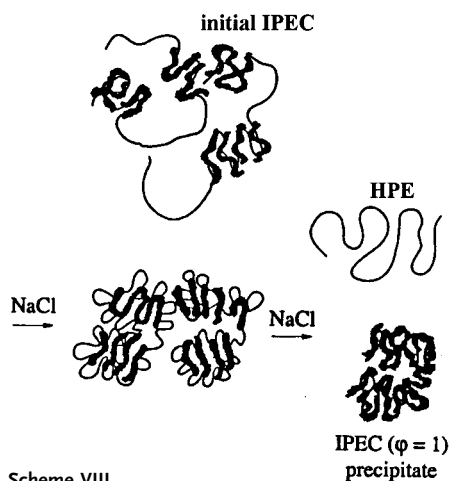
#### Transformation of Interpolyelectrolyte Complexes in External Salt Solutions

Fig. 2.8 (a) represents typical ionic strength dependences of reduced turbidity,  $\tau/\tau_{\max}$ , for HPE–GPE mixtures in water at  $Z < \varphi_c$ ,  $\Theta$  close to 1, and HPE content below its crossover concentration range. Homogeneity region I corresponds to dilute solutions of the equilibrated nonstoichiometric IPECs in which IPEC species behave similarly to individual polyelectrolytes. Region I is important, where  $Z = \varphi$  is broader the lower is  $\varphi$ , i.e. an occupancy of HPE by GPEs. Homogeneity region II corresponds to the solution of the individual polyelectrolyte components, released as a result of IPEC decomposition caused by shielding of paired ionic groups by small counterions. A series of inhomogeneity regions observed for various  $Z$  at intermediate salt concentrations corresponds to phase separation. Fig. 2.8 (b) depicts sedimentograms of the HPE–GPE system at various salt concentrations compared with those for the individual HPE and GPE (patterns 4 and 5). Patterns 1 and 2, characterized by a single sedimentation mode, relate to homogeneity region I. Pattern 3, revealing two sedimentation modes, relates to the inhomogeneity region [3, 72].



Detailed studies of phase behavior of nonstoichiometric mixtures of oppositely charged polyelectrolytes in external salt solutions accomplished by using light scattering, analytical and preparative ultracentrifugation, fluorimetry in the systems containing fluorescent tagged HPEs and GPE quenchers, the composition analysis of separated phases etc. [72–79] have led to an understanding of the whole picture.

Increasing salt concentration within homogeneity region I (Fig. 2.8(a)) decreases the thermodynamic quality of the solvent, resulting in a decrease in the size of the dissolved IPEC species. At the same time the ultimate extent of HPE populated by GPE chains,  $\varphi_c(I)$ , which, to maintain IPEC homogeneity, should not be exceeded, also decreases. This means that the higher the original  $\varphi$  value,  $\varphi_0 = Z$ , the lower is the critical ionic strength,  $I_c$ , sufficient to reduce  $\varphi_c(I)$  to  $\varphi_0$ , and the broader is region I (Fig. 2.8(a), curves 1–4). To minimize the free energy of the whole system at  $I > I_c$  IPEC species should lose some GPE chains. This occurs due to their disproportionation via GPE interchange and redistribution resulting in formation of stoichiometric IPEC, which phase separates, while nonstoichiometric IPEC species of  $\varphi' = \varphi_c(I) < Z$  remain in solution. A further increase in salt concentration within the inhomogeneity region (Fig. 2.8(a)) results in an increase in the amount of phase separated stoichiometric IPEC in equilibrium with soluble IPEC species of decreasing  $\varphi'$ . It is clear that under conditions when  $\Theta$  is close to 1,  $\varphi'$  cannot become smaller than the ratio of GPE to HPE degrees of polymerization,  $DP_{GPE}/DP_{HPE}$ . Under this condition, on stoichiometric IPEC separation at  $\varphi_c(I) < DP_{GPE}/DP_{HPE}$  the free HPE remains in the supernatant as shown in Scheme VIII [80]. The ultimate HPE concentration in the supernate may reach  $[HPE]_{\infty} = [HPE]_0(1 - \varphi)$ , where  $[HPE]_0$  is its initial concentration.



It is noteworthy that the above phase behavior of IPECs in external salt solutions is not uniquely determined by ionic strength. The  $I_c$  value for a given IPEC substantially depends on the nature of HPE counterions [72]. Fig. 2.9 shows the

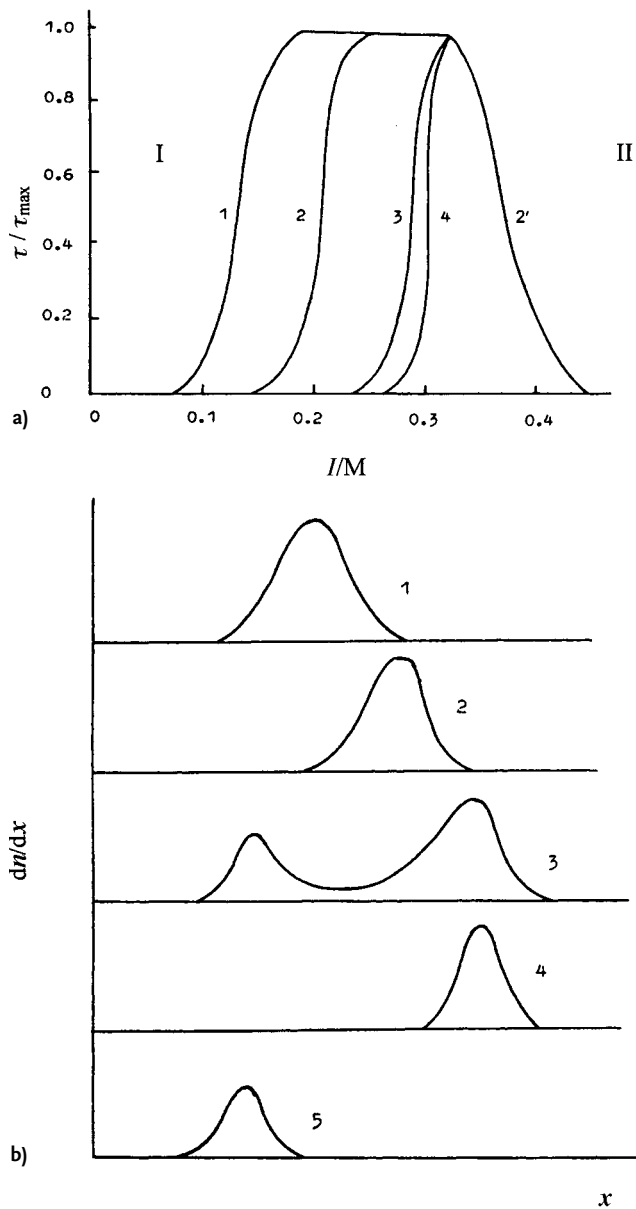


**Fig. 2.8** Phase behavior of Na PMA ( $M_w=2.6 \times 10^5$ )-PVP ( $M_w=6.0 \times 10^4$ ) mixtures on ionic strength varied by adding NaBr, pH 7.5, 20 °C [70]. (a) Ionic strength ( $I=[\text{NaBr}]$ ) dependences of reduced turbidity ( $\tau/\tau_{\max}$ ) at  $Z$ : (1) 0.40, (2.2') 0.33, (3) 0.25,

(4) 0.20. (b) Sedimentograms of the mixture, at  $Z=0.14$ ,  $C=0.3$  wt.%,  $w=56$  100 rpm, sedimentation time 60 min at various  $I=[\text{NaBr}]$ : (1) 0.2 M, (2) 0.35 M, (3) 0.48 in comparison with free Na PMA (4) and free PVP (5) at  $[\text{NaBr}]=0.48$  M.

turbidimetric titration curves of Na PMA (HPE)–IB (GPE) IPEC ( $\varphi=0.33$ ) with various salts with different cations or anions. Comparing curves 1–4 one can see that for the series of cations:  $(\text{CH}_3)_4\text{N}^+$ ,  $\text{K}^+$ ,  $\text{Na}^+$ ,  $\text{Li}^+$ ,  $I_c$  decreases in parallel with an increase in their affinity to  $-\text{COO}^-$  groups [80]. At the same time  $I_c$  does not depend on the nature of the HPE co-ions, in particular  $\text{F}^-$ ,  $\text{Cl}^-$  and  $\text{Br}^-$  (Fig. 2.9, curves 2'–2'''). The above data correlate with more recent measurements of ionic strength dependences of sedimentation coefficients,  $S_c$ , for PMA (HPE)–PVP (GPE) IPEC ( $\varphi=0.37$ ) and free Na PMA at low external salt concentrations, i.e. under conditions of full IPEC stability [76]. It was found that in the ionic strength range  $0 < I < 0.1$  M addition of NaCl resulted in a substantial  $S_c$  increase either for the IPEC (from 1.7 to 4.35 Sv), or for free Na PMA (from 1.3 to 2.5 Sv) indicating their compaction due to binding of  $\text{Na}^+$  counterions to negatively charged PMA repeating units. However, the same increase in ionic strength accomplished by adding tetramethylammonium (TMA) chloride affected the measured  $S_c$  values only slightly. Similar effects might also be expected for nonstoichiometric IPECs formed by cationic HPEs and anionic GPEs but with respect to the nature of external salt anions. In fact, it has been shown that IPEC ( $\varphi=0.33$ ) consisting of poly(*N*-ethyl-4-vinylpyridinium fluoride) separates at  $[\text{NaF}]_c=0.2$  M,  $[\text{NaCl}]_c=0.03$  M and  $[\text{NaBr}]_c=0.01$  M. This order corresponds to increasing affinity of halide anions to HPE pyridinium rings. At the same time  $I_c$  is not dependent at all on the nature of the alkali metal cations [81].

The salt concentrations at which phase separated IPEC systems homogenize again (region II in Fig. 2.8) due to IPEC splitting with release of the original polyelectrolytes depend on the nature of both shielding counterions [77, 78]. Fig. 2.10

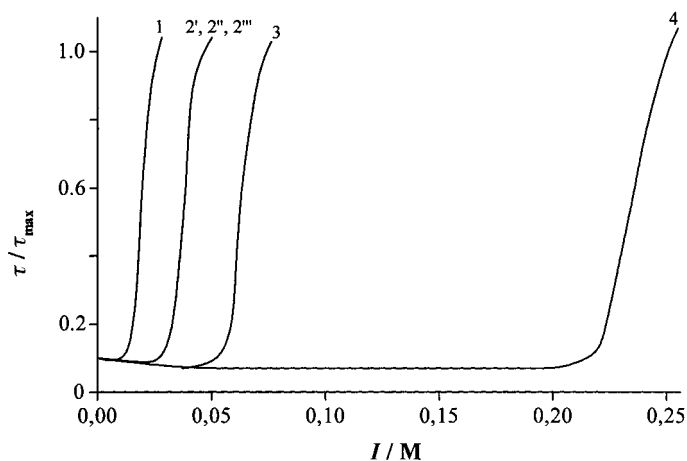
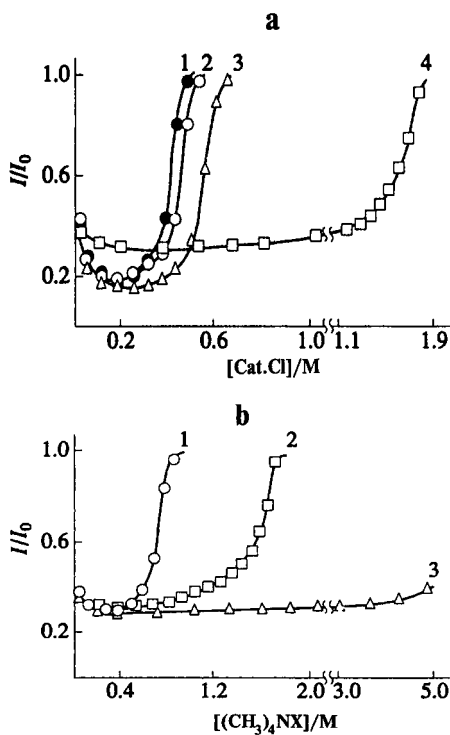


Fig. 2.9 Ionic strength dependences of reduced turbidity ( $\tau/\tau_{\max}$ ) at titration of IPEC formed in Na PMA ( $M_w=1.8 \times 10^5$ )–IB ( $M_w=1.4 \times 10^4$ ) mixture ( $Z=\varphi=0.33$ ) with different salt solutions: (1) LiCl; (2'–2''') NaX, where X is  $\text{F}^-$  (2'),  $\text{Cl}^-$  (2'')  $\text{Br}^-$  (2'''); (3) KCl; (4)  $(\text{CH}_3)_4\text{NCl}$ . The concentration of IPEC in solution is 0.01 wt.%; pH 8.5, 20 °C [72].



**Fig. 2.10** Reduced fluorescence intensity ( $I/I_0$ ) of the solution of IPEC formed by Na PMA\* ( $\text{DP}_w=2150$ ) and PVP ( $\text{DP}_w=390$ ) vs. concentration of different salts,  $Z=\phi=0.3$ ,  $[\text{PMA}^*]=2\times 10^{-3}$  base-mol  $\text{l}^{-1}$ , pH 9.5,  $20^\circ\text{C}$  ( $I_0$  is the fluorescence intensity of free HPE in the same salt solution) [76]; (a) Cat. is: Li<sup>+</sup> (1), Na<sup>+</sup> (2), K<sup>+</sup> (3) and  $(\text{CH}_3)_4\text{N}^+$  (4). (b) X is: Br<sup>-</sup> (1), Cl<sup>-</sup> (2) and F<sup>-</sup> (3).

shows reduced fluorescence intensity of pyrenyl tagged PMA\* (HPE) originally incorporated in soluble nonstoichiometric PMA\*–PVP IPEC, vs. the concentration of various external simple salts. The fluorescence intensity of the initial IPEC is small because of quenching by GPE pyridinium rings. The increase in fluorescence on titration of the IPEC solution by the salt solutions presumably indicates dissociation of the IPEC to the constituent polyelectrolytes. Fig. 2.10 (a) shows the fluorometric titration curves of PMA\* (HPE)–PVP (GPE) solution with solutions of various alkali metal chlorides and tetramethylammonium chloride. A comparison of these curves demonstrates that the ability of cations to induce IPEC dissociation tends to decrease in the following order:  $\text{Li}^+ > \text{Na}^+ > \text{K}^+ \gg (\text{CH}_3)_4\text{N}^+$ . As mentioned above, a similar trend has been observed for the affinity of cations to poly(carboxylic) polyanions [80]. Fig. 2.10 (b) depicts the fluorometric titration curves of the same IPEC with solutions of various TMA halides. As seen, in the case of bromide, the salt concentration (ionic strength) required for IPEC decomposition is the lowest, while decomposition was not observed at all even at very high salt concentration in the case of fluoride. We note that the affinity of halide anions to PVP polycation decreases in the same order [81].

The above fluorometric titration curves reveal the salt concentration dependence of the fraction of HPE fluorescent tags, contacting with GPE repeating units, each one a fluorescence quencher. Each HPE chain contains only one pyrenyl tag per

few hundred units. In support of the fluorescence studies, sedimentation studies of Na PMA\*–PVP IPEC behavior in corresponding salt solutions using high speed analytical centrifugation with selective UV detection have shown that the curves of Fig. 2.10 in fact quantitatively describe the extent of IPEC decoupling [79]. Fig. 2.10(a) also shows substantial fluorescence intensity decrease at concentrations of alkali metal halides which are still far from those sufficient for IPEC decomposition. It is likely that compaction of IPEC species upon specific binding of alkali metal ions by excess of PMA repeating units facilitates intra-IPEC quenching. Such a decrease is not observed in the case of TMA salts because of the much lower affinity of  $(\text{CH}_3)_4\text{N}^+$  cations to  $-\text{COO}^-$  groups [78].

The threshold concentration of a given external salt required for IPEC decomposition, independent of DP for HPE, sharply increases with increasing DP for GPE oligomers, but then approaches a limit for sufficiently long GPE chains (Fig. 2.11) [79]. It is noteworthy, however, that clarification of IPEC systems due to dissolution of a stoichiometric IPEC phase does not necessarily mean complete separation of GPE and HPE chains, especially for GPEs of a high molecular mass. Some of them may retain a certain number of dynamic contacts even in solution above the clearing point as shown by sedimentation analysis. Such contacts fully dissociate only at higher concentrations of external salts [77].

We stress that phase separation in nonstoichiometric IPEC solutions upon addition of external salts does not occur if GPE interchange is restricted for some reason. In particular, the above-mentioned PA (PMA)–PTBA IPEC solutions were phase separated on adding NaCl at room temperature, but remained homogeneous at 40–60 °C where GPE interchange was suppressed by hydrophobic interactions [58]. PA (HPE)–PE (GPE) IPECs solutions do not phase separate even at high concentrations of an external salt, if HPE–GPE electrostatic binding is superimposed with a covalent link [73–76]. At salt concentration sufficient to break in-

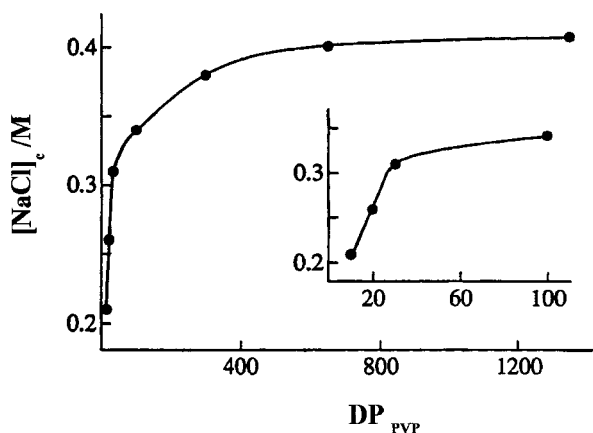


Fig. 2.11 Threshold sodium chloride concentration required for dissociation of PVP–PMA\* IPEC vs. PVP degree of polymerization; DP<sub>w</sub> of PMA\* is  $3.9 \times 10^3$ ,  $\phi = 0.30$ , 20 °C.

terpolyelectrolyte ion pairs such IPECs behave just as graft co-polymers in a common solvent for a main chain and grafts.

Recently a novel family of soluble IPECs based on block copolymers containing ionic and nonionic water soluble blocks has been described [82–85]. Such IPECs termed as “block ionomer complexes” (BIC) may retain solubility even at  $Z = \varphi = 1$ , where  $Z$  relates to polyelectrolyte entities. An example is the BIC formed between diblock copolymer consisting of Na PMA, DP=188, and poly(ethylene oxide) (PEO), DP=176 blocks, and PVP, DP=100 [82]. At  $Z = \varphi = 1$  this BIC contains hydrophobic domains of PMA neutralized with PVP (i.e. stoichiometric PMA–PVP IPEC), and hydrophilic free PEO segments. So it essentially represents an amphiphilic polymer species revealing a typical c.m.c. behavior. Indeed, at concentrations above c.m.c. these BICs microsegregate and form polymeric micelles with an insoluble core and PEO corona providing their solubility in water and stability with respect to further aggregation. At the same time the micellar species formed undergo polyelectrolyte interchange reactions with Na PSS or Na PMA homopolymers, and in contrast to any other polymeric micelles dissociate upon adding external salts. The dissociation occurs due to decoupling IPEC domains similar to the phenomena above describing ordinary IPECs [82].

Finally, polyelectrolyte adsorption on large oppositely charged surfaces may also be considered in terms of IPEC formation. Adsorption of PVP on carboxylated poly(styrene) latex species has been studied from this point of view [86–91]. The latex particles had a diameter of  $5 \times 10^2$  nm; much higher than a polyelectrolyte contour length. The surface carboxyl groups density was ca.  $5 \text{ nm}^{-2}$ , their  $pK_a = 6.8$ . The initial electrophoretic mobility (EPM) of the latex species at pH 9 when all carboxyl groups were ionized, had a negative sign. Fig. 2.12 demonstrates the dependence of EPM on  $Z = [\text{PVP}]/[-\text{COO}^-]$ . One can see that the surface charge decreases with increasing  $Z$  and approaches 0 at  $Z = 1$ . However, it is likely that in this case a substantial number of constituent ionic sites at the surface and in PVP chains remain unpaired at the isoelectric point because of steric limitations, in contrast to equilibrated stoichiometric IPECs formed by fully ionized linear polyions. These surface sites, as well as those in loops and free tails of adsorbed PVP, are neutralized by corresponding low molecular weight counterions. Therefore, an interface formed at the isoelectric point retains a resource for adsorbing either excess polycations (charge reversal) or polyanions, if they are added.

At  $Z > 1$  charge reversal is observed, indicating adsorption of some excess PVP polycations. At the same time the EPM vs.  $Z$  plot does not depend on the concentration of latex species, indicating a strong binding of PVP to the surface. Indeed, free PVP is not detected on titration of the latex with PVP solution until the surface is fully saturated. Nonetheless, the latex particles easily interchange adsorbed polycations on collisions. This was proved by mixing the original negatively charged latex (arrow **a** in Fig. 2.12) with the same latex but by first charge reversed with adsorbed PVP (arrow **b** in Fig. 2.12). Such a mixing is followed by aggregation of oppositely charged latex species. Then these aggregates dissociate again to form the “unimers” of the original size. However, the EPM of the redispersed species takes the intermediate value (arrow **c** in Fig. 2.12) indicating PVP chain redistribution (Scheme IX).

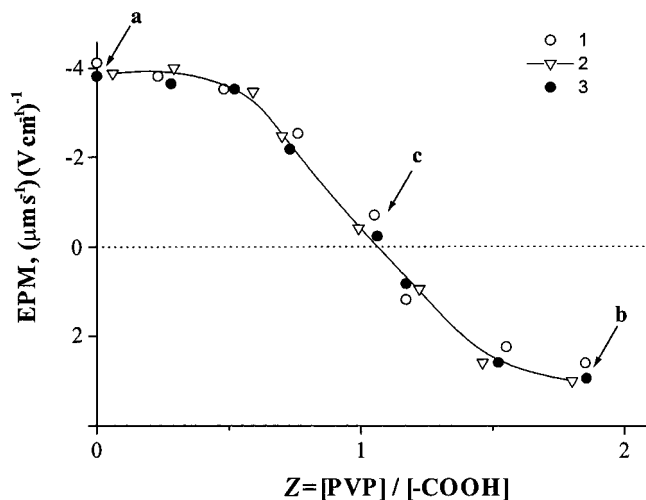
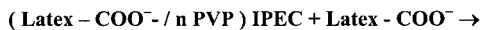


Fig. 2.12 Electrophoretic mobility of latex–PVP system vs. its interface composition,  $Z$ . Latex particles concentration:  $1.8 \times 10^{12} \text{ l}^{-1}$  (1),  $1.8 \times 10^{11} \text{ l}^{-1}$  (2),  $9.0 \times 10^9 \text{ l}^{-1}$  (3), pH 9.0, 20°C (a, b, c see explanation in the text).



#### Scheme IX

Similar behavior has been observed for negatively charged small unilamellar liquid liposomes (SUL)s, upon interaction with PVP [91, 92]. Addition of PVP solution to a suspension of the SULs formed by the zwitterionic lipid, phosphatidylcholine (or dipalmitoylphosphatidylcholine) and anionic lipid, cardiolipin is followed by strong adsorption of the polycation on the surface of the SULs. However, addition of Na PA solution results in a fast PVP removal from the surface of the SULs due to the formation of a stronger (PA–PVP) IPEC. Addition of external salts (e.g. NaCl) leads to dissociation of the SUL–PVP complex. In both the above cases transformations are accompanied by complete regeneration of the original SULs.

The examples cited above demonstrate “ideal” behavior of polyelectrolytes interacting with oppositely charged surfaces unique to such systems with nearly pure electrostatic adsorption. If some other attraction forces (hydrogen bonding, hydrophobic interaction, charge transfer etc.) are substantially involved neither polyion interchange, nor replacement, nor desorption in salt solutions occurs. For example, the SULs mentioned above do not desorb PVP copolymers containing hydrophobic sites in contrast to PVP with a  $\beta$  value exceeding 90% [92].

It is probable that *nonideal* electrostatic or strong nonelectrostatic adsorption of soluble polyelectrolytes on surfaces leads to formation of an initial interface favorable for consecutive deposition of IPEC nanolayers to obtain multilayer composites. At the same time the factors restricting polyelectrolyte interchange reactions

apparently favor preservation of the integrity of the layers already formed and the reproduction of a “sticky” interface for every successive deposition.

### 2.3

#### Complexation of Polyelectrolytes with Oppositely Charged Hydrogels

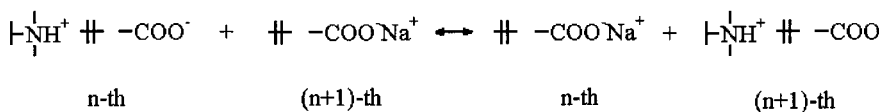
This topic was introduced with the absorption of linear polyelectrolytes by macroscopic pieces of lightly cross-linked oppositely charged polyelectrolyte hydrogels (# PE) from aqueous solutions to form crossed-linked interpolyelectrolyte complexes (# IPECs) [93, 94]. The hydrogels had 1–2 chemical crosslinks per 200 repeating units. Their initial equilibrium degree of swelling was of the order of  $10^3$ . The interpolyelectrolyte reaction is thermodynamically controlled by the same factors as complexation between oppositely charged linear polyelectrolytes. In the case of weak polyelectrolyte counterparts the pH region of # IPEC stability is shown in Fig. 2.1.

It has been shown that absorption causes a sharp decrease in the volume of a reacted hydrogel by 2–3 orders of magnitude. In the course of interpolyelectrolyte reaction a distinctly differentiated weakly swollen # IPEC shell coexists with a highly swollen original # PE core as shown in Scheme X.



Scheme X

The mechanism is based on two independent interpolyelectrolyte reactions. The rate determining stage is a “relay-race” transfer of polyion segments from one fragment of the # PE network to the other initially vacant via interpolyelectrolyte exchange reaction similar to those described in Section 2.2.1 (Scheme XI).

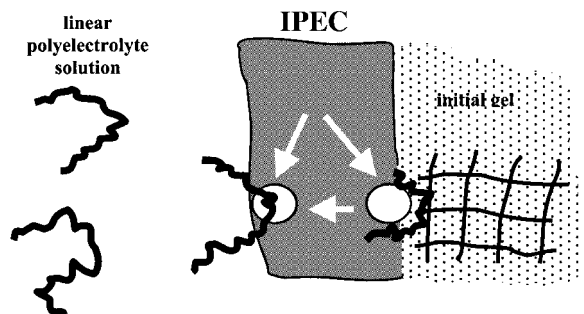


Scheme XI

Each transfer step occurring at the shell/core interface and directed towards the # PE hydrogels phase produces a vacancy in the # IPEC shell available for another polyion segment to transfer in the same direction (Scheme XII) etc.

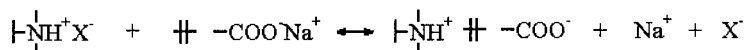
As a result the shell/core interface moves taking up the original # PE hydrogel, while vacancies move outward, finally reaching the outer solution/#IPEC shell interface where interpolyelectrolyte coupling with dissolved polyions occurs (Scheme XIII). This reaction provides the driving force for polyions to migrate into the oppositely charged # PE hydrogel. In other words, the free energy of Scheme XIII is consumed for polyion transport within the hydrogel phase pushing forward Scheme XI [93]. This means that # IPEC formation is *thermodynamically* con-





Scheme XII

trolled by Scheme XIII occurring only under the conditions (pH or degree of ionization of the polyelectrolyte components,  $\alpha$ , ionic strength), when the equilibrium of Scheme XIII is shifted to the right. Correspondingly, already-formed # IPEC dissociates when the equilibrium of Scheme XIII is shifted to the left, so that linear polyions are released to the surrounding solution and the original # PE gel completely recovers. The composition of the final # IPEC is also controlled by  $\alpha$ .



Scheme XIII

# IPEC formation can be stopped at any intermediate stage by termination of linear polyion supply from the environment. Then the shell/core sharp boundary structure of the hydrogel composite shown in Scheme X is fixed and remains stable for an infinitely long time if the conditions of IPEC stability are met. So the thickness of the # IPEC shell can be easily controlled. At the same time formation of # IPEC is *kinetically* controlled by Scheme XI [94]. It is faster for higher ionic strength (in the range of IPEC stability) and for lower degree of polymerization of a linear polyion. If the interpolyelectrolyte exchange reaction is restricted by some specific factors, linear polyions do not interpenetrate into the # PE hydrogel. In that case only a thin # IPEC skin (of a polyion size) is formed on the original hydrogel surface [95]. Tab. 2.7 represents a manner of complexation of various # PE hydrogels with various linear counterparts. One can see that the entities restricting interchange reactions in linear polyelectrolyte systems (hydrophobes, sulfate or sulfonate groups) also restrict an unbounded interpenetration of linear polyions into the investigated hydrogels.

# PE are also able to absorb oppositely charged globular proteins to form corresponding # IPEC. This was first reported for highly cross-linked poly(sodium acrylate) hydrogel (# Na PA) interacting with lysozyme [96], then extended to cytochrome *c* and protamine, and studied in detail [97, 98]. In salt-free systems the number of salt bonds formed between  $\text{---COO}^-$  groups of # Na PA and amine groups of complexed protein as well as the equilibrium composition of final # IPECs at excess of protein is determined by the pH and coincides with the com-

**Tab. 2.7** Manner of complexation between cross-linked polyelectrolyte hydrogels and oppositely charged linear polyelectrolytes (20 °C)

<b>Hydrogel</b>	<b>Linear polyelectrolyte</b>	<b><math>M_w</math></b>	<b>Character of complexation</b>	
# Na PA	PVP	$3 \times 10^5$	Interpenetration	
		$1.5 \times 10^5$	Interpenetration	
		$0.5 \times 10^5$	Interpenetration	
	PDMAEM	$6 \times 10^4$	Interpenetration	
		PEI (linear)	$6 \times 10^4$	Interpenetration
		chitosane	$2 \times 10^5$	Interpenetration
# PDMAEM	PVPD <sup>a)</sup>	$1.7 \times 10^3$	Surface adsorption	
	Na PA	$3.5 \times 10^5$	Interpenetration	
	Na PMA	$2.7 \times 10^4$	Interpenetration	
		$1.6 \times 10^4$	Interpenetration	
	Na PSS	$3.0 \times 10^5$	Surface adsorption	
	Na PVS <sup>b)</sup>	$4.4 \times 10^3$	Surface adsorption	
	heparine	$1.0 \times 10^5$	Surface adsorption	

a) N-ethyl-4-vinylpyridinium/N-dodecyl-4-vinylpyridium copolymer 70/30.

b) Poly(sodium vinylsulfate).

position of the corresponding IPEC formed by titration of linear Na PA solution with the protein. Absorption of proteins from salt-free water solutions proceeds so that the distinctly differentiated contracted zone of # IPEC formed surrounds the highly swollen # Na PA hydrogel core. However, in contrast to # PE/linear polyelectrolyte systems considered above, addition of external salts influences not only the kinetics but also drastically changes the distribution of a protein within the partly converted hydrogel from fully inhomogeneous to nearly uniform [98].

## 2.4

### Structural and Mechanical Properties of Interpolyelectrolyte Complexes in the Bulk

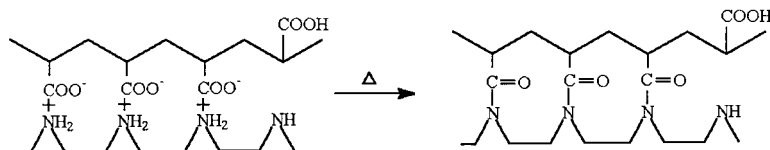
Initial analysis of the equilibria in polyelectrolyte coupling reactions led to a concept of IPECs as polymers with a structure in which more or less lengthy sequences of oppositely charged polyelectrolyte repeating units form tight, interpolyelectrolyte ion pairs alternating with loops and tails containing separate units. The latter may be considered as structural defects [99]. The fraction of paired domains is more the higher is  $\theta$  (see Fig. 2.1). The fraction of unpaired hydrophilic units included in loops and tails determines the ultimate degree of swelling of IPECs in water, which is limited by cooperatively stabilized ion-paired sequences.

Non-soluble stoichiometric complexes, even those formed in dilute aqueous solutions, in contrast to equilibrated nonstoichiometric IPECs aggregate into compact globular species, of size usually no less than tenths of a micron [100–102].

The presence of defects in stoichiometric IPECs may be caused by “freezing” of random interchain contacts occurring in the early stages of the rapidly proceeding

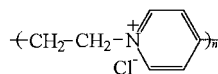
coupling reaction. Then, in the phase separated IPEC, subsequent rearrangements required for defects “healing” proceed very slowly, especially in the absence of an external salt. Slow relaxation of the nonequilibrium IPEC structure formed upon neutralization of strong polyacids by strong polybases was observed in [14, 102]. If the cause of formation of nonequibrated IPEC structure is eliminated, e.g. by using polymerization of ionic monomers on oppositely charged polyelectrolyte templates to prepare IPECs, the resulting products may be rather highly ordered [103–106].

In general, however, one should keep in mind that the major factor determining the defectiveness of IPECs is the absence of steric conformity between the polyelectrolyte counterparts. Most known IPECs are the products of coupling of sterically irregular polymer chains. Such IPECs are amorphous by X-ray diffraction. They contain at least 20–30% of pairs of separate units as has been shown by ion-exchange equilibria studies [107]. In particular, even the product of complete reaction between linear PEI and atactic PAA, whose macromolecules are characterized by quite a good steric fit to each other, is amorphous by X-ray. About 20% of carboxyl and imine groups are not ion-paired in this IPEC obtained at  $Z=1$ , i.e. located in structural defects as shown by IR spectroscopy [108]. On the other hand, the ion-paired domains in PEI–PA IPEC are fairly close. This is indicated by the fact that interpolyelectrolyte salt bonds quantitatively transform to amide bonds upon heating the dry IPEC film to form a ladder structure as shown in Scheme XIV. Carboxyl and amine groups located in defects do not participate in this reaction [108–110].



Scheme XIV

The aforesaid does not mean that all IPECs obtained by the direct mixing of oppositely charged polyelectrolyte components cannot be crystallized. The IPECs formed from the ionene (Structure 6) and isotactic Na PA [106] or Na PP [111, 112] have been described as highly crystalline materials. In any event, one may assume that stereoregularity and a certain steric conformity of the polyelectrolyte counterparts are the necessary conditions for IPEC crystallization.



Structure 6

Important data on single chain conformations in the bulk of IPECs consisting of high molecular mass PMA and chitosan ( $M_w=1.9\times 10^5$ ) at  $Z=1$  were obtained by small angle neutron scattering (SANS) measurements [113]. A mixture of ordinary PMA (PMA (H),  $M_w=3\times 10^5$ ) with 2% of deuterated PMA (PMA(D),  $M_w=1.1\times 10^5$ ,  $M_w/M_n=1.25$ ) was used as a polyanionic component. The IPEC

samples in the form of homogeneous films, 0.1 mm thick, were prepared from formic acid (3.5%) water solution of the polyelectrolytes, thoroughly washed after solvent evaporation and dried in vacuum as described in [114]. A reference PMA sample was also prepared in the form of a film from aqueous solution, containing 2 mol% PMA(D) and 98 mol% PMA(H). This was used for measuring the unperturbed dimensions of PMA(D) chains, while a PMA(H) film served as a background sample. The SANS measurements were carried out in the range of scattering vectors,  $Q$ ,  $4 \times 10^{-5} \leq Q \leq 8 \times 10^{-4} \text{ nm}^{-1}$ , where  $Q = 4\pi \sin\theta/\lambda$ ,  $2\theta$  is the scattering angle,  $\lambda = 3.03 \times 10^{-2} \text{ nm}$  is the average wavelength of the incident neutron beam. The half-width of the spectra was  $\Delta\lambda/\lambda = 0.35$ .

In the case of PMA(D) highly “diluted” with PMA(H) the intermolecular interference from the contrasting PMA(D) component may be neglected. Then for coil-like chains the Debye approximation

$$I(Q)^{-1} = I(0)^{-1}(1 + Q^2 R_g^2/3) \quad (10)$$

is valid at  $QR_g < 1$ , where  $I(Q)$  is the scattering intensity at  $Q \neq 0$ ,  $I(0)$  is the scattering intensity at  $\theta = 0$ .

From Eq. (10) the  $R_g$  of PMA(D) chains in the IPEC has been determined in so far that chitosan and PMA(H) have practically equal scattering length densities. Fig. 2.13 shows  $I(Q)^{-1}$  vs.  $Q^2$  plots for the IPEC and the reference PMA samples in the range of small  $Q$  values. The observed equality of extrapolated  $I(Q)^{-1}$  values for the both samples evidences that contrasting PMA(D) macromolecules are uniformly distributed and not aggregated. In fact the  $R_g = 10.2 \pm 0.3 \text{ nm}$  obtained for PMA(D) in a PMA(H) matrix exactly corresponds to the expected unperturbed size. By contrast the  $R_g = 17.5 \pm 0.5 \text{ nm}$  obtained for PMA(D) in the IPEC matrix indicates a substantial extension of PMA coils interacting with chitosan. However,

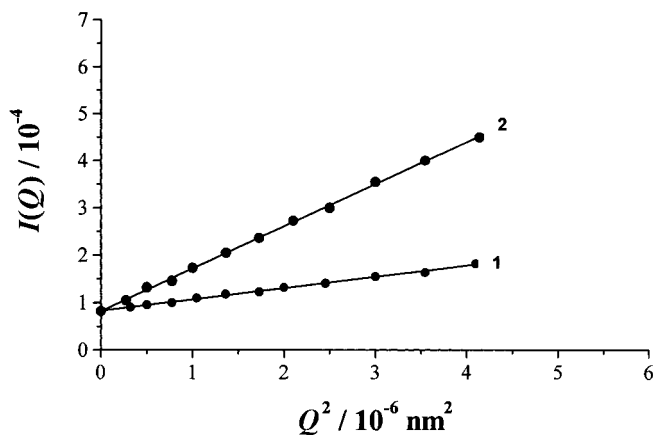


Fig. 2.13 The initial parts of SANS curves: PMA(D) in PMA(H) matrix (1); PMA(D) in PMA–chitosane IPEC matrix (2).

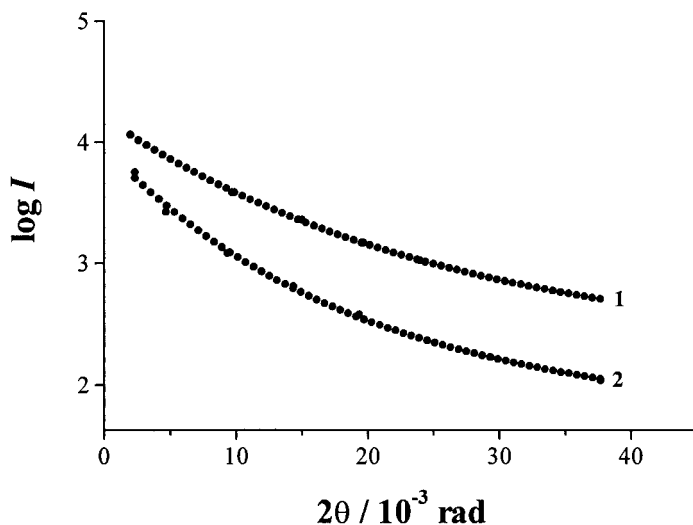


Fig. 2.14 Full experimental SANS curves: PMA(D) in PMA(H) matrix (1); PMA(D) in PMA-chitosane IPEC matrix (2).

their shape only slightly deviates from a Gaussian coil. The treatment of the experimental neutron scattering data (Fig. 2.14, curves 1 and 2) at  $QR > 5$  gives  $I(Q) \sim Q^{-2}$  for PMA(D) in a PMA(H) matrix that exactly corresponds to Gaussian behavior, and  $I(Q) \sim Q^{-2.2}$  for PMA(D) in the IPEC matrix.

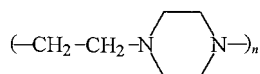
Unfortunately, the above study is the only example of SANS application for investigation of IPEC structure in the bulk known to the author. There is no question that further systematic investigations in this field would be most beneficial.

Air-dry amorphous IPECs in the bulk represent transparent brittle materials. Water is a common plasticizer for most of these materials. Slightly water swollen (tens of per cent at  $Z=1$ ) IPEC films are flexible elastic bodies. A homogeneous IPEC film can be formed from a solution of the corresponding polyelectrolytes initially protected from electrostatic coupling. In the case of a pair of strong polyelectrolytes a mixed water-organic solvent should be used containing a shielding salt, such as NaCl or NaBr, and a volatile organic component, such as acetone or dioxane to avoid salting out the polymers. After solvent evaporation the formed film should be repeatedly washed with water to remove inorganic salts [1, 14, 115].

In the case of weak polyelectrolytes their premature interaction can be prevented simply by shifting the pH to either the acidic or alkaline region outside the region of IPEC stability (see Fig. 2.1). This can be done by using a volatile acid, such as formic or acetic acid, or a volatile base, such as ammonia or trimethylamine [114].

The mechanical properties of IPECs consisting of pairs of strong polyelectrolytes have never been investigated systematically. However, it was noted that the strongest water swollen IPEC films studied as potential membranes for ion exchange and salt separation, could be prepared at  $Z=1$ , i.e. at a maximum content of interpolyelectrolyte salt bonds [1].

The relationship is more complicated in the case of IPEC membranes consisting of weak polyelectrolytes [114] in particular the IPEC formed from poly(ethylenepiperasine) (PEP,  $M_n=3\times 10^5$ ) (Structure 7) and PAA ( $M_n=3\times 10^5$ ), whose mechanical behavior was thoroughly investigated in [116]. The IPEC films of various composition  $Z=[\text{PAA}]/[\text{PEP}]$  were cast from 50% water solution of formic acid. The stress-strain curves for equilibrium swollen PAA-PEP IPEC films measured in water environment are presented in Fig. 2.15 (a). These curves reveal a visco-elastic behavior of the investigated samples in the broad range of  $Z\geq 1$ . Such behavior is typical for most water swollen IPECs. However, in contrast to IPECs formed from strong polyelectrolytes the highest yield stress (Fig. 2.15 (a)) and elastic moduli (Fig. 2.15 (b)) are observed not at  $Z=1$ , but at  $Z=1.5$  i.e. for the PAA-PEP IPEC films somewhat enriched with PAA. This IPEC composition also corresponds to a minimum swelling (about 35%). At  $Z<1$  the films are still weaker. Undoubtedly intermolecular salt bonds play an important role here reinforcing the film structure as well as in the case of strong polyelectrolytes. In particular, it follows from the stress-strain curves represented in Fig. 2.15 (c). One can see that the sample originally exposed in NaCl solution and then tested in the same environment has substantially lowered initial modulus and yield stress. This is due to shielding of intermolecular ion pairs. At the same time replacing water by water-dioxane mixtures and pure dioxane one can observe a considerable



Structure 7

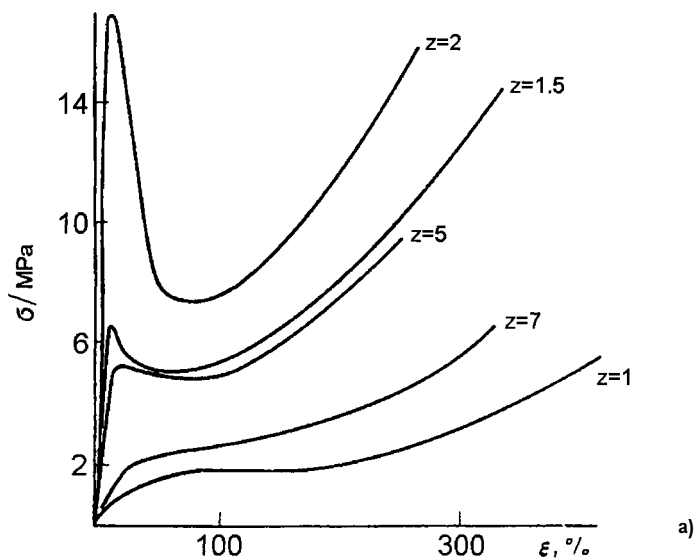
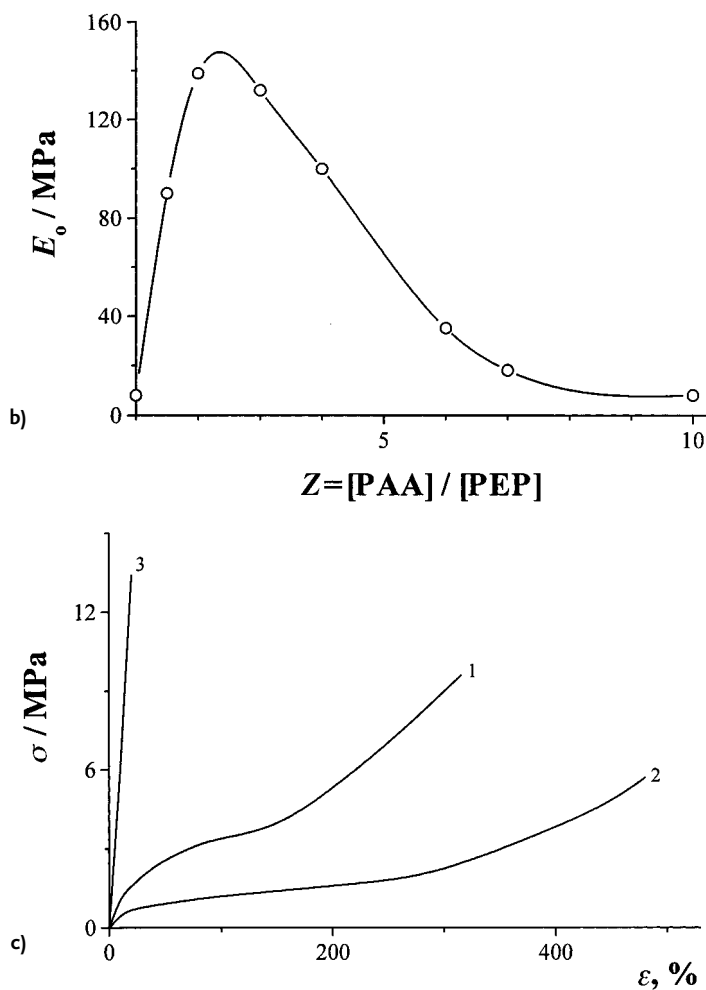


Fig. 2.15a



**Fig. 2.15** Visco-elastic behavior of PAA-PEP IPECs. (a) Stress-strain curves of PAA-PEP IPECs of various composition in water environment, pH 6.0, 20°C. (b) Initial elastic modulus of PAA-PEP IPECs vs. their composition  $Z$ . (c) Stress-strain curves for PAA-PEP IPECs ( $Z=1$ ) in water (1), 5 wt.% NaCl water solution (2), pH 6.0, 10°C; and dioxane (3).

strengthening of the IPEC films due to increasing stability of ion pairs with decreasing environmental polarity. Nevertheless the effect of excess PMA suggests that hydrogen bonding contributes markedly to the IPEC mechanical behavior. The contributions of interpolymer salt bonds and hydrogen bonds apparently become optimum at  $Z=1.5$ . Fig. 2.16 demonstrates the decrease in IPEC strength with increasing temperature, which is much sharper and looks more cooperative in the case of the IPEC enriched with PAA (Fig. 2.16(b)).

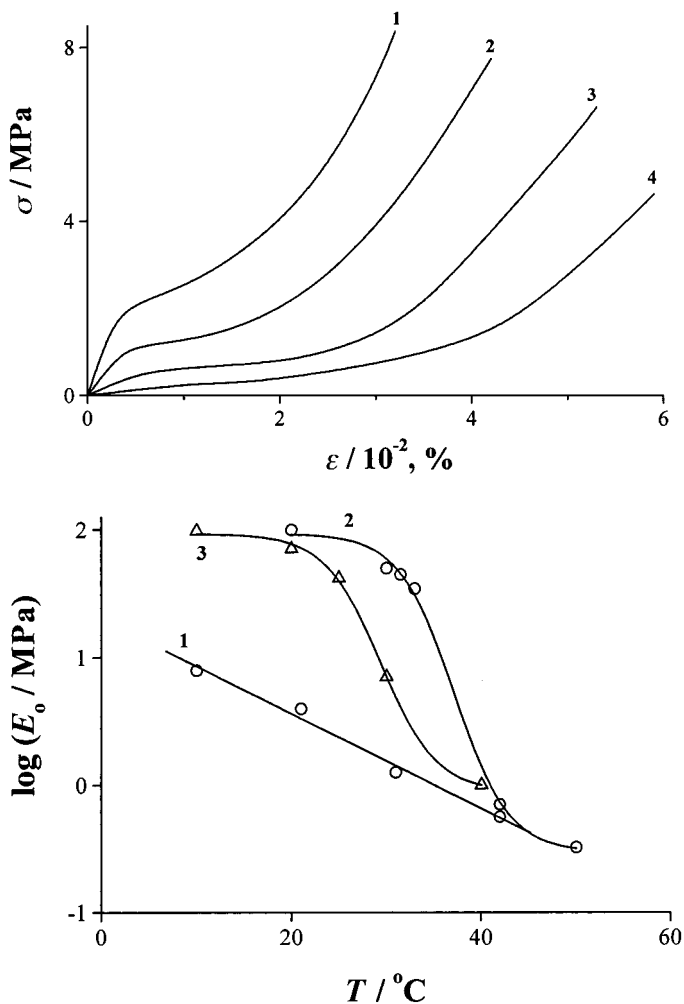


Fig. 2.16 Effect of temperature on visco-elastic behavior of PAA-PEP IPECs in water environment, pH 6.0. (a) Stress-strain curves measured at various temperatures: 10°C (1), 20°C (2), 30°C (3), 40°C (4). (b) Initial electric modulus vs. temperature;  $Z=1$  (1),  $Z=3$  (2),  $Z=5$  (3).

## 2.5 Conclusion

Vitally important functions of biology, except precisely designed building blocks, are provided by self-assembly and rearrangements. The structure of supramolecular biological entities form on balancing various superimposing multisite interactions (hydrogen, hydrophobic and donor-acceptor bonding, electrostatic attraction and repulsion etc.), some of them opposing. Hence, hand in hand with an extra-



ordinary stability over a certain range of conditions, a possibility of substantial structural rearrangements arises with only slight changes in the environment. These peculiarities are also characteristic to some extent of the behavior of synthetic IPECs. The trends and considerations set forth in this chapter may be useful for controlling the synthesis, structure and properties of various IPECs including those forming interfaces between polyelectrolyte nanolayers in multilayered composites.

### Acknowledgement

The author is deeply grateful to Professor A. B. Zezin for discussing some key aspects of this chapter and Natalya Lokshin, MSU PhD student for kindly helping to arrange the manuscript.

## 2.6

### References

- 1 H. A. BIXLER, A. S. MICHAELS, in *Encyclopedia of Polymer Science and Technology*, ed. board: H. F. MARK, N. G. GAYLORD (ex. ed.) N. M. BIKALES (ed.), Interscience Publishers, New York, London, Sydney, Toronto, 1969, vol. 10, p. 765.
- 2 V. A. KABANOV, *Pure Appl. Chem., Macromol. Chem.*, 1973, 8, 121–145.
- 3 V. A. KABANOV, A. B. ZEZIN, *Soviet Sci. Rev., Ser. B, Chem. Rev.*, 1982, 4, 207–282.
- 4 E. TSUCHIDA, K. ABE, *Adv. Polym. Sci.*, 1982, 45, 1–130.
- 5 V. A. KABANOV, A. B. ZEZIN, *Macromol. Chem., Suppl.*, 1984, 6, 259–276.
- 6 A. B. ZEZIN, V. V. LUTSENKO, V. B. ROGA-CHEVA, O. A. ALEKSINA, R. I. KALYUZH-NAYA, V. A. KABANOV, V. A. KARGIN, *Vysokomol. Soedin., Ser. A*, 1972, 14, 772–779.
- 7 H. G. BUNGENBERG DE JONG, *Trans. Faraday Soc.*, 1932, 28, 27.
- 8 H. G. BUNGENBERG DE JONG, W. A. DEK-KER, *Kolloidchem. Beih.*, 1936, 43, 143, 213.
- 9 H. G. BUNGENBERG DE JONG, in *Colloid Science*, 1949, vol. 2, ch. 10, p. 335 ed. H. R. KRUYT, Elsevier, Amsterdam, New York
- 10 I. MICHAELI, J. TH. G. OVERBEEK, M. J. VOORN, *J. Polym. Sci.*, 1957, 23, 443.
- 11 M. J. VOORN, *Fortschr. Hochpolym.-Forsch.*, 1959, 1, 192.
- 12 A. S. MICHAELS, R. G. MIEKKA, *J. Phys. Chem.*, 1961, 65, 1765.
- 13 A. S. MICHAELS, L. MIR, N. S. SCHNEIDER, *J. Phys. Chem.*, 1965, 69, 1447.
- 14 A. S. MICHAELS, G. L. FALKENSTEIN, N. S. SCHNEIDER, *J. Phys. Chem.*, 1965, 69, 1456.
- 15 V. A. KABANOV, A. B. ZEZIN, V. A. KASAI-KIN, A. A. JAROSLAVOV, D. A. TOPCHIEV, *Usp. Khim.*, 1991, 60(3), 595–601.
- 16 A. B. ZEZIN, B. S. ELTSEFON, A. R. RUD-MAN, N. A. VENGEROVA, R. I. KALYUZH-NAYA, S. P. VALUEVA, E. M. KOPILOVA, A. K. CHEPUROV, *Khim-Farm. Zh.*, 1987, 21(7), 788–801.
- 17 R. MILLER, D. BACH, *Biopolymers*, 1968, 6, 169.
- 18 E. TSUCHIDA, Y. OSADA, K. SANADA, *J. Polym. Sci., Polym. Chem. Ed.*, 1972, 10, 3397.
- 19 V. A. KABANOV, A. B. ZEZIN, A. V. KHA-RENKO, R. I. KALYUZH-NAYA, *Dokl. Akad. Nauk SSSR*, 1976, 230, 139–142.
- 20 ZH. G. GULYAIEVA, O. A. POLETAIEVA, A. A. KALACHEV, V. A. KASAIKIN, A. B. ZEZIN, V. A. KABANOV, *Vysokomol. Soedin., Ser. A*, 1976, 18, 2800–2805.
- 21 V. A. KABANOV, A. B. ZEZIN, V. B. ROGA-CHEVA, ZH. G. GULYAIEVA, M. F. ZANSO-CHOVA, J. G. H. JOOSTEN, J. BRACKMAN, *Macromolecules*, 1999, 32, 1904–1909.
- 22 W. CHEN, N. J. TURRO, D. A. TOMALIA, *Langmuir*, 2000, 16, 15.

- 23 V.A. KABANOV, V.G. SERGEYEV, O.A. PYSHKINA, A.A. ZINCHENKO, A.B. ZE-ZIN, J.G.H. JOOSTEN, J. BRACKMAN, K. YOSHIKAWA, *Macromolecules*, **2000**, *33*, 9587–9593.
- 24 A.V. KABANOV, V.A. KABANOV, *Bioconjugate Chem.*, **1995**, *6*, 7–20.
- 25 *Self-assembling Complexes for Gene Delivery*, ed. A.V. KABANOV, P.L. FELGNER, L.W. SAYMOUR, Wiley, Chichester, 1998, part 4, pp. 167–273.
- 26 V.A. KABANOV, in *Polymerization in Organized Media*, ed. C.M. PALEOS, Gordon & Breach, Philadelphia, 1992, pp. 369–454.
- 27 V.A. KABANOV, V.P. EVDAKOV, M.I. MUSTAFAEV, A.D. ANTIPINA, *Mol. Biol. (Moscow)*, **1977**, *11*, 582–597.
- 28 V.A. KABANOV, A.B. ZE-ZIN, M.I. MUSTAFAEV, V.A. KASAIKIN in *Polymeric Amines and Ammonium Salts*, ed. E.J. GOETHALS, Pergamon, Oxford, 1980, pp. 173–192.
- 29 V.S. ZAITSEV, V.A. IZUMRUDOV, A.B. ZE-ZIN, V.A. KABANOV, *Dokl. Akad. Nauk SSSR*, **1992**, *322*, 318–323.
- 30 Z.KH. IBRAGIMOVA, E.M. IVLEVA, N.V. PAVLOVA, T.A. BORODULINA, V.A. EFREMOV, V.A. KASAIKIN, A.B. ZE-ZIN, V.A. KABANOV, *Polym. Sci.*, **1992**, *34*, 808–812.
- 31 Z.KH. IBRAGIMOVA, V.A. KASAIKIN, A.B. ZE-ZIN, V.A. KABANOV, *Vysokomol. Soedin., Ser. A*, **1986**, *28*, 1640–1646.
- 32 E.A. LYSCHENKO, T.K. BRONICH, V.A. KASAIKIN, A.B. ZE-ZIN, V.A. KABANOV, *Polym. Sci.*, **1994**, *36*, 175–178.
- 33 T.A. KOROBKO, V.A. IZUMRUDOV, A.B. ZE-ZIN, V.A. KABANOV, *Polym. Sci.*, **1994**, *36*, 179–183.
- 34 YU. V. KHANDURINA, V.B. ROGACHEVA, A.B. ZE-ZIN, V.A. KABANOV, *Polym. Sci.*, **1994**, *36*, 184–188.
- 35 YU. V. KHANDURINA, A.T. DEMBO, V.B. ROGACHEVA, A.B. ZE-ZIN, V.A. KABANOV, *Polym. Sci.*, **1994**, *36*, 189–194.
- 36 YU. V. KHANDURINA, V.B. ROGACHEVA, A.B. ZE-ZIN, V.A. KABANOV, *Polym. Sci.*, **1994**, *36*, 195–199.
- 37 E. TSUCHIDA, Y. OSADA, *Macromol. Chem.*, **1974**, *175*, 603.
- 38 A.V. KHARENKO, E.A. STARIKOVA, V.V. LUTSENKO, A.B. ZE-ZIN, V.A. KABANOV, *Vysokomol. Soedin., Ser. A*, **1976**, *18*, 1604–1608.
- 39 ZH.G. GULYAEVA, M.F. ZANSOKHOVA, E.F. RAZVODOVSKII, V.S. EFIMOV, A.B. ZE-ZIN, V.A. KABANOV, *Vysokomol. Soedin., Ser. A*, **1983**, *25*, 1238–1244.
- 40 V.A. IZUMRUDOV, A.P. SAVITSKII, K.N. BAKEEV, A.B. ZE-ZIN, V.A. KABANOV, *Macromol. Chem., Rapid Commun.*, **1984**, *5*, 709–714.
- 41 V.A. IZUMRUDOV, T.K. BRONICH, A.B. ZE-ZIN, V.A. KABANOV, *J. Polym. Sci., Polym. Lett. Ed.*, **1985**, *23*, 439–444.
- 42 V.A. KABANOV, A.B. ZE-ZIN, V.A. IZUMRUDOV, T.K. BRONICH, K.N. BAKEEV, *Macromol. Chem., Suppl.*, **1985**, *13*, 137–155.
- 43 A.B. ZE-ZIN, V.A. IZUMRUDOV, V.A. KABANOV, *Frontiers of Macromolecular Science*, Blackwell, Oxford, 1989, pp. 219–225.
- 44 K.N. BAKEEV, V.A. IZUMRUDOV, A.B. ZE-ZIN, V.A. KABANOV, *Dokl. Akad. Nauk SSSR*, **1988**, *299*, 1405–1408.
- 45 K.N. BAKEEV, V.A. IZUMRUDOV, S.I. KUCHANOV, A.B. ZE-ZIN, V.A. KABANOV, *Dokl. Akad. Nauk SSSR*, **1988**, *300*, 132–135.
- 46 K.N. BAKEEV, V.A. IZUMRUDOV, S.I. KUCHANOV, A.B. ZE-ZIN, V.A. KABANOV, *Macromolecules*, **1992**, *25*, 4249–4254.
- 47 V.A. IZUMRUDOV, T.K. BRONICH, O.S. SABUROVA, A.B. ZE-ZIN, V.A. KABANOV, *Makromol. Chem. Rapid Commun.*, **1988**, *9*, 7–12.
- 48 M.G. KRAKOVYAK, E.V. ANUFRIEVA, S.S. SKOROKHODOV, *Vysokomol. Soedin. Ser. A*, **1972**, *14*, 1127–1131.
- 49 N.R. PAVLOVA, YU.E. KIRSH, V.A. KABANOV, *Vysokomol. Soedin. Ser. A*, **1979**, *21*, 2062–2069.
- 50 V.A. KABANOV, M.V. ZHIRYAKOVA, S.I. KARGOV, A.B. ZE-ZIN, V.A. IZUMRUDOV, *Dokl. Akad. Nauk*, **1993**, *329*, 66–70.
- 51 V.A. KABANOV, M.V. ZHIRYAKOVA, S.I. KARGOV, A.B. ZE-ZIN, V.A. IZUMRUDOV, *Dokl. Akad. Nauk*, **1993**, *332*, 722–726.
- 52 V.A. IZUMRUDOV, S.I. KARGOV, M.V. ZHIRYAKOVA, A.B. ZE-ZIN, V.A. KABANOV, *Biopolymers*, **1995**, *35*, 523–531.
- 53 V.A. IZUMRUDOV, V.A. KASAIKIN, L.M. ERMAKOVA, A.B. ZE-ZIN, *Vysokomol. Soedin. Ser. A*, **1978**, *20*, 400–406.
- 54 L.N. ERMAKOVA, YU.G. FROLOV, V.A. KASAIKIN, A.B. ZE-ZIN, V.A. KABANOV, *Vysokomol. Soedin. Ser. A*, **1981**, *23*, 2328–2340.

- 55 L. N. ERMAKOVA, P. V. NUSS, V. A. KASAIIKIN, A. B. ZEZIN, V. A. KABANOV, *Vysokomol. Soedin. Ser. A*, **1983**, 25, 1391–1399.
- 56 V. A. KASAIIKIN, N. V. PAVLOVA, A. B. ZEZIN, V. A. KABANOV, *Dokl. Akad. Nauk SSSR*, **1985**, 281, 888–892.
- 57 L. N. ERMAKOVA, T. A. ALEXANDROVA, P. V. NUSS, A. M. VASSERMAN, V. A. KASAIIKIN, A. B. ZEZIN, V. A. KABANOV, *Vysokomol. Soedin. Ser. A*, **1985**, 1845–1851.
- 58 V. A. KASAIIKIN, N. V. PAVLOVA, L. N. ERMAKOVA, A. B. ZEZIN, V. A. KABANOV, *Kolloidn. Jurnal*, **1988**, 48, 452–460.
- 59 R. I. KALYUZHNAJA, KH. KHUL'CHAEV, V. A. KASAIIKIN, V. A. KABANOV, *Polym. Sci.*, **1994**, 36, 209–214.
- 60 V. A. KABANOV, A. B. ZEZIN, V. B. ROGACHEVA, N. V. GRISHINA, E. J. GOETHALS, M. VAN DE VELDE, *Macromol. Chem.*, **1986**, 187, 1151–1158.
- 61 O. A. KHARENKO, A. V. KHARENKO, R. I. KALYUZHNAJA, V. A. IZUMRUDOV, V. A. KASAIIKIN, A. B. ZEZIN, V. A. KABANOV, *Vysokomol. Soedin. Ser. A*, **1979**, 21, 2719–2725.
- 62 V. A. KASAIIKIN, O. A. KHARENKO, A. V. KHARENKO, A. B. ZEZIN, V. A. KABANOV, *Vysokomol. Soedin. Ser. B*, **1979**, 21, 84–85.
- 63 O. A. KHARENKO, A. V. KHARENKO, V. A. KASAIIKIN, A. B. ZEZIN, V. A. KABANOV, *Vysokomol. Soedin. Ser. A*, **1979**, 21, 2726–2733.
- 64 V. A. EFREMOV, N. V. PAVLOVA, E. M. IVLEVA, V. A. KASAIIKIN, *Vysokomol. Soedin. Ser. A*, **1990**, 32, 2458–2460.
- 65 H. YAMAKAWA, *J. Chem. Phys.*, **1967**, 46, 973.
- 66 O. A. KHARENKO, V. A. IZUMRUDOV, A. V. KHARENKO, V. A. KASAIIKIN, A. B. ZEZIN, V. A. KABANOV, *Vysokomol. Soedin. Ser. A*, **1980**, 22, 218–225.
- 67 E. G. DONNAN, E. A. GUGGENHEIM, *Z. Phys. Chem.*, **1932**, 162, 346.
- 68 N. KARIBYANTS, H. DAUTZENBERG, H. GOLFEN, *Macromolecules*, **1997**, 30, 7803–7809.
- 69 H. DAUTZENBERG, *Macromolecules*, **1997**, 30, 7810–7815.
- 70 N. KARIBYANTS, H. DAUTZENBERG, *Langmuir*, **1998**, 14, 4427–4434.
- 71 H. DAUTZENBERG, N. KARIBYANTS, *Macromol. Chem. Phys.*, **1999**, 200, 118–125.
- 72 V. A. IZUMRUDOV, O. A. KHARENKO, A. V. KHARENKO, ZH. G. GULYAEVA, V. A. KASAIIKIN, A. B. ZEZIN, V. A. KABANOV, *Vysokomol. Soedin., Ser. A*, **1980**, 22, 692–699.
- 73 V. A. KABANOV, A. B. ZEZIN, V. B. ROGACHEVA, V. A. IZUMRUDOV, S. V. RYZHYKOV, *Dokl. Akad. Nauk SSSR*, **1982**, 262, 1419–1422.
- 74 V. A. KABANOV, A. B. ZEZIN, V. B. ROGACHEVA, S. V. RYZHYKOV, *Dokl. Akad. Nauk SSSR*, **1982**, 267, 862–865.
- 75 V. B. ROGACHEVA, S. V. RYZHYKOV, A. B. ZEZIN, V. A. KABANOV, *Vysokomol. Soedin., Ser. A*, **1984**, 26, 1674–1680.
- 76 V. B. ROGACHEVA, S. V. RYZHYKOV, A. B. ZEZIN, V. A. KABANOV, *Vysokomol. Soedin., Ser. A*, **1984**, 26, 2417–2427.
- 77 ZH. G. GULYAEVA, I. V. ALDOSHINA, M. F. ZANSOKHOVA, V. B. ROGACHEVA, A. B. ZEZIN, V. A. KABANOV, *Vysokomol. Soedin., Ser. A*, **1990**, 32, 776–783.
- 78 D. V. PERGUSHOV, V. A. IZUMRUDOV, A. B. ZEZIN, V. A. KABANOV, *Polym. Sci.*, **1993**, 35, 940–944.
- 79 D. V. PERGUSHOV, V. A. IZUMRUDOV, A. B. ZEZIN, V. A. KABANOV, *Polym. Sci.*, **1995**, 37, 1081–1087.
- 80 U. P. STRAUSS, Y. P. LEUNG, *J. Am. Chem. Soc.*, **1965**, 87, 1476.
- 81 N. K. NEFEDOV, T. G. ERMAKOVA, V. A. KASAIIKIN, A. B. ZEZIN, V. A. LOPYREV, *Vysokomol. Soedin., Ser. A*, **1985**, 27, 1496–1499.
- 82 A. V. KABANOV, T. K. BRONICH, V. A. KABANOV, K. YU. A. EISENBERG, *Macromolecules*, **1996**, 29, 6797–6802.
- 83 A. HARADA, K. KATAOKA, *Macromolecules*, **1998**, 28, 5294–5299.
- 84 A. V. KABANOV, S. V. VINOGRADOV, Y. G. SUZDALTSEVA, V. YU. ALAKHOV, *Bioconjugate Chem.*, **1995**, 6, 639–643.
- 85 K. KATAOKA, H. TOGAWA, A. HARADA, K. YASUGI, T. MATSUMOTO, S. KATAYASE, *Macromolecules*, **1996**, 29, 8556–8557.
- 86 V. A. KABANOV, A. S. POLYNSKY, A. A. YAROSLAVOV, O. S. CHECHIK, *Dokl. Akad. Nauk SSSR*, **1986**, 283, 845–847.
- 87 S. A. SUKHISHVILI, A. S. POLYNSKY, A. A. YAROSLAVOV, O. S. CHECHIK, V. A. KABANOV, *Dokl. Akad. Nauk SSSR*, **1988**, 302, 640–643.
- 88 A. A. YAROSLAVOV, A. S. POLYNSKY, S. A. SUKHISHVILI, V. A. KABANOV, *Makromol.*

- Chem., Macromol. Symp.*, **1989**, 26, 265–280.
- 89 V. A. KABANOV, A. A. YAROSLAVOV, S. A. SUKHISHVILI, A. S. POLINSKY, O. S. CHECHIK, *FEBS Lett.*, **1990**, 275, 231–234.
- 90 V. A. KABANOV, A. A. YAROSLAVOV, O. V. BORONINA, S. A. SUKHISHVILI, I. R. NAZAROVA, *J. Bioact. Compat. Polym.*, **1995**, 10, 41–50.
- 91 V. A. KABANOV, A. A. YAROSLAVOV, S. A. SUKHISHVILI, *J. Controlled Release*, **1996**, 39, 173–189.
- 92 A. A. YAROSLAVOV, E. G. YAROSLAVOVA, A. A. RAKHNYANSKAYA, F. M. MENGER, V. A. KABANOV, *Colloids Surf., B*, **1999**, 16, 29–43.
- 93 V. A. KABANOV, A. B. ZEIN, V. B. ROGACHEVA, V. A. PREVISH, *Macromol. Chem.*, **1989**, 190, 2211–2216.
- 94 A. M. CHUPYATOV, V. B. ROGACHEVA, A. B. ZEIN, V. A. KABANOV, *Polym. Sci.*, **1994**, 36, 169–174.
- 95 A. B. ZEIN, V. B. ROGACHEVA, V. A. KABANOV, *Macromol. Symp.*, **1997**, 126, 123–141.
- 96 SH. NAGAMATSU, Y. NABESHIMA, A. S. HOFFMAN, *Polym. Prepr. (ACS, Div. Polym. Chem.)*, **1992**, 33, 478.
- 97 V. B. KARABANOVA, V. B. ROGACHEVA, A. B. ZEIN, V. A. KABANOV, *Polym. Sci., Ser. A*, **1995**, 37, 1138–1143.
- 98 V. B. SKOBELEVA, V. B. ROGACHEVA, A. B. ZEIN, V. A. KABANOV, *Dokl. Phys. Chem.*, **1996**, 347, 52–55.
- 99 A. B. ZEIN, V. B. ROGACHEVA, in *Uspekhi Khimii I Phiziki Polymerov*, Khimia, Moscow, 1973, pp. 3–32.
- 100 N. F. BAKEEV, V. S. PSHEZHETSII, V. A. KARGIN, *Vysokomol. Soedin. Ser. B*, **1959**, 1, 1812.
- 101 A. S. MICHAELS, *Ind. Eng. Chem.*, **1965**, 57(10), 32.
- 102 V. B. ROGACHEVA, S. YA. MIRLINA, V. A. KARGIN, *Vysokomol. Soedin., Ser. B*, **1970**, 12, 340–343.
- 103 V. A. KABANOV, O. V. KARGINA, M. V. UL'YANOVA, *Vysokomol. Soedin., Ser. B*, **1974**, 16, 795–796.
- 104 A. BLUMSTEIN, S. R. KAKIVAYA, J. C. SALAMONE, *J. Polym. Sci., Part B*, **1974**, 12, 651.
- 105 A. BLUMSTEIN, S. R. KAKIVAYA, R. BLUMSTEIN, T. SUZUKI, *Macromolecules*, **1975**, 8, 435.
- 106 V. A. KABANOV, O. V. KARGINA, M. V. UL'YANOVA, *J. Polym. Sci., Polym. Chem. Ed.*, **1976**, 14, 2351–2356.
- 107 I. MICHAELI, T. BEJERANO, *J. Polym. Sci., Part C*, **1967**, 22, 909–915.
- 108 A. B. ZEIN, V. B. ROGACHEVA, V. S. KOMAROV, E. F. RAZVODOVSKY, *Vysokomol. Soedin., Ser. A*, **1975**, 17, 2637–2643.
- 109 V. S. KOMAROV, V. B. ROGACHEVA, A. A. BEZUBOV, A. B. ZEIN, *Vysokomol. Soedin., Ser. B*, **1976**, 784–786.
- 110 V. S. KOMAROV, V. B. ROGACHEVA, A. B. ZEIN, *Vysokomol. Soedin., Ser. A*, **1978**, 20, 1629–1633.
- 111 A. N. GVOZDETSKII, O. V. KIM, V. I. SMETANYUK, V. A. KABANOV, V. A. KARGIN, *Vysokomol. Soedin., Ser. A*, **1971**, 13, 2409.
- 112 V. A. KABANOV, O. V. KARGINA, L. A. MISHUSTINA, S. YU. LABANOV, K. KATUZYNSKI, S. PENCZEK, *Macromol. Chem., Rapid Commun.*, **1981**, 2, 343–346.
- 113 M. M. AGAMALYAN, V. A. KASAIKIN, V. L. ALEXEEV, R. I. KALYUZHNAJA, G. A. EVMENENKO, E. E. SKORIKOVA, *Preprint 1627 of Leningrad Institute of Nuclear Physics*, **1990**, 1–14.
- 114 R. I. KALYUZHNAJA, A. R. RUDMAN, N. A. VENGEROVA, E. F. RAZVODOVSKII, B. S. ELTSEFON, A. B. ZEIN, *Vysokomol. Soedin., Ser. A*, **1975**, 27, 86–92.
- 115 A. S. HOFMAN, R. LEWIS, A. MICHAELS, *Polymer Preprints*, **1969**, 10, 916–917.
- 116 R. I. KALYUZHNAJA, A. L. VOLYNSKII, A. R. RUDMAN, N. A. VENGEROVA, E. F. RAZVODOVSKII, B. S. ELTSEFON, A. B. ZEIN, *Vysokomol. Soedin., Ser. A*, **1976**, 28, 71–76.

### 3

## **Polyelectrolyte Adsorption and Multilayer Formation**

JEAN-FRANCOIS JOANNY and MARTIN CASTELNOVO

### **Abstract**

In this chapter, we review our recent theoretical work on the formation of polyelectrolyte multilayers. The first layer is obtained by polyelectrolyte adsorption on a surface with an opposite charge. The adsorbed polyelectrolyte charge is sufficient to invert the charge of the surface. Each subsequent layer is bound to the previous one by the formation of a polyelectrolyte complex. Using a Debye-Hückel-like theory to describe the complexation, we obtain the adsorbance (the adsorbed amount) of each layer and the thickness of the layers.

### 3.1

#### **Introduction**

Recent experiments on polyelectrolyte multilayers, formed by consecutive adsorption of negatively charged and positively charged polyelectrolytes, have shown that, upon addition of a new layer, the number of charges carried by the incorporated polymer is large enough to neutralize the charge of the previous layer and even to invert the sign of the zeta potential (or the global charge of the layer). Neutron experiments also clearly indicate that the newly incorporated layer strongly interpenetrates the previous layer and even the one before but that there is not complete mixing between the layers, each layer keeping its identity [1].

All these results raise a number of theoretical questions that we try to address briefly in this chapter. The first question concerns the first layer of the assembly. It is obtained by adsorption of polyelectrolyte chains on an oppositely charged surface; the adsorption must overcompensate the charge of the surface and the layer must be “strongly anchored to the surface” so that in many cases a polymer such as polyethyleneimine that is different from the polymer used for the following layers is used. Polyelectrolyte adsorption has been studied extensively over recent years and we will summarize the conditions under which charge inversion can occur and the influence of ionic strength on polyelectrolyte adsorption [2].

Starting from the second layer, the new adsorbing layer is formed by adsorption of polyelectrolyte chains of a given charge, interacting with the polyelectrolyte

chains of the previous layer that have an opposite charge. When they are mixed in solution in water, oppositely charged polyelectrolytes form polyelectrolyte complexes and in most cases precipitate. There is a vast literature on polyelectrolyte complexes, in particular due to the Russian school of Kabanov [3]. Theoretical models have appeared recently that give some predictions for the phase diagram of the complex [4, 5]. We will assume here that polyelectrolyte complexation is the driving force for multilayer formation and that the polymer density inside the multilayer is the density in the dense phase of the polymer mixture (the complex).

An important step in the formation of multilayers is the rinsing step between two consecutive adsorptions. This step is aimed at eliminating the non-adsorbed (or the weakly adsorbed) polyelectrolyte. In many experiments, the properties of the multilayer depend for example on the duration of the rinsing step. This indicates that the formation of the multilayers is not an equilibrium process and that one should build a kinetic theory which does not seem to be available at the present time. We will thus limit ourselves here to a thermodynamic theory and impose a constrained equilibrium; for example, polyelectrolyte adsorption is assumed to be irreversible in the sense that the amount of adsorbed polymer remains constant, even in contact with pure solvent during the rinsing step, and that there is no desorption; however we allow for free equilibration of the chain conformations at each step under this constraint that the adsorbed amount is constant. Another important problem that is not discussed here is the interdiffusion between the layers. It certainly plays a major role in defining some of the properties of the layers when they are used for applications.

The properties of polyelectrolyte multilayers are controlled by many parameters such as ionic strength, temperature, pH, the electrostatic charges and the stiffnesses of the two polymers etc. At each step of the formation, parameters such as the ionic strength can be changed allowing a fine tuning of the multilayer properties. The layer properties also strongly depend on the experimental procedure. In many experiments, the layer is dried at each step, the polymers in the multilayer become glassy and their conformation is frozen. For simplicity, we will assume here that all parameters are fixed during the multilayer formation: there is no change in the salt concentration or in the temperature during the various steps of the formation and that there is no drying of the layers at each step, so that the polymers remain in a liquid state and that a thermodynamic or a constrained thermodynamic equilibrium can be reached. This condition is not fulfilled in most experiments but has been carefully imposed in some recent experiments probing the structure of the monolayers [6].

This short review is organized as follows. In the next section, we give a short summary of the properties of flexible polyelectrolyte in solution. Polyelectrolyte adsorption is considered in the following section and the formation of polyelectrolyte complexes in Section 3.4. All these results are used in Section 3.5 to give a rather rough discussion of the structure of polyelectrolyte multilayers. The last section gives some concluding remarks and discusses some open issues.

## 3.2

## Polyelectrolytes in Solution

In this section, we very briefly summarize the solution properties of polyelectrolytes [7]. We first consider a very dilute polyelectrolyte solution in water that we assimilate to a  $\Theta$  solvent. Each chain comprises  $N$  monomers of size  $a$  and a fraction  $f$  of the monomers are charged. If the charge is very low, the electrostatic interactions do not play any role and the chain is Gaussian, its end to end distance is  $R_0 = N^{1/2}a$ . If the charge is higher, it is stretched by the repulsive electrostatic interactions between monomers. In the presence of a concentration  $n$  of added salt, the coulombic interaction between two charges at a distance  $r$  is given by the Debye-Hückel potential  $(r) = \frac{kTl_B}{r} \exp -\kappa r$  where  $l_B = \frac{q^2}{4\pi\epsilon kT}$  is the so-called Bjerrum length ( $q$  is the elementary charge and  $\epsilon$  the dielectric constant of water) and  $\kappa^{-1} = (8\pi n l_B)^{-1/2}$  is the Debye screening length. In the absence of added salt, the Debye-Hückel interaction reduces to the standard Coulomb interaction.

In the absence of added salt, the interaction is long ranged and the chains are highly stretched; their size  $R$  is given by [8]

$$R \sim Na(f_B^2/a)^{1/3} . \quad (1)$$

A weakly charged polyelectrolyte chain is not fully stretched but it can be viewed as an elongated chain of Gaussian electrostatic blobs of size  $\zeta_{el} \sim a(\frac{f^2 l_B}{a})^{-1/3}$  containing each  $g_{el} \sim (\frac{l_B^2}{a})^{-2/3}$  monomers as sketched in Fig. 3.1). The size of the blob is such that the electrostatic interaction inside a blob is of the order of  $kT$ . As salt is added, the local blob structure of the chain is not affected but if the screening length is smaller than the size of the chain, the chain is no longer fully elongated and bends. It is in general characterized by a persistence length  $l_p$  which is the length over which it remains stretched.

Depending on the theoretical approach, the persistence length is predicted to decrease with the salt concentration as  $\kappa^{-1}$  or  $\kappa^{-2}$ . Experimental results have not allowed us to discriminate between these two results. At very high ionic strength, the electrostatic interaction is short range and is equivalent to an excluded volume interaction, the corresponding excluded volume parameter is  $\zeta_{el} = 4\pi l_B \frac{f^2}{\kappa^2}$ .

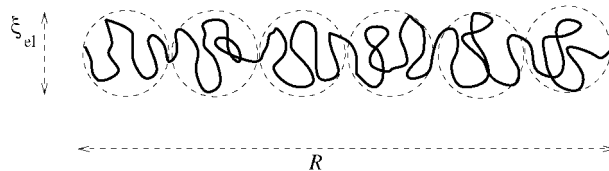


Fig. 3.1 Electrostatic blob model.

When their concentration is increased, polyelectrolyte chains interact strongly and eventually overlap. The electrostatic interaction between chains is much larger than the thermal excitation when the concentration is close to overlap (i.e. when the distance between the chains is of the order of their size). This could induce an ordering of the chains but there is no clear evidence for that experimentally. We will thus assume here that semi-dilute polyelectrolyte solutions are a disordered and isotropic liquid. We will view them as interpenetrated chains of blobs that have a local structure identical to that of isolated polyelectrolyte chains shown in Fig. 3.1.

The most prominent feature of a polyelectrolyte solution in a scattering experiment is a strong peak in the structure factor  $S(q)$  that measures the concentration correlations. At large values of the scattering vector  $q$ , the structure factor probes the internal structure of the chains that is roughly the same as in a dilute solution, it thus decays as  $S(q) \sim 1/q^2$  if  $q\xi_{\text{el}} \gg 1$  (characterizing the Gaussian chain structure inside the electrostatic blobs) and  $S(q) \sim 1/q$  if  $q\xi_{\text{el}} < 1$  (characterizing the elongated structure). At zero wave-vector the structure factor is obtained from the global electroneutrality constraint from the Stillinger-Lovett sum rule  $S(q=0) = 1/f$ . At intermediate wave-vectors the structure factor shows a peak at a wave-vector  $q^*$ ; as for neutral polymers in a semidilute solution, the corresponding wave-length  $2\pi/q^*$  is the mesh size of the temporary network formed by the overlapping chains. The wave-vector  $q^*$  can be obtained by a scaling argument from the radius of a chain in a dilute solution (1)  $q^* \sim (ca)^{1/2}(f^2l_B/a)^{1/6}$ .

In a concentrated polyelectrolyte solution ( $q^*\xi_{\text{el}} > 1$  or  $ca^3 > (f^2l_B/a)^{1/3}$ ) the mesh size of the solution is smaller than the electrostatic blob size; the chains are no longer stretched and have Gaussian statistics at any length scale. The effect of the electrostatic interaction is small and the chain structure factor can be calculated from the so-called Random Phase Approximation used for neutral polymers; the position of the peak in the structure factor is given by [9, 10]

$$q^* = (48\pi f^2 l_B c / a^2)^{1/3}. \quad (2)$$

When salt is added to a semidilute or a concentrated polyelectrolyte solution, the peak in the structure factor shifts to lower wave-vector and disappears when  $\kappa \simeq q^*$ . At this point, the electrostatic interactions are sufficiently screened and can be considered as short range. The polyelectrolyte solution behaves as a neutral polymer solution (the polymers having eventually an electrostatic persistence length [7]). The structure factor decreases monotonically with the wave-vector.

### 3.3

#### Polyelectrolytes at Interfaces

We now discuss the adsorption of a polyelectrolyte solution on a solid surface that carries an electrical charge per unit area  $q\sigma$  with a sign opposite to that of the polymer [2]. The electric field in the very vicinity of the surface is



$E = (kT/q)(4\pi\sigma l_B)$ . The field created by the surface decays with the distance from the surface because of the screening by the surface counterions and by the salt molecules. In a first approximation, the electric field can be calculated from the Poisson-Boltzmann equation. In the absence of salt, the screening is due to the counterions. The counterions are confined in the vicinity of the surface within a length  $\lambda = 1/(2\pi\sigma l_B)$  which is called the Gouy-Chapman length and the electric field decays with the distance  $z$  as  $E \simeq \frac{2}{z + \lambda}$ . If a sufficient amount of salt is added (so that  $\kappa^{-1} < \lambda$ ), screening becomes dominated by the salt and  $E \simeq \frac{2}{\lambda} \exp - \kappa z$ .

In a very low ionic strength solution, a single polyelectrolyte chain is attracted by the electric field of the surface and gets confined within a distance  $\delta$  from the surface. If the surface charge is large enough  $\delta < \lambda$  and the chain feels the surface field. The balance between the electrostatic force and the confinement force for a Gaussian chain gives [11]

$$\delta \sim (a^2/f\sigma l_B)^{1/3}.$$

This thickness is independent of the chain molecular weight and decreases weakly with the surface charge; it is, in most cases, in the range of a few nanometers. Note that we have considered here flexible chains and that the thickness of a rigid polyelectrolyte chain adsorbed on an oppositely charged surface would be even smaller [12].

When salt is added to the solution, the structure of the adsorbed chain is not changed as long as the screening length  $\kappa^{-1}$  is smaller than the chain thickness  $\delta$ . At higher ionic strength, if there is no short range non-electrostatic attraction between the chain and the surface, the chain desorbs. Adsorption can be induced by a sufficient short range attraction of the chain to the surface.

When a dilute polyelectrolyte solution is put in contact with a surface of opposite charge, even if the bulk concentration is rather low, adsorbed chains on the surface overlap. Polyelectrolytes in an adsorbed layer at thermal equilibrium do not develop large loops at very low ionic strength and the thickness of the adsorbed layer is of the order of the thickness  $\delta$  of a single adsorbed chain, as shown by a mean field calculation [13]. The adsorbed chains however have a strong electrostatic interaction between them and it is not clear whether they form a two-dimensional isotropic solution or whether the strong interaction induces liquid crystalline or even crystalline order in the direction of the adsorbing plane. Most existing theories predict an overcompensation of the charge of the surface by the adsorbed polymer i.e. the electric charge per unit area due to the adsorbing polymer is larger than the bare charge of the solid surface by  $\delta\sigma > 0$ . The global charge is small in the limit of low ionic strength, a mean field theory based on the Edwards equation for the chain conformation [13] predicts  $\delta\sigma/\sigma \sim \kappa\delta(1 + \zeta_{el}^2/\delta^2)$ . This theory is expected to be valid at the scaling level.

In the limit of large ionic strength, the polymer behaves as a neutral polymer with excluded volume interactions in the bulk. If the adsorbing surface is a pure

hard wall with no attractive interactions, there is no adsorption; the adsorption of the monomers to the wall is strongly screened and is not sufficient to compensate the hard wall constraint. If there is a strong enough short range attraction between the adsorbing surface and the monomers, the polymer adsorbs like a neutral polymer. All the results obtained for the adsorption of neutral polymers can be used. The thickness of the layer is the size of the largest loops and is of the order of the size of a polyelectrolyte in dilute solution at the same ionic strength. The monomer concentration profile decays as a power law of the distance  $z$  from the solid surface. In a mean field approach

$$c(z) = \frac{\kappa^2 a^2}{12\pi l_B f^2 (z + d_{\text{eff}})^2} \quad (4)$$

where  $d_{\text{eff}}$  measures the interaction of the polymer with the surface (both electrostatic and non-electrostatic). A large charge overcompensation is then expected. If the short range attraction exactly compensates the hard wall constraint, the mean field theory predicts an overcompensation  $\delta\sigma/\sigma = 1$ ; for stronger attraction, the overcompensated charge increases as  $\delta\sigma/\sigma \sim \kappa^2$ .

One should however keep in mind that the mean field theory based on the Edwards equation for the chain conformations ignores the excluded volume correlations and that this result should be only qualitatively correct (one expects a strong overcompensation of the charge that increases with an unknown power of ionic strength). Another limitation of the mean field theory is that it neglects the in-plane concentration fluctuations; other theories [12, 14] that overestimate these fluctuations by assuming that the chains form an ordered array on the surface also predict a strong charge inversion.

### 3.4 Polyelectrolyte Complexes

When two polyelectrolyte solutions of opposite charges (a polyanion and a polycation) are mixed, the polymers have a tendency to form a dense phase and to separate from the solvent. The dense phase is called a polyelectrolyte complex. Polyelectrolyte complexes have been studied extensively experimentally and show a rich variety of behavior depending on the stoichiometry (the relative molecular weights and charge contents of the two polymers), ionic strength, temperature [3] etc. For simplicity we consider here only symmetric complexes where the two polymers have the same molecular weight  $N$ , the same charge fraction  $f$  and the same concentration  $c$ . We also only consider very large molecular weights; in this limit the two polyelectrolytes precipitate and form a dense complex in equilibrium with pure water; the critical concentration for complex formation is extremely low. Even in this simplified limit, the phase diagram of the polymer mixture in water is not very simple [15, 16]. In general, the backbones of the two polymers are not compatible and repel each other. The repulsion is characterized by a Flory interac-

tion parameter  $\chi$ . When the charge fraction is low, the backbone repulsion is dominant and the solution separates into two phases each containing mostly one of the polymers. At high charge fraction, the attractive electrostatic interactions between the polymers dominate and they precipitate to form a complex. In an intermediate range of charge fraction, the equilibrium state can be a mesophase where the two polymers only separate microscopically. A tentative theoretical description of the phase diagram is given in reference [5]. If the two polymers are asymmetric in charge or in mass, more complex structures such as aggregates can form.

We only consider here the properties of the complex phase for symmetric polyelectrolyte mixtures in the limit of high ionic strength, which corresponds to most of the experimental results on polyelectrolyte multilayers. The complex is in equilibrium with a very dilute phase (containing salt however and therefore the osmotic pressure of the complex is equal to the osmotic pressure of the simple electrolyte forming the dilute phase). The osmotic pressure difference between the two phases  $\Delta\Pi$  has two contributions, an excluded volume contribution and an electrostatic contribution. We will consider here that the two polymers are in a  $\Theta$  solvent and the excluded volume osmotic pressure is written as  $\Delta\Pi_{\text{ev}} = \frac{kT}{3}w^2c^3$  where  $c$  is the total polymer concentration. It is dominated by three body interactions and  $w^2$  is the third virial coefficient;  $w$  is a volume of the order of the monomeric volume  $a^3$ . At the mean field level, the average charge in the polyelectrolyte complex vanishes and the electrostatic energy also vanishes. In order to calculate the electrostatic free energy of the polyelectrolyte complex one must take into account the concentration fluctuations, as one does for example in the classical Debye-Hückel theory of simple electrolytes [4]. The fluctuation free energy is however different from that of a simple electrolyte because the charges are connected along the polymer chains. An important point is that, in a polyelectrolyte complex, there are free ions due to the added salt but there are also counterions associated with the two polyelectrolytes. We will suppose that these ions are identical and consider them as added salt. Note however that, in certain experiments, the counterions can be dialyzed out. In the limit where the salt concentration is large, the electrostatic pressure can be written as  $\Delta\Pi_{\text{el}} \sim -\frac{kT}{\zeta_c^3}$  where  $\zeta_c \sim \frac{\kappa a}{(4\pi l_B f^2 c)^{1/2}} \sim \kappa/q^{*2}$  is the relevant correlation length inside the complex ( $q^*$  is the wave-vector characteristic of the charge fluctuations in a dense polyelectrolyte solution given by Eq. (2)). The polymer concentration in the complex is then [17]

$$c_c \sim \frac{f^2}{nw^{4/3}a^2}. \quad (5)$$

## 3.5

**Multilayer Formation**

We now use the results presented in the previous sections on polyelectrolyte adsorption and polyelectrolyte complexation to build up a theory for multilayer formation [17]. We start from a positively charged surface. The first layer is obtained by adsorbing a solution of negatively charged polyelectrolyte at high ionic strength. As explained above, there is a strong inversion of the charge and this inversion is higher if there exists a short range non electrostatic attraction between the polymer and the surface. A strong adsorption of the first layer is necessary to anchor the polymer on the surface and in most experimental cases, the first layer is made with a different polymer known for its good adsorption properties. We call  $\Gamma_1$  the adsorbance of this first layer. If the short range attraction of the monomers to the surface is large  $\Gamma_1 \gg 2\sigma/f$ .

The layer is then rinsed. We will suppose that the layer is not dried in any of the rinsing steps and that it is rinsed in water at the same ionic strength as the adsorbing solution. We moreover will make these assumptions for all the following rinsing steps. This ensures that the multilayer is always liquid and never becomes glassy and that it is always in contact with water at the same ionic strength. These restrictions are usually not necessary when multilayers are prepared for various applications but they largely simplify the theoretical analysis and they correspond to the recent experiments of Ladam and coworkers [6]. We will also consider that polyelectrolyte adsorption is irreversible, in the sense that when the adsorbed layer is put in contact with the simple electrolyte solution, no polymer desorbs. The amount of polymer in the first layer remains equal to  $\Gamma_1$  even after the rinsing step. We therefore ignore for the first layer (and for all the consecutive layers) the small desorption that may occur during the rinsing step. We do not however consider the adsorbed layer as frozen and we allow for reequilibration of the local chain conformation during the following steps of the multilayer build-up. Multilayer formation is a non-equilibrium process; we treat here the multilayer as a thermodynamic system under constrained equilibrium: the quantity of adsorbed polymer in each layer remains fixed.

After the rinsing step, the surface with the first layer is put in contact with a solution of positively charged polyelectrolytes. The positively charged polyelectrolyte is excluded from the vicinity of the solid surface that has the same electrostatic charge over a layer of thickness  $\zeta_c$  (the correlation length of the polyelectrolyte complex). It complexes all of the available negatively charged polyelectrolytes of the first layer by forming a complex of concentration  $c_c$  given by Eq. (5). The thickness of this complexed layer is  $L_1 = 2\Gamma_1/c_c$ . The surface carries only a quantity  $\Gamma_1$  of negatively charged polymer and the concentration of negatively charged polymer decays rapidly to zero from the value  $c_c/2$  over the complex correlation length  $\zeta_c$  at the edge of the layer. The positively charged polymer is in equilibrium with a bulk solution and can form loops anchored in the complex and dangling into the electrolyte solution. The loop structure is the same as in an adsorbed polyelectrolyte layer and is given by Eq. (4) where the cut-off length is cho-

sen by imposing that at  $z = 0$  (at the edge of the complex layer), the concentration matches to that in the complex  $c_c/2$ . The quantity of polymer in these loops is obtained by integration

$$\Delta\Gamma \sim \frac{1}{w^{2/3}} \left( 1 - \frac{f^2}{n^{3/2} l_B^{1/2} a^2 w^{2/3}} \right). \quad (6)$$

The first term is readily obtained from the results on polyelectrolyte complexation of the previous section. It is however independent of ionic strength and the dependence on ionic strength is due to the first correction to this result that requires a more detailed analysis of the polyelectrolyte complexes. The loops in the electrolyte solution create an overcompensation of the charge of the multilayer (with an effective surface charge  $f\Delta\Gamma$ ). They serve to anchor the next layer by complexation with negatively charged polyelectrolyte. A qualitative plot of the concentrations in the first two layers is sketched in Fig. 3.2. The build-up process can then be iterated. Each consecutive layer has an adsorbance of order  $\Delta\Gamma$  and the thickness of all the layers starting from the third one is

$$L_3 \sim \Delta\Gamma/c_c \sim \frac{w^{2/3} n a^2}{f^2}. \quad (7)$$

In this picture the effective surface charge of the multilayer oscillates between the values  $f\Delta\Gamma$  and  $-f\Delta\Gamma$  after deposition of the successive layers (starting from the second layer) and the amount of polymer per unit area in each layer (starting from the third one) increases very weakly with the ionic strength as given by Eq. (6). This is in agreement with the experiments of reference [6].

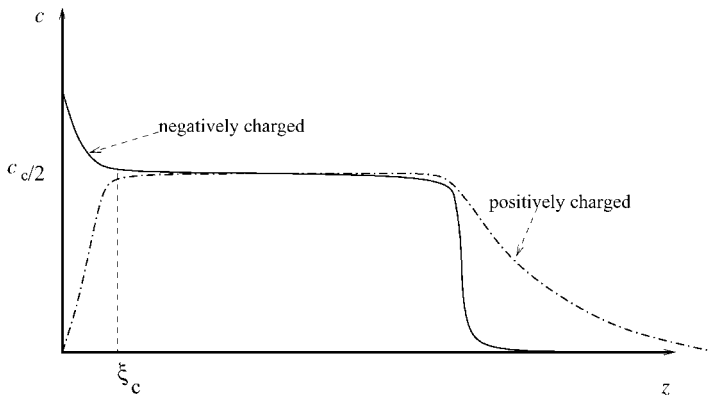


**Fig. 3.2** Concentration profiles of the negatively charged (full line) and positively charged (dash-dotted line) polymers after the formation of the second layer on a positively charged surface.

## 3.6

**Concluding Remarks**

We have summarized in this short review a model for polyelectrolyte multilayer formation which is based on the complexation between consecutive layers. This model is clearly valid for flexible polyelectrolytes only. Even in that case it is rather rough and makes important approximations.

The model has been presented for high ionic strength only. Experimentally, the structure of a polyelectrolyte multilayer does not seem to be strongly affected by ionic strength and we believe that the model could be used for weaker ionic strength as well. For weak ionic strength, the electrostatic pressure in a polyelectrolyte complex scales as  $\Delta\Pi \sim -kTq^{*3}$ , the polymer density in a polyelectrolyte complex varies as  $c_c \sim \frac{l_B^{1/3} f^{2/3}}{a^{2/3} w^{8/9}}$  and the adsorbance of the layers is  $\Delta\Gamma \sim \frac{a^{2/3} n^{1/2} l_B^{1/6}}{f^{2/3} w^{4/9}}$ .

We have also ignored in the model the effect of the short range repulsive interactions between the polymer backbones. It has been argued [18] that the short range interaction could lead to the formation of mesophases. The formation of mesophases is studied in detail in reference [5] and they do not seem to be stable at high ionic strength. The experimental results also prove clearly that the multilayer build-up is a non-equilibrium process and not only due to the orientation of lamellar mesophases along the solid substrate.

The whole theory is based on linear electrostatics at the level of the Debye-Hückel theory and can certainly not be applied if the local density of charges is too large. It is thus valid only for weakly charged polymers. In the limit of strongly charged polymers, a model based on the formation of ion pairs would certainly be more adequate [19].

A final important limitation is that we have used a quasi-equilibrium approach treating the irreversibility as constraints on the thermodynamics. This should be a reasonable approximation to describe the internal structure of the monolayers but does not explain the fact that the dynamics inside the monolayers seems frozen and that the layers keep their identity.

One of the major interest of polyelectrolyte multilayers is their versatility. In any layer, polyelectrolytes can be replaced by other charged objects (surfactants, colloids, proteins etc.) and they seem to be obtained for all kinds of polyelectrolytes. Our model is rather specific for flexible polyelectrolytes. If the polymers are too rigid, interpenetration between different layers is difficult and the complexation mechanism is different. In reference [12], a model has been proposed in the other extreme limit where the polyelectrolytes are rodlike. In this case the charge inversion in the first layer is due to the strong correlations between adsorbed chains that form an ordered array and each layer is treated as adsorbing on an effective surface formed by the previous layers.

## 3.7

## References

- 1 G. DECHER, *Science* **1997**, 277, 1232. See also the other chapters of this book.
- 2 D. ANDELMAN, J.F. JOANNY, *C. R. Acad. Sci. Paris IV* **2000**, 1, 1153.
- 3 E. BEKTUROV, A. BAKAUOVA, *Synthetic Water Soluble Polymers in Solution*, Hütig and Wopf Verlag, Berlin 1986; B. PHILIPP, H. DAUTZENBERG, K. LINOW, J. KÖTZ, W. DAWYDOFF, *Prog. Polym. Sci.* **1998**, 14, 823.
- 4 V.I. BORUE, I. ERUKHIMOVICH, *Macromolecules* **1990**, 23, 3625.
- 5 M. CASTELNOVO, J.F. JOANNY, *Eur. Phys. J. E* **2001**, 6, 377.
- 6 G. LADAM, P. SCHAAD, J.C. VOEGEL, P. SCHAAF, G. DECHER, F. CUISINIER, *Langmuir* **2000**, 16, 1249.
- 7 J.L. BARRAT, J.F. JOANNY, *Adv. Chem. Phys.* **1996**, XCIV, 1.
- 8 P.G. DE GENNES, P. PINCUS, R. VELASCO, F. BROCHARD, *J. Phys. Paris* **1976**, 37, 1461.
- 9 V.I. BORUE, I. ERUKHIMOVICH, *Macromolecules* **1988**, 21, 3240.
- 10 L. LEIBLER, J.F. JOANNY, *J. Phys. Paris* **1990**, 51, 545.
- 11 O. BORISOV, E. ZHULINA, T. BIRHSTEIN, *J. Phys. II Paris* **1994**, 4, 913.
- 12 R. NETZ, J.F. JOANNY, *Macromolecules* **1999**, 26, 2026.
- 13 J.F. JOANNY, *Eur. Phys. J. B* **1999**, 9, 117.
- 14 T. NGUYEN, A. GROSBERG, B. SHKLOVSKII, *J. Chem. Phys.* **2000**, 113, 1110.
- 15 S. DJADOUN, R. GOLDBERG, H. MORAWETZ, *Macromolecules* **1977**, 10, 1015.
- 16 A. KHOKHLOV, I. NYRKOVA, *Macromolecules* **1992**, 25, 1493.
- 17 M. CASTELNOVO, J.F. JOANNY, *Langmuir* **2000**, 16, 7524.
- 18 F. SOLIS, M. OLVERA DE LA CRUZ, *J. Chem. Phys.* **1999**, 110, 11517.
- 19 K. ZELDOVITCH, A. KHOKHLOV, preprint 2000.

## 4

# Charge Balance and Transport in Polyelectrolyte Multilayers

JOSEPH B. SCHLENOFF

### Abstract

Quantitative descriptions of the way charge is balanced between polyelectrolytes and small ions are essential for understanding the growth mechanism and permeability of polyelectrolyte multilayers. Using radioisotope-labeled constituents, it is shown that multilayers contain minimal bulk counterions (“salt” ions) in their nascent state, and that all excess polymer charge resides at the surface. The thickness of this excess charge, which is spread over several “layers”, determines the ultimate rate of multilayer buildup. Salt, introduced into the multilayers under an external chemical potential, moderates the ion pairing interaction energy between oppositely charged polymer segments. Salt also creates ion-exchange sites that facilitate the transport of other ions via a hopping mechanism. It is thus possible, using salt to reversibly “dope” multilayers, to control both the flux and selectivity of ions traveling through multilayer membranes.

### 4.1

#### Introduction

The extraordinary recent growth in the field of thin films made by sequential adsorption, detailed in Chapter 1, has led to a variety of film compositions with a multitude of potential applications [1–4]. Synthetic or natural [5, 6] polyelectrolytes, alone or in combination with nanoparticulates such as dendrimers [7], metal colloids [8], silica [9, 10], latices, clay minerals [11, 12] or other inorganic particles [13, 14], provide a broad palette of materials that can be tailored into functional multilayers.

The majority of multilayer studies have involved only two components alternately adsorbed. Nanoparticle/polyelectrolyte combinations, where polymer “glues” the particles together, often require some subtle optimization of parameters. The assembly of an ultrathin film using highly charged synthetic polyelectrolytes alone is more straightforward and yields uniform blends. Thus, multilayers made from polyelectrolyte components only (polyelectrolyte multilayers or PEMUs) are typically amorphous, with neighboring layers extensively interpenetrated [15–19]. Because of this intermingling, actual stratification, or composition modulation, in



PEMUs is observed only if components are separated by several “layers” of material which include a third component [15, 16, 19]. The definition of a “layer” is rather loose, and, for the majority of films, really means a thickness increment following an adsorption step. Although the lack of layering may make the thin film less intriguing from a structural point of view, it simplifies the theoretical treatment, since the film is represented by an average composition with a mean field response to external stimuli.

A researcher entering the field of polyelectrolyte multilayers and related systems will quickly discover the historical precedent set by polyelectrolyte complexes, PECs, formed by mixing solutions of dissolved, oppositely charged macromolecules [20]. Indeed, the duality between PECs and PEMUs is extensive [21]. Properties of polyelectrolyte complexes made from highly-charged polyelectrolytes, as described in the 1960s by Alan Michaels and coworkers [22–24], include the following: insolubility in common solvents [24], infusibility [24], amorphous structure [24], blending of constituents on a molecular level [25], virtually no salt counterions within the complex [24], high dielectric constant when wet [26], permeable to water and electrolytes [24], impermeable to macrosolutes [24], and swelling and plasticizing by aqueous electrolytes [24]. Principal projected uses [24] were as membranes for dialysis, ultrafiltration, battery separators, fuel cell membranes, electrically conductive coatings, medical devices including contact lenses, and chemical sensors. In addition to Chapter 2 on PECs by Kabanov, the reader is referred to a couple of review articles [23, 24].

Given the several decades elapsed and the paucity of applications of PECs currently in play, one may ask what PEMUs have to offer that PECs do not. A brief comparison of these two methods for producing complexed polyelectrolytes will help to illuminate the ways they differ: although certain solvent systems dissolve PECs, permitting them to be prepared in various morphologies, the main differences between PECs and PEMUs are in the area of processing. In the latter, each adsorption step (“layer”) leads to surface charge reversal, and the adsorbed amount is self-limiting. These two properties induce steady state layer-by-layer propagation, as detailed in Decher’s pioneering work a decade ago [17, 27]. Because of the sequential adsorption approach, PEMUs form ultrathin, uniform, smooth, contour following films. The exceptional thinness, not accessible with solvent cast PECs, of defect-free PEMU membranes provides high flux for selective separations. PEMUs are better suited to surface modification, where uniformity is at a premium and a minimal thickness of a mechanically weak film is advantageous. A few nanometers of PEMU controls wetting [28], biocompatibility [29], and surface charge in microchannels for microfluidics [30, 31].

Further distinguishing features of PEMUs are evidenced by the demonstration of actual layering in PEMUs and related systems. For example, ultrathin strata of polymers may be isolated by layers of clay nanosheets for light-emitting devices [32]. Layers of magnetic nanoparticles have been separated by clay minerals [33]. Layered systems composed of polymers only may be obtained when one of the components is a liquid crystalline polyelectrolyte [34]. We have prepared multilayered “onion skins” that decompose to yield free membranes [35].

Some degree of molecular orientation is possible in PEMUs, an additional advantage. Second order nonlinear optical responses [36–38] are a clear indication of molecular ordering in PEMUs comprising azobenzene polyelectrolytes. From a scale-up perspective, organic solvents and high salt conditions used to process PEC into films are environmentally less acceptable than are pure aqueous salt solutions. Finally, a PEC processing solvent may also be incompatible with the substrate or materials, such as enzymes [5, 6], that must be incorporated into the polymer complex for specific applications.

This chapter focuses on PEMUs, but by symmetrical arguments many of the phenomena described for PEMUs will also apply to PECs. The system treated here, composed of two synthetic polyelectrolytes, salt ions and water, is the simplest of multi-component thin films described throughout this book. In this chapter we track all PEMU ingredients and show that focusing on the way charged components contribute to overall electrical neutrality at the surface and in the bulk helps one to understand the formation and function of PEMUs. The importance of salt, which controls buildup, permeability and stability, is immediately apparent, but will be no surprise to scientists acquainted with the peculiarities of charged polymers: charged microions are expected to modify electrostatic interactions between polymers [20].

The balance of this chapter is organized in three parts. First, we will consider the forces holding constituent polymers together and the way salt counterions govern these forces and participate in charge balance. Then, a view of how excess surface charge, the key to propagating layer-by-layer buildup, is spread out through the multilayer will provide a semiquantitative model for their construction. Finally, we will show how the internal counterion population, regulated by external salt, controls the transport of charged species through PEMUs.

## 4.2 Interactions

### 4.2.1

#### **Mechanism: Competitive Ion Pairing**

Consideration of the response of polyelectrolyte systems to salt usually starts with electrostatic theory [20, 39]. The local electrostatic potential caused by the local charge density is determined by the Poisson equation. Using a mean-field approximation, local ionic concentrations are then expressed as a Boltzmann distribution. Typically, the Poisson–Boltzmann equation is linearized by assuming low charge density (Debye–Hückel approximation) or more elaborate non-linear solutions are sought. For polyelectrolytes, concepts of local stiffness, or persistence length, and excluded volume have been introduced, as well as sophisticated scaling concepts. Interactions are not specific and there is no dependence of interaction energy on the chemical identity of the charges. The interaction energy between like and opposite charges is modified by screening, the characteristic decay length (Debye length) of electric potential being shorter in solutions of higher salt concentration [20, 39].

In this chapter, a more “chemical” perspective is taken in dealing with salt ions, where they are to be found, and how they modify polymer–polymer interactions. In spite of the imposing precision and complexity of electrostatic theory, it does not take into account the polarizability of functional groups, their degree of hydration and, more specifically, differential hydration. Here, precise values of interactions, obtained from electrostatic first principles, are forgone in favor of a combination of equilibrium constants that must be experimentally obtained, but can be rationalized and categorized post hoc by intuitive arguments based on entropy, hydrophobicities, polarizabilities, polymer excluded volume and other fundamental physical-chemical constructs.

The complexation of polyelectrolytes is known to be virtually athermal [23, 24]. The overall free energy change of complexation is derived mainly from the release of counterions (“escaping tendency” i.e. increase in entropy [23]). Small free energy changes per segment are additive, to a point [40], due to the cooperative nature of polyelectrolyte complexation, yielding strong association on a per-molecule basis. Since ions are well hydrated, the release of waters of hydration, specifically the differential levels of solvation between free, solvated polymer and associated complex, should also be considered in the net energy equation. The term “hydrophobicity” is used here to denote the relative numbers of waters of hydration released. As shown for calorimetric studies of small ions, hydration also has an enthalpic component, especially for hydrophobic species [41].

The equilibria considered here are variations of place-exchange or ion-exchange reactions. In its most generic form, the interaction between charged polymer segments is represented by Fig. 4.1. Upon complexation, polyelectrolyte segments form ion pairs and relinquish their counterions. Electrostatic neutrality is maintained and no chemical bonds are formed in the reshuffling of charged species. The term “ion pairing” is used to describe an energetically favorable pairing of polymer segments, driven by the loss of water and counterions.

From the perspective of a single polyelectrolyte segment, an oppositely-charged segment and a counterion compete to balance the charge. There are two arenas where this competition for charge takes place. The first is in the initial formation of the PEMU (or PEC). Individual solution phase macromolecules come together, expelling their counterions as they complex. There may be some conceptual fuzziness, with a long history [20], as to exactly where the counterions are and how closely they are associated with the polymer chain, but for simplicity we assume they are predominantly “condensed” [42] on the polymer chain. For a polyelectrolyte adsorbing to an oppositely-charged surface, the surface counterions are dis-

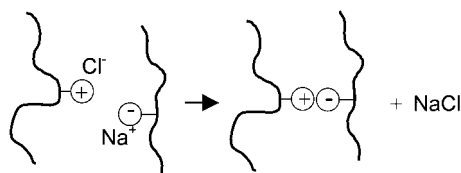


**Fig. 4.1** Complexation between positive polyelectrolyte segment and negative polyelectrolyte segment releasing counterions.

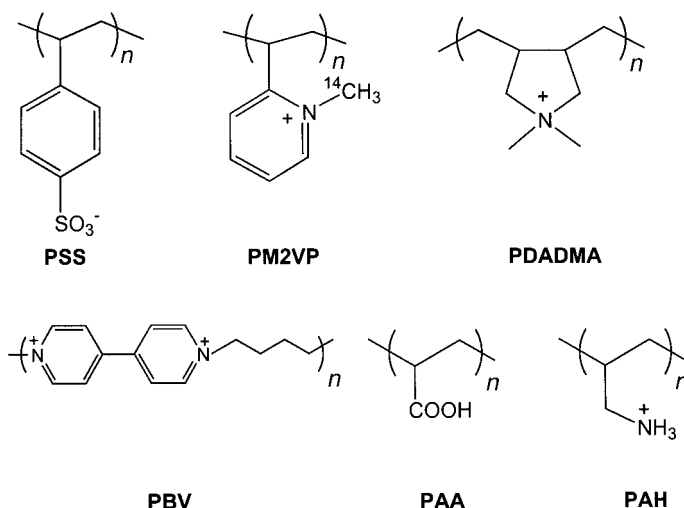


Fig. 4.2 Structures of representative polyelectrolytes.

placed by adsorbing polymer segments, a process that can be directly tracked by radiochemical labeling techniques [43].

In the second arena, the chemical potential of salt in solution can cause swelling or infiltration of ions into a bulk polyelectrolyte complex *after* it has been formed. For assembled multilayers there is a clear phase change on going from complexed polymer to solution. Waters of hydration can be added into the equation, but these are more difficult to follow and will be only implied during discussions of “hydrophobicity.”

On consideration of the equilibria above it is clear that electroneutralization is the dominant mechanism [44], but an analysis of the overall driving force must include consideration of all charged species. The situation cannot be described simply by vacuum electrostatics between naked, isolated charges, which would yield enormous free energy changes. The driving force is ion pairing between polyelectrolyte segments, driven by release of counterions and water. Additional salt ions modify the overall free energy of interaction by competing for polymer charge. Given this, the mechanism is better defined as competitive ion pairing [45].

Systems without added salt are at the theoretical maximum strength of interaction, but are also poorly defined, since the ionic strength is that of the polyelectrolyte and its attendant counterions. Multilayers have been created using small components of low charge, but, in the absence of specific interactions, must be assembled at low ionic strength [46–48].

## 4.2.2

**Intrinsic vs. Extrinsic Charge Compensation**4.2.2.1 **Key Equilibria**

Initially, in constructing a multilayer, there seem to be a host of experimental options, each with potential impact on formation [45]. Variables include exposure time, temperature, polymer type, polymer molecular weight, polymer concentration, salt concentration, salt identity, pH, and solvent composition. Fortunately, since almost all work is performed with high molecular weight material at room temperature in aqueous NaCl solutions the only significant variables are polymer type, and salt concentration, and also pH if one of more of the polymers is a weak acid/base [28, 49]. Even then, the process is extraordinarily robust (forgiving) and some form of multilayering is easily obtained (as long as the substrate is properly cleaned!).

We begin with a multilayer that has been formed, for example, with a pair of oppositely charged polymers selected from those shown in Fig. 4.2. Following sequential adsorption of polyelectrolytes to the desired film thickness, the PEMU is typically rinsed in pure water to remove excess polymer and salt.

One can envisage two scenarios, shown in Fig. 4.3, of how net charge neutrality is maintained, by a combination of polymer repeat units and salt ions, within the as-made film. In one case, termed *intrinsic* compensation, polymer positive charge is balanced by a negative charge, also on a polymer [50]. Alternatively, polymer charge is balanced by salt counterions derived from the bathing solution used to construct the multilayers (*extrinsic* charge compensation) [50]. A continuum of intrinsic  $\rightarrow$  extrinsic composition is available, with the proviso that fully extrinsic multilayers are not realistic since, in the absence of other interaction mechanisms, the PEMU would decompose back into isolated molecules.

The presence of salt ions would have a substantial impact on the performance of PEMUs in certain applications. For electronic devices, mobile counterions would control the dielectric constant and the conductivity of thin film PEMU insulators, and would degrade electrical contacts. Intrinsic compensation controls transport of charged species through PEMUs when they are employed as membranes, as discussed below.

An interesting physiological question arises when considering intrinsic compensation: how can the polymers undergo the contortions required to match each

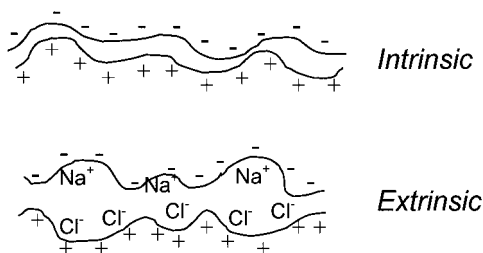


**Fig. 4.3** Comparison of intrinsic and extrinsic charge compensation in polyelectrolyte multilayers.

positive segment with each negative segment and obviate the need for salt ions, especially if the spacings of charged units along the polyelectrolyte backbone are very different? In considering this question for PECs, Michaels [23, 24] concluded that polyelectrolytes do not complex as “ladders,” where a polymer is associated with only one other, complementary, molecule (DNA-like), rather, they form amorphous “scrambled salts.” Our experiments, described below, confirm the intrinsic compensation mode for the bulk of PEMUs.

Although as-made PEMUs contain no salt ions it is possible to introduce them by increasing their external (solution) concentration (chemical potential). In the following equilibrium, polyelectrolyte/polyelectrolyte ion pairs are replaced by polyelectrolyte/salt ion pairs. The process is a type of ion exchange [51], the difference being that the polyelectrolyte segments are not free to leave the PEMU matrix. The system, believed to be under rapid, reversible equilibrium control for NaCl [52], as it involves the transport of small ions with minimal displacement of polyelectrolyte segments, is represented by



where  $\text{Pol}^+$  and  $\text{Pol}^-$  are respective positive and negative polyelectrolyte repeat units. The subscript “m” refers to components in the multilayer phase. The equilibrium constant may be written as

$$K' = \frac{\gamma^2}{(1-\gamma)[\text{NaCl}]_{\text{aq}}^2} = \left( \frac{\gamma^2}{[\text{NaCl}]_{\text{aq}}^2} \right)_{\gamma \rightarrow 0} \quad (2)$$

where  $\gamma$  is the fraction of the multilayer in the extrinsic form and  $1-\gamma$  is the intrinsic fraction [52]. It is clear, from this equilibrium, how salt directly controls the degree of association or interaction between polymer segments. Note that the number of positive and negative counterions is equal, unlike the example for “as-made” PEMUs shown in Fig. 4.3. These ions are, themselves, available for exchange with other ions. We have termed these systems, having matched positive and negative immobile ion pairs in their as-made state, “reluctant exchangers,” since exchangeable ions can be forced into them with external chemical potential as in the equilibrium above [52].

We are avoiding here any close scrutiny of the question of how closely each ion is associated with its polyelectrolyte segment. We believe the counterion is localized near the polyelectrolyte charge, especially for dilute extrinsic charges, but this semantics problem does not affect the net equilibrium.

“Interaction energy” means, in the present context, the free energy of ion pairing between polyelectrolyte segments, which is the reverse of Eq. (1). Different pairs of polyelectrolytes are expected to have different strengths of interaction. Note that the energetics of interaction in pre-formed multilayers will not be the same as for individual solution phase polyelectrolytes precipitating to form insoluble complexes [53]. Although the same trends and magnitudes are expected, so-

lution polyelectrolytes lose configurational and translational degrees of freedom on precipitation, and may also lose additional water molecules. In a slightly different approach, the free energy of complexation has been further broken down into individual contributions from electrostatics, hydration, ionic atmosphere, and hydrophobics [54, 55].

#### 4.2.2.2 Swelling and Smoothing: Estimating Interaction Energies

One would expect multilayers to expand as ions (and additional waters of hydration) enter the film. Direct measurements of swelling have been sparse, however [56, 57]. Sukhorukov *et al.* measured the expansion of PEMUs by salt *ex situ* using X-ray reflectivity on dried films [56]. We have employed atomic force microscopy (AFM) to determine swelling *in situ* of representative pairs of polyelectrolytes [58]. The first measurement for each PEMU was made on the “dry” film (exposed to ambient atmosphere of approximately 30% relative humidity). Pure water was then added to the cell, followed by salt solutions. All films expanded on immersion in water. Very different swelling behavior, Fig. 4.4, is observed for the three combinations of “typical” polyelectrolytes: poly(styrene sulfonate), PSS/poly(acrylic acid), PAA; PSS/poly(diallyldimethylammonium), PDADMA; PSS/poly(allylamine hydrochloride), PAH. These differences are presumed to reflect the relative degree of association of oppositely charged polyelectrolyte segments. Polymer pairs which

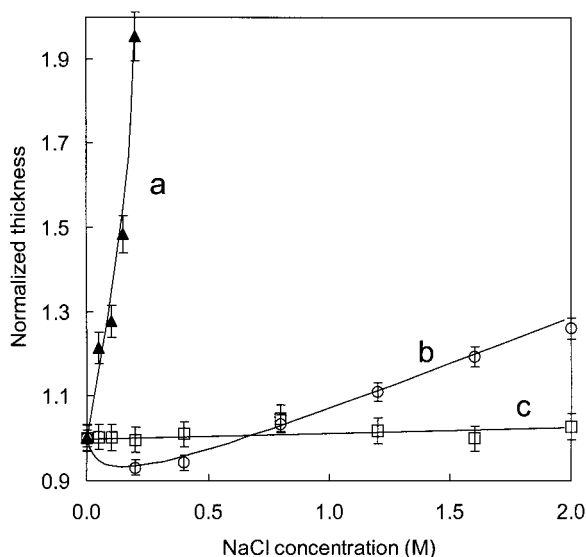


**Fig. 4.4** Thickness (normalized to  $[\text{NaCl}]_{\text{aq}}=0$ ) as a function of NaCl concentration for three multilayers: (a) PAA/PDADMA; (b) PSS/PDADMA; (c) PSS/PAH. For these

PEMUs, “wet” (immersed in pure water)/ “dry” (ca. 30% r.h.) thickness ( $\text{\AA}$ ): (a) 2330/640=3.64; (b) 3550/1750=2.03; (c) 600/490=1.22. Solid lines are a guide to the eye.

form more hydrophobic complexes are expected to associate more strongly in contact with aqueous solutions and would thus be less prone to swelling by salt ( $K'$  smaller). Swelling curves were reproducible for the same sample provided  $[\text{NaCl}]_{\text{aq}}$  did not exceed 2 M (for PSS/PDADMA) or 0.3 M (for PAA/PDADMA), after which concentrations the films started to decompose.

The ratio of the “wet” to “dry” thicknesses, given in the caption for Fig. 4.4, may be used as a relative index of hydrophobicity of polyelectrolyte pairs. The water content for PSS/PDADMA in contact with liquid water is in approximate agreement with prior estimates [21]. A quantitative measure of salt infiltration can be provided by defining a volume swelling coefficient,  $Q_{\text{swell}}$  (the slope from Fig. 4.4),

$$Q_{\text{swell}} = \frac{\% \text{swelling}}{[\text{salt}]} \quad (3)$$

$Q_{\text{swell}}$  values for PAA/PDADMA, PSS/PDADMA, and PSS/PAH are about 400, 20, and  $<1 \text{ M}^{-1}$ , respectively. Swelling involves sorption of both salt and additional waters of hydration, since polyelectrolyte segments paired with salt counterions will be more hydrophilic. The dimensional changes here cannot be resolved into individual contributions from these two swelling components, but if we assume that a salt ion plus additional waters of hydration have the same volume as a polyelectrolyte segment, respective  $K'$  values are 16, 0.04 and  $<1 \times 10^{-4}$ . These values may be translated into free energies of association of polymer segments, the reverse of Eq. (1), using  $\Delta G^\circ = -RT \ln K'^{-1}$ . Respective  $\Delta G^\circ$ s, in  $\text{kJ mol}^{-1}$ , are +6.9, -8.0, and -22.8. These free energies are a measure of the affinity, or “interaction energy” of polyelectrolyte segment pairs under standard conditions. Interaction energies under non-standard conditions (i.e. for salt concentrations other than 1 M) are given by  $\Delta G = \Delta G^\circ + RT \ln [\text{NaCl}]_{\text{aq}}^2$ .

The detailed behavior of each PEMU is of interest. PSS/PDADMA exhibits a (reproducible) decrease in thickness at low salt concentrations. We interpret this as the drawing out of water molecules unassociated with specific ion pairs (“liquid water”) under an increasing external osmotic pressure. PAA/PDADMA exhibits a “hyperswelling” behavior, consistent with the observation that the films actually decompose at intermediate salt concentrations [53]. Different salts are expected to yield different  $Q_{\text{swell}}$ , depending on their hydrophobicity and charge.

Swelling curves are reversible and reproducible. Salt concentration jump experiments on the permeability of redox active probe ions through PSS/PDADMA multilayers have demonstrated that swelling is very rapid and the equilibrium swelling level is also attained quickly [52]. During the normal course of multilayer buildup, where the substrate is alternately immersed in salt solutions and salt-free rinse water, the multilayer undergoes cyclic swelling and shrinking as ions rush in and out of the film under changing conditions of solution salt concentration – a phenomenon we term “ion breathing.”

During exposure of our freshly-prepared PEMUs to salt solutions a significant decrease in the surface roughness was observed [58]. Smoothing of the surface, shown in Fig. 4.5, was especially rapid in solutions of high salt concentration.



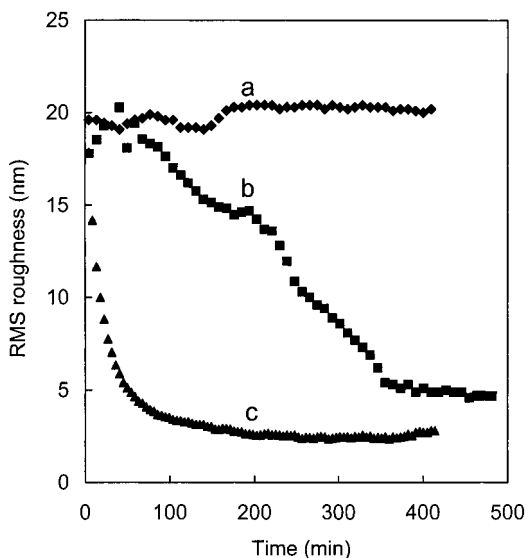


**Fig. 4.5** RMS surface roughness factors vs. time, determined *in situ*, of PSS/PDAMA multilayers annealed in (a) 0.1 M NaCl; (b) 0.5 M NaCl; and (c) 1.0 M NaCl. Results for pure water were similar to those for 0.1 M NaCl.

Higher salt concentrations are known to enhance the mobility of charge-paired polyelectrolyte chains [59–62], presumably by freeing up “frozen” segments via Eq. (1). As a PEMU surface smooths, to reduce the PEMU/solution interfacial contact area, the material in the “peaks” diffuses into the “valleys”. For a PSS/PDADMA multilayer prepared from 1.0 M NaCl, a characteristic peak–valley dimension,  $\Delta$ , of 150 nm was found. This value, inserted into the well known [63] relationship  $\Delta = (2Dt)^{1/2}$ , provides values for the polyelectrolyte interdiffusion coefficient,  $D$ , of order  $6 \times 10^{-15}$  and  $5 \times 10^{-14} \text{ cm}^2 \text{ s}^{-1}$  for 0.5 and 1.0 M salt, respectively. The strongly nonlinear effect of salt in “lubricating” the motions of one charged polymer against another [64], as discussed for the diffusion of a polyelectrolyte into an oppositely-charged gel [65, 66], indicates the cooperative properties of polyelectrolyte segments in retarding interdiffusion.

Samples not used immediately after preparation displayed an induction period before the smoothing effect started, possibly a result of the aggregation of hydrophobic domains within the multilayer. For practical purposes, a brief annealing period in high salt concentration is generally recommended for applications where PEMU roughness is undesired. The optimum annealing conditions are probably a function of  $Q_{\text{swell}}$ .

#### 4.2.2.3 Multilayer Decomposition

Fig. 4.4 suggests it is possible to reverse polyelectrolyte association at sufficiently high salt concentrations [67]. At some critical salt concentration,  $[\text{NaCl}]_{\text{crit}}$ , the extrinsic compensation is pushed to the point,  $\gamma_{\text{crit}}$ , where the few remaining polymer/polymer ion pairs are no longer capable of holding the PEMU together and the individual polyelectrolytes surrender to the entropic forces driving dissocia-

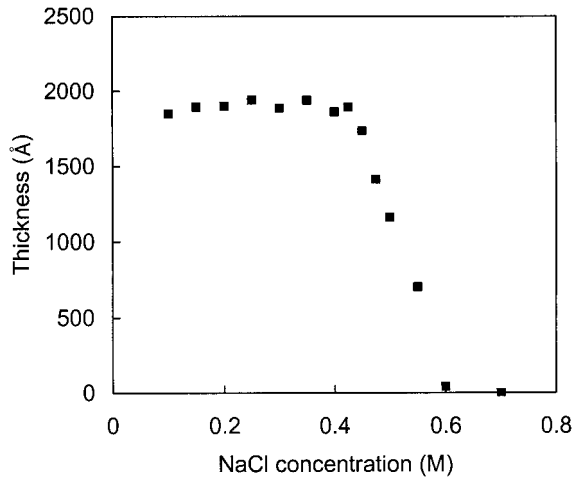


**Fig. 4.6** Thickness of 20-layer PAA/PDADMA film, prepared with 84 500 MW PAA, as a function of salt concentration. The deposition, soaking and rinsing solutions were maintained at pH 11.

tion. Fig. 4.6 demonstrates this effect for a PAA/PDADMA system [53]. The multilayer is stable to salt concentrations up to about 0.4 M, after which point the system decomposes. The deconstruction of PEMUs may actually yield very loosely associated complexes, i.e. not a true solution of individual polyelectrolyte molecules.

The concept of minimum charge density along the backbone needed to form a stable multilayer has been addressed previously [3, 68]. We add here the proviso that this minimum charge density depends on the salt concentration and salt type, and also very strongly on the chemical identity of the charged units being relied on to form the thin film. We have used the preferential decomposition of “weak” multilayers, inserted between more salt-resilient ones, to prepare onion-skin PEMUs that, on exposure to salt or pH changes, delaminate to yield free ultrathin membranes [35].

### 4.3

#### Excess Charge

##### 4.3.1

#### Surface vs. Bulk Polymer Charge

Fig. 4.7 depicts a typical growth vs. layer number for a strongly dissociated pair of polyelectrolytes (in this case, PSS and PM2VP) [50]. These particular polymers have been radiolabeled [43, 62, 69, 70], making it a simple task to accurately track their surface concentration. A strong dependence of the amount deposited on the solution salt concentration is observed. Other typical multilayer growth features

include a slight upwards curvature of the amount per layer towards the beginning of the plot (for 0.1 M salt) followed by a very linear behavior. The linear portion of the curve is evidence that the eventual thickness increment per cycle does not depend on the amount already deposited, and thus the controlling features of multilayer growth must be related to properties at or near the surface. The total molar charge of positive and negative polyelectrolytes balance for Fig. 4.7 [50], which points towards intrinsic bulk compensation, but does not prove it conclusively.

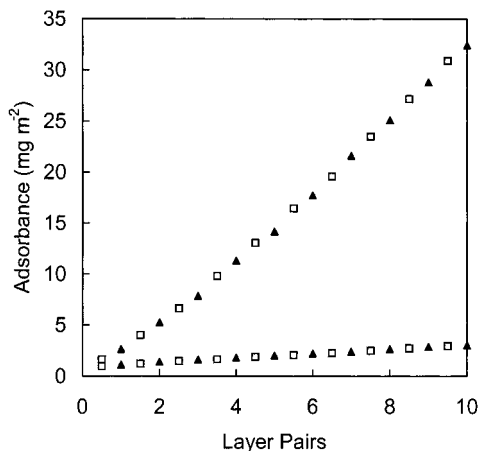


Fig. 4.7 Buildup of a multilayer of PM2VP (squares) and PSS (triangles) from 0.1 M NaCl<sub>aq</sub> (upper curve) and pure water (lower curve).

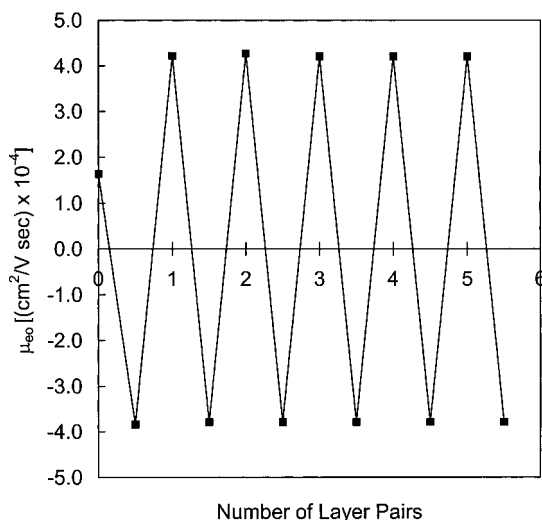
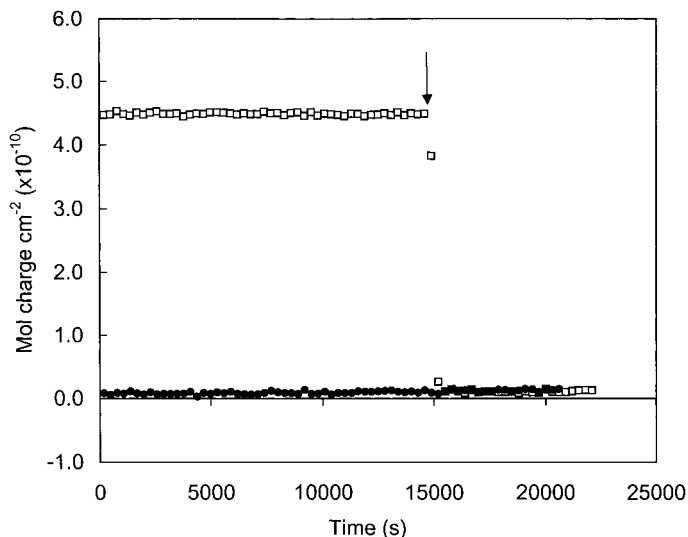


Fig. 4.8 Demonstration of surface charge reversal using capillary electrophoresis. PDADMA and PSS were alternately deposited from 0.5 M NaCl<sub>aq</sub>. Acetone was used as a neutral

marker to measure electroosmotic flow, with detection at 254 nm. Capillary length 37 cm, 50  $\mu$ m I.D. column, 15 kV applied voltage. 20 mM phosphate buffer.

The non-intuitive reversal of surface charge that occurs on each adsorption step, critical for multilayer buildup, was recognized at the outset [2, 27]. The sign of the surface charge and its reversal are shown by electroosmotic flow experiments on capillaries coated with multilayers [30, 31]. The direction of electroosmotic flow in these microfluidic systems depends on the sign of the wall charge. As shown in Fig. 4.8, the flow is reversed as each new polymer layer is added. The apparent charge density, which is taken to be the net charge density presented to the solution/multilayer interface, is much less than the total integrated areal excess (net) polymer charge density and is also remarkably constant. Surface charge reversal is also seen in the conceptually inverted arrangement of PEMU coated particles moving under an electric field [71].

Direct evaluation of the total areal excess charge density of a multilayer was accomplished using radiolabeled counterions and multilayers terminated with either a positive or a negative polyelectrolyte [50]. For both types of multilayer, ion self-exchange experiments indicate the presence of positive or negative salt ions within the film. For the example in Fig. 4.9 a PSS/PDADMA multilayer of thickness 245 Å, having either PSS or PDADMA as the “capping” layer, was exposed to a solution of radiolabeled calcium ions ( $^{45}\text{Ca}^{2+}$ , details on this type of radiochemical experiment may be found in [43, 62, 69, 70, 72]). At the point indicated, an excess of *unlabeled* calcium ions was added, which would self-exchange with any labeled calcium in the film. For the film capped with PSS (negative surface) an excess



**Fig. 4.9** Salt cation content, in terms of areal charge density, of a PDADMA/PSS multilayer deposited from 0.1 M NaCl, with PDADMA as the top layer (circles, 10.5 layer pairs) or PSS as the top layer (squares, 10 layer pairs).  $^{45}\text{Ca}^{2+}$  ( $10^{-4}$  M) has been used as a probe. At

the point indicated an excess of unlabeled  $\text{Ca}^{2+}$  was added to self-exchange salt cations in the PEMU. The multilayer contains exchangeable positive charge, at the surface only, when PSS is the top layer.

positive polymer charge was detected from the self-exchange, but the positive-capped film has no detectable salt cations. Symmetrical results were obtained for a negative radiolabeled probe ion ( $^{14}\text{CH}_3\text{COO}^-$ ) [50]. These results were interpreted as showing that there are no salt ions within the bulk of as-made multilayer (within the limit of detection of ca. 100 ppm. Salt concentrations at the low ppm level may be inferred from AC dielectric measurements [73]) and only one type of salt ion exists at the surface.

The absence of salt ions within the bulk of as-made multilayers is consistent with prior, but less sensitive, studies using XPS [18, 74], and with thermal gravimetric analysis [21], which shows no inorganic residue on thermolysis of multilayers. It is also consistent with the strong exclusion of ions when multilayers are used as membranes. Of course, salt added to the external solution contacting the multilayer can introduce extrinsic charge, as in Eq. (1) and Fig. 4.1.

The absence of extrinsic charge within as-made multilayers is an important and interesting property. It confirms the strong driving forces leading to complete ion pairing, and supports strong interpenetration [16] of “layers” and the scrambled or amorphous structure [23, 24]. It seems to be a property of a bulk polyelectrolyte complex that excess polymer charge is *extruded* towards the surface, much like a bulk conductor localizes excess electronic charge on the surface.

Despite the fact that strong ion pairing defeats many attempts to induce actual layering of material within PEMUs [3], several strategies may be invoked to create extrinsic charge and thereby layering in 2-component systems. (Layering in 3-component polyelectrolyte systems is possible provided the spacing of one of the components, such as a deuterated layer, is greater than a few layer thicknesses [16,

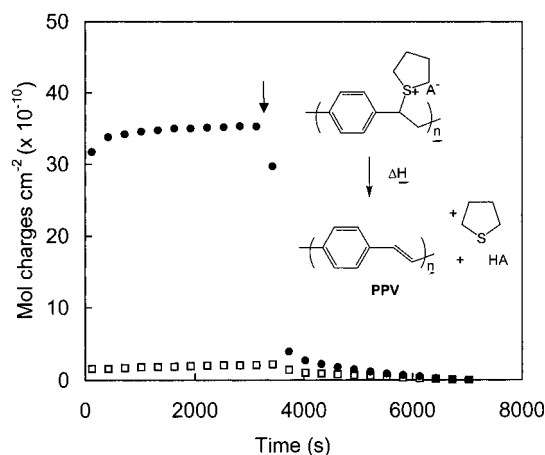


**Fig. 4.10** Cation content, in terms of areal charge density, of a 10.5 layer-pair PPV precursor/PSS multilayer following 0 h (squares) and 1 h (circles) thermal elimination at 90 °C. The PEMU was allowed to equilibrate with

$10^{-4}$  M  $^{45}\text{Ca}^{2+}$  and, at the point indicated, labeled  $\text{Ca}^{2+}$  was self-exchanged with an excess of unlabeled  $\text{Ca}^{2+}$ . Inset: thermal elimination scheme for PPV precursor.

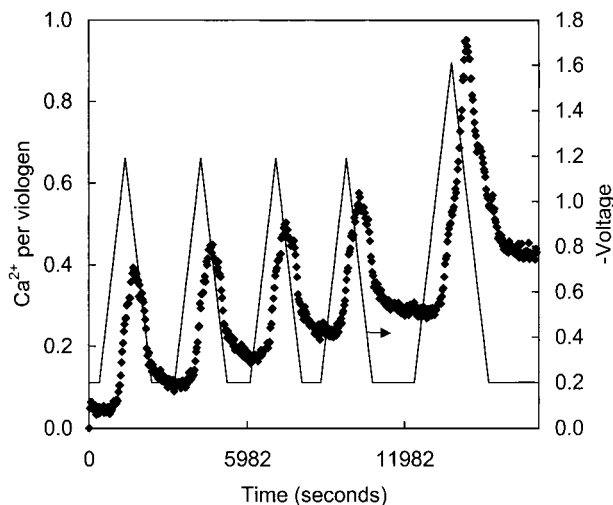


**Fig. 4.11**  $\text{Ca}^{2+}$  ion content (diamonds) of an eight layer-pair PEMU of PBV/PSS, deposited from 0.5 M KBr, cycled electrochemically on gold-coated plastic scintillator under  $\text{N}_2$  in 1 mM  $^{45}\text{CaCl}_2$  using the potential:time profile

depicted in the solid line. The charge density of the PEMU is *ca.*  $1.5 \times 10^{-9}$  mol layer $^{-1}$  cm $^{-2}$ . The first four cycles are in the 1-electron reduction regime of PBV, whereas the last one is a 2-electron reduction. Scan rate 1 mV s $^{-1}$ .

19].) In 2-component polyelectrolyte systems, a fundamental requirement for layering with periodicity greater than the width of a polymer chain is the presence of extrinsic compensation; layering is not possible for completely mixed intrinsic materials. Layering with particle/polymer combinations is observed due to the inability of components to mix.

Post-assembly processing steps can induce excess polymer charge of one type within a multilayer. Such steps include thermolytic or photolytic elimination of charged groups, electrochemical injection of charge into the multilayer, or the introduction of charge via pH changes when the multilayer includes weakly acidic polyelectrolytes [28, 49]. For example [50], the polycationic precursor to poly(phenylene vinylene), PPV, when incorporated into a multilayer, will, on heating, eliminate thiophene, as shown in Fig. 4.10. The excess negative sites left behind are compensated by extrinsic cations, in this case radiolabeled calcium.

Fig. 4.11 demonstrates the strategy of drawing ions into a multilayer by electrochemistry [18, 50, 75–77]. An electrochemical cell having a gold film electrode covering a scintillation detector enables an *in situ* assay of the radiolabel during electrochemical cycling. The electroactive polymer is a polyviologen, PBV, which undergoes a 1-electron reduction at  $-0.6$  V vs. SCE followed by another 1-electron reduction at  $-1.0$  V. Calcium ions enter the PEMU to compensate electrons injected into the film during reduction. Not all calcium ions are expelled (anions enter the film instead) when the polyviologen is restored to its neutral state, as the cyclic radiovoltammograms reveal residual extrinsic compensation ( $\text{Ca}^{2+}$  ions). Intrinsic compensation is gradually recovered after long times.

Extrinsic charges produced by mechanisms other than “reluctant” swelling may be thermodynamically unstable and may relax towards intrinsic compensation with *extrusion* to the surface and possible *expulsion* of excess polyelectrolyte charge from the multilayer. Immobilization of polymers, for example by crosslinking, may be required to prevent this type of relaxation.

#### 4.3.2

##### Distribution of Surface Charge in Layer-by-Layer Buildup: Mechanism

Surface excess polyelectrolyte charge is known to be compensated, then overcompensated, on the addition of oppositely-charged polymer [1–4]. It is understood that the increment per deposition cycle depends on the magnitude of this excess surface charge. For the PEMU pair of PSS and PDADMA, commonly employed in multilayer studies, we have shown [45] that the film thickness is an approximately linear function of the salt concentration used in the deposition solution,  $[\text{NaCl}]_{\text{build}}$ . This implies that the surface excess charge must also be proportional to salt concentration. We have verified this relationship using radiolabeled probes ( $^{35}\text{SO}_4^{2-}$ ) of the net areal surface charge density [78]. As shown in Fig. 4.12, the areal surface charge density of a multilayer capped with PDADMA shows a

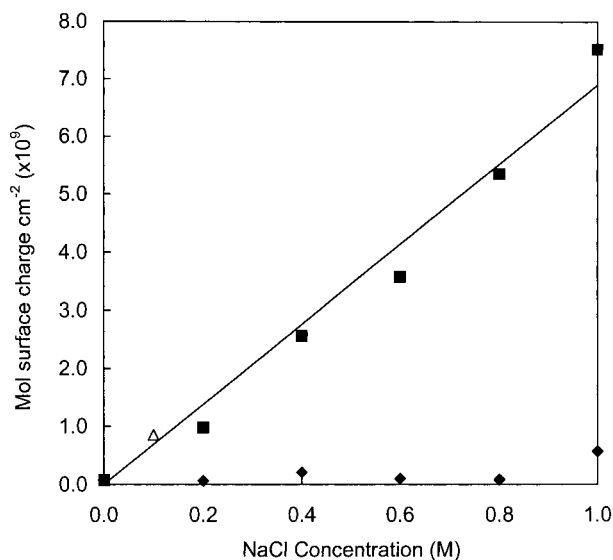


**Fig. 4.12** Positive surface areal charge density for 15-layer PSS/PDADMA multilayers (PDADMA-capped, squares), and 14-layer multilayers (PSS-capped, diamonds) made from solutions containing 1 mM polymer and different  $[\text{NaCl}]_{\text{build}}$ . The probe for surface charge was  $^{35}\text{S}$ -labeled sulfate ion. No surface

or bulk positive polymer excess charge is observed for the PSS-capped multilayer (i.e. the multilayer contains no negative salt ions). The solid line is a guide to the eye. The open triangle is from a similar strongly-dissociated polyelectrolyte system [50].

roughly linear dependence on  $[\text{NaCl}]_{\text{bulk}}$ , whereas the same multilayer capped with PSS contains neither surface nor bulk negative counterions.

If deposition is performed from concentrated salt solutions, several equivalent monolayers of polymer accrue on a single deposition step [45]. We have suggested [45, 50] that this large polymer excess charge is accommodated in the substrate-perpendicular direction over a length scale equal to several “layer thicknesses.” Such a spreading of polymer charge is depicted in Fig. 4.13, which shows contributions to volume charge density from both polyelectrolytes, with an exponential decay of positive excess polymer charge from the surface to the bulk having a characteristic length  $l_{cp}$ . The excess polymer charge density is mirrored by a counteranion profile, required to maintain net neutrality.

Fig. 4.13 incorporates several elements discussed above and found in the literature. First, the bulk of the PEMU is intrinsically compensated, in contrast to the

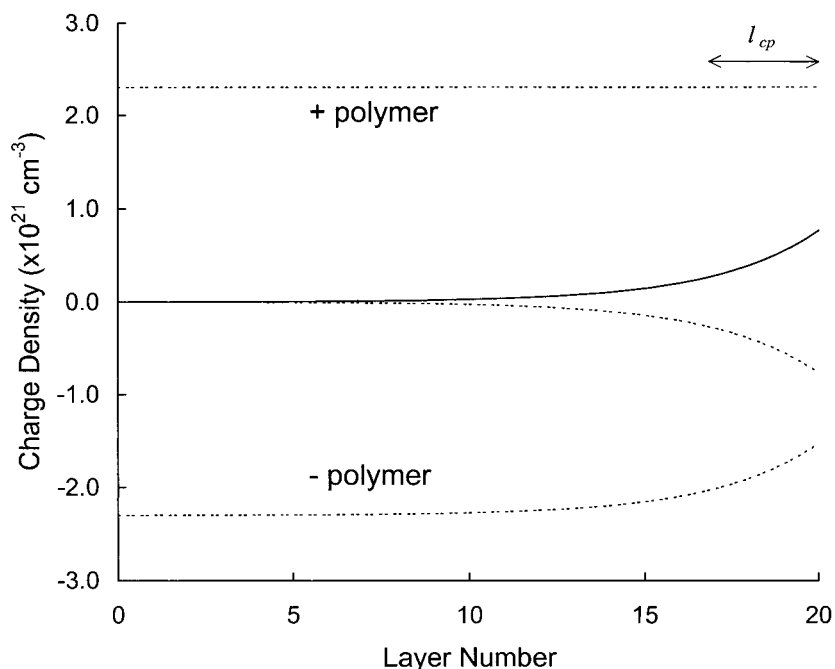


**Fig. 4.13** Sketch of charge density vs. distance from the substrate (in terms of nominal layer number) for an as-made 20 layer pair PSS/PDADMA multilayer measured under dry conditions. The curves were modeled according to Eq. (4) and (5) with  $l_{cp}=200 \text{ \AA}$  and  $\varphi=1.5$ . The system assumes intrinsic compensation within the bulk of the multilayer (layers 0 to 10), that is, 1:1 polymer charge stoichiometry and no salt ions. The final deposition is

from PDADMAC. Contributions from positive and negative polymer are shown as dotted lines and the net polymer charge density is shown as the solid line. The area under the latter curve would represent the polymer excess “surface” charge. Chloride counterions are represented by the dashed line. Charge density is estimated assuming a bulk density of  $1.2 \text{ g cm}^{-3}$  and a segment ion pair molecular weight of  $310 \text{ g mol}^{-1}$ .



region near the surface, where salt counterions balance excess polymer charge [50]. Second, both polymers are present at all points, since they are interpenetrating [16, 17]. This coexistence extends to the surface, allowing excess polymer to be distributed smoothly into the multilayer, rather than remain a thick surface layer of loops and tails.

At the multilayer/solution interface the charge of the last-added polymer compensates the previous one by a factor  $\varphi$ . If  $\varphi=1$  the opposite polymer charges are in exact stoichiometric ratio.  $\varphi-1$  is the surface overcompensation level. In our model, overcompensation, essential for multilayer growth, is driven by entropy gains due to the adsorbing polymer preserving some configurational degrees of freedom despite being immobilized on the multilayer surface. Going into the multilayer, segment density increases, the polymer/polymer ion pairs become denser, and the restrictions against polymer excluded volume increase, making overcompensation unprofitable from an entropic viewpoint. Thus, at increasing lengths  $l$  from the interface, overcompensation decreases in an exponential fashion (decay rate  $l_{cp}$ ).

Attractive interactions between oppositely charged polymer segments are moderated by external salt via Eq. (1). Increasing the external salt concentration makes it easier to separate polymer segments, allowing the overcompensation to penetrate further into the multilayer (greater  $l_{cp}$ ). The overall energy balance is one of enhanced entropy from overcompensation against decreasing available volume and separation of polyelectrolyte ion pairs.

In order to estimate the amount of polymer added in each deposition step, the area under the exponential polymer excess charge profile is integrated and doubled, since the adding polymer compensated the multilayer then overcompensates by the same amount. Assuming we are modeling the buildup of a PSS/PDADMA multilayer, thickness  $t$ , from 1.0 M NaCl, shown in Fig. 4.14, the thickness increments,  $t_n^+$  and  $t_n^-$ , for odd (PDADMA) and even (PSS) layers, respectively, are

$$t_n^+ = 2l_{cp} \left( \frac{\varphi - 1}{\varphi} \right) f^+ (1 - e^{-t/l_{cp}}) \quad (4)$$

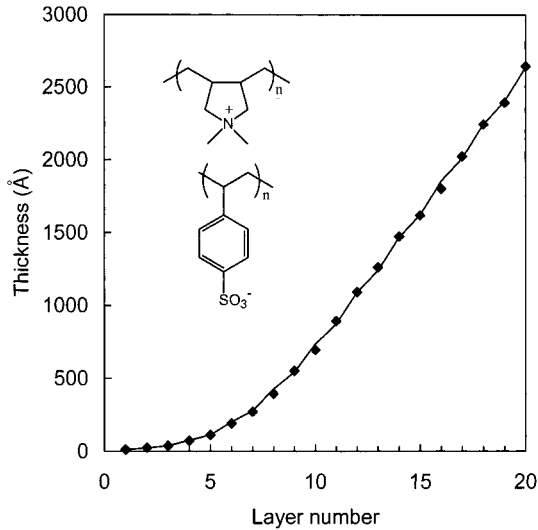
$$t_n^- = 2l_{cp} \left( \frac{\varphi - 1}{\varphi} \right) f^- (1 - e^{-t/l_{cp}}) \quad (5)$$

The thickness increment from each layer is limited, at the beginning of buildup, by truncation of the excess charge profile by the substrate, represented by the right-most term in Eq. (4) and (5). At sufficient thicknesses, or smaller  $l_{cp}$ s, the growth is a linear function of layer number. The overall thickness of a film is the sum of thickness increments

$$t = \sum t_n = t_1 + \sum t_n^+ + \sum t_n^- \quad (6)$$

Where  $t_1$  is the anomalous, but small, thickness of the first layer.

**Fig. 4.14** Thickness as a function of the number of layers for a PSS/PDADMA multilayer deposited on silicon wafer from polymer solutions containing 1.0 M  $[\text{NaCl}]_{\text{build}}$ . Odd layers are from PDADMA; even from PSS. Polymer concentration 10 mM; 5 min deposition time with 3 water rinses in between layers. Solid line is a fit to Eq. (4), (5) and (6) with  $\phi=1.86$  and  $l_{\text{cp}}=425 \text{ \AA}$ . The thickness of the first layer,  $t_1$ , was measured to be 12  $\text{\AA}$ .



An iterative computer program [78] yields thicknesses for specific values of  $\phi$  and  $l_{\text{cp}}$ . The model using the optimum pair of  $\phi$  and  $l_{\text{cp}}$  is also presented in Fig. 4.14. The experimental data are reproduced well with these two parameters. Note that the linear portion of the curve yields the product  $\phi l_{\text{cp}}$ . Clear separation between  $\phi$  and  $l_{\text{cp}}$  can only be obtained if there is initial curvature to the data, since  $l_{\text{cp}}$  effectively delays the onset of steady-state growth.

The model shows how excess charge is spread over several “layers” ( $l_{\text{cp}}$  is about 2.5 nominal “layers”) so that  $\phi$  does not need to be high, even for very “thick” films. A significant preliminary finding was that values of  $\phi$  for the PSS/PDADMA multilayer system were almost independent of salt concentration and film growth is almost entirely controlled by  $l_{\text{cp}}$ . For salt concentration  $M$ , the approximate relationship is  $l_{\text{cp}}(\text{\AA})=400 M$  in the present case. The independence of  $\phi$  on salt concentration is consistent with results from electroosmotic flow measurements of capillaries coated with multilayers [30], where it was found that the apparent surface charge remained strictly constant as a function of the salt concentration (layer thickness) [79].

The invariability of apparent surface charge with salt is a very useful property for microfluidics [30, 31], such as capillary zone electrophoretic separations, from the perspective of reproducibility. The drawback is that one cannot vary fluid flow: in particular, it is not possible to obtain “turbocharged” flow from high wall charge. It may be possible to vary  $\phi$  by changing the solvent or by using different pairs of polyelectrolytes.

## 4.3.3

**Equilibrium vs. non-Equilibrium Conditions for Salt and Polymer Sorption**

It is appropriate to view discussions concerning the distribution of excess polymer charge, based on thermodynamic arguments, with caution. Although the adsorption/desorption of salt ions (swelling) is fast and reversible [52], the adsorption of polymer is irreversible. The latter fact, generally acknowledged from the outset of research into multilayered systems [1–4], was demonstrated using radiolabeled polyelectrolyte [45], which, when incorporated into a PEMU as the top layer, did not exchange with unlabeled solution polyelectrolyte on the time scale of the assembly. Irreversibility is an essential and fortuitous property. If desorption were not kinetically limited, multilayer polymer could be stripped from the surface on exposure to a solution of its oppositely charged partner [53]. Indeed, polymers with sufficiently low molecular weight can be prised off the surface by this process, suppressing PEMU growth [80]. Polymer stripping using a very large excess of oppositely charged polyelectrolyte may yield soluble complexes, which, having more configurational and translational entropy, might be more stable than precipitated complexes. Salt, again, mediates the removal of surface polyelectrolyte by loosening the interactions between polymers via competitive ion exchange. Adsorbed polyelectrolyte conformational changes are known to be accelerated by the addition of salt [59, 62]. For successful PEMU growth the competition between polymer addition to the surface and the loss of complex to solution favors the former on the time scale of the experiment. In the presence of salt, the kinetic balance is tipped towards polymer addition by sufficient molecular weight.

Small but measurable gradual changes in the adsorbed amount with time or polymer concentration attest to nonequilibrium conditions [45]. Yet, the amount of polymer added for each deposition step is precisely reproducible, is self-limiting and shows little dependence on molecular weight for sufficiently large macromolecules. As a compromise in the face of this paradox, the process of multilayer formation may be considered to be under “local” thermodynamic control: one can invoke the chemical potential gradient in Fig. 4.13, which requires only the transport of small ions and short distance (short correlation length) rearrangements of polymer segments. These rearrangements are much less demanding than complete removal of an entire polyelectrolyte chain from the surface, necessary for desorption.

## 4.4

**Equilibria and Transport**

## 4.4.1

**Ion Transport through Multilayers: the “Reluctant” Exchange Mechanism**

PEMUs have been employed as selective membranes for the separation of gases [81, 82] and dissolved species [83–86]. Multilayers offer several advantages for use as membranes: they are uniform, easily prepared on a variety of substrates, con-

tinuous, resistant to protein adsorption [30], fairly rugged, the thickness is reproducible, very thin layers allow high permeation rates, and there are a wide range of possible compositions of polymers and particles. Separation by pervaporation of volatiles [87–89], for example water and ethanol, has achieved very high separation factors. Membrane selectivity for ions of low charge has been demonstrated using conductivity [84] or redox electrochemical [85, 86] methods. Post-deposition thermal crosslinking of polyamine/polyacrylic acid PEMUs significantly decreases ion permeability [85]. The ion flux through a dendrimer multilayer composite may be controlled by the external pH [90]. The reader is referred to Chapter 17 by M. Bruening and Chapter 15 by B. Tiede et al. on the design and use of PEMUs as separation membranes.

In the remainder of this chapter, ionic transport through PEMUs will be rationalized in terms of the kinetics and distribution of charged species within multilayers. The latter is elucidated by considering various equilibria governing reluctant exchange.

We employ a rotating disk electrode, RDE, coated with a multilayer, to evaluate the permeation of electrochemically active ionic probes [52]. For reversible redox species, such as ferrocyanide,  $\text{Fe}(\text{CN})_6^{4-}$ , this apparatus yields an S-shaped redox wave with a steady state limiting current,  $i_l$ , at the plateau [91]. Fig. 4.15 depicts,

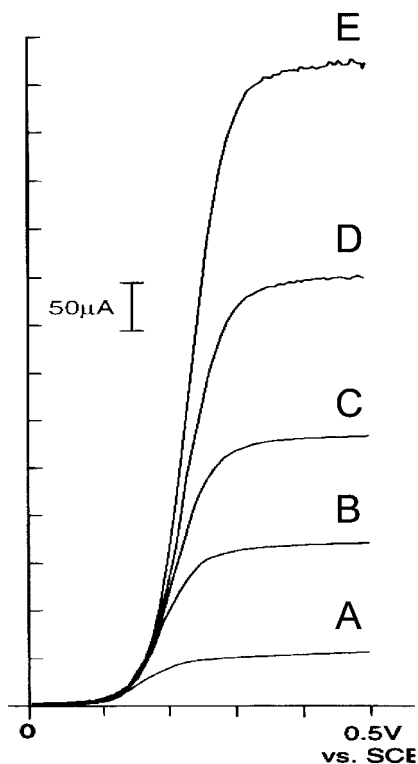


**Fig. 4.15** Linear scan voltammograms of a rotating disc electrode; uncoated (E), and coated with a PSS/PDADMA multilayer of thickness 700 Å (A–D). Polymer solutions used to make the 20-layer membrane were 1 mM in polyelectrolyte and 0.25 M salt. The last layer (PSS) was deposited from 10 mM salt to provide a pseudo-neutral surface. The electrolyte for voltammograms contained 1 mM potassium ferrocyanide and 1.2 M (A); 1.6 M (B); 1.8 M (C); 2.0 M (D) salt. Electrode was 8 mm diameter platinum, temperature  $(22 \pm 0.1)^\circ\text{C}$ , rotation rate 1000 rpm.

for example, the response of a RDE coated with 700 Å of PSS/PDADMA to a solution of 1 mM ferrocyanide with various  $[\text{NaCl}]_{\text{aq}}$ . A striking and unconventional feature of the electrochemistry at the PEMU-coated RDE is the increase of current as the  $[\text{NaCl}]_{\text{aq}}$  increases.

The flux, or current, to the membrane-coated RDE electrode is limited by convective diffusion through a stagnant layer of electrolyte next to the membrane and by diffusion through the membrane [92, 93]. The effect of these two series resistances to mass transport is expressed as follows:

$$\frac{1}{i_l} = \frac{1}{i_m} + \frac{1}{i_{\text{bare}}} \quad (7)$$

where  $i_m$  is the membrane-limited current and  $i_{\text{bare}}$  is the current at the bare electrode, area  $A$ . The latter is given, with precision for this system with well-defined hydrodynamics, by the Levich equation [91]

$$i_{\text{bare}} = 0.620nFAD_{\text{aq}}^{2/3}\omega^{1/2}\nu^{-1/6}C_{\text{aq}} \quad (8)$$

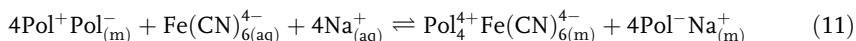
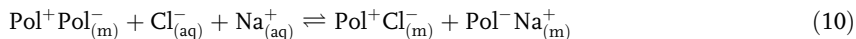
where  $n$  is the number of electrons transferred (1 in this case),  $F$  is Faraday's constant,  $D_{\text{aq}}$  is the solution diffusion coefficient of electroactive species,  $\omega$  is the angular velocity,  $\nu$  is the kinematic viscosity of the electrolyte (approximately  $0.01 \text{ cm}^2 \text{ s}^{-1}$  for dilute aqueous solutions) and  $C_{\text{aq}}$  is the solution concentration ( $\text{mol cm}^{-3}$ ). With plots of  $i_l$  vs.  $\omega^{1/2}$  on coated and bare electrodes,  $i_m$  is easily extracted.

Steady-state diffusion-limited flux,  $J_m$ , through a membrane of thickness  $d$  is given by [94]

$$J_m = -\frac{\bar{D}\bar{C}}{d} \quad (9)$$

where  $\bar{D}$  and  $\bar{C}$  are, respectively, the diffusion coefficient and concentration of the probe species within the membrane. Note that the flux, which is converted to current by  $i_m = J_m nFA$ , is purely diffusive, i.e. does not contain an electric field driven, or migration, component. Evidence that this is the case for the electrochemical system in Fig. 4.15 comes from the fact that the limiting plateau is flat instead of ramped. The electric field is suppressed by the presence of salt ions within the multilayer. Given Eq. (9) one would expect current to decrease for thicker films. This is indeed observed (see Fig. 4.16).

The distribution of charged species within the multilayer is governed by the chemical potential of external salt. The competition between intrinsic and extrinsic compensation in the presence of pure salt solutions is characterized, for the ferrocyanide system used in our studies, by the following equilibria



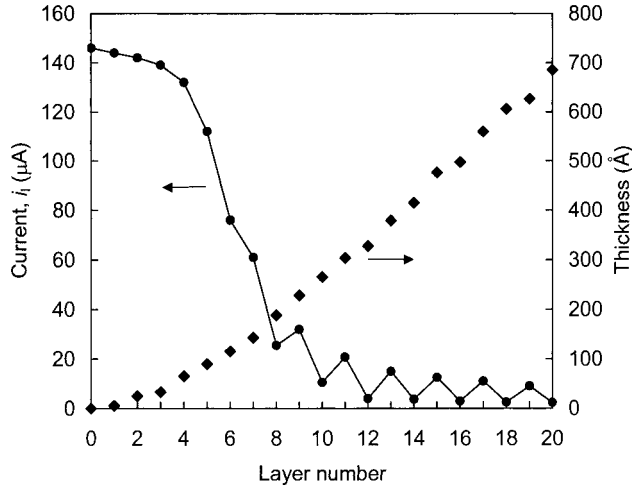
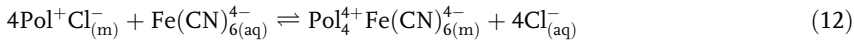


**Fig. 4.16** Current and thickness vs. layer number for the buildup of a 20-layer PEMU from 0.25 M salt, as in Fig. 4.15. The flux of ferrocyanide through the membrane after the addition of each layer was measured in 1 mM  $\text{Fe}(\text{CN})_6^{4-}$  and 0.6 M NaCl. The 20th (PSS) layer was deposited from 10 mM salt. Rotation rate 1000 rpm.

A third equilibrium represents competition between solution anion species for positive polymer segments.



Assuming activity coefficients are unity

$$K_1 = \frac{[\text{Pol}^+\text{Cl}^-]_m [\text{Pol}^-\text{Na}^+]_m}{[\text{Pol}^+\text{Pol}^-]_m [\text{Cl}^-]_{aq} [\text{Na}^+]_{aq}} \quad (13)$$

$$K_2 = \frac{[\text{Pol}_4^{4+}\text{Fe}(\text{CN})_6^{4-}]_m [\text{Pol}^-\text{Na}^+]_m^4}{[\text{Pol}^+\text{Pol}^-]_m^4 [\text{Fe}(\text{CN})_6^{4-}]_{aq} [\text{Na}^+]_{aq}^4} \quad (14)$$

$$K_3 = \frac{[\text{Pol}_4^{4+}\text{Fe}(\text{CN})_6^{4-}]_m [\text{Cl}^-]_{aq}^4}{[\text{Pol}^+\text{Cl}^-]_m^4 [\text{Fe}(\text{CN})_6^{4-}]_{aq}} \quad (15)$$

Where  $K_3 = K_2 / K_1^4$ .

At this point, it is worth comparing the differences in ion exchange behavior between salt-swollen PEMUs and classical ion exchanger resins. Resins are typically prepared with one type of polyelectrolyte, charge balanced completely via exchangeable salt ions, and crosslinked to prevent the polymer from dissolving [51]. These classical exchangers exhibit permselective Donnan exclusion of like-charged

mobile species and inclusion of oppositely charged ones [50]. This selectivity sets up a concentration gradient, and therefore chemical potential, across the membrane/solution interface. Competition between solution species for a fixed number of ion exchanging sites in classical exchangers is represented by an equilibrium of the type shown in Eq. (12). The difference with reluctant exchangers is that additional exchanging sites are also *created* by external ions (Eq. (10) and (11)). The number of sites is controlled by the external ion concentration.

There are some examples of reluctant exchangers in the literature. It is possible to synthesize resins containing equal numbers of *fixed* positive and negative groups (so-called “amphoteric” exchangers) [95], which, if intrinsically compensated, would be reluctant. More relevant examples are the “snake cage” exchangers developed by Dow Chemical in the 1950s [96]. These interesting systems are prepared by polymerizing ionic counterions (making “snakes”) inside an ion exchanger matrix (the “cage”). If polymerization were complete, the system would be fully intrinsic as made. Snake cage resins also exhibit the characteristic reluctant properties of swelling in electrolyte (unlike Donnan exchangers, which shrink) and non-permselectivity [96]. There are examples where solution-precipitated PECs have been formed into membranes [20, 97, 98]. These materials, having similar morphologies to PEMUs also exhibit selective transport for ions of low charge.

Some unusual oscillating features (Fig. 4.16), also seen in other work [4], are observed in the current as the PEMU is built layer by layer. For our negatively charged probe ion, multilayers terminated with a positive layer yield larger membrane currents than those ending with a negative layer [99]. These features may be explained by Donnan inclusion of ferrocyanide into the positively charged surface layer shown in Fig. 4.13. This inclusion increases the membrane concentration  $\bar{C}$ , leading to greater  $J_m$  as predicted by Eq. (9). Examples of representative profiles at steady state through membranes with purely reluctant exchange, compared to a Donnan-enhanced mechanism are depicted in Fig. 4.17. The finding

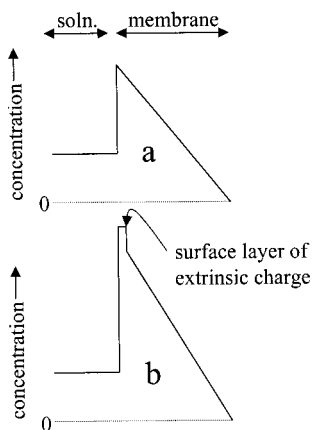


**Fig. 4.17** Concentration profile, going from solution into the multilayer for a redox probe species favored by the latter; (a) assumes population of redox probe in multilayer is controlled by pure reluctant exchange; (b) shows additional probe ion included into the surface of the multilayer by polymer excess surface charge.

that the currents with positive-capped multilayers approach those of negative capped ones as the multilayer sits in electrolyte for extended periods is indirect evidence of excess positive charge sinking into the multilayer to yield the eventual “equilibrium” profiles given in Fig. 4.13.

Manipulation of the equilibrium expressions above in the limit of high  $[\text{NaCl}]_{\text{aq}}$  leads to some important conclusions. If the solution concentration of NaCl is much greater than that of the ferrocyanide, we make the following approximations:  $[\text{Pol}^+\text{Cl}^-]_{\text{m}} \gg [\text{Pol}_4^{4+}(\text{Fe}(\text{CN})_6^4-)]_{\text{m}}$  and  $[\text{Pol}^+\text{Cl}^-]_{\text{m}} \approx [\text{Pol}^+\text{Na}^+]_{\text{m}}$ , and  $[\text{Cl}^-]_{\text{aq}} = [\text{Na}^+]_{\text{aq}}$ . In the limit of low swelling,  $(1-\gamma) \rightarrow 1$  and  $[\text{Pol}^+\text{Pol}^-]_{\text{m}} \approx C_{\text{t}}$ , where  $C_{\text{t}}$  is the total concentration of intrinsically plus extrinsically compensated polymer, which remains constant if the volume is constant, which is the case for small  $\gamma$ . Thus,

$$\bar{C} = [\text{Pol}_4^{4+}\text{Fe}(\text{CN})_6^4-]_{\text{m}} = K_3 K_1^2 C_{\text{t}}^2 [\text{Fe}(\text{CN})_6^4-]_{\text{aq}} \quad (16)$$

The linear dependence of  $J_{\text{m}}$  on  $[\text{Fe}(\text{CN})_6^4-]_{\text{aq}}$  through  $\bar{C}$  was verified experimentally. From Eq. (2)

$$\gamma = [\text{NaCl}]_{\text{aq}} \sqrt{K'} \quad (17)$$

Two important facts emerge from the foregoing treatment of the high salt concentration limit: (1) ferrocyanide concentration in the PEMU is independent of solution salt; the ferrocyanides in the multilayer displaced by chloride ions are compensated by the fact that the chlorides *also* open up an equal number of new, reluctant, ferrocyanide-occupied anion exchanging sites. (2) The total exchanger capacity ( $\gamma$ ) is directly proportional to the external salt ion concentration, at least for low  $\gamma$ . Given finding (1), i.e.  $\bar{C}$  is constant as  $[\text{NaCl}]_{\text{aq}}$  increases, *all enhancement of flux by  $[\text{NaCl}]_{\text{aq}}$  is due to an increase in  $\bar{D}$ .*

The constancy of redox probe ion concentration,  $\bar{C}$ , in the PEMU as a function of  $[\text{NaCl}]_{\text{aq}}$  is a critical feature of the “reluctant” ion exchange mechanism and the ultimate control of the flux by  $\bar{D}$  (Eq. (9)). (This constancy may be generalized for all combinations of probe ion and salt ion charge.) Other mechanisms for exchange and accounting of flux posit an increase of  $\bar{C}$  with increasing salt, for example, by producing more sodium-paired, free salt form of ferrocyanide (i.e.  $[\text{Na}_4\text{Fe}(\text{CN})_6]$ ) within the membrane. We have obtained direct experimental evidence for the constancy of  $\bar{C}$ . Multilayers were exposed to salt solutions containing ferrocyanide and the PEM content of this ion was measured using FTIR absorption spectroscopy and the conveniently-strong CN stretch at  $2050 \text{ cm}^{-1}$ . The clear ferrocyanide absorption band (spectra not shown) remained roughly constant as the multilayer was immersed in 0.6 and 2.0 M NaCl solutions with 1 mM ferrocyanide (over this range the flux changes by a factor of ca. 100). Using ferrocyanide complexed with PDADMA (mole ratio 4:1) as a reference, we estimated a multilayer mole ratio of PDADMA:ferrocyanide of approximately 150:1 (i.e. 0.7 mol% redox probe), which translates to a  $\bar{C}$  of approximately  $3 \times 10^{-5} \text{ mol cm}^{-3}$ . This permits the separation of  $\bar{D}$  and  $\bar{C}$  and an estimate for  $\bar{D}$ . A similar treatment for



multilayer immersed in 1 mM ferricyanide yielded a multilayer concentration of  $8 \times 10^{-5} \text{ mol cm}^{-3}$  for this ion.

Membrane currents extracted from  $i_l$  using Eq. (7) are plotted as a function of the activity of NaCl (determined by the product of  $[\text{NaCl}]_{\text{aq}}$  and a tabulated activity coefficient) in Fig. 4.18 for ferro- and ferricyanide. The dependence of flux on salt activity (or  $[\text{NaCl}]_{\text{aq}}$ ) is clearly nonlinear. On inspection of the data, we established the following empirical fit for transport of ions of charge  $n$  through PEMUs

$$J_m = ka_{\text{NaCl}}^n = c\gamma^n \quad (\text{since } \gamma \text{ scales with } a_{\text{NaCl}}) \quad (18)$$

where  $c$  is another constant. The fits with  $n=3$  or 4 for ferri- or ferrocyanide, respectively, are shown in Fig. 4.18.

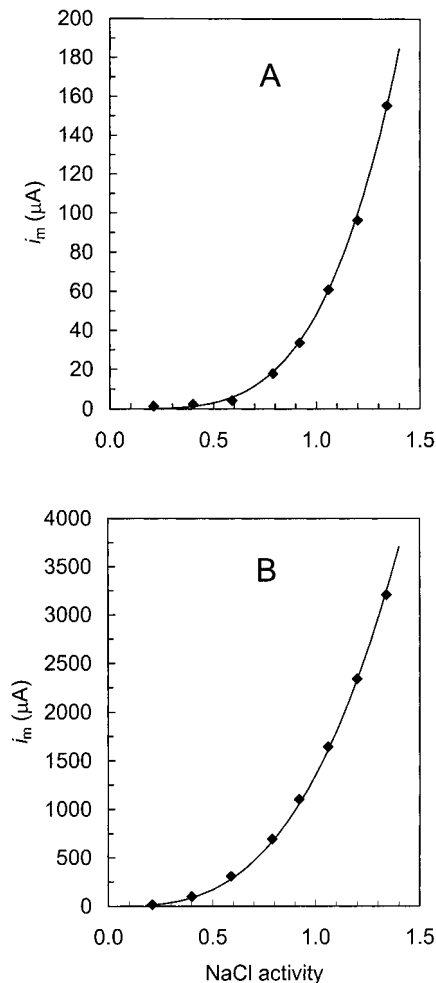


**Fig. 4.18** Membrane flux, in terms of  $i_m$ , vs. activity of salt  $a_{\text{NaCl}}$ . The solid line represents an empirical fit of  $J_m = Ka_{\text{NaCl}}^4$  for 1 mM ferrocyanide ( $k=48$ , Panel A); and for  $J_m = Ka_{\text{NaCl}}^3$  1 mM ferricyanide ( $k=1350$ , Panel B).

The nonlinear control of diffusion coefficient on external salt represents a fascinating new paradigm for the transport of charge through “soft” condensed matter. The phenomenological trends in Fig. 4.18 suggest transport of ions within the PEMU occurs via hopping from site to site. Each site that is occupied by a small ion (mostly  $\text{Cl}^-$  and  $\text{Na}^+$ ) acts as a charge carrier. Positive charge carriers,  $[\text{Pol}^+\text{Cl}^-]_m$  sites, are introduced, or “doped,” into the PEM by the external chemical potential of the salt solution. The  $n$ th power relationship to the site exchanger site concentration,  $[\text{Pol}^+\text{Cl}^-]_m$  (or normalized concentration,  $\gamma$ ) is reasonable, since each ion requires the simultaneous displacement of  $n$  adjacent chloride ions from  $\text{Pol}^+$  sites. The probability that this occurs is a function of  $\gamma^n$ . A hopping-type mechanism would be thermally activated, as observed [52].

A further implication of the charge carrier argument for ion transport through reluctant exchangers is that polyelectrolyte multilayers will be much more permeable to species of lower charge. This trend has been observed previously [83, 85, 86], and is confirmed in a quantitative fashion for the ferro/ferricyanide data (Fig. 4.19). Selectivity, regulated by salt concentration, tends to higher values as  $[\text{salt}] \rightarrow 0$ . A summary of the dependence of flux on salt concentration and probe charge, for ions of different charge, is presented in Fig. 4.20. Note that the positive and negative trivalent ions exhibit comparable membrane currents. Also, the neutral species shows almost no dependence of flux on  $[\text{NaCl}]_{\text{aq}}$ , as expected.

Monte Carlo simulations of reluctant exchanger films with extrinsic ions support the selectivity according to charge and the  $\gamma^n$  dependence of flux [100]. In these simulations, probe ions of charge  $n$  are assumed to hop only if  $n$  oppositely charged sites are generated, by random movement of extrinsic salt counterions, within a specified range.

An interesting comparison may be made of the mechanism of ion transport in the system described with electron transport. Some electron transport materials,

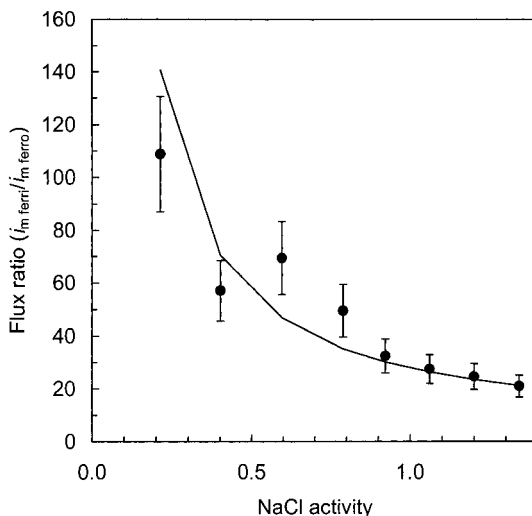


**Fig. 4.19** Flux ratio  $J_{\text{ferric}}/J_{\text{ferro}}$  taken from Fig. 4.18 for various salt concentrations. The solid line is taken from the equations used to fit Fig. 4.18.

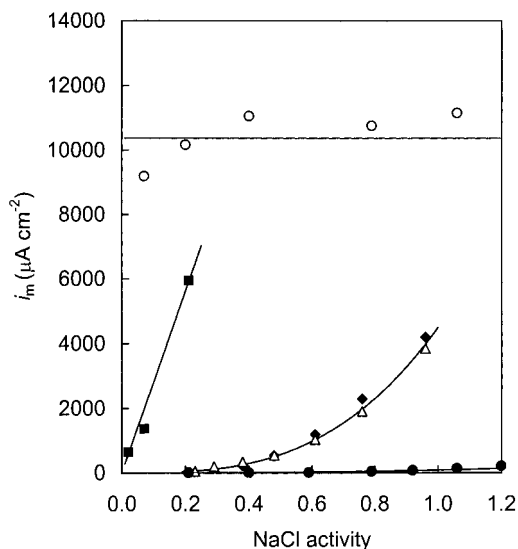


**Fig. 4.20** Membrane limited current density, as a function of salt activity, through a 700 Å thick multilayer of PSS/PDADMA on a rotating Pt electrode as in Fig. 4.16, using species of different charge, all  $1 \times 10^{-3}$  M concentration. Hydroquinone (open circles) was uncharged; iodide (charge  $-1$ , squares); ferricyanide ( $-3$ , diamonds); ferric ion ( $+3$ , triangles); and ferrocyanide ( $-4$ , solid circles). Solid lines are fits using the scaling behavior: flux  $\sim a_{\text{NaCl}}^{\text{charge}}$ .

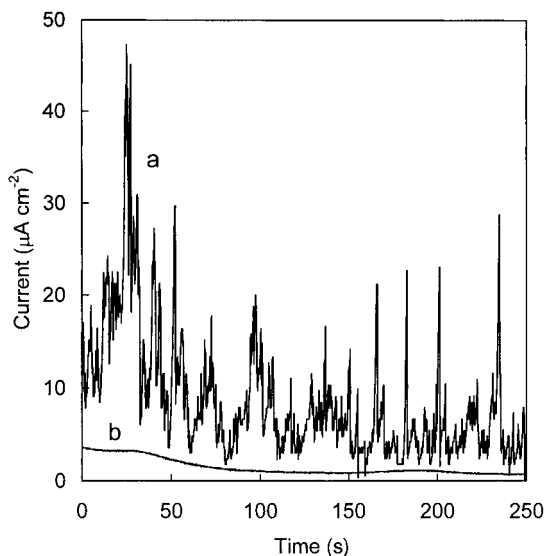
such as conducting polymers, exhibit strongly nonlinear increases in conductivity with doping level [101, 102]. However, since electrons, or holes, are of unit charge, a dependence of transport on the charge of the carrier is not an issue.

#### 4.4.2

#### Practical Consequences: Trapping and Self-Trapping

Many practical considerations follow from the control of permeability and selectivity by salt. For membrane separations with PEMUs, the selectivity for species of differing charge, in addition to being high, may be tuned by salt. As is commonly encountered in membrane separations, enhanced selectivity comes at the cost of flux. For the trapping of molecules, such as drugs and biomolecules, by PEMU microcapsules, [71,103–105] detailed by other contributors to this volume, salt will play a strong role in loading and in the rate of release. Selective transportation of species with lower charge provides a convenient mechanism for loading PEMU membranes or capsules: under conditions of high salt, PEMU capsules, rendered significantly more permeable, may be loaded with polyvalent molecules. When the system is exposed to fresh water, ions of low charge rush out leaving the lumbering highly-charged species trapped within the capsule. Selective transport, giving trapped extrinsic charge in a PEMU, was seen above for the radiolabeled calcium experiment. “Self-trapping” is possible for single ionic species only (i.e. no other salts are added) when the overall ionic content of a film falls to a value that does not support diffusion. Self-trapping for ions of higher charge is a nonlinear (power law) positive feedback mechanism, as fewer ions within the film mean significantly decreased  $\bar{D}$ . Thus, notably more polyvalent ions will be self-trapped, as is probably the case for multiply charged dyes probes [48]. Self-trapping implies

**Fig. 4.21** Current vs. time in the metastable pitting region (0.6 V vs. SCE) for (a) a bare steel wire; (b) wire coated with 70 nm PDADMA/PSS in 0.1 M  $\text{NaCl}_{\text{aq}}$ .



that it is impossible to rid a multilayer of all salt ions on immersion into pure water, although their concentration may be below the detection limit.

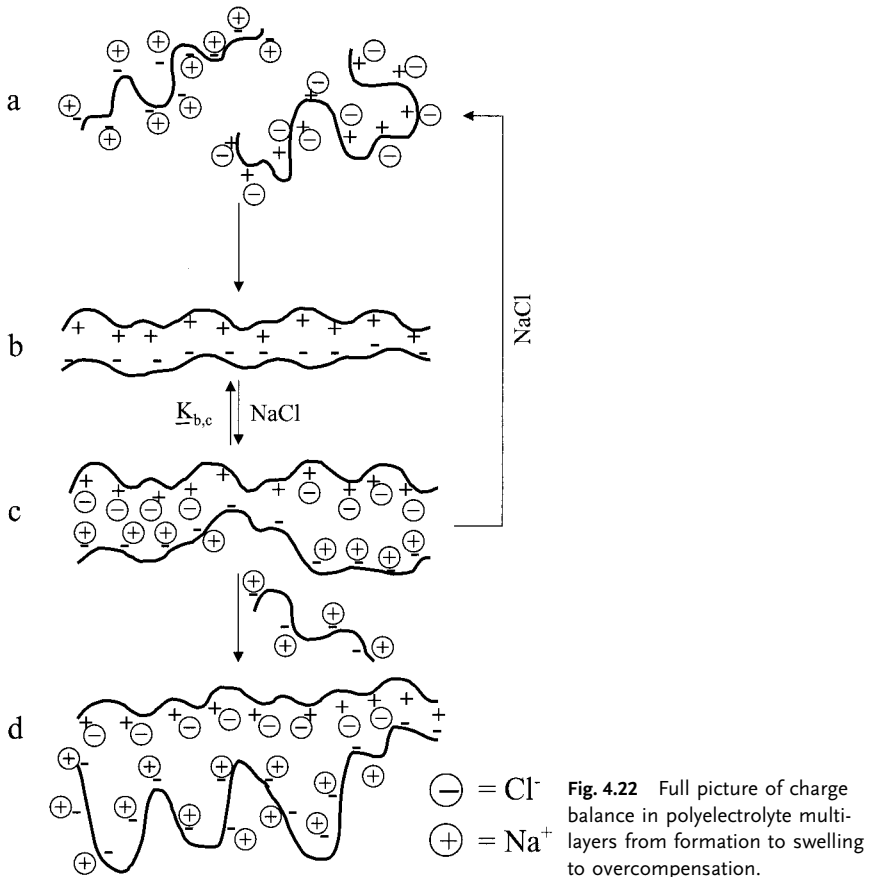
As an example of another potential application, we have shown that PEMUs are useful in preventing corrosion [106]. The effectiveness of PEMUs in suppressing corrosion of steel in salt water, surprising in the light of the fact that the films contain appreciable amounts of water and salt, was attributed partially to the exclusion of “liquid” water, or water that is not occupied in hydrating ion pairs (see Fig. 4.4). In addition, the partial mobility, in the presence of salt, of polymeric material in PEMUs, evidenced in Fig. 4.5, was thought to allow small defects in the ultrathin film to heal over. Fig. 4.21 depicts corrosion current vs. time in the metastable pitting region of stainless steel. A 70 nm layer of PEMU is extremely effective at suppressing pitting events.

The transport of biomolecules or bioactive molecules across reluctant exchangers is potentially controlled in two “dimensions”: salt and pH. Changes in solution pH have the possibility of creating extrinsic charge if the membrane materials comprise weak acids/bases. Alternatively, pH can modify the charge, thus mobility, of the species attempting to traverse the membrane. Both ionic strength and pH effects can work in concert. One wonders whether the reluctant transport mechanism plays a role in natural membranes [107].

## 4.5

## Conclusions

This chapter concludes with an overall look at the role of salt in multilayer formation and function. A pictorial summary of ion-controlled phenomena discussed in this chapter is provided in Fig. 4.22. In (a) the solution phase polymers are compensated by counterions. When the polymers associate during multilayer formation, (b), and after the final rinse step, polymer charges are compensated by other polymer charges (polymer/polymer ion pairs, intrinsic compensation). Salt added to the external bathing solution forces some swelling (extrinsic compensation), (c). If the swelling is sufficient, the multilayer decomposes (shown by the arrow) back into individual, or perhaps loosely associated, solution-phase polymer strands. In the presence of additional polyelectrolyte of one type (here negative), overcompensation occurs near the surface (d), giving the excess surface charge reversal required for adsorption of the next polyelectrolyte. During the adsorption of a poly-



electrolyte layer in multilayer buildup, steps  $b \rightarrow c \rightarrow d$  occur simultaneously. Although we focus on PEMUs here, the same ideas of swelling and surface overcompensation may be extended to particles of solution precipitated complexes (PECs). Interestingly, Dautzenberg [108] has recently suggested a similar picture of PEC particles which are charged balanced on the interior, but which have a surface excess of one of the polyelectrolytes.

Several trends may be predicted/rationalized if  $K'$  (Eq. (2)), characterizing the extent of swelling, is known. First, stronger ion pairing (smaller  $K'$ ) will likely decrease both  $\phi$  and  $l_{cp}$ , leading to thinner “layers” during PEMU buildup. Stronger ion pairing will also yield more stable multilayers, able to withstand higher salt concentration. Second, the permeability of multilayers to ions depends on the ability of salt to swell multilayers, producing carriers, and will thus be greater with larger  $K'$ . Last, hydrophobic salt ions, more effective at displacing polymer/polymer ion pairs ( $K'$  larger), will give thicker films, but will cause decomposition of the PEMU sooner. The former effect has been observed experimentally [45].

Finally, a glossary of terms used in this chapter relating to charge balance in PEMUs is given below:

*Charge penetration length.* Characteristic length scale over which excess polymer surface charge is distributed.

*Hydrophobicity index.* The relative water content of a multilayer under defined conditions.

*Intrinsic or extrinsic compensation.* The absence or presence of salt ions participating in balancing charge of bulk polyelectrolyte segments.

*Ion breathing.* Ingress and expulsion of salt ions as multilayer is cycled between salt-containing and salt-free solutions.

*Ion doping.* Creation of extrinsic charge carrier sites within a PEMU by external salt concentration.

*Ion filtering.* Selective transport of ions through a PEMU membrane.

*Ion-assisted decomposition.* The dissociation of a PEMU when the salt concentration is sufficiently high.

*Ion lubrication.* The acceleration of extremely slow interdiffusion of polyelectrolytes in a polyelectrolyte complex by the presence of salt ions, which reduce the number of polymer/polymer ion pairs.

*Ion swelling.* Transformation of an intrinsic to an extrinsic system by the chemical potential of external salt.

*Ion trapping.* The selective, based on charge, transport of ions through a PEMU membrane leading to kinetic trapping of higher-charged species.

*Ion self-trapping.* The autoretardation of ion diffusion through a PEMU as the total ionic content of the film decreases.

*Polymer charge extrusion.* The extrusion to the surface of a polyelectrolyte complex of excess polymer charge.

*Reluctant exchanger.* An intrinsically compensated system, having well matched immobile charged polymer segments, capable of being transformed to an extrinsic system under the influence of small, exchangeable ions in the external solution.

*Unconstrained overcompensation.* Overcompensation of one polyelectrolyte by another in the presence of an excess of one polymer with no excluded volume constraints.

#### 4.6

#### References

- 1 G. DECHER, J. SCHMITT, *Prog. Colloid Polym. Sci.* **1992**, *89*, 160–164.
- 2 G. DECHER in *Comprehensive Supramolecular Chemistry*, J.P. SAUVAGE, M.W. HOSSEINI, Eds. Pergamon Press, Oxford, **1996**, Vol 9, Ch. 14.
- 3 P. BERTRAND, A. JONAS, A. LASCHEWSKY, R. LEGRAS, *Macromol. Rapid. Commun.* **2000**, *21*, 319–348.
- 4 Y. LVOV in *Protein Architecture. Interfacing Molecular Assemblies and Immobilization Biotechnology*, Y. LVOV, H. MÖHWALD, Eds. Marcel Dekker, New York, **2000**.
- 5 M. ONDA, Y. LVOV, K. ARIGA, T. KUNITAKE, *Biotech. Bioeng.* **1996**, *51*, 161–167.
- 6 Y.M. LVOV, Z. LU, J.B. SCHENKMAN, J.F. RUSLING, *J. Am. Chem. Soc.* **1998**, *120*, 4073–4080.
- 7 S. WATANABE, S.L. REGAN, *J. Am. Chem. Soc.* **1994**, *116*, 8855–8856.
- 8 D.L. FELDHEIM, K.C. GRABAR, M.J. NATAN, T.C. MALLOUK, *J. Am. Chem. Soc.* **1996**, *118*, 7640–7641.
- 9 Y. LVOV, K. ARIGA, M. ONDA, I. ICHINOSE, T. KUNITAKE, *Langmuir* **1997**, *13*, 6195–6203.
- 10 K. ARIGA, Y. LVOV, M. ONDA, I. ICHINOSE, T. KUNITAKE, *Chem. Lett.*, **1997**, 125–126.
- 11 E.R. KLEINFELD, G.S. FERGUSON, *Science* **1994**, *265*, 370–373.
- 12 YU. LVOV, K. ARIGA, I. ICHINOSE, T. KUNITAKE, *Langmuir*, **1996**, *12*, 3038–3044.
- 13 R.K. ILER, *J. Colloid Interfac. Sci.* **1966**, *21*, 569–594.
- 14 N.A. KOTOV, I. DEKANY, J.H. FENDLER, *J. Phys. Chem.* **1995**, *99*, 13065–13069.
- 15 J. SCHMITT, T. GRÜNEWALD, G. DECHER, P.S. PERSHAN, K. KJAER, M. LÖSCHE, *Macromolecules* **1993**, *26*, 7058–7063.
- 16 M. LÖSCHE, J. SCHMITT, G. DECHER, W.G. BOUWMAN, K. KJAER, *Macromolecules* **1998**, *31*, 8893–8906.
- 17 G. DECHER, *Science* **1997**, *277*, 1232–1237.
- 18 D. LAURENT, J.B. SCHLENOFF, *Langmuir* **1997**, *13*, 1552–1557.
- 19 G. DECHER, Y. LVOV, J. SCHMITT, *Thin Solid Films* **1994**, *244*, 772–777.
- 20 H. DAUTZENBERG, W. JAEGER, J. KÖTZ, B. PHILIPP, C.H. SEIDEL, D. STSCHERBINA, *Polyelectrolytes: Formation, Characterization and Application*, Hanser, Munich, **1994**.
- 21 T. FARHAT, G. YASSIN, S.T. DUBAS, J.B. SCHLENOFF, *Langmuir* **1999**, *15*, 6621–6623.
- 22 A.S. MICHAELS, G. MIEKKA, *J. Phys. Chem.* **1961**, *65*, 1765–1773.
- 23 H.J. BIXLER, A. MICHAELS, in *Encyclopedia of Polymer Science and Technology*, Interscience, New York, **1969**, Vol.10, p. 765.
- 24 A.S. MICHAELS, *Ind. Eng. Chem.*, **1965**, *57*, 32–40.
- 25 H.T. OYAMA, C.W. FRANK, *J. Polym. Sci. B, Polym. Phys.* **1985**, *24*, 1813–1821.
- 26 A.S. MICHAELS, G.L. FALKENSTEIN, N.S. SCHNEIDER, *J. Phys. Chem.* **1965**, *69*, 1456–1465.

- 27 G. DECHER, J.D. HONG, J. SCHMITT, *Thin Solid Films* **1992**, 210–211, 831–839.
- 28 D. YOO, S.S. SHIRATORI, M.F. RUBNER, *Macromolecules* **1998**, 31, 4309–4318.
- 29 M. MÜLLER, T. RIESER, K. LUNKWITZ, J. MEIER-HAACK, *Macromol. Rapid Commun.* **1997**, 20, 607–611.
- 30 T.W. GRAUL, J.B. SCHLENOFF, *Anal. Chem.* **1999**, 71, 4007–4013.
- 31 S.L.R. BARKER, M.J. TARLOV, H. CANAVAN, J.J. HICKMAN, L.E. LOCASCIO, *Anal. Chem.* **2000**, 72, 4899–4903.
- 32 M. ECKLE, G. DECHER, *Nano Lett.* **2001**, 1, 45–49.
- 33 A. MAMEDOV, J. OSTRANDER, F. ALIEV, N.A. KOTOV, *Langmuir* **2000**, 16, 3941–3949.
- 34 X. ARYS, A. LASCHEWSKY, A.M. JONAS, *Macromolecules* **2001**, 34, 3318–3330.
- 35 S.T. DUBAS, T. FARHAT, J.B. SCHLENOFF, *J. Am. Chem. Soc.* **2001**, 123, 5368–5369.
- 36 A. LASCHEWSKY, B. MAYER, E. WISCHERHOFF, X. ARYS, P. BERTRAND, A. DELCORTE, A. JONAS, *Thin Solid Films* **1996**, 284, 334–337.
- 37 M.J. ROBERTS, G.A. LINDSAY, W.N. HERMAN, K.J. WYNNE, *J. Am. Chem. Soc.* **1998**, 120, 11202–11203.
- 38 J.R. HEFLIN, C. FIGURA, D. MARCIU, Y. LIU, R.O. CLAUS, *Appl. Phys. Lett.* **1999**, 74, 495–497.
- 39 T. RADEVA, *Physical Chemistry of Polyelectrolytes*, Marcel Dekker, New York, **2001**.
- 40 E. TSUCHIDA, Y. OSADA, *Makromol. Chem.* **1974**, 175, 593–601.
- 41 Y. MARCUS in *Liquid-Liquid Interfaces. Theory and Methods*, A.G. VOLKOV, D.W. DEAMER, Eds. CRC Press, Boca Raton, FL, **1996**.
- 42 G.S. MANNING, *J. Chem. Phys.* **1969**, 51, 924–933.
- 43 J.B. SCHLENOFF, M. LI, *Ber. Bunsen-Ges. Phys. Chem.* **1996**, 100, 943–948.
- 44 Although alternative interactions between macromolecules, such as hydrogen bonding, charge transfer and stereocomplexation have been identified for multilayer buildup, charge is the predominantly-employed mechanism.
- 45 S.T. DUBAS, J.B. SCHLENOFF, *Macromolecules* **1999**, 32, 8153–8160.
- 46 K. ARIGA, Y. LVOV, T. KUNITAKE, *J. Am. Chem. Soc.* **1997**, 119, 2224–2231.
- 47 J. KIM, H. WANG, J. KUMAR, S.K. TRIPATHY, K.G. CHITTIBABU, M.J. CAZECA, W. KIM, *Chem. Mater.* **1999**, 11, 2250–2256.
- 48 C. TEDESCHI, F. CARUSO, H. MÖHWALD, S. KIRSTEIN *J. Am. Chem. Soc.* **2000**, 122, 5841–5848.
- 49 S.S. SHIRATORI, M.F. RUBNER, *Macromolecules* **2000**, 33, 4213–4219.
- 50 J.B. SCHLENOFF, H. LY, H. LI, *J. Am. Chem. Soc.* **1998**, 120, 7626–7634.
- 51 F. HELFFERICH, *Ion Exchange*, McGraw-Hill, New York, **1962**.
- 52 T. FARHAT, J.B. SCHLENOFF, *Langmuir* **2001**, 17, 1184–1192.
- 53 S.T. DUBAS, J.B. SCHLENOFF, *Macromolecules* **2001**, 34, 3736–3740.
- 54 N.A. KOTOV, *Nanostr. Mater.* **1999**, 12, 789–796.
- 55 Electrostatic arguments also lead to the conclusion that salt modifies interactions by a screening mechanism usually having a nonlinear response to salt concentration.
- 56 G.B. SUKHORUKOV, J. SCHMITT, G. DECHER, *Ber. Bunsen-Ges. Phys. Chem.* **1996**, 100, 948–953.
- 57 J. RUTHS, F. ESSLER, G. DECHER, H. RIEGLER, *Langmuir* **2000**, 16, 8871–8878.
- 58 S.T. DUBAS, J.B. SCHLENOFF, *Langmuir*, in press.
- 59 E. PEFFERKORN, A.C. JEAN-CHRONBERG, R. VAROQUI, *Macromolecules* **1990**, 23, 1735–1741.
- 60 N. KARIBYANTS, H. DAUTZENBERG, *Langmuir* **1998**, 14, 4427–4434.
- 61 H. DAUTZENBERG, *Macromolecules* **1997**, 30, 7810–7815.
- 62 J.B. Schlenoff in *Colloid-Polymer Interactions*, P.DUBIN, R. FARINATO, Eds., Wiley, New York, **1999**.
- 63 J. CRANK, *The Mathematics of Diffusion*, Clarendon Press, Oxford, **1975**.
- 64 MICHAELS [23, 24] discusses a salt-induced rubber transition. Although the dependence of multilayer smoothing on salt is nonlinear it does not appear to be a distinct glass → rubber phase transition.
- 65 A.B. ZEZIN, V.B. ROGACHEVA, V.A. KABANOV, *Macromol. Symp.* **1997**, 126, 123–141.
- 66 J.B. SCHLENOFF, M. LI, *PMSE Prepr. ACS* **1995**, 72, 269–270.
- 67 Such a decomposition is presumed during the dissolution of PECs in specialized ternary solvents developed for this



- purpose (see [23, 24]). These solvents have both concentrated salt and an organic solvent mixed with water to coax the polyelectrolytes apart.
- 68 N.G. HOOGEVEEN, M.A. COHEN STUART, G.J. FLEER, M.R. BÖHMER, *Langmuir* **1996**, *12*, 3675–3681.
  - 69 R. WANG, J.B. SCHLENOFF, *Macromolecules* **1998**, *31*, 494–500.
  - 70 T. GRAUL, J.B. SCHLENOFF, *J. Phys. Chem. B* **1999**, *103*, 2718–2723.
  - 71 F. CARUSO, E. DONATH, H. MÖHWALD, *J. Phys. Chem. B*, **1998**, *102*, 2011–2016.
  - 72 M. LI, J.B. SCHLENOFF, *Anal. Chem.* **1994**, *66*, 824–829.
  - 73 M.F. DURSTOCK, M.F. RUBNER, *Langmuir*, in press.
  - 74 D. KORNEEV, Y. LVOV, G. DECHER, J. SCHMITT, S. YARADAIKIN, *Physica B* **1995**, *213*, 214, 954–956.
  - 75 J. STEPP, J.B. SCHLENOFF, *J. Electrochem. Soc.* **1997**, *144*, L155–L157.
  - 76 J.B. SCHLENOFF, D. LAURENT, H. LY, J. STEPP, *Adv. Mater.* **1998**, *10*, 347–349.
  - 77 J.B. SCHLENOFF, D. LAURENT, H. LY, J. STEPP, *Chem. Eng. Technol.* **1998**, *21*, 757–759.
  - 78 J.B. SCHLENOFF, S.T. DUBAS, *Macromolecules* **2001**, *34*, 592–598.
  - 79 Also, from electrostatics, apparent surface charge density tends towards a constant limiting value at high surface charge.
  - 80 Z. SUI, J.B. SCHLENOFF, *ACS Proc. PMSE* **2001**, *84*, 672–673.
  - 81 P. STROEVE, V. VASQUEZ, M.A.N. COELHO, J.F. RABOLT, *Thin Solid Films* **1996**, *284*, 708–712.
  - 82 J. LEVASALMI, T.J. MCCARTHY, *Macromolecules* **1997**, *30*, 1752–1757.
  - 83 J.J. HARRIS, M.L. BRUENING, *Langmuir* **2000**, *16*, 2006–2013.
  - 84 L. KRASEMANN, B. TIEKE, *Langmuir* **2000**, *16*, 287–290.
  - 85 J.J. HARRIS, P.M. DEROSE, M.L. BRUENING, *J. Am. Chem. Soc.* **1999**, *121*, 1978–1979.
  - 86 J.J. HARRIS, J.L. STAIR, M.L. BRUENING, *Chem. Mater.* **2000**, *12*, 1941–1946.
  - 87 L. KRASEMANN, B. TIEKE, *J. Membr. Sci.* **1998**, *150*, 23–30.
  - 88 F. VAN ACKERN, L. KRASEMANN, B. TIEKE, *Thin Solid Films* **1998**, 327–329, 762–766.
  - 89 L. KRASEMANN, B. TIEKE, *Chem. Eng. Technol.* **2000**, *23*, 211–213.
  - 90 Y. LIU, M. ZHAO, D.E. BERGBREITER, R.M. CROOKS, *J. Am. Chem. Soc.* **1997**, *119*, 8720–8721.
  - 91 A.J. BARD, L.R. FALKNER, *Electrochemical Methods*, Wiley, New York, 1980, Ch. 8.
  - 92 D.A. GOUGH, J.K. LEYPOLDT, *Anal. Chem.* **1979**, *51*, 439–444.
  - 93 T. IKEDA, R. SCHMEHL, P. DENISEVICH, K. WILLMAN, R.W. MURRAY, *J. Am. Chem. Soc.* **1982**, *104*, 2683–2691.
  - 94 See Ch. 8 in [51].
  - 95 H.Z. FRIEDLANDER, *Encycl. Pol. Sci. Technol.* **1968**, *8*, 620–638. Eds. H.F. MARK, N.G. GAYLORD, N.M. BIKALES, Interscience, New York
  - 96 M.J. HATCH, J.A. DILLON, H.B. SMITH, *Ind. Eng. Chem.* **1957**, *49*, 1812–1819.
  - 97 L.E. BROMBERG, *J. Membr. Sci.* **1991**, *62*, 131–143.
  - 98 M. URAIRI, T. TSURU, S. NAKAO, S. KIMURA, *J. Membr. Sci.* **1992**, *70*, 153–162.
  - 99 If it were simply a matter of electrostatic repulsion by like-charged surface, and screening thereof by added salt, the current should not show a dependence on film thickness.
  - 100 T.R. FARHAT, J.B. SCHLENOFF, to be published.
  - 101 J.C.W. CHIEN, *Polyacetylene. Chemistry, Physics, and Materials Science*, Academic Press, Orlando, 1984.
  - 102 *Handbook of Conducting Polymers*. T.A. SKOTHEIM, Ed., Marcel Dekker, New York, 1986.
  - 103 E. DONATH, G.B. SUKHORUKOV, F. CARUSO, S.A. DAVIS, H. MÖHWALD, *Angew. Chem. Int. Ed. Engl.* **1998**, *37*, 2202–2205.
  - 104 F. CARUSO, H. LICHTENFELD, M. GIERSIG, H. MÖHWALD, *J. Am. Chem. Soc.* **1998**, *120*, 8523–8534.
  - 105 F. CARUSO, R.A. CARUSO, H. MÖHWALD, *Science* **1998**, *282*, 1111–1114.
  - 106 FARHAT and SCHLENOFF, *Electrochem. and Solid State Lett.* **2002**, *5*, B13–B15.
  - 107 Polymer with charge-variable backbone, weak acid, thermal or photoelimination, can enhance transport considerably, especially for weakly-swelling complexes made, for example, from hydrophobic constituents.
  - 108 H. DAUTZENBERG, Ch. 20 in [39].

## 5

# pH-Controlled Fabrication of Polyelectrolyte Multilayers: Assembly and Applications

M. F. RUBNER

### Abstract

The pH-controlled layer-by-layer assembly of weak polyelectrolytes provides enormous flexibility in controlling both the molecular organization and properties of polyelectrolyte multilayer thin films. With suitable adjustments of the pH of the dipping solutions, it is possible to manipulate dramatically the molecular organization, composition, surface properties and chemistry of the multilayer assemblies created by this process. This new type of molecular-level blending process has been used to create multilayer films that can be used as nanoreactors for nanoparticle synthesis, as templates for the selective electroless deposition of metals and as microporous films of low dielectric constant, to name a few. In addition, by controlling the composition of the basic bilayer building blocks of these films and their surface composition, it is possible to create light emitting thin film devices based on conjugated polymers with significantly improved performance. The development of new patterning schemes for weak polyelectrolyte multilayers further expands their utility in electronic and biomaterial applications.

### 5.1

#### Introduction

Control over surface and interface properties is critically important in many existing and emerging technologies, particularly those that are based on electroactive organic and polymeric materials and bioactive or bioresponsive materials. Inevitably, one would like to design and engineer surfaces and interfaces at the molecular level, where oftentimes subtle changes in organization and composition can result in dramatic performance enhancement. The wettability of a polymer film, for example, is determined, in many cases, by only the first 5–10 Å of its outermost surface. The ability to manipulate surface composition and surface chemistry at such length scales is clearly highly desirable. The layer-by-layer processing of polyelectrolytes into multilayer thin films is ideally suited for this task. By controlling simple processing parameters such as solution pH and ionic strength, it is possible to assemble molecular-scale layers of oppositely charged polymers onto a vari-

ety of surfaces [1–3]. Since there is extensive interpenetration of the layers [1, 4], this can be viewed as a molecular-level blending process carried out one layer at a time. As will be discussed in this chapter, the pH-controlled assembly of weak polyelectrolytes provides an amazingly rich environment for creating polyelectrolyte multilayer thin films. Even in the simplest case, i.e., the multilayer assembly of only two weak polyelectrolytes (a single bilayer building block of a polycation and polyanion), there exists the potential to manipulate dramatically the resultant bulk and surface properties by simply controlling the manner in which these two polymers are blended together.

Weak polyelectrolytes are ionic polymers with linear charge densities that are tunable by simple pH adjustments: typically in the pH range of 2–10. When both the polycation and polyanion are weak polyelectrolytes, the pH of a dipping solution can be used to control the charge density of an adsorbing polymer, of a previously adsorbed polymer (i.e., the surface charge density) or both [5, 6]. This provides great flexibility over the multilayer assembly process and hence the manner in which this novel type of molecular-level blending process is carried out. The net result is the ability to control in a predictable manner the thickness, ionic crosslink density and conformation (flat versus loopy chain arrangement) of each adsorbed layer. From a blending perspective, this means that both the internal and surface composition (relative amount of polycation and polyanion) of a multilayer thin film can be selectively tuned to achieve specific properties. In addition, since pH determines the fraction of functional groups that will be ionized during the assembly process, it is possible to control the density of non-ionic, reactive functional groups, such as acid or amine groups, that are available for subsequent internal or surface chemistry. Finally, since the multilayer thin film is comprised of pH sensitive polymers, it is also possible to induce both reversible and irreversible morphological changes after the assembly process is complete. Specific examples of what can be accomplished with weak polyelectrolyte multilayer assembly are provided below. In all cases to be discussed, no salt ions were added to the dipping or rinsing solutions beyond what is required to adjust pH.

## 5.2

### Layer-by-Layer Assembly of Weak Polyelectrolyte Multilayers

Fig. 5.1 shows the two weak polyelectrolytes that we have most extensively studied. Both of these polymers are essentially fully charged at neutral pH. As solution pH is lowered from neutral, the charge density of poly(acrylic acid) (PAA) decreases as its acid groups become protonated, whereas when pH is increased, the charge density of poly(allylamine hydrochloride) (PAH) decreases as its ammonium groups become deprotonated. The solution  $pK_a$ s of PAA and PAH are about 5.0 and 9.0 respectively. It should be noted however, that the actual  $pK_a$  of a weak polyelectrolyte is very sensitive to its local ionic environment and may shift significantly from the solution value. Such shifts have clearly been observed when weak polyelectrolytes and other pH sensitive molecules are incorporated into multilayer films [5–9].

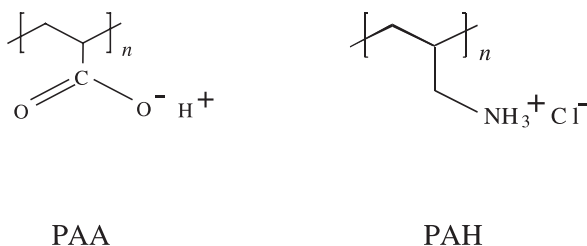


Fig. 5.1 Repeat unit structures of PAA and PAH.

Fig. 5.2 shows how the average incremental layer thickness (measured in the dry state after the deposition of each layer) of an adsorbed PAA and PAH layer can vary when solution pH is varied [6]. In this case, both the PAA and PAH dipping solutions were at the same indicated pH values. At neutral pH, these polymers assemble into a highly ionically crosslinked multilayer comprised of molecularly thin, well-interpenetrated layers in which the polymer chains adopt flattened conformations. As expected for polymer chains adopting a flat conformation, the thickness of an adsorbed layer in this case, about 3–5 Å, is independent of polymer molecular weight over a range of at least 3000–10<sup>6</sup> g mol<sup>-1</sup> [6]. If the pH of the dipping solutions used to fabricate a multilayer film is either increased or decreased, dramatic increases in the layer thickness of both PAA and PAH are observed. For example, with both dipping solutions set at pH 5.0, the thickness contributed by a PAH and PAA layer is 80 and 45 Å respectively. To achieve such thicknesses, the polymer chains must adopt a conformation dominated by loops and tails. Consistent with the formation of a more “loopy” conformation is the fact that the thickness of an adsorbed layer now is found to depend on molecular weight and scales approximately as  $T \propto M^{0.3}$  [6]. The dramatic increase in thickness that is observed over a very narrow pH range when the pH is increased or

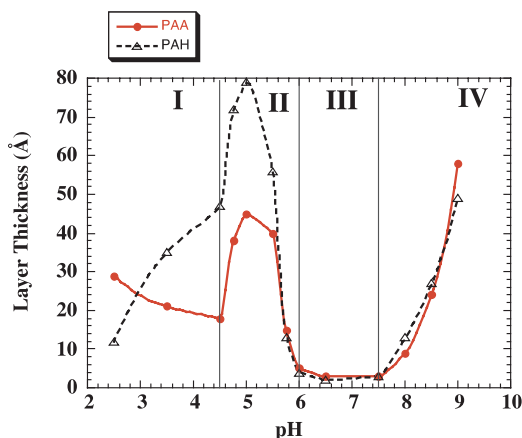


Fig. 5.2 Average incremental thickness contributed by a PAA and PAH adsorbed layer as a function of solution pH. Both the PAA and PAH dipping solutions were at the same indicated pH. The solid line represents the PAA layer thickness and the dashed line is the PAH thickness. Reproduced from [6] by permission of the American Chemical Society.

decreased from neutral, occurs when the surface charge density experienced by an adsorbing, fully charged polyelectrolyte drops below the critical value needed to overcome chain coiling entropy effects. A theoretical model that explains the origin of this interesting pH dependent change from very thin adsorbed layers to unusually thick layers has been developed by Mayes and coworkers [10].

It is clear from Fig. 5.2 that the relative amount of PAA and PAH “blended” into a multilayer film can be varied over a wide range by suitable pH adjustment. A more complete pH matrix showing how the layer thickness of PAA and PAH varies when the pH of the dipping solutions is varied over the range of pH from 2.5 to 9.0 has been published [6]. It should be pointed out that these studies have revealed that surface roughness can also influence the thickness of an adsorbed layer, with thicker layers being formed on multilayers of high roughness. This effect reflects the fact that “conformationally” rough surfaces, such as those produced from layers adsorbed with a high segmental population of loops and tails, promote the deposition of larger amounts of an adsorbing polymer. This becomes particularly important when one is building more complex multilayer heterostructures as it cannot be assumed that the layer thickness determined from studies of a single bilayer system will be the same when the layers are assembled onto a different bilayer system [6, 11].

A useful consequence of the pH-controlled assembly of weak polyelectrolytes is the ability to manipulate both internal and surface composition. In other words, it is possible to control the amount of PAA and PAH utilized to construct the multilayer film as well as the segmental population of these two polymers at the surface of the multilayer film. One obvious way to accomplish this is to simply construct the multilayer film with either an odd or even number of layers. In this case, the surface properties will, in principle, be dominated by segments of the outermost layer polymer. We and others [5, 12, 13] have shown that this is generally a good way to control surface wettability. More often than not, however, the polycation and polyanion chains are highly interpenetrated thereby producing a surface that is a mixture of both polymers. Thus, even though it is now well established that the surface charge reverses with the addition of each new polymer layer [14], it is not always safe to assume that the surface is comprised only of segments of the outermost polymer layer. With weak polyelectrolytes, it is possible to adsorb a polymer chain at a low charge density and subsequently increase the surface charge density by adsorbing the next layer at a pH that ionizes the remaining segments of the previously adsorbed layer. As will be discussed shortly, this strategy makes it possible to create surfaces that are clearly dominated by segments of the outermost layer even though the internal layers may be completely interpenetrated.

Fig. 5.3 highlights the key structural features of three different PAA/PAH bilayer systems that exhibit particularly interesting properties. When the PAA and PAH layers are assembled with both dipping solutions maintained at a low pH, for example PAA/PAH 2.5/2.5, the degree of ionization of the PAA chains is kept low during each polymer adsorption step. The PAH chains, on the other hand, are fully ionized at this low pH. This results in a non-stoichiometric pairing of repeat units and a bilayer composition that is rich in PAA chains (ca. 70% PAA,

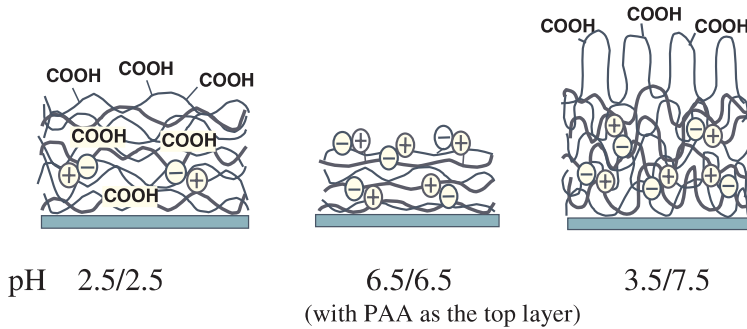


**Fig. 5.3** Schematic representation of the molecular organization of PAA/PAH multilayer films assembled with the dipping solutions at different pH levels.

30% PAH) with a low degree of ionization (ca. 30–40%) [5]. The net result is a readily swellable multilayer film with a relatively low ionic crosslink density and a high concentration of reactive acid groups, both within the multilayer and at its surface (regardless of whether PAA or PAH is the outermost layer). When PAA/PAH layers are assembled at neutral pH (6.5/6.5), where both polymers are in their essentially completely ionized forms, a more highly ionically crosslinked multilayer film [15] is created with near equal amounts of PAA and PAH found within the multilayer and at its surface. In this case, most of the PAA and PAH ionized segments are ion-paired and therefore not available for subsequent chemistry. In the third example of Fig. 5.3, the PAA/PAH chains are assembled at a pH of 3.5 and 7.5 for the PAA and PAH dipping solutions respectively. In this case, the PAA chains adsorb at a low pH with a low degree of ionization onto fully charged chains of PAH. This produces a loopy conformational arrangement and a PAA surface layer with a high density of free acid groups. During the adsorption of the PAH chains, however, the pH is increased and the remaining acid groups of PAA become fully ionized. The PAH chains penetrate into the PAA surface layer and neutralize this extra charge, thereby creating an internal bilayer organization that is mostly ion-paired, but a surface that is enriched in PAH segments. Thus, when PAA is the outermost layer, the surface contains a significant fraction of free acid groups, whereas there are essentially no free acid groups on the surface when PAH is the outermost layer. Specific examples of how the pH-controlled assembly of weak polyelectrolytes like PAA and PAH can be utilized to create multilayers with a wide range of useful properties are provided below.

### 5.3 Light Emitting Thin Film Devices

The layer-by-layer processing technique is ideal for the fabrication of thin film devices based on electronically active polymeric materials [16–35]. Using this approach, it is possible to coat large areas with films of uniform thickness, low

surface roughness and very low pin-hole densities [18]. In addition, complex multilayer heterostructures including compositionally graded heterostructures are easily realized [19, 22, 28]. Perhaps most importantly, it also provides one of the few effective ways available to modify electrode surfaces and interfaces with uniform, ultra-thin polymer films of specified functionality.

As indicated above, the pH-controlled deposition of weak polyelectrolytes can be used to blend two oppositely charged polyelectrolytes together with molecular-level control over composition and surface functionality. We have used this approach to fabricate multilayer thin film devices comprised of PAA (or poly(methacrylic acid) PMA) as the pH tunable polyanion and a light emitting polymer (or precursor polymer) as the polycation. Green light emitting devices were fabricated from the cationic precursor polymer to poly(*p*-phenylene vinylene) (PPV) [18, 19] whereas red-light emitting devices were fabricated with a water soluble polycation containing the light emitting Ru(II) complex [22]. In both cases, it was found that dramatic enhancements in device performance could be realized by varying the composition of the multilayer film and its surface properties. For example, with the Ru(II) complex polycation, external quantum efficiencies could be varied from 0.006 to 3% by simply changing the pH of the dipping solutions. The highest device efficiencies were realized with low pH assembly (both dipping solutions at pH 3.5). The resultant multilayer in this case is comprised of light emitting Ru(II) complexes dispersed in a matrix rich in PAA chains, thereby enhancing device efficiency by reducing Ru(II) complex self-quenching effects. It should be noted that spin cast films of the Ru(II) complex polycation exhibited device efficiencies of about 0.2%. Thus, the use of a multilayer assembly process increased the device efficiency possible with this material by more than an order of magnitude. In addition, devices that emitted light only in the forward bias, only in the reverse bias, or in both forward and reverse bias were fabricated by constructing compositionally graded multilayers or by adding thin PAA/PAH insulating bilayers to the electrode interfaces [22].

In the PPV case, pH-controlled assembly also produced devices with significantly enhanced efficiency as well as increased luminance levels. For example, the external quantum efficiency of a 3.5/4.5 PAA/precursor-PPV multilayer device, after thermal conversion to create light emitting PPV, increased by about an order of magnitude relative to what is typically found for spin-coated PPV devices with ITO and aluminum electrodes [34]. Luminance levels as high as  $1000 \text{ cd m}^{-2}$  were also achieved with the multilayer film. Such brightness levels and high efficiencies from a PPV single component device with an aluminum top electrode are very unusual. In the early stages of this work, we also demonstrated that device performance could be dramatically improved by placing ultra-thin electrically conductive PPV bilayers at the ITO electrode interface or by adding insulating PMA/PAH bilayers to the aluminum electrode interface [18, 19, 35]. In the former case, it was found that bilayers assembled from sulfonated-polystyrene (SPS) and PPV could be used to facilitate hole injection in a PMA/PPV multilayer device [19]. Amazingly, the assembly of SPS/PPV multilayers onto the ITO electrode with a total thickness of only 16–80 Å resulted in nearly an order of magnitude increase in

light output and a four-fold increase in device efficiency. It has also been demonstrated that the placement of layer-by-layer assembled thin films of electrically conductive polymers like polyaniline [16] onto an ITO electrode can be used to enhance hole injection in devices based on spin-coated films of PPV and its derivatives [26, 27]. In a powerful demonstration of the unique capabilities of the layer-by-layer processing scheme, Ho and coworkers have fabricated “graded” electrically conductive multilayers to facilitate hole injection at the ITO interface of MEH-PPV devices [28].

## 5.4

### Microporous Thin Films

Polyelectrolyte multilayers fabricated from weak polyelectrolytes exhibit the unique feature that, once assembled, the films may undergo pH-driven morphological reorganizations. For example, we have found that multilayers of PAA/PAH assembled with the PAA solution at pH 3.5 and the PAH solution at pH 7.5 (PAA/PAH 3.5/7.5) will undergo a pH-driven spinodal decomposition to produce microporous thin films [7]. As suggested in Fig. 5.3, this multilayer system is assembled in such a manner that the internal structure is comprised of a complex array of essentially fully charged, loopy chains randomly stitched together. The more cooperatively stitched structure of the PAA/PAH 6.5/6.5 multilayers (Fig. 5.3) represents a more energetically favorable arrangement of fully charged chains in a polyelectrolyte complex. Hence, if a suitable pathway is provided, the polymer chains of the 3.5/7.5 multilayer system will reorganize into this more coordinated ionic-paired conformation. This can be accomplished by simply exposing a 3.5/7.5 PAA/PAH multilayer to acidic water of pH  $\sim 2.4$ , for a brief period of time (as short as 15 s) followed by rinsing with neutral water or blow drying with air. With this treatment, the multilayer film undergoes a dramatic increase in thickness as it phase separates into a microporous structure.

The reason for this transformation of a dense multilayer film to a microporous multilayer film is as follows. The low pH treatment protonates many of the carboxylate ions within the multilayer film, thus breaking numerous electrostatic cross-links and temporarily freeing the structure. A microporous morphology develops rapidly as the now much more mobile chains can reorganize and re-pair in more favorable stitching arrangements. FTIR spectroscopy confirms that the carboxylic acid groups of PAA in the initial non-porous film are nearly 90% charged, but only about half remain charged after exposure to acidic water. Rinsing with neutral water returns the number of ionized carboxylate groups to  $\sim 80\%$ .

The level and type of microporosity that develops depends on parameters such as the pH of the acidic water, temperature and exposure times to the treatment baths (acidic solution and rinsing solution). Fig. 5.4a shows an atomic force microscopy (AFM) image of the original, non-porous 3.5/7.5 PAA/PAH multilayer. A typical 21 layer film in the dry state is  $\sim 1000$  Å thick and possesses a fairly rough surface (RMS roughness  $\sim 50$  Å) with a unique surface texture. Fig. 5.4 b



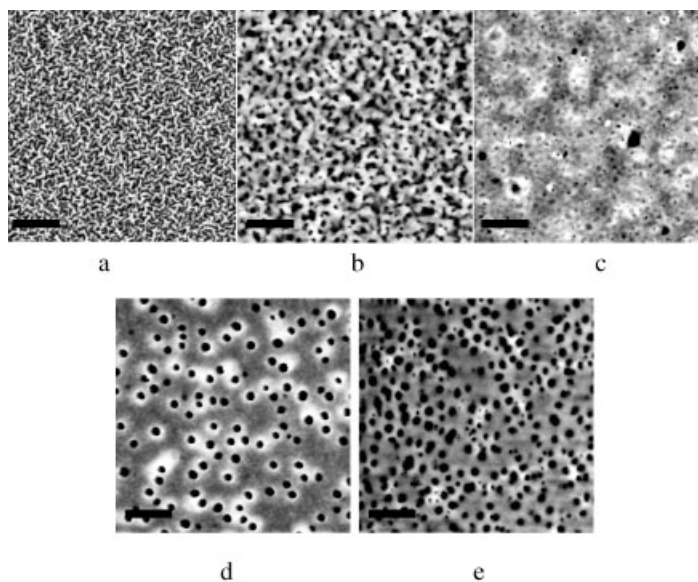


**Fig. 5.4** AFM images of (a) a typical non-porous 3.5/7.5 PAA/PAH multilayer, (b) a 3.5/7.5 film after a 1 min exposure to pH  $\sim$ 2.4 water at 20°C without any subsequent neutral water rinsing, (c) the same as (b) but with a subsequent 15 s neutral water rinse, (d) the same as (b) but processed in pH  $\sim$ 2.4 water at 50°C, (e) the same as (b) but followed by an extended exposure for 10 h at 20°C in neutral water. Scale bar = 1  $\mu$ m.

presents a similar film after being immersed in pH  $\sim$ 2.4 water for 1 min at room temperature without subsequent rinsing with neutral water. The acid-immersed film exhibits a highly-interconnected, percolating microporous network that is much rougher (RMS roughness  $\sim$  300 Å) and  $\sim$ 1.5 times thicker than the original film. In addition, the refractive index of the treated film (measured in the dry state) decreases from an original value of  $\sim$ 1.55 to a value of  $\sim$ 1.3. If the film is briefly rinsed ( $\sim$ 15 s) with neutral water, as shown in Fig. 5.4c, further changes take place. In this case, a more poorly-defined surface is observed that is much smoother than in the non-rinsed case. This microporous structure exhibits a refractive index of  $\sim$ 1.2 and a thickness  $\sim$ 2.5 times greater than the original 3.5/7.5 film. If the temperature of the acidic treatment bath is increased to 50°C, both rinsed and non-rinsed films develop a discrete, through-pore morphology, as displayed in Fig. 5.4d. In both cases, the film refractive index has dropped from  $\sim$ 1.55 to  $\sim$ 1.2–1.4, the roughness has increased to 250–500 Å, and the thickness has increased  $\sim$ 1.5 times. A similar through-pore morphology as shown in Fig. 5.4e develops if the 3.5/7.5 films are immersed in neutral water for many hours after the initial acidic water treatment. These porous films exhibit thickness and refractive index values approaching that of the original, non-porous films.

The above results suggest that the energetically-favorable structure for the 3.5/7.5 multilayers after transformation is a discrete, through-pore morphology. Non-porous 3.5/7.5 multilayers can reach such a structure via two different paths: 1. rapidly, upon contact with acidic solutions at elevated temperatures (e.g., 40–50 °C) for only a few seconds to minutes, or 2. slowly, by being briefly exposed to the acidic solution and then to neutral water for many hours, all at room temperature.

PAA/PAH combinations assembled under conditions similar to the 3.5/7.5 system also show some tendency to become microporous with acidic water treatment (such as PAA/PAH 4.5/7.5). In sharp contrast, no pH-driven porosity transformations have been observed with PAA/PAH films assembled under conditions that produce more cooperatively stitched chains such as PAA/PAH 6.5/6.5 multilayers. Recently, it has been reported [36] that microporosity can be also be developed in PAA/PAH 5.0/5.0 multilayers assembled with added salt in the dipping and rinsing solutions. In this case, microporosity is introduced by dipping the assembled multilayer film into salt-free neutral water. The PAA/PAH 5.0/5.0 multilayer system is also an example of a molecular organization that is comprised of a complex array of essentially fully charged, loopy chains randomly stitched together [6]. With the proper choice of assembly conditions, it should be possible to induce microporosity in other polyelectrolyte multilayer systems via similar mechanisms and with treatments that cover a wide range of pH and/or ionic strength.

Numerous applications of microporous multilayers are possible, including low dielectric constant and low refractive index thin film coatings, separation filters, biocompatible membranes for controlled release and encapsulation systems and anti-reflection coatings.

## 5.5

### Nanoreactors, Electroless Plating and Ink-jet Printing

In addition to manipulating the physical structure of weak polyelectrolyte multilayers, it is also possible to use pH control to manipulate the chemical functionality of both their surfaces and internal structures. This, in turn, makes it possible to prepare thin film inorganic nanocomposites and templates for selective electroless metal plating. For example, we have used PAA/PAH multilayers to bind, through ion-exchange with the protons of the PAA carboxylic acid groups, metal cations from aqueous solution. The metal cations can be selectively bound to specific regions of the surface of the multilayer or in specific regions within a multilayer. This is accomplished by simply choosing the appropriate assembly conditions, the last adsorbed polyelectrolyte (i.e., PAH or PAA), the duration of metal cation exchange and suitable patterning approaches if necessary. Once the metal cations are selectively bound to the PAA acid groups, they can be used, among other things, to synthesize nanoparticles [11] or to catalyze the deposition of electrolessly deposited metals [37].

In the case of nanoparticle synthesis, this approach can be used to synthesize, *in situ*, a variety of inorganic particles, including noble metals and chalcogenides

[11]. This is in contrast to the direct assembly approach involving the manipulation of preformed nanoparticles into multilayers using the layer-by-layer processing scheme [38–43]. The two approaches are complementary and offer different advantages in the design of nanocomposite thin films. The PAA/PAH multilayers most useful for use in *in situ* nanoparticle synthesis schemes are those assembled at low pH (e.g., less than pH 4.0). Such multilayers, exemplified by the 2.5/2.5 PAA/PAH system shown in Fig. 5.3, contain a high fraction of free carboxylic acid groups that are available for metal cation binding.

Fig. 5.5 shows a multilayer heterostructure comprised of the following bilayers: [(PAH/PAA)<sub>10</sub>(PAH/SPS)<sub>30</sub>(PAH/PAA)<sub>1</sub>(PAH/SPS)<sub>30</sub>(PAH/PAA)<sub>10.5</sub>]. In this case, all of the polyelectrolyte layers were assembled at pH 3.5 onto a polystyrene substrate. The organization of the SPS/PAH bilayers of this heterostructure is similar to the schematic of the 6.5/6.5 PAA/PAH multilayers shown in Fig. 5.3. Since PAH and SPS are fully-charged during adsorption, they completely pair up with each other in the multilayer leaving no functional groups available for binding metal cations. The 3.5/3.5 PAA/PAH bilayers, on the other hand, contain a significant fraction of free acid groups, similar to the 2.5/2.5 PAA/PAH multilayers illustrated in Fig. 5.3. When immersed into a silver acetate aqueous solution, silver cations will only bind to the free carboxylic acid groups of PAA. Subsequent reduction by hydrogen, forms zero-valent silver nanoparticles within the PAA/PAH bilayers, while the SPS/PAH bilayers remain free of nanoparticles. The nanoparticles formed selectively within the PAA/PAH layers are typically small, ~ 2 nm in diameter, and are homogeneously distributed throughout the PAH/PAA bilayer because of extensive interpenetration of the individual layers. Note that even with only a single layer of PAA sandwiched between SPS/PAH bilayers, it is possible to grow a clearly discernible “row” of silver nanoparticles. The spatial confinement of silver nanoparticles within a single PAA layer suggests the possibility of creating nanocomposites with well-defined layered architectures. In addition, once the nanoparticles are formed, the acid groups are available for additional reloading of metal ions to create more complex nanocomposites. A variety of such useful na-

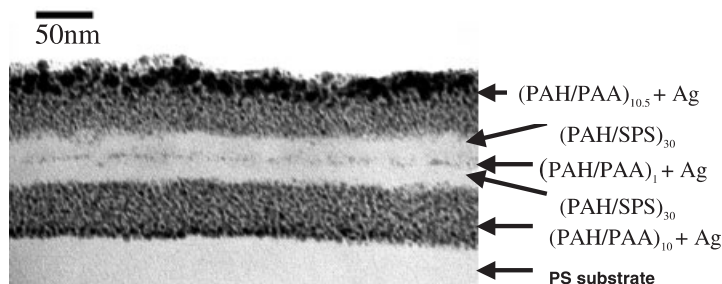


**Fig. 5.5** Cross-section TEM image of a Ag nanoparticle loaded multilayer heterostructure comprised of the following bilayers: [(PAH/PAA)<sub>10</sub>(PAH/SPS)<sub>30</sub>(PAH/PAA)<sub>1</sub>(PAH/SPS)<sub>30</sub>(PAH/PAA)<sub>10.5</sub>]. In this case, all of the polyelectrolyte layers were assembled at pH 3.5 onto a polystyrene substrate.

noreactor schemes has been developed extensively by the Cohen group at MIT [44].

Although the above nanoreactor scheme is useful for creating nanoparticle assemblies within specific regions of a multilayer thin film, the loading level is typically small and percolating nanoparticle systems can only be created via a multiple loading process [45]. In an attempt to create percolating metal-loaded multilayers in one shot, we have been examining selective electroless plating schemes. A similar approach has been utilized to grow metals within microphase separated block copolymers [46]. This work is currently ongoing, however, as discussed below, we have recently found that this is also an ideal way to activate surfaces for electroless metal plating [37].

A particularly useful metal cation to incorporate into PAA/PAH multilayers for this purpose is palladium: a metal ion that is used to promote the electroless deposition of metals like nickel and copper. Selective surface binding to create metal patterns can be accomplished in a number of different ways. Using the 3.5/7.5 PAA/PAH multilayer system, for example, it is possible to create surfaces that are dominated by either PAH or PAA depending on the last adsorbed layer. When PAA is the outermost layer, palladium cations will bind to the free acid groups present at the surface. With PAH as the outermost layer, no binding sites are available. Thus, a patterned surface comprised of PAA outermost layer regions and PAH outermost layer regions will selectively direct the electroless plating process to the PAA regions. A simple way to accomplish this is by first depositing 10 bilayers of 3.5/7.5 PAA/PAH (starting with PAH) on a substrate followed by half-dipping the substrate into the 7.5 PAH solution. This creates a substrate that has a bottom half with PAH as the outermost layer and a top half with PAA as the outermost layer. After immersion into a palladium cation solution followed by a nickel electroless plating bath, a uniform film of electrically conductive nickel metal is found to deposit only onto the top half of the substrate [37]. With short exposure times to the palladium solution, mass transport limits the metal cation binding essentially to the outermost PAA surface layers. The adhesion of the metal to the multilayer/substrate surface is excellent, suggesting that this is a very simple and effective way to prepare any surface for electroless plating.

To produce high-resolution metal patterns on polyelectrolyte multilayers, we have used both ink-jet printing and micro-contact printing techniques. In the former case, with the help of the Yang Yang group of UCLA [47], we have modified a commercial Epson ink-jet printer to print aqueous solutions onto substrates as thick as a typical glass slide [37]. First a 3.5/7.5 PAA/PAH multilayer thin film is deposited onto the substrate with PAH as the last deposited layer. A pattern of PAA is then created on the PAH-topped multilayer by inkjet printing of the PAA solution. After printing the PAA, the entire multilayer is immersed in a tetraaminepalladium(II) chloride aqueous solution where the palladium complex cation binds only to the PAA pattern. In the subsequent immersion into a standard electroless nickel-plating solution, nickel deposition is only catalyzed on the palladium containing-PAA pattern. Fig. 5.6 shows an example of a metal pattern created with this approach. Using an inexpensive, readily available ink-jet printer, we

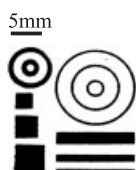


**Fig. 5.6** Selectively nickel plated 3.5/7.5 PAA/PAH multilayer film created by ink-jet printing a pattern of PAA onto a PAH outermost layer film followed by selective palladium complex deposition and a nickel electroless plating process.

are able to create feature sizes as small as  $200\ \mu\text{m}$  (and possibly as small as  $50\ \mu\text{m}$ ). As will be discussed later, micro-contact printing techniques can be used to create patterned multilayers with feature sizes down to at least  $1\ \mu\text{m}$ .

## 5.6

### Surface Modification via Selective Adsorption of Block Copolymers

The ability to use pH to control readily the surface chemistry of weak polyelectrolyte multilayers coupled with their strong adhesion to many different substrates makes them ideally suited for surface modification applications. Functional groups at the surface of a multilayer film can be utilized as physical or chemical binding sites to anchor other molecules and polymers with a specific affinity for these functional groups. After successful anchoring, the polyelectrolyte multilayer surface acquires the specific physical or chemical properties of the newly attached molecules. Amphiphilic block copolymers are ideally suited for this task. In this case, an anchoring block is used to attach the copolymer to the multilayer surface leaving the remaining block available to modify surface properties. It is also possible to selectively adsorb an amphiphilic block copolymer to specific regions of a patterned multilayer surface. Using this approach, surface properties such as wettability, adhesion, surface chemistry and biocompatibility can be easily and dramatically modified.

To explore the basic concept of block copolymer surface modification, we have studied the adsorption of the amphiphilic block copolymer polystyrene-block-poly(acrylic acid) (PS-PAA) from tetrahydrofuran (THF) solutions onto weak polyelectrolyte multilayers of PAH and PAA [48]. Under such conditions, the PAA block anchors onto the multilayer surface primarily by hydrogen-bonding interactions with PAH segments. This in turn means that surfaces that are rich in PAH segments will promote block copolymer adsorption, whereas surfaces rich in PAA segments will resist block copolymer adsorption. For example, when a 3.5/7.5 PAH top layer or 6.5/6.5 PAA or PAH top layer multilayer film is immersed in a THF solution of a PS-PAA block copolymer (PAA block molecular weight;  $4500\ \text{g mol}^{-1}$ , PAH block molecular weight  $66\ 000\ \text{g mol}^{-1}$ ), the advancing and receding water droplet contact angles of the film increase to a value close to that of a polystyrene surface; greater than  $85^\circ$ . The significance of this observation becomes important when it is recognized that all PAA/PAH multilayer films become highly wettable after contact with water, i.e. they exhibit very low receding contact angles of  $10^\circ$  or less. The hydrophobic surfaces created by PS-PAA block

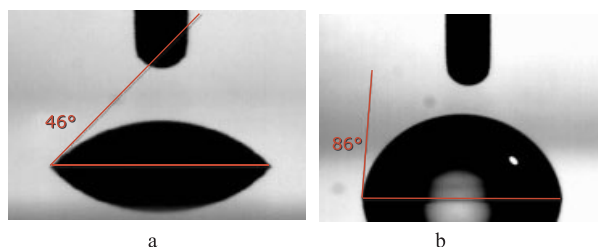


**Fig. 5.7** Images of water droplets on 3.5/7.5 (PAA/PAH)<sub>7.5</sub> multilayer films: (a) as-prepared and (b) after immersing the multilayer film into a PS-PAA block copolymer solution. Numbers represent advancing contact angles, PAH is the outermost layer prior to block copolymer adsorption.

copolymer adsorption are very stable to exhaustive washing with both pure THF and water, indicating that the hydrogen bonded PAA block is well anchored to the surface. Fig. 5.7 shows the dramatic change in hydrophobicity that occurs when a PS-PAA block copolymer is adsorbed onto a 3.5/7.5 multilayer film with PAH as the outermost layer. The advancing contact angle of this multilayer film increases by about  $40^\circ$  as a result of this treatment. The thickness of the adsorbed block copolymer in this case is only in the range of 30–80 Å.

In contrast to PAA/PAH multilayer films assembled to produce surfaces that are rich in PAH segments, the 2.5/2.5 PAA/PAH multilayer system with PAA as the top layer completely resists the adsorption of the PS-PAA block copolymer. After immersion in the PS-PAA block copolymer solution, both the advancing and receding contact angles remain characteristic of a highly wettable surface ( $\theta_{\text{adv}} = 15 \pm 5^\circ$  and  $\theta_{\text{rec}} < 10^\circ$ ). Thus, when a patterned surface comprised of regions rich in PAA segments and regions rich in PAH segments is immersed in the block copolymer solution, the block copolymer will selectively adsorb to the PAH rich regions. This can be accomplished by simply half-coating a PAA outermost layer multilayer film with an additional layer of PAH or by micro-contact printing techniques as described next.

## 5.7

### Patterning of Weak Polyelectrolyte Multilayers

The ability to create patterned polyelectrolyte multilayers is clearly desirable for many of the applications envisioned for these materials. Although, in principle, standard photolithographic-type approaches can be used, there is a growing interest in identifying techniques that are fast, inexpensive and complementary to the very simple fabrication possibilities provided by layer-by-layer, water based processing. Currently, we have explored three different approaches to creating patterned polyelectrolyte multilayers ranging in resolution capability from very low (cm scale) to very high (micron scale). These include partial last layer dip coating, ink-

jet printing and micro-contact printing. As will be discussed later, we are also pursuing photolithographic approaches. The first technique is used just as a very simple way of studying selective surface properties that result from different outermost layer effects. Examples of how this works have already been described. With ink-jet printing, we have developed both additive and subtractive techniques. In the former case, mentioned earlier, the final polyelectrolyte layer to be deposited is ink-jet printed onto a multilayer film to form patterns with feature sizes in the range of 100–200  $\mu\text{m}$ . The second case involves the selective removal of regions of a preformed multilayer film in a manner analogous to the solvent development of a crosslinked photoresist. In this section, we describe briefly the application of micro-contact printing approaches to the patterning of weak polyelectrolyte multilayers as well as the second ink-jet printing process.

### 5.7.1

#### **Micro-Contact Printing**

The techniques needed to create patterned polyelectrolyte multilayers have been developed extensively by the Hammond group of MIT [49]. Using the micro-contact printing process first introduced by the Whitesides group at Harvard [50], Hammond's group has pioneered the development of a variety of extremely useful schemes for fabricating both patterned polyelectrolyte multilayers and multilayers with patterned surfaces. The first approach involves the directed assembly of multilayers onto patterned substrates [49]. The second approach is accomplished by the direct printing of a polymer layer onto a preformed multilayer; a process called polymer-on-polymer printing [51]. Details concerning these techniques and the types of unique structures that can be created with them can be found in Chapter 10 by Hammond. Here we describe a collaborative effort with the Hammond group that is aimed at the patterning of weak polyelectrolyte multilayers via the polymer-on-polymer micro-contact printing approach.

Fig. 5.8 illustrates the basic concept of the polymer-on-polymer stamping process. Specifically, it shows the micro-contact printing of a PAH outermost layer onto a PAA/PAH multilayer film with PAA as the top layer. To start this process, a plasma treated poly(dimethyl siloxane) (PDMS) stamp is inked with the PAH solution. Control over the ink's concentration is critical. The best results are obtained by using a concentration in the range of 5–10 mM (based on the repeat unit). Next, the stamp is dried and then brought into contact with the multilayer surface. Finally, the stamp is removed leaving a pattern of PAH on top of the PAA outermost layer multilayer platform.

The pH of the solution used to ink the stamp is clearly important when dealing with weak polyelectrolytes. The ability to create high quality, large area patterns requires that the polymer ink uniformly coats the stamp and is transferred uniformly onto the surface. It is therefore important to identify a suitable pH to accomplish this task. The best results for PAH stamping are obtained when the inking solution is below the  $\text{p}K_{\text{a}}$  of PAH, with the best patterns being formed at a pH of 6.5. Raising the pH above the  $\text{p}K_{\text{a}}$  of PAH results in a stronger adhesion

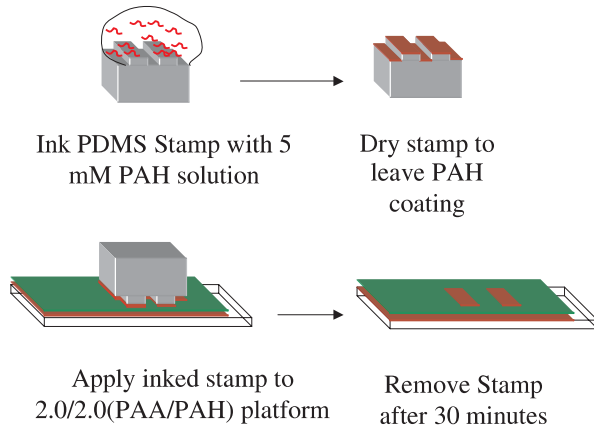


**Fig. 5.8** Process for stamping a PAH layer onto a 2.0/2.0 PAA/PAH multilayer film.

between the polymer and the stamp, often resulting in PDMS residue on the surface. Fig. 5.9 shows a microscope image of a 10 bilayer film of 2.0/2.0 PAA/PAH patterned with a stamp that was inked with a 5 mM PAH solution at a pH of 6.5. In this case, the stamp was left in contact with the surface for 30 min. The patterned multilayer film was stained with Methylene Blue to provide a contrast between the PAH stamped and PAA unstamped regions. This figure demonstrates that high quality, uniform patterns are possible over a wide area of the stamped

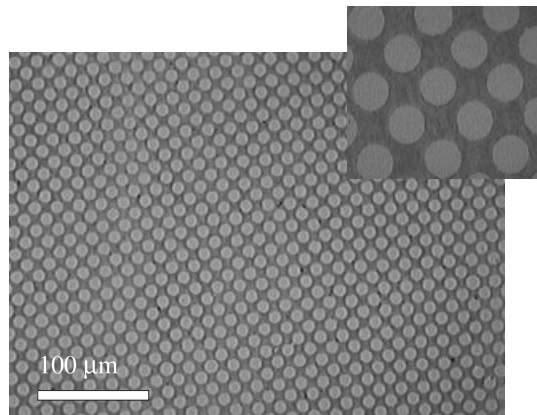


**Fig. 5.9** Optical microscope image of the surface of a 10 bilayer film of 2.0/2.0 PAA/PAH micro-contact printed with a layer of PAH. The film was stained with Methylene Blue to provide contrast; the lighter elements are the PAA regions selectively stained with Methylene Blue. Inset shows a higher magnification of the same film.



region. With this approach, feature sizes as small as one micron are easily obtained.

A few comments about the Methylene Blue staining process are appropriate at this time. In the past we have suggested that Methylene Blue, a cationic dye, will only bind to multilayer surfaces that contain free carboxylic acid groups [5, 6]. At neutral pH, the free acid groups of PAA become ionized and readily bind this dye. Acid groups that are ion paired with PAH segments, on the other hand, are not capable of binding Methylene Blue. For example, a 2.5/2.5 PAA/PAH film turns deep blue after immersion in a pH 7.0 Methylene Blue solution whereas a 6.5/6.5 film remains clear. Thus, this is simple way to probe the level of ion-pairing and availability of free acid groups in PAA/PAH multilayer films. If the immersion times in the Methylene Blue solution are short, typically 15 min or less, then the dye only has time to diffuse into the outermost few layers. These conditions are ideal for probing the surfaces of PAA/PAH multilayer films. This was the way the multilayer film in Fig. 5.9 was treated. In this case, Methylene Blue surface staining only occurs on the regions of the film with PAA as the outermost layer and is resisted by the regions stamped with PAH. Longer immersion times result in a deeper penetration of the dye onto the film, thereby making it possible to probe the internal structure as well. It should be noted that we have recently found that a very fast and uniform loading of PAA/PAH multilayer films with Methylene Blue can be accomplished with the use of buffered solutions [52]. This is due, in part, to the increased level of swelling of the film that occurs as a result of the higher ionic strength of the buffered Methylene Blue solution. In this case, PAA/PAH films with available acid binding sites can be uniformly loaded in 15 min with no limiting penetration depth observed in films up to 2000 Å in thickness. These results demonstrate that polyelectrolyte multilayers can become highly permeable in solutions of modest ionic strength, a fact that has implications in controlled drug release applications [52].

The polymer-on-polymer micro-contact printing process can be used to create patterned surfaces with coexisting regions of positive and negative charge. Such regions, in-turn, can selectively direct the adsorption of other molecules, like amphiphilic block copolymers or dyes or promote selective electroless plating to make circuit patterns. Using weak polyelectrolyte platforms and the plating techniques described earlier, for example, we have used this approach to create micron-scale patterns of electrolessly plated metals [53]. This simple yet effective tool for patterning surfaces should find wide application in the design of electronic and photonic devices as well in the biosensor area.

### 5.7.2

#### **Ink-jet Printing of Hydrogen-Bonded Multilayers**

The second ink-jet printing process that we have developed for creating patterned polyelectrolyte multilayers utilizes multilayer films assembled via hydrogen-bonding interactions. Although most of the work in this field has been directed at electrostatic layer-by-layer assembly, our work [54] and the work of Wang et al. [55] es-

tablished early on that hydrogen-bonding interactions can also be used to assemble multilayer films. More recently, Granick and coworkers have demonstrated [56] that hydrogen-bonded multilayers containing weak polyacids can be assembled and then readily dissolved by simply increasing the degree of ionization of the acid groups by increasing the pH. This intriguing result opens the door to some novel patterning possibilities based on the selective dissolution of a multilayer film. In order to use hydrogen-bonded multilayers in subtractive patterning schemes, however, it is critically important to identify simple crosslinking methodologies for stabilizing the film. We now describe two such methodologies.

Hydrogen-bonded multilayer thin films containing a weak polyelectrolyte were fabricated with polyacrylamide (PAAm) and PAA [57]. To start the process, a single layer of PAH was deposited onto the substrate to facilitate adhesion. Alternating layers of PAAm and PAA were then deposited at pH 3.0 to form a uniform multilayer thin film. At this pH, most of the carboxylic acid groups of the PAA chains in solution exist in their non-ionized form and are therefore available for hydrogen bond formation. The pH of both the dipping and rinsing solutions was adjusted to 3.0 with aqueous HCl and no salt was added to the solutions. Operating at low pH is critical to the assembly process as dissolution occurs if the film is rinsed in pH neutral water. Fig. 5.10 shows the incremental mass growth of two PAA/PAAm multilayer films as monitored by an *in situ* quartz crystal microbalance set-up [58]. The two films were assembled with a 90 K molecular weight PAA sample and either a 5000 K or 800 K molecular weight PAAm sample. The multilayer film assembled with the lower molecular weight PAAm shows the usual linear growth observed in many multilayer systems. The film assembled with the higher molecular weight PAAm, on the other hand, exhibits a non-linear growth pattern. Ellipsometric measurements confirm a non-linear growth process with bilayer thicknesses of about 40 Å at 4 bilayers, 150 Å at 8 bilayers and 400 Å at 12 bilayers. Nevertheless, all films fabricated with the PAA/PAAm system were uniform, of relatively low surface roughness (ca. 60 Å rms roughness for a 1200 Å thick film as determined by AFM) and optically transparent up to at least 14 bi-

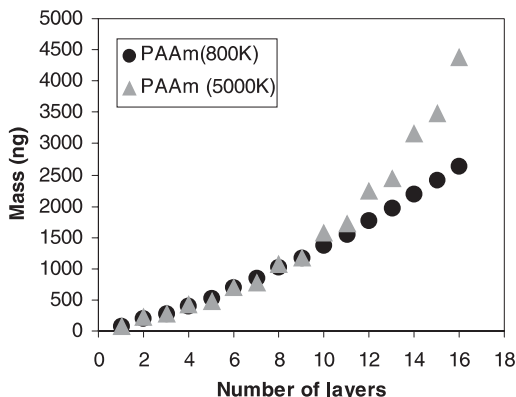


**Fig. 5.10** Mass versus number of deposited layers plots of the PAA/PAAm multilayer system assembled with two different molecular weight samples of PAAm.

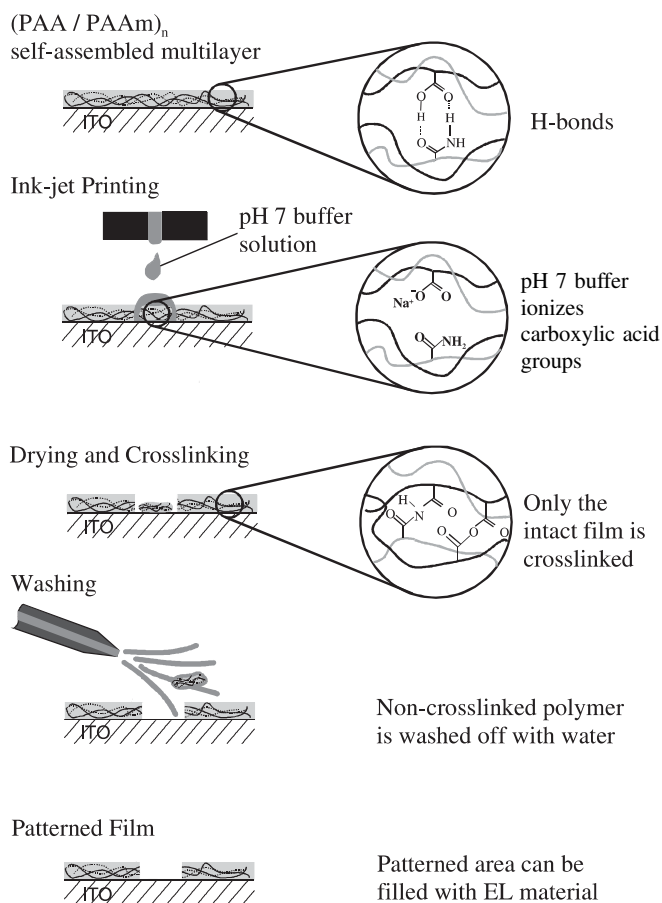


**Fig. 5.11** Schematic of the patterning of PAA/PAAm hydrogen-bonded multilayers by the subtractive ink-jet printing process.

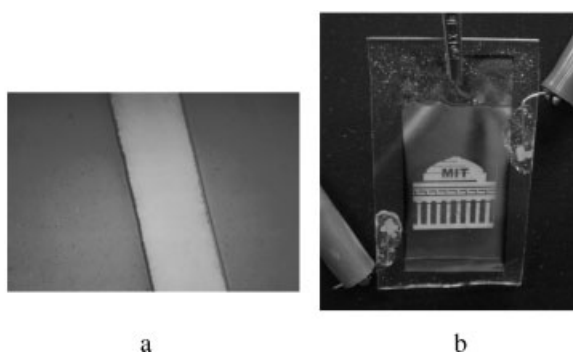
layers. In addition, FTIR measurements confirm the formation of hydrogen bonds between the acid groups of PAA and amide groups of PAAm [57].

As expected, the PAA/PAAm multilayers dissolved quickly in pH 4.5 or higher aqueous solutions. In particular, the multilayers were found to dissolve within a few seconds in a pH 7.0 phosphate buffer solution. However, if the multilayer film is thermally treated at 90 °C for 8 h (or shorter times at higher temperatures), it becomes insoluble in these higher pH solutions. The insolubility appears to be the result of thermally induced crosslinking reactions that produce both anhydride and imide linkages (confirmed by FTIR). Thus, with a simple thermal treatment, water soluble PAA/PAAm multilayers can be rendered insoluble. This makes them very useful for patterning applications.

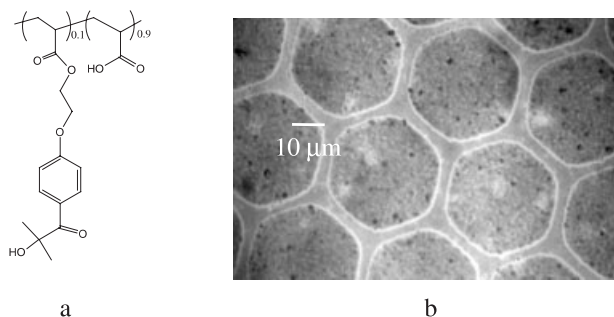
Fig. 5.11 shows a schematic of how PAA/PAAm multilayers in conjunction with ink-jet printing can be used to create simple micro-patterns. In this process, a substrate is first coated with PAA/PAAm multilayers by assembly at low pH. A pH 7.0 aqueous buffer solution is then ink-jet printed onto the film to create the desired pattern. The PAA chains in the regions printed by the buffer solution become ionized and dissolution of the multilayer begins. The printed film is then dried and thermally crosslinked to render the non-printed regions insoluble in water. The printed regions remain water soluble due to the disruption of the hydrogen-bonded multilayer that occurs when the PAA acid groups become ionized. A final water rinse removes the soluble material from the printed regions to produce a patterned film.

Fig. 5.12 shows a patterned PAA/PAAm multilayer film and a patterned light emitting device fabricated with this process. In the former case, the multilayer film was deposited onto a glass slide. This shows that the ink-jet printed region of the multilayer film has been cleanly removed from the substrate revealing the bare glass surface. The width of this line is 300  $\mu\text{m}$ . In the second example, this new process has been used to fabricate a patterned light-emitting device with patterned elements as small as about 100  $\mu\text{m}$  [59]. The PAA/PAAm multilayer film was deposited onto an ITO coated glass slide and selectively removed by the ink-jet process. A red-orange light emitting tris-bipyridyl Ru(II) complex [60] was then spin coated onto the substrate followed by evaporation of an aluminum top electrode. Light is only emitted from the regions removed by ink-jet printing where a direct conduction path exists between the two conductive electrodes. The remaining PAA/PAAm film acts as an excellent insulator thereby preventing the flow of current and hence light emission.

Finally, we note that standard photolithographic techniques can also be used to create patterned films of PAA/PAAm. In this case, we utilized a photoinitiator-labeled PAA copolymer to generate free radicals that are capable of crosslinking the PAA/PAAm multilayer film [57]. Fig. 5.13 shows the structure of this copolymer



**Fig. 5.12** Ink-jet printed PAA/PAAm multilayer films showing (a) a 300  $\mu\text{m}$  width line of material removed from a glass substrate and (b) a light emitting device patterned by the subtractive ink-jet process.



**Fig. 5.13** (a) Chemical structure of a new photo-initiator labeled PAA copolymer. (b) Optical microscope image of the pattern created by UV-crosslinking a PAA/PAAm multilayer film through a TEM microscope grid. Dark regions are 100 nm thick hexagons of the PAA/PAAm multilayer film that were rendered insoluble by photo-crosslinking.

as well as a simple pattern created by UV exposure of a PAA/PAAm film through a microscope grid with 35  $\mu\text{m}$  “holes” followed by a brief washing in water. The irradiated regions of the film become insoluble whereas the non-irradiated regions are washed away with the water rinse. The photoinitiator-labeled PAA was simply adsorbed onto the multilayer film as the last deposited layer. Apparently, the radicals generated by the UV irradiation of this copolymer are capable of rendering the film insoluble. We are currently working on understanding the mechanism of this crosslinking reaction.

## 5.8

### Conclusions and Future Prospects

The pH-controlled layer-by-layer assembly of weak polyelectrolytes can be used to create multilayer thin films with a wide range of useful properties. The future for this type of assembly looks extremely promising as we continue to find novel applications for these materials based on their precisely tunable optical, electrical and physical properties. New developments to be disclosed shortly include the fabrication of metallo-dielectric stacks exhibiting the properties of a one-dimensional photonic band-gap, tunable anti-reflection coatings and “bio-inert” thin film coatings that can be used to resist the adhesion and spreading of mammalian cells.

### Acknowledgements

This work was supported by the following organizations: the MIT MRSEC Program of the National Science Foundation, the National Science Foundation, the Office of Naval Research, the MURI Program of the Office of Naval Research and CibaVision.

## 5.9

## References

- 1 G. DECHER, *Science* **1997**, *277*, 1232.
- 2 P. T. HAMMOND, *Colloid Interface Sci.* **2000**, *4*, 430.
- 3 P. BERTRAND, A. JONAS, A. LASCHEWSKY, R. LEGRAS, *Macromol. Rapid Commun.* **2000**, *21*, 319.
- 4 J. BAUR, M. F. RUBNER, J. R. REYNOLDS, S. KIM, *Langmuir* **1999**, *15*, 6460.
- 5 D. YOO, S. S. SHIRATORI, M. F. RUBNER, *Macromolecules* **1998**, *31*, 4309.
- 6 S. S. SHIRATORI, M. F. RUBNER, *Macromolecules* **2000**, *33*, 4213.
- 7 J. D. MENDELSON, C. J. BARRETT, V. V. CHAN, A. J. PAL, A. M. MAYES, M. F. RUBNER, *Langmuir* **2000**, *16*, 5017.
- 8 R. V. KLITZING, H. MOHWALD, *Langmuir* **1995**, *11*, 3554.
- 9 A. F. XIE, S. GRANICK, *J. Am. Chem. Soc.* **2001**, *123*, 3175.
- 10 S. Y. PARK, C. J. BARRETT, M. F. RUBNER, A. M. MAYES, *Macromolecules* **2001**, *34*, 3384.
- 11 S. JOLY, R. KANE, L. RADZILOWSKI, T. WANG, A. WU, R. E. COHEN, E. L. THOMAS, M. F. RUBNER, *Langmuir* **2000**, *16*, 1354.
- 12 D. YOU, M. F. RUBNER, *SPE-Antec Boston* **1995**, *95*, 2568.
- 13 W. CHEN, T. J. MCCARTHY, *Macromolecules* **1997**, *30*, 78.
- 14 F. CARUSO, H. LICHTENFELD, E. DONATH, H. MÖHWALD, *Macromolecules* **1999**, *32*, 2317.
- 15 M. F. DURSTOCK, M. F. RUBNER, *Langmuir* **2001**, in-press.
- 16 (a) J. H. CHEUNG, A. C. FOU, M. F. RUBNER, *Thin Solid Films* **1994**, *244*, 1232; (b) A. C. FOU, M. F. RUBNER, *Macromolecules* **1995**, *28*, 7115; (c) J. H. CHEUNG, B. STOCKTON, M. F. RUBNER, *Macromolecules* **1997**, *30*, 2712.
- 17 (a) M. FERREIRA, J. H. CHEUNG, M. F. RUBNER, *Thin Solid Films* **1994**, *244*, 806; (b) M. FERREIRA, M. F. RUBNER, *Macromolecules* **1995**, *28*, 7107.
- 18 A. C. FOU, O. ONITSUKA, M. FERREIRA, M. F. RUBNER, B. R. HSIEH, *J. Appl. Phys.* **1996**, *79*, 7501.
- 19 O. ONITSUKA, A. C. FOU, M. FERREIRA, B. R. HSIEH, M. F. RUBNER, *J. Appl. Phys.* **1996**, *80*, 4067.
- 20 H. MATTOUSSI, M. F. RUBNER, F. ZHOU, J. KUMAR, S. K. TRIPATHY, L. Y. CHIANG, *Appl. Phys. Lett.* **2000**, *77*, 1540.
- 21 H. MATTOUSSI, L. RADZILOWSKI, B. DABBOUSI, E. L. THOMAS, M. BAWENDI, M. F. RUBNER, *J. Appl. Phys.* **1998**, *83*, 7965.
- 22 A. WU, D. YOO, J.-K. LEE, M. F. RUBNER, *J. Am. Chem. Soc.* **1999**, *121*, 4883.
- 23 H. HONG, D. DAVIDOV, Y. AVANY, H. CHAYET, E. Z. FARAGGI, R. NEUMANN, *Adv. Mater.* **1995**, *7*, 846.
- 24 J. TIAN, C. C. WU, M. E. THOMPSON, J. C. STURM, R. A. REGISTER, M. J. MARSELIA, T. M. SWAGER, *Adv. Mater.* **1995**, *7*, 395.
- 25 M. ONODA, K. YOSHINO, *Jpn. J. Appl. Phys.* **1995**, *34*, L260.
- 26 R. ADVINCULA, *IEICE Trans. Electron.* **2000**, *E83C*, 1104.
- 27 P. K. H. HO, M. GRANSTROM, R. H. FRIEND, N. C. GREENHAM, *Adv. Mater.* **1998**, *10*, 769.
- 28 P. K. H. HO, J. S. KIM, J. H. BURROUGHES, H. BECKER, S. F. Y. LI, T. M. BROWN, F. CACIALLI, R. H. FRIEND, *Nature* **2000**, *404*, 481.
- 29 X. WANG, S. BALASUBRAMANIAN, L. LI, X. JIANG, D. J. SANDMAN, M. F. RUBNER, J. KUMAR, S. K. TRIPATHY, *Macromol. Rapid Commun.* **1997**, *18*, 451.
- 30 M. ECKLE, G. DECHER, *Nanoletters* **2001**, *1*, 45.
- 31 J. W. BAUR, S. KIM, P. B. BALANDER, J. R. REYNOLDS, M. F. RUBNER, *Adv. Mater.* **1998**, *10*, 1452.
- 32 S. L. CLARK, E. S. HANDY, M. F. RUBNER, P. H. HAMMOND, *Adv. Mater.* **1999**, *11*, 1031.
- 33 M. GAO, B. RICHTER, S. KIRSTEIN, *Adv. Mater.* **1997**, *9*, 802.
- 34 M. F. DURSTOCK, M. F. RUBNER, *Proc. SPIE* **1997**, *3148*, 126.
- 35 (a) M. FERREIRA, O. ONITSUKA, A. C. FOU, B. HSIEH, M. F. RUBNER, *Mater. Res. Soc. Symp. Proc.* **1996**, *413*, 49; (b) A. C. FOU, O. ONITSUKA, M. FERREIRA, M. F. RUBNER, *Mater. Res. Soc. Symp. Proc.* **1995**, *369*, 575.

- 36 A. FERY, B. SCHOLER, T. CASSAGNEAU, F. CARUSO, *Langmuir* **2001**, *17*, 3779.
- 37 T. C. WANG, B. CHEN, M. F. RUBNER, R. E. COHEN, *Langmuir* **2001**, *17*, 6610.
- 38 N. A. KOTOV, I. DÉKÁNY, J. H. FENDLER, *J. Phys. Chem.* **1995**, *99*, 13069.
- 39 N. A. KOTOV, S. MAGONOV, E. TROPSHA, *Chem. Mater.* **1998**, *10*, 886.
- 40 (a) K. ARIGA, Y. LVOV, M. ONDA, I. ICHINOSE, T. KUNITAKE, *Chem. Lett.* **1997**, *125*; (b) Y. LVOV, K. ARIGA, M. ONDA, I. ICHINOSE, T. KUNITAKE, *Langmuir* **1997**, *13*, 6195.
- 41 (a) E. R. KLEINFELD, G. FERGUSON, *Science* **1994**, *265*, 370; (b) Y. J. LIU, A. B. WANG, R. CLAUS, *J. Phys. Chem. B.* **1997**, *101*, 1385.
- 42 J. SCHMITT, G. DECHER, W. J. DRESSICK, S. L. BRANDOW, R. E. GEER, R. SHASHIDHAR, J. M. CALVERT, *Adv. Mater.* **1997**, *9*, 61.
- 43 S. W. KELLER, H.-N. KIM, T. E. MALLOUK, *J. Am. Chem. Soc.* **1994**, *116*, 8817.
- 44 (a) R. T. CLAY, R. E. COHEN, *Supramol. Sci.* **1995**, *2*, 183; (b) J. Yue, R. E. COHEN, *Supramol. Sci.* **1994**, *1*, 117; (c) B. H. SOHN, R. E. COHEN, *Chem. Mater.* **1997**, *9*, 264; (d) R. T. CLAY, R. E. COHEN, *Supramol. Sci.* **1997**, *4*, 113; (e) R. T. CLAY, R. E. COHEN, *Supramol. Sci.* **1998**, *5*, 41.
- 45 T. C. WANG, M. F. RUBNER, R. E. COHEN, *Langmuir* **2002**, *18*, 3370.
- 46 Y. BOONTONGKONG, R. E. COHEN, M. F. RUBNER, *Chem. Mater.* **2000**, *12*, 1628.
- 47 J. BHARATHAN, Y. YANG, *Appl. Phys. Lett.* **1998**, *72*, 2660.
- 48 J. CHOI, M. F. RUBNER, *J. Macromol. Sci., Pure Appl. Chem.* **2001**, *A38*, 1191.
- 49 (a) P. T. HAMMOND, G. M. WHITESIDES, *Macromolecules* **1995**, *28*, 7569; (b) S. L. CLARK, M. MONTAGUE, P. T. HAMMOND, *Supramol. Sci.* **1997**, *4*, 141; (c) S. L. CLARK, M. MONTAGUE, P. T. HAMMOND, *Macromolecules* **1997**, *30*, 7237; (d) S. L. CLARK, P. T. HAMMOND, *Adv. Mater.* **1998**, *10*, 1515.
- 50 A. KUMAR, G. M. WHITESIDES, *Science* **1994**, *263*, 60.
- 51 X. P. JIANG, P. T. HAMMOND, *Langmuir* **2000**, *16*, 8501.
- 52 A. J. CHUNG, M. F. RUBNER, *Langmuir* **2002**, *18*, 1176.
- 53 X. P. JIANG, P. T. HAMMOND, R. E. COHEN, B. CHEN, T. C. WANG, M. F. RUBNER, to be submitted for publication.
- 54 W. B. STOCKTON, M. F. RUBNER, *Macromolecules* **1997**, *30*, 2717.
- 55 L. WANG, Z. WANG, X. ZHANG, J. SHEN, L. CHI, H. FUCHS, *Macromol. Rapid Commun.* **1997**, *18*, 509.
- 56 A. SUKHISHVILI, S. GRANICK, *J. Am. Chem. Soc.* **2000**, *122*, 9550.
- 57 S. Y. YANG, M. F. RUBNER, *J. Am. Chem. Soc.* **2002**, *124*, 2100.
- 58 Y. OKAYAMA, T. ITO, S. SHIRATORI, *Thin Solid Films* **2001**, *393*, 132.
- 59 H. RUDMANN, S. Y. YANG, M. F. RUBNER, to be submitted for publication.
- 60 H. RUDMANN, M. F. RUBNER, *J. Appl. Phys.* **2001**, *90*, 4338.

## 6

### Recent Progress in the Surface Sol–Gel Process and Protein Multilayers

I. ICHINOSE, K. KUROIWA, Y. LVOV, and T. KUNITAKE

#### Abstract

Positively charged organic and inorganic compounds adsorb densely on metal oxide gel films prepared by the surface sol–gel process. For example, linear cationic polymers and a cadmium polynuclear complex ( $[\text{Cd}_{10}(\text{SCH}_2\text{CH}_2\text{OH})_{16}]^{4+}$ ) were alternately assembled with ultrathin metal oxide layers. Multilayer assemblies of heme proteins such as cytochrome c and myoglobin were similarly prepared. Thus, the surface sol–gel process becomes a useful tool for designing functional organic/inorganic nanocomposite films. In this chapter, we describe recent progress in the preparation of ultrathin films composed of metal oxides, polymers, small organic molecules and proteins. In particular, we demonstrate herein molecular recognition of amino acid derivatives in ultrathin  $\text{TiO}_2$ -gel films, molecular filtration via two-dimensionally cross-linked polymer films, enzyme multilayers as a nano-reactor, and encapsulation and release of proteins in and from microshells from the viewpoint of biochemical applications.

#### 6.1

##### Alternating Adsorption

##### 6.1.1

##### Surface Sol–Gel Process

Preparative techniques of ultrathin films via the stepwise adsorption from solution have been developed rapidly in the last decade. These techniques enable us to fabricate various nano-composite films containing polymers [1], dye molecules [2], bio-molecules [3], nanoparticles [4], two-dimensional inorganic sheets [5], and molecular aggregates [6] by controlling their thicknesses with molecular precision. While the majority of the nano-composite layers have been assembled via electrostatic interaction between oppositely charged materials, other interactions such as hydrogen bonding [7], charge-transfer interactions [8], biochemical affinity [9], and stereocomplex formation [10] were also effective for layer-by-layer assembly. Such diversity in materials and in chemical interactions led to their extensive applications in molecular architectures with novel functionalities.



We have reported a preparative technique for ultrathin metal oxide films based on the stepwise adsorption of metal alkoxides, where solid substrates with hydroxyl (or carboxyl) groups are immersed in the alkoxide solution, rinsed with adequate organic solvent, and the chemisorbed alkoxides are hydrolyzed. Ultrathin metal oxide gel films with molecular thickness are formed on the substrate surface. At this stage, hydroxy groups are regenerated on the film surface, which can be employed for further chemisorption of metal alkoxides. This process, which we named the surface sol–gel process, is applicable to various alkoxides of titanium, zirconium, aluminum, silica, indium, tin, and vanadium metals [11]. Fig. 6.1a illustrates sequential chemisorption of metal alkoxides in the surface sol–gel process. The increase in thickness in one adsorption cycle is adjusted to a precision of less than 1 nm. Generation of the surface hydroxy group is achieved by hydrolysis of chemisorbed alkoxides as well as by chemisorption of polyhydroxyl compounds (Fig. 6.1b) [12]. For example, by repeating chemisorption of titanium butoxide ( $\text{Ti}(\text{O}^n\text{Bu})_4$ ) and poly(acrylic acid) (PAA), alternating layers of 1 nm thick  $\text{TiO}_2$ -gel and PAA are formed on the substrate. Similar multilayer assemblies are obtainable from various combinations of metal alkoxides and polyhydroxy compounds. We have used this methodology to incorporate organic dyes, protected amino acids, and sugar compounds into metal oxide gel films to conduct molecular imprinting as described later [13].

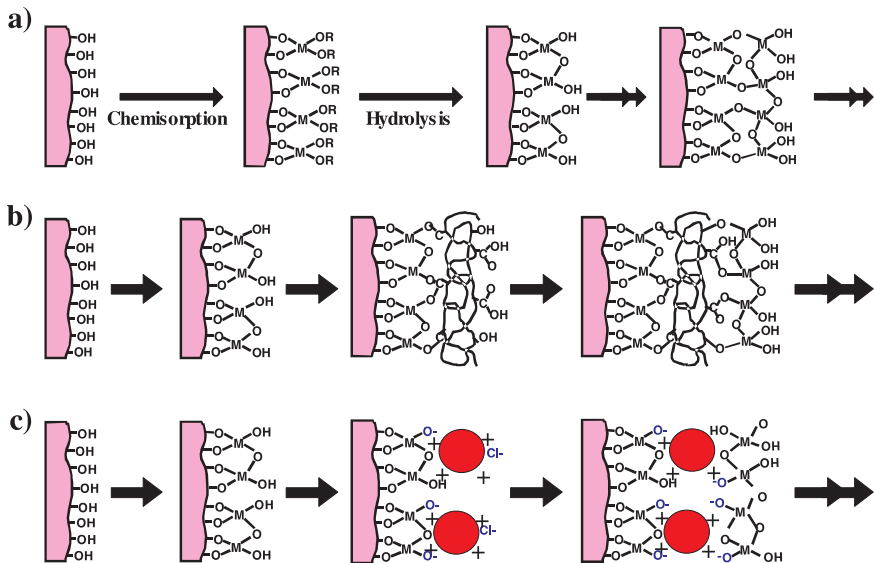


**Fig. 6.1** Schematic illustrations of three types of layer-by-layer adsorption based on the surface sol–gel process. Stepwise adsorption of metal alkoxides (a), alternate adsorption of

metal alkoxides and polyhydroxyl compounds (b), and alternate adsorption of metal alkoxide and cationic compounds (c).

Very recently, it was found that the metal oxide gel strongly adsorbs positively charged compounds. Abundant hydroxy groups on the gel surface are readily dissociated to give negative charges. This new feature leads to new types of nanocomposite films made of metal oxide and water-soluble compounds such as metal complexes, polyelectrolytes, and proteins (Fig. 6.1c). Since we have published review articles on the surface sol-gel process elsewhere, the present chapter focuses on further developments of this process.

### 6.1.2

#### Adsorption of cationic compounds on metal oxide gels

Alternating adsorption of metal alkoxides and cationic compounds was studied by the quartz crystal microbalance (QCM) technique. Minute mass changes on the QCM electrode are detected as frequency changes ( $-\Delta F$ ). In our system (9 MHz resonator, manufactured by USI system, Japan), a 1 Hz decrease in frequency corresponds to a mass increase of 0.9 ng. A gold-coated QCM electrode was modified with mercaptoethanol to introduce hydroxy groups onto the surface. The electrode was immersed in  $\text{Ti}(\text{O}^n\text{Bu})_4$  in toluene/ethanol (1/1 vol/vol) for 3 min, rinsed in ethanol, dipped into ion-exchanged water for 1 min to hydrolyze the chemisorbed alkoxide, and dried by flushing with nitrogen gas. The frequency shift was then measured to estimate the mass of  $\text{TiO}_2$ -gel layer formed. In general, the thickness increase for one adsorption cycle was less than 1 nm. The electrode was immersed in an aqueous solution of cadmium polynuclear complex ( $[\text{Cd}_{10}(\text{SCH}_2\text{CH}_2\text{OH})_{16}]^{4+} \cdot 4\text{ClO}_4$ ) for 1 min, rinsed, and dried with nitrogen gas. Fig. 6.2 shows QCM frequency shifts during alternating adsorption of  $\text{Ti}(\text{O}^n\text{Bu})_4$  and the polynuclear complex. Regular film growth was observed when the adsorption of  $\text{Ti}(\text{O}^n\text{Bu})_4$  was repeated twice for every adsorption of the polynuclear complex. The average frequency decrease was  $102 \pm 67$  Hz for the polynuclear complex, and the frequency change for two adsorption cycles of  $\text{TiO}_2$ -gel was ca. 30 Hz. The size of the spherical polynuclear complex is ca. 15 Å in diameter, the molecular weight is 2756, not including its counter anions, and the complex has four positive charges [14]. Supposing hexagonal close packing of the spherical complex on both sides of a QCM resonator ( $0.32 \text{ cm}^2$ ), an estimated mass increase would be 75.0 ng corresponding to the frequency change of 83.3 Hz. Though the experimental frequency change (102 Hz) is slightly larger than the calculated value, the polynuclear complex can be considered to form a close-packed monolayer on  $\text{TiO}_2$ -gel.

Multilayer assembly of the polynuclear complex and  $\text{TiO}_2$ -gel was subjected to X-ray photoelectron spectroscopy (XPS) measurements. The film formed on a quartz plate gave XPS peaks of oxygen and titanium atoms that are attributed to  $\text{TiO}_2$ -gel, along with peaks of cadmium and sulfur atoms derived from the polynuclear complex (Fig. 6.3). A carbon peak is also seen in Fig. 6.3. The elemental composition estimated from these peak intensities is Ti:O:C: Cd:S = 2.5:10.3:5.6:1.0:0.35. The composite film contains one cadmium complex ( $[\text{Cd}_{10}(\text{SCH}_2\text{CH}_2\text{OH})_{16}]^{4+}$ ) per 25 titanium atoms. The ratio of cadmium and sul-

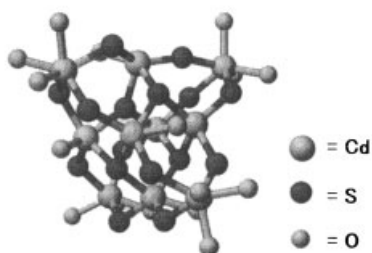
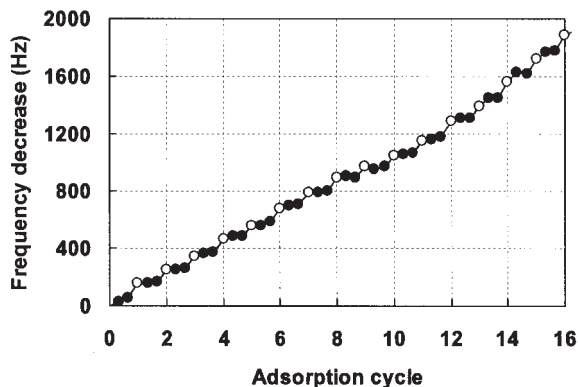


**Fig. 6.2** QCM frequency shifts due to alternate adsorption of  $\text{Ti}(\text{O}^i\text{Bu})_4$  and cadmium polynuclear complex  $[(\text{Cd}_{10}(\text{SCH}_2\text{CH}_2\text{OH})_{16})^{4+} \cdot 4\text{ClO}_4]$ .  $\text{Ti}(\text{O}^i\text{Bu})_4$  was adsorbed twice for every adsorption of the polynuclear complex. The left shows the inner structure of the polynuclear complex, where carbon and hydrogen atoms are omitted. The whole size is ca. 15 Å in diameter.

fur atoms is significant. The polynuclear complex is composed of 10 cadmium atoms and 16 sulfur atoms. However, the ratio estimated by XPS is  $\text{Cd}:\text{S}=1.0:0.35$ . This inconsistency probably arises from partial decomposition of the cadmium complex. A part of the mercaptoethanol molecule that is coordinated to cadmium ions may be removed in the composite film. Such a structure is shown in Fig. 6.3, in which a cluster structure composed of ten cadmium atoms and four sulfur atoms is drawn in the  $\text{TiO}_2$ -gel matrix, consistent with the XPS results.

The surface sol–gel process is, of course, a convenient way to form ultrathin mixed metal oxide films from more than one kind of metal alkoxide. Incorporation of polynuclear complexes provides an additional means to introduce inorganic components that are not available as metal alkoxides. Ultrathin metal oxide gels possess negative charges even at neutral pH, and adsorb cationic polynuclear complexes. Therefore, negatively charged polynuclear complexes such as  $[\text{V}_{10}\text{O}_{28}]^{6-}$  cannot adsorb on the gel surface at all. On the other hand, metal alkoxide is readily adsorbed on the surface of the polynuclear complex  $[(\text{Cd}_{10}(\text{SCH}_2\text{CH}_2\text{OH})_{16})^{4+}]$ .

Cationic polymers are similarly adsorbed on the metal oxide gel layer. Alternating adsorption of metal alkoxides and cationic polymers, such as poly(allylamine) (PAH), poly(ethyleneimine) (PEI), poly(dimethyldiallylammonium bromide) (PDDA), and poly(butanylviologen) (PBV), has been investigated in our laboratory. The chemical structures of these polymers are shown in Fig. 6.4.

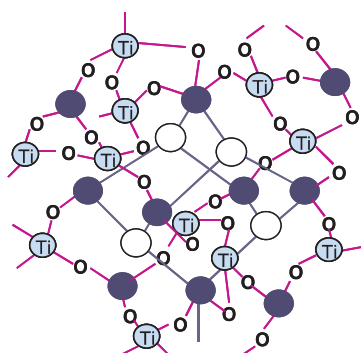
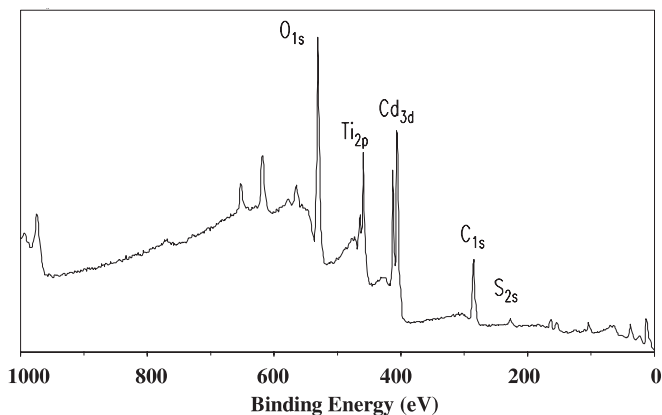


**Fig. 6.3** XPS spectrum of a polynuclear complex/TiO<sub>2</sub>-gel composite film and a schematic representation of a polynuclear cadmium cluster in TiO<sub>2</sub>-gel matrix. Open and closed circles denote sulfur and cadmium atoms, respectively.

The typical procedure for the preparation of a PDDA/TiO<sub>2</sub>-gel composite film is as follows: A QCM electrode modified with mercaptoethanol was immersed in Ti(O<sup>n</sup>Bu)<sub>4</sub> in 1/1 toluene/ethanol for 3 min, rinsed in ethanol, dipped in ion-exchanged water for 1 min to hydrolyze the chemisorbed alkoxide, and dried by flushing with nitrogen gas. Then the electrode was immersed in aqueous PDDA (1 mg ml<sup>-1</sup>, pH 7.0) for 3 min, rinsed in pure water, and dried. These assembly procedures were repeated for 40 cycles. Fig. 6.5 shows a scanning electron microscope (SEM) image of a PDDA/TiO<sub>2</sub>-gel film on an Au-coated resonator. The film has a uniform thickness of 90±10 nm and looks like a cloven timber. The total QCM frequency shift during the adsorption of 40 cycles is 5499 Hz. The film density ( $\rho$ ) is estimated from the QCM frequency shift ( $-\Delta F$ , 5499 Hz) and the thickness ( $d$ , 90 nm) in SEM using the following equation.

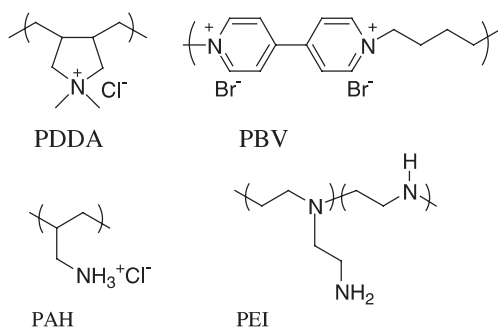
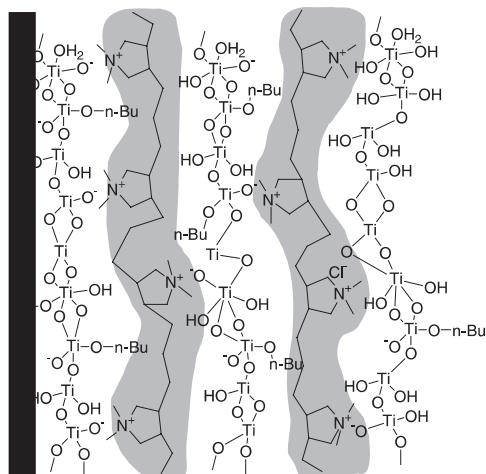


**Fig. 6.4** Structures of cationic polymers used for the surface sol-gel process and a schematic illustration of a PDDA/TiO<sub>2</sub>-gel multilayer.

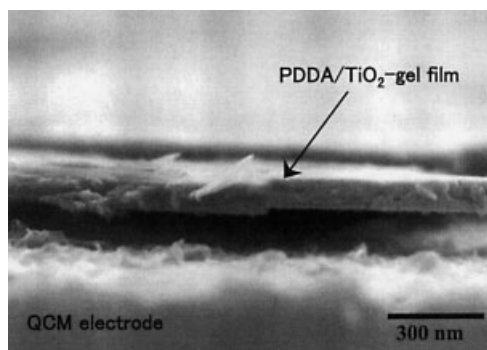


$$2d(\text{\AA}) = -\Delta F(\text{Hz})/1.832\rho(\text{g cm}^{-3}) \quad (1)$$

The estimated density is  $1.67 \text{ g cm}^{-3}$ , and is considerably larger than that of PDDA ( $1.3 \text{ g cm}^{-3}$ ) and is almost equal to the density of bulk TiO<sub>2</sub>-gel ( $1.6 \text{ g cm}^{-3}$ ) prepared by the conventional sol-gel process. Both components, PDDA and TiO<sub>2</sub>-gel, appear to be densely mixed with each other. In the QCM experiment, the average frequency change is  $107 \pm 40 \text{ Hz}$  for Ti(O<sup>n</sup>Bu)<sub>4</sub> adsorption, and is  $43 \pm 21 \text{ Hz}$  for PDDA. The thickness increase per cycle is calculated to be  $2.5 \text{ nm}$  from the density ( $1.67 \text{ g cm}^{-3}$ ) and the frequency change ( $150 \text{ Hz}$ ) using Eq. (1). Individual thicknesses of the polymer and metal oxide layers in the PDDA/TiO<sub>2</sub>-gel composite film are estimated to be  $1.0$  and  $1.5 \text{ nm}$ , respectively.

The elemental composition of the PDDA/TiO<sub>2</sub>-gel film estimated by XPS measurements is Ti:C:N:Cl=1.0:5.5:0.45:0.09. PDDA has one nitrogen atom and one chlorine atom in the monomer unit. The smaller chlorine ratio in the composite film (N:Cl=0.45:0.09) indicates that the positive charge of PDDA is mainly

**Fig. 6.5** A scanning electron microscopy image of the cross-sectional view of a PDDA/TiO<sub>2</sub>-gel composite film.



neutralized by the negative charge of the TiO<sub>2</sub>-gel. From the XPS data, 80% of the monomer units of PDDA should bind to the TiO<sub>2</sub>-gel layer by ion-pair formation. The film has at least two titanium atoms per monomer unit of PDDA from the ratio of titanium to nitrogen (Ti:N=1.0:0.45).

Details of the alternating adsorption of metal alkoxides and various polymers are summarized in Tab. 6.1. It is obvious that the surface sol-gel process can be widely used for the preparation of ultrathin polymer/metal oxide composite films. In the combination of Ti(O<sup>n</sup>Bu)<sub>4</sub> and cationic polymers, the frequency change for Ti(O<sup>n</sup>Bu)<sub>4</sub> adsorption is in the range 43–71 Hz, and those of the polymers are in the range 69–116 Hz. It is worthy of note that the Cl(or Br)/N ratio estimated by XPS measurements is in the range 0.13–0.35 for all cases. This indicates that most of the positive charges of the polymers are neutralized by the TiO<sub>2</sub>-gel layer.

**Tab. 6.1** Alternate adsorption of metal alkoxides and polymer

<i>Metal alkoxide</i> <sup>a)</sup>	<i>Polymer</i> <sup>b)</sup>	<i>Frequency decrease/HZ</i>		<i>XPS measurement</i>	
		<i>Metal alkoxide</i>	<i>Polymer</i>	<i>N/metal atom</i>	<i>Cl (or Br)/N</i>
Ti(O <sup>n</sup> Bu) <sub>4</sub>	PDDA (pH 4.0)	71 ± 20	69 ± 23	0.32	0.23
	PDDA (pH 7.0)	43 ± 21	107 ± 40	0.45	0.21
	PDDA (pH 10.0)	69 ± 54	101 ± 23	0.67	0.15
	PBV (pH 7.0)	55 ± 32	116 ± 40	0.51	0.23
	PAH (pH 7.0)	55 ± 42	109 ± 44	0.55	0.18
In(OEtOMe) <sub>3</sub>	PDDA	84 ± 16	49 ± 15	0.26	0.19
In(OEtOMe) <sub>3</sub>	PBV	72 ± 23	55 ± 11	0.32	0.21
Si(OMe) <sub>4</sub>	PDDA	81 ± 23	107 ± 20	0.43	0.13
Zr(O <sup>n</sup> Bu) <sub>4</sub>	PDDA	68 ± 39	103 ± 34	0.40	0.23
Al(O <sup>n</sup> Bu) <sub>3</sub>	PDDA	161 ± 108	100 ± 23	0.03	0.10
Nb(O <sup>n</sup> Bu) <sub>5</sub>	PDDA	510 ± 82	194 ± 26	0.27	0.35

a) Concentrations are 100 mM for Ti(O<sup>n</sup>Bu)<sub>4</sub>, In(OEtOMe)<sub>3</sub>, and Zr(O<sup>n</sup>Bu)<sub>4</sub>, 10 mM for Al(O<sup>n</sup>Bu)<sub>3</sub> and Nb(O<sup>n</sup>Bu)<sub>5</sub>, and 500 mM for Si(OMe)<sub>4</sub>. Proper solvent and adsorption conditions were chosen for each metal alkoxide.

b) Concentration of polymers is 1 mg/mL.

When PDDA is used, the Cl/N ratio decreases with increasing pH. The negative charge on the  $\text{TiO}_2$ -gel surface increases in basic conditions, neutralizing more effectively the positive charge of the polymer.

Zirconium butoxide ( $\text{Zr}(\text{O}^n\text{Bu})_4$ ), indium methoxyethoxide ( $\text{In}(\text{OEtOMe})_3$ ), and tetramethoxysilane ( $\text{Si}(\text{OMe})_4$ ) give QCM frequency changes of 68–84 Hz. The frequency change for PDDA is a little smaller when alternately adsorbed with  $\text{In}(\text{OEtOMe})_3$  (49 Hz), and is ca. 100 Hz in the case of  $\text{Zr}(\text{O}^n\text{Bu})_4$  and  $\text{Si}(\text{OMe})_4$ . The thickness increases per cycle are in the range of 2.0–3.0 nm. The surfaces of PDDA/ $\text{ZrO}_2$ -gel and PDDA/ $\text{In}_2\text{O}_3$ -gel films have roughness of a few tenths of a nanometer. Their XPS data show the Cl(or Br)/N ratio of 0.13–0.23 in all three cases, indicating that electrostatic neutralization between PDDA and the metal oxide gel layer occurs as in the case of PDDA/ $\text{TiO}_2$ -gel composite film. Since the reactivity of aluminum butoxide ( $\text{Al}(\text{O}^n\text{Bu})_3$ ) is relatively low, the reaction temperature is set at 45°. Then, regular film growth is observed with frequency shifts of  $161 \pm 108$  Hz for  $\text{Al}(\text{O}^n\text{Bu})_3$  and  $100 \pm 23$  Hz for PDDA. The film had many wrinkles ca. 100 nm high over a wide area, as observed by SEM.  $\text{Al}(\text{O}^n\text{Bu})_3$  seems not to be particularly suitable for forming uniform composite films. In contrast, the reactivity of niobium butoxide ( $\text{Nb}(\text{O}^n\text{Bu})_5$ ) is very high, giving a frequency change of  $510 \pm 82$  Hz on the surface of PDDA. The PDDA/ $\text{Nb}_2\text{O}_5$ -gel film has a fairly smooth surface, as confirmed by SEM. The thickness increase per adsorption cycle is 23 nm.

The highly charged surface of the metal oxide gel layer electrostatically absorbs cationic polymers. The resulting polymer layer is approximately 1 nm thick, and can absorb metal alkoxides. The composite film formed may not necessarily assume a multilayer structure. A more plausible morphology may be a partially interpenetrated structure of both components, as seen in the electrostatic alternating adsorption of oppositely charged polymers [15]. In any event, nanocomposites of polymers and metal oxides at the molecular level will bring about superior mechanical properties. Furthermore, optical and electronic characteristics of metal oxides may be altered by proper selection of polymers.

### 6.1.3

#### Multilayer Assembly of Metal Oxides and Proteins

Multilayer assemblies of water-soluble proteins have been developed by the above-mentioned technique. Cytochrome c (Cyt.c) is a globular protein performing electron transfer in several biological systems. The protein has a size of  $2.5 \times 2.5 \times 3.7 \text{ nm}^3$ , a molecular weight of 12000–13000, and an isoelectric point (pI) of 10 [16]. Many of the basic amino acid residues on the protein surface are positively charged at neutral pH. A clean quartz plate was immersed in 100 mM  $\text{Ti}(\text{O}^n\text{Bu})_4$  (in toluene/ethanol, 1/1) for 3 min, then rinsed in organic solvent and hydrolyzed in water. Then the substrate was immersed in a Cyt.c solution (1 mg  $\text{ml}^{-1}$  in water) for 3 min, and rinsed with pure water. Fig. 6.6 shows UV–vis absorption changes upon repeated adsorption cycles. The peak intensity at 409 nm, attributed to the heme unit of Cyt.c, regularly increases, at least up to 13 cycles. It

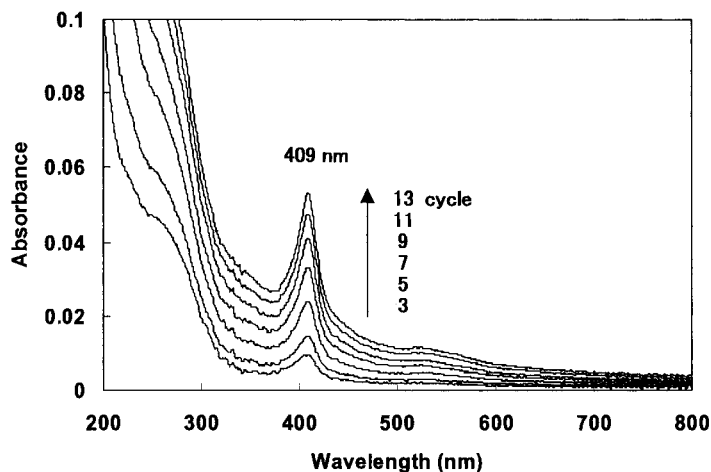


Fig. 6.6 UV-vis absorption changes due to alternate adsorption of cytochrome c and  $\text{Ti}(\text{O}^i\text{Bu})_4$ .

is apparent that a fixed amount of Cyt.c is adsorbed on each cycle. The amount of Cyt.c was calculated from the molar extinction coefficient ( $\epsilon$ :  $106 \text{ mM}^{-1} \text{ cm}^{-1}$ ) and the absorbance change at 409 nm (absorption change; 0.0046 per cycle) as  $0.13 \text{ molecule nm}^{-2}$ . Assuming that spherical Cyt.c of 3 nm diameter is adsorbed uniformly in hexagonal packing, the protein density should be  $0.128 \text{ molecule nm}^{-2}$ . The agreement of the experimental and calculated values of protein density supports the fact that adsorbed Cyt.c forms a monolayer. It is worth noting that the absorption maximum (409 nm) of Cyt.c in a Cyt.c/ $\text{TiO}_2$ -gel multilayer is the same as that of native Cyt.c in water. This means that the environment surrounding the heme is not altered in the protein incorporated in the multilayer assembly.

Fig. 6.7 shows QCM frequency shifts of the alternating adsorption of  $\text{Zr}(\text{O}^n\text{Pr})_4$  (100 mM in propanol) and Cyt.c ( $1 \text{ mg ml}^{-1}$  in water), where the pH of the protein solution is adjusted to 4.0, 7.0, and 10.0. The linear frequency decrease indicates regular growth of Cyt.c/ $\text{ZrO}_2$ -gel composite films in all cases. Average QCM frequency changes due to Cyt.c adsorption are  $33 \pm 25 \text{ Hz}$  for pH 4 solution,  $168 \pm 30 \text{ Hz}$  at pH 7, and  $114 \pm 44 \text{ Hz}$  at pH 10. Frequency changes due to  $\text{Zr}(\text{O}^n\text{Pr})_4$  adsorption are  $34 \pm 48 \text{ Hz}$  (pH 4),  $35 \pm 23 \text{ Hz}$  (pH 7), and  $6 \pm 31 \text{ Hz}$  (pH 10). The thickness of the  $\text{ZrO}_2$ -gel layer varies widely, depending on the pH of the Cyt.c solution.

Adsorption of Cyt.c is low at pH 4 probably due to fewer negative charges on the  $\text{ZrO}_2$ -gel layer. On the other hand, the adsorption of Cyt.c is not large at pH 10 in comparison with the case of pH 7, even though the  $\text{ZrO}_2$ -gel is highly negatively charged. This must be caused by smaller positive charges on Cyt.c near the isoelectric point. Cyt.c adsorption becomes maximal under neutral conditions, in which both components, Cyt.c and  $\text{ZrO}_2$ -gel, can be oppositely charged. It is



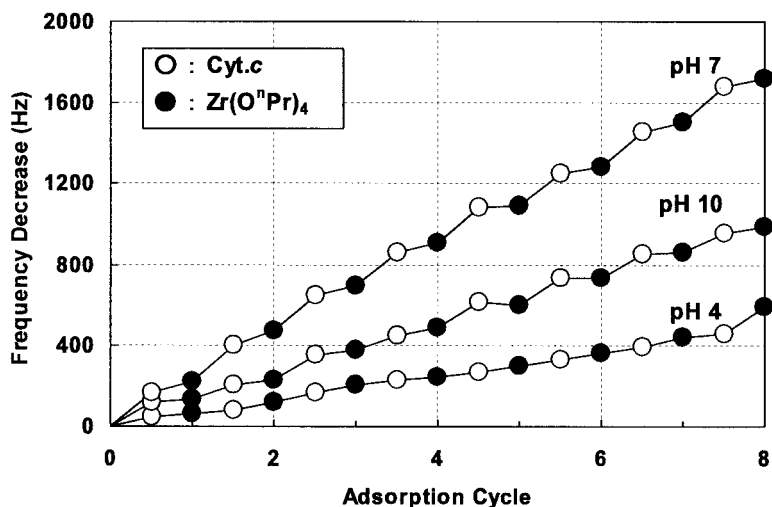


Fig. 6.7 QCM frequency changes due to alternate adsorption of Cyt.c and  $Zr(O^iPr)_4$ .

clear that the electrostatic factor is dominant in these assembly processes. We have reported that linear polymers with carboxyl groups, such as poly(acrylic acid) (PAA), adsorb strongly on metal oxide gel surfaces. In an analogous fashion, the carboxyl group of the Cyt.c molecule may also provide additional binding sites for the  $ZrO_2$ -gel layer.

Fig. 6.8c (s. page 166) shows scanning electron micrographs of Cyt.c/ $ZrO_2$ -gel composite films. All the samples are coated with 2 nm thick platinum to prevent charge buildup by the electron beam. Numerous granular structures of diameter 20 nm are observed on the surface of the film formed from the pH 4 Cyt.c solution, as shown in Fig. 6.8a. These structures are probably caused by aggregation of the protein. In sharp contrast, the film formed from the Cyt.c solution of pH 10 has a very smooth surface over a wide area (Fig. 6.8c). While some spherical aggregates are observed, the film is mostly smooth for the case of pH 7 (Fig. 6.8b). Fig. 6.8d shows a cross-sectional view of the film (pH 7). The composite film located on a gold electrode has a thickness of  $120 \pm 15$  nm. Since the film was obtained by repeating the adsorption of Cyt.c and  $Zr(O^iPr)_4$  for 50 times, the thickness increase per cycle can be estimated to be 2.4 nm. This value agrees with the molecular size of Cyt.c (2–3 nm in diameter). However, UV measurements revealed that the amount of Cyt.c in the composite film is 1.4 times larger than expected for monolayer adsorption. This increment must arise from the formation of globular aggregates on the film surface. The amount of the protein incorporated in the film reaches about 80 wt.% of the total film weight, as estimated by QCM measurements. Adsorption modes of Cyt.c on the  $ZrO_2$ -gel layer are schematically illustrated in Fig. 6.9. Cyt.c adsorption at pH 10 is rather small in comparison with the case of pH 7. The protein coverage is 63%, as estimated by UV adsorption. The film has an extremely smooth surface. On the other hand, the low charge density of a  $ZrO_2$ -gel layer at

pH 4 tends to generate granular structures on the film surface, and gives protein coverage of less than 20%. Such low coverage is probably attributed to the weak electrostatic interaction of Cyt.c and the  $\text{ZrO}_2$ -gel layer.

Nanocomposite films of proteins and metal oxides can be prepared by combining the surface sol-gel process with electrostatic adsorption of positively charged proteins. It is clear that the ultrathin metal oxide gel layer is an excellent substrate for the two-dimensional arrangement of proteins. Such novel combinations of biomolecules and metal oxides are expected to give rich applications in separation, biosensing, and the preparation of biocompatible materials.

#### 6.1.4

#### **Protein/Polyelectrolyte Multilayer Assembly**

Protein multilayers can be prepared by electrostatic alternating adsorption of linear polyelectrolytes and oppositely charged proteins. The preparative details have been reported in other papers and reviews [3, 17]. In this technique, water-soluble polymers are used without limitation as long as they possess charges opposite to those of the proteins. For example, linear cationic polymers such as poly(allylamine) (PAH), poly(ethyleneimine) (PEI), poly(dimethyldiallylammonium chloride) (PDDA), and anionic polymers such as poly(styrenesulfonic acid) (PSS) and poly(anilinesulfonic acid) (PANPS), and biopolymers like DNA are employed. Inorganic sheets like clay minerals are also useful for alternating assembly with proteins.

Experimental results of protein/polyion alternate multilayer assembly are summarized in Tab. 6.2. Cyt.c, positively charged in aqueous solutions at pH 4.5, can be adsorbed alternately with negatively charged PSS. Mass increases due to Cyt.c adsorption on the PSS layer have been estimated by QCM measurements to be  $3.6 \text{ mg m}^{-2}$ , which corresponds to a thickness increase of 2.4 nm. The thickness increase for the PSS adsorption step is 1.6 nm. Lysozyme, histone, and myoglobin produce alternating layers with PSS in a similar way. In contrast, cationic polymers are employed for the alternating adsorption of negatively charged proteins such as bacteriorhodopsin, albumin, and glucoamylase, which have isoelectric points in the acidic region. The alternating adsorption with polyelectrolytes is not restricted by the molecular weight of proteins, and is applicable to huge proteins such as IgG ( $M_w$ : 150 000) and Diaphorase ( $M_w$ : 600 000). In most cases, thickness increases for protein adsorption are roughly consistent with the size of the proteins. A schematic illustration of protein multilayer assembly is shown in Fig. 6.10. As mentioned below, positively charged glucose oxidase (GOD) and negatively charged peroxidase (POD) can be alternately adsorbed on a substrate in combination with oppositely charged polymers such as poly(styrenesulfonic acid) and poly(ethyleneimine), respectively.

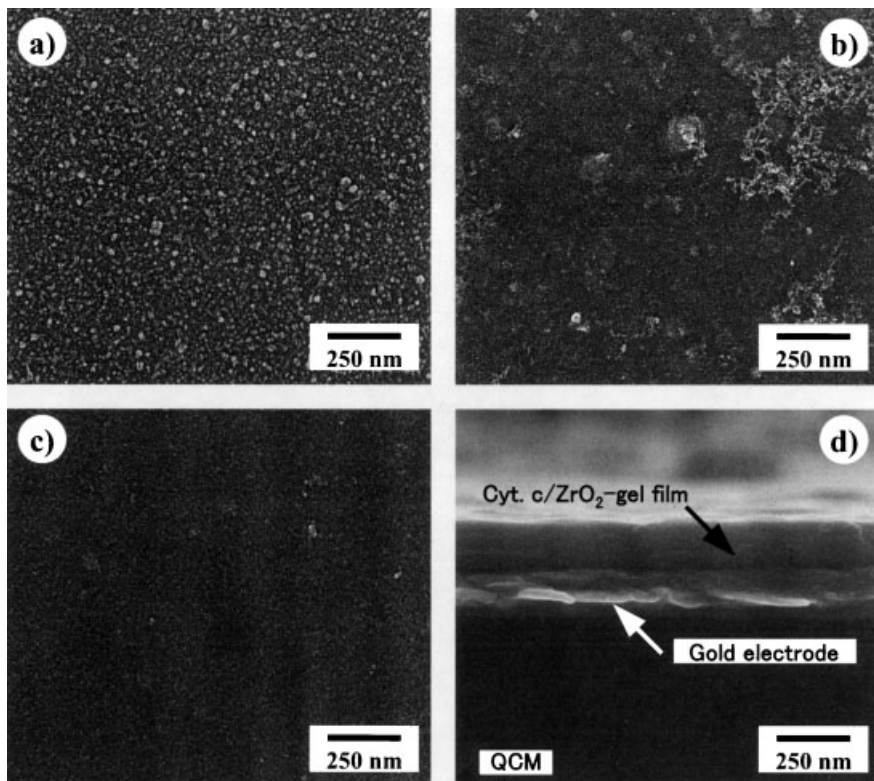


**Fig. 6.8** SEM images of Cyt.c/ZrO<sub>2</sub>-gel multilayer films assembled by using Cyt.c solutions of pH 4.0 (a), pH 7.0 (b), and pH 10.0 (c) and a cross-sectional view of the composite film of pH 7 (d).

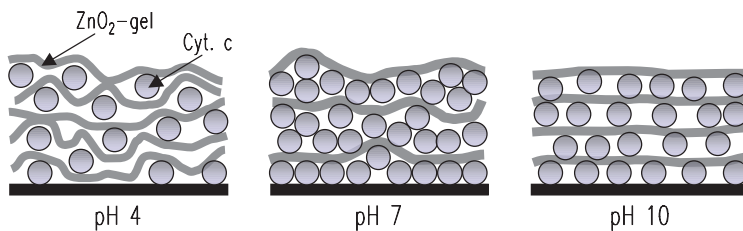


**Fig. 6.9** Schematic representations of Cyt.c/ZrO<sub>2</sub>-gel multilayer films assembled by using Cyt.c solutions of pH 4.0, pH 7.0, and pH 10.0.

Tab. 6.2 Protein/polyelectrolyte alternate multilayer assembly

Protein	Molecular weight	Isoelect. point	pH used	Counter-polymer	Protein mass coverage ( $\text{mg}/\text{m}^2$ )	Thickness of protein + polymer bilayer (nm)	Protein size (nm)
Cytochrome c	12 400	10.1	4.5	PSS <sup>-</sup>	3.6	2.4+1.6	2.5×2.5×3.7
Lysozyme	14 000	11	4	PSS <sup>-</sup>	3.5	2.3+1.9	3.0×3.0×4.5
Histone f3	15 300	11	7	PSS <sup>-</sup>	3.3	2.2+2.0	3.4 (diameter)
Myoglobin	17 800	7.0	4.5	DNA, PSS <sup>-</sup>	6	4.0+2.0	2.5×3.5×4.5
Bacteriorhodopsin	26 000	6	9.4	PDDA <sup>+</sup>	7.5	5.0+1.0	5.0 (diameter)
Carbonic anhydrase	29 000	5.5	8.3	PEI <sup>+</sup>	2.8	2.2 (bilayer)	1.5×2.2×2.5
Pepsin	35 000	1	6	PDDA <sup>+</sup>	4.5	3.0+0.6	3.0 (diameter)
Peroxidase	42 000	8.0	4.2	PSS <sup>-</sup>	5.3	3.5 (bilayer)	3.5 (diameter)
Hemoglobin	64 000	6.8	4.5	PSS <sup>-</sup>	26	17.5+3.0	5.0×5.5×6.5
			9.2	PEI <sup>+</sup>	27	18.2 (bilayer)	
Albumin	68 000	4.9	8	PDDA <sup>+</sup>	23	16.0+1.0	11.6×2.7×2.7
Glucoamylase	95 000	4.2	6.8	PDDA, PEI <sup>+</sup>	4	2.6+0.5	6.3 (diameter)
Photosynt. RC	100 000	5.5	8	PDDA <sup>+</sup>	13	9.0+1.0	13×7.5×4.0
Concanavalin	104 000	5	7	PEI <sup>+</sup>	8.6	5.7+0.8	3.9×4.0×4.2
Alcohol dehydrogenase	141 000	5.4	8.5	PDDA <sup>+</sup>	12.2	8.5+1.0	9.0×4.0×4.0
IgG	150 000	6.8	7.5	PSS <sup>-</sup>	15	10.0 (bilayer)	14×10×5
Glucose oxidase	186 000	4.1	6.8	PDDA <sup>+</sup>	12	8.0 (bilayer)	8 (diameter)
Catalase	240 000	5.5	9.2	PEI <sup>+</sup>	9.6	6.4+0.8	9.0 (diameter)
Diaphorase	600 000	5	8	PEI <sup>+</sup>	31	21.0 (bilayer)	11.5 (diameter)

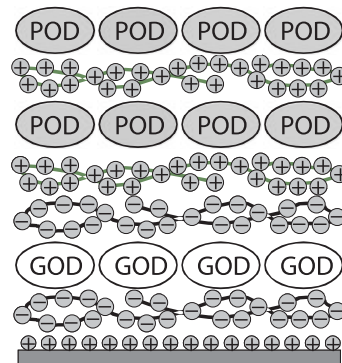


Fig. 6.10 A schematic illustration of a protein/polymer multilayer assembly.

## 6.2

### Recent Topics in Biological Applications

The surface sol–gel process is a superior method for the preparation of metal oxide gel films with nanometer thickness control. This technique enables one to introduce various organic molecules, inorganic clusters, polymers, and biomolecules into ultrathin oxide gel films. Metal oxide gel layers are capable of not only covalently binding hydroxyl and carboxyl groups of organic molecules but also of electrostatically binding positively charged macromolecules. The latter capability is a useful alternative to polyelectrolyte multilayers that have been studied extensively for water-soluble polymers and biomolecules. In this section, we describe recent progress in applications of ultrathin nano-composite films to biochemical problems.

#### 6.2.1

##### Biosensors

Molecular recognition is one of the main principles that sustain the biological process. Ultrathin metal oxide films have been used as a matrix for molecular imprinting because they can memorize the size and shape of small molecules. This capability was extended to the imprinting of protected amino acids [13].

Ti(O<sup>n</sup>Bu)<sub>4</sub> and carbobenzyloxy-L-alanine (Cbz-L-Ala) were mixed in organic solvents, followed by the addition of a small amount of water, and stirred for a few hours. This mixture was subjected to the surface sol–gel process to form a Cbz-L-Ala/TiO<sub>2</sub>-gel composite film on a QCM electrode. Uniform film growth was observed up to at least 15 cycles with frequency shifts of 140 to 160 Hz per cycle. The template molecule, Cbz-L-Ala, was removed from the gel film by dipping in 1 wt.% aqueous ammonia. The resulting film shows selective binding for protected amino acids. In situ QCM frequency changes for re-binding of the original template and other guest molecules are shown in Fig. 6.11. The binding is rapid and saturates in 30 to 60 s. Among the amino acid derivatives employed, Cbz-Gly showed the strongest binding (53 Hz) and the extent of binding became suppressed with increasing size of the side chain. It is noteworthy that the original template, Cbz-L-Ala (43 ± 3 Hz), is less efficiently bound than the smaller Cbz-Gly. However, the binding efficiency is not determined solely by the size of the guest molecules. For example, adamantane-1-carboxylic acid, 1-AdCO<sub>2</sub>H, gave much weaker binding than all the amino acid derivatives. Organic carboxylic acids such as benzoic acid and cinnamic acid also gave relatively low binding efficiencies. Imprinted TiO<sub>2</sub>-gel film memorizes the shape of the template molecule. The film appears to achieve such precise recognition through coordination bonds, hydrogen bonds, hydrophobic interactions, and shape selectivity, as illustrated in Fig. 6.11 b.

More recently, molecular imprinting was applied to a field-effect transistor (FET) device that is highly sensitive to the change in the surface potential [18]. A mixture of titanium alkoxide and chloroaromatic acetic acid was deposited onto an ion-sensitive FET device with a SiO<sub>2</sub> gate. The sol–gel polymerization resulted in a TiO<sub>2</sub>-gel film with the embedded carboxylate. Treatment of the composite film

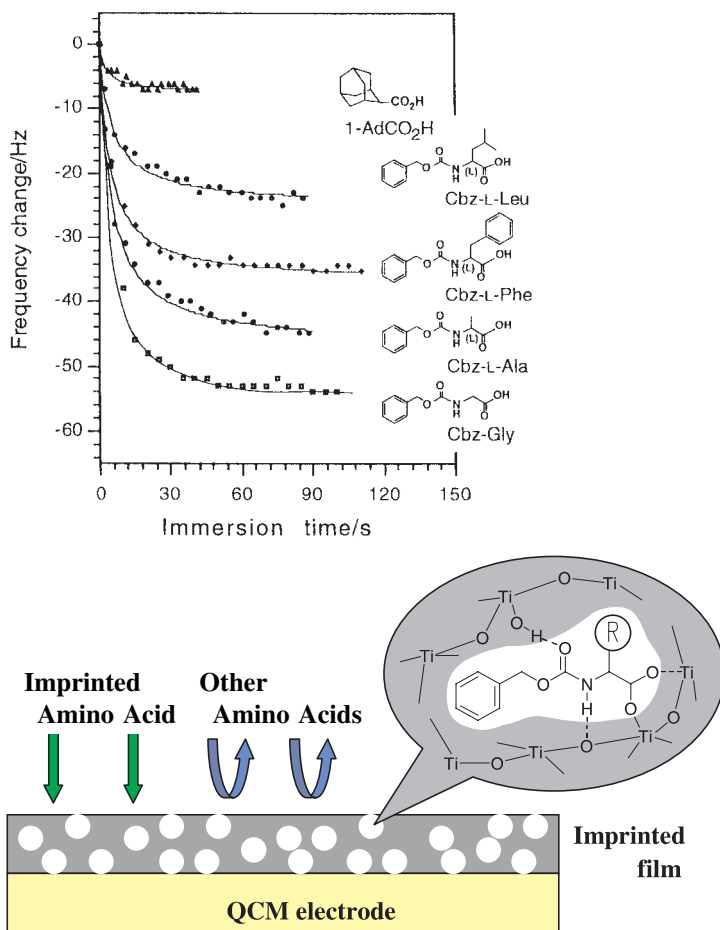


**Fig. 6.11** In situ QCM frequency decreases due to binding of a series of guest molecules in a TiO<sub>2</sub>-gel imprinted with Cbz-L-Ala (above) and a schematic illustration of a QCM biosensor (below).

with aqueous ammonia resulted in the elimination of the carboxylic acid. The hydroxytitanate residue of the imprinted film undergoes deprotonation and the resulting negative charge on the SiO<sub>2</sub> gate interface affects its potential. Rebinding of the carboxyl compounds generates a titanium ester that depletes the hydroxyl function and reduces the negative charges on the gate interface. The gate-source voltage is significantly changed by rebinding. The lowest limit of detection of the device is ca.  $1.0 \times 10^{-5}$  M for aromatic acetic acids. The high selectivity of the sensing is attributed to the large equilibrium constant for the complexation of imprinted TiO<sub>2</sub>-gel and the template molecule.

## 6.2.2

**Nano-filtration**

The fabrication of ultrathin cross-linked polymer films has been actively studied because of its prospects for high mechanical strength and designable separation properties for molecules and nano-materials. Ultrathin films prepared by covalent connection of individual layers in polyelectrolyte multilayers appear suitable for this purpose [19], and cross-linking of a multilayer assembly of poly(allylamine) (PAH) and (methyl vinyl ether)-alt-(monomethyl maleate) copolymer (MMC) was examined [20]. In alternating adsorption of these weak polyelectrolytes the thicknesses of the individual layer are strongly dependent on the pH of the polymer solutions. This feature was used to control the composition of polyelectrolyte multilayers. For instance, when PAH solution of pH 6 ( $1 \text{ mg ml}^{-1}$ , in pure water) and MMC solution of pH 7 ( $1 \text{ mg ml}^{-1}$ , in potassium phosphate buffer) are assembled

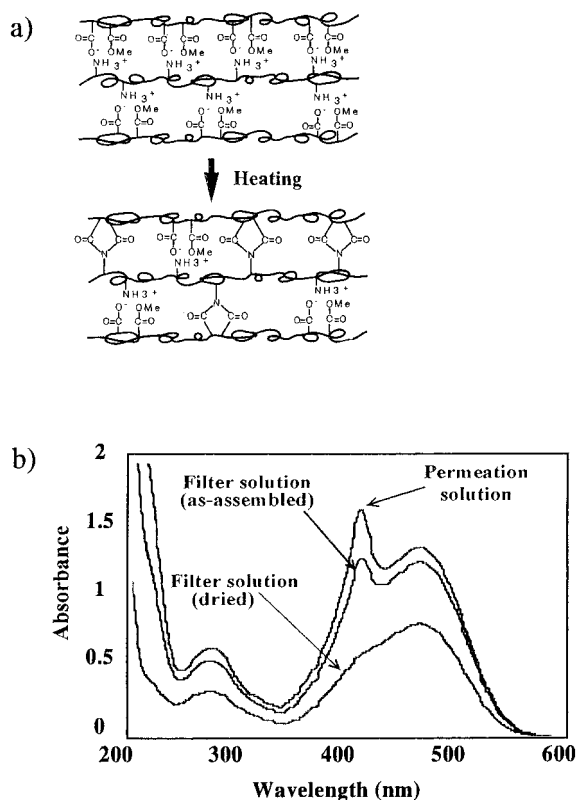


**Fig. 6.12** A schematic illustration of cross-linking of a PAH/MMC multilayer assembly (a) and UV–Vis absorption spectra of myoglobin/Methyl Orange mixture and the filtered solutions through a PAH/MMC film (b).

on a QCM electrode, the thickness increases for PAH and MMC were 2.5 nm and 0.8 nm, respectively, from QCM frequency changes. The composition of the two polymers was PAH/MMC=11, as confirmed by XPS measurements. When PAH solution of pH 6 and MMC solution of pH 8 were used, the thickness of the PAH and MMC layers were 1.7 nm and 0.9 nm, respectively, with the composition of PAH/MMC=7.

Upon heating the PAH/MMC multilayer films at 125 ° for 12 h under reduced pressure, the amino group of PAH and the maleic acid moiety of MMC formed imide bonds, and highly cross-linked ultrathin films were obtained (Fig. 6.12). In the course of the cross-linking, the IR peak intensity of the methyl ester of MMC (1739  $\text{cm}^{-1}$ ) weakened, and characteristic peaks of the imide unit (1774, 1850  $\text{cm}^{-1}$ ) appeared. Imide formation was also confirmed by XPS spectra. The N 1s peaks due to ammonium nitrogen (401.3 eV) and free amine (398.9 eV) of PAH were weaker, and the peak of imide nitrogen (400 eV) intensified following heating. From these data, the extent of imide conversion was estimated to be 50% of the amino groups of PAH. Interestingly, the imide conversion proceeds slowly, even at room temperature. The film assembled by electrostatic alternating adsorption is composed of polymer layers with molecular thickness, and contains carboxylate/ammonium ion pairs. This pre-organization is favorable for efficient imide formation at elevated and room temperatures.

We carried out permeation experiments in order to examine the network properties of the cross-linked PAH/MMC film. First, one side of a polycarbonate membrane filter with pores of diameter 0.2  $\mu\text{m}$  was covered with 2 nm thick platinum layer, and was treated with 3-mercaptopropionic acid. The negatively charged surface was immersed into PAH solution (1  $\text{mg ml}^{-1}$ ; pH 10) for 5 min, and rinsed with hydrochloric acid (pH 3). Then, the membrane filter was immersed in PSS solution (3  $\text{mg ml}^{-1}$ ; pH 3) for 5 min, and rinsed with pure water. After repeating these procedures four times, all the pores of the membrane filter were covered by PAH/PSS multilayer. Subsequently, the membrane filter was immersed alternately in PAH solution (1  $\text{mg ml}^{-1}$ , pH 6) and in MMC solution (1  $\text{mg ml}^{-1}$ , pH 7) for four cycles, and subjected to permeation experiments at a constant pressure.

An aqueous mixture of myoglobin (12.5  $\mu\text{M}$ ) and methyl orange (0.1 mM) was selected as a permeation solution. Myoglobin and Methyl Orange have absorption peaks at 410 nm and 463 nm, respectively. Fig. 6.12b shows UV-Vis spectra of permeation solution and filter solution. The as-assembled film shows a high permeability at a pressure of 1.5  $\text{kg cm}^{-2}$ . The permselectivity is not very high, since 78% of myoglobin permeated against 90% of Methyl Orange. Interestingly, permselectivity was enhanced and permeability diminished after drying this film for one week at room temperature. Then, myoglobin was detected only as a shoulder of the Methyl Orange peak, as filtered at 3.0  $\text{kg cm}^{-2}$ . When two-fifths (by volume) of the solution was filtered, the myoglobin concentration in the permeation solution increased by 20% against the original solution. Myoglobin is an elliptical molecule of 3–4 nm in diameter, and the molecular length of Methyl Orange is ca. 2 nm. The porous multilayer can discriminate between these sizes.



## 6.2.3

**Bioreactors**

Most of the sophisticated functions in biological systems are derived from the cooperative mechanism of spatially organized proteins. Typical examples are found in the light-harvesting system of photosynthesis and in sequential reactions in multi-enzyme systems [21]. Layer-by-layer adsorption of proteins has advantages for fabrication of two-dimensional assemblies of water-soluble proteins with a view to designing artificial biochemical systems.

Glucose oxidase (GOD) and poly(ethyleneimine) (PEI) were alternately adsorbed on a glass substrate, and followed by alternate adsorption of peroxidase (POD) and poly(styrenesulfonic acid) (PSS). When the substrate was immersed into an aqueous solution of DA67 dye and glucose, the solution turned blue because of oxidation of the DA67 dye. GOD can catalyze oxidation of glucose to gluconolactone to generate hydrogen peroxide as a product. The hydrogen peroxide is decomposed by POD, and simultaneously DA67 is oxidized to the blue colored oxidant. That is to say, sequential redox reactions of glucose,  $\text{H}_2\text{O}_2$ , and DA67 are achieved by the combination of GOD and POD. Activities of these enzymes are not lost in the multilayer assembly.

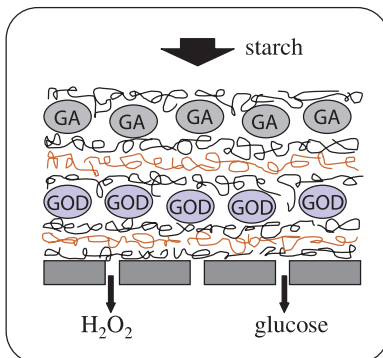
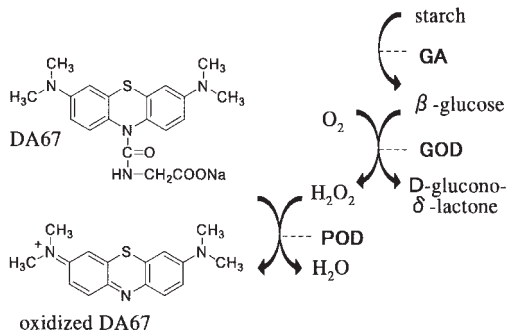


**Fig. 6.13** Sequential enzymatic process based on glucoamylase (GA) and glucose oxidase (GOD) and its experimental setup.

An enzyme multilayer was prepared on a membrane filter [22]. A PEI/PSS precursor film was assembled on an ultrafiltration membrane (Molcut II LC, 5 kDa). Subsequently, a PEI/GOD multilayer, an intermediate layer, and then a multilayer of PEI and glucoamylase (GA) that catalyzes decomposition of starch to glucose were assembled in this order. The resulting film has an internal structure of [filter + (PEI/PSS)<sub>4</sub> + (PEI/GOD)<sub>2</sub> + (PEI/PSS)<sub>10</sub> + (PEI/GA)<sub>2</sub> + PEI]. The enzymatic activity of this film was examined using the experimental setup shown in Fig. 6.13. An aqueous solution of “water-soluble starch” was employed for the permeation solution. As illustrated in Fig. 6.13, GA decomposes starch to glucose, and GOD converts glucose to gluconolactone and generates hydrogen peroxide as the product. Concentrations of hydrogen peroxide and glucose in the filtered solution were determined by monitoring the coloring reaction of DA67 dye in both POD alone and in POD–GOD mixed solutions.

Under these experimental conditions, the molar ratios of glucose and H<sub>2</sub>O<sub>2</sub> in the filtrate are 59/41. This means that about 40% of the glucose produced by the GA layer was converted to H<sub>2</sub>O<sub>2</sub> by the GOD layer. The efficiency of the conversion of glucose to H<sub>2</sub>O<sub>2</sub> was affected by the thickness of the PEI/PSS intermediate layer, flow rate, and starch concentration.

#### 6.2.4

#### Protein Capsule and Protein Shell

The immobilization of protein/polyion multilayers is not limited to solid substrates and membrane filters. Various chemical and biological applications are anticipated if the protein multilayer is applied to surfaces of tubes, fibers, colloidal particles, molecular aggregates, and the stationary phase of column chromatography.

The coating of negatively charged latex particles with positively charged linear polymers is straightforward [23]. In general, excess polymer is added to suspensions of the aqueous latex, and the mixture is allowed to stand until the adsorption saturates. Isolation of the polymer-coated latex is carried out by ultracentrifugation (generally, 10 min at 10000 G for 400 nm diameter cores). Polyelectrolyte multilayers surrounding the latex are obtainable by repeated adsorption of oppositely charged polymers and subsequent ultracentrifugation. Proteins are readily incorporated into the shell of the polyelectrolyte (Fig. 6.14).

Stable hollow capsules are also obtainable by removal of the core from the above core/shell particles, making encapsulation of proteins feasible. For example,

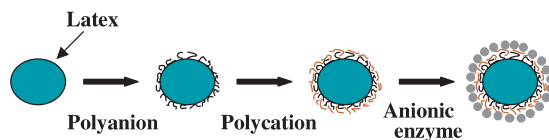
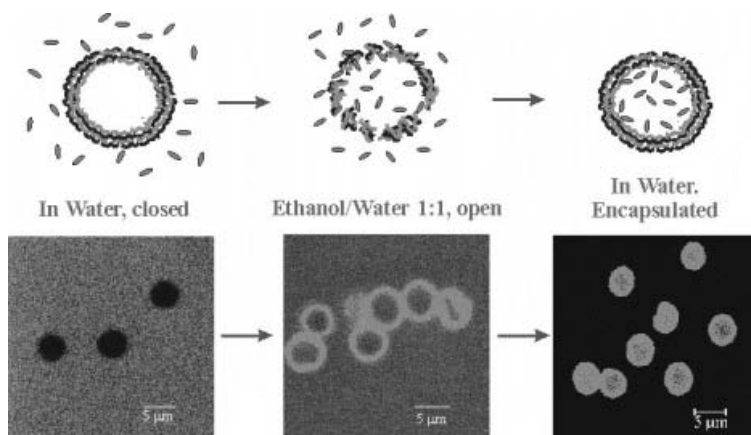


Fig. 6.14 Enzyme assembly on a spherical microtemplate coated with a polyion multilayer.



**Fig. 6.15** Permeation and encapsulation of urease-FITC into polyion multilayer capsules in water (left) and in water/ethanol 1:1 mixture (middle) and encapsulated urease (right).

PAH and PSS were alternately assembled on melamine–formaldehyde microparticles (5  $\mu\text{m}$ ) for four cycles, and the core particle was decomposed at pH 1. The obtained capsule is non-permeable against large molecules dissolved in water, but becomes permeable in a water/ethanol mixture. We examined loading of proteins into the hollow capsule by using urease that was labeled with fluorescent dye, fluorescein-4-isothiocyanate (FITC) [24]. The confocal fluorescence image in Fig. 6.15 (left) shows that FITC-labeled urease is excluded from the core by the polyelectrolyte shell. The interior of the capsule remains dark and the background containing FITC-urease is fluorescent outside the capsule. The center image shows the capsule after addition of ethanol to give a 1:1 water ethanol mixture. In this case, the fluorescence coming from the interior of the capsule is the same as the outside background fluorescence, indicating penetration of the protein into the capsule. The transition between the open and closed states of the polyelectrolyte multilayer capsule due to ethanol addition is reversible. When the capsule is transferred into water, the polyion shell becomes closed to urease molecules.

The mechanism of the reversible permeability change is not yet fully understood. It may be related to segregation and/or expansion of the polyion network in water/ethanol media. Such changes can lead to defects in the shell, and pores big enough to pass 5 nm urease molecules. These results can be applied to fabrication of enzymatic micro- and nanoreactors. In addition, if loaded enzymes are released out of the capsules under certain conditions (pH or salt concentration), the capsule could find some applications in drug delivery and sustained release.

## 6.3

## References

- 1 G. DECHER, J.D. HONG, J. SCHMITT, *Thin Solid Films* **1992**, 210–211, 831–835; G. DECHER, *Comprehensive Supramolecular Chemistry*, Pergamon Press, New York, **1996**, vol. 9, pp. 507–528.
- 2 T.M. Cooper, A.L. Campbell, R.L. Crane, *Langmuir*, **1995**, 11, 2713–2718; K. ARIGA, Y. LVOV, T. KUNITAKE, *J. Am. Chem. Soc.* **1997**, 119, 2224–2231.
- 3 S.W. KELLER, H.-N. KIM, T.E. MALLOUK, *J. Am. Chem. Soc.* **1994**, 116, 8817–8818; Y. LVOV, K. ARIGA, I. ICHINOSE, T. KUNITAKE, *J. Am. Chem. Soc.*, **1995**, 117, 6117–6123.
- 4 M. CAO, X. ZHANG, B. YANG, F. LI, J. SHEN, *Thin Solid Films* **1996**, 284/285, 242–245.
- 5 E.R. KLEINFELD, G.S. FERGUSON, *Science* **1994**, 265, 370–373.
- 6 I. ICHINOSE, K. FUJIYOSHI, S. MIZUKI, Y. LVOV, T. KUNITAKE, *Chem. Lett.* **1996**, 257–258.
- 7 W.B. STOCKTON, M.F. RUBNER, *Macromolecules*, **1997**, 30, 2717–2725.
- 8 Y. SHIMAZAKI, M. MITSUISHI, S. ITO, M. YAMAMOTO, *Langmuir* **1997**, 13, 1385–1387.
- 9 Y. LVOV, K. ARIGA, I. ICHINOSE, T. KUNITAKE, *J. Chem. Soc., Chem. Commun.* **1995**, 2313–2314.
- 10 T. SERIZAWA, K. HAMADA, T. KITAYAMA, N. FUJIMOTO, K. HATADA, M. AKASHI, *J. Am. Chem. Soc.* **2000**, 122, 1891–1899.
- 11 I. ICHINOSE, H. SENZU, T. KUNITAKE. *Chem. Lett.* **1996**, 831–832; I. Ichinose, H. Senzu, T. Kunitake. *Chem. Mater.* **1997**, 9, 1296–1298.
- 12 I. ICHINOSE, T. KAWAKAMI, T. KUNITAKE, *Adv. Mater.* **1998**, 10, 535–539.
- 13 S.-W. LEE, I. ICHINOSE, T. KUNITAKE, *Langmuir* **1998**, 14, 2857–2863; S.-W. Lee, I. Ichinose, T. Kunitake, *Chem. Lett.* **1998**, 1193–1194.
- 14 R.A. HABERKORN, L. QUE, W.O. GILLUM, R.H. HOLM, C.S. LIU, R.C. LORD, *Inorg. Chem.* **1976**, 15, 2408–2414.
- 15 G. DECHER, *Science* **1997**, 277, 1232–1237.
- 16 F.S. MATHEWS, *Prog. Biophys. Mol. Biol.* **1985**, 45, 1–56.
- 17 Y. LVOV and H. MÖHWALD, *Protein Architecture: Interfacial Molecular Assembly and Immobilization Biotechnology*. Marcel Dekker, New York, **2000**.
- 18 M. LAHAV, A.B. KHARITONOV, O. KATZ, T. KUNITAKE, I. WILLNER, *Anal. Chem.* **2001**, 73, 720–723.
- 19 B. TIEKE, F. V. ACKERN, L. KRASEMANN, A. TOUTIANOUSH, *Euro. Phys. J. E* **2001**, 5, 29–39.
- 20 I. ICHINOSE, S. MIZUKI, S. OHNO, H. SHIRAISHI, T. KUNITAKE, *Polymer J.* **1999**, 31, 1065–1070.
- 21 M. ONDA, Y. LVOV, K. ARIGA, T. KUNITAKE, *Biotechnol. Bioeng.* **1996**, 51, 163–167.
- 22 M. ONDA, Y. LVOV, K. ARIGA, T. KUNITAKE, *J. Fermentation Bioeng.* **1996**, 82, 502–506.
- 23 Y. LVOV, A.A. ANTIPOV, A. MAMEDOV, H. MÖHWALD, G.B. SUKHORUKOV, *Nano Letters*, **2001**, 1, 125–128. E. DONATH, G. SUKHORUKOV, F. CARUSO, S. DAVIS, H. MÖHWALD, *Angew. Chem., Int. Ed. Engl.* **1998**, 37, 2202–2205; G. SUKHORUKOV, M. BRUMEN, E. DONATH, H. MÖHWALD, *J. Phys. Chem. B* **1999**, 103, 6434–6440; A. ANTIPOV, G. SUKHORUKOV, E. DONATH, H. MÖHWALD, *J. Phys. Chem. B* **2001**, 105, 2281–2284.
- 24 Y. LVOV, F. CARUSO, *Anal. Chem.* **2001**, 73, 4212–4217.

## 7

### Internally Structured Polyelectrolyte Multilayers

K. GLINEL, A. M. JONAS, A. LASCHEWSKY, and P. Y. VUILLAUME

#### Abstract

We report on the internal structure of a series of layer-by-layer (LBL) self-assembled polyelectrolyte films, mostly analyzed by X-ray reflectometry. Most binary (A/B)<sub>n</sub> systems based on organic polyelectrolytes do not form well-defined strata in LBL-films. However, we found a category of polycations giving rise to much better stratified (A/B)<sub>n</sub> multilayers: Stratification results from prestructuring of the polycations in the swollen layer adsorbed at the film/water interface, due to the formation of lamellar lyotropic mesophases. We compare the internal structure of such organic films with that of binary (A/B)<sub>n</sub> hybrid multilayers made from clay platelets and a large set of organic polycations. The main difference between these systems lies in the compliance of the lamellae and its consequences on ordering, which for organic systems may extend over very long ranges, or be destroyed completely during complexation in the film, while being limited to a few tens of Å for hybrid films. For both types of internally structured binary LBL films, there is no direct correspondence between the number of strata deposited and the number of dipping cycles and so it is impossible to control the composition of each stratum in turn. Therefore, other strategies have to be developed in order to design well compartmentalized assemblies allowing the confinement of functional molecules at precise positions within the stratified structure. This is possible by the construction of superlattices containing organic compartments of well-defined and tunable thickness separated by hybrid organic/inorganic barriers.

#### 7.1

##### Introduction

Nanoscale control of the structure of organic materials is a prerequisite to the fabrication of sophisticated organic functional devices. The ability to position chemical units precisely in these devices, and similarly to align or to orient them, allows one to fine tune the function of such (macro)molecular assemblies [1, 2]. Furthermore, as transfer mechanisms like electron tunneling or non-radiative energy transfer depend extremely on the distance between active centers in the range of a few Å

or nanometers [3, 4], positional control of functional groups must obviously be realized with a very high spatial resolution. In this respect, Nature excels in delicately knitting molecules at the nanoscale to provide elaborate functions, as illustrated, e.g., by light harvesting centers in photosynthetic bacteria [5, 6].

In this context, organic multilayers are particularly simple systems wherein nanoscale control of the structure in one direction is easily attainable. There are different ways to build organic or hybrid organic/inorganic multilayers, among which the Langmuir–Blodgett deposition technique [7] and chemical self-assembly [8] (using, e.g., functional silanes [9], thiols [10], or  $\alpha,\omega$ -biphosphonic acids [11]) were mostly known one decade ago. Layer-by-layer (LBL) self-assembly, also known as electrostatic self-assembly (ESA), is the most recent addition to this collection of techniques, and a very promising one indeed, owing to its versatility, simplicity and environmental friendliness [12, 13]. However, by contrast with older methods, LBL provides essentially amorphous films, with profuse interpenetration of neighbouring “layers” [13 e]. This may certainly be seen as one of the advantages of the technique, since it avoids defect propagation from layer to layer, a nagging problem of other multilayer construction techniques [14]. On the other hand, it remains to be assessed to what extent these traits, interpenetration of “layers” and amorphous chain conformations, may be compatible with true nanoscale control of film structure.

Before proceeding, one should define what will be considered here to be a nanostructured multilayer. We define a “*stratum*” as a lamellar spatial region of close to homogeneous composition, running parallel to a substrate, and bordered on each side by strata of different compositions. A structured multilayer is a collection of such strata stacked vertically, with limited interpenetration of successive strata (i.e., the thickness of a stratum should be much larger than the thickness of the transition region between strata). Nanostructured multilayers are made from strata thinner than about 10 nm, much thinner strata being desirable for reasons explained above. Of importance here is also the lateral extent of the strata; for reasons which will be discussed later, we consider that a stratum should run parallel to the substrate over several micrometers.

It is well-known that, in most films LBL-deposited from two organic polyelectrolytes only (i.e.,  $(A/B)_n$  systems), no strata can be defined: Due to profuse interpenetration of successively deposited A and B “layers”, the film composition appears homogeneous along the sample normal [13 a, 13 e]. The molecular-level blending of A and B polyelectrolytes [15] is unambiguously testified by the absence of Bragg reflections in the X-ray or neutron grazing-angle scattering by such films, even when every second “layer” is deuterated [16, 17 b, c]. There are, however, notable exceptions to this seemingly general rule [18], which are presented and discussed in Section 7.3 of this Chapter.

If one of the flexible organic macromolecules is substituted by a rigid and charged thin inorganic platelet (clay, zirconium phosphate,...),  $(A/B)_n$  hybrid organic/inorganic films displaying some stratification may also be obtained [19–26]. However, strata only exist very close to the substrate, stratification being lost for distances larger than a few nanometers from the substrate [27]. This is a general

characteristic of such hybrid films, irrespective of the type of materials used, as will be shown in Section 7.4.

In order to attain higher degrees of stratification, construction of superlattices of the  $\{(A/B)_m/(C/D)_p\}_n$ -type (or more complex sequences) is required, as was performed successfully by a series of workers in the field (see e.g. [20a, 25c, 25e, 28–48]). Studies on hybrid organic/inorganic superlattices, aiming at the control of strata formation while simultaneously decreasing the repeat period of the nanostructured films, are presented in Section 7.5. This strategy effectively allows one to obtain small organic 2D compartments separated by thin insulating inorganic barriers.

## 7.2

### Experimental Considerations

With the recent observation that linear variations of UV absorbance with the number of deposition cycles do not necessarily correspond to regular growth of a multilayer, but may instead be due to progressive lateral filling of incomplete layers [49], it becomes obvious that one may not deduce film microstructure (or even quality) from techniques only sensitive to the amounts of adsorbed polyelectrolytes (such as ellipsometry, UV or IR absorbance, quartz crystal microbalance, etc.). It is also unsafe to assume that the sequence of strata in a film coincides with the sequence of adsorption events. In addition, because the free surface and the film/substrate interface most probably differ in structure and composition from the core of the film [50, 51], surface characteristics of LBL-films, such as obtained from X-ray photoelectron spectroscopy (XPS), static secondary ion mass spectroscopy (SSIMS), contact angle measurements or atomic force microscopy (AFM) may not be used *alone* to deduce film structure. This in part results from the highly dynamic nature of polyelectrolyte adsorption and from the penetration of newly adsorbed polyelectrolyte “layers” into previously deposited “layers”.

Hence, a proper evaluation of the internal structure of LBL films requires resorting to high resolution but indirect techniques, such as X-ray diffuse scattering (XDS) to probe the lateral internal features of films, and X-ray (or neutron) reflectometry (XRR or NR) to probe composition fluctuations perpendicular to the interfaces. Transmission electron microscopy (TEM) may also provide structural information normal and parallel to the substrate. TEM images of transverse cuts of  $\{(A/B)_m/(C/D)_p\}_n$  films have been published [36], clearly showing the existence of strata in such films provided that  $m$  and  $p$  are large enough. Differential staining of one type of strata is required to obtain contrast, although electron energy loss spectroscopy may be used in the future to avoid staining. Although very appealing aesthetically, TEM suffers from the time-consuming preparation of the sample and from the limited number of substrates which are compatible with the method: Typically, films are deposited on polymers such as corona-treated poly(styrene) [36] or cellulose acetate [52] to allow microtoming of the sample. In addition, spatial resolution still seems insufficient to image the structure of multilayers having

small internal repeat periods. For instance, recent attempts to observe in our group the internal structure of hybrid clay/polyelectrolyte multilayers deposited on silicon substrates (having  $\sim 14 \text{ \AA}$  as internal repeat period) were unsuccessful, even with a high-resolution TEM (field emission gun, 200 kV acceleration voltage) and microtoming samples with focussed ion beams.

Provided that the substrates are flat and smooth enough, reflectometry techniques are currently among the most powerful methods of characterizing the internal structure of thin films. In this context, neutron reflectometry on films containing selectively deuterated layers  $\{(A/B)_m/(deuterated-A/B)_p\}_n$  and related systems) provides unique pieces of information about thickness and interpenetration of polyelectrolyte “layers” [16, 17, 43]. The very large difference between the scattering lengths of deuterium and hydrogen [53] is responsible for the unique sensitivity of neutron reflectometry to specific features of multilayers labeled at different locations. By contrast, X-ray reflectivity is sensitive to electron densities, which are rather close for most organic polyelectrolytes. It is thus a common belief that X-ray reflectometry may not reveal the internal structure of LBL-films, and the absence of Bragg reflections in most X-ray reflectograms of  $(A/B)_n$  multilayers is considered as supporting evidence for this statement. However, the absence of Bragg reflections does not result essentially from the weak electron density difference between most polyelectrolytes, but rather from the strong interpenetration of A and B “layers” in  $(A/B)_n$  films, which smooths out completely the compositional fluctuations. This is also evidenced by the absence of Bragg reflections in neutron reflectograms of  $(deuterated-A/B)_n$  multilayers and is also supported by the detection of Bragg peaks in the X-ray reflectograms of some organic  $\{(A/B)_m/(C/D)_p\}_n$  films [43 a, 54]. In Fig. 7.1, we present simulations of the X-ray reflectivity of  $\{(A/B)_1/(A/C)_1\}_6$  superlattices deposited on silicon wafers (reflectivities are presented vs.  $K_{z0}$ , the component perpendicular to the interface of the wavevector *in air*). The values of roughness for the air interface (12  $\text{\AA}$ ), internal roughness between A/B and A/C layer pairs (14  $\text{\AA}$ ), and thickness of an A/C layer pair (42  $\text{\AA}$ ) were taken from experimental values published for the poly(styrene sulfonate) (PSS)/poly(allyl amine hydrochloride) (PAH) layer pair deposited from 0.5 M NaCl solutions [17 c]. The roughness of the silicon substrate was set to a typical value (3  $\text{\AA}$ ), and the thickness of the A/B layer pair was set arbitrarily to 29  $\text{\AA}$ . The electron densities of each layer pair were then varied, and the reflectivity computed. From the reflectivity, a Patterson function was computed by Fourier transformation using [55]:

$$P(r) = \frac{1}{2\pi} \int_{-\infty}^{\infty} \frac{R(K_{z1})}{R_F(K_{z1})} e^{2iK_{z1}r} dK_{z1} ,$$

where  $K_{z1}$  is the component perpendicular to the interface of the wavevector *in the film* and  $R_F(K_{z1})$  is the Fresnel reflectivity of the bare and perfectly smooth substrate computed at  $K_{z1}$ . In the limit of validity of the first Born approximation, the Patterson function can be shown to be equivalent to the normalized autocorrelation function of the electron density gradient [56]:



$$P(r) = \frac{1}{\varrho_s^2} \int_{-\infty}^{\infty} \frac{d\varrho(z)}{dz} \frac{d\varrho(z+r)}{dz} dz,$$

where  $\varrho_s$  is the electron density of the substrate and  $\varrho(z)$  is the electron density in the film at  $z$ , laterally averaged over the coherence area of the photons. Put simply,  $P(r)$  is proportional to the probability of finding an interface at a distance  $r$  from another one, positive peaks being associated with correlations between interfaces of both positive or both negative slopes, negative peaks being associated with interfaces having slopes of opposite signs. Alternatively, one may consider  $P(r)$  to be the spectral power density of the reflectogram scaled by the reflectivity of the bare substrate. As can be judged from Fig. 7.1, already modest electron density fluctuations may be detected in Patterson functions and X-ray reflectograms. The electron density profile of curve 3 in Fig. 7.1 simulates a  $\{(\text{PAH}/\text{PVS})_1/(\text{PAH}/\text{PSS})_1\}_6$  superlattice (where PVS stands for poly(vinyl sulfate)), with electron densities being estimated from group contributions to the molar volume of polymers [57]. In this case, a fluctuation of about 8% suffices to induce significant perturbations in the simulated reflectograms and Patterson functions. X-ray reflectometry may thus be used to characterize the internal structure of LBL-assembled superlat-

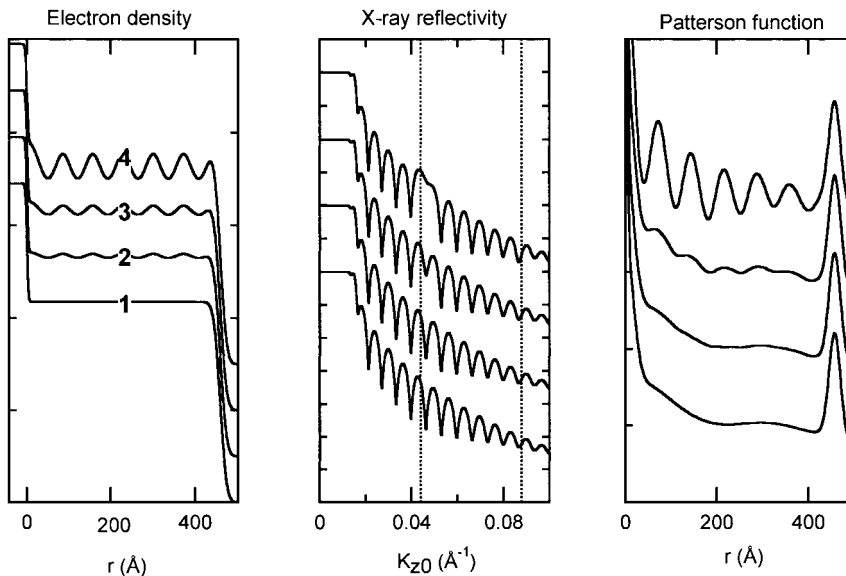


**Fig. 7.1** Simulations of the X-ray reflectivity (middle graph) by multilayers displaying the electron density profiles shown in the left graph. The right graph presents Patterson functions computed from the simulated reflectivities. The peak-to-valley fluctuations of electron density in the films amount to 0, 3.5,

8 and 24% of the average film density for curves 1, 2, 3 and 4, respectively. Curve 3 simulates a  $\{(\text{PAH}/\text{PVS})_1/(\text{PAH}/\text{PSS})_1\}_6$  superlattice deposited on a silicon wafer. The dashed vertical lines in the middle graph indicate the expected positions of Bragg peaks. All curves are displaced vertically for clarity.

tices, unless the difference in electron density between successive strata is below 5–10%. The use of Patterson functions is particularly easy and interesting in this context. For more sophisticated analyses, we refer the reader to ref. [18a, 18c].

Finally, it is appropriate to comment on the effects on the reflectivity of the internal roughness of the strata and of the photon coherence. It may be shown that reflectometry is actually sensitive to the electron density *laterally averaged over the coherence area of the incoming particles* [58, 59]. This has important consequences as shown in Fig. 7.2, which presents schematically a set of four lamellar structures having increasing internal roughness of the strata, the corresponding electron density profiles laterally averaged over the width of the images, and the variation with film thickness of the area of the Bragg peak which would be detected in a typical specular scan if photon coherence were of the order of image size. All samples may be considered as *locally* stratified. However, the smoothing out of fluctuations in the averaged density profiles, resulting from internal roughness, leads to a severe damping of Bragg peaks. Critical here is the lateral size over which electron density is integrated, i.e., the photon coherence area, which effectively depends on the resolution of the setup (usually via slit widths). For most X-ray reflectometers, typical values of coherence lengths are in the range of a few micrometers in at least one direction parallel to the substrate. In Section 7.4, the variation of Bragg peak area with film thickness will be used to explore stratification as a function of distance from the substrate.

### 7.3

#### Stratified Binary (A/B)<sub>n</sub> Organic Multilayers

As stated in the Introduction, most LBL-films made of two organic polyelectrolytes A and B do not contain strata. Even though polyelectrolytes adsorb in layers running parallel to the substrates, it was demonstrated by neutron reflectometry that A and B layers interpenetrate to such an extent that no compositional fluctuation can be detected along the sample normal, irrespective of the ionic strength of the deposition solutions. Although layer thickness increases with ionic strength, the distance of interpenetration increases in proportion, with no benefit as concerns formation of strata [17c]. Hence, the internal structure of binary LBL films may be considered to be akin to a scrambled-egg polyelectrolyte complex [60], as schematized in Fig. 7.3. Preliminary reports on the appearance of Bragg peaks in the X-ray reflectograms of a specific (A/B)<sub>n</sub> system [61] were initially essentially considered as exotic results, with little significance to the field. Since then, the structure of this specific system has been explored in much greater detail [18a, 18c], and systematic variations of the chemical architecture of the polycation have been performed, allowing one to disclose new stratified binary systems and to elucidate their peculiarities [18b, 18c].

Tab. 7.1 presents the polycations tested to grow ordered multilayers in combination with poly(vinyl sulfate) (PVS), poly(vinyl sulfonate) (PVSo), or poly(styrene sulfonate) (PSS) (Fig. 7.4). These polycations are ionenes, differing in the nature

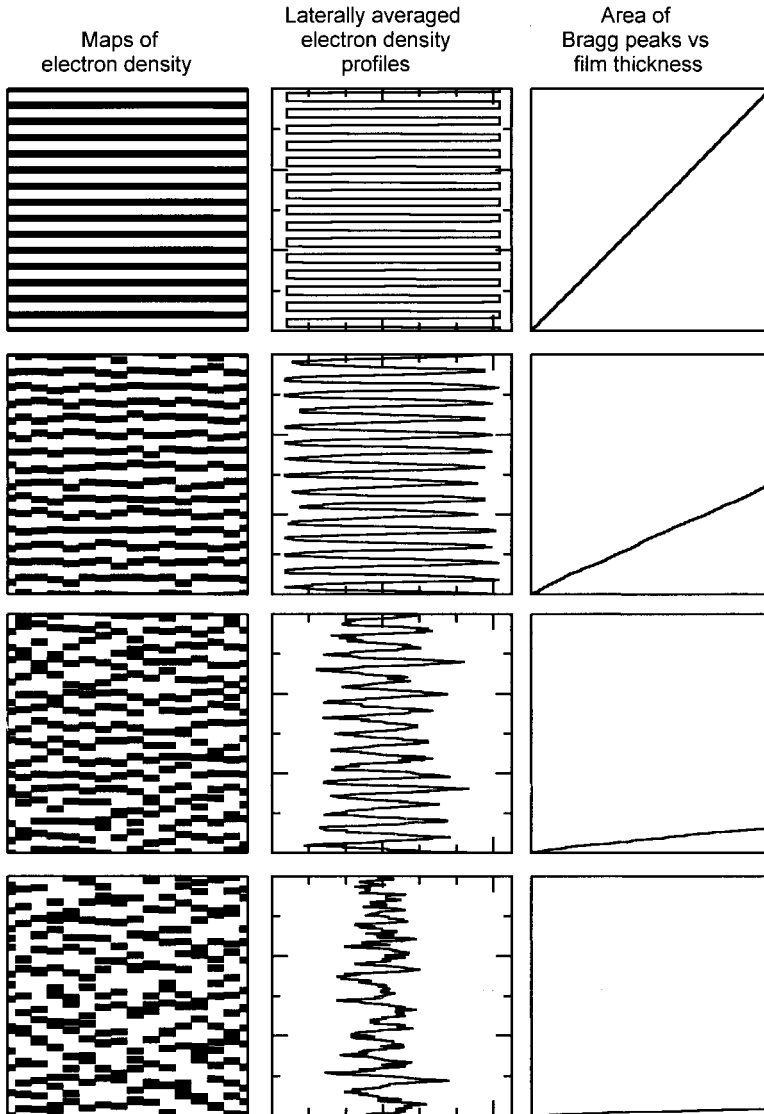
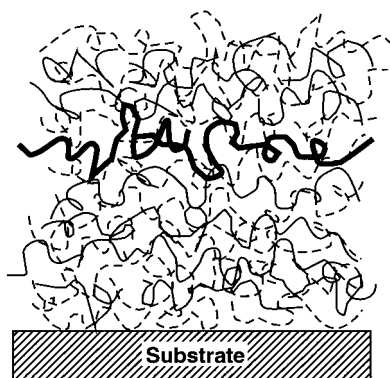
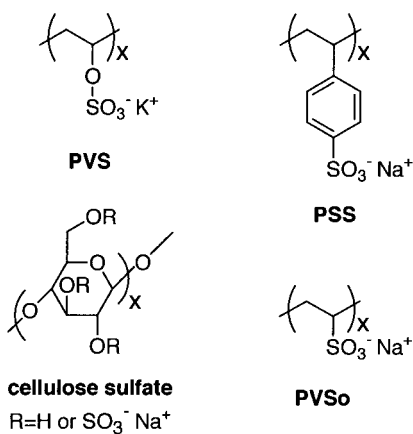


Fig. 7.2 Left: Schematic representation of a set of four lamellar structures with increasing internal roughness of the strata. Middle: Corresponding electron density profiles laterally averaged over the width of the images. Right: Variation with film thickness of the area of

the Bragg peak which would be detected in a typical specular scan if photon coherence were of the order of the image size. The scales of the graphs have been kept constant for all simulations.



**Fig. 7.3** Schematic description of the structure of binary  $(A/B)_n$  films LBL self-assembled from two flexible organic polyelectrolytes. Due to profuse interpenetration between neighboring layers, the composition is homogeneous perpendicular to the substrate. The highlighted layer is made of polyelectrolyte chains deposited during a single adsorption step in the fabrication process.

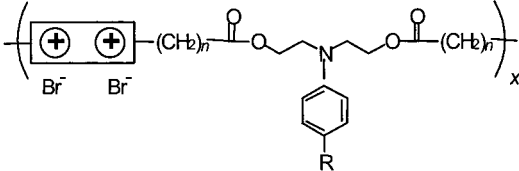
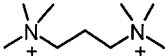
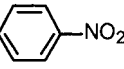
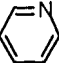
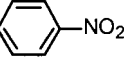
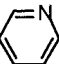
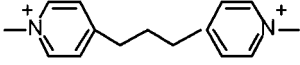
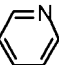
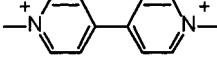
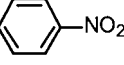


**Fig. 7.4** Organic polyelectrolytes used as counter-polyanions of the ionenes of Table 7.1.

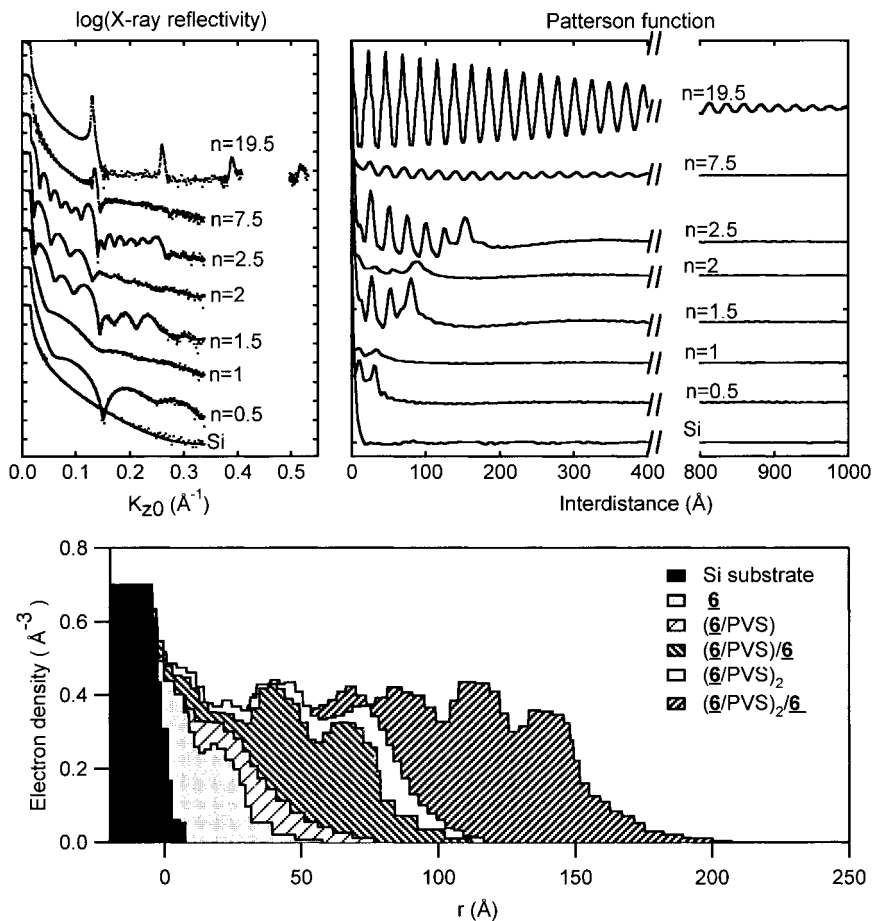
of the pendent group, the length of the aliphatic spacer in the main chain, and the nature of the quaternized ammonium groups. As indicated in Tab. 7.1, a significant number of these polycations gives rise to at least partially ordered films when combined with the proper polyanion, as judged from the presence of Bragg peaks in X-ray reflectograms and of regular oscillations in Patterson [18]. Among these systems, the highly ordered multilayers obtained by combining **6** with PVS were studied in great detail [18a].

Fig. 7.5 presents selected X-ray reflectograms, together with computed Patterson functions and electron density profiles, for the system  $(\mathbf{6}/\text{PVS})_n$  deposited on silicon wafers. The presence of regularly packed strata in the films is readily apparent. Also obvious is the fact that more than one stratum appears per deposition cycle, which can be deduced as well from the fact that the increment of thickness per deposition cycle ( $88 \text{ \AA}$ ) is much larger than the distance between two strata ( $\sim 24 \text{ \AA}$ ). It was also noted that strata already appear just after the first deposition of the ionene, before any deposition of the polyanion. Since it was shown that the ionene presents a lyotropic mesophase in water, it was concluded that the ionene

**Tab. 7.1** Ionenes tested for the construction of (A/B)<sub>n</sub> binary multilayers, and internal structure of multilayers made by combining these ionenes with poly(vinyl sulfate) (PVS), poly(vinyl sulfonate) (PVSo), or poly(styrene sulfonate) (PSS).

	R	n	No- men- cla- ture	Internal organization of multilayers, <sup>a)</sup> ionene being combined with		
				PVS	PVSo	PSS
	—H	3	1	am.	No gr.	am.
	—N=N—  —NO <sub>2</sub>	3	2	sl. 24 Å	—	am.
	—N=N— 	3	3	am.	am.	am.
	—H	10	4	part. 34 Å ± 3	am.	part. 29 Å
	—N=N—  —NO <sub>2</sub>	10	5	sl. 18 Å	—	sl. 18 Å
	—N=N— 	10	6	ord. 24 Å	ord. 24 Å	am.
	—H	3	7	am.	—	—
	—N=N— 	3	8	No gr.	—	—
	—N=N—  —NO <sub>2</sub>	3	9	sl. 26 Å	ord. 23.5 Å	am.

a) “—”: system not tested; “No gr.”: no growth of multilayer; “am.”: amorphous, i.e., no strata in multilayer (no Bragg reflection); “sl.”: slightly ordered, i.e., hints of a Bragg peak observed in X-ray reflectograms, 2–3 very weak oscillations detected in Patterson functions; “part.”: partially ordered, i.e., small Bragg peaks observed in X-ray reflectograms, marked oscillations detected in Patterson functions over a limited spatial range; “ord.”: ordered, i.e., strong Bragg peaks observed in X-ray reflectograms, marked oscillations detected in Patterson functions over distances comparable to film thickness. For ordered systems, the repeat periods in the film are also indicated.



**Fig. 7.5** Top left: Selected X-ray reflectograms of  $(\underline{6}/\text{PVS})_n$  multilayers deposited on silicon wafers. Dots: experimental data; lines: fits. Curves are displaced vertically for clarity.  $n=x.5$  means that  $x$  cycles of deposition were performed, followed by an extra deposition of polycation  $\underline{6}$ . Top right: Patterson functions

computed from the reflectivity data. Curves are displaced vertically for clarity. Bottom: electron density profiles computed by fitting box models to the reflectivity data. Profiles are superimposed to help following changes as growth proceeds.

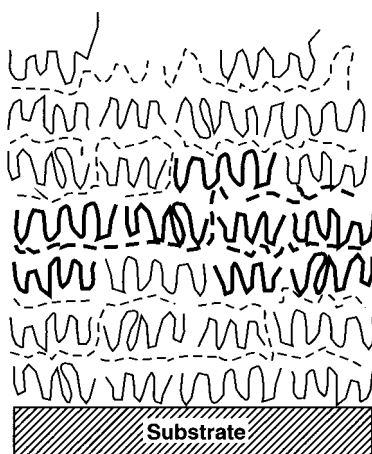
pre-organizes into a lamellar phase in the swollen layer adsorbed at the film/water interface. Depending on the amount of adsorbed ionene, which is controlled by charge balance considerations, a few lamellar layers of the ionene form onto the growing film per adsorption cycle. Also remarkable is the alternation of the quality of the structure (Fig. 7.5): After ionene adsorption, the amplitudes of Bragg reflections and the oscillations in the Patterson functions are strong; after adsorption of PVS, these parameters decrease, showing unambiguously that PVS

penetrates over some distance into the previously adsorbed film, partially destroying the previous ordering. Strata in the LBL film thus result from a surface-constrained complexation between the polyanion and a prestructured ionene deposit, which ensues diffusion of the polyanion in the previously deposited film.

It was also demonstrated that strata run over the whole film thickness (at least for films up to 0.2  $\mu\text{m}$  thickness), and that the quality of the ordering is dependent on adsorption time, or post-annealing time in water. In the best cases, strata may be parallel to the substrate within  $0.05^\circ$ , and partial alignment of the chromophore groups in the films is detected. The quality of the ordering is also extremely dependent on the nature of the polyanion: For instance, replacing PVS by PSS results in the loss of stratification [18a]. This observation confirms that penetration of the polyanion in the pre-organized adsorbed ionene layer indeed occurs, resulting in the reorganization of the internal structure with possible destruction of the initial ordering. A schematic representation of multilayer structure is presented in Fig. 7.6, and should be contrasted with the one of classical LBL films shown in Fig. 7.3.

The growth and the internal structure of multilayers made of ionenes shown in Tab. 7.1 combined with PVS, PVSo and PSS were monitored, and compared to the structure of the corresponding bulk polyelectrolyte complexes [18b–c]. It was shown that the internal structure of the multilayers is often similar, but not necessarily identical to that of the bulk complexes, pointing out the importance of the surface of the substrate in directing the structuring of the films. More importantly, it was observed that highly ordered multilayers could only be obtained with ionenes **6** and **9**, which are the only two ionenes for which lyotropic mesophases in water were found. In addition, restricted ordering was also observed for ionenes **2**, **4** and **5** which, although not forming lyotropic mesophases (as detected by polarized optical microscopy), bear either a long hydrophobic spacer in the main chain, or a 4-(4'-nitrophenylazo)-phenyl mesogenic side group. Ionenes

**Fig. 7.6** Schematic description of the structure of binary (A/B)<sub>n</sub> films LBL self-assembled from structure-forming ionenes of Table 7.1. Lamellar layers of the ionene separate polyanion-rich regions. The highlighted region is made of chains adsorbed during one complete cycle of deposition, corresponding to more than one lamellar stratum.



not bearing any long hydrophobic spacer or mesogenic side group never gave rise to any ordering. In all cases, ordering is extremely dependent on the nature of the polyanion, as was also confirmed by experiments performed with **6** combined with a set of cellulose sulfates (Fig. 7.4) of systematically varied degrees of substitution [62].

From this, it may be safely concluded that the presence of strata in the films indeed results from preorganization of the ionene in the swollen adsorbed layer, and that the subsequent penetration of the polyanion into this layer may improve, or not, the pre-ordering of the ionene deposits. An important consequence of this mechanism is that, although strata are present in the films, there is no direct, one-to-one, correspondence between film structure and sequence of deposition: Since more than one stratum may be formed per cycle of adsorption, it becomes impossible to control the composition of each stratum in turn. This diminishes the practical interest of such multilayers with respect to our initial goals; however, the partial alignment of functional groups in such films remains particularly attractive for applications in optics.

#### 7.4

#### Stratified Binary (A/B)<sub>n</sub> Hybrid Organic/Inorganic Multilayers

Another strategy to strata-containing binary LBL multilayers has been explored in recent years by exploiting the sequential adsorption of two heterospecies, namely a (semi)flexible organic polyelectrolyte together with rigid (i.e., two-dimensional) inorganic nanoplatelets, as obtained by exfoliation of layered crystals. The usual incompatibility between silicates and organic polymers is overcome by strong electrostatic interactions prevailing between the two complementary components [63]. Phyllosilicates from the smectite group such as the negatively charged hectorite [19] and montmorillonite [20, 21] (Fig. 7.7), or the positively charged hydroxalcite (from the carbonate hydroxide class) [20b, 23] have proved to be particularly appropriate for LBL films. Exfoliated transition metal oxides [24b], metal disulfide [24a], metal phosphates [25, 64] and perovskites [26] as well as graphite oxide [65] and titania nanosheets [66] have also been used. The morphology of these nano-

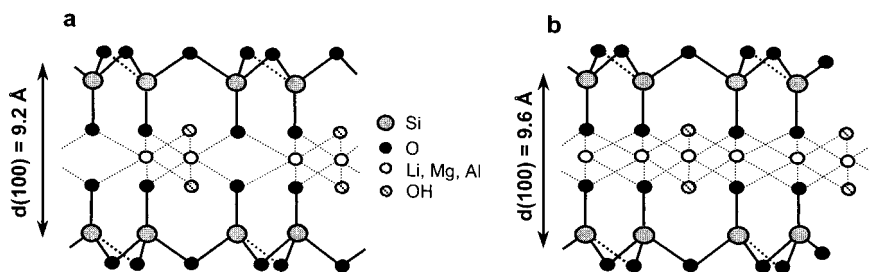


Fig. 7.7 Schematic representation of the crystal structures of montmorillonite (a) and hectorite (b) according to ref. [81].



sheets seems appropriate to provide stratified assemblies: Due to the shape anisotropy, the high surface area and the rigidity of the platelets, tiling might be expected to occur in a regular fashion.

#### 7.4.1

#### Initial Studies on Hybrid Assemblies

First uses of exfoliated smectites, such as hectorite or bentonite, go back to the initial studies by Iler [67]. More detailed pioneering studies [19, 20b, 30, 31] used poly(diallyl dimethyl ammonium) chloride, PDADMAC (**13**, Fig. 7.8) [68], a strong polyelectrolyte. Bragg diffraction peaks were observed in X-ray studies performed on films built from **13** and Laponite (**L**), a synthetic hectorite, demonstrating

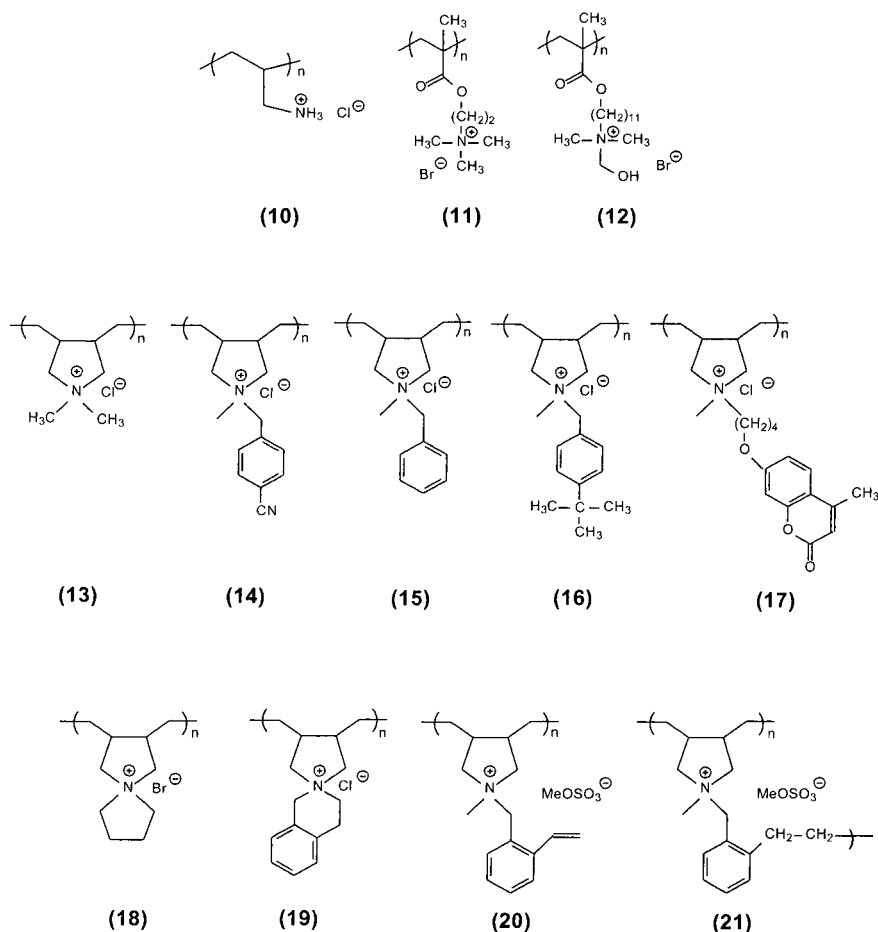


**Fig. 7.8** Poly(diallyl ammonium) salts used as organic counter-polycations of negatively charged Laponite platelets for the preparation of (A/B)<sub>n</sub> hybrid multilayers.

some degree of internal order in such films [19a]. The relative positions of the peaks in reciprocal space were consistent with a lamellar structure of a period close to the 14 Å basal spacing of hectorite. It was assumed that the flexible organic polyelectrolyte is intercalated between the inorganic sheets, the period of 14 Å being attributed to the (13/L) interlayer spacing. It was also observed that approximately two hectorite layers are adsorbed per adsorption cycle. Other ordered assemblies were reported with montmorillonite (M) platelets by Kotov and co-workers [20b]. But, different from (13/L)-based assemblies, atomic force microscopy (AFM) suggested the presence of unexfoliated clay particles. It was therefore concluded that the observed Bragg peaks reflect the basal period of small stacks of pure clay, rather than the (13/M) interlayer spacing [20b]. Similar observations were reported for systems based on exfoliated graphite oxide (GO) and PDADMAC [65b]. In these studies, two different Bragg peaks in the small-angle region of the diffractograms were found, which were attributed to the interlayer spacing of (13/GO), as well as to small stacks of pure platelets. Alternative systems using rigid inorganic polyanions employ exfoliated zirconium phosphate ( $\alpha$ -ZrP) and protonated poly(allyl amine) PAH (10, Fig. 7.8) [25c], or titania nanosheets and poly(dimethyl diallyl ammonium chloride) [66], providing other systems well-suited for forming ordered LBL films with internal structure.

#### 7.4.2

### Layered Assemblies from Analogous Poly(diallyl ammonium) Salt Derivatives and Hectorite Platelets

#### 7.4.2.1 General Structural Observations

The most documented initial studies on LBL clay-based systems were made on PDADMAC 13 combined with the synthetic hectorite Laponite (L). Given the paucity of variations of this outstanding parent system, we explored several series of polycations of systematically varied molecular architecture. Polycations mainly of the poly(diallyl ammonium) family, complemented by a small set of other polycations, were tuned with respect to their hydrophilic/hydrophobic balance, as well as to their bulkiness and the length of pendent side groups [27a, 69]. The molecular structures of various polymers tested are listed in Fig. 7.8. Some representative X-ray reflectograms of hybrid films assembled on silicon wafers using Laponite with various polycations are shown in Fig. 7.9. Broad Bragg peaks are observed in all cases, irrespective of the solvent used for building the assembly and of the detailed nature of the polycation employed. A Bragg peak was even observed for the system based on 9 which contains only a low charge density, but bears multiple mesogens [27a]. This indicates that the general system (polycation/L) is remarkably robust for structure formation.

The position of the Bragg peak is only moderately modulated by the details of the chemical structure. The Bragg spacing lies between 14.4 Å for (13/L) and 18.6 Å for (19/L), and between 18.5 Å for (17/L) and 19.6 Å for (16/L)-based assemblies built, respectively, from water and water/ethanol solutions. From these data alone, it was, however, not obvious whether the variations in the interlamellar

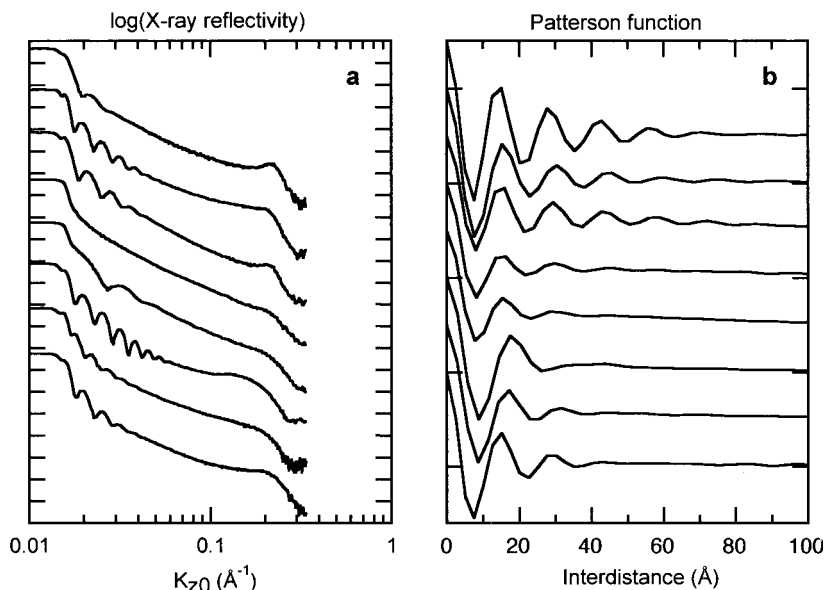


**Fig. 7.9** (a) X-ray reflectograms of (A/B)<sub>n</sub> hybrid multilayers. From top to bottom: (13/L)<sub>16</sub>, (19/L)<sub>15</sub>, (15/L)<sub>15</sub>, (20/L)<sub>15</sub>, (21/L)<sub>15</sub>, (17/L)<sub>15</sub>, (12/L)<sub>25</sub>, (11/L)<sub>25</sub>. Note the log–log scale. Curves are displaced vertically for clarity. (b) Patterson functions computed from the reflectivity data. Curves are displaced vertically for clarity.

spacing were due to the specific nature of the complexed polycation, or to a change in the extent of hydration of unexfoliated silicate layers [20b]. The basal spacing of layered silicates indeed expands significantly with degree of hydration. Nevertheless, detailed thermal analysis coupled with X-ray reflectivity measurements demonstrated that the polyelectrolyte is truly intercalated between the inorganic sheets [27a]. Exfoliated platelets of Laponite deposit thus as individual sheets, and not as an unexfoliated stack of clay platelets. This behavior contrasts with that of natural clays for which a much more difficult exfoliation is expected due to the higher degree of crystallinity and the larger size of the individual platelets [20b].

By contrast, the increment of thickness per adsorption cycle was found to be much more dependent on the nature of the polycation. As a result, the ratio (increment of thickness per adsorption cycle/Bragg spacing) is frequently not equal to 1, and was found to vary between 0.8 and 2.1, depending on the nature of the polycation and the type of platelet [27 a, 19 a, 20 b]. This is similar to what was found for the purely organic ordered (A/B)<sub>n</sub> multilayers discussed in the previous section, and suggests that film growth cannot be explained by the simple alternate deposition of monolayers of platelets and polycation, as was proposed by Mallouk and coworkers for the system (13/*α*-ZrP)<sub>13</sub> [25 d]. Rather, a more dynamic deposition process takes place, involving the adsorption of more than one monolayer of platelets for each cycle of deposition, followed by restructuring of the film upon adsorption and penetration of the polycation.

tion. The adsorption of more than one layer of silicate platelets per deposition cycle is easy to understand, considering their low surface charge density: Charge balance simply requires a given amount of platelets to (over)compensate the previous charge of the surface layer. Considering the relatively high mobility of organic polyelectrolytes in the swollen outer layer of the films, reorganization ensues, as proposed initially by Kleinfeld and Fergusson [19a].

#### 7.4.2.2 Detailed Analysis of the Structure of Laponite-Based Hybrid LBL Films

An examination of Patterson functions computed from the X-ray reflectivity of Laponite based LBL films indicates that such films are only partially ordered (Fig. 7.9). Although oscillations do appear in these curves, they are exponentially damped and disappear for interdistances larger than a few tens of Å. In reciprocal space, this observation translates into an increase in the width of the Bragg peaks with the order of the reflection, as reported in the past for  $(13/\text{Laponite})_n$  films [19a].

The limitation of order seen in Patterson functions may arise either from the existence of vertical disordering in the positions of silicate strata (i.e., paracrystallinity of the stacking), or from the disappearance of strata as the distance from the substrate increases. In the first case, because of cumulative displacement of silicate strata in the vertical direction, the positions of the strata are no longer defined with respect to an ideal lattice, but only with respect to the positions of the adjacent strata [70, 71]: The limited range of oscillations seen in the Patterson functions corresponds thus to the coherence of the vertical stacking. In the second case, due to the random tiling of platelets, strata can only be defined close to the substrate: Further away, lateral averaging effectively smoothes out the density fluctuations perpendicular to the substrate (see Section 7.2).

The validity of the second hypothesis is demonstrated by a series of observations [27b]. First, from X-ray reflectograms of  $(18/L)_n$  LBL films (Fig. 7.10a), electron density profiles were computed for increasing values of  $n$  (Fig. 7.10b). They showed that strata become less apparent and thicker as the distance from the substrate increases. Second, AFM measurements on a  $(18/L)_1$  film show a broadening of the distribution of the heights of the platelets as their distance from the substrate increases, in good agreement with the density profile obtained by reflectometry (Fig. 7.11). Third, the Bragg peak area varies according to a linear regime for small film thickness, but progressively saturates for thicker films (Fig. 7.12). In agreement with Fig. 7.2, this would correspond to a first region, close to the substrate, where silicate platelets would be laterally aligned, and to a second region where the strata would progressively disappear. Finally, off-specular and specular reflectivity measurements performed with different instrumental resolutions were also found to be compatible with the second hypothesis, as will be reported elsewhere [27b]. The schematic picture which emerges from these studies is presented in Fig. 7.13, which is *quantitatively* compatible with the experimental data.

For all systems tested to date, the spatial extent of the really stratified region is limited to about 100 Å. The extent of this region is moderately affected by the details of the chemical structure of the flexible polycation, the size of the ordered re-

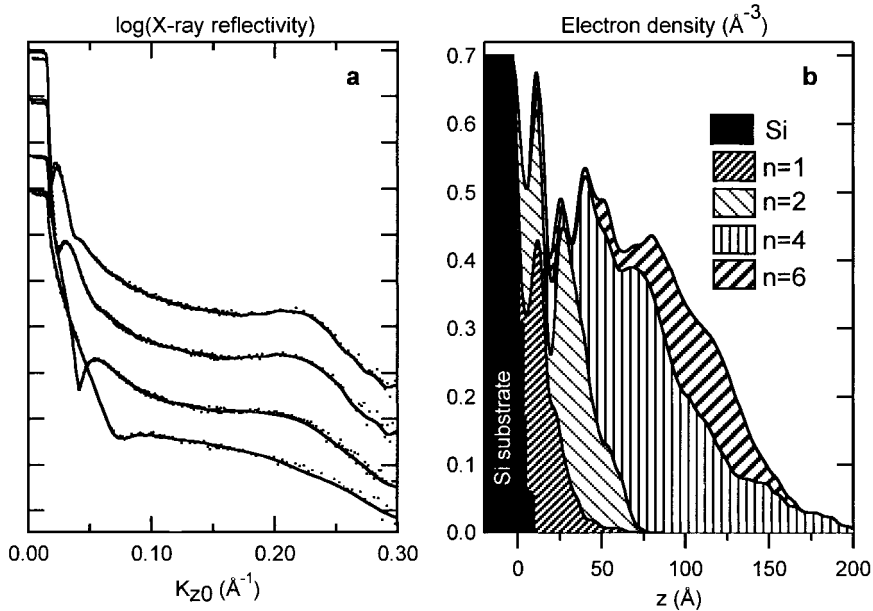


**Fig. 7.10** (a) X-ray reflectograms of  $(18/L)_n$  multilayers with, from bottom to top,  $n=1, 2, 4$  and  $6$ . Dots: experimental data; lines: fits. Curves are displaced vertically for clarity.

(b) Electron density profiles computed by fitting box models to the reflectivity data. Profiles are superimposed to help following changes as growth proceeds.

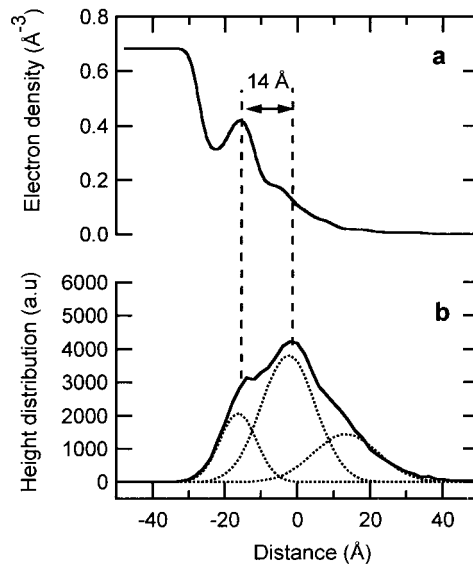


**Fig. 7.11** (a) Electron density profiles computed by fitting box models to the reflectivity data of a  $(18/L)_1$  film. (b) Height distribution of the surface of a  $(18/L)_1$  film as obtained from a  $1\ \mu\text{m} \times 1\ \mu\text{m}$  AFM image. Dashed curves are the result of a decomposition of the height histogram into a trimodal distribution.

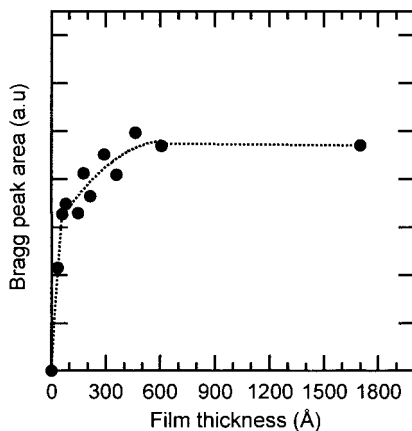


Fig. 7.12 Variation with film thickness of the area of the Bragg peak of  $(18/L)_n$  multilayers.

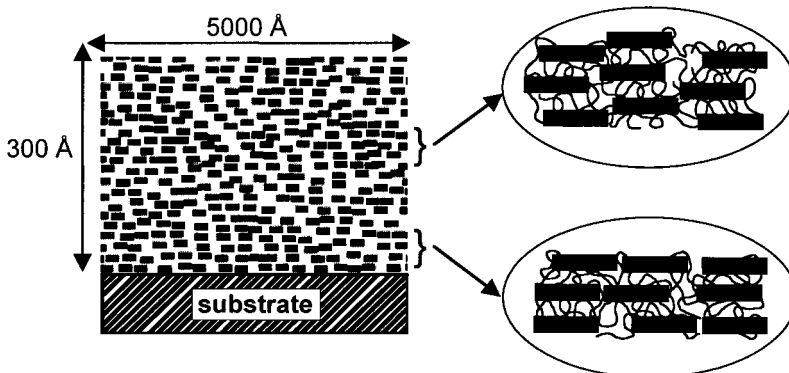


Fig. 7.13 Schematic representation of the internal structure of a hybrid (organic polycation/Laponite) $_n$  multilayer. Due to a cumulative disorder in the vertical tiling of platelets, strata can only be defined close to the substrate, as shown in the magnifications.

gions lying between about 20 and 100 Å. Interestingly, the bulkiness of the polycations within the series 13, 18 and 19 seems to have no impact on the extent of the stratified region. By contrast, the hydrophilic/lipophilic balance does seem to have an influence as the stratified regions of films formed from the rather hydrophobic polycations 16 and 17 are of very limited size.

### 7.4.3

#### Ordering in Hybrid Assemblies Employing Functional Polyions

##### 7.4.3.1 Photocrosslinkable Polyelectrolytes

To prepare hybrid films with a set of strata with high coherence lengths, we tried to limit the reorganization in the lowermost layers by in situ crosslinking of the flexible polyelectrolyte prior to the tiling process. One may imagine hampering

the interpenetration between heterospecies by freezing the mobility of the uppermost organic layer, not only on the timescale of the adsorption of the platelets. But even for purely organic LBL films, crosslinking strategies have received little attention [72–75]. In the few cases studied so far, crosslinking led to a more regular adsorption of hydrophobic polycations in purely organic films [73]. Besides the beneficial effects expected in terms of regularity in the stacking of the strata, the crosslinking approach should help to stabilize the films, for instance, by improving the barrier functionality of the inorganic layers as well as controlling the permeability between sublayers [76].

In this context, we prepared a new rigid unsaturated polycation of the poly(diallyl ammonium) family **20** and self-assembled the reactive polycation with hectorite from DMSO/water based systems [69]. UV spectroscopy studies indicate that the photoreaction is complete after short exposure to UV light. The occurrence of a broad Bragg peak in the X-ray reflectograms, similar in shape for both crosslinked (**21/L**)<sub>15</sub> and uncrosslinked (**20/L**)<sub>15</sub> films, demonstrates that the assemblies dispose of an internal structure, and that the cross-linking process does not interfere markedly with the structure formation. But in any case, the cross-linking did not improve significantly the coherence domains of the strata.

#### 7.4.3.2 The Use of Mesomorphic Polyions

Alternatively, and similarly to the strategy employed for organic films (see Section 7.3), we explored whether the introduction of mesomorphic polyelectrolytes or liquid crystalline ionomers in hybrid thin films could favor internal order. Indeed, both shape anisotropy and amphiphilic character may promote lamellar order and induce mesomorphic organization in supramolecular assemblies [77]. As discussed above, the use of liquid crystalline polyelectrolytes can indeed induce the formation of well defined strata. One might think that the combination of rigid platelets with liquid crystalline polymers would improve the ordering even more. In any case, the multiplication of the interfaces (mesogens–platelets) should promote the induction of local orientation. Therefore, the formation of the hybrid film has been investigated for both anionic and cationic exfoliated inorganic crystals in combination with liquid crystalline ionomers. Hydrotalcite nanosheets (Ht), for example, were deposited together with negatively charged main chain liquid crystals **22** and **23** (Fig. 7.14) [13b, 23]. Alternatively, montmorillonite sheets (M) were deposited with liquid crystalline cationic ionomer **24**, or with polycation **9** even bearing two different mesogens, namely the viologen group and the azobenzene moiety [23, 72]. All these ionomers, **6**, **9** and **24**, present thermotropic or lyotropic nematic or smectic phases [78]. They could be easily and regularly assembled with their inorganic partners to films like (**22/Ht**)<sub>n</sub>, (**23/Ht**)<sub>n</sub>, (**24/M**)<sub>n</sub> or (**9/M**)<sub>n</sub> [13b, 23, 72], exhibiting regular film growth according to ellipsometry or UV/vis spectroscopy. However, X-ray reflectometry indicated the formation of films without defined internal sublayers. The lack of structure might be explained by the low charge density of the polyions applied, that is close to the limiting case of the LBL self-assembly method, eventually combined with the high flexibility of some of the ionomers.

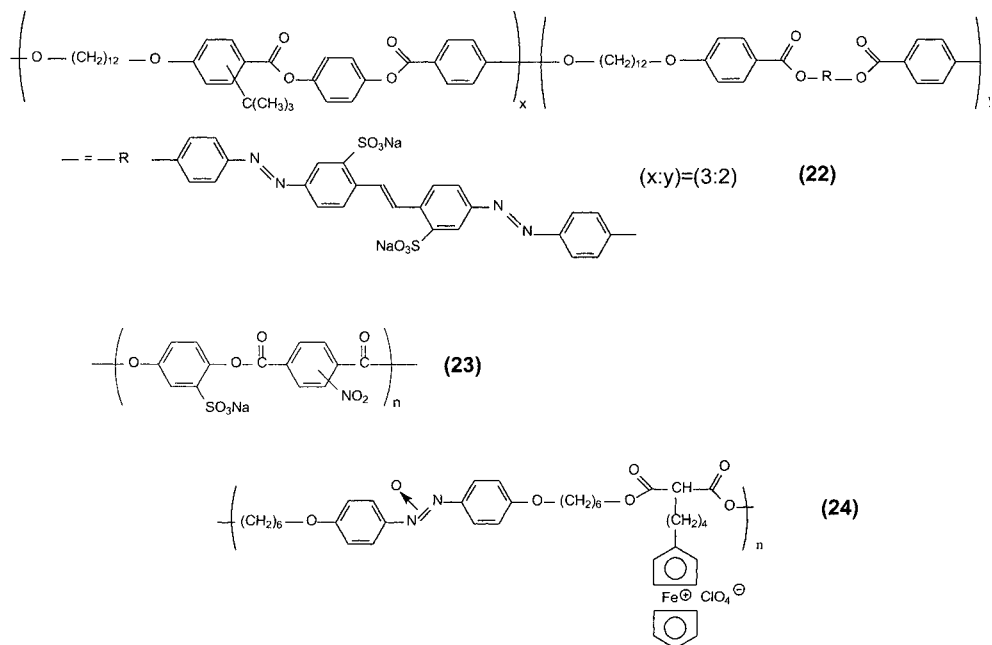


Fig. 7.14 Mesomorphic polyelectrolytes used for building (A/B)<sub>n</sub> hybrid multilayers.

Independent of the induction of well defined strata, charged polymers bearing mesogenic groups may, alternatively, improve the alignment of functional fragments within the films. For (9/M), UV/vis spectroscopy measurements suggest the formation of J-aggregates (implying in-line alignment of adjacent chromophores) [13a, 72]. Most interestingly, for polymer 9 whose mesogens are substituted to provide good second-order non linear optical properties, second harmonic generation (SHG) studies revealed an average orientation of the mesogens in the hybrid films (9/M)<sub>n</sub> [72]. But the extent of orientation is presumably weak, and disappears for thicker layers due to the dynamic character of LBL films. This illustrates the *a priori* low degree of organization of many such hybrid films, at least in their final state. Nevertheless, the picture that emerges from these results is that some local alignment of functional fragments may be obtained. By contrast, organization on a larger scale, such as the formation of lamellar structures, i.e. of distinguishable strata in the films, remains a challenge.

## 7.5

### Hybrid Superlattices of the {(A/B)<sub>m</sub>/(C/D)<sub>p</sub>}<sub>n</sub> Type

So far, only binary multilayers of the (A/B)<sub>n</sub> type have been discussed. Another approach to the fabrication of strata-containing LBL films consists in using two different (A/B) and (C/D) layer pairs as building blocks to create superlattices of



the  $\{(A/B)_m/(C/D)_p\}_n$  type. For such superlattices, strata may be expected, consisting of homogeneous  $(A/B)_m$  and  $(C/D)_p$  molecular-level blends. Obviously, the number of possible combinations is now very large, and complete exploration of the possibilities offered by this strategy is far from being achieved. In the following, we review briefly previous works in this field, then describe in more detail our own work on hybrid organic/inorganic superlattices.

### 7.5.1

#### Literature Survey

Several reports have dealt with the construction of LBL superlattices to incorporate active components in spatially separated compartments. For example, proteins [28–31], enzymes [32–34], viruses [35], metal nanoparticles [36–41], magnetite particles [42], conjugated polymers [25 e, 43–45] and optical dyes [25 c, 43 b, 46–48] were incorporated in LBL superlattices to prepare devices displaying the desired biosensing, electrical, optical or chemical properties. Unfortunately, most of these reports paid little attention to the detailed internal structure of the superlattices in relation to the specific sequence of deposition events.

Organic strata were demonstrated in self-assemblies containing more than two organic polyelectrolytes [13 e, 17 a, 43 a, b, 54]. As stated in the Introduction, the fuzziness of the strata, resulting from layer interpenetration, could be established in most cases. In order to decrease fuzziness, intercalation of more rigid blocks between  $(A/B)_m$  organic blocks was attempted. For instance, lipid bilayers were used to separate polyelectrolyte layers by a combination of Langmuir–Blodgett transfer and LBL self-assembly [79]. Other examples of superlattices include the insertion between  $(A/B)_m$  blocks, of inorganic layers made from metal or metal oxide particles [20 a, 38–41], of exfoliated platelets of metal phosphates [25 e], or of clays [20, 30]. The resulting films are composed of organic compartments sandwiched between hybrid barriers. Among these different examples, rigid inorganic nanoplatelet spacers seem to be particularly suitable for the control of the superlattice architecture on the nanometer scale. Indeed, the high aspect ratio of two-dimensional nanoplatelets should result in minimal interpenetration of successive organic strata. Moreover, by contrast with spherical nanoparticles, nanometer-thick platelets may form sharp and dense barriers inhibiting the transfer of active components from a stratum to its neighbors. The permeability of the barrier can be easily fine-tuned by adjusting the number of hybrid bilayers deposited between organic  $(A/B)_m$  blocks. Such a strategy was previously described for systems containing montmorillonite [76], zirconium phosphate ( $\alpha$ -ZrP) or HTiNbO<sub>5</sub> platelets [25 c, 38, 25 e]. However, no evidence for the effective control of the supramolecular structure was provided in these works.

## 7.5.2

**Hybrid Organic/Inorganic Compartmentalized Multilayers from Clay Platelets**

Given the limited information available on the internal structure of hybrid organic/inorganic superlattices, we have followed the structure of such compartmentalized multilayers during their build-up [27b]. Multilayers were prepared by alternate adsorption of hybrid and organic blocks.  $(A/B)_m$  hybrid blocks were obtained by LBL deposition of **18** (A) and Laponite platelets (B).  $(A/C)_p$  organic blocks were made by LBL assembly of **18** (A) and poly(styrene sulfonate) (C). The influence of  $m$ ,  $p$  and  $n$  on the structure of  $\{(A/B)_m/(A/C)_p\}_n$  deposited on silicon wafers was investigated in detail by X-ray reflectometry and ellipsometry. Here, we restrict the scope to  $\{(A/B)_2/(A/C)_p\}_n$  films, and report only on selected examples of such multilayers.

The variation of film thickness vs. number of “supercycles” of deposition ( $n$ ) is presented in Fig. 7.15. Thickness increases linearly with  $n$ , indicating regular film growth. The increments of thickness by supercycle are 53 and 125 Å, for  $p$  equal to 2 and 10, respectively. Fig. 7.16a depicts reflectograms obtained for  $\{(A/B)_2/(A/C)_2\}_{5.5}$  and  $\{(A/B)_2/(A/C)_{10}\}_6$  films. For the sake of comparison, the reflectogram of an  $(A/B)_6$  film is also shown. All multilayers present a broad Bragg peak at about  $0.22 \text{ \AA}^{-1}$  (corresponding to a repeat distance of 14 Å) resulting from the stratification of Laponite platelets close to the surface of the substrate (see Section 7.4). It is obvious that the deposition of (A/C) layers atop the  $(A/B)_2$  block does not significantly disturb the stratified arrangement of the latter block. The numerous Kiessig fringes seen in the reflectograms testify to the low roughness of the film/air interface. The most interesting feature of reflectograms of the superlattices is the presence of supplementary Bragg reflections at lower scattering angles, with up to three orders detected for the  $\{(A/B)_2/(A/C)_{10}\}_6$  superlattice. These results clearly indicate the presence of an ordered stratified superlattice structure in the multilayers, of 45 and 113 Å repeat period for the  $\{(A/B)_2/(A/$

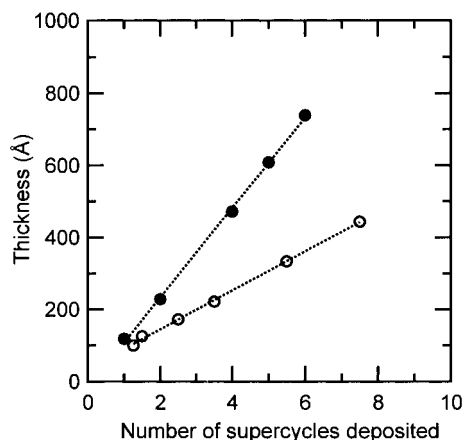


**Fig. 7.15** Variation of sample thickness versus number of supercycles of deposition for  $\{(A/B)_2/(A/C)_2\}_n$  (O) and  $\{(A/B)_2/(A/C)_{10}\}_n$  (●) hybrid superlattices. Dashed lines are linear fits to the data.

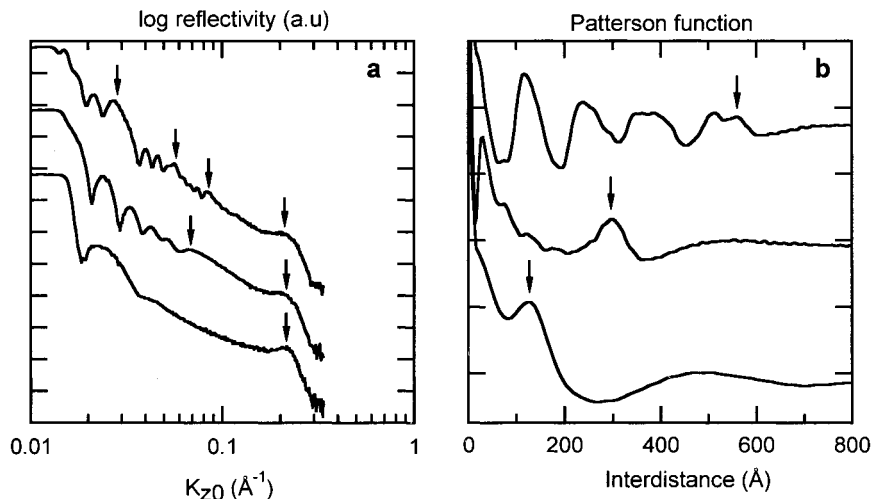


**Fig. 7.16** (a) X-ray reflectivity of  $\{(A/B)_2/(A/C)_p\}_n$  and  $(A/B)_n$  hybrid superlattices. From top to bottom: sample  $\{(A/B)_2/(A/C)_{10}\}_5$ ,  $\{(A/B)_2/(A/C)_2\}_{5.5}$  and  $(A/B)_6$ . Vertical arrows indicate the positions of Bragg reflections. Note the

log-log scale. Curves are displaced vertically for clarity. (b) Patterson functions of the same samples computed over  $0.01 \leq K_{z0} \leq 0.1 \text{ \AA}^{-1}$ . Vertical arrows indicate the film thickness. Curves are displaced vertically for clarity.

$C)_2\}_{5.5}$  and  $\{(A/B)_2/(A/C)_{10}\}_6$  films, respectively. These numbers are very close to the increments of thickness per supercycle of deposition, indicating complete control over the superstructure of the film by the deposition process.

More information about the spatial extent of the order in these self-assemblies can be obtained by analyzing Patterson functions computed from the first part ( $0.01 \leq K_{z0} \leq 0.1 \text{ \AA}^{-1}$ ) of the reflectograms (Fig. 7.16 b). Due to the absence of a superlattice in the  $(A/B)_6$  film, a single peak appears in the corresponding Patterson function, resulting from the correlations between substrate/film and film/air interfaces. By contrast, the weak oscillations in the Patterson function of  $\{(A/B)_2/(A/C)_2\}_{5.5}$ , and the much stronger ones observed for  $\{(A/B)_2/(A/C)_{10}\}_6$ , unambiguously signal the existence of a superlattice in these samples. However, the spatial extent of the stratification depends on the thickness of the organic compartment, being limited to the first deposited layers (75  $\text{\AA}$ ) for  $\{(A/B)_2/(A/C)_2\}_{5.5}$ , while extending over the total film thickness for  $\{(A/B)_2/(A/C)_{10}\}_6$ . The loss of coherence of the stacking for the sample with  $p=2$  results from the large interfacial roughness of the hybrid spacer compared to the value of the repeat period. In order to obtain multi-compartmentalized films over large vertical distances, it is necessary to smooth out the roughness of the hybrid spacer layer by depositing an organic block of sufficiently large thickness. A similar conclusion was drawn by Decher et al. for nanoparticle-based  $\{(PSS/PAH)_m/(Au/PAH)\}_n$  systems [41].

In order to decrease the number of deposition cycles necessary to smooth the barrier layer while fine-tuning the thickness of organic compartments and decreasing the total time for multilayer buildup, we deposited  $(A/C)_p$  organic layer

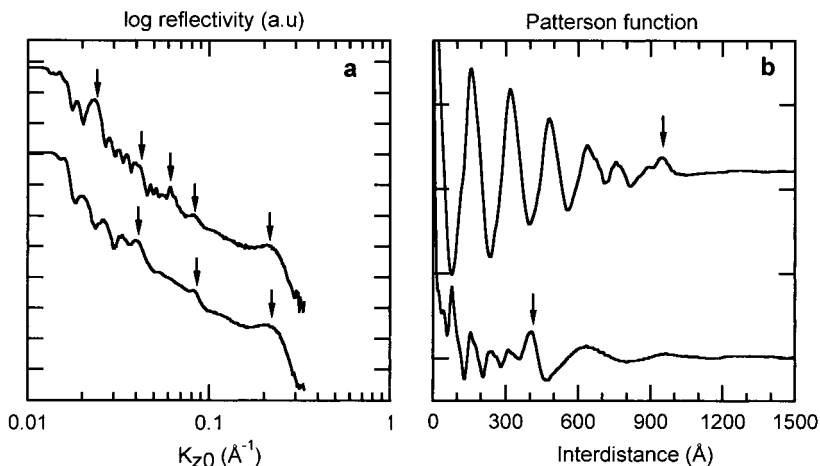


**Fig. 7.17** (a) X-ray reflectivity of  $\{(A/B)_2/(A/C)_p\}_n$  hybrid superlattices, with the  $(A/C)_p$  block deposited from 0.1 M NaCl water solutions. Top curve:  $\{(A/B)_2/(A/C)_5\}_{5.5}$ ; bottom curve:  $\{(A/B)_2/(A/C)_2\}_{5.5}$ . Vertical arrows indicate the locations of Bragg reflections. Note

the log–log scale. Curves are displaced vertically for clarity. (b) Patterson functions of the same samples calculated over  $0.01 \leq K_{z0} \leq 0.1 \text{\AA}^{-1}$ . Vertical arrows indicate the film thickness. Curves are displaced vertically for clarity.

pairs from 0.1 M NaCl aqueous solutions. These conditions are known to increase the thickness of adsorbed polyelectrolyte layers [80]. The X-ray reflectograms of two samples  $\{(A/B)_2/(A/C)_2\}_{5.5}$  and  $\{(A/B)_2/(A/C)_5\}_6$  fabricated by this process are displayed in Fig. 7.17a, while Patterson functions computed from the data in the first part of the reflectograms ( $0.01 \leq K_{z0} \leq 0.1 \text{\AA}^{-1}$ ) are shown in Fig. 7.17b. The repeat distances of the superlattices are 76  $\text{\AA}$  and 156  $\text{\AA}$  for samples with  $p=2$  and 5, respectively, and the coherence lengths of the superlattices equal to film thickness for both samples. These experiments clearly show that well-ordered multilayers can be fabricated with a smaller number of deposition cycles of the organic

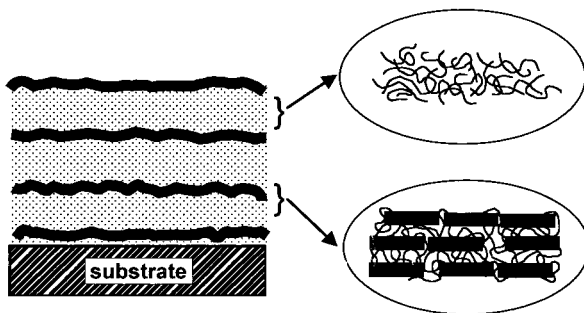


**Fig. 7.18** Schematic representation of the internal structure of  $\{(A/B)_2/(A/C)_p\}_n$  hybrid superlattices.

layer pair. However, the use of increased ionic strength during the deposition of the organic layer pairs also results in larger values of thickness for the organic compartments, which may be detrimental for some applications. To summarize, a schematic representation of the structure of the superlattices is depicted in Fig. 7.18.

## 7.6

### Conclusions

We have explored the internal structure of a series of LBL-assembled polyelectrolyte films. Usually, for binary  $(A/B)_n$  systems based on two organic polyelectrolytes only, no strata can be defined in LBL-assembled films; Fig. 7.3 exemplifies the internal structure of such films, as derived from previous studies in the field [13].

However, we have found a category of polycations giving rise to much better stratified  $(A/B)_n$  multilayers. These polycations form organized concentrated water solutions (i.e., lyotropic mesophases), or at least contain groups capable of driving structuring (long hydrophobic spacers, mesogenic groups, ...). This preorganization occurs in the swollen layer adsorbed at the film/water interface, and may be enhanced or destroyed upon adsorption of the polyanion and its subsequent diffusion in this layer. The generality of this finding was tested with a complete set of polycations of systematically varied architecture. In the best cases, the surface-constrained complexation between polycation and polyanion may lead to films stratified over very long distances (0.2  $\mu\text{m}$ ). Fig. 7.6 illustrates schematically the structure of such LBL films.

It is interesting to compare these multilayers with hybrid binary multilayers made from clay platelets and simple polycations (Fig. 7.13). Both types of multilayers share common traits: they are at least partially internally stratified; they grow by the deposition of more than one internal repeat period per deposition cycle, due to the decoupling between amounts adsorbed (which is governed by charge balance) and internal structuring (related to macromolecular architecture and specific complexation between polyelectrolytes after diffusion in the film). In addition, both result from some lamellar organization of polyelectrolytes: for silicates platelets, the anisotropy of the platelets by itself suffices to define lamellae, while for ionenes, microphase separation in the swollen layer adsorbed at the film/water interface is most probably responsible for the formation of lamellar-shaped aggregates. However, the main difference between these two systems lies in the compliance of the lamellae, and its consequences on ordering. Soft ionene lamellar aggregates may not resist the complexation with a given polyanion, resulting in loss of internal order in the films, or may gently yield to the requirements of stratified complexation, leading to extremely well-ordered assemblies. By contrast, rigid silicate platelets will not suffer, nor benefit, from the complexation with a counter-polyelectrolyte; as a result, strata always exist in hybrid films, but order is restricted to regions close to the substrate, due to the lack of compliance of platelets with the requirements of stratified complexation. On the positive side,

silicate platelets can accommodate with a wide range of functional polyelectrolytes, such as poly(diallyl ammonium) salts, polymethacrylates or ionenes. Bulky, hydrophobic, amphiphilic or photocrosslinkable polyelectrolytes can be incorporated while still keeping strata close to the substrate.

For both types of internally structured binary LBL films, there is no direct correspondence between the number of strata deposited and the number of dipping cycles. It is thus impossible to control the composition of each stratum in turn. Therefore, other strategies have to be developed in order to design well compartmentalized assemblies allowing the confinement of functional molecules at precise positions within the stratified structure. This is possible through the construction of superlattices containing organic compartments of well-defined and tunable thickness separated by hybrid barriers. We have shown here preliminary results in this direction. Similarly, others [76] have recently used hybrid strata placed at specific locations along the sample normal to tune the light-emitting properties of LBL self-assemblies. The influence of ionic strength and the use of different  $\{(A/B)_m/(A/C)_p\}_n$  combinations are currently being investigated in our laboratory in order to obtain organic compartments with a tunable thickness on the nanometer scale.

### Acknowledgements

It is appropriate to first acknowledge the dedication of many people who significantly contributed in our groups to the work reported here: X. Arys, P. Fischer, M. Koetse, B. Laguitton, B. Mayer, A. Moussa and E. Wischerhoff. The authors also greatly benefited at different stages from scientific discussions with P. Bertrand, G. Decher, J.-L. Habib-Jiwan, R. Legras and B. Nysten, and many researchers from the LBL self-assembly community. Financial support was provided by the Belgian National Fund for Scientific Research, and by the DG Recherche Scientifique of the French Community of Belgium (Action de Recherches Concertée, conventions 94/99-173 and 00/05-261).

### 7.7

#### References

- 1 D. LI, M.A. Ratner, T. Marks, C.H. Zhang, J. Yang, G.K. Wong, *J. Am. Chem. Soc.* **1990**, *112*, 7389–7390; (b) S.B. UNGASHE, W. L. WILSON, H.E. KATZ, G.R. SCHELLER, *J. Am. Chem. Soc.* **1992**, *114*, 8717–8719.
- 2 H. BYRD, E.P. SUPONEVA, A.B. BOCARSLY, M.E. THOMPSON, *Nature* **1996**, *380*, 610–612.
- 3 L. LANDAU, E. LIFCHITZ, *Mécanique Quantique: Théorie Non Relativiste*, MIR, Moscow, 2nd edn., 1967.
- 4 J.R. LAKOWICZ, *Principles of Fluorescence Spectroscopy*, Kluwer Academic Press, New York, 2nd edn., 1999.
- 5 G. MCDERMOTT, S.M. PRINCE, A.A. FREER, A.M. HAWTHORNTHWAITTE-LAWLESS, M.Z. PAPIZ, R.J. COGDELL, N.W. ISAACS, *Nature* **1995**, *374*, 517–521.

- 6 J. KOEPKE, X. HU, C. MUENKE, K. SCHULTEN, H. MICHEL, *Structure* **1996**, *4*, 581–597.
- 7 M. C. PETTY, *Langmuir-Blodgett Films: An Introduction*, Cambridge University Press, Cambridge, 1996.
- 8 ULMAN, *Chem. Rev.* **1996**, *96*, 1533–1554.
- 9 L. NETZER, J. SAGIV, *J. Am. Chem. Soc.* **1983**, *105*, 674–676.
- 10 S. D. EVANS, A. ULMAN, K. E. GOPPERT-BERARDUCCI, L. J. GERENSER, *J. Am. Chem. Soc.* **1991**, *113*, 5866–5868.
- 11 H. LEE, L. J. KEPLEY, H.-G. HONG, T. E. MALLOUK, *J. Am. Chem. Soc.* **1988**, *110*, 618–620.
- 12 G. DECHER, J. D. HONG, *Ber. Bunsen-Ges. Phys. Chem.* **1991**, *95*, 1430–1434.
- 13 See review articles: (a) X. ARYS, A. M. JONAS, A. LASCHEWSKY, R. LEGRAS, in *Supramolecular Polymers*, Ed. A. Cifferi, Marcel Dekker, New York, 2000, p 505–563; (b) P. BERTRAND, A. M. JONAS, A. LASCHEWSKY, R. LEGRAS, *Macromol. Rapid Commun.* **2000**, *21*, 319–348; (c) M. RAPOSO, O. N. OLIVEIRA, *Braz. J. Phys.* **1998**, *28*, 392–404; (d) G. DECHER, M. ECKLE, J. SCHMITT, B. STRUTH, *Curr. Opin. Colloid Interface Sci.* **1998**, *3*, 32–39; (e) G. DECHER, *Science* **1997**, *277*, 1232–1237; (f) W. KNOLL, *Curr. Opin. Colloid Interface Sci.* **1996**, *1*, 137–143; (g) G. DECHER, in *The Polymer Materials Encyclopedia: Synthesis, Properties and Applications*, Ed. J. C. Salamone, CRC Press, Boca Raton, 1996, p. 4540–4546; (h) G. DECHER, *Comprehensive Supramolecular Chemistry (Templating, Self-Assembly and Self-Organization)*, Eds. J. P. SAUVAGE, M. W. HOSSEINI, Pergamon Press, Oxford, 1996, vol. 9, p. 507; (i) M. SANO, Y. LVOV, T. KUNITAKE, *Annu. Rev. Mater. Sci.* **1996**, *26*, 153–187; (j) Y. M. LVOV, G. DECHER, *Crystallogr. Rep.* **1994**, *39*, 628–647.
- 14 LASCHEWSKY, *Eur. Chem. Chronicle* **1997**, *2*, 13–24.
- 15 WU, D. YOO, J. K. LEE, M. F. RUBNER, *J. Am. Chem. Soc.* **1999**, *121*, 4883–4891.
- 16 G. J. KELLOGG, A. M. MAYES, W. B. STOCKTON, M. FERREIRA, M. F. RUBNER, S. K. SATIJA, *Langmuir* **1996**, *12*, 5109–5113.
- 17 (a) J. SCHMITT, T. GRÜNEWALD, G. DECHER, P. S. PERSHAN, K. KJAER, M. LÖSCHE, *Macromolecules* **1993**, *26*, 7058–7053; (b) D. KORNEEV, Y. LVOV, G. DECHER, J. SCHMITT, S. YARADAIKIN, *Physica B* **1995**, *213&214*, 954–956; (c) M. LÖSCHE, J. SCHMITT, G. DECHER, W. G. BOUWMAN, K. KJAER, *Macromolecules* **1998**, *31*, 8893–8906.
- 18 (a) X. ARYS, A. M. JONAS, A. LASCHEWSKY, *Macromolecules* **2001**, *34*, 3318–3330; (b) X. ARYS, E. WISCHERHOFF, P. FISCHER, R. LEGRAS, A. LASCHEWSKY, A. M. JONAS, submitted; (c) X. ARYS, *PhD Thesis*, Université Catholique de Louvain, 2000.
- 19 (a) E. R. KLEINFELD, G. S. FERGUSON, *Science* **1994**, *265*, 370–373; (b) *Chem. Mater.* **1995**, *7*, 2327–2331; (c) *Chem. Mater.* **1996**, *8*, 1575–1578.
- 20 (a) N. A. KOTOV, I. DÉKÁNY, J. H. FENDLER, *J. Phys. Chem.* **1995**, *99*, 13065–13069; (b) N. A. KOTOV, T. HARASZTI, L. TURI, G. ZAVAL, R. E. GEER, I. DÉKÁNY, J. H. FENDLER, *J. Am. Chem. Soc.* **1997**, *119*, 6821–6832.
- 21 K. ARIGA, Y. LVOV, I. ICHINOSE, T. KUNITAKE, *Appl. Clay Sci.* **1999**, *15*, 137–152.
- 22 (a) N. G. HOOGVEEN, M. A. C. STUART, G. J. FLEER, *J. Colloid Interface Sci.* **1996**, *182*, 133–145; (b) N. G. HOOGVEEN, M. A. C. STUART, G. J. FLEER, *J. Colloid Interface Sci.* **1996**, *182*, 146–157.
- 23 D. COCHIN, M. PASSMANN, G. WILBERT, R. ZENTEL, E. WISCHERHOFF, *Macromolecules* **1997**, *30*, 4775–4779.
- 24 (a) P. J. OLLIVIER, N. I. KOVYUKHOVA, S. W. KELLER, T. E. MALLOUK, *Chem. Commun.* **1998**, 1563–1564; (b) Z. H. CHEN, Y. A. YANG, J. B. QIU, J. N. YAO, *Langmuir* **2000**, *16*, 722–725.
- 25 (a) S. W. KELLER, N. H. KIM, T. E. MALLOUK, *J. Am. Chem. Soc.* **1994**, *116*, 8817–8818; (b) S. W. KELLER, S. A. JOHNSON, E. S. BRIGHAM, E. H. YONEMOTO, T. E. MALLOUK, *J. Am. Chem. Soc.* **1995**, *117*, 12879–12880; (c) D. M. KASCHAK, T. E. MALLOUK, *J. Am. Chem. Soc.* **1996**, *118*, 4222–4223; (d) H. N. KIM, S. W. KELLER, T. E. MALLOUK, J. SCHMITT, G. DECHER, *Chem. Mater.* **1997**, *9*, 1414–1421; (e) D. M. KASCHAK, J. T. LEAN, C. C. WARAKSA, G. B. SAUPE, H. USAMI, T. E. MALLOUK, *J. Am. Chem. Soc.* **1999**, *121*, 3435–3445; (f) J. KERIMO, D. M. ADAMS, P. F. BARBARA, D. M. KASCHAK, T. E. MALLOUK, *J. Phys. Chem. B* **1998**, *102*, 9451–

- 9460; (g) S. W. KELLER, H. N. KIM, T. E. MALLOUK, *J. Am. Chem. Soc.* **1994**, *116*, 8817–8818.
- 26 R. E. SCHAACK, T. E. MALLOUK, *Chem. Mater.* **2000**, *12*, 2513–2516.
- 27 (a) K. GLINEL, A. LASCHEWSKY, A. M. JONAS, *Macromolecules* **2001**, *34*, 5267–5274; (b) K. GLINEL, A. LASCHEWSKY, A. M. JONAS, submitted.
- 28 M. LI, B. LI, L. JIANG, T. TUSSILA, N. TKACHENKO, H. LEMMETYINEN, *Chem. Lett.* **2000**, 266–267.
- 29 F. CARUSO, K. NIIKURA, D. N. FURLONG, Y. OKAHATA, *Langmuir* **1997**, *13*, 3427–3433.
- 30 Y. LVOV, K. ARIGA, I. ICHINOSE, T. KUNITAKE, *J. Am. Chem. Soc.* **1995**, *117*, 6117–6123.
- 31 Y. LVOV, K. ARIGA, I. ICHINOSE, T. KUNITAKE, *Thin Solid Films* **1996**, *284*–285, 797–801.
- 32 M. K. RAM, M. ADAMI, S. PADDEU, C. NICOLINI, *Nanotechnology* **2000**, *11*, 112–119.
- 33 M. ONDA, Y. LVOV, K. ARIGA, T. KUNITAKE, *Biotechnol. Bioeng.* **1996**, *51*, 163–167.
- 34 M. ONDA, Y. LVOV, K. ARIGA, T. KUNITAKE, *J. Ferment. Bioeng.* **1996**, *82*, 502–506.
- 35 Y. LVOV, H. HASS, G. DECHER, H. MÖHWALD, *Langmuir* **1994**, *10*, 4232–4236.
- 36 S. JOLY, R. KANE, L. RADZIŁOWSKI, T. WANG, A. WU, R. E. COHEN, E. L. THOMAS, M. F. RUBNER, *Langmuir* **2000**, *16*, 1354–1355.
- 37 D. L. FELDHEIM, K. C. GRABAR, M. J. NATAN, T. E. MALLOUK, *J. Am. Chem. Soc.* **1996**, *118*, 7640–7641.
- 38 D. L. FELDHEIM, H. N. KIM, H. G. HONG, S. W. KELLER, K. C. GRABAR, M. J. NATAN, T. E. MALLOUK, *NATO ASI Series C* **1997**, *499*, 41–51.
- 39 E. HAO, B. YANG, H. REN, X. QIAN, T. XIE, J. SHEN, D. LI, *Mater. Sci. Eng. C* **1999**, *10*, 119–122.
- 40 Y. LIU, A. ROSIDIAN, R. O. CLAUS, *J. Clust. Sci.* **1999**, *10*, 421–428.
- 41 J. SCHMITT, G. DECHER, W. J. DRESSICK, S. L. BRANDOW, R. E. GEER, R. SHASHIDHAR, J. M. CALVERT, *Adv. Mater.* **1997**, *9*, 61–65.
- 42 A. MAMEDOV, J. OSTRANDER, F. ALIEV, N. A. KOTOV, *Langmuir* **2000**, *16*, 3941–3949.
- 43 (a) M. TARABIA, H. HONG, D. DAVIDOV, S. KIRSTEIN, R. STEITZ, R. NEUMANN, Y. AVNY, *J. Appl. Phys.* **1998**, *83*, 725–732; (b) H. HONG, R. STEITZ, S. KIRSTEIN, D. DAVIDOV, *Adv. Mater.* **1999**, *10*, 1104–1108; (c) S. KIRSTEIN, H. HONG, R. STEITZ, D. DAVIDOV, *Synth. Met.* **1999**, *102*, 1067–1068.
- 44 M. FERREIRA, M. F. RUBNER, *Macromolecules* **1995**, *28*, 7107–7114.
- 45 J. W. BAUR, M. F. RUBNER, J. R. REYNOLDS, S. KIM, *Langmuir* **1999**, *15*, 6460–6469.
- 46 K. M. LENAHAN, Y. LIU, R. O. CLAUS, *SPIE* **1999**, 3675, 74–83.
- 47 B. RICHTER, S. KIRSTEIN, *J. Chem. Phys.* **1999**, *111*, 5191–5200.
- 48 A. V. NABOK, F. DAVIS, A. K. HASSAN, A. K. RAY, R. MAJEED, Z. GHASSEMLOOY, *Mater. Sci. Eng. C* **1999**, 8–9, 123–126.
- 49 J. W. OSTRANDER, A. A. MAMEDOV, N. A. KOTOV, *J. Am. Chem. Soc.* **2001**, *123*, 1101–1110.
- 50 G. LADAM, P. SCHAAD, J. C. VOEGEL, P. SCHAAF, G. DECHER, F. CUISINIER, *Langmuir* **2000**, *16*, 1249–1255.
- 51 J. B. SCHLENOFF, S. T. DUBAS, *Macromolecules* **2001**, *34*, 592–598.
- 52 A. A. MAMEDOV, N. A. KOTOV, *Langmuir* **2000**, *16*, 5530–5533.
- 53 J. S. HIGGINS, H. C. BENOIT, *Polymers and Neutron Scattering*, Clarendon Press, Oxford, 1994.
- 54 G. DECHER, Y. LVOV, J. SCHMITT, *Thin Solid Films* **1994**, *244*, 772–777.
- 55 C. BOLLINNE, V. W. STONE, V. CARLIER, A. M. JONAS, *Macromolecules* **1999**, *32*, 4719–4724.
- 56 P. S. PERSHAN, J. ALS-NIELSEN, *Phys. Rev. Lett.* **1984**, *52*, 759–762.
- 57 D. W. VAN KREVELEN, *Properties of Polymers: Their Correlation with Chemical Structure; Their Numerical Estimation and Prediction from Additive Group Contributions*, Elsevier, Amsterdam, 1990.
- 58 M. TOLAN, *X-ray Scattering from Soft-Matter Thin Films*, Springer, Berlin, 1999.
- 59 J. DAILLANT, A. GIBAUD, *X-Ray and Neutron Reflectivity: Principles and Applications*, Springer, Berlin, 1999.



- 60 B. PHILIPP, H. DAUTZENBERG, K.-J. LINOW, J. KÖTZ, W. DAWYDOFF, *Prog. Polym. Sci.* **1989**, *14*, 91–172.
- 61 (a) A. LASCHEWSKY, B. MAYER, E. WISCHERHOFF, X. ARYS, A. M. JONAS, *Ber. Bunsen-Ges. Phys. Chem.* **1996**, *100*, 1033–1038; (b) X. ARYS, A. M. JONAS, B. LA-GUITTON, R. LEGRAS, A. LASCHEWSKY, E. WISCHERHOFF, *Prog. Org. Coat.* **1998**, *34*, 108–118; (c) P. FISCHER, A. LASCHEWSKY, E. WISCHERHOFF, X. ARYS, A. M. JONAS, R. LEGRAS, *Macromol. Symp.* **1999**, *137*, 1–24.
- 62 M. KOETSE, PhD Thesis, Université catholique de Louvain, 2001.
- 63 A. J. BARD, T. E. MALLOUK, in *Molecular Design of Electrode Surfaces (Techniques of Chemistry; Vol. 22)*, Ed. R. W. MURRAY; Wiley-Interscience, New York, **1992**, 271–312.
- 64 (a) H. G. HONG, *Bull. Korean Chem. Soc.* **1995**, *16*, 1145–1147; (b) J. S. DO, T. H. HA, J. D. HONG, K. KIM, *Bull. Korean Chem. Soc.* **1998**, *19*, 257–261.
- 65 (a) N. A. KOTOV, I. DÉKÁNY, J. H. FENDLER, *Adv. Mater.* **1996**, *8*, 637–641; (b) J. H. FENDLER, *Chem. Mater.* **1996**, *8*, 1616–1624; (c) J. H. FENDLER, *Croat. Chem. Acta* **1998**, *71*, 1127–1137; (d) T. CASSAGNEAU, J. H. FENDLER, *Adv. Mater.* **1998**, *10*, 877–881; (e) T. CASSAGNEAU, N. A. KOTOV, J. H. FENDLER, *J. Disper. Sci. Technol.* **1999**, *20*, 1517–1517; (f) N. I. KOVTYUKHOVA, P. J. OLLIVIER, B. R. MARTIN, T. E. MALLOUK, S. A. CHIZHIK, E. V. BUZANEVA, A. D. GORCHINSKIY, *Chem. Mater.* **1999**, *11*, 771–778.
- 66 T. SASAKI, Y. EBINA, M. WATANABE, G. DECHER, *Chem. Commun.* **2000**, 2163–2164.
- 67 R. K. ILER, *J. Colloid Interface Sci.* **1966**, *21*, 569–594.
- 68 C. WANDREY, J. HERNÁNDEZ-BARAJAS, D. HUNKELER, *Adv. Polym. Sci.* **1999**, *145*, 123–192.
- 69 A. LASCHEWSKY, P. Y. VUILLAUME, unpublished results.
- 70 R. HOSEMANN, S. N. BAGCHI, *Direct Analysis of Diffraction by Matter*, North-Holland, Amsterdam, 1962.
- 71 (a) A. GUINIER, *Théorie et Technique de la Radiocristallographie*, Dunod, Paris, 2nd edn. 1950, p. 490; (b) F. J. BALTÁ-CALLEJA, C. G. VONK, *X-Ray Scattering of Synthetic Polymers*, Elsevier, New York, 1989, p. 134.
- 72 I. A. LASCHEWSKY, E. WISCHERHOFF, M. KAURANEN, A. PERSOONS, *Macromolecules* **1997**, *30*, 8304–8309.
- 73 A. LASCHEWSKY, E. WISCHERHOFF, P. BERTRAND, A. DELCORTE, *Macromol. Chem. Phys.* **1997**, *198*, 3239–3253.
- 74 (a) J. DAI, A. W. JENSEN, D. K. MOHANTY, J. HERDT, M. L. BRUENING, *Langmuir* **2001**, *17*, 931–937; (b) I. ICHINOSE, S. MIZUKI, S. OHNO, H. SHIRAIISHI, T. KUNITAKE, *Polym. J.* **1999**, *31*, 1065–1070.
- 75 I. PASTORIZA-SANTOS, B. SCHÖLER, F. CARUSO, *Adv. Funct. Mater.* **2001**, *11*, 122–128.
- 76 M. ECKLE, G. DECHER, *Nano Lett.* **2001**, *1*, 45–49.
- 77 R. ZENTEL, *Liquid Crystal*, Steinkopff Verlag, Darmstadt, 1994, p. 103.
- 78 (a) A. WIESEMANN, R. ZENTEL, *Liq. Cryst.* **1994**, *16*, 349–350; (b) A. WIESEMANN, R. ZENTEL, G. LIESER, *Acta Polym.* **1995**, *46*, 25–36.
- 79 Y. LVOV, F. ESSLER, G. DECHER, *J. Phys. Chem.* **1993**, *97*, 13773–13777.
- 80 S. T. DUBAS, J. B. SCHLENOFF, *Macromolecules* **1999**, *32*, 8153–8160.
- 81 W. KLEBER, *Einführung in die Kristallographie*, VEB Verlag Technik, Berlin, 1956.

## 8

# Layer-by-Layer Assembly of Nanoparticles and Nanocolloids: Intermolecular Interactions, Structure and Materials Perspectives

N. A. KOTOV

### Abstract

Nanoparticles (NPs) of diameter 1–100 nm and nanocolloids (i.e., species with one or two dimension in the nanometer scale) can be assembled with polyelectrolytes following layer-by-layer deposition (LBL) protocols producing high-quality thin films. This technique can be considered a convenient method for processing NPs and related materials into a variety of thin-film devices. Materials properties of the assemblies depend on both the packing of the NPs and layer sequence and, therefore, approaches to structural control of NP LBL films need to be established. The effect of different experimental parameters and morphological characteristics of NP on the structure of LBL films are considered on the basis of intermolecular interactions between NP and polyelectrolytes. Their combination and, in particular, appropriate surface modification of colloids, make possible the preparation of densely packed films, which follow regular LBL deposition with growth direction parallel to the surface normal, for virtually any nanoscale dispersion. For such layers, one can design stratified materials, whose functional properties may be controlled and optimized by ordering the layers according to a predetermined pattern. Several examples of such assemblies demonstrating the effect of layer sequence on the mechanical, magnetic and optical properties are highlighted.

### 8.1

#### Introduction

Advanced materials from inorganic nanoparticles are currently one of the most dynamic areas of today's science. They represent significant fundamental and commercial interest with a wide range of applications including the next generation optics, electronics, and sensors [1–6]. Synthetic methods of colloidal chemistry afford manipulation of their size, surface structure and, hence, their properties [7]. In optical, electrical and magnetic devices, NPs will be mostly used as thin films. Currently, such films are typically made by spin coating, spraying, or sometimes by simple painting of nanoparticle–matrix mixtures. Layer-by-layer assembly is one of the most promising new methods of thin film deposition, which is often

used for oppositely charged polyelectrolytes (PE) [8, 9]. It has also been successfully applied to thin films of NPs and various other inorganic materials [10–33]. One of the major advantages of LBL is simplicity: the process requires neither sophisticated hardware nor high purity of the components. At the same time under optimal conditions, the method produces high quality coatings with thickness controllable at the nanometer level [26]. This deposition technique is also quite universal: for virtually any aqueous dispersion of NPs, one can find a matching polyelectrolyte and deposition conditions yielding a steady film build-up [34]. The lateral packing of the NPs in individual adsorption layers can also be controlled by different means producing densely packed coatings [15, 27, 34]. LBL coatings are also highly homogeneous, unlike the composite polymer/NP coatings obtained by other means [35], where phase separation may occur [36]. Last but not least, LBL allows one to combine NPs with other functional materials often used in this technique such as dyes, proteins, and DNA, leading to a palette of multifunctional nanostructured materials [37]. In essence, LBL can be a convenient method for processing NPs in thin films, which opens broad perspectives for this technique, both in research and in industry. This review attempts to summarize the current status of understanding of LBL deposition of NPs, the structure of the films produced and the future applications of these materials.

## 8.2

### **Layer-by-layer Assembly of Nanoparticles and Nanocolloids**

Layer-by-layer assembly can be described as the sequential adsorption of positively and negatively charged species, A and B, by dipping a substrate alternately into their solutions. Rinsing with water between adsorption steps removes the excess of the previous solution and leaves a thin layer of charged species on the surface, thereby preparing the surface for the next adsorption step. The dynamic development of LBL that we have seen recently was sparked mainly by its great success with the assembly of PEs associated with the work of Decher, Möhwald, Lvov, Rubner and Mallouk [9, 30, 38–40]; however, similar ideas were previously used by Iler [41] for the assembly of colloids, by Nicolau for production of semiconductor films [42, 43], and by Bruce et al. for the assembly of NP/PE magnetic films [10]. Description of the experimental details of the technique can be found in other contributions to this book and in the original publications of the respective authors.

From the analysis of the abundant literature on LBL, one can say that A and B are chosen preferentially to be of relatively high molecular weight. The experimental work on polymers with different chain lengths indicates that increase in the molecular mass of species promotes stable LBL growth [15, 44–46], which is related to the diverse nature of intermolecular interactions involved in the process (see Section 8.3.1). Although for relatively low molecular weight species such as multicharged metal ions [47–51] and molecular dyes [52–54], LBL assembly has also been reported, their tendency to leach out should be stressed [55]. A heavy

mass and multiple points of attachment of A and B render the adsorption sufficiently irreversible to allow for deposition of the next layer. Either A or B is almost always a PE, while the other LBL partner can be a dispersion of NPs, clay sheets, proteins, dyes, vesicles, DNA, viruses or other species. The omnipresence of PEs in LBL assemblies, that acquired popularity in the 1990s, is explained by their ability to cover irregularities owing to the rod-like conformation of the charged macromolecules in aqueous solutions [9, 56]. As evidenced by AFM images of different PEs adsorbed to the surface of a silicon wafer from aqueous solutions (Fig. 8.1), this conformation is likely to be retained in the LBL films as well. For more rigid polymers such as poly(2-vinylpyridine)  $M_w$  200 000–400 000 (Fig. 8.1a), the polymer chains tend to be less intertwined than for more flexible macromolecules such as poly(diallyldimethylammonium chloride)  $M_w$  400 000–

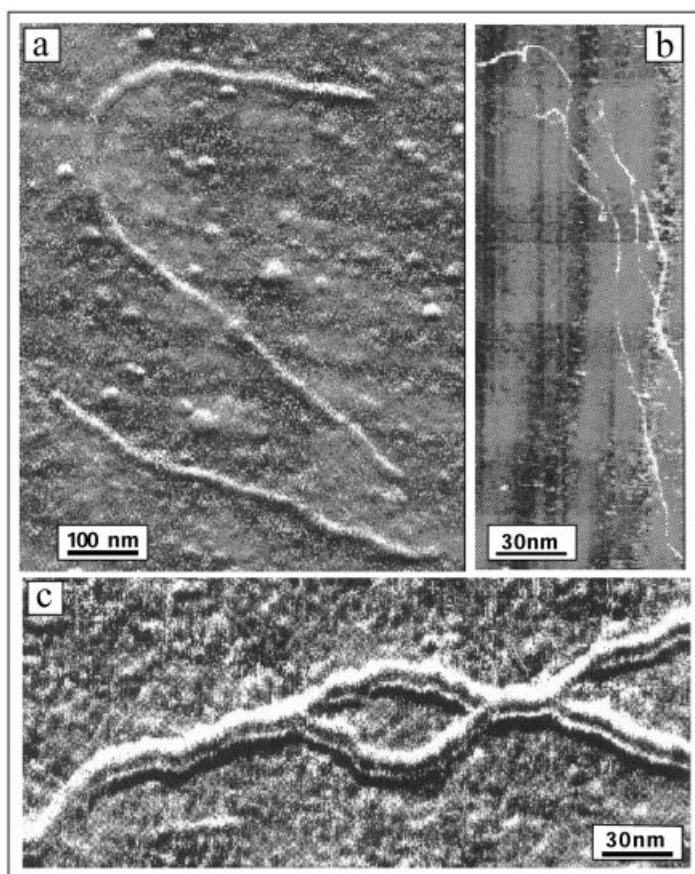


**Fig. 8.1** Phase contrast AFM images of (a) poly(2-vinylpyridine)  $M_w$  200 000–400 000, (b) poly(diallyldimethylammonium) chloride  $M_w$  400 000–500 000 and (c) (poly(4-vinyl-1-methyl-pyridinium) bromide  $M_w$  50 000 deposited on silicon wafers by adsorption from dilute solutions at pH 2–3.

500000 (Fig. 8.1 b) and poly(4-vinyl-*N*-methyl pyridinium bromide)  $M_w$  50000 sometimes even forming double chains (Fig. 8.1 c).

An LBL film obtained after  $n$  deposition cycles can be generically referred to as  $(A/B)_n$ , and this notation will be used throughout the chapter. It is important to note that the  $(A/B)_n$  abbreviation describes primarily the *deposition procedure* rather than the actual sequence of the multilayers obtained as a result of it. Films where the adjacent layers deposited in one cycle can be clearly distinguished from each other are difficult to obtain because of the strong interpenetration of PE chains [57–59] blurring the border between the adjacent layers. Although significant improvement of layer sharpness has been made recently by combining LBL with spin-coating [61] and by selecting an LB pair with low degree of interpenetration [26], one needs to point out that in the majority of polymer pairs the result of LBL assembly can be characterized best as a molecular blend of A and B [62, 63]. The same conclusion can be made for many PE assemblies with spherical colloids, with the exception of anisotropic particles, such as clay platelets, that may have preferential orientation in LBL films.

NPs are commonly defined as crystallites of inorganic materials with a diameter from 1 to 100 nm exemplified by NPs of CdS and  $Fe_3O_4$  in Fig. 8.2 a, b. Quite often, NPs with an additional layer of a different inorganic material epitaxially or non-epitaxially deposited around the core have more refined electrical optical and magnetic properties than “naked” NPs. The core–shell NPs (Fig. 8.2 c, d) can also be assembled by LBL and will also be considered here. Since there are no abrupt transitions in the PE–NP interactions associated with size, if necessary, other systems with physical dimensions outside the 1–100 nm range will be discussed, too.

The LBL process for NPs follows that used for the other systems [20, 34, 35]. Their layer-by-layer assembly is typically monitored by the increase in the UV–VIS absorbance, O.D., when the particles are deposited on a transparent substrate. The hallmark of this technique is the linear rise of the O.D. with the number of layers, which was observed for many LBL pairs [9, 52, 64–69]. Typically, the distribution of the deposited species in macroscale (mm range) is very uniform, and the substrate appears very homogeneously colored. Notably, the O.D. vs.  $n$  linearity shows the equality of the amounts of the material transferred on the substrate in every deposition cycle. It cannot serve as a proof for the structural organization of the film, although ordered layered stacks, for instance Langmuir–Blodgett films, also revealed the same behavior. For NPs, the linear growth of the multilayers on planar substrates (similar to that in Fig. 8.3) has been demonstrated by many authors. The nanocrystalline materials used in such multilayers include CdS [20, 70–72], CdSe [18, 31, 73], CdTe [70, 74], ZnS [75], PbS [76],  $TiO_2$  [20, 71–73, 76–78],  $ZrO_2$  [79], Ag [27, 80], Au [21, 81–83],  $SiO_2$  [12, 23, 24],  $MoO_2$  [84], polyoxometallates [85, 86], HgTe [35],  $Fe_3O_4$  [26, 87]. Nanocolloids, i.e. dispersions with particles with only one or two spatial dimensions in the nanometer scale range, exhibit similar behavior and include exfoliated clay platelets [12, 26, 28, 29, 37, 56, 88–90], zirconium phosphate [31, 91–94], lamellar Hofmann clathrates [30], perovskites [95–97], graphite oxide [33, 80, 98–100], and gold/platinum nanorods [101]. Significant research efforts have been devoted to LBL assemblies of

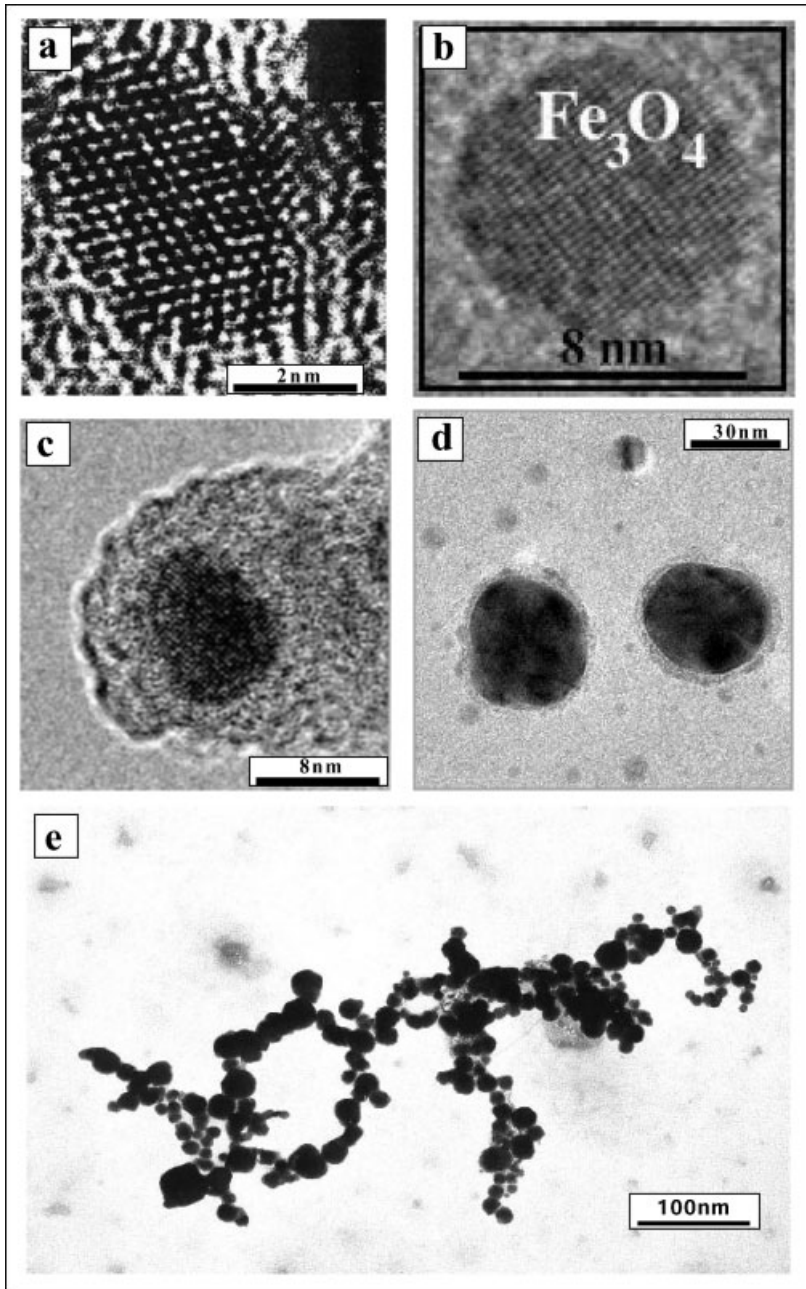


**Fig. 8.2** Transmission electron microscopy images of different NPs: (a) CdS, (b)  $\text{Fe}_3\text{O}_4$ , (c)  $\text{SiO}_2$ -coated core-shell  $\text{Fe}_3\text{O}_4$ , (d)  $\text{TiO}_2$ -coated Ag NP, and (e) YIG.

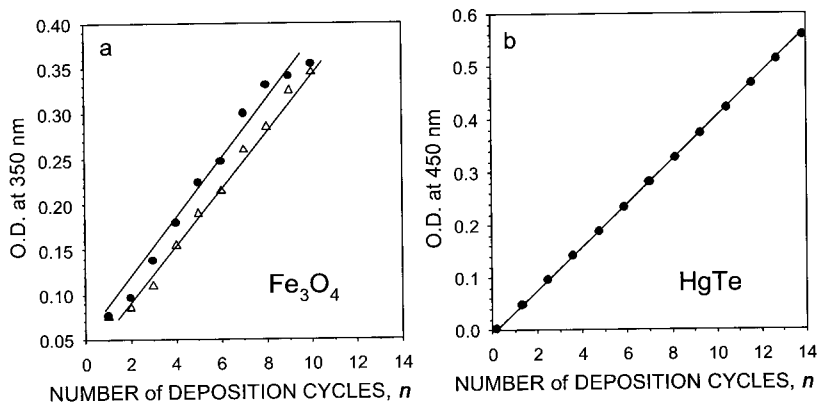


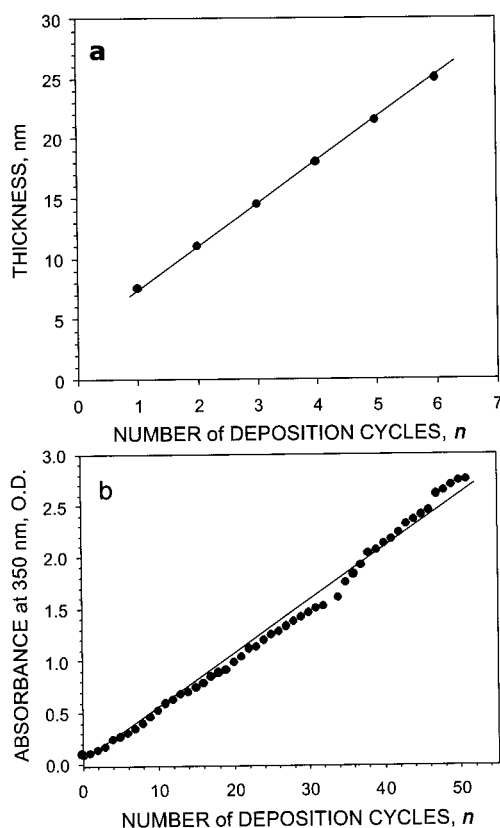
**Fig. 8.3** Dependence of optical density of (a) (PDDA/naked  $\text{Fe}_3\text{O}_4$ ) $_n$  (triangles), (PDDA/ $\text{SiO}_2$  coated  $\text{Fe}_3\text{O}_4$ ) $_n$  (circles), and (b) (PDDA/HgTe) $_n$  LBL films on the number of deposition cycles.

NPs around micron-scale colloids, which demonstrated that the multilayer growth behavior did not appear to be different from that on planar substrates, as evidenced by single particle light scattering experiments, at least when the radius of curvature of the colloids was much greater than that of the NPs [13, 14, 102–104].

The thickness of the coating calculated from ellipsometric or quartz crystal microbalance measurements followed the linear behavior of the O.D. vs.  $n$  plots. The thickness increment added in one deposition cycle often approached that of a monolayer of PE or NPs [24, 53, 97]. Sometimes it exceeded the average NP diameter; for instance, HgTe NPs formed 2–3 monolayers in each deposition cycle [35]. The same could be seen for gold NPs stabilized by citrate forming dense LBL films with a characteristic metallic shine [105] and for relatively large latex colloids when salt is added to the dispersion [106]. In general, one can say that assembly from solutions on the verge of instability should result in thicker films. In turn, the role of the previously deposited PE is then to selectively destabilize the particle in the vicinity of the substrate. The increase in thickness associated with such accelerated deposition may also increase the roughness of the coating.

In some cases, such as ca. 32 nm yttrium iron garnet (YIG) (Fig. 8.2e), as well as for some other relatively large hydrophilic NPs made from oxides, the thickness obtained was noted to be significantly lower than the average value expected for densely packed layers of NPs of this diameter. The thickness increment, which was added to the coating by a single PDDA/YIG layer, was 3.5 nm (Fig. 8.4a). This thickness corresponded to the average surface density of YIG of one particle per 32300 nm<sup>2</sup>. Such a small thickness of absorption layer and low density of particles contradicted the structure of LBL nanoparticles films found in previously studied LBL pairs [11, 18, 23, 24, 26, 35, 74, 79, 81]. Despite this, stable growth of YIG/PDDA multilayers was observed for as long as 50 deposition cycles (Fig. 8.4b).

**Fig. 8.4** Dependence of (a) ellipsometric thickness and (b) optical density of  $(\text{PDDA}/\text{YIG})_n$  multilayers on the number of deposition cycles assembled with 1 h YIG adsorption step. Same deposition time was used for other YIG data unless otherwise specified. Elongation of the assembly time did not result in significant change of layer thickness and O.D.



It is commonly understood that both A and B in LBL pairs form a *complete* (mono)layer on the surface, which is dense enough to reverse the surface charge in each layer. Indeed, for many combinations of oppositely charged compounds, each adsorption step produced a thin and uniform layer of a corresponding compound. However, for many combinations of PEs with compact colloidal species, organic or inorganic, the growth of the LBL assembly was shown to be very slow or irregular, for reasons that remain poorly understood. Considering the requirement of surface charge switching, the fact that sustained build-up of the multilayers was seen in Fig. 8.4b was quite surprising and raised questions about the actual mechanism of the layer-by-layer growth in this and similar cases.

The SEM images of  $(\text{YIG}/\text{PDDA})_n$  multilayers revealed that the repetition of adsorption cycles resulted not in the sandwich-like layering of organic and inorganic strata [21, 23, 24, 26, 27, 35, 37, 79, 81, 107, 108] but rather in the growth of fairly isolated YIG islands (Fig. 8.5). In layer 1, the film consisted of YIG domains of 0.5–1.5  $\mu\text{m}$  in diameter (Fig. 8.5a), which increased to 1–3  $\mu\text{m}$  in deposition cycle 2 (Fig. 8.5b), and 3–4  $\mu\text{m}$  in deposition cycle 3 (Fig. 8.5c). The domains were expanding laterally along the substrate surface, accompanied by an increase in their aver-



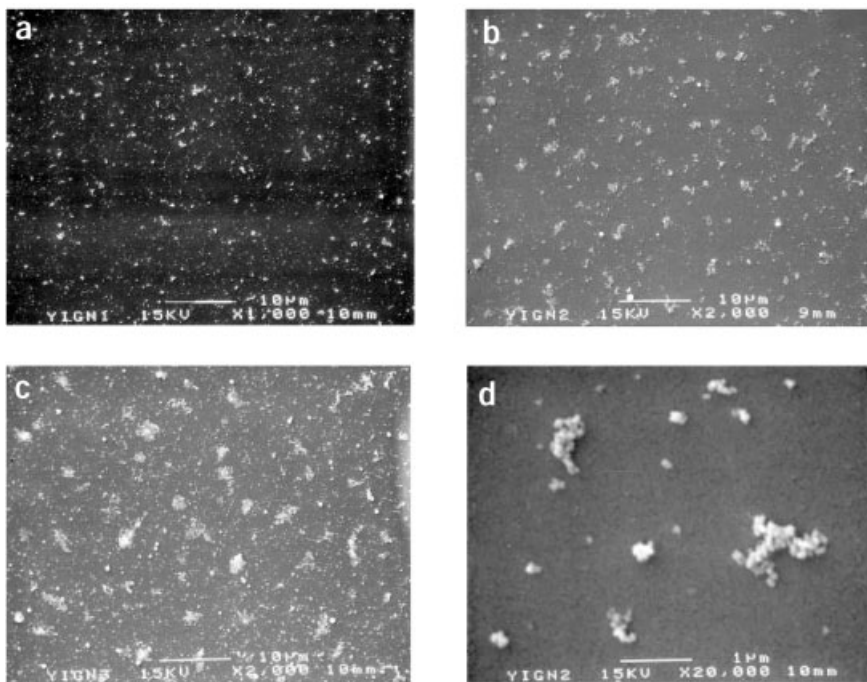


**Fig. 8.5** Scanning electron microscopy images of  $(\text{PDDA}/\text{YIG})_n$  films with (a)  $n=1$ , (b) and (c)  $n=2$ , and (d)  $n=3$ .

age height. In the close-up, one could see that the YIG islands were 3D agglomerates of YIG NPs (Fig. 8.5d), growing in size with increasing  $n$ . This demonstrated that the particles deposited in the LBL deposition cycles adhered predominantly to the existing domains rather than to the bare PDDA-covered surface, although the total number of domains may also increase.

The growth pattern of the isolated YIG domains, which for convenience is referred to here as a lateral expansion mode [109], was initially regarded as the result of poor quality substrates, possibly carrying hydrophobic patches, as seen for modified silica surfaces [88]. However, for glass slides and silicon wafers thoroughly cleaned with hot piranha solution for as long as 30 min as well as for glass slides treated with a promoter of ionic adsorption 3-aminopropylsiloxane, identical deposition patterns were observed. Effective elimination of a potential substrate effect could be accomplished by precoating with a  $(\text{PDDA}/\text{PAA})_n$  multilayer to form a precursor film, which made the surface virtually uniform in properties.  $(\text{PDDA}/\text{PAA})_n$  and similar PE pairs have been shown by many authors to form excellent coatings on a variety of surfaces [110–114]. We used acidic, pH 3.5, PAA solution, when the PAA was only slightly ionized, to increase the thickness of the adsorption layers [111]. The high molecular weight of PAA of 1 000 000 allowed it to bridge over possible undesirable spots. Five  $(\text{PDDA}/\text{PAA})$  bilayers were

made on a substrate producing a film of ca. 20 nm and topped with an additional layer of PDDA. This rendered the substrate hydrophilic with a contact angle of  $37 \pm 3$  degrees. Regardless of the very hydrophilic nature of  $(\text{PDDA}/\text{PAA})_n\text{PDDA}$  film, a new series of SEM images revealed that the cyclic repetition of adsorption steps resulted in the same growth pattern (Fig. 8.6) as for the bare silicon wafers without the precursor film, the size of the YIG domains expanded from 1.5–2  $\mu\text{m}$  for the first dipping cycle (Fig. 8.6a) to 3–5  $\mu\text{m}$  for cycle 2 (Fig. 8.6b) and 5–7  $\mu\text{m}$  for cycle 3 (Fig. 8.6c). Between the YIG islands, the texture of the underlying precursor layer could be seen on both the low magnification and high magnification images (compare Fig. 8.5d with Fig. 8.6d).

Thus, one could conclude that the pattern of film growth seen in Figs. 8.5 and 8.6 was a feature of the NP/PE pair rather than the substrate effect. Since the forces between YIG and PDDA are of a rather general nature, i.e. not specific to the YIG–PE pair, the similar growth pattern is likely to occur in other systems involving NPs or other colloids. Indeed, the similar lateral domain expansion was seen for 40 nm barium ferrite NPs (Fig. 8.7a,b) and 200 nm polystyrene latex (Fig. 8.7c,d).

Considering the structure of the films in Fig. 8.5–8.7, it must be pointed out that there is an aspect of the deposition process that is quite difficult to rational-

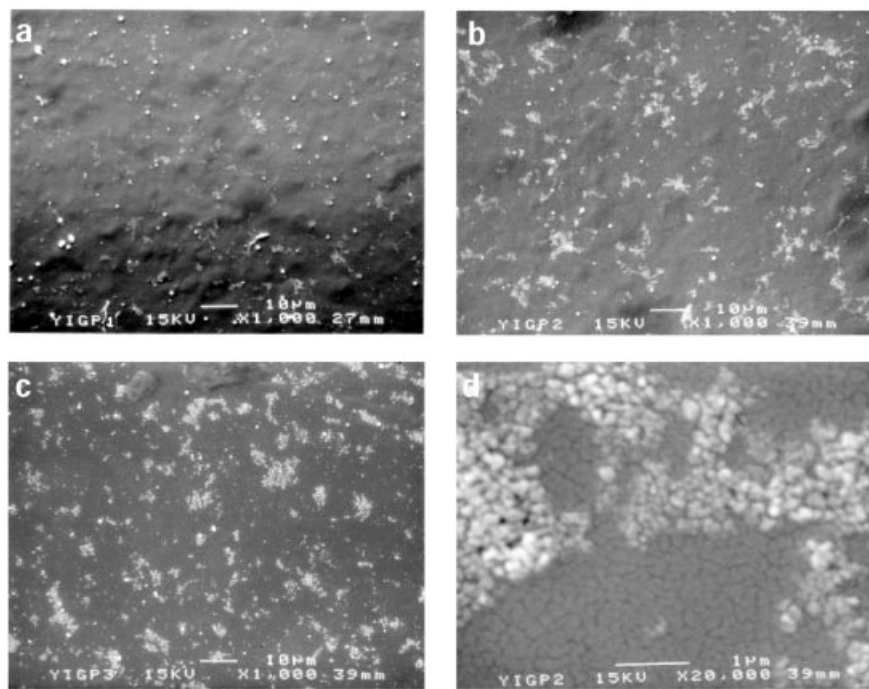


**Fig. 8.6** Scanning electron microscopy images of  $(\text{PDDA}/\text{YIG})_n$  films with (a)  $n=1$ , (b) and (d)  $n=2$ , and (c)  $n=3$  assembled on a precursor layer  $(\text{PDDA}/\text{PAA})_5\text{PDDA}$ .

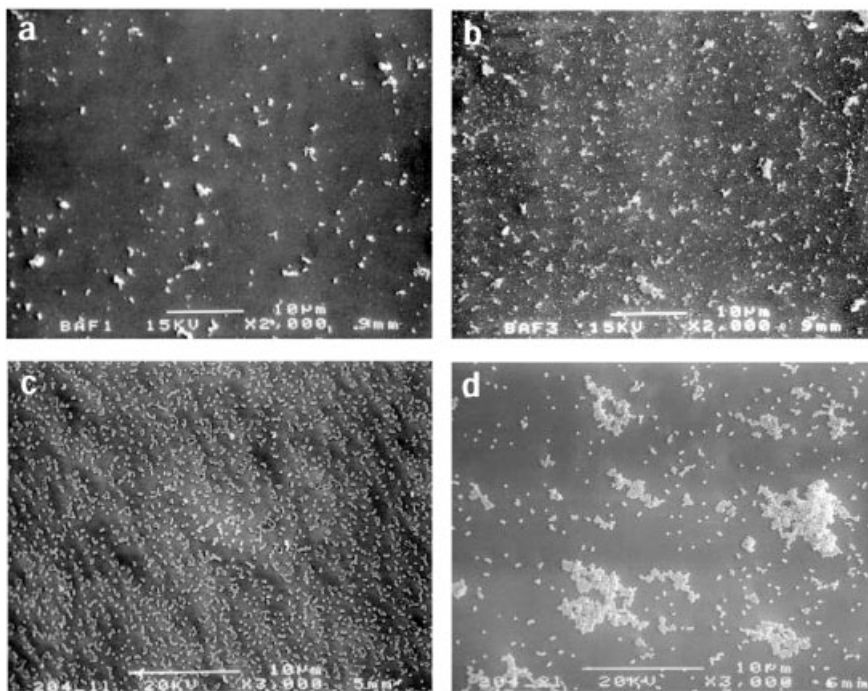


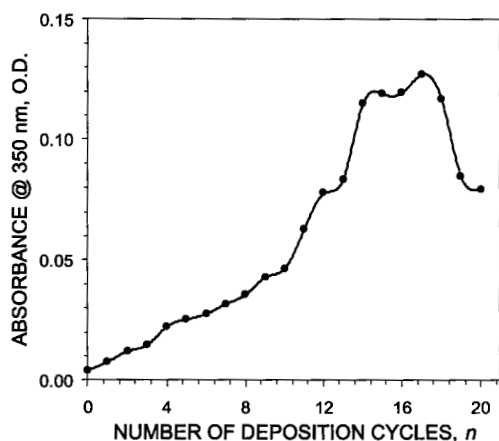
**Fig. 8.7** Scanning electron microscopy images of  $(\text{PDDA}/\text{barium ferrate})_n$  films with (a)  $n=1$  and (b)  $n=2$ , and  $(\text{PDDA}/\text{latex})_n$  films with (c)  $n=1$ , and (d)  $n=2$ .

ize at the moment. The constantly expanding area of YIG islands was supposed to increase the amount of the material transferred in each deposition cycle and, therefore, should have resulted in a constantly increasing optical density increment. Particularly surprising in the growth pattern of YIG and others was the fact that the O.D. vs.  $n$  plot remained linear throughout the deposition process without any sign of upturn. This indicates that there was a compensation effect reducing the number of adsorbed particles as the area of the film expanded. There can be several possible mechanisms of the compensation:

1. Partial desorption of previously adsorbed particles during the adsorption of the next PE layer;
2. increased electrostatic repulsion between like charged components as the film grows; and
3. dependence of the amount of the adsorbed material on film/substrate roughness.

The presence of the NP desorption process associated with the deposition of the new PDDA layers can be clearly seen in Fig. 8.8. The reduction of the YIG UV absorbance with increasing  $n$  for unoptimized deposition conditions can only be explained by the partial removal of YIG particles performing the standard LBL pro-

**Fig. 8.8** Dependence of the optical density of  $(\text{PDDA}/\text{YIG})_n$  film with 20 min YIG absorption step (unoptimized conditions).



cedure [115]. The reduction of the number of isolated latex spheres after the second deposition is also visible in Fig. 8.7d. A recent report on the adsorption of pyrene label in the LBL layers also showed that with every new PE layer some amount of the label was removed [54]. The increase in electrostatic repulsion and the influence of roughness on the amount of adsorbed material can be predicted on the basis of work on PE adsorption on solid surfaces [116]. Hence, compensation mechanisms are assumed to be operative in the system. Nevertheless, the question concerning why the superposition of all these effects results in a linear growth and not in a higher order curve remains open. In order to clarify this and other issues of LBL assembly, such as obtaining better organized layers, we need to look into the molecular processes responsible for LBL.

### 8.3

#### Structural Factors of Individual Adsorption Layers

##### 8.3.1

##### Intermolecular Interactions in the LBL Process

As can be seen from the previous section, the seemingly simple nature of the process may camouflage the complexity of the interactions responsible for the layer-by-layer build-up. Significant insights into the mechanism of the LBL process have been recently attained [64, 111, 117–121], and various complementary aspects of the theoretical foundation of LBL are presented in several chapters of this book. Nevertheless, the fact that the theoretical understanding of the process is significantly lagging behind the numerous experimental realizations of the technique needs to be recognized. To a large extent, LBL is the manifestation of a large class of novel phenomena that were revealed recently for intermolecular interactions of high molecular weight

compounds [122–125]. Without hesitation, one can anticipate more of these unique effects related to the concerted action of different forces as we learn more about the different aspects of LBL and expand the number of LBL pairs to include, in particular, more anisotropic species such as some NPs and nanocolloids.

Perspectives of LBL assemblies as new materials require structural control over the deposited films and therefore a fairly detailed picture of the intermolecular interactions involved in the process. The important consensus among many researchers in this field achieved in recent years is that short range interactions i.e. hydrophobic, ion–dipole, dipole–dipole forces and hydrogen bonding, are not merely the supporting actors in the LBL but rather, at least, equal partners as compared to commonly accepted electrostatic interactions, and may have a profound influence on the structure of LBL assemblies. To some extent, this is an evident conclusion that can be made on the basis of abundant experimental data obtained for PE complexes made from positive and negative chains in solutions [126–129] because the LBL PE–PE systems actually represent their special case [130]. It also coincides with the current understanding of the nature of the PE absorption [131–135]. Non-ionic and, in particular, hydrophobic interactions, which can be exceptionally strong in aqueous media, were also shown to play a major role in the systems that resemble the LBL assemblies such as PE complexes with surfactants [136–139], micelles [140], and inorganic colloids [141, 142]. It would not be necessary to make this point except that hydrophobic and other short-range interactions have sometimes been overlooked when considering LBL [143]. The explicit inclusion of hydrophobic and other “weak” forces changes the view on the driving forces of PE adsorption, which were previously considered to be virtually exclusively electrostatic [21, 29, 79, 144–150].

In publications on the role of interactions other than ion–ion in film build-up, theoretical [119] and experimental data [34, 119, 151–155] reflecting their influence on the adsorption of different components are discussed in great detail. Particularly relevant to the discussion of the driving forces of LBL are the reports on processes with no PE involved. Polymeric multilayers, which are based exclusively on non-ionic interactions include multilayers bound by charge transfer complexes [156], hydrogen bonding [155, 157], hydrophobic interactions [154] and dispersive attraction between complementary stereoregular polymers [158]. Contrary to the established classical LBL procedure with charge alternation, the assembly of similarly charged species has been observed when non-ionic interactions are maximized [118, 159].

In the case of NPs, non-ionically bonded multilayers have also been reported [73, 83, 160]. Together with the non-ionic polymeric LBL pairs, they represent experimental proof of the theoretically predicted crucial contribution of secondary interactions [119] to multilayer build-up. Since most of the NP dispersions are water-based and highly charged, it is important to evaluate the roles of ionic and van der Waals interactions in their assembly. In this respect, it is instructive to mention two experiments revealing the important role of hydrophobic interactions in the build-up of NP multilayers with PEs. In the first experiment, the composition of the NP stabilizer(s), i.e. the organic shell around the inorganic core made

of molecules strongly adsorbed by a functional group to the NP, was varied during the synthesis of NPs. The fairly dense stabilizer shell not only protects the NPs from further growth and aggregation, but is also responsible for their solubility and intermolecular interactions. CdS clusters can be stabilized almost equally well by many short-chain thiols, and therefore, a mixture of ethyl mercaptan, EtSH, and thiolactic acid,  $\text{CH}_3\text{CH}(\text{SH})\text{COOH}$ , was chosen for their preparation according to standard procedure [20, 161]. Different ratios of EtSH and thiolactic acid resulted in NPs with different hydrophobic/hydrophilic balance. EtSH, attached to the CdS core via the mercaptan end, presents the hydrophobic Et part to the outside, while thiolactic acid in the stabilizer shell presents polar  $-\text{COOH}$  groups to the outside making the NPs more hydrophilic. The CdS NPs with different shells were assembled with poly(diallyldimethylammonium chloride) (PDDA) using the same procedure [162]. The amount of the NPs in the films was evaluated by the optical density of five PDDA/CdS bilayers. As can be seen in Fig. 8.9, the average number of NPs transferred in each cycle depended on the structure of the organic shell around them and went through a maximum when the molar ratio of thiolactic acid/EtSH was about 0.3 [163]. Importantly, one could observe a precipitous decline of particle density with increase in the thiolactic acid portion of the stabilizer, imparting negative charge to the NPs. Therefore, the decline in NP affinity to the PE was accompanied by an *increase* in electrostatic attraction to the substrates coated with positively charged PDDA. These data indicate that there exists an optimum ratio between the number of hydrophobic Et and hydrophilic  $-\text{COOH}$  groups on the NP surface for efficient adsorption of NP to PE. When the surface charge exceeds an optimum value, determined by the balance between the long-range electrostatic attraction and the short-range hydrophobic forces associated with TLA and EtSH respectively, the hydrated state becomes more preferable for the NPs. Consequently, they can be easily removed from the substrate during the rinsing step. For insufficiently charged particles, both very low solubility in  $\text{H}_2\text{O}$  and the lack of long-range attraction to the substrate contribute to the poor film formation. The point of maximum surface density of NPs corresponds to the optimum combination of strong electrostatic attraction and firm binding to the PE via hydrophobic interactions, which make the adsorbed layer thermodynamically more preferable than the dissolved state.

The strong influence of NP coating on the efficiency of NP adsorption on PE can also be seen for the surface modification of yttrium iron garnet NPs (Fig. 8.10) [34]. In this case, the particle density and their distribution on the substrate surface were evaluated by atomic force microscopy. The native surface of YIG is very hydrophilic and negatively charged. YIG NPs could be assembled on positively charged PDDA; however LBL deposition followed the lateral expansion mode (see above, Fig. 8.5–8.7) with vast areas (on the nm scale) devoid of NPs (Fig. 8.10a). The surface between the agglomerates was coated only with PDDA, which could be seen in the magnified AFM images (Fig. 8.10b).

As for many oxide surfaces, alkylsiloxanes can be grafted to YIG. Hence, 3-aminopropyl siloxane was used, which rendered the NPs positively charged in acidic media due to the exposed  $-\text{NH}_3$  group. The LBL assembly for 3-aminopropyl-silox-

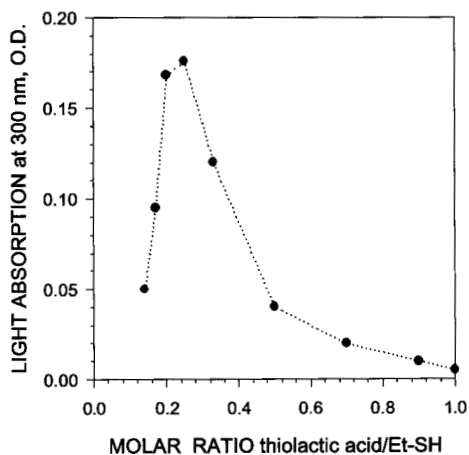


**Fig. 8.9** The dependence of optical density of (PDDA/CdS)<sub>5</sub> multilayer stack on the composition of the stabilizer shell around CdS NPs.

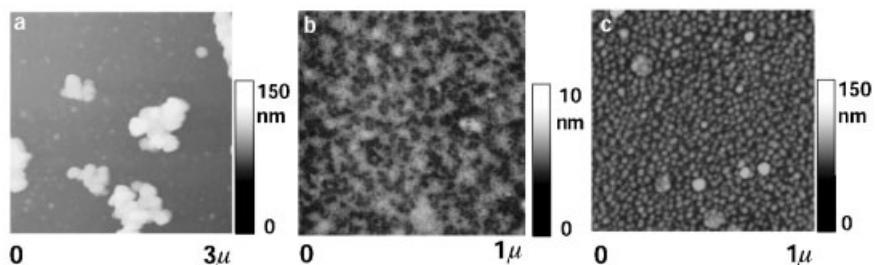


**Fig. 8.10** Atomic force microscopy images of (a) original YIG NPs adsorbed to PDDA layer, (b) the same sample with the scan area

chosen to be between the particle clusters, (c) 3-aminopropyl siloxane surface-modified YIG NPs adsorbed to a PAA layer.

ane-modified YIG NPs was performed with negatively charged PEs such as poly(styrenesulfonate) (PSS) and poly(acrylic acid) (PAA). AFM revealed a great improvement in the film structure: the NPs were densely packed after only one deposition cycle (Fig. 8.10c). The change in the film morphology can be understood by considering the new forces introduced by the surface modification. When YIG was modified with 3-aminopropyl siloxane, both the electrostatic and the van-der-Waals components of NP-PE interactions were changed and, in addition, the native and modified YIG had a different electrical charge. However, the difference in the behavior of the modified YIG could not be attributed to the difference in the electrostatic *attraction* between the NPs and corresponding PEs. The zeta potentials of the modified YIG and PSS at pH 3.5 were +12 mV and +15 mV, while the zeta potentials of the naked YIG and PDDA at pH 11 were -17 mV and -12 mV. As one can see, the magnitudes of the potentials were virtually the same for both LBL pairs and, therefore, the long-distance Coulomb interaction between the NPs and the PE-coated substrate is nearly the same for both pairs. At

this point, it is necessary to add that the initial use of both bare and modified particles at their corresponding pH on the PE covered surfaces caused electrostatic repulsion between the particle and the substrate because the zeta potentials were of the same sign for each pair under the assembly conditions. Apparently, this did not prevent the layer-by-layer process because the PEs at the physical border between the PDDA or PSS and water remained largely ionized, whereas the zeta-potential reflected the integral potential from the Stern layer and a part of the diffuse layer. The electrostatic repulsion of the outer layers of the ionic atmospheres created a barrier for adsorption, which was overcome by the kinetic energy of the heavy NPs followed by the engagement of short-range attractive interactions.

Thus, the increase in surface density of the NPs for modified YIG was primarily attributed to attractive interactions between hydrocarbon groups or organic modifier and the PE chains adsorbed to the substrate, i.e. hydrophobic interactions. Their amplification increased the attraction of the NPs both to PE and to each other. In turn, this switched the deposition mode from the lateral expansion to the normal mode, which means that the direction of film growth was directed along the normal of the substrate surface [34].

The problem of intermolecular interactions in LBL has not only academic interest; understanding the role of different forces acting during the LBL process becomes particularly important for attaining desirable materials properties of multilayers. Having characteristic length  $f$  1–100 nm, they determine the nanometer scale organization of the layers. Fine tuning the film structure is particularly important for nanotechnological devices reported recently for LBL such as light-emitting diodes [31, 62, 90, 164–167], photovoltaic cells [63, 150, 168–172], conductive coatings [21, 98, 173, 174], complex patterned films [175–177], nonlinear optical coatings [178–180], ultrathin resists [28, 56, 95, 97], and magnetic media [11, 16, 26, 87]. The molecular engineering of species to be assembled, bearing in mind the modes of their interaction in the film, can lead to desirable organization of individual adsorption layers, improved ordering of species and, ultimately, improved performance of the material. Recently, we found that the LBL assembly of fullerene derivatives in which the C<sub>60</sub> sphere is connected to a fulleropyrrolidinium ion via a rigid all-sigma-bonded framework of androstane bridges, results in a surprisingly high level of intermolecular organization. In every adsorption layer, they self-assemble into linear superstructures (nanowires) [168]. Adsorption of the positively charged C<sub>60</sub>-fulleropyrrolidinium dyad on the negatively charged PSS resulted in the formation of rod-like superstructures 1–3 μm long. Similarly films from fullerene-ferrocene dyads connected by a flexible oligoethylene bridge did not reveal any intralayer self-organization. The supramolecular organization of films of the fullerene salt was accompanied by the presence of a donor-acceptor fullerene-ferrocene electron transfer pair, which made the system particularly appealing for photoconversion. Indeed, the photocurrent obtained from a PDDA/PSS/dyad LBL film under deoxygenated conditions reveals up to a 90-fold enhancement relative to an earlier flexible dyad with oligoethylene bridge [171]. This performance improvement can be attributed to the charge conductance along the fullerene nanowires enhancing the efficiency of the energy conversion.



## 8.3.2

**Ionic Conditions**

The ionic conditions refer to experimental parameters affecting the NP and PE ionization states and long-range electrostatic interactions. They include, primarily, pH and ionic strength, which affect the ionization of the species the most. Increasing the ionic strength of NP dispersions often increases NP density in the adsorption layer presumably via the reduction of NP–NP electrostatic repulsion [34, 181, 182], which correlates with observations on PE–PE LBL films [9, 183]. At the same time, increasing ionic strength is not sufficient to switch the mode of deposition from lateral expansion to normal for YIG NPs [34].

The pH of any of the LBL components has a strong and multifaceted effect on the structure of the adsorption layer, and, unlike an increase in ionic strength, its influence is not monotonic. For LBL films of TiO<sub>2</sub>-on-Ag NPs (Fig. 8.2d) assembled with PAA [27] and for titanium niobate sheets assembled on poly(allylamine hydrochloride) (PAH) [97], the existence of an optimum pH, for which the density of NPs in the film reached a maximum, was observed. Taking the TiO<sub>2</sub>-on-Ag NPs as an example, the current understanding of the pH effect on NP/PE multilayers can be considered. The core–shell TiO<sub>2</sub>-on-Ag NPs displayed the highest coating density at pH 2.5 (Fig. 8.11c), while the best ordering was obtained at pH 2.0, when they formed closely packed films (Fig. 8.11d). Deviations in pH in both directions from the optimal range of 2.0–2.5 yielded a decrease in NP density. At low pH 2.0, the adsorption of protons on the TiO<sub>2</sub> shells resulted in a high surface charge of NPs (isoelectric point of TiO<sub>2</sub> is pH 6.5–5.2) [184]. Consequently, strong repulsion between them dominated other intermolecular forces. Additionally, the degree of PAA ionization was decreased. Both factors made adsorption thermodynamically less favorable and dilute layers of individual NPs were produced (Fig. 8.11a,b), which were similar to those seen for YIG (Fig. 8.5). At pH 2.0, the surface charge of TiO<sub>2</sub> decreased and so did the interparticle repulsion. The relative contribution of the electrostatic and van der Waals attractions to the PAA-coated surface increased, which resulted in the alteration of film structure and an increase in the NP density. The situation when the repulsion and attraction both remained strong, while balancing each other, promoted uniform structures as can be seen in Fig. 8.11c. A further increase in pH, to 2.5, shifted the balance toward nonspecific attractive interactions (hydrogen bonding, dipole–dipole, hydrophobic, etc) of NPs with each other and with PAA macromolecules. In response to that, the films became thicker and less organized with fairly large aggregates distributed all over the surface (Fig. 8.11d). At a relatively high pH of 3.0, the kinetics of adsorption became very slow, presumably due to a smaller charge on TiO<sub>2</sub> and the corresponding weakness of long-range electrostatic attraction of NPs to the substrate, which resulted in dilute films consisting of 3D clusters of many particles (Fig. 8.11e,f). Notably, the NP agglomeration patterns transformed as pH changed (compare Fig. 8.11a,f), which was not observed for YIG colloids. Thus, the pH-induced changes in the nature of NP–NP and NP–PE interactions are quite specific for particular LBL pairs due to an intricate inter-

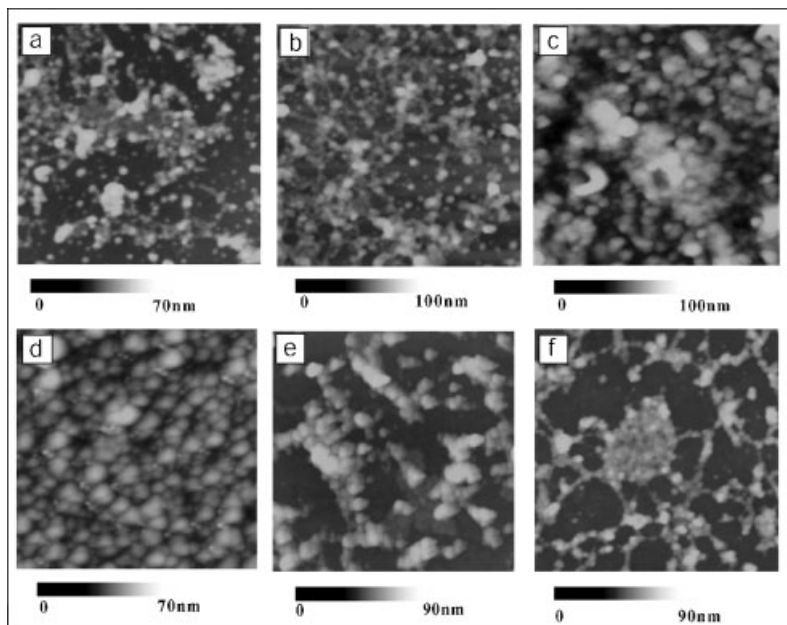


**Fig. 8.11** AFM images of PDPA(PAA/TiO<sub>2</sub>-on-Ag)<sub>1</sub> layers assembled at different pH of NP dispersion: (a) pH 1.0 (b) pH 1.5 (c) pH 2 (d) pH 2.5 (e) pH 3.0 (f) pH 3.5. Exposure time for NP dispersion was 1 h. PDPA and PAA were adsorbed at pH 3.6 and pH 3.5 respectively with exposure time of 5 min.

play of the large number of interactions involved. Therefore, structural transformations that happen with different NP LBL films are likely to be unique for each system, and one should expect a number of interesting phenomena with agglomeration meso/nanostructures. As an example of such phenomena, the restacking of assembled titanium niobate lamellae for pH below 7.0 can be cited, while monolayers of TiNbO<sub>5</sub> sheets were observed at higher pH [97]. Adding further to the complexity of the process and to the factors that control the ordering in such systems is the presence of loose segments of PE chains protruding into the solution [185], which change their conformation with pH. They are suspected to stimulate particle aggregation during the adsorption process [16].

Variations of pH and ionic strength are the most powerful tools now available in the arsenal for control of LBL film structure. This refers to both NP-PE and PE-PE LBL systems. For the latter, remarkably abrupt transitions from smooth to porous films and large thickness variations were observed [40, 110, 111]. Therefore, it is important both to optimize and to monitor the ionic conditions and, in particular, the pH value, for every step of the assembly including rinsing.

## 8.3.3

**Effect of Particle Shape on the Density of the Adsorption Layer**

Another influential factor to consider for LBL assembly of NPs, is the shape of the adsorbed species. Although it may appear that one has little control over shape for a particular material set by the crystal lattice, advances in NP synthesis now permit molding nanocrystallites into different shapes [186–195]. The performance of photonic, electronic and optical devices is expected to depend strongly on the connectivity of the NPs, determined among other factors by their shape [196]. Therefore, the design of an LBL thin film suitable for a specific application is affected by the choice of NP geometry.

It would be interesting to trace a dependence of particle shape on the NP density in LBL films, although this is an inherently difficult problem because shape alterations are coupled to, in part, some change in the physical make up of intermolecular interactions at the atomic level. Bearing this in mind, NPs and nanocolloids of “naked” YIG, barium ferrite and montmorillonite were chosen. All of them are highly hydrophilic negatively charged particles with oxide surfaces. Reasonable similarities between them, especially when they are compared to other LBL pairs with NP coated with an organic layer of stabilizers, afford a qualitative evaluation of the shape effect, although other factors, such as isoelectric point differences, will inevitably be convoluted into the results. All the colloids were assembled on PDDA in basic media at pH 8.5. The spherical YIG NPs after a total of 5 deposition cycles form a very dilute film similar to those discussed above (Fig. 8.12a). The density in the disk-like barium ferrite nanocolloid after the same number of layers was significantly greater than that for YIG for the same 5 deposition cycles (Fig. 8.12b). When large clay sheets were adsorbed on PDDA, even after one deposition cycle the particle density was enough to virtually completely cover the surface of the substrate (Fig. 8.12c). These data confirmed a fairly obvious fact that an increase in anisotropy of NPs must lead to an increase in their density in LBL films. Spherical NPs provide the least surface area for interaction with the substrate, whatever these interactions may be, while the geometry of more anisotropic particles such as disks, sheets and rods, provides greater specific surface area for interactions, the highest for thin sheets, which was reflected in the particle density of montmorillonite clay (Fig. 8.12c). An analysis of LBL publications shows that nanocolloids with sheet-like morphology can virtually always form high quality LBL films [12, 26, 30, 31, 33, 45, 56, 84, 89, 92, 95–98, 197]. Considering this, a focused search and synthesis of semiconductor materials with planar particle morphologies can lead to better performing LBL devices. As such, NPs of  $\text{In}_2\text{S}_3$  shaped as thin sheet were recently made in our laboratory, taking advantage of its orthogonal crystal lattice for which layered crystals are typical [198]. Unlike clay and other nanocolloids,  $\text{In}_2\text{S}_3$  is a semiconductor with great doping capacity. Additionally, it revealed excitonic luminescence in the UV (Fig. 8.13). Both properties can lead to significant improvement in LBL-produced electronic and photonic devices due to facilitation of charge transfer between the layers. The preparation of uniformly sized NPs of more complex asymmetric

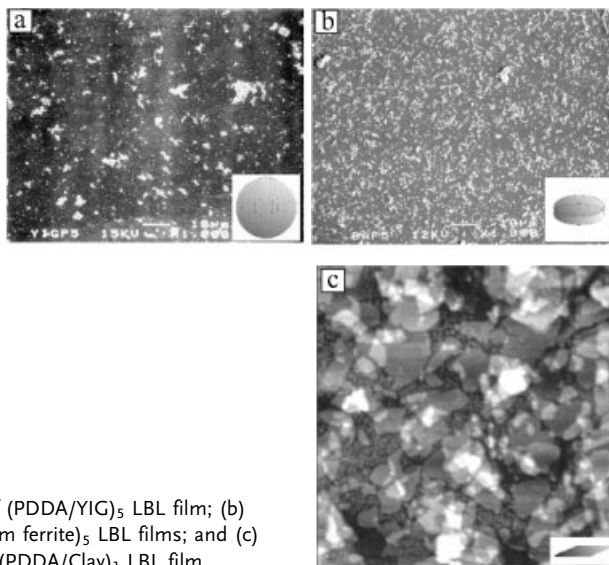


**Fig. 8.12** (a) SEM image of (PDDA/YIG)<sub>5</sub> LBL film; (b) SEM image of (PDDA/barium ferrite)<sub>5</sub> LBL films; and (c) 1 μm×1 μm AFM image of (PDDA/Clay)<sub>1</sub> LBL film.

shape, which is a difficult experimental problem, can possibly lead to their self-assembly in LBL films in supramolecular structures of the higher degree of order that we could see for rigid fullerene derivatives.

Some shape effects could be seen for proteins of different geometry [64, 199–202], but they were not as pronounced as for NPs, because of their lower degree of anisotropy and stronger overall attraction to Pes [118].

## 8.4

### Stratified LBL Assemblies of Nanoparticles and Nanocolloids

One of the advantages of LBL is the possibility of using the layer-by-layer nature of the deposition to manufacture complex stratified materials. This task requires the assurance that the multilayer build-up occurs in the normal mode rather than in lateral expansion mode; otherwise, the organization of the subsequently deposited layers will be largely compromised owing to patchy growth and the tendency of the adsorbing species to detach from the surface when the next layer is added. By using the entire spectrum of methods for tuning intermolecular interactions between NP and PE discussed above, i.e. pH, ionic strength, surface derivatization, and shape selection, one can obtain dense monolayer coverage for NPs from probably any desirable material, and the strict correspondence between the (A/B)<sub>n</sub> deposition procedure and the expected stack sequence will be attained. Therefore, the effect of the *sequence* of the layers on the materials properties of the NP assemblies will be the focus of this Section.

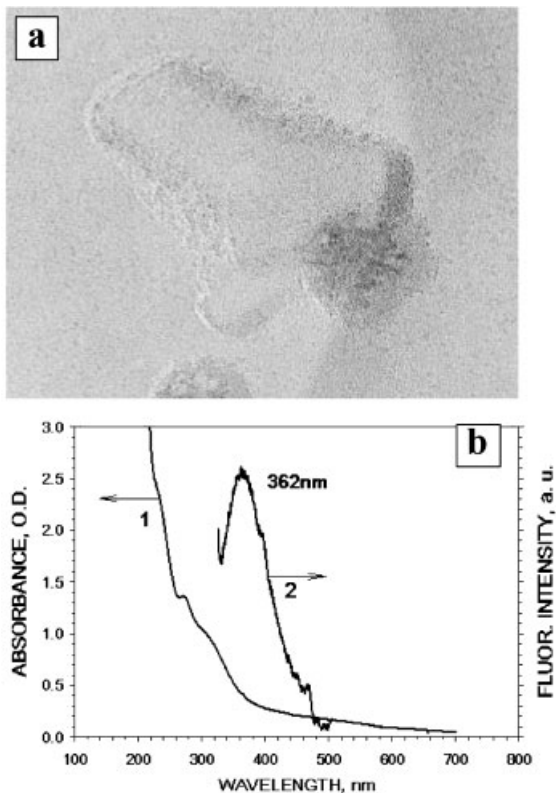


Fig. 8.13 (a) TEM image of thiol-stabilized  $\text{In}_2\text{S}_3$  NPs. (b) Absorption (1) and luminescence spectra (2) of  $\text{In}_2\text{S}_3$  NPs.

The layer order should be viewed as a very potent fundamental parameter for the control of functional properties of LBL stacks. Combined with the versatility of the LBL technique, this approach can afford multifunctional materials with permutations of properties, which are difficult or impossible to obtain by bulk techniques of composite synthesis. The effect of ordering films on photovoltaic response was first demonstrated in a publication on LBL of CdS and  $\text{TiO}_2$  NPs [20]. Since then, it has been shown that the LBL architecture strongly affects biological reactions in PE-PE assemblies [203–205], their AFM topography [201], energy/electron transfer [98, 206–209], the course of chemical reactions in them [112] and the performance of LBL-based PE light emitting diodes [62, 90, 210]. For multilayers made from NPs, the layer sequence is particularly influential because their optical, electronic and magnetic properties depend strongly on interparticle communication and, therefore, their nanometer scale organization [4, 211–217]. Here, several examples of the new methods of molecular engineering of NP materials using programmed variation in film properties will be highlighted.

## 8.4.1

**Self-standing LBL films**

One of the new modalities in NP materials afforded by LBL processing and stratification is free-standing ultrathin films. They are interesting from both the fundamental and practical points of view. Possible applications for free-standing NP films range from implantable biosensors and retina mimics to membranes for gas separation, micromechanical devices, and advanced catalysis. The degree of structural organization of thin composite membranes that can be made in this way is hard to attain by traditional methods of production. At the same time, free-standing films allow experimental techniques applicable to bulk materials, such as nuclear magnetic resonance and differential scanning calorimetry, to be used for fundamental studies of LBL films and related systems.

The principle of making free-standing LBL assembled films is quite simple. The LBL deposition process is carried out on a solid substrate and, when desirable thickness and stratification are achieved, the LBL assembly is lifted off by dissolving the substrate in an organic solvent, melting it, delaminating the film or any other suitable technique. The first realization of free-standing LBL films was done by the “assemble-and-dissolve” method [37] which was recently followed by the “weak-point” technique. In the latter approach, a change in pH or ionic strength induced the decomposition of the LBL film, formed by a weak PE, while the top LBL stratum was preserved and thereby delaminated off the substrate [218]. Both methods have pros and cons. The assemble-and-dissolve technique imposes two major requirements on the substrate: 1. the organic solvents used in the lift-off step must not damage the film and 2. the substrate must be hydrophilic with a positively or negatively charged surface. The weak-point technique does not impose any limitations on the substrate material, but allows for the preparation of free-standing films only from strong macromolecular electrolytes, which are rare among NPs. Destabilization of the protective organic shell around the NPs originating in the strong electrostatic repulsion between stabilizer molecules is the cause of the predominant utilization of weak electrolytes in the NP synthesis.

Free-standing films were obtained from  $(\text{PDDA}/\text{Fe}_3\text{O}_4)_n$  NP multilayers with  $n=15\text{--}30$  by depositing them on cellulose acetate-coated glass followed by its dissolution in acetone [37]. (A TEM image of these NPs is given in Fig. 8.2b). As expected, the thin film retained the magnetic properties of NPs: it moved in a magnetic field and had a room-temperature magnetization curve similar to that of the original NPs [11]. Importantly, from the suspended state, the films could be transferred onto any solid or porous substrate. However, they were quite fragile, which was not surprising considering that the thickness of the films, such as  $(\text{PDDA}/\text{Fe}_3\text{O}_4)_{15}$  and  $(\text{PDDA}/\text{Fe}_3\text{O}_4)_{30}$ , was in the range of a few hundred nanometers.

Magnetite NPs form well packed LBL layers (Fig. 8.14a), and hence, the layer-by-layer assembly affords effective manipulation of the order of the deposited layers. For self-standing membranes, the natural direction for their further improvement would be the search for a layer sequence that could strengthen the film. At the same time, this could serve as a qualitative demonstration of the ef-

fect of the layer sequence on the mechanical properties of the film. Towards this, every other layer of magnetite was replaced with a layer of exfoliated montmorillonite clay platelets, thereby producing an assembly with a (PDDA/Clay/PDDA/ $\text{Fe}_3\text{O}_4$ )<sub>n</sub> sequence (Fig. 8.14d). The clay platelets used in this case had lateral dimensions of 150–300 nm. On PEs, they formed a layer of overlapping aluminosilicate sheets (Fig. 8.14b) with an average thickness of  $3.8 \pm 0.3$  nm [56, 219]. Being adsorbed virtually parallel to the surface of the substrate, they permitted circumvention of the problem of interdigitation of the adjacent PE films by closing large areas of the surface [45, 56]. Their large size and parallel orientation allowed them to cover ca. 400 nanoparticles at once, thereby cementing the assembly. (PDDA/Clay/PDDA/ $\text{Fe}_3\text{O}_4$ )<sub>30</sub> free-standing film prepared following the procedure outlined above could be easily picked up with tweezers, transferred, cut, moved around the solid surface, and handled in any other way. Taking advantage of this architecture, we were able to make a free-standing film with as few as 8 repeating (PDDA/Clay/PDDA/ $\text{Fe}_3\text{O}_4$ ) units, which was impossible without the aluminosilicate framework. Besides stratification, the enhanced mechanical strength of the composite clay/magnetite/PDDA film, as compared to the NP/PE assembly, should be also attributed to ordering within the individual LBL layers – parallel orientation of the clay platelets. Similar films were made recently by the assemble-and-dissolve method from luminescent (quantum yield 15–20%) CdTe nanocrystallites that had the layer sequence (PDDA/PAA)<sub>3</sub>(PDDA/Clay/PDDA/CdTe)<sub>20</sub> (Fig. 8.15).

The (PDDA/Clay/PDDA/ $\text{Fe}_3\text{O}_4$ )<sub>30</sub> assembly was imbedded in epoxy resin, and its cross-section was investigated by optical and transmission electron microscopy. The film could be clearly seen in an optical microscope as a continuous black band of uniform thickness (Fig. 8.16a). The thickness was determined from the electron microscopy image (Fig. 8.16b) to be  $350 \pm 30$  nm. One can also estimate this parameter by adding up the thicknesses of the M and C layers. For (PDDA/Clay/PDDA/ $\text{Fe}_3\text{O}_4$ )<sub>30</sub> film, this gives  $(3.8+8.0) \times 530 = 354$  nm, which coincides well with the TEM measurements. The films were homogeneous with no apparent

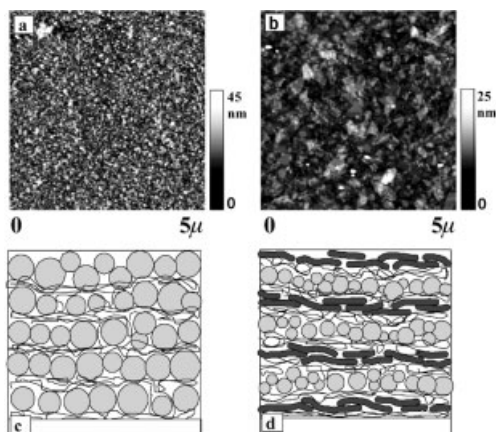


**Fig. 8.14** (a) and (b) AFM images of (PDDA/ $\text{Fe}_3\text{O}_4$ )<sub>n</sub> and (PDDA/Clay)<sub>1</sub> films on silicon wafers. Fine-grain texture of the left image is characteristic for the magnetite film. Montmorillonite adsorption time in image (b) was shortened from regular 1 min, to 25 s to reveal better the shape and size of the platelets. (c) and (d) model structures of (PDDA/ $\text{Fe}_3\text{O}_4$ )<sub>n</sub> and (PDDA/ $\text{Fe}_3\text{O}_4$ /PDDA/Clay)<sub>n</sub> multilayers. Not drawn to scale.

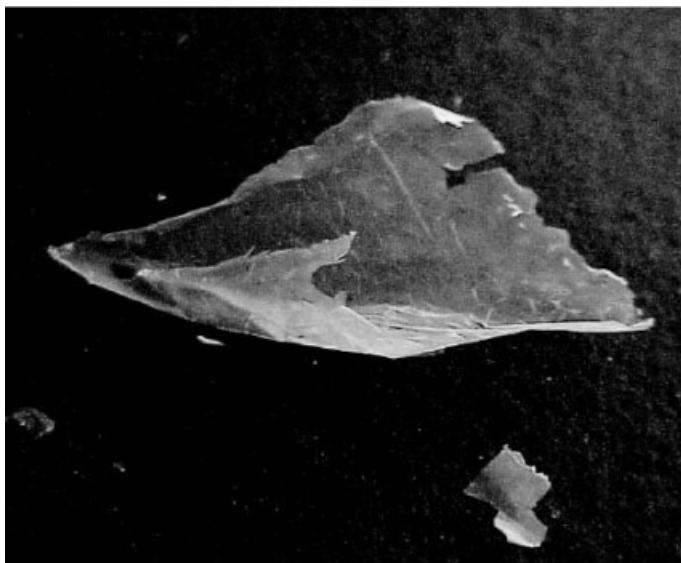


**Fig. 8.15** Photograph of the self-sustained  $(\text{PDDA}/\text{PAA})_3(\text{PDDA}/\text{Clay}/\text{PDDA}/\text{CdTe})_{20}$  floating in water taken under black light illumination. CdTe NPs used here were *ca.* 2 nm in diameter and assembled at pH 8.5.

phase boundaries between components. Their NP nature can be seen in a thin cross-section (Fig. 8.16c).

Unfortunately, the low TEM contrast of montmorillonite does not allow the direct visualization of the clay layers in the cross-sections. Nevertheless, indirect proof of their preferential orientation in the stack may be obtained by detailed examination of the TEM images. It was noticed that the films showed some longitudinal cracks from cross-sectioning (Fig. 8.16b). The obvious anisotropy of the physical damage caused by the diamond knife should be attributed to the existence of montmorillonite stacks with sheets oriented parallel to each other and to the substrate. Note that the aluminosilicate platelets are flexible and conform to the surface topography, unlike what may be expected from them due to their fairly rigid aluminosilicate lattice [45]. The physical properties of clay sheets resemble those of a nanoscale version of fiberglass fabric rather than rigid bricks. The ability of thin inorganic sheets to wrap around the nanoparticles can also be seen for graphite oxide colloids [220].

## 8.4.2

### Magnetic Properties of the Stratified LBL Assemblies of Nanoparticles

Besides the sheet-like morphology, aluminosilicate clays have other useful qualities, for instance, they can be excellent insulators. Mica sheets, often used as elec-



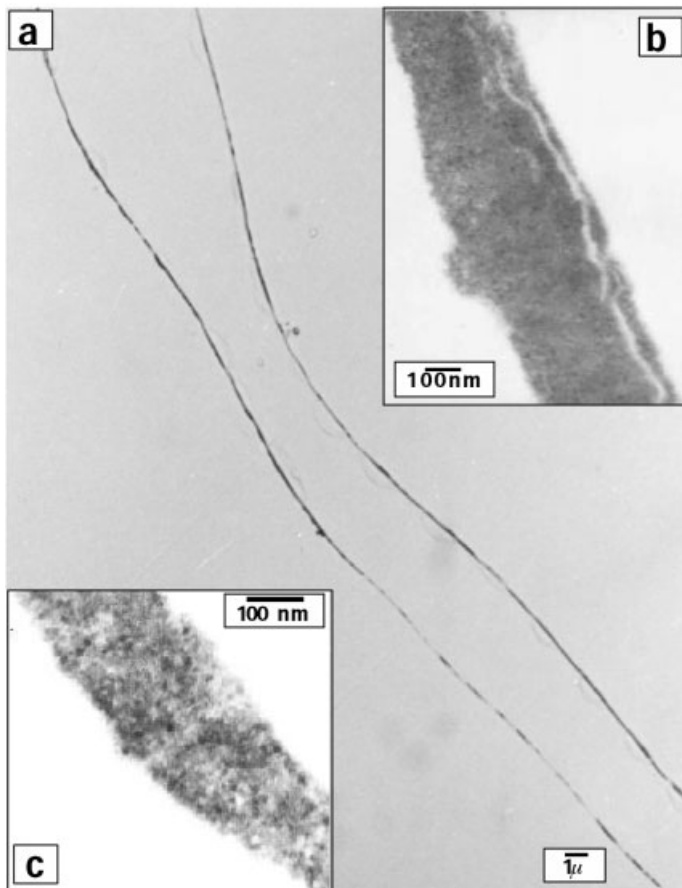
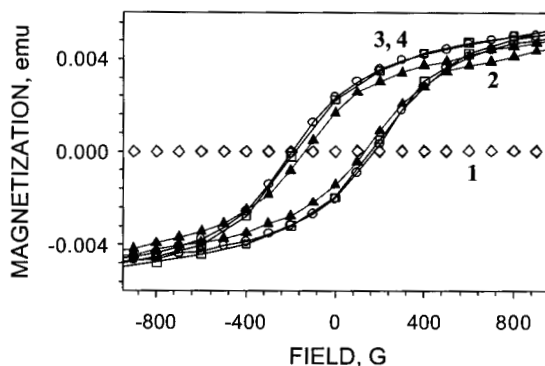


**Fig. 8.16** (a) Optical micrograph of the cross-section of the (PDDA/Fe<sub>3</sub>O<sub>4</sub>/PDDA/Clay)<sub>30</sub> assembly. Two strands of the film can be seen; some parts of the film were folded during imbedding in epoxy resin. (b) and (c) Transmission electron micrographs of the cross-sections of (PDDA/Fe<sub>3</sub>O<sub>4</sub>/PDDA/Clay)<sub>30</sub> assembly.

trode spacers, are members of this family. The insulating properties of LBL layers of clay and similar materials [97] can be utilized in many devices involving electron transfer such as sensors, light-emitters [90], and on-chip capacitors. Many magnetic phenomena in NP on the nanoscale are strongly dependent on the electronic communication between the NP, and insulating coatings can strongly affect the magnetic behavior of the NP solids [11]. Therefore, as a part of the investigation of the effects of order, it would be interesting to see how the magnetic properties of LBL films respond to changes in the stack architecture.

For this study, “naked” Fe<sub>3</sub>O<sub>4</sub> NPs were deposited on poly(ethyleneterephthalate) skins 25 μm thick, which were pretreated with 0.1 M NaOH to render their sur-

**Fig. 8.17** Low field magnetization loops taken at 10 K for LBL films with different layer sequence: [PDDA/Clay]<sub>10</sub> (1), [PDDA/Fe<sub>3</sub>O<sub>4</sub>]<sub>10</sub> (2), [PDDA/Clay/PDDA/Fe<sub>3</sub>O<sub>4</sub>]<sub>10</sub> (3), and [(PDDA/Clay)<sub>2</sub>PDDA/Fe<sub>3</sub>O<sub>4</sub>]<sub>10</sub> (4).



face more hydrophilic. The departure from conventional LBL substrates (glass, silicon wafers, quartz, gold, etc.) was necessary to reduce the background magnetic signal. Multilayers of the layer sequences [PDDA/Fe<sub>3</sub>O<sub>4</sub>]<sub>10</sub>, [PDDA/Clay/PDDA/Fe<sub>3</sub>O<sub>4</sub>]<sub>10</sub>, and [(PDDA/Clay)<sub>2</sub>PDDA/Fe<sub>3</sub>O<sub>4</sub>]<sub>10</sub>, were built. Magnetization plots of LBL films at room temperature with all these architectures revealed a typical superparamagnetic behavior with coercive field  $H_c=0$  G [26].

An effect of the stack sequence on magnetic behavior becomes visible for the normalized magnetization loops taken at low field amplitudes at  $T=10$  K, (Fig. 8.17). The magnetization curves for [PDDA/Clay/PDDA/Fe<sub>3</sub>O<sub>4</sub>]<sub>10</sub> and [(PDDA/Clay)<sub>2</sub>PDDA/Fe<sub>3</sub>O<sub>4</sub>]<sub>10</sub> coincided within ca. 5% deviation, whereas the magnetization loop of [PDDA/Fe<sub>3</sub>O<sub>4</sub>]<sub>10</sub> displayed slightly lower hysteresis than that for the clay-containing multilayers [26]. According to the Stoner–Wolfarth model, the magnetization reversal can be pictured as the concerted spin flipping of adjacent magnetic domains coupled to each other by exchange and dipole–dipole interactions. The range of electron exchange interactions does not exceed 2 nm, and therefore they can be successfully interrupted by isolation with clay layers whose thickness is 2.5–3.0 nm. Since there is little difference in the magnetization curves observed between multilayers of different architecture, the coupling between layers should be mostly attributed to the dipole–dipole interactions with significantly longer characteristic distance.

#### 8.4.3

##### Nanorainbows: Graded Semiconductor Films from Nanoparticles

In the previous examples, physical effects were observed due to the combination of two different species in a layered composite. At the same time, stratified layered assemblies of NPs could also be made from only one material by organizing NPs according to their size as pictured schematically in Fig. 8.18a. Such organization of the layers is particularly interesting for semiconductor quantum dots displaying a strong dependence of the band gap on particle size. Since the abso-

lute energy of both conduction and valence bands of semiconductors are affected by the confinement of the excitonic wavefunction [239–243], films with a gradual change of particle diameter should display similarly gradual evolution of the valence and conduction band energies along the normal to the substrate (Fig. 8.18b). Such assemblies can be compared to, so-called, graded semiconductor films known for exceptional capabilities as photodetectors, bipolar transistors, waveguides, and other optical and electronic devices [244–248]. This type of material also revealed new phenomena in charge injection, charge carrier dynamics, and light trapping [249–257]. Traditional graded semiconductors are difficult to make. Expensive and complex methods, such as molecular beam epitaxy and plasma enhanced chemical vapor deposition, are required for their preparation. They also utilize hazardous organometallic precursors. Taking advantage of the LBL assembly, one can build graded semiconducting material by laying down water soluble NPs on a substrate, which is a safe and inexpensive procedure. It may be performed in virtually any high school chemical laboratory, although such simplicity also has a trade-off. The movement of charge carriers in NP solids is frustrated by the organic shell around the NPs [212, 213] and, in perspective, this problem needs to be addressed by molecular engineering of the stabilizer molecules or surface modification of NP after the assembly. At the present stage, it would be necessary to demonstrate that the gradual change in valence and conduction band energies can indeed be prepared by NP LBL.

The first examples of NP graded films were prepared from luminescent CdTe nanocrystals stabilized by thioglycolic acid. They are negatively charged, therefore positively charged PDDA was utilized as an LBL partner PE. The CdTe NPs formed closely packed layers on PDDA, as could be evidenced by the phase contrast AFM image in Fig. 8.19, which distinguishes them from NP films that can be made by the Langmuir–Blodgett technique [258]. The graded NP films were assembled using four different CdTe dispersions with luminescence maxima at 495–505, 530–545, 570–585, and 605–620 nm which display respectively green, yellow, orange and red luminescence (Fig. 8.20a). Layer-by-layer assembly was carried out on glass and plastic substrates and typically 5–10 CdTe NP bilayers of each of four luminescent colors were deposited.

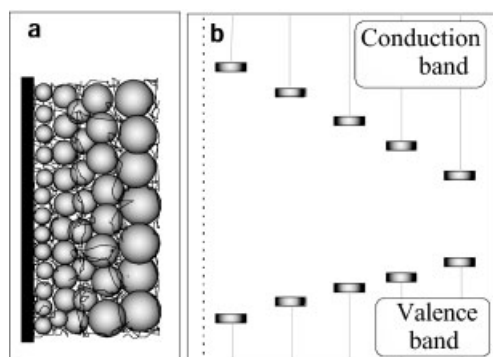


**Fig. 8.18** Graphic representation of the graded semiconductor film assembled from NPs. (a) Schematic sequence of NP layers. (b) Approximate profile of the absolute energies of valence and conduction bands. Not drawn to scale.

Fig. 8.19  $1\ \mu\text{m}\times 1\ \mu\text{m}$  AFM phase contrast image of (PDDA/CdTe)<sub>n</sub> LBL film.

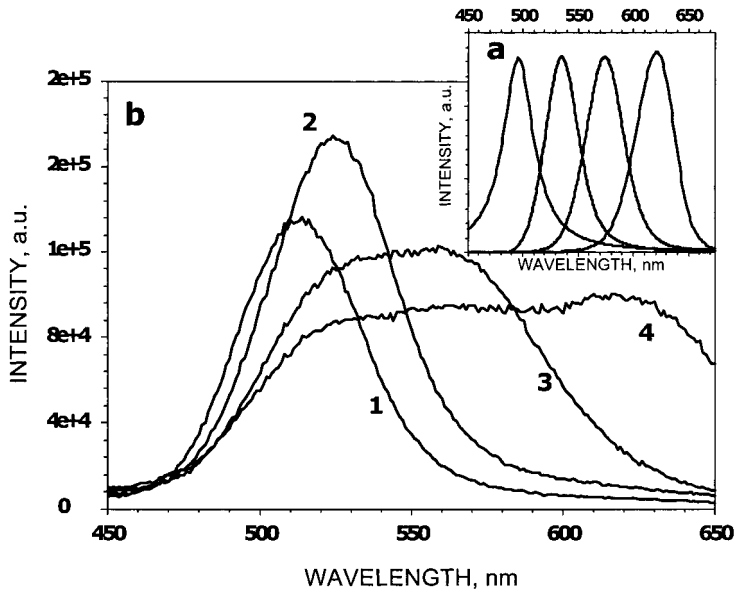
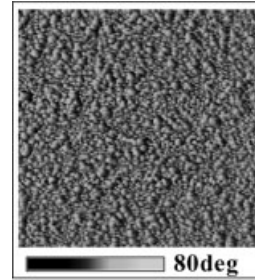


Fig. 8.20 Luminescence spectra of (a) exemplary CdTe NPs used in this work and (b) thin films obtained after the sequential deposition of 5 bilayers of (1) “green”, (2) “yellow” (3) “orange”, and (4) “red” CdTe.

The assembly started from the smallest NPs (“green”) and proceeded to the biggest ones (“red”) according to the visible light spectral sequence (rainbow). With the addition of new layers from bigger NPs, the luminescence of the assembly shifted toward the red part of the spectrum while also becoming broader (Fig. 8.20b). Finally, the luminescence spectrum of the stack of all four NP diameters had a plateau appearance reflecting almost equal emission intensity over a wide range of wavelengths. As compared to the original spectra of CdTe NPs, the prevalence of the red emission (red shift) should be attributed to the excitation energy transfer from smaller NPs to bigger ones [214].

A cross-sectional slice of the NP stack was analyzed by TEM. The asymmetry of the film could be seen in the difference in electron diffracting power of the “red”

and “green” sides of the assembly (Fig. 8.21 a, b). The layers of bigger NPs appeared noticeably darker in the TEM image due to the greater percentage of heavier elements on this side of the multilayer stack (Fig. 8.21 a, b). The high resolution TEM images of single NPs in the network of the PE matrix (identified as areas of CdTe crystallinity) were observed to be different, being 2–3 nm in the “green” and “yellow” parts and 5–6 nm in the “red” side of the assembly (Fig. 8.21 c, d).

The graded nature of the prepared NP film was also established by confocal optical microscopy. The sample was assembled on a glass slide and a series of luminescence images was obtained at different focus depths inside the assembly. The images were processed by confocal microscope software and a cross-sectional image without physical sectioning of the film was obtained (Fig. 8.22 a). The image clearly showed the gradual change in the luminescence emission wavelength from green at the bottom to red on the top of the stack and the corresponding increase in the NP diameters. The schematic dependence of the valence and conduction band energies on the position along the axes normal to the surface of the film is given in Fig. 8.22 b. Since there is a certain degree of interpenetration of the nanoparticle layers, the deviation from the ideal graded film in Fig. 8.18 is reflected by the overlap of the energy distribution in each layer.

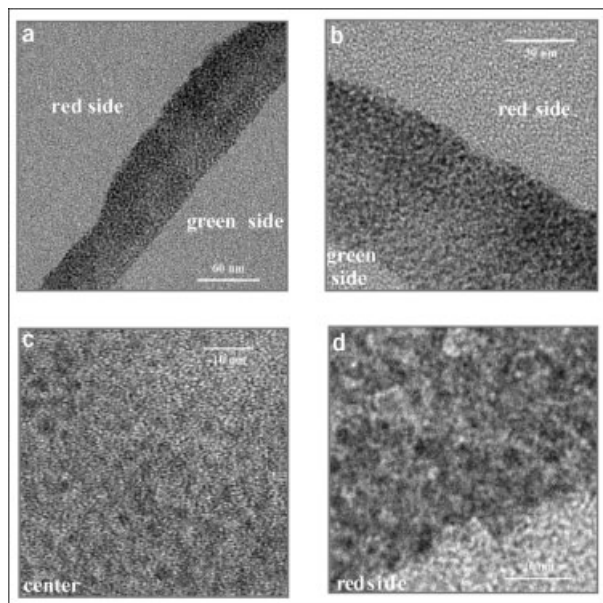


**Fig. 8.21** Transmission electron microscopy images of the graded film cross-sections made from 5 bilayer of “green”, “yellow”, and “red (total 15): NPs. (a) and (b) are survey images; (c) and (d) are high resolution TEM images of the center section and “red” side of the NP film.

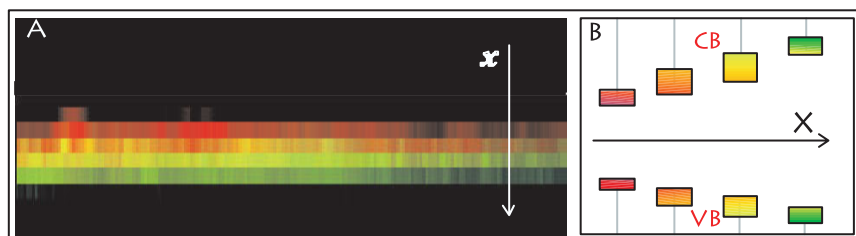


**Fig. 8.22** (a) Cross-sectional confocal microscopy image of the graded LBL film of CdTe NPs made of 10 bilayers of “green”, yellow”, “orange”, and “red” NPs (total 40). Small NPs are assembled in the lower part (green and yellow luminescence), while bigger NPs

are assembled on top of them (orange and red luminescence). The total thickness of the film was estimated to be  $220 \pm 20$  nm by the same technique. (b) Schematic arrangement of the conduction and valence energy levels of the film in (a).

The combination of size quantization and the gradient nature of the material opens the possibility for new optical and electrical effects, as well as for the optimization of existing applications of NP thin films based on charge transfer. The benefits of the graded media and ordered LBL assemblies have already been demonstrated by the markedly better light-emitting performance when the homogeneous media in polymer light-emitting diodes was replaced with a spatially-organized one [210]. At the same time, one needs to point out that the physical distance for which programmed change in properties in the LBL films can be obtained is greater than in vacuum epitaxial methods, although LBL is sometimes also called “molecular beaker epitaxy” [32]. Its lower limit is set by the intrinsic roughness of the LBL layers and the average diameter of species being deposited from cycle to cycle. For PDDA/CdTe multilayers, the characteristic distances of graded properties should exceed ca. 100 nm, i.e. be several times greater than the NP diameter. Importantly, this limitation does not prevent NP layers from being organized on a scale smaller than the wavelength of visible light. One can engineer polarizability, refractive index and other parameters on the molecular level in such assemblies so that the overall interaction of electromagnetic waves with the film will be significantly different than in the traditional optically uniform material.

## 8.5

### Conclusion

Over the last decade, layer-by-layer assembly research has experienced rapid growth, which was initially aimed at expanding the number of coatings and other nanostructured objects that can be obtained by this technique. Lately, great advances in understanding the driving forces of, and ordering in, LBL deposition have been made. As a result, multilayers have reached substantial sophistication in terms of structure and variety of components, which has opened the door for

complex functionality. At this stage, one should expect significant research effort to be directed at fine-tuning film morphology to improve specific functionalities, such as conductivity, porosity, phase transitions of composites and others. Additionally, more work on the utilization of stack architecture for improving materials properties of thin films and membranes made by LBL should be anticipated.

Microcapsules made by LBL paved the way for drug delivery research with PE-PE multilayers. The inherent hydrophilicity of the films, preservation of protein activity in LBL layers, polyelectrolyte nature of many biomolecules, and the characteristic distances of spatial control, either by patterning or by stratification, possible for such films, point towards numerous biomedical applications of planar LBL films in the future, which we are beginning to see now. The incorporation of NP in such multilayers will enable design of new biocomposites, which are organized on the nm scale and incorporate unique functionalities of the nano-sized state of matter. This area of research will probably be one of the most exciting in the field because of the elegance of the method and the novelty of the materials.

## 8.6

### References

- 1 A. P. ALIVISATOS, *J. Phys. Chem.* **1996**, *100*, 13226–13239.
- 2 D. L. KLEIN, R. ROTH, A. K. L. LIM, A. P. ALIVISATOS, P. L. MCEUEN, *Nature* **1997**, *389*, 699–701.
- 3 M. BRUCHEZ, JR., M. MORONNE, P. GIN, S. WEISS, A. P. ALIVISATOS, *Science* **1998**, *281*, 2013–2016.
- 4 M. G. BAWENDI, *Abstr. Pap. Am. Chem. Soc.* **1996**, *212*, 149-Inv.
- 5 H. WELLER, *Curr. Opin. Colloid Interface Sci.* **1998**, *3*, 194–199.
- 6 W. C. W. CHAN, S. NIE, *Science* **1998**, *281*, 2016–2018.
- 7 A. P. ALIVISATOS, *Science* **1996**, *271*, 933–937.
- 8 G. DECHER, J. D. HONG, *Ber. Bunsen-Ges. Phys. Chem.* **1991**, *95*, 1430.
- 9 G. DECHER, *Science* **1997**, *277*, 1232–1237.
- 10 C. A. BRUCE, A. M. HOMOLA, M. R. LORENTZ, *US Pat.*, 1982, 259,270 [4, 333, 961].
- 11 F. ALIEV, M. CORREA-DUARTE, A. MAMEDOV, J. W. OSTRANDER, M. GIERSIG, L. LIZ-MARZAN, N. KOTOV, *Adv. Mater.* **1999**, *11*, 1006–1010.
- 12 K. ARIGA, Y. LVOV, I. ICHINOSE, T. KUNITAKE, *Appl. Clay Sci.* **1999**, *15*, 137–152.
- 13 F. CARUSO, H. LICHTENFELD, M. GIERSIG, H. MÖHWALD, *J. Am. Chem. Soc.* **1998**, *120*, 8523–8524.
- 14 F. CARUSO, R. A. CARUSO, H. MÖHWALD, *Science* **1998**, *282*, 1111–1114.
- 15 M. A. CORREA-DUARTE, M. GIERSIG, N. A. KOTOV, L. M. LIZ-MARZAN, *Langmuir* **1998**, *14*, 6430–6435.
- 16 M. A. CORREA-DUARTE, M. GIERSIG, N. A. KOTOV, L. M. LIZ-MARZAN, *Langmuir* **1998**, *14*, 6430–6435.
- 17 D. L. FELDHEIM, K. C. GRABAR, M. J. NANTAN, T. E. MALLOUK, *J. Am. Chem. Soc.* **1996**, *118*, 7640–7641.
- 18 M. Y. GAO, B. RICHTER, S. KIRSTEIN, H. MÖHWALD, *J. Phys. Chem. B* **1998**, *102*, 4096–4103.
- 19 M. GAO, S. KIRSTEIN, A. L. ROGACH, H. WELLER, H. MÖHWALD, *Adv. Sci. Technol.* **1999**, *27*, 347–358.
- 20 N. A. KOTOV, I. DEKANY, J. H. FENDLER, *J. Phys. Chem.* **1995**, *99*, 13065–13069.
- 21 Y. LIU, Y. WANG, R. O. CLAUS, *Chem. Phys. Lett.* **1998**, *298*, 315–319.
- 22 Y. LIU, W. ZHAO, Y. X. WANG, R. O. CLAUS, *Proc. SPIE-Int. Soc. Opt. Eng.* **1998**, *3324*, 45–48.

- 23 Y. LVOV, K. ARIGA, M. ONDA, I. ICHINOSE, T. KUNITAKE, *Langmuir* **1997**, *13*, 6195–6203.
- 24 Y.M. LVOV, J.F. RUSLING, D.L. THOMSEN, F. PAPADIMITRAKOPOULOS, T. KAWAKAMI, T. KUNITAKE, *Chem. Commun.* **1998**, 1229–1230.
- 25 Y. LVOV, K. ARIGA, M. ONDA, I. ICHINOSE, T. KUNITAKE, *Langmuir* **1997**, *13*, 6195–6203.
- 26 A. MAMEDOV, J. OSTRANDER, F. ALIEV, N.A. KOTOV, *Langmuir* **2000**, *16*, 3941–3949.
- 27 I. PASTORIZA-SANTOS, D.S. KOKTYSH, A.A. MAMEDOV, M. GIERSIG, N.A. KOTOV, L.M. LIZ-MARZAN, *Langmuir* **2000**, *16*, 2731–2735.
- 28 G.S. FERGUSON, E.R. KLEINFELD, *Adv. Mater.* **1995**, *7*, 414–416.
- 29 E.R. KLEINFELD, G.S. FERGUSON, *Science* **1994**, *265*, 370–373.
- 30 C.M. BELL, M.F. ARENDT, L. GOMEZ, R.H. SCHMEHL, T.E. MALLOW, *J. Am. Chem. Soc.* **1994**, *116*, 8374–8375.
- 31 T. CASSAGNEAU, T.E. MALLOW, J.H. FENDLER, *J. Am. Chem. Soc.* **1998**, *120*, 7848–7859.
- 32 S.W. KELLER, H.N. KIM, T.E. MALLOW, *J. Am. Chem. Soc.* **1994**, *116*, 8817–8818.
- 33 N.I. KOVIYUKHOVA, P.J. OLLIVIER, B.R. MARTIN, T.E. MALLOW, S.A. CHIZHIK, E.V. BUZANEVA, A.D. GORCHINSKIY, *Chem. Mater.* **1999**, *11*, 771–778.
- 34 J.W. OSTRANDER, A.A. MAMEDOV, N.A. KOTOV, *J. Am. Chem. Soc.* **2001**, *123*, 1101–1110.
- 35 A.L. ROGACH, D.S. KOKTYSH, M. HARRISON, N.A. KOTOV, *Chem. Mater.* **2000**, *12*, 1526–1528.
- 36 H. MATTOUSSI, L.H. RADZIŁOWSKI, B.O. DABBOUSI, D.E. FOGG, R.R. SCHROCK, E.L. THOMAS, M.F. RUBNER, M.G. BAWENDI, *J. Appl. Phys.* **1999**, *86*, 4390–4399.
- 37 A.A. MAMEDOV, N.A. KOTOV, *Langmuir* **2000**, *16*, 5530–5533.
- 38 G. DECHER, J.D. HONG, *Macromol. Chem., Macromol. Symp.* **1991**, *46*, 321.
- 39 M. FERREIRA, J.H. CHEUNG, M.F. RUBNER, *Thin Solid Films* **1994**, *244*, 806–809.
- 40 Y. LVOV, G. DECHER, H. MÖHWALD, *Langmuir* **1993**, *9*, 481–486.
- 41 I.J. ILER, *J. Colloid Interface Sci.* **1966**, *21*, 569.
- 42 Y.F. NICOLAU, *Appl. Surf. Sci.* **1985**, *22–23*, 1061–1074.
- 43 Y.F. NICOLAU, J.C. MENARD, *J. Cryst. Growth* **1988**, *92*, 128–142.
- 44 Y. SHIMAZAKI, R. NAKAMURA, S. ITO, M. YAMAMOTO, *Langmuir* **2001**, *17*, 953–956.
- 45 N.A. KOTOV, S. MAGONOV, E. TROPASHA, *Chem. Mater.* **1998**, *10*, 886–895.
- 46 W.B. STOCKTON, M.F. RUBNER, *Macromolecules* **1997**, *30*, 2717–2725.
- 47 S.H. LEE, J. KUMAR, S.K. TRIPATHY, *Langmuir* **2000**, *16*, 10482–10489.
- 48 B.A. SNOPOK, Y.G. GOLTSOV, E.V. KOSTYUKEVICH, L. MATKOVSKAYA, I.A. KOSHETS, E.V. RENGEVICH, P.E. STRIZHAK, Y.M. SHIRSHOV, E.F. VENGER, Book of Abstracts, 219th ACS National Meeting, San Francisco, CA, March 26–30, 2000.
- 49 H. HONG, I. BENJAMIN, S. KIRSTEIN, Y. AVNY, R. NEUMANN, D. DAVIDOV, *Synth. Met.* **1999**, *102*, 1215–1216.
- 50 J. KIM, S.K. TRIPATHY, J. KUMAR, K.G. CHITTIBABU, *Mater. Sci. Eng., C* **1999**, *7*, 11–18.
- 51 J. KIM, H.C. WANG, J. KUMAR, S.K. TRIPATHY, K.G. CHITTIBABU, M.J. CAZECA, W. KIM, *Chem. Mater.* **1999**, *11*, 2250–2256.
- 52 K. ARIGA, Y. LVOV, T. KUNITAKE, *J. Am. Chem. Soc.* **1997**, *119*, 2224–2231.
- 53 C. TEDESCHI, H. MÖHWALD, S. KIRSTEIN, *J. Am. Chem. Soc.* **2001**, *123*, 954–960.
- 54 C. TEDESCHI, F. CARUSO, H. MÖHWALD, S. KIRSTEIN, *J. Am. Chem. Soc.* **2000**, *122*, 5841–5848.
- 55 D.S. KOKTYSH, N.A. KOTOV, unpublished results for Rhodamine 6G in PAA/PDDA films, **2001**.
- 56 N.A. KOTOV, T. HARASZTI, L. TURI, G. ZAVALA, R.E. GEER, I. DEKANY, J.H. FENDLER, *J. Am. Chem. Soc.* **1997**, *119*, 6821–6832.
- 57 G. DECHER, Y. LVOV, J. SCHMITT, *Thin Solid Films* **1994**, *244*, 772–777.
- 58 Y. LVOV, G. DECHER, H. MÖHWALD, *Langmuir* **1993**, *9*, 481–486.
- 59 Y. LVOV, G. DECHER, H. HAAS, H. MÖHWALD, A. KALACHEV, *Physica B* **1994**, *198*, 89–91.



- 60 M. TARABIA, H. HONG, D. DAVIDOV, S. KIRSTEIN, R. STEITZ, R. NEUMANN, Y. AVNY, *J. Appl. Phys.* **1998**, *83*, 725–732.
- 61 a) (H. HONG, R. STEITZ, S. KIRSTEIN, D. DAVIDOV, *Adv. Mater.* **1998**, *10*, 1104–1108; b) (J. CHO, K. CHAR, J.-D. HONG, K.-B. LEE, *Adv. Mater.* **2001**, *13*, 1076–1078.
- 62 A. WU, D. YOO, J. K. LEE, M. F. RUBNER, *J. Am. Chem. Soc.* **1999**, *121*, 4883–4891.
- 63 D. YOO, S. S. SHIRATORI, M. F. RUBNER, *Macromolecules* **1998**, *31*, 4309–4318.
- 64 Y. LVOV, IN *Protein Architecture*, Eds. Y. Lvov, H. Möwald, Marcel Dekker, New York, 2000, pp. 125–167.
- 65 F. CARUSO, D. G. KURTH, D. VOLKMER, M. J. KOOP, A. MUELLER, *Langmuir* **1998**, *14*, 3462–3465.
- 66 J. Q. SUN, Y. P. SUN, S. ZOU, X. ZHANG, C. Q. SUN, Y. WANG, J. C. SHEN, *Macromol. Chem. Phys.* **1999**, *200*, 840–844.
- 67 M. SCHUTTE, D. G. KURTH, M. R. LINFORD, H. COLFEN, H. MÖHWALD, *Angew. Chem., Int. Ed. Engl.* **1998**, *37*, 2891–2893.
- 68 M. FERREIRA, M. F. RUBNER, *Macromolecules* **1995**, *28*, 7107–7114.
- 69 G. J. KELLOGG, A. M. MAYES, W. B. STOCKTON, M. FERREIRA, M. F. RUBNER, S. K. SATIJA, *Langmuir* **1996**, *12*, 5109–5113.
- 70 C. LESSER, M. GAO, S. KIRSTEIN, *Mater. Sci. Eng., C* **1999**, *8–9*, 159–162.
- 71 E. HAO, B. YANG, H. REN, X. QIAN, T. XIE, J. SHEN, D. LI, *Mater. Sci. Eng., C* **1999**, *10*, 119–122.
- 72 E. HAO, X. QIAN, B. YANG, D. WANG, J. SHEN, *Mol. Cryst. Liq. Cryst. Sci. Technol., Sect. A* **1999**, *337*, 181–184.
- 73 E. HAO, T. LIAN, *Langmuir* **2000**, *16*, 7879–7881.
- 74 M. GAO, C. LESSER, S. KIRSTEIN, H. MÖHWALD, A. L. ROGACH, H. WELLER, *J. Appl. Phys.* **2000**, *87*, 2297–2302.
- 75 J. SUN, E. HAO, Y. SUN, H. ZHANG, B. YANG, S. ZOU, J. SHEN, S. WANG, *Thin Solid Films* **1998**, *327–329*, 528–531.
- 76 Y. SUN, E. HAO, X. ZHANG, B. YANG, J. SHEN, L. CHI, H. FUCHS, *Langmuir* **1997**, *13*, 5168–5174.
- 77 Y. J. LIU, A. B. WANG, R. CLAUS, *J. Phys. Chem. B* **1997**, *101*, 1385–1388.
- 78 E. HAO, B. YANG, J. ZHANG, X. ZHANG, J. SUN, J. SHEN, *J. Mater. Chem.* **1998**, *8*, 1327–1328.
- 79 A. ROSIDIAN, Y. J. LIU, R. O. CLAUS, *Adv. Mater.* **1998**, *10*, 1087.
- 80 T. CASSAGNEAU, J. H. FENDLER, *J. Phys. Chem. B* **1999**, *103*, 1789–1793.
- 81 W. SCHROF, S. ROZOUVAN, E. VANKEUREN, D. HORN, J. SCHMITT, G. DECHER, *Adv. Mater.* **1998**, *10*, 338–341.
- 82 J. A. HE, R. VALLUZZI, K. YANG, T. DOLUKHANYAN, C. SUNG, J. KUMAR, S. K. TRIPATHY, L. SAMUELSON, L. BALOGH, D. A. TOMALIA, *Chem. Mater.* **1999**, *11*, 3268–3274.
- 83 E. HAO, T. LIAN, *Chem. Mater.* **2000**, *12*, 3392–3396.
- 84 I. ICHINOSE, H. TAGAWA, S. MIZUKI, Y. LVOV, T. KUNITAKE, *Langmuir* **1998**, *14*, 187–192.
- 85 F. CARUSO, D. KURTH, D. VOLKMER, M. J. KOOP, A. MÜLLER, *Langmuir* **1998**, *14*, 3462–3465.
- 86 I. MORIGUCHI, J. H. FENDLER, *Chem. Mater.* **1998**, *10*, 2205–2211.
- 87 Y. J. LIU, A. B. WANG, R. O. CLAUS, *Appl. Phys. Lett.* **1997**, *71*, 2265–2267.
- 88 G. FERGUSON, E. KLEINFELD, *Chem. Mater.* **1996**, *8*, 1575–1578.
- 89 Y. LVOV, K. ARIGA, I. ICHINOSE, T. KUNITAKE, *Langmuir* **1996**, *12*, 3038–3044.
- 90 M. ECKLE, G. DECHER, *Nano Lett.* **2001**, *1*, 45–49.
- 91 M. M. FANG, C. H. KIM, A. C. SUTORIK, D. M. KASCHAK, T. E. MALLOUK, IN *Amorphous And Crystalline Insulating Thin Films*, Eds. (W. L. WARREN, R. A. DEVINE, M. MATSUMURA, S. CRISTOLOVEANU, Y. HOMMA, J. KANICKI, Materials Research Society, Warrendale **1997**, pp. 377–381.
- 92 M. M. FANG, D. M. KASCHAK, A. C. SUTORIK, T. E. MALLOUK, *J. Am. Chem. Soc.* **1997**, *119*, 12184–12191.
- 93 S. W. KELLER, S. A. JOHNSON, E. S. BRIGHAM, E. H. YONEMOTO, T. E. MALLOUK, *J. Am. Chem. Soc.* **1995**, *117*, 12879–12880.
- 94 J. KERIMO, D. M. ADAMS, P. F. BARBARA, D. M. KASCHAK, T. E. MALLOUK, *J. Phys. Chem. B* **1998**, *102*, 9451–9460.
- 95 R. E. SCHAACK, T. E. MALLOUK, *Chem. Mater.* **2000**, *12*, 3427–3434.
- 96 R. E. SCHAACK, T. E. MALLOUK, *Chem. Mater.* **2000**, *12*, 2513–2516.
- 97 M. FANG, C. H. KIM, G. B. SAUPE, H. N. KIM, C. C. WARAKSA, T. MIWA, A. FU-

- JISHIMA, T.E. MALLOUK, *Chem. Mater.* **1999**, *11*, 1526–1532.
- 98 N.A. KOTOV, I. DEKANY, J.H. FENDLER, *Adv. Mater.* **1996**, *8*, 637.
- 99 T. CASSAGNEAU, J.H. FENDLER, *Adv. Mater.* **1998**, *10*, 877.
- 100 N.I. KOVTYUKHOVA, E.V. BUZANEVA, A.D. GORCHINSKY, P.J. OLLIVIER, B.R. MARTIN, C.C. WARAKSA, T.E. MALLOUK, *NATO ASI Ser.* **2000**, *6*, 331–346.
- 101 J.S. YU, J.Y. KIM, S. LEE, J.K.N. MBINDYO, B.R. MARTIN, T.E. MALLOUK, *Chem. Commun.* **2000**, 2445–2446.
- 102 F. CARUSO, A.S. SUSHA, M. GIERSIG, H. MÖHWALD, *Adv. Mater.* **1999**, *11*, 950–953.
- 103 F. CARUSO, R.A. CARUSO, E. DONATH, H. MÖHWALD, G. SUKHORUKOV, *US Pat.*, 1999, E.V. 99-EP1854[9947253].
- 104 A.S. SUSHA, F. CARUSO, A.L. ROGACH, G.B. SUKHORUKOV, A. KORNOWSKI, H. MÖHWALD, M. GIERSIG, A. EYCHMULLER, H. WELLER, *Colloids Surf., A* **2000**, *163*, 39–44.
- 105 D.S. KOKTYSH, N.A. KOTOV, unpublished results. The layers have blue coloration characteristic for closely packed Au particles and strong reflection. Interestingly, despite metallic shine, no noticeable conductivity was seen in these films.
- 106 T. SERIZAWA, H. TAKESHITA, M. AKASHI, *Langmuir* **1998**, *14* 4088–4094.
- 107 M. GAO, X. ZHANG, B. YANG, F. LI, J. SHEN, *Thin Solid Films* **1996**, *284–285*, 242–245.
- 108 Y. LIU, A. WANG, R.O. CLAUS, *Appl. Phys. Lett.* **1997**, *71*, 2265–2267.
- 109 This term is used with the understanding that, concomitantly with the lateral expansion, the domains also grow in thickness accumulating new layers of particles similar to the normal (sandwich) mode.
- 110 J.D. MENDELSON, C.J. BARRETT, V.V. CHAN, A.J. PAL, A.M. MAYES, M.F. RUBNER, *Langmuir* **2000**, *16*, 5017–5023.
- 111 S.S. SHIRATORI, M.F. RUBNER, *Macromolecules* **2000**, *33*, 4213–4219.
- 112 S. JOLY, R. KANE, L. RADZILOWSKI, T. WANG, A. WÜ, R.E. COHEN, E.L. THOMAS, M.F. RUBNER, *Langmuir* **2000**, *16*, 1354–1359.
- 113 F. CARUSO, D.N. FURLONG, K. ARIGA, I. ICHINOSE, T. KUNITAKE, *Langmuir* **1998**, *14*, 4559–4565.
- 114 W. CHEN, T. J. MCCARTHY, *Macromolecules* **1997**, *30*, 78–86.
- 115 The substrates with YIG/PDDA films were air-dried between the deposition cycles and removed slowly from the adsorption baths. The accelerated drying in the stream of gas was intentionally avoided because of indications that the hydrodynamic conditions in all LBL steps affect the thickness of NPs and PE layers. The thickness of the films decreased very strongly when the process was performed in the rapid flow of the liquid.
- 116 P.G. HARTLEY, P.J. SCALES, P.J. *Langmuir* **1998**, *14*, 6948–6955; N. HOOGVEEN, M.A. COHEN STUART, G.J. FLEER, *J. Colloid Interface Sci.* **1996**, *182*, 146–157; S. SUKHISHVILI, S. GRANICK, *J. Chem. Phys.* **1998**, *109*, 6869–6878; S. SUKHISHVILI, S. GRANICK, *J. Chem. Phys.* **1998**, *109*, 6861–6868; T. WALLIN, P. LINSE, *J. Chem. Phys.* **1998**, *109*, 5089–5100.
- 117 J.B. SCHLENOFF, H. LY, M. LI, *J. Am. Chem. Soc.* **1998**, *120*, 7626–7634.
- 118 G. LADAM, P. SCHAAP, F.J.G. CUISINIER, G. DECHER, J.C. VOEGEL, *Langmuir* **2001**, *17*, 878–882.
- 119 N.A. KOTOV, *Nanostruct. Mater.* **1999**, *12*, 789–796.
- 120 S.Y. PARK, C.J. BARRETT, M.F. RUBNER, A.M. MAYES, *Macromolecules* **2001**, *34*, 3384–3388.
- 121 P.T. HAMMOND, *Curr. Opin. Colloid Interface Sci.* **2000**, *4*, 430–442.
- 122 D.A. WEITZ, *Nature (London)* **1996**, *381*, 475–476.
- 123 H. ARANDA-ESPINOZA, Y. CHEN, N. DAN, T. C. LUBENSKY, P. NELSON, L. RAMOS, D.A. WEITZ, *Science* **1999**, *285*, 394–397.
- 124 K.H. LIN, J.C. CROCKER, V. PRASAD, A. SCHOFIELD, D.A. WEITZ, T.C. LUBENSKY, A.G. YODH, *Phys. Rev. Lett.* **2000**, *85*, 1770–1773.
- 125 U. GASSER, E.R. WEEKS, A. SCHOFIELD, P.N. PUSEY, D.A. WEITZ, *Science* **2001**, *292*, 258–262.
- 126 A. POLDERMAN, *Biopolymers* **1975**, *14*, 2181–2195.

- 127 V.A. IZUMRUDOV, V.A. KASAIKIN, L.N. YERMAKOVA, M.I. MUSTAPAEV, A.B. ZEZIN, V.A. KABANOV, *Polym. Sci. USSR* **1981**, *23*, 1512–1525.
- 128 J. MIKULIK, Z. VINKLAREK, M. VONDRUSKA, *Collect. Czech. Chem. Commun.* **1993**, *58*, 713–747 And References Therein.
- 129 B. PHILLIP, H. DAUTZENBERG, K.-J. LINDNOW, J. KÖTZ, W. DAWYDOFF, *Prog. Polym. Sci.* **1989**, *14*, 91 and references therein.
- 130 A. LASCHEWSKY, B. MAYER, E. WISCHERHOFF, X. ARYS, A. JONAS, *Ber. Bunsen-Ges. Phys. Chem.*, **1996**, *100*, 1033.
- 131 H.G.M. STEEG, M.A. COHEN STUART, A. KEIZER, B. H. BIJSTERBOSCH, *Langmuir* **1992**, *8*, 2538.
- 132 F.V. GOELER, M. MUTHUKUMAR, *J. Chem. Phys* **2001**, *100*, 7802.
- 133 T. WALLIN, P. LINSE, *Langmuir* **1996**, *12*, 314.
- 134 J.B. SCHLENOFF, H. XU, *Langmuir* **1994**, *10*, 241–245.
- 135 E.M. LEE, D. KANELLEAS, J.E. MILNES, K. SMITH, N. WARREN, M. WEBBERLEY, A.R. RENNIE, *Langmuir* **1996**, *12*, 1270–1277.
- 136 F.M. WINNIK, S.T.A. REGISMOND, E.D. GODDARD, *Langmuir* **1997**, *13*, 111–114.
- 137 J.-M. SEQUARIS, *Langmuir* **1997**, *13*, 653–658.
- 138 C.K. OBER, G. WEGNER, *Adv. Mater.* **1997**, *9*, 17–31 and references therein.
- 139 O. ANTONY, R. ZANA, *Langmuir* **1996**, *12*, 1967–1975.
- 140 S. LUDEMANN, R. ABSEHER, H. SCHREIBER, O. STEINHAUSER, *J. Am. Chem. Soc.* **1997**, *119*, 4206–4213.
- 141 D.J. NEIVANDT, M.L. GEE, C.P. TRIPP, M.L. HAIR, *Langmuir* **1997**, *13*, 2519–2526.
- 142 P.M. MACDONALD, A. TANG, JR., *Langmuir* **1997**, *13*, 2259–2265 and references therein.
- 143 Electrostatic (or ionic) self-assembly (ESA) are terms occasionally used in the scientific literature for the LBL process. It appears to be a double misnomer because the theoretical and experimental data point to the conclusion that electrostatic forces alone cannot produce the sequentially adsorbed films. There are also several examples of LBL process where no oppositely charged PEs are involved, or the electrostatic interactions are even unfavorable for adsorption. Additionally, the notion of self-assembly implies that there is a certain degree of lateral order within the film similar to, for instance, self-assembled films of thiols on gold, which has not been achieved yet for PE/PE or PE/colloid LBL pairs. In the first publications, we also described LBL sequential adsorption as self-assembly (see for instance(N. KOTOV, A. DEKANY, J.H. FENDLER, *J. Phys. Chem.* **1995**, *99* 13065–13069), but later most of the researchers in the field including us prefer to associate the word “assembly” with it, which then does not bear the meaning of self-organization of the individual adsorption layers.
- 144 N.G. HOOGVEEN, M.A. COHEN STUART, G.J. FLEER, *J. Colloid Interface. Sci.* **1996**, *182*, 146–157.
- 145 N.G. HOOGVEEN, M.A.C. COHEN STUART, G. J. FLEER, M.R. BOHMER, *Langmuir* **1996**, *12*, 3675–3681.
- 146 Y. LVOV, K. ARIGA, I. ICHINOSE, T. KUNITAKE, *J. Am. Chem. Soc.* **1995**, *117*, 6117–6123.
- 147 Y. LVOV, H. HAAS, G. DECHER, H. MÖHWALD, A. KALACHEV, *J. Phys. Chem.* **1993**, *97*, 12835–12841.
- 148 J. HODAK, R. ETCHENIQUE, E. CALVO, K. SINGHAL, P.N. BARTLETT, *Langmuir* **1997**, *13*, 2708–2716.
- 149 T.M. COOPER, A.L. CAMPBELL, R.L. CRANE, *Langmuir* **1995**, *11*, 2713–2718.
- 150 Y.J. LIU, Y. WANG, H. LU, R.O. CLAUS, *J. Phys. Chem.A.* **1999**, *103*, 2035–2036.
- 151 S.L. CLARK, P.T. HAMMOND, *Langmuir* **2000**, *16*, 10206–10214.
- 152 S. T. DUBAS, J.B. SCHLENOFF, *Macromolecules* **1999**, *32*, 8153–8160.
- 153 P. FISCHER, A. LASCHEWSKY, *Macromolecules* **2000**, *33*, 1100–1102.
- 154 T. SERIZAWA, S. HASHIGUCHI, M. AKASHI, *Langmuir* **1999**, *15*, 5363–5368.
- 155 T. SERIZAWA, K. YAMAMOTO, M. AKASHI, *Langmuir* **1999**, *15*, 4682–4684.
- 156 Y. SHIMAZAKI, M. MITSUISHI, S. ITO, M. YAMAMOTO, *Langmuir* **1998**, *14*, 2768–2773.
- 157 L.Y. WANG, Z.Q. WANG, X. ZHANG, J.C. SHEN, L. CHI, H. FUCHS, *Macromol. Rapid Commun.* **1997**, *18*, 509–514.

- 158 T. SERIZAWA, K. I. HAMADA, T. KITAYAMA, N. FUJIMOTO, K. HATADA, M. AKASHI, *J. Am. Chem. Soc.* **2000**, *122*, 1891–1899.
- 159 P. FISCHER, A. LASCHEWSKY, *Macromolecules* **2000**, *33* 1100–1102.
- 160 E. HAO, L. WANG, J. ZHANG, B. YANG, Z. XI, J. SHEN, *Chem. Lett.* **1999**, 5–6.
- 161 T. VOSSMEYER, L. KATSIKAS, M. GIERSIG, I. G. POPOVIC, K. DIESNER, A. CHEMSEDINE, A. EYCHMUELLER, H. WELLER, *J. Phys. Chem.* **1994**, *98*, 7665–7673.
- 162 The adsorption time of NP and PDDA layers was 24 h and 0.5 h respectively. The pH of CdS was 8.5, while the pH of PDDA was 7.0. The ionic strength for all NP dispersions was presumably identical because they were made in identical conditions. Ionic strength of PDDA was not adjusted. All the CdS NPs synthesized from different ratios of the stabilizers had a fairly broad size distribution with UV–vis absorption edge at 440 nm.
- 163 The relative amounts of thiolactic acid and Et-SH in the shell around the NP are likely to be somewhat different than those taken for the synthesis. Nevertheless, the inclusion of different stabilizers in the NP coating should follow the statistical probability of their binding to CdS nanocrystals.
- 164 C. H. LYONS, E. D. ABBAS, J. K. LEE, M. F. RUBNER, *J. Am. Chem. Soc.* **1998**, *120*, 12100–12107.
- 165 J. W. BAUR, S. KIM, P. B. BALANDA, J. R. REYNOLDS, M. F. RUBNER, *Adv. Mater.* **1998**, *10*, 1452–1455.
- 166 E. S. HANDY, A. J. PAL, M. F. RUBNER, *J. Am. Chem. Soc.* **1999**, *121*, 3525–3528.
- 167 T. SASAKI, Y. EBINA, M. WATANABE, G. DECHER, *Chem. Commun.* **2000**, 2163–2164.
- 168 D. M. GULDI, C. LUO, D. S. KOKTYSH, N. A. KOTOV, T. DA ROSS, S. BOSI, M. PRATO, *Nano Letters* **2002**, *2*, 775–780.
- 169 A. WU, J. LEE, M. F. RUBNER, *Thin Solid Films* **1998**, *327–329*, 663–667.
- 170 H. MATTOUSSI, M. F. RUBNER, F. ZHOU, J. KUMAR, S. K. TRIPATHY, L. Y. CHIANG, *Appl. Phys. Lett.* **2000**, *77*, 1540–1542.
- 171 C. LUO, D. M. GULDI, M. MAGGINI, E. MENNA, S. MONDINI, N. A. KOTOV, M. PRATO, *Angew. Chem., Int. Ed. Engl.* **2000**, *39*, 3905–3909.
- 172 A. C. FOU, O. ONITSUKA, M. FERREIRA, M. F. RUBNER, B. R. HSIEH, *J. Appl. Phys.* **1996**, *79*, 7501–7509.
- 173 S. JOLY, R. KANE, L. RADZIŁOWSKI, T. WANG, A. WU, R. E. COHEN, E. L. THOMAS, M. F. RUBNER, *Langmuir* **2000**, *16*, 1354–1359.
- 174 Y. BOONTONGKONG, R. E. COHEN, M. F. RUBNER, *Chem. Mater.* **2000**, *12*, 1628–1633.
- 175 S. L. CLARK, P. T. HAMMOND, *Adv. Mater.* **1998**, *10*, 1515–1519.
- 176 S. L. CLARK, M. F. MONTAGUE, P. T. HAMMOND, *Macromolecules* **1997**, *30*, 7237–7244.
- 177 S. L. CLARK, E. S. HANDY, M. F. RUBNER, P. T. HAMMOND, *Adv. Mater.* **1999**, *11*, 1031–1035.
- 178 A. LASCHEWSKY, B. MAYER, E. WISCHERHOFF, X. ARYS, P. BERTRAND, A. DELCORTE, A. JONAS, *Thin Solid Films* **1996**, *284–285*, 334–337.
- 179 A. LASCHEWSKY, E. WISCHERHOFF, M. KAURANEN, A. PERSOONS, *Macromolecules* **1997**, *30*, 8304–8309.
- 180 A. LASCHEWSKY, B. MAYER, E. WISCHERHOFF, X. ARYS, A. JONAS, M. KAURANEN, A. PERSOONS, *Angew. Chem., Int. Ed. Engl.* **1998**, *36*, 2788–2791.
- 181 T. SERIZAWA, H. TAKESHITA, M. AKASHI, in Book of Abstracts, 216th ACS National Meeting, Boston, August 23–27, **1998**, MACR-044.
- 182 F. CARUSO, H. MÖHWALD, *Langmuir* **1999**, *15*, 8276–8281.
- 183 Y. LVOV, H. HAAS, G. DECHER, H. MÖHWALD, *J. Phys. Chem.* **1993**, *97*, 12835–12841.
- 184 D. E. MACDONALD, B. MARKOVIC, A. L. BOSKEY, P. SOMASUNDARAN, *Colloid Surf. B.* **1998**, *11*, 131–139; A. Szymczyk, P. Fievet, J. C. Reggiani, J. Pagetti, *Desalination*, **1998**, *115*, 129–134.
- 185 E. DONATH, D. WALTHER, V. N. SHILOV, E. KNIPPEL, A. BUDDE, K. LOWACK, C. A. HELM, H. MÖHWALD, *Langmuir* **1997**, *13*, 5294–5305.
- 186 T. TERANISHI, R. KURITA, M. MIYAKE, *J. Inorg. Organomet. Polym.* **2000**, *10*, 145–156.
- 187 A. A. PATEL, F. WU, J. Z. ZHANG, C. L. TORRES-MARTINEZ, R. K. MEHRA, Y. YANG, S. H. RISBUD, *J. Phys. Chem. B* **2000**, *104*, 11598–11605.

- 188 J. ZHU, S. LIU, O. PALCHIK, Y. KOLTYPIN, A. GEDANKEN, *Langmuir* **2000**, *16*, 6396–6399.
- 189 M. M. MAYE, W. ZHENG, F. L. LEIBOWITZ, N. K. LY, C. J. ZHONG, *Langmuir* **2000**, *16*, 490–497.
- 190 J. M. PETROSKI, Z. L. WANG, T. C. GREEN, M. A. EL SAYED, *J. Phys. Chem. B* **1998**, *102*, 3316–3320.
- 191 M. P. PILENI, A. HAMMOUDA, I. LISIECKI, L. MOTTE, N. MOUMEN, J. TANORI, *NATO ASI Ser., Ser. 3* **1996**, *12*, 413–429.
- 192 T. S. AHMADI, Z. L. WANG, T. C. GREEN, A. HENGLEIN, M. A. EL SAYED, *Science* **1996**, *272*, 1924–1926.
- 193 T. E. MALLOUK, *Science* **2001**, *291*, 443–444.
- 194 Z. A. PENG, X. PENG, *J. Am. Chem. Soc.* **2001**, *123*, 1389–1395.
- 195 X. PENG, U. MANNA, W. YANG, J. WICKHAM, E. SCHER, A. KADAVANICH, A. P. ALLVISATOS, *Nature* **2000**, *404*, 59–61.
- 196 W. U. HUYNH, X. PENG, A. P. ALIVISATOS, *Adv. Mater.* **1999**, *11*, 923–927.
- 197 R. E. SCHAAK, T. E. MALLOUK, *J. Am. Chem. Soc.* **2000**, *122*, 2798–2803.
- 198 D. K. NAGESHA, X. LIANG, A. A. MAMEDOF, G. GAINER, M. EASTMAN, M. GIER SIG, J.-J. SONG, T. NI, N. KOTOV, *J. Phys. Chem. B* **2001**, *105*, 7490–7498.
- 199 Y. M. LVOV, G. B. SUKHORUKOV, *Biol. Membr.* **1997**, *14*, 229–250.
- 200 Y. M. LVOV, Z. Q. LU, J. B. SCHENKMAN, X. L. ZU, J. F. RUSLING, *J. Am. Chem. Soc.* **1998**, *120*, 4073–4080.
- 201 F. CARUSO, D. N. FURLONG, K. ARIGA, I. ICHINOSE, T. KUNITAKE, *Langmuir* **1998**, *14*, 4559–4565.
- 202 F. CARUSO, K. NIJKURA, D. N. FURLONG, Y. OKAHATA, *Langmuir* **1997**, *13*, 3427–3433.
- 203 M. ONDA, Y. LVOV, K. ARIGA, T. KUNITAKE, *J. Ferment. Bioeng.* **1996**, *82*, 502–506.
- 204 M. ONDA, Y. LVOV, K. ARIGA, T. KUNITAKE, *Biotechnol. Bioeng.* **1996**, *51*, 163–167.
- 205 A. NARVAEZ, G. SUAREZ, I. C. POPESCU, I. KATAKIS, E. DOMINGUEZ, *Biosens. Bioelectron.* **2000**, *15*, 43–52.
- 206 J. W. BAUR, M. F. RUBNER, J. R. REYNOLDS, S. KIM, *Langmuir* **1999**, *15*, 6460–6469.
- 207 D. M. KASCHAK, J. T. LEAN, C. C. WARAKSA, G. B. SAUPE, H. USAMI, T. E. MALLOUK, *J. Am. Chem. Soc.* **1999**, *121*, 3435–3445.
- 208 D. M. KASCHAK, T. E. MALLOUK, *J. Am. Chem. Soc.* **1996**, *118*, 4222–4223.
- 209 F. CARUSO, E. DONATH, H. MÖHWALD, *J. Phys. Chem. B* **1998**, *102*, 2011–2016.
- 210 P. K. H. HO, J. S. KIM, J. H. BURROUGHES, H. BECKER, F. Y. L. SAM, T. M. BROWN, F. CACIALLI, R. H. FRIEND, *Nature* **2000**, *404*, 481–484.
- 211 C. B. MURRAY, C. R. KAGAN, M. G. BAWEN DI, *Science* **1995**, *270*, 1335–1338.
- 212 C. A. LEATHERDALE, C. R. KAGAN, N. Y. MORGAN, S. A. EMPEDOCLES, M. A. KASTNER, M. G. BAWEN DI, *Phys. Rev. B* **2000**, *62*, 2669–2680.
- 213 C. A. LEATHERDALE, N. Y. MORGAN, C. R. KAGAN, S. A. EMPEDOCLES, M. G. BAWEN DI, M. A. KASTNER, *Mater. Res. Soc. Symp. Proc.* **2000**, *571*, 191–196.
- 214 C. R. KAGAN, C. B. MURRAY, M. G. BAWEN DI, *Phys. Rev. B* **1996**, *54*, 8633–8643.
- 215 U. BANIN, J. C. LEE, A. A. GUZELIAN, A. V. KADAVANICH, A. P. ALIVISATOS, *Superlattice Microstruct.* **1997**, *22*, 559–567.
- 216 C. A. MIRKIN, *MRS Bull.* **2000**, *25*, 43–54.
- 217 R. C. MUCIC, J. J. STORHOFF, C. A. MIRKIN, R. L. LETSINGER, *J. Am. Chem. Soc.* **1998**, *120*, 12674–12675.
- 218 S. T. DUBAS, T. R. FARHAT, J. B. SCHLENOFF, *J. Am. Chem. Soc.* **2001**, *123*, 5368–5369.
- 219 N. A. KOTOV, S. MAGONOV, E. TROP SHA, *Chem. Mater.* **1998**, *10*, 886–895.
- 220 T. CASSEGNEAU, J. H. FENDLER, *J. Phys. Chem. B* **1999**, *103*, 1789–1793.
- 221 F. J. HIMPSEL, J. E. ORTEGA, G. J. MANKEY, R. F. WILLIS, *Adv. Phys.* **1998**, *47*, 511–597.
- 222 E. C. STONER, E. P. WOHLFARTH, *Philos. Trans. R. Soc. London, Ser. A.* **1948**, *240*, 599.
- 223 D. E. SPELIOTIS, W. LYNCH, *J. Appl. Phys.* **1991**, *69*, 4496–4498.
- 224 M. EL HILO, R. W. CHANTRELL, K. O'GRADY, *J. Appl. Phys.* **1998**, *84*, 5114–5122.
- 225 G. CHOE, S. J. CHUNG, R. M. WALSER, *Thin Solid Films* **1995**, *259*, 231–236.
- 226 Y. TAKAHASHI, *Phys. Rev. B* **1997**, *56*, 8175–8182.
- 227 H. NESS, F. GAUTIER, *Phys. Rev. B* **1995**, *52*, 7352–7361.

- 228 P. C. KUO, Y. D. YAO, J. W. CHEN, H. C. CHIU, *IEEE Trans. Magn.* **1998**, *34*, 1156–1158.
- 229 Z. CELINSKI, B. HEINRICH, *J. Magn. Magn. Mater.* **1991**, *99*, L25–L30.
- 230 K. VANLANGENBERG, S. R. BATTEN, K. J. BERRY, D. C. R. HOCKLESS, B. MOUBARAKI, K. S. MURRAY, *Inorg. Chem.* **1997**, *36*, 5006–5015.
- 231 V. LAGET, C. HORNICK, P. RABU, M. DRILLON, P. TUREK, R. N. ZIESSEL, *Adv. Mater.* **1998**, *10*, 1024.
- 232 V. LAGET, P. RABU, C. HORNICK, F. ROMERO, R. ZIESSEL, P. TUREK, M. DRILLON, *Mol. Cryst. Liq. Cryst. Sci. Technol. A* **1997**, *305*, 291–301.
- 233 K. NAKAMURA, H. HASEGAWA, T. OGUCHI, K. SUEOKA, K. HAYAKAWA, K. MUKASA, *Phys. Rev. B* **1997**, *56*, 3218–3221.
- 234 A. MURAYAMA, K. HYOMI, K. OHSHIMA, M. MIYAMURA, M. MAEKAWA, S. KONDOH, *J. Appl. Phys.* **1997**, *81*, 3925–3927.
- 235 A. MURAYAMA, K. OHSHIMA, M. MIYAMURA, M. MAEKAWA, S. KONDOH, *J. Appl. Phys.* **1996**, *79*, 7916–7919.
- 236 R. MUKAI, K. YAMANAKA, M. OSHIKI, *J. Appl. Phys.* **1997**, *81*, 3931–3933.
- 237 W. H. LIU, S. FLEMING, B. M. LAIRSON, *J. Appl. Phys.* **1996**, *79*, 3651.
- 238 I. KAITSU, A. INOMATA, I. OKAMOTO, M. SHINOHARA, *IEEE Trans. Magn.* **1998**, *34*, 1591–1593.
- 239 A. I. EKIMOV, A. EFROS, A. A. ONUSHCHENKO, *Solid State Commun.* **1985**, *56*, 921–924.
- 240 A. EFROS, M. ROSEN, M. KUNO, M. NIRMAL, D. J. NORRIS, M. BAWENDI, *Phys. Rev. B* **1996**, *54*, 4843–4856.
- 241 A. L. EFROS, A. L. EFROS, *Fiz. Tëkh. Poluprovodn. (Leningrad)* **1982**, *16*, 1209–1214.
- 242 L. BRUS, *J. Phys. Chem.* **1986**, *90*, 2555–2560.
- 243 L. E. BRUS, *J. Chem. Phys.* **1983**, *79*, 5566–5571.
- 244 L. AIGOUY, V. MATHET, F. LIACI, B. GIL, O. BRIOT, N. BRIOT, T. CLOITRE, M. AVEROUS, R. L. AULOMBARD, *Phys. Rev. B* **1996**, *53*, 4708–4721.
- 245 A. K. NEWMAN, J. M. LIU, *J. Appl. Phys.* **1997**, *82*, 4637–4646.
- 246 J. H. LEE, S. S. LI, M. Z. TIDROW, W. K. LIU, K. BACHER, *Appl. Phys. Lett.* **1999**, *75*, 3207–3209.
- 247 F. CAPASSO, B. F. LEVINE, *J. Lumin.* **1985**, *30*, 144–153.
- 248 F. CAPASSO, *NATO ASI Ser., Ser. B* **1988**, *180*, 659–682.
- 249 S. VLAEV, V. R. VELASCO, F. GARCIA-MOLLNER, *Phys. Rev. B* **1994**, *49* 11222–11229.
- 250 M. R. GELLER, *Phys. Rev. Lett.* **1997**, *78*, 110–113.
- 251 B. S. SOKOLOVSKII, *Phys. Status Solidi A* **1997**, *163*, 425–432.
- 252 R. TOMASIUNAS, I. PELANT, B. HONERLAGE, R. LEVY, T. CLOITRE, R. L. AULOMBARD, *Phys. Rev. B* **1998**, *57*, 13077–13085.
- 253 H. FUJIWARA, J. KOH, C. R. WRONSKI, R. W. COLLINS, J. S. BURNHAM, *Appl. Phys. Lett.* **1998**, *72*, 2993–2995.
- 254 G. AICHMAYR, M. D. MARTIN, H. VAN DER MEULEN, C. PASCUAL, L. VINA, J. M. CALLEJA, F. SCHAFER, J. P. REITHMAIER, A. FORCHEL, *Appl. Phys. Lett.* **2000**, *76*, 3540–3542.
- 255 S. K. CHATTOPADHYAYA, V. K. MATHUR, *Phys. Rev. B* **1971**, *3*, 3390–3399.
- 256 B. S. SOKOLOVSKII, *Phys. Status Solidi A* **1997**, *161*, 105–110.
- 257 B. S. SOKOLOVSKII, *Phys. Status Solidi A* **1997**, *163*, 425–432.
- 258 A. SAMOKHVALOV, M. BERFELD, M. LAHAV, R. NAAMAN, E. RABANI, *J. Phys. Chem. B.* **2000**, *104*, 8631–8634.

## 9

# Layer-by-Layer Self-assembled Polyelectrolytes and Nanoplatelets

J. H. FENDLER

### Abstract

Preparation, characterization and potential utilization of ultrathin films composed of alternating layers of cationic polyelectrolytes and anionic clay (Montmorillonite, M, for example) and graphite oxide (GO) nanoplatelets are surveyed. There are several benefits of using nanoplatelets. First, they can effectively cover and smooth large areas. Second, expansion of the basal spacing between incompletely exfoliated nanoplatelets in a suitable solvent provides opportunities for molecular architecture by pillaring with or reversibly intercalating desired materials. Third, in situ reduction of GO permits controllable lateral current conduction in self-assembled films. Potential applications are illustrated by 1) pollutant photodestruction by semiconductor–clay nanocomposites and layer-by-layer self-assembled clay platelets and semiconductor nanoparticles; 2) construction of ultrathin rectifiers by the self-assembly of semiconductor nanoparticles, polyelectrolytes, ruthenium complexes and GO; and 3) by the demonstration of superior charge storage in an electrochemical cell which contains a layer-by-layer self-assembled, polyelectrolyte, polymer and GO electrode.

### 9.1

#### Introduction

Following the seminal report on the layer-by-layer adsorption of oppositely charged colloidal particles [1], there has been an exponential growth in the investigation of the sequential self-assembly of polyelectrolytes, nanoparticles and nanoplatelets on a variety of substrates. The relative ease of preparation, versatility, potential of scalability and applicability have prompted this progress. Indeed, layer-by-layer self-assembly has become recognized as a sub-field of colloid chemistry and the exponentially increasing research publications are listed at a website [2]. That a large variety of molecules, polyelectrolytes, nanoparticles and nanoplatelets can be layer-by-layer adsorbed, in any desired order, is the greatest advantage of self-assembly. The oppositely charged species are held together by strong ionic attractions and form long-lasting, uniform and stable films which are often imper-

vious to solvents. No special film balance is required for the self-assembly; indeed the method has been referred to as a “Molecular Beaker Epitaxy” [3].

Self-assembly is governed by a delicate balance between adsorption and desorption equilibria. The layer-by-layer preparation of ultrathin films, as detailed in Chapter 1, is deceptively simple. In the self-assembly of clay nanoplatelets, for example, the efficient adsorption of one (and only one) layer of exfoliated clay platelets onto the oppositely charged substrate surface is the objective of the immersion step. Desorption of clay platelets forming a second and additional layers (and preventing the desorption of the first added layer) is the purpose of the rinsing process. The self-assembly of clay platelets can be optimized by the judicious selection of stabilizer(s) and exfoliating agents as well as by the careful control of the kinetics of the adsorption and desorption [4].

The present survey is limited to the preparation, characterization and applications of ultrathin films, layer-by-layer self-assembled from polyelectrolytes and clay or graphite oxide nanoplatelets. There are several beneficial properties of nanoplatelets in self-assembled films. First, the unique morphology of nanoplatelets (typically, irregularly shaped,  $100 \pm 50$  nm long,  $80 \pm 30$  nm wide and 1 nm thick) ensures the coverage and smoothing of large areas. Second, expansion of the basal spacing between incompletely exfoliated nanoplatelets (say 2–3 sheets) in an appropriately selected solvent provides opportunities for molecular architecture by pillaring with or reversibly intercalating desired materials. Third, in situ reduction of graphite oxide permits controllable lateral current conduction in self-assembled films.

## 9.2

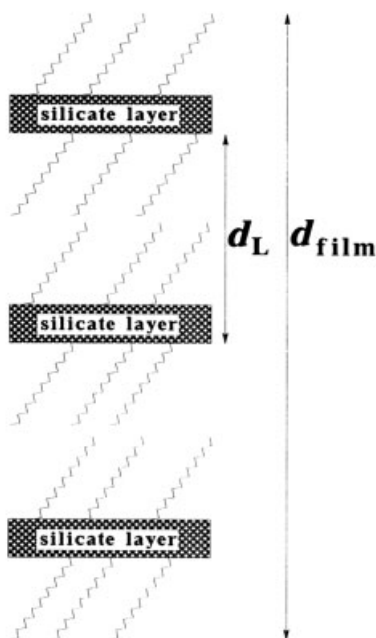
### Self-assembled Polyelectrolytes and Clay Nanoplatelets

Montmorillonites are colloidal, layered aluminosilicates (clays) with exchangeable cations distributed over their external and internal surfaces [5, 6]. The layers, each consisting of a sheet (typically  $100 \text{ nm} \times 100 \text{ nm}$  and 1 nm thick) of  $\text{AlO}_4(\text{OH})_2$  octahedra sandwiched between two sheets of  $\text{SiO}_4$  tetrahedra, are stacked parallel to one another to form plates. The flat, composite aluminosilicate lattice carries a net negative charge as a result of isomorphous substitution of Al and Si atoms by atoms of lower valence, as well as of crystal defects. Usually, positive vacancies are occupied by calcium or sodium cations (Ca or Na forms of montmorillonite) which can be easily replaced by other cations.

In our work we have exchanged the cations by hexadecylammonium (**A**) and dioctadecylammonium (**B**) cations to form organic clay-complexes (Fig. 9.1) [7]. The presence of hydrophobic moieties render **A** and **B** dispersible in organic solvents (in contrast to the native montmorillonite which gives a stable optically transparent dispersion in water). A 1:1 (v/v) mixture of butanol and benzene was found to be the best dispersing medium for **A**. The mean hydrodynamic diameter of **A** in this mixture was determined to be  $190 \pm 10$  nm by dynamic light scattering. **B** could be best dispersed in a 3:7 butanol:benzene mixture to produce nano-



**Fig. 9.1** Schematics of a stack of organic clay-complexes, swollen in an organic solvent (butanol:benzene=1:1, v/v, for example).  $d_L$ =basal spacing and  $d_{film}$ =the thickness of a stack of organic clay-complexes spread on an aqueous electrolyte. Depending on the extent of swelling and on the surface pressure,  $d_{film}$  can contain 3–5 silicate layers. The cationic alkylammonium surfactants, indicated by the squiggly lines, have replaced the exchangeable cations on the silicate layers.



platelets with mean hydrodynamic diameters of  $650 \pm 30$  nm. These measurements indicated the negligible association of **A** in the butanol:benzene dispersing medium, in contrast to **B**, which is likely to be present as agglomerates of several primary platelets. Spreading of **A** on water surfaces resulted in the formation of whitish patches, which coalesced upon compression into a rather contiguous film (curve A in Fig. 9.2). Surface pressure ( $\Pi$ ) vs. reduced surface area (AR) isotherms and Brewster angle microscopic measurements (Fig. 9.2), ex situ, and in situ transmission electron microscopy (TEM) measurements established the formation, of a 5.0–13.0 nm thick layer of overlapping clay nanoplatelets at the aqueous solution/air interface (Fig. 9.3) [7]. Multilayers of clay nanoplatelets could also be prepared by the Langmuir–Blodgett technique (Fig. 9.4 and 9.5) [7].

We have also layer-by-layer self-assembled positively charged polyallyldimethylammonium chloride, PDDA, and montmorillonite, M, ultrathin films, S-(PDDA/M) $_n$ , on a variety of different substrates (S) [4]. Surface plasmon resonance reflectivity and X-ray diffraction measurements indicated the thickness of a layer of PDDA to be  $1.60 \pm 0.4$  nm and that of a layer of M to be  $2.4 \pm 0.5$  nm. These values should be compared to those reported for the thickness of PDDA (2.2 nm [8] and 0.5 nm [9]) and M (1.4 nm [8] and 1.0 nm [9]) in self-assembled films. Apparently, M had not been exfoliated into single sheets (the observed thickness corresponds to an average of 1.7 platelets). The greater than unity number of M nanoplatelets in the self-assembled film is indicative of the incomplete neutralization of the surface charge on PDDA with one layer of irregularly shaped clay sheets.

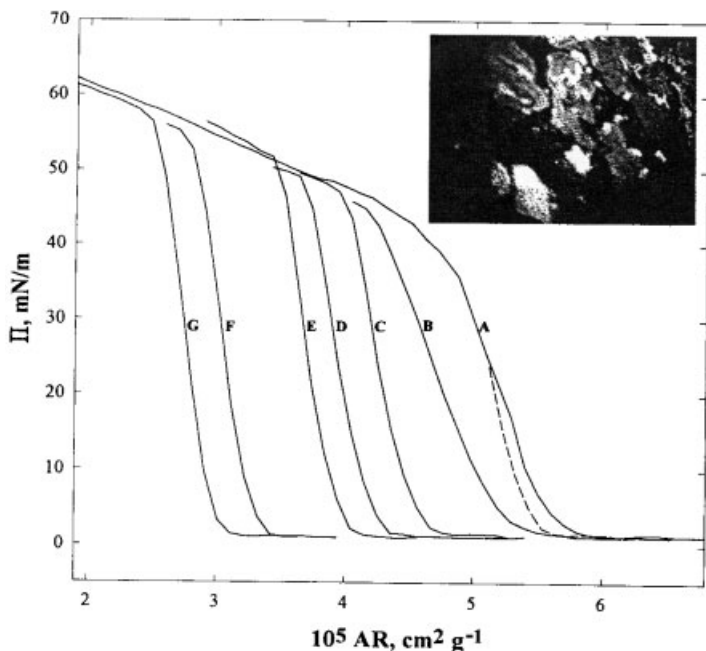


**Fig. 9.2** Surface pressure ( $\Pi$ ) vs. reduced surface area (AR) isotherms of **A** spread on a water subphase in a Langmuir film balance. Stopping the compression at surface pressures below the collapse of the film permitted the observation of repeated reversible expansion–compression cycles (A, expansion = bro-

ken line). Conversely, no reversibility was observed if the films were compressed fully to collapse pressure (and beyond). Repeated compression isotherms shifted progressively to smaller surface areas (B to G). A Brewster-angle microscopic image of **A** (curve A, at  $\Pi = 5 \text{ mN m}^{-1}$ ) is illustrated in the insert.

The observation of the basal spacing reflection in the X-ray diffraction pattern also supports the fact that the M layer is formed by short stacks of platelets, rather than completely exfoliated sheets, which are intercalated with the polymer. AFM images have also revealed overlapping clay nanoplatelets within the M layer. This stacking also manifests itself in the broadening of the X-ray diffraction of the PDDA/M repeating units (expected at  $2\theta \sim 2^\circ$  corresponding to 4.0 nm thick repeating PDDA/M units) to such an extent that it could barely be observed. Taking these results together, the structure of a sandwich unit of (PDDA/M) is best described by stacking irregular M platelets intercalated by PDDA (Fig. 9.6). In general, M nanoplatelets smoothed the surface of self-assembled films. We observed, by atomic force microscopy (AFM), the coverage of large etched pits, up to 700 nm in diameter and 30 nm in depth during the PDDA/M deposition [9]. The thickness of both M and PDDA could be altered by applying a potential during the self-assembly. The thickness of the M layer was found to increase from  $2.4 \pm 0.5$  to  $4.8 \pm 0.3$  nm by changing the bias from 0 to +0.7 V during the self-assembly of M (Fig. 9.6a, b). Brief rinsing did not re-establish the original thickness of the layer;

**Fig. 9.3** Schematic representation of the structures formed on spreading **A** on an aqueous electrolyte solution at very low (A), medium (B), and high (>40 mN m<sup>-1</sup>; C) surface pressures.

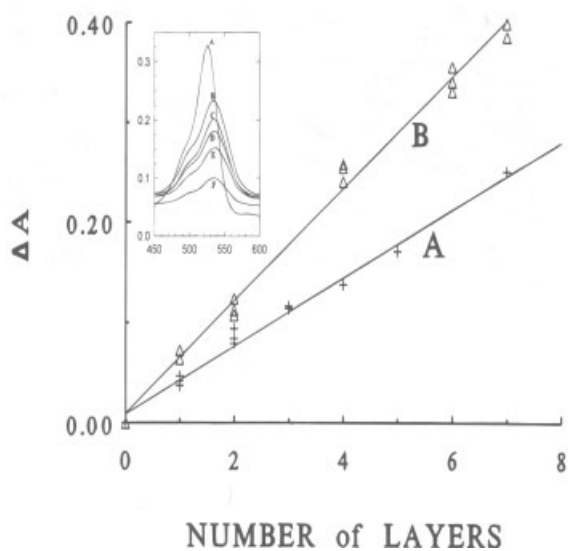
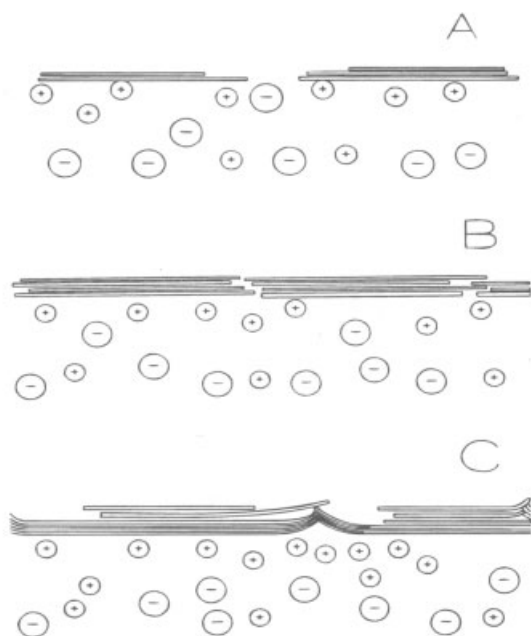


**Fig. 9.4** Dependence of the differential absorption peak height at 532 nm (Rhodamine 6G containing LB films, blank LB films) on the number of layers of **A** and **B** transferred to a quartz plate at  $\Pi=30$  mN m<sup>-1</sup>. The insert shows the absorption spectra (absorption vs. wavelength) of a diluted solution of Rhodamine 6G in water (A) and adsorbed onto 5 (B), 4 (C), 3 (D), 2 (E), and 1 (F) layers of **A** in air.

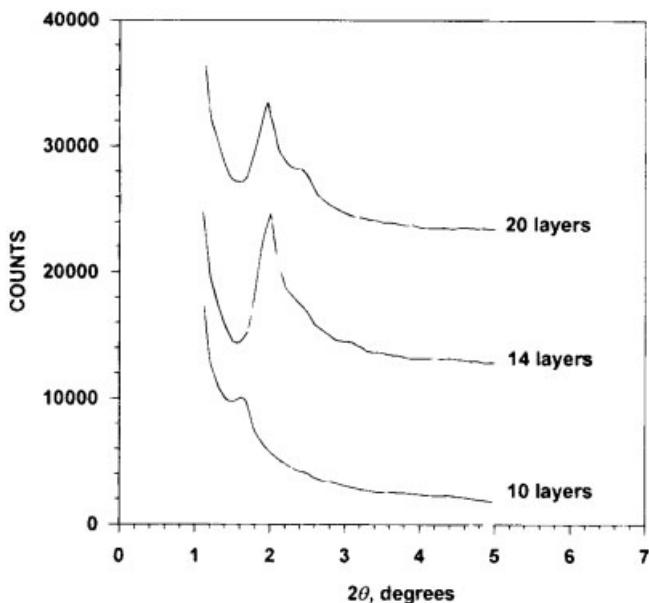


**Fig. 9.5** SAXS diffraction patterns of 10, 14, and 20 layers of organic clay-complexes on a quartz substrate. For clarity, curves for 14 and 20 layers have been shifted upwards along the y-axis.

indicating a kinetic, rather than a thermodynamic control of the process. Application of a negative voltage ( $-0.3$  V) during the self-assembly of M also resulted in a noticeable augmentation of the thickness (Fig. 9.6c). This effect was rationalized in terms of the attraction of positively charged edges of M to the electrode and corresponding tilting of the adsorbed nanoplatelets [9].

### 9.3

#### Self-assembled Polyelectrolytes and Graphite Oxide Nanoplatelets

The recognized beneficial properties of polymer-graphite composites [10–13] have prompted our interest in constructing ultrathin graphite-polymer films by self-assembly. Since graphite, G, cannot be dispersed in water and since it forms micrometer-sized irregular aggregates in organic solvents, our approach involved the preparation of exfoliated graphite oxide, GO, nanoplatelets in water, the layer-by-layer self-assembly of GO and PDDA films and the subsequent, in situ, reduction of GO to G [4]. GO nanoplatelets were prepared by the repeated oxidation of graphite flakes (by heating in concentrated  $\text{HNO}_3$  containing  $\text{NaClO}_3$  for 24 hours), washing, ball milling and dispersion. The oxidation results in the formation of dangling  $-\text{OH}$  and  $-\text{COOH}$  groups which, when ionized, provide the necessary negative charges for adsorption onto the cationic PDDA.

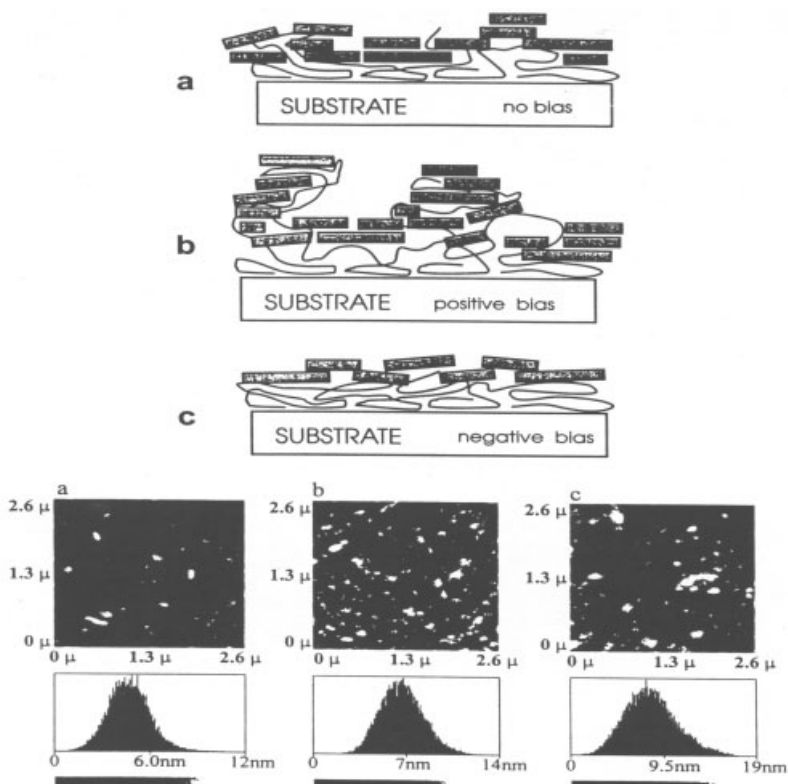


**Fig. 9.6** A simplified representation of the effect of external potential (top) and TEM images and size distributions (bottom) on the self-assembly and PDDA/M film. Application of a positive potential (b) repulses loose

parts of the polymer chain which results in increased disorganization and roughness of the subsequent layers of M; application of a negative potential results in improved morphology and denser packing of P(c).

Self-assembly of the  $(\text{PDDA}/\text{GO})_n$  films was monitored by absorption spectrophotometry (Fig. 9.7). The observed good linearity in the plot of absorbancies vs.  $n$  indicates the uniformity of the sandwich unit that self-assembled (Fig. 9.7b) [14]. Surface plasmon resonance reflectivity (SPR) measurements permitted the layer-by-layer monitoring of the self-assembly of the  $(\text{PDDA}/\text{GO})_n$  film (Fig. 9.8). Importantly, SPR measurements indicated very little change in the thicknesses of the successive PDDA and GO layers, their average being  $1.6 \pm 0.3$  nm and  $1.6 \pm 0.3$  nm, respectively [14]. AFM images revealed the height of each GO sheet to be between 1.8 nm and 2.8 nm in the self-assembled film (Fig. 9.9) indicating incomplete exfoliation of GO (basal spacing of GO sheets = 0.73 nm [14]); i.e., the presence of 2–3 sheets. This is quite similar to that observed for the self-assembled  $(\text{PDDA}/\text{M})_n$  films [4].

The X-ray diffraction (XRD) spectrum of a  $(\text{PDDA}/\text{GO})_{30}$  film is illustrated in Fig. 9.10 [14]. Characteristic maxima were observed at  $1.95^\circ$  (4.5 nm, very intense,

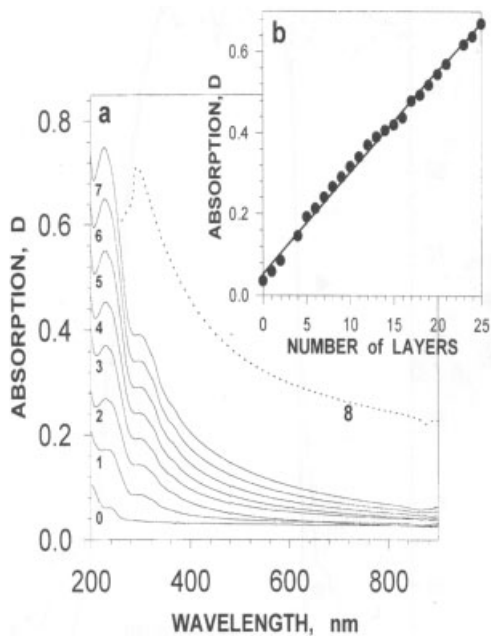


**Fig. 9.7** (a) Absorption spectra of the  $(\text{PDDA}/\text{GO})_n$  films, self-assembled onto a quartz slide. The number of sandwich layers ( $n$ ) are indicated next to given spectrum. Curve 8 denotes the absorption spectrum of a  $(\text{P}/\text{GO})_{10}$  film after reduction by exposure to 50% hydrazine for 24 h. (b) A plot of absorbance at 300 nm vs. the number of deposited PDDA/GO sandwich layers.

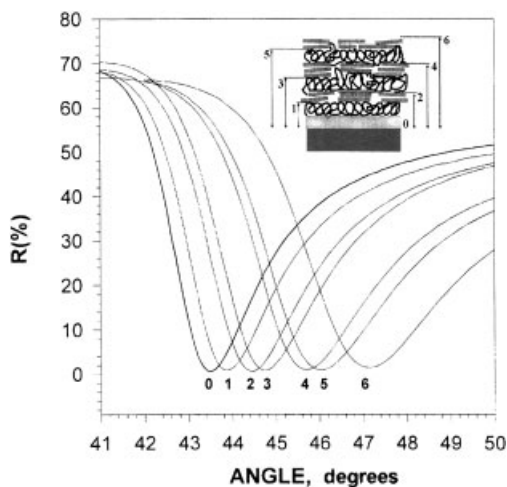


**Fig. 9.8** Surface plasmon reflectivity curves for the sequential deposition of self-assembled layers: 0=bare gold film; 1=PDDA on gold; 2=PDDA/GO on gold; 3=(PDDA/GO)PDDA on gold; 4=(PDDA/GO)<sub>2</sub> on gold; 5=(PDDA/GO)<sub>2</sub>/PDDA on gold; 6=(PDDA/GO)<sub>3</sub> on gold. Fitting parameters  $\ell_{\text{PDDA}}=2.25$ ,  $\ell_{\text{GO}}=2.24$ .

sharp and narrow),  $9.78^\circ$  (0.93 nm, small, not very pronounced), and at  $20.6^\circ$  (0.43 nm, very intense and broad). The peak at  $978^\circ$  corresponds to the basal spacing of GO in the multilayer film (0.93 nm, see Fig. 9.10b). This value is larger than that obtained for the basal spacing of GO (0.74 nm) due to the presence of the surrounding polymer chains and difficulties of forming tight lamellas. Strong X-ray diffraction in the region between  $20^\circ$  to  $30^\circ$  (Fig. 9.10c) is the ear-

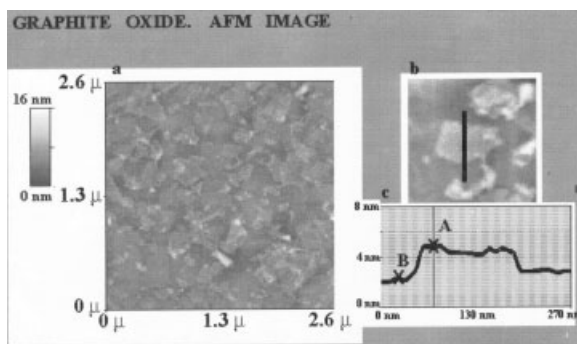
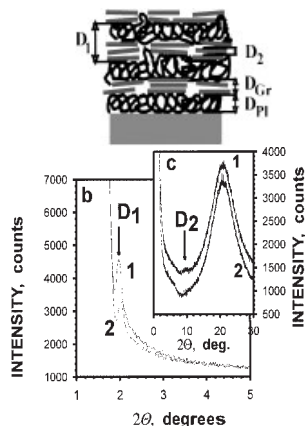


**Fig. 9.9** Atomic microscopic images of GO in a PDDA/GO film self-assembled onto a freshly cleaved mica (a). The image selected for analysis (b) indicated a height difference of 2.7 nm between A and B (in c).

mark of GO intercalation compounds. Broad reflection at  $20.6^\circ$  corresponds to intercalation of water between GO sheets. The peak at  $1.95^\circ$  (4.5 nm, Fig. 9.10b) does not appear in the X-ray patterns of the original GO powder or that of the flocculated mixture of polyelectrolyte and aqueous GO dispersion. It should be assigned to  $D_1$ , the repeating distance of the  $(\text{PDDA}/\text{GO})_n$  unit (Fig. 9.10a). This assignment is supported by combined AFM and SPR measurements. AFM images indicated the height of a GO layer to be  $2.5 \pm 0.5$  nm (Fig. 9.8c) and SPR measurements gave  $1.6 \pm 0.3$  nm for the thickness of a PDDA layer. The sum of these two values ( $2.5 \pm 0.5$  nm +  $1.6 \pm 0.3$  nm =  $4.4 \pm 0.8$  nm) is close to the X-ray repeating distance  $D_1 = 4.5$  nm. The slight deviation originates from the fact that the SPR technique yields the average thickness of a presumed uniform film.

Reduction of GO in the  $(\text{PDDA}/\text{GO})_n$  films to G could be accomplished either chemically or electrochemically. The chemical reduction involved the immersion

**Fig. 9.10** (a) Graphical representation of the structure of a self-assembled  $(\text{PDDA}/\text{GO})_n$  film:  $D_1$ , repeat distance of the multilayers;  $D_2$ , basal spacing of GO. (b) and (c) XRD of a  $(\text{PDDA}/\text{GO})_{30}$  film prior (1) and subsequent (2) to reduction by hydrazine.



of the self-assembled film into an aqueous hydrazine hydride (50%, w/v) solution for 1–24 h or into a 0.10 M HCl solution which contained Zn powder (i.e., into a *nascent* hydrogen generator) for 2–3 h. The electrochemical reduction of GO (in the  $(\text{PDDA}/\text{GO})_n$  film, self-assembled on metal or glassy carbon electrodes) was performed by scanning the potential from +0.7 V to –1.5 V vs. SCE and was monitored by cyclic voltammetry. The peak at  $-0.95 \pm 0.05$  V corresponds to electrochemical reduction of GO to G. The amplitude of the peak was found to increase initially with the number of GO layers; it levels off when  $n$  reaches 8–10 units. Both chemical and electrochemical reduction was accompanied by drastic darkening of the film which can be seen in Fig. 9.7 (curve 8). Such effect is to be expected provided that this process induces the restoration of an extended  $\pi$ -orbital conjugated system along carbon sheets.

X-ray diffraction measurements indicated that the reduction of GO to G was accompanied by a slight diminishing of the interlayer spacing (from 4.5 nm to 4.4 nm for the hydrazine reduction, and from 5.6 nm to 4.5 nm for the electrochemical reduction). As expected, the small peak at 0.93 nm, corresponding to the GO basal spacing, does not appear in the X-ray diffraction pattern of the reduced GO.

The lateral resistivity of  $(\text{PDDA}/\text{GO})_{10}$  film was measured between two 3 mm wide gold stripes evaporated on a glass slide at a distance of 2 mm between them. Self-assembled graphite oxide films were deposited on top of them over the whole surface of the slide. The as-deposited  $(\text{PDDA}/\text{GO})_{10}$  film had an  $R$  value of 32 M $\Omega$  at the 2 mm gap. After reduction by hydrogen, evolving *in situ*, the  $R$  value dropped to 12 K $\Omega$ , which amounts to a 27 000-fold decrease in the overall resistance. This corresponds to the change in volume conductivity from  $1.2 \times 10^4 \Omega^{-1} \text{m}^{-1}$  to  $3.1 \times 10^7 \Omega^{-1} \text{m}^{-1}$ . Roughening the substrate surface (by multiple diamond knife grooves along the electrode direction) *prior to* the deposition of multilayers rendered the resistivity decrease (which accompanied GO reduction) to be less pronounced (only a 370-fold increase in conductivity was observed). This was the consequence of imperfect self-assembly on a disturbed surface which resulted in broken films and less than uniform in-plane contacts of the GO platelets.

The effect of the nonconductive to conductive state transition was also observed in photo-electrochemical measurements in composite self-assembled  $(\text{PDDA}/\text{GO})$  films into which CdS semiconductor nanoparticles had been incorporated. It was found that the semiconductor crystallite acquired a pancake-like structure and adhered to the GO surface, being constrained between layers. The photocurrent,  $i_p$ , denoting the difference between the steady state current in the dark and during the illumination period, was found to be negligible in  $(\text{PDDA}/\text{GO})_{10}$  in the absence of incorporated semiconductor nanoparticles. At 0.7 V vs. a gold electrode bearing 10 layers of  $\text{PDDA}/\text{GO}$  composite films (in the nonconducting state, with CdS particles synthesized therein)  $i_p = 204$  nA was produced. Subsequent to *in situ* reduction of the GO layers to their conductive G state by scanning the potential of the working electrode between –0.1 V and –1.8 V for 20 min,  $i_p$  was found to increase to 1050 nA (i.e., a 5-fold increase). Since the photocurrent originated from the photoxidation of water, the porous matrix of polyelectrolyte chains maintained a satisfactory mass transport between the CdS semiconductor nanoparticles



and species in solution, while the highly conductive G platelets produced in the reduction step improved the electrical contact with the underlying electrode. The smaller effect of the GO to G reduction on the photocurrent than on the lateral resistivity (see above) is explicable in terms of the considerably higher lateral than perpendicular electrical conductivities in organic thin films.

Disruption of the organization of the multilayer system by roughening the surface, by overloading the film with micron-sized semiconductor particles, or by casting a mixture of GO, PDDA, and CdS, did not increase the photocurrent upon GO to G conversion; instead the  $i_p$  for films which contained G was some 15–30% smaller than for those which contained GO. This observation underscores the importance of supramolecular ordering in self-assembled films.

Self-assembled composite (PDDA/GO) films were found to be remarkably stable in concentrated acid or basic solutions and resisted photodegradation. These properties constitute substantial advantages of the (PDDA/GO) $_n$  films over the conductive organic thin films prepared by Langmuir–Blodgett (LB) techniques or self-assembly. The demonstrated lateral conductivities and the relative ease of transition between the nonconductive GO state and the conductive G state render these films inherently interesting and potentially useful as components of advanced optical and electronic devices.

Exfoliated GO sheets were found to be able to cap 10 nm diameter silver particles [15]. Sodium borohydride reduction of silver ions in aqueous dispersions of exfoliated graphite oxide (GO) resulted in the formation of remarkably monodis-

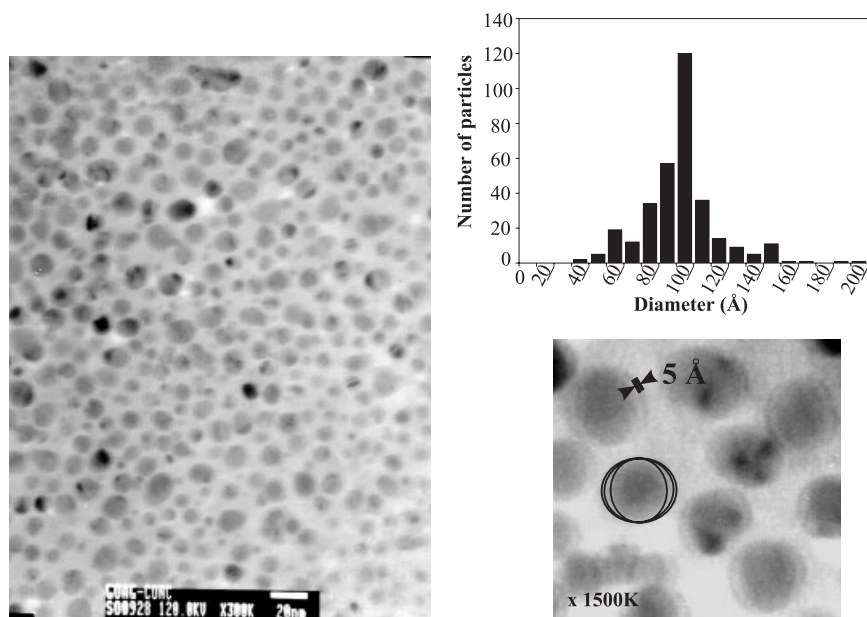
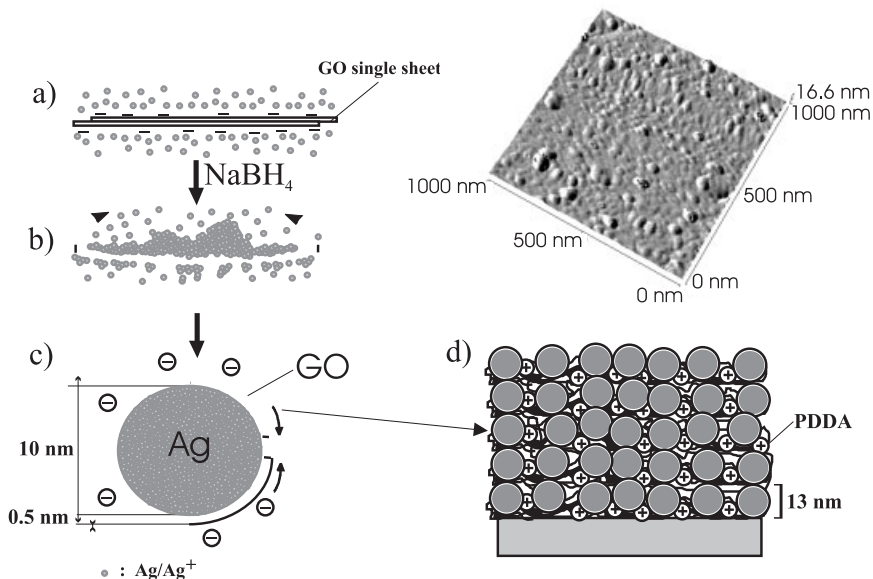


Fig. 9.11 Transmission electron microscopic images of Ag-GO nanoparticles.



**Fig. 9.12** Schematics of Ag-GO formation mechanism: adsorption of silver cations onto the GO nanosheets (a) followed by a reductive treatment to form Ag clusters preferentially on the surface of the GO sheets (b) and the wrapping of the GO around the Ag clus-

ters to form Ag-GO (c). The layer-by-layer self-assembly of PDDAP and Ag-GO nanoparticles onto a given substrate leads to highly organized arrays (d) with high density of surface coverage, as illustrated by the AFM image.

perse 100 Å diameter oblate Ag particles which are effectively protected by 5 Å thick GO sheets, Ag-GO (Figs. 9.11 and 9.12) [15]. Ag-GO could be self-assembled onto poly(diallyldimethylammonium) chloride, PDDA, coated substrate; subsequent layer-by-layer self-assembly of Ag-GO and PDDA led to well ordered ultrathin films of S-(PDDA/Ag-GO)<sub>n</sub> [15].

## 9.4

### Potential Applications

#### 9.4.1

##### Pollutant Photodestruction

Semiconductor nanoparticles have been advantageously employed for pollutant photodestruction [16, 17]. The principle of this approach is that (i) photoexcitation of the semiconductor nanoparticles (N) results in the formation of conduction band electrons and valence band holes:



(ii) the conduction band electrons readily react with oxygen to produce oxygen anion radicals and a variety of other oxidizing agents:



and, importantly, (iii) both the  $h_{vb}^+$  (Eq. (1)) and the  $O_2^{\bullet -} + \text{other oxidizing agents}$  (Eq. (2)) oxidatively destroy the hydrocarbon pollutants. The advantage of nanoparticles is that they provide large surface area to volume ratios and that they are size quantized. Therefore, the interaction with the pollutants is facilitated and the non-desirable recombination:



is minimized. Of all the nanoparticles, titanium dioxide has been used most extensively.

In our laboratories we have prepared semiconductor–clay platelet nanocomposites and showed them to be highly efficient catalysts for pollutant photodegrada-

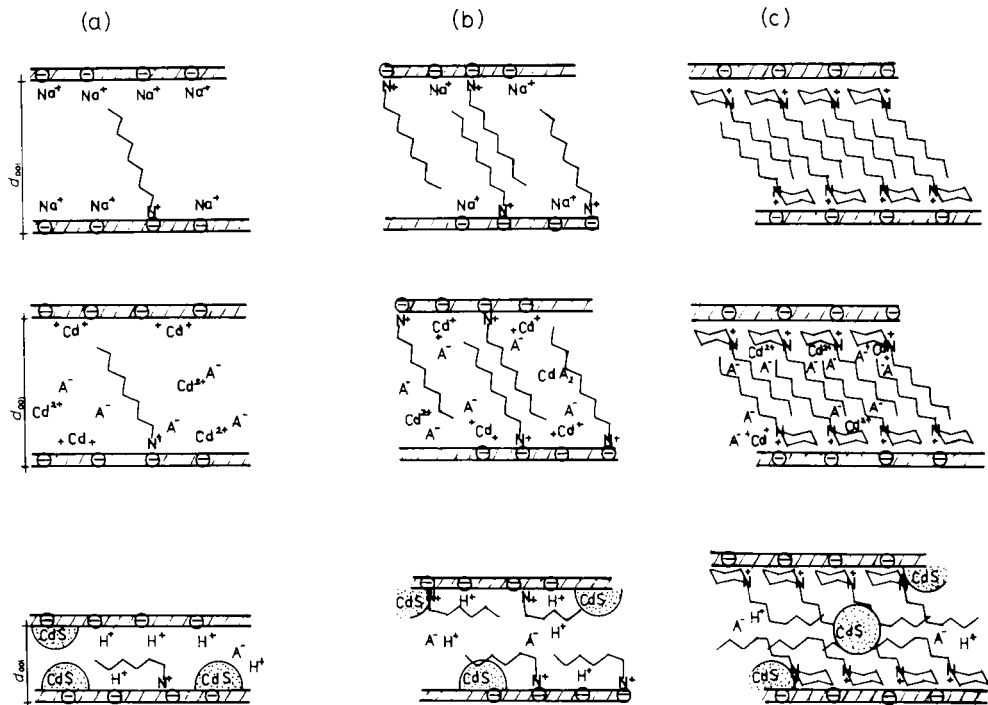


Fig. 9.13 An oversimplified representation of the proposed mode of cadmium ion (a) and/or undissociated cadmium salt (b) and CdS (c) incorporation into organic clay-complexes. Swollen organic clay-complexes prior (top)

and subsequent (middle) to the introduction of cadmium ions; partially swollen organic clay-complexes subsequent to the in situ formation (pillaring) of CdS (bottom).

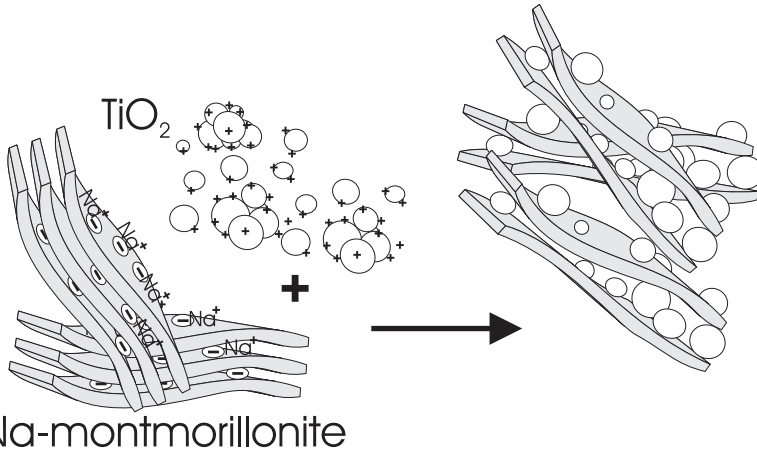


Fig. 9.14 Schematics of  $\text{TiO}_2$  and montmorillonite heterocoagulation.

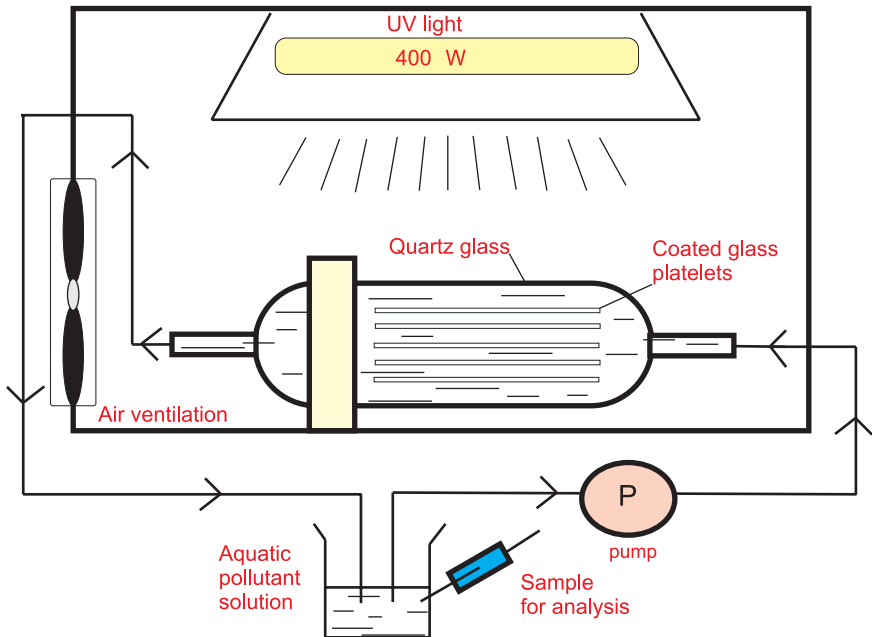


Fig. 9.15 Schematics of the photoreactor used for aquatic pollutant photodestruction

by semiconductor–nanoparticle–clay platelet films self-assembled onto glass slides.

tion [18–20]. Two different methods were employed for the preparation of the semiconductor–clay platelet nanocomposites. In the first method, the semiconductor precursors were adsorbed onto/into the clays and (Fig. 9.13) allowed to react therein. The second method involved the heterocoagulation of oppositely charged

semiconductor nanoparticles and clay platelets (Fig. 9.14). Additionally, negatively charged clay platelets and cationic semiconductor nanoparticles were layer-by-layer self-assembled (Fig. 9.15) [20]. By placing these self-assembled semiconductor nanoparticle–clay platelet thiol films into a solar reaction, efficient photodestruction of aqueous pollutants has been demonstrated [20].

#### 9.4.2

#### Electronic Applications

Judicious manipulation of the chemical structure permits the adsorption of fully conducting, completely isolating or semiconducting (or anything between these extremes) layers in the self-assembled film. Equally importantly, the order the layers are adsorbed allows the fabrication of ultrathin electronic (and electro-optical) devices. Suitably selected chemicals can also change the Schottky energy barrier in a heterojunction by functioning as an oriented dipole layer. Creating a metal/insulator/metal junction and/or connecting a wire to the self-assembled films remain, however, a formidable challenge. Evaporation of a metal (aluminum or gold, for example) layer onto or the use of silver paints on the self-assembled film may well cause damage and/or electrical shorting. Attempts to overcome this problem included, special evaporation techniques [21], the construction of 10 or more sandwich layers of the self-assembled film or the design of nanowires [22].

We have layer-by-layer assembled n-type  $\text{TiO}_2$  nanoparticles, poly(diallyldimethylammonium chloride), PDDA, a ruthenium complex, RuP, and polyanions (PSS or GO) on conductive indium tin oxide (ITO)-coated glass, antimony tin oxide (ATO)-coated glass, mercaptoethylamine-modified gold, and insulating quartz substrates [23]. The thicknesses of the PDDA/ $\text{TiO}_2$  layers, estimated from surface plasmon reflectivity measurements to be  $0.7 \pm 0.2$  nm and  $2.2 \pm 0.3$  nm, increased linearly with the number of layers deposited. Self-assembly of RuP with PSS or GO was also found to be linear, as evidenced by the regular increase of the MLCT absorbance of RuP at 480 nm (Fig. 9.16). The electrostatic nature of the GO interaction with RuP was confirmed by dipping a quartz-PDDA/(GO/RuP)<sub>30</sub> film in an acidic solution (pH 1), which induced rapid exfoliation and the complete desorption of the film from the substrate. Atomic force microscopic images of the multilayer film sequence quartz-PDDA/PSS/RuP/GO showed full coverage by 2.0 nm-thick GO sheets with a tilted morphology (Fig. 9.17), which ensured the efficient compartmentalization of the  $\text{TiO}_2$  and RuP layers.

A systematic investigation of the rectifying properties of the different layer sequences of these polyelectrolytes was conducted, beginning from the simplest and progressing to more complex devices [23]. The system ITO/(PDDA/ $\text{TiO}_2$ )<sub>10</sub>/Au exhibited a rectifying behavior (current flowed when the ITO electrode was biased negative, but not in the opposite direction) indicative of the formation of a Schottky diode at the  $\text{TiO}_2$ /Au interface [24]. In contrast, the system ITO/(PDDA/GO)<sub>30</sub>/Au gave linear  $i$ - $V$  behavior, consistent with ohmic ITO/GO and GO/Au interfaces. The  $\text{TiO}_2$ /GO interface was specifically studied by preparing the system ITO/(PDDA/ $\text{TiO}_2$ )<sub>10</sub>/(PDDA/GO)<sub>30</sub>/Au. Curve 1 in Fig. 9.18 shows current flow at

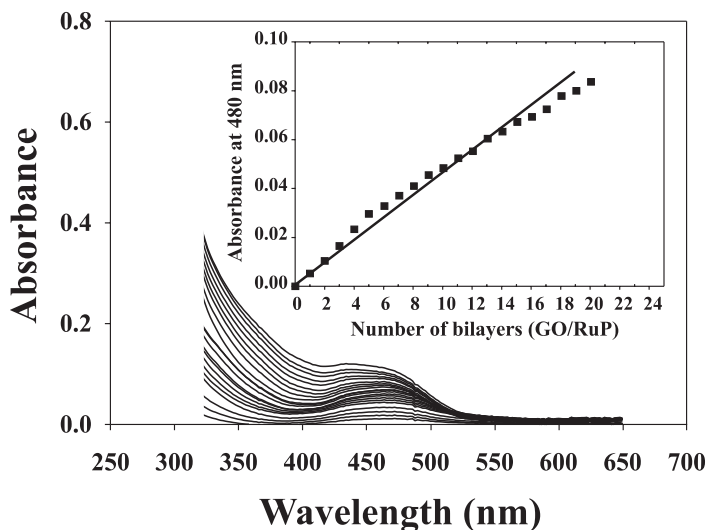
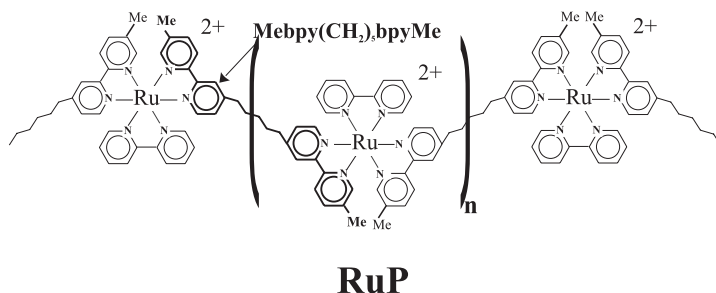


**Fig. 9.16** Absorption spectra of a (PDDA/ $\text{TiO}_2$ )<sub>10</sub>/(GO/RuP)<sub>n</sub> film self-assembled on a quartz substrate. The inset shows the regular increase of the metal to ligand charge transfer band, monitored at 480 nm, with the number of (GO/RuP) bilayers.

negative bias originating from this rectifying interface. In this case the forward bias current can be thought of as a redox process in which  $\text{TiO}_2$  reduces GO with minimum overpotential, and electrons travel through the film to Au, where reduced GO is re-oxidized. A barrier height energy of 0.42 eV, which corresponds to the difference in Fermi levels [24] at the  $\text{TiO}_2$ /GO interface, was calculated by fitting the  $i$ - $V$  characteristics to the Schottky diode equation. This gives a work function for GO in the multilayer film of 4.8 eV below the vacuum level (Fig. 9.19).

Substantial differences were observed between the electronic behavior of these films in the solid state and in electrolyte solutions (in a standard electrochemical cell where the working electrode constituted the self-assembled film). At negative bias, the electrode ATO/(PDDA/ $\text{TiO}_2$ )<sub>10</sub>, showed a reversible reduction at  $-1.13$  V vs. SCE, corresponding to a redox level and conduction band edge 3.6 eV below

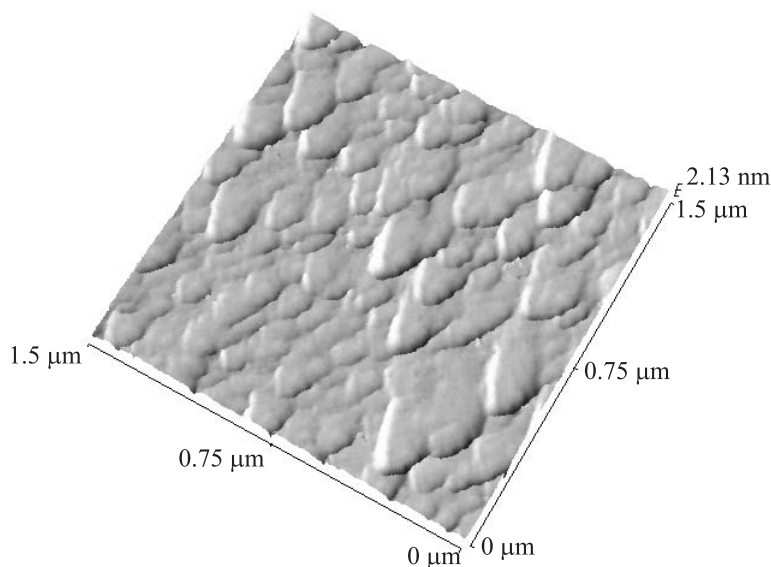


**Fig. 9.17** Typical 1.5 mm×1.5 mm AFM topographical images obtained after depositing a layer of GO sheets onto a PDDA/PSS/RuP

film self-assembled onto a quartz substrate. The average thickness of the GO layer was 2.0 nm.

the vacuum level. The cathodic current began to increase at the flat band potential (estimated to be  $-0.5$  V vs. SCE). When 10 bilayers of (PSS/RuP) were added to  $\text{ATO}/(\text{PDDA}/\text{TiO}_2)_{10}$  with a terminal layer of PSS or 30 bilayers (GO/RuP) with a top-layer of GO, additional redox waves were observed at  $-1.38$  V ( $\text{Ru}^{\text{I}}/\text{Ru}^{\text{II}}$ ) vs. SCE (reversible wave) and  $+1.00$  V ( $\text{Ru}^{\text{II}}/\text{Ru}^{\text{III}}$ ) vs. SCE, (quasi-reversible wave). The positions of these waves correspond to those of RuP ( $-1.52$  V and  $+1.12$  V, respectively) in solution. Consistent with this assignment, the quantity of charge passed in the cathodic wave for the  $\text{Ru}^{\text{II}}/\text{Ru}^{\text{III}}$  process ( $1.07 \times 10^{-8}$  mol  $\text{cm}^{-2}$  for a 10 bilayer PSS/RuP film) agreed closely with the amount of RuP determined by UV-visible spectroscopy ( $1.04 \times 10^{-8}$  mol  $\text{cm}^{-2}$ ). These results show that, in contact with a liquid electrolyte solution, charge transfer through the multilayer and oxidation/reduction of the RuP film are facile processes. This was true for both polyelectrolytes (GO and PSS) used as charge-compensating layers for RuP.

In contrast, dry films prepared with Au top contacts behaved differently. The system  $\text{ITO}/(\text{PDDA}/\text{TiO}_2)_{10}/(\text{PSS}/\text{RuP})_n/\text{PSS}/\text{Au}$  with  $n=10$  to 30, exhibited resistive behavior. Interestingly,  $\text{ITO}/(\text{PDDA}/\text{TiO}_2)_{10}/(\text{GO}/\text{RuP})_{30}/\text{GO}/\text{Au}$  were rectifying at both positive and negative voltages and the  $i$ - $V$  curve was dissymmetric (Fig. 9.18A, curve 2). The emergence of current in the positive branch (at bias  $>1.8$  V) is consistent with electron injection into  $\text{TiO}_2$  via the  $\text{Ru}^{\text{I}}/\text{II}$  couple, whereas the negative branch corresponds to electron transfer from  $\text{TiO}_2$  to GO and/or  $\text{Ru}^{\text{III}}$ . It should be noted that this result was obtained after pre-cycling the

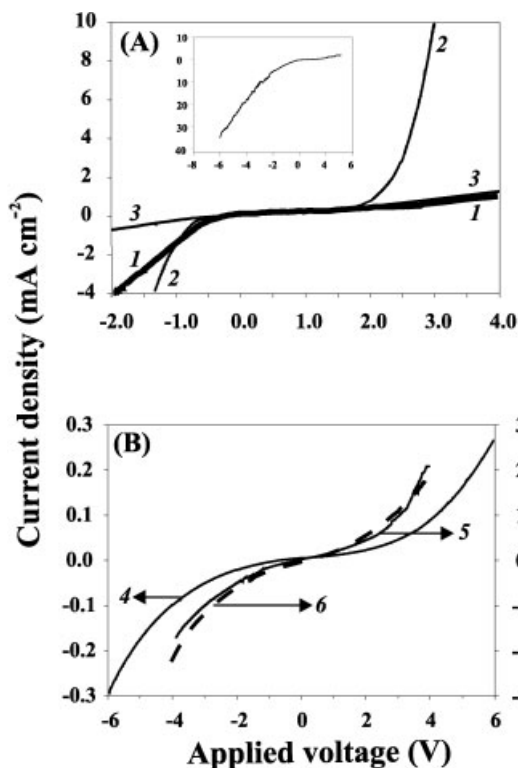


**Fig. 9.18**  $i$ - $V$  characteristics of (A) rectifying junctions: ITO/(PDDA/TiO<sub>2</sub>)<sub>10</sub>/(PDDA/GO)<sub>30</sub>/Au, curve 1 (inset shows the reverse bias region on a larger scale), ITO/(PDDA/TiO<sub>2</sub>)<sub>10</sub>/(GO/RuP)<sub>30</sub>/GO/Au, curve 2, ITO/PDDA/(GO/RuP)<sub>30</sub>/GO/Au, curve 3, and (B) junctions with fully reversible interfaces: ITO/(PDDA/PSS)<sub>10</sub>/(GO/RuP)<sub>30</sub>/GO/Au, curve 4, ITO/(PDDA/PSS)<sub>10</sub>/(PSS/RuP)<sub>30</sub>/PSS/Au, curve 5, and ITO/(PDDA/TiO<sub>2</sub>)<sub>10</sub>/PDDA/(PSS/RuP)<sub>30</sub>/PSS/Au, curve 6.

films 10 times between 0 and 2 V. A pronounced charging hysteresis was observed during this pre-cycling treatment, however, past this treatment the electrical response of the junctions was reproducible and reversible. We believe that the thinness of the bilayer RuP/GO and the fact that GO platelets are both electronically and ionically conductive might explain the fast reversal of the concentration gradients upon further cycling.

Several control experiments were conducted with the fixed-site strong acid polyelectrolyte PSS in place of TiO<sub>2</sub> or GO, or with PDDA in place of RuP. These experiments underscore the necessity for electronically conducting TiO<sub>2</sub> nanoparticles and mobile ions from GO layers in making high conductance devices. The film ITO/(PDDA)/(GO/RuP)<sub>30</sub>/GO/Au (Fig. 9.18A, curve 3) shows poor conductivity relative to ITO/(PDDA/TiO<sub>2</sub>)<sub>10</sub>/(GO/RuP)<sub>30</sub>/GO/Au, and no current rectification. The conductivity becomes progressively lower with ITO/(PDDA/PSS)<sub>10</sub>/(GO/RuP)<sub>30</sub>/GO/Au (Fig. 9.18B, curve 4) and ITO/(PDDA/PSS)<sub>10</sub>/(PSS/RuP)<sub>30</sub>/PSS/Au (Fig. 9.18B, curve 5), which contain insulating PDDA/PSS sequences. Although these two systems differed only in the nature of the spacer between the RuP layers, the dramatic change observed upon substituting GO for PSS shows that in the dry state PSS cannot rearrange to provide the ion gradient necessary for redox conduction in the RuP layers. Layer-by-layer assembly of polyelectrolyte films is



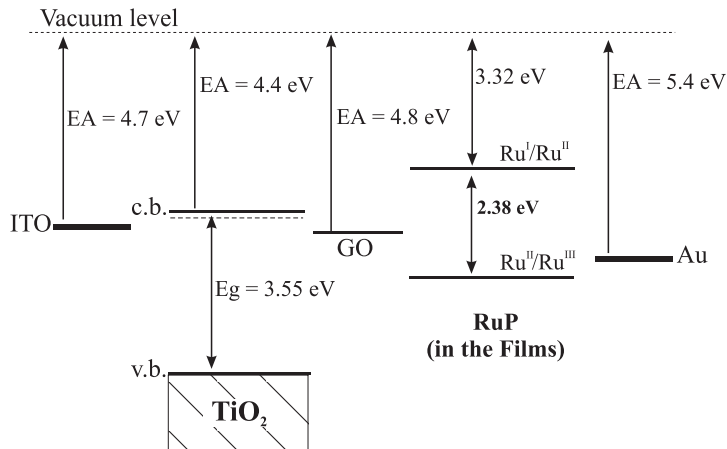


**Fig. 9.19** Energy level diagram of the different materials used in the construction of the rectifying devices (ITO, TiO<sub>2</sub> nanoparticles, GO, RuP and Au) at zero applied potential. All energy levels are calculated relative to the vacuum level. EA is the electron affinity (or

work function in the case of a metal),  $E_g$  is the band gap energy, c.b. is the conduction band, and v.b. is the valence band. The dashed line below the conduction band edge of TiO<sub>2</sub> corresponds to the Fermi level.

based on the displacement of their counterions, and the process often leads to multilayers containing few or no mobile ions. To compensate, a very high voltage must be applied (up to 10–15 V) when polyelectrolytes such as PSS are adsorbed alternately with a Ru(bpy)<sub>3</sub><sup>2+</sup>-containing polymers [24].

These results indicated that: 1. a direct contact between quantum-size TiO<sub>2</sub> particles and RuP is not required for promoting efficient electron transfer in a diode-like junction; 2. the interconnection of the RuP layers via thin GO sheets allows the electroactivity of the junction to be observed at positive bias; and 3. that the interface TiO<sub>2</sub>/GO is also rectifying at negative bias.

### 9.4.3

#### Charge Storage

Lithium batteries are the recognized choice for high energy density power supply [25, 26]. On discharge, the metallic anode of a lithium battery supplies Li<sup>+</sup>-ions to the Li<sup>+</sup>-ion electrolyte and electrons to the external circuit; the cathode is an electronically conducting host into which Li<sup>+</sup>-ions are inserted as guest species and the charge is compensated by electrons from the external circuit (Fig. 9.20). The chemical reactions at the anode and the cathode of a secondary (rechargeable) battery must be reversible. On charge, the removal of the electrons from the cathode by an external field releases Li<sup>+</sup>-ions back into the electrolyte to restore the parent host structure and the addition of the electrons to the anode by the external field attracts charge compensating Li<sup>+</sup>-ions back to the anode. A battery is said to be re-

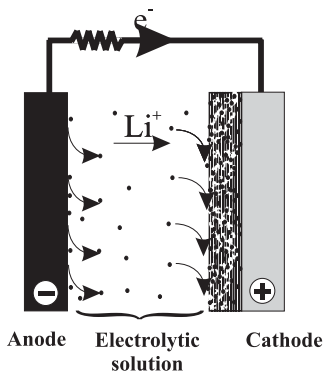


**Fig. 9.20** Principle of operation of a lithium battery in a liquid electrolytic medium. Upon discharge (as shown here) the metallic anode supplies  $\text{Li}^+$  to the surrounding electrolyte while electrons flow to the external circuit toward the cathode. The cathode is an electronically conducting host into which  $\text{Li}^+$  ions are inserted as guest species and charge is compensated by electrons from the external circuit. The chemical reactions at the anode and

cathode of a lithium secondary battery must be reversible. In that case, on charge, removal of the electrons from the cathode is achieved by applying an external opposite current to restore the difference of chemical potential between the anode and the cathode. During the charge, lithium ions are released back into the electrolyte with the concomitant formation of metallic lithium at the negative electrode.

chargeable when charging is complete (or quasi-complete) even after a large number of discharge and charge cycles (typically 1000 times for commercial use).

Lithium is a good material for the anode because of its intrinsic high negative potential and its low density and graphite and carbonaceous hosts have often constituted the cathode. Batteries based on  $\text{Li}^+$ -ion intercalation into graphite or carbonaceous hosts have the highest specific energies (energy per unit weight) and energy densities (energy per unit volume). While the specific capacity of graphite does not exceed  $372 \text{ mAh g}^{-1}$  ( $\text{LiC}_6$ ), high-capacity carbonaceous materials, prepared by thermal treatment of organic precursors (epoxy or phenolic resins, sugars, petroleum pitch, polymers) between  $550^\circ\text{C}$  and  $1000^\circ\text{C}$ , show reversible specific charges of  $400 \text{ mAh g}^{-1}$  ( $1.2 \times 5$  in  $\text{Li}_x\text{C}_6$ ) [26].

A correlation was shown to exist between the H/C atomic ratio and the capacity of the carbonaceous materials [27]. Alternatively, high charging capacities have been rationalized in terms of disordered carbons in the carbonaceous materials [28]. Two different sites for  $\text{Li}^+$ -ion intercalation have been suggested based on  $^7\text{Li}$  NMR investigations [28]. The first site was believed to be restricted by the graphite intercalation carbon stoichiometry (ionic site). The second site was proposed to be restricted only by the geometrical limit of the host and the formation of  $\text{Li}_2$  was believed to act as a capacity reservoir in this type of site [28]. These results suggested that the presence of hydrogen and oxygen atoms in the carbonaceous material as well as defects and disorders was likely to increase the charging capacity of lithium batteries.

Additional sites for  $\text{Li}^+$ -ion insertion could also be generated by the oxidation of graphite. Graphite oxidation is usually carried out by heating in a mixture of  $\text{NaClO}_3/\text{HNO}_3$  or  $\text{KMnO}_4/\text{H}_2\text{SO}_4$ . Cathodes have then been fabricated by simply blending the graphite oxide with a polymer, poly(vinylidene fluoride), PVDF, to prevent the direct exposure of the graphite to the liquid electrolyte [29]. Layer-by-layer self-assembly of graphite oxide (GO), polyethylene oxide (PEO), and poly(diallyldimethylammonium chloride), PDDA, onto an ITO substrate has recently been demonstrated to provide an efficient  $\text{Li}^+$ -ion intercalation cathode in an experimental lithium cell consisting also of a metallic lithium anode and  $\text{LiAsF}_6$  electrolyte, dissolved in a mixture of ethylene carbonate and methyl formate (Fig. 9.21) [30]. An open circuit voltage (typically of 2.3 V) between the electrodes triggers the flow of electrons from the anode (lithium metal) to the cathode (the ultrathin film self-assembled onto ITO) and the concomitant intercalation of lithium ions into the self-assembled films to compensate for the charges. The rate of charge transfer can also be controlled by the application of an appropriate current to the cathode, allowing further quantitative and qualitative studies of the intercalation reactions and charging properties. As electrons flow toward the cathode, the electromotive force decreases and the cell undergoes a discharge. To restore the initial electromotive force a current must be applied, leading to recharge of the cell.

Different self-assembled films fabricated as cathods (Film I = ITO-(PDDA/GO)<sub>10</sub>; Film II = ITO-PDDA/(GO/PEO)<sub>10</sub>; Film III = ITO-(PDDA/GO/PEO)<sub>10</sub>; Film IV = ITO-(PDDA/PEO)<sub>10</sub>; Film V = ITO-(PDDA/MO (montmorillonite)/PEO)<sub>10</sub>) were

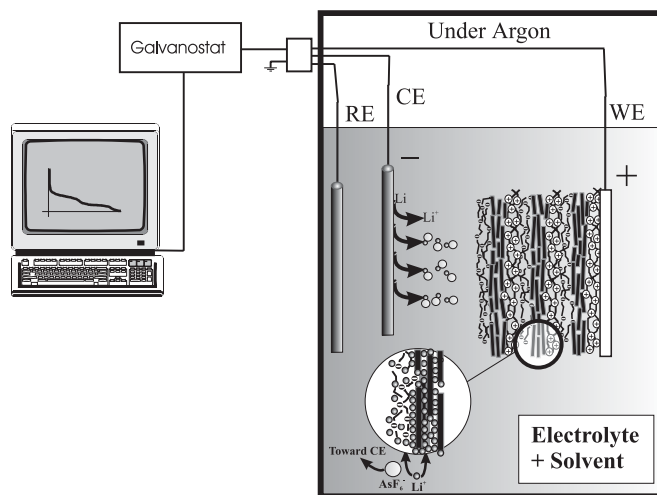


**Fig. 9.21** Schematics of the electrochemical cell used. A multilayer formed by the sequential adsorption of polyelectrolyte (PDDA), graphite oxide nanoplatelets (GO) and poly(ethylene oxide) (PEO) constitutes the

cathodic film in the cell. Metallic lithium is used as reference and counter electrodes. The cell is isolated and under an inert atmosphere.

characterized by surface plasmon reflectivity measurements, optical absorption and atomic force microscopy, in order to determine precisely the thickness and the amount of the different materials laid down after each adsorption cycle [30]. Tab. 9.1 summarizes the main charging characteristics of the multilayers and indicates the effective thickness of the GO layers in the different films.

Fig. 9.22 shows the chronopotentiometric curves obtained on discharging and charging the different films with a current density of  $50 \mu\text{A cm}^{-2}$ . It can be seen that although Film I contained the largest amount of GO, the capacity (number of charge equivalents taken by the system per unit time and surface area of electrode) was the lowest in the series. This result indicated that self-assembled PDDA/GO films were poor ionic conductors, preventing the penetration of  $\text{Li}^+$  ions into the film and their further intercalation into GO. This issue was addressed by introducing PEO into the self-assembled films. In Film II, a thin layer (0.5 nm) of PEO, self-assembled onto the GO layers, is seen to have greatly im-

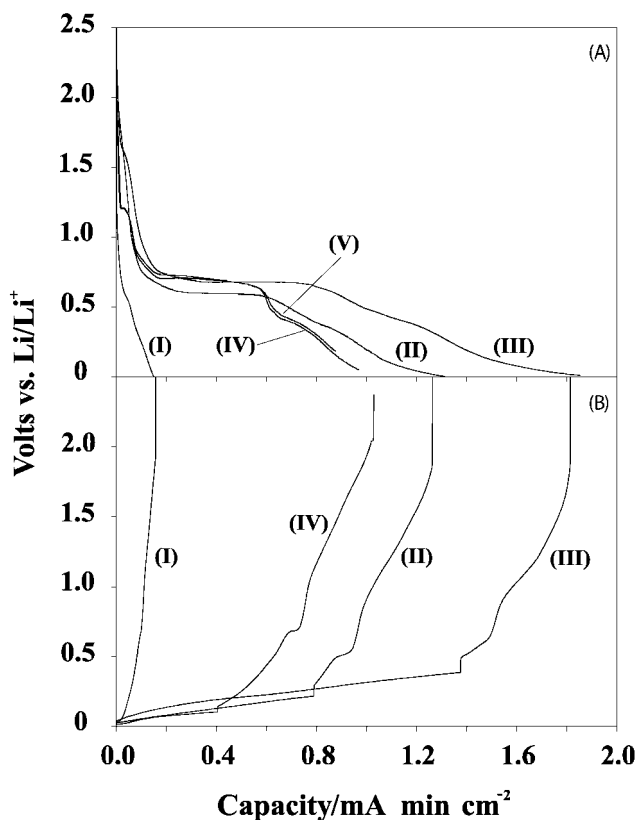


**Fig. 9.22** Chronopotentiometric curves, discharge (A) and charge (B), obtained for Film I (S-(PDDA/GO-33)<sub>10</sub>, Curve I); Film II (S-PDDA/(GO-33)/PEO)<sub>10</sub>, Curves II); Film III

(S-(PDDA/GO-33)/PEO)<sub>10</sub>, Curves III); Film IV (S-(PDDA/PEO)<sub>10</sub>, Curve IV) and Film V (S-(PDDA/PEO)<sub>10</sub>, Curve V).

Tab. 9.1 Properties of the different self-assembled electrodes

Self-assembled Film	Q/C cm <sup>-2</sup> (charging) <sup>a)</sup>	Q/C cm <sup>-2</sup> (discharging)	Thickness of the GO Layers/Å		LiC <sub>n</sub> (graphite) <sup>c)</sup>	Specific Capacity <sup>d)</sup> mAh g <sup>-1</sup>	
			From AFM	Data			From UV-visible
			Coverage of the GO layer (%)	T <sub>sep</sub> <sup>GO</sup> /Å			T <sub>film</sub> <sup>GO</sup> /Å
Film I: S-(PDDA/GO) <sub>10</sub>	0.009 0.009	0.009 0.009	80	80 <sup>e)</sup>	n = 11.98 n = 12.22	— 182	
Film II: S-PDDA/(GO/PEO) <sub>10</sub>	0.078 0.078	0.075 0.075	45	20 <sup>f),g)</sup>	n = 1.36 <sup>h)</sup> n = 1.80 <sup>h)</sup>	— 1232	
Film III: S-(PDDA/GO/PEO) <sub>10</sub>	0.109 0.109	0.105 0.105	80	70	n = 1.90 <sup>h)</sup> n = 1.89 <sup>h)</sup>	— 1174	
Film IV: S-(PDDA/PEO) <sub>10</sub>	0.060	0.061	—	—	—	—	
Film V: S-(PDDA/MO/PEO) <sub>10</sub>	0.060	0.060	—	—	—	—	

a) Calculated values based on thicknesses determined by AFM (top) and by absorption spectra (on bottom).

b) Calculated from absorption spectra, taking  $\epsilon_{2,30} \text{ nm} = 21412$ .

c) Calculated from the charging process.

d) Calculated for the graphitic layers only, by taking into account the amount of carbon deduced from absorption spectroscopy.

e) In good agreement with the AFM image histogram of a window of 1  $\mu\text{m}^2$ , indicating a maximum distribution at 8.5 nm.

f) This thickness corresponds to a GO layer sandwiched between PEO layers only.

g) In good agreement with the AFM image histogram of a window of 1  $\mu\text{m}^2$ , indicating a maximum distribution at 25 Å.

h) By assuming that PEO layers contribute for 0.060 C cm<sup>-2</sup>.

proved the specific capacity of battery. To precisely determine the contribution of the GO layers in Films II, it was necessary to subtract the lithium uptake due to PEO layers. Film IV did not contain GO, therefore, the capacity difference between Film II and Film IV provided the contribution due to GO and was characteristic of a lithium intercalation compound  $\text{LiC}_2$ . Introducing an inert layer of clay platelets (montmorillonite, M) between PDDA and PEO, in Film V, did not change the chronopotentiometric profile, overlapping with the profile obtained with Film IV. However substituting GO for M, allowed a twofold increase in capacity, as more GO platelets were present in these films than in Films II, but the intercalation compound was also found to be  $\text{LiC}_2$ . This last result indicates that the existence of well-defined interfaces PEO/GO in the films was crucial in discharging the platelets, with the ability to convey lithium ions into GO layers of at least 5.5–6.0 nm thick. Film III was electronically and ionically conductive enough to undergo a significant discharge, though the GO layer was thicker than in Film II. These intercalation compounds corresponded to a specific capacity of about  $1200 \text{ mA g}^{-1}$  (for the graphite oxide only) and were comparable to the values measured for polyacenic compounds (PAS) materials,  $1100 \text{ mA g}^{-1}$ . The self-assembly approach [30] allows one to minimize the surface of GO in direct contact with the solution, avoiding the formation of a so-called chemically bonded solid electrolyte interface (CB-SEI film) [31], consuming part of the electrons and lithium ions in a side reaction involving the carboxy and alkoxy moieties attached to the GO surface and leading to the formation of stabilizing salts containing irreversible reduction products of solvent at the first cycle.

### Acknowledgments

Support of this work by the National Science Foundation is gratefully acknowledged.

### 9.5

#### References

- 1 R. K. ILER, *J. Colloid Interface Sci.* **1966**, *21*, 569–594.
- 2 <http://www.chem.fsu.edu/multilayers/>
- 3 S. W. KELLER, H. N. KIM, T. E. MALLOW, *J. Am. Chem. Soc.* **1994**, *116*, 8817–8818.
- 4 N. A. KOTOV, T. HARASZTI, L. TURI, G. ZAVALA, R. E. GEER, I. DÉKÁNY, J. H. FENDLER, *J. Am. Chem. Soc.* **1997**, *119*, 6821–6832.
- 5 H. VAN OLPHEN, *An Introduction to Clay Colloid Chemistry*, Wiley, New York, 1977.
- 6 G. W. BRINDLEY, G. BROWN, *Mineral Soc. Monogram No. 5*, **1980**.
- 7 N. A. KOTOV, F. C. MELDRUM, J. H. FENDLER, E. TOMBACZ, I. DEKANY, *Langmuir*, **1994**, *10*, 3797–3804.
- 8 Y. LVOV, K. ARIGA, I. ICHINOSE, T. KUNITAKE, *Langmuir* **1996**, *12*, 3038–3044.
- 9 E. R. KLEINFELD, G. S. FERGUSON, *Sci. China* **1994**, *265*, 370–373.
- 10 M. SANO, M. SANDBERG, S. YOSHIMURA, *Langmuir* **1994**, *10*, 3815–3819.

- 11 M. SANO, M.O. SANDBERG, S. YOSHIMURA, *Langmuir* **1994**, *10*, 3815; M. SANO, D.Y. SASAKI, T. KUNITAKE, *J. Chem. Soc., Chem. Commun.* **1992**, 1326; M. SANO, D.Y. SASAKI, T. KUNITAKE, *Macromolecules* **1992**, *25*, 6961; M. SANO, D.Y. SASAKI, T. KUNITAKE, *Science* **1992**, *258*, 441
- 12 E.J.H. CHEN, R.B. CROMAN, *Compos. Sci. Technol.* **1993**, *48(1-4)*, 173; D.S. SAUNDERS, S.C. GALEA, G.K. DEIMENDJIAN, *Composites* **1993**, *24*, 309; J.O. IROH, J.P. BELL, D.A. SCOLA, J.P. WESSON, *Polymer* **1994**, *35*, 1306; R.C. DON, J.W. GILLESPIE, C.L. T. LAMBING, *Polym. Eng. Sci.* **1992**, *32*, 620; P.R. DUFOUR, A.W.J. GEE, J.A. KINGMA, J.W.M. MENS, *Wear* **1992**, *156*, 85; H.Y. CHOI, F.K. CHANG, *Polym. Eng. Sci.* **1991**, *31*, 1294.
- 13 M.C. LEE, N.A. PEPPAS, *J. Appl. Polym. Sci.* **1993**, *47*, 1349.
- 14 J.R. DAHN, A.K. SLEIGH, H. SHI, J.N. REIMERS, Q. ZHONG, B.M. WAY, *Electrochim. Acta* **1993**, *38*, 1179–1191.
- 15 T. CASSAGNEAU, J.H. FENDLER, *J. Phys. Chem. B* **1999**, *103*, 1789–1793.
- 16 M.R. HOFFMANN, S.T. MARTIN, W. CHOI, D.W. BAHNEMANN, *Chem. Rev.* **1995**, *95*, 69–96.
- 17 U. STAFFORD, K.A. GRAY, P.V. KAMAT, *Heterogeneous Chem. Rev.* **1996**, *3*, 77–104.
- 18 I. DEKANY, L. TURI, G. GALBACS, J.H. FENDLER, *J. Colloid Interface Sci.* **1999**, *213*, 584–591.
- 19 I. DEKANY, L. NAGY, L. TURI, Z. KIRALY, N.A. KOTOV, J.H. FENDLER, *Langmuir* **1996**, *12*, 3709–3715.
- 20 I. DEKANY, J.H. FENDLER, unpublished work, 2001
- 21 T. XU, I.R. PETERSON, M.V. LAKSHMIKANTHAM, R.M. METZGER, *Angew. Chem. Int. Ed. Engl.* **2001**, *40*, 1749–1752.
- 22 N. GROBERT, M. MAYNE, M. TERRONES, J. SLOAN, R.E. DUNIN-BORKOWSKI, R. KAMALAKARAN, T. SEEGER, H. TERRONES, M. RUHLE, D.R.M. WALTON, H.W. KROTO, J.L. HUTCHISON, *Chem. Commun.* **2001**, 471–472.
- 23 T. CASSAGNEAU, J.H. FENDLER, S.A. JOHNSON, T.E. MALLOUK, *Adv. Mater.* **2000**, *12*, 1363–1366.
- 24 T. CASSAGNEAU, J.H. FENDLER, T.E. MALLOUK, *Langmuir* **2000**, *16*, 241–246.
- 25 P.G. BRUCE, *Philos. Trans. R. Soc. London, Ser. A*, **1996**, *354*, 1577–1593.
- 26 J.R. OWEN, *Chem Soc Rev* **1997**, *26*, 259–267.
- 27 T. ZHENG, J.S. XUE, J.R. DAHN, *Chem. Mater.* **1996**, *8*, 389–393.
- 28 N. TAKAMI, A. SATOH, T. OHSAKI, M. KANDA, *J. Electrochem. Soc.*, **1998**, *145*, 478–482.
- 29 Y. EINELI, V.R. KOCH, *J. Am. Chem. Soc.* **1997**, *144*, 2968–2973.
- 30 T. CASSAGNEAU, J.H. FENDLER, *Adv. Mater.* **1998**, *10*, 877–881.
- 31 E. PELED, C. MENACHEM, D. BARTOW, A. MELMAN, *J. Electrochem. Soc.* **1996**, *143*, 4.

10

## **Chemistry Directed Deposition via Electrostatic and Secondary Interactions: A Nonlithographic Approach to Patterned Polyelectrolyte Multilayer Systems**

P. T. HAMMOND

### **Abstract**

The development of an array of electroactive polymer materials, combined with the advent of a number of versatile nonlithographic approaches to patterning, has created new opportunities for the application of conducting and conjugated polymers as electronic and optical devices made for common, everyday applications. Further advances in the development of cheap plastic electronics rely on a greater understanding of how to manipulate the deposition of these materials using self- or directed-assembly. Surface directed templating and assembly is particularly promising for the creation of single and multi-component devices on a range of substrates. Two important concepts and aspects of this work are discussed. The first is based on selective deposition of materials from solution to a pre-patterned substrate. By utilizing two or more surface groups as templates for various components of the film, each component can be directed to a specific region of the surface, resulting in multi-component devices created using simple adsorption processes based on electrostatic and secondary interactions. The second concept expands the directed assembly concept to a variety of surfaces through the direct stamping of functional polymers and block copolymers. This polymer-on-polymer stamping concept allows the micron scale patterning of plastic, glass, and many other common substrates without the need for traditional silane or thiol chemistry. The resulting chemically patterned surfaces can be used as templates for materials deposition. These two techniques have been applied to the selective deposition and patterning of colloidal particles atop polyelectrolyte multilayer arrays, illustrating the extension of the work to the adsorption of mesoscale objects, as well as charged polyion systems. Finally, specific multilayer functional systems that have been targeted in this work include organic/polymer light-emitting diodes (LEDs), electrochromic materials and patterned conducting polymer films.



## 10.1

### Introduction and Overview

Developments in the electrostatic layer-by-layer assembly process have progressed significantly since its inception, bringing with them a new approach to creating polymeric materials with unique, multifunctional properties through the sequential adsorption, and effective nanoscale blending, of polymeric, organic and inorganic materials into a stable ultrathin film. Due to the ease of processing of this technique, and its applicability to a variety of substrates ranging from noble metals such as gold, to semiconductors and oxides such as silicon oxide, and plastic and flexible polymer film surfaces, the multilayer assembly approach has been adopted for use in microelectronics materials, light-emitting devices, conducting films, catalytic membranes, dielectric layers, biomaterials surfaces and delivery vehicles. Applications of these polymer thin films in integrated optics, microelectronic devices, chemical and biological sensors, and ordered arrays for photonic and micro- to nanostructured material surfaces require control of film deposition and ordering as well as control of the supramolecular architecture. To be able to incorporate layer-by-layer multifunctional thin films into arrays and devices, it is necessary to pattern them onto surfaces on micron to millimeter length scales. For example, polymers used for electro-optical applications must, to be useful, be incorporated into an integrated optical device by some patterning method, and micro-sensor devices may require small patterned arrays of polymer.

Current techniques used for the patterning of organic thin films are ultimately based on photolithographic techniques [1]. Unfortunately, these techniques rely on the transformation of polymer in an ultrathin film upon exposure to UV light or the electron beam; this leads to the additional requirement that new polymeric materials for micron-scale multilayer devices be photopolymerizable, photodegradable or deconstructable under a specific set of conditions, thus limiting the potential composition of the film. These requirements are also nontrivial; good photoresist materials require efficient response to irradiation, high contrast, or degree of chemical change, upon exposure, and high resolution [2]. Other methods used to form patterned organic thin films include selective poling of films, spincoating of polymer into topographic channels on a silicon or polymer substrate, UV-photo-bleaching or exposure through a negative mask. These procedures often require additional processing steps, or are specific to the chemistry of the polymeric material used. None of the above-named approaches provides a general means of selectively depositing complex multilayered films onto a surface in situ. Furthermore, none of these techniques allows for the introduction of complex, multiple component systems on surfaces without numerous processing steps.

In response to the challenge of incorporating ultrathin functional polymeric films into integrated devices, we have developed new approaches to the patterning of polymeric microfeatures using the concept of surface directed assembly [3]. This method utilizes chemically patterned surfaces which act as templates for the deposition of polymers on surfaces. A nonlithographic process, microcontact printing, is used to generate the chemical pattern with a micron featured polydi-

methylsiloxane stamp [4–6]. The patterned features are then used as a template for the selective deposition of polymeric multilayers. The result is a cheap, simple procedure to produce patterned thin films and devices that can be performed on a laboratory benchtop rather than in a clean room.

In this review, new methods that have been developed to manipulate the deposition of polyelectrolyte multilayer systems to create patterned single and multiple component thin films on a vast range of surfaces will be addressed. During the course of the past several years, we have developed a new approach to patterning polyion thin films on a micron length scale using nonlithographic techniques that involve the manipulation of surface functionality and the use of the layer-by-layer adsorption technique. The key to this approach is the use of secondary, or non-specific interactions, in combination with steric repulsion and electrostatic interactions to chemically direct the deposition of polyelectrolytes on chemically patterned surfaces [7–9]. Recent work has been along two directions: 1) An understanding of secondary interactions between polymer and surface functional groups, and use of that understanding to direct specific materials systems to different regions of a surface (selective deposition or “surface sorting”) [9, 10], and [2]. Development of an accessible means of printing polymers on surfaces (*polymer-on-polymer stamping*), and application of this technique to create chemically patterned templates for materials deposition and surface modification. Finally, we have applied the concepts developed in both areas, and applied them to the deposition of micron scale charged colloidal particles, applying the same concepts to mesoscale systems as for the polyion adsorption. Each of these areas is discussed in detail in the sections below.

## 10.2

### Selective Deposition of Polyelectrolyte Multilayer Systems

#### 10.2.1

##### Selective Deposition of Strong Polyelectrolytes

###### 10.2.1.1 Basis of Selective Adsorption and Ionic Strength Effects

The general concept of selective deposition of polyions on a surface is based on the ability to form alternating regions on the substrate that allow or resist the deposition of charged polymers under a given set of adsorption conditions. In much of the work described in this review, we chose to use carboxylic acid (COOH) functionalized monolayer surfaces as regions for deposition, and oligoethylene glycol (EG) functionalized surfaces to discourage polyion deposition. A number of other charged or ionizable groups, such as sulfonate and amino surfaces, have been successfully used in place of the COOH surface as a deposition region. On the other hand, the EG system was chosen for its success in the prevention of protein adsorption on gold surfaces in aqueous solution due to steric and hydration forces [11–14], and under appropriate conditions, can serve to prevent the deposition of a number of charged systems from solution, including synthetic poly-

electrolytes. Microcontact printing, a unique nonlithographic printing method introduced by the Whitesides group [4, 6, 15] is used to form chemical patterns on gold using alkanethiols or on silicon oxide surfaces using triethoxysilanes. This method entails the creation of a polydimethylsiloxane (PDMS) stamp molded atop a topographically defined master mold created using traditional photolithography. The stamp that is formed, as well as the mold itself, can be stored and used numerous times, making this process a simple, facile, and inexpensive means of introducing patterns. The microcontact printing process presents the advantages of high resolution, bench-top processing, and low cost. Once the surface is patterned, it is alternately dipped into solutions containing polycation and polyanion respectively to build up a multilayered polyelectrolyte thin film. Polyions adsorb predominantly to the COOH surface, allowing the build-up of a very well-defined pattern. This process is shown in the schematic in Fig. 10.1.

In the first systematic patterning studies of directed patterning of layer-by-layer films, we examined the adsorption of the simple strong polyelectrolytes, sulfonated polystyrene (SPS) and poly(diallyldimethylammonium chloride) (PDAC), and found that the selective deposition of the multilayers resulted in well defined patterned polymeric microstructures with sharp edges [3, 7]. In further investigations using strong polyelectrolyte adsorption, the addition of an electrolyte to the polyanion solutions was used to determine the effect of ionic shielding on adsorption selectivity for the COOH surface during the adsorption process [8, 16]. The thickness of the film on each self-assembled monolayer (SAM) was determined using atomic force microscopy (AFM) to ascertain the selectivity of adsorption for these two surface regions; on introduction of additional electrolyte, NaCl, several interesting changes were observed in the nature of the adsorption and selectivity to the COOH and EG surfaces. Fig. 10.2 (a–c) contains AFM images of SPS/PDAC multilayers consisting of 13 bilayers that were adsorbed at varying ionic strengths. At NaCl concentrations of 0 to 0.01 M, small, but measurable amounts of adsorption of the polyions on the EG resist regions can be observed; however, at intermediate concentrations of NaCl, ranging up to 0.1 M, the resist regions become cleaner, with noticeably less polyanion adsorption than that observed without

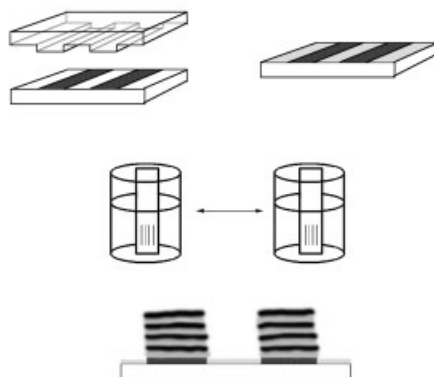


**Fig. 10.1** Schematic of patterning process for layer-by-layer polyanion films.

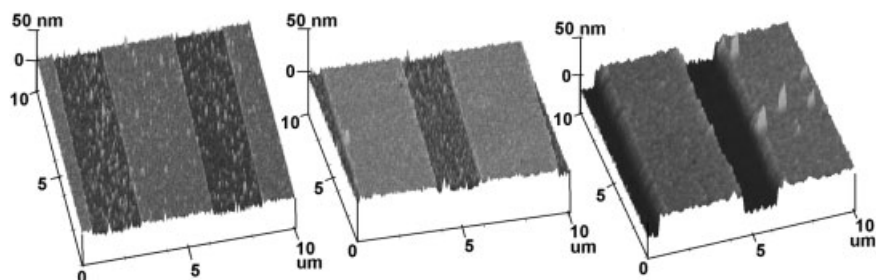


**Fig. 10.2** Films formed from varying amounts of added electrolyte (NaCl): (a) 0.001 M NaCl, (b) 0.01 M NaCl and (c) 0.1 M NaCl solutions of SPS and PDAC.

added salt, as seen in Fig. 10.2c, at 0.1 M NaCl concentration. At these conditions, optimal selectivity is achieved for the SPS/PDAC system, with thicker films formed on the COOH surface, and very little, if any, deposition on the EG surface. The effects of shielding result in the adsorption of thicker SPS/PDAC multilayer films due to shielding of the polyion chains, which leads to a lowering of self-repulsive interactions between segments, and loopier, thicker adsorbed layers. This screening enhanced adsorption has been observed by a number of researchers in studies of continuous films of single polyelectrolytes and polyelectrolyte multilayers [17–21]. The interesting observation that the EG surface becomes a more effective resist at moderate salt concentrations is believed to be due to the fact that sodium ions intercalate into the matrix of the oligoethylene glycol monolayer, which can act as a ligand for small metal cations. This intercalation of ions increases the degree of hydration of the EG surface, bolstering the hydration shell; similar effects have been observed and reported by the Grunze group for protein adsorption on oligoethylene glycol surfaces [11, 12].

Large increases in the ionic strength serve to screen attractive ionic interactions between the solvated polyion and the surface until, ultimately, polyelectrolyte deposition is no longer observed on the COOH regions of the surface due to shielding of the COOH surface regions. In contrast, the EG surface changes from an area that resists polyion adsorption at low ionic strengths (Fig. 10.3a) to a region that promotes adsorption at high ionic strength in Fig. 10.3b). Above approximately 1 M NaCl concentrations, the salt ions, when coupled with the nitrogen drying step, dehydrate the EG monolayer and allow the macroscopic deposition of the polyelectrolytes [8]. These two simultaneous behaviors work in conjunction to reverse the templating of the ionic multilayers, resulting in negative selectivity on the surface, as illustrated in the electron micrographs in Fig. 10.33. If the ions used as electrolytes are changed, the ionic strength at which this transition is observed is shifted based on the relative affinity of the ions to each surface region [16].

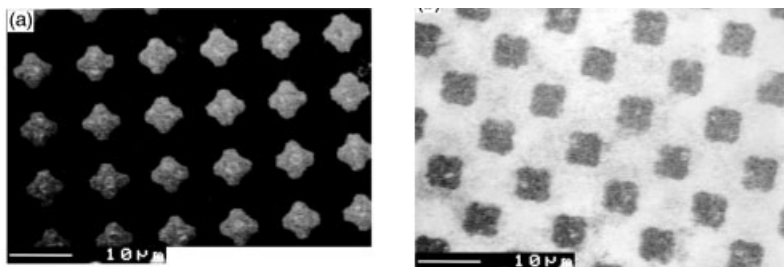


**Fig. 10.3** SEM micrographs of SPS/PDAC polyion pairs deposited onto a patterned SAM for which the ionic content was (a) 0.1 M NaCl and (b) 1.0 M NaCl.

### 10.2.1.2 Formation of Complex Multilayer Structures

The ability to direct the deposition of polyions to specific regions of a surface is central to the concept of patterning polymer thin films. The reversal of the deposition behavior, such as that observed with SPS/PDAC multilayers at high ionic content, presents a useful new tool for fabricating complex microstructures from one or more sets of polyion pairs [22]. For example, an initial set of SPS/PDAC polyelectrolyte multilayers can be patterned onto a surface templated with COOH/EG surface groups at optimal adsorption conditions, resulting in selective deposition of a series of lines on the COOH surface. A second set of polyion pairs can then be adsorbed onto the original patterned multilayer at a new set of adsorption conditions with high ionic strength. In this second case, deposition occurs on the EG surface, and on the top surfaces of the original SPS/PDAC film structures. The result is the formation of a blanket layer of polymer film over the original structures, as demonstrated in Fig. 10.4 (a–d). As the number of bilayers is increased from 2, 3 and 5 negative polyion pairs respectively, the ridges between the polymer begin to fill; ultimately, at 6 bilayers and greater, a continuous film surface is

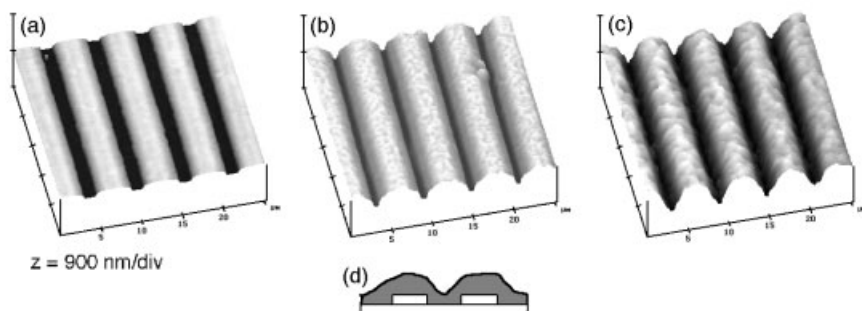


**Fig. 10.4** Result of negative deposition at high salt concentrations onto a 10 polyion pair patterned film [22]. Film growth occurs over both the resist and the polyelectrolyte layer regions, resulting in a blanketing of the

entire structure. (a) 2 negative polyion pairs; (b) 3 negative polyion pairs; (c) 5 negative polyion pairs; (d) schematic illustration of cross-section.

observed. This approach leads to the formation of a cladding layer, which can be applied to the formation of complex microstructures for a number of different applications from waveguide elements, to insulating layers, or as a means of advancing a third level in the formation of a 3D film structure.

### 10.2.2

#### **Understanding and Utilizing Secondary Interactions in Selective Deposition**

At low to moderate ionic strength, strong, highly charged polyelectrolytes such as sulfonated polystyrene or poly(diallyldimethyl ammonium chloride) deposit almost solely on the COOH regions, with very little deposition on the EG resist, creating well-defined, highly selective patterned polymer thin films [22]. For strong polyelectrolytes, it is essentially the electrostatic interactions that play the predominant role in determining the selectivity of deposition on the patterned surface [22], and, as discussed in the previous section, selectivity can be reversed at high ionic strengths. On the other hand, weak polyelectrolytes such as polyamines and polyacids are more likely to undergo additional secondary interactions such as hydrogen bonding and hydrophobic interactions, particularly as a function of the degree of ionization, or pH. By understanding the interfacial interactions between the polyelectrolyte and the chemical functional group at the surface, it is possible to manipulate the deposition of polyion pairs based on electrostatic, hydrogen bonding and hydrophobic interactions. These variations in the interactions between the polyion and the surface groups can lead to new and interesting means of manipulating selective deposition of multilayer films. Specifically, studies of weak polyion multilayer systems have led to a greater understanding of the importance of secondary interactions for these materials.

##### **10.2.2.1 Establishing the Rules for Weak Polyelectrolyte Deposition**

A systematic study of selective deposition of multilayers containing structurally different weak polyions, including polyamines and polyacids, was carried out to determine the role of molecular architecture and chemical structure on selectivity. It was found that for certain sets of synthetic polyelectrolytes, the oligoethylene oxide functional group appears to promote rather than discourage deposition over a certain pH range. Weak polyelectrolytes that are hydrophobic by nature, including polymethacrylic acid (PMAA), which has a pendant methyl group, and poly(allylamine hydrochloride) (PAH) which has a hydrophobic backbone, will preferentially adsorb to an oligoethylene oxide functionalized self-assembled monolayer (EG SAM) versus an acid functionalized monolayer (COOH SAM). More specifically, Fig. 10.5 contains the structures of three synthetic polyamines with similar atomic compositions, but different molecular architectures; the two surface functional groups, the COOH and EG SAMs, are also shown. These polyamines are an ideal choice for an examination of hydrophobic versus hydrophilic secondary interactions, electrostatic forces, and steric interactions, because their architectures are so different, with an all hydrocarbon backbone in one case

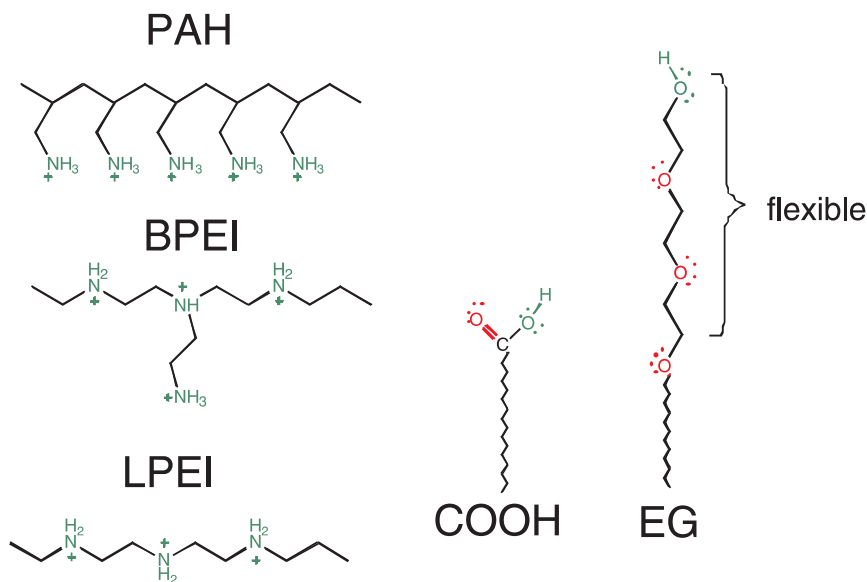


**Fig. 10.5** Chemical structures of polyamines and surface functional groups used in selective adsorption studies.

(PAH), and a heteroatomic, hydrophilic backbone at the other extreme (linear polyethyleneimine or LPEI). These polyamines were co-adsorbed with polyacrylic acid to form polyelectrolyte multilayers on continuous and patterned films of the two surface groups [9]. Selectivity was measured on patterned films using atomic force microscopy; the amount of film adsorbed on both surfaces was determined and used to calculate the selectivity. We found that LPEI, a weak polyelectrolyte with hydrophilic backbone, will direct the multilayers to adsorb preferentially on the charged COOH surface at medium pH condition; while PAH, a weak polyelectrolyte with hydrophobic backbone, has maximal selectivity towards the neutral EG surface at medium pH condition. Intermediate, pH dependent behavior was observed for branched polyethyleneimine (BPEI), which has both hydrophobic and hydrophilic groups in its branched backbone structure. It was hypothesized that strong secondary interactions between PAH and the EG surface lead to the negative selectivity of the PAH/PAA films. In particular, the hydrophobic nature of the PAH backbone can induce dispersion, or hydrophobic interactions with the ethylene groups in PEO. These interactions would not be possible with LPEI, which is highly hydrated in aqueous solution, thus introducing strong steric and hydration repulsions with the similarly hydrated EG oligomer. This hypothesis was supported by similar experiments in which the COOH and EG surfaces were replaced by sulfonated ionic surfaces and a methyl surface; under the same pH conditions, PAH adsorbs to the methyl surface preferentially.

### 10.2.2.2 Confirming the Rules of Selective Adsorption: SFM Investigations

To better elucidate the nature of the interactions that seemed to dominate adsorption at certain pH ranges, surface force microscopy (SFM) was used to examine the relationships between polyions and both charged acid surface groups (COOH) and neutral oligoethylene oxide (EG) functionalized surfaces. Polymer surface modified colloidal particles were used as force probes to examine the interactions of polyamines with hydrophilic backbones, such as LPEI, and those with hydrophobic backbones, such as PAH, on alkanethiol monolayers. The adsorption and force curves of these two model polyamines with COOH and EG surfaces at a range of pH values were determined with a sensitive molecular force probe [23]. Figure 10.6 contains force curves derived for PAH and LPEI on each surface at pH 4.8, when large differences in adsorption behavior are observed.

Polyamine modified polystyrene latex colloids were prepared successfully by surface grafting via electron beam irradiation and used as force probes. The surface force probe results indicate that the architecture of the polyion chain, as well as its charge density, can greatly influence the selectivity of deposition on charged versus neutral EG surfaces. The adhesion of the more hydrated LPEI on the COOH surface was dominated by ionic attractions at intermediate and high pH; whereas hydration forces led to steric repulsion of LPEI from the EG surface due to the hydrated nature of the LPEI backbone. In contrast, the adhesion of PAH to the COOH surface was reduced with respect to that of LPEI, but strong and very favorable adhesive interactions take place between the hydrophobic PAH polyamine and the EG surface at pH 4.8. This observation confirmed the adsorption studies described in the earlier section, in which LPEI based multilayers deposit preferentially on the COOH surface to yield positive selectivity, but PAH based multilayer films deposit preferentially on the EG surface, resulting in negative selectivities, at pH 4.8. Chemical force microscopy has proven to be a valuable tool in discerning the interactions which can drive self-assembly and selective deposition.

### 10.2.2.3 Using the Rules: Side-by-side Structures

We have taken advantage of the differences in adsorption behavior of these and other polymers, using directed adsorption as a tool to effectively control the region of film deposition and create two component, laterally patterned polyelectrolyte multilayer films on the surface [24]. A demonstration of side-by-side multilayer adsorption using LPEI and PAH was accomplished by first adsorbing multilayers of LPEI with polyacrylic acid (PAA) onto the COOH surface, followed by the adsorption of PAH/polyanion based multilayers onto the EG regions of the surface. The red sulfonated ruthenium dye,  $\text{Ru}(\text{phen})_3^{4+}$ , was chosen as the multiply charged anionic species to be directed to the EG regions by PAH. The resulting composite structure, shown in the AFM micrograph in Fig. 10.7a, consists of the PAH/ $\text{Ru}(\text{phen})_3^{4+}$  surrounded by a continuous region of LPEI/PAA multilayers. This technique can be extended to demonstrate the adsorption of two independent dye systems on one substrate, as shown by the images in Fig. 10.7b. The permanently charged polycation, poly(diallyldimethylammonium chloride) (PDAC)



was used to assemble patterned films with a sulfonated poly-*p*-phenylene (PPP<sup>(-)</sup>) blue dye on the COOH regions. PAH was then co-adsorbed with the ruthenium dye at pH 4.8, resulting in the adsorption of the red dye on the EG circular re-

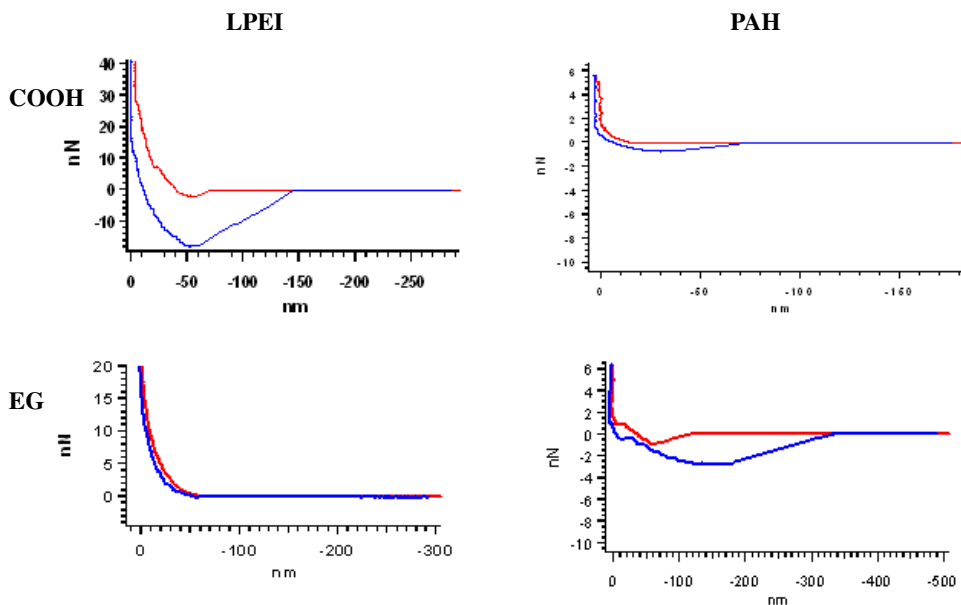


**Fig. 10.6** Surface force curves obtained from chemical force microscopy utilizing a molecular force probe with a polyamine modified colloid functionalized tip and COOH and EG

SAMs on gold. Force measurements shown were made at a pH of 4.8. Advancing curve is shown in red; retracting curve is in blue. Area under the curve indicates adhesion force.

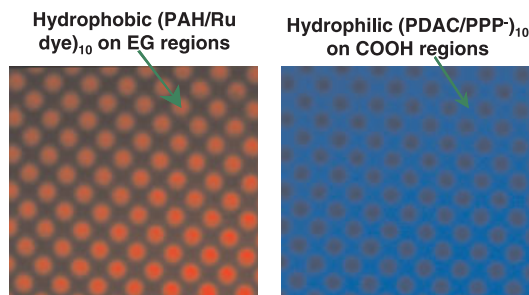


**Fig. 10.7** (a) An AFM topographic image of patterned (LPEI/PAA) multilayers adsorbed on a patterned COOH SAM surface (outer regions) and (LPEI/PAA)<sub>10</sub>(LPEI/Ru(phen<sup>4+</sup>)) adsorbed on the EG surface respectively (circular dots). Schematic shows cross-sectional view. (b) Laterally patterned bicolor OLED model structure, containing 10(PDAC/PPP<sup>(-)</sup>)

on COOH surface and 5(PAH/PAA)<sub>10</sub>(PAH/Ru(phen<sup>4+</sup>)) on the EG surface. The image on the left is a fluorescence micrograph taken with the filter for red dye on the EG surface and the image on the right is the same sample taken with the fluorescence filter for the blue dye on the COOH surface.

gions. The result was an alternating surface pattern of red and blue luminescent dye multilayers on a single surface.

#### 10.2.2.4 The Next Steps: Surface Sorting of Multilayers and Other Elements

In the previous studies described above, it was found that secondary interactions such as hydrophobicity can be used to selectively direct deposition of specific charged polymers, despite the presence of strong competing ionic attractions. These findings suggest that such interactions might be used, in conjunction with electrostatic interactions and steric forces, to guide the assembly of multi-element arrays of polymers on surfaces. This idea has been demonstrated with the use of the polyamines LPEI and PAH to direct the deposition of two different dyes to alternating regions of a surface. The ability to use different chemical functional groups as a guide to directing assembly leads to the simple concept that we have termed “surface sorting”, a process by which elements with different chemical functionality are drawn to specific complementary surface sites. This idea has been used successfully in biological fields, in which specific binding sites are created with DNA segments or proteins such streptavidin and biotin, for the creation of sensors or arrays. The schematic in Fig. 10.8 illustrates a general approach which may be used to form a three component array; the “objects” indicated in the schematic can represent polyions, molecular dyes or chromophores, nanometer scale quantum dots, or micron sized particles. An adaptation of this approach can be used to create complex electro-optical devices, three color pixel displays, biological arrays for sensors, and even biomaterials surfaces for co-cell cultures.

In the example of this concept given above, with red and blue luminescent dye systems, surface groups are used which can promote adhesion of one polymer, but resist or repel deposition of other polyion types, leading to the formation of laterally patterned, or side-by-side, multilayer thin films. More complex multiple layer assemblies can be formed by using surfaces which are selective to one polyion multilayer system, but not another, allowing the creation of blanket layers such as those described in Section 10.2.1 with strong polyelectrolytes, as well as multiple component lateral films. *This approach can lead to novel approaches to device fabrication which would be difficult to emulate with traditional photolithography.* In particular, a single patterned surface can be prepared at low cost to guide deposition of materials in situ without further processing steps. Photolithography

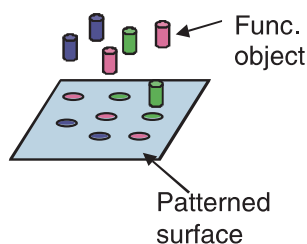


**Fig. 10.8** Schematic representation of the concept of surface sorting with multiple surface components during the adsorption process. Cylinders represent charged functional “objects” present in solution ranging from macromolecules to micron sized particles with a specific binding group. Colored dots on the surface indicate surface regions with complementary functionality which act as regions for deposition.

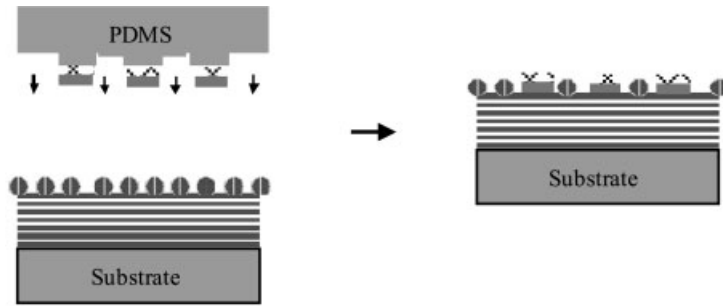
traditionally involves masking and etching processes that are required subsequent steps following each materials deposition to form a lateral or vertically patterned film. This concept is universal, in that it can apply to polymers, low molar mass dyes and other small molecules, as well as mesoscale systems and objects, as will be discussed in the section on colloidal assembly.

### 10.3

#### Polymer-on-Polymer Stamping

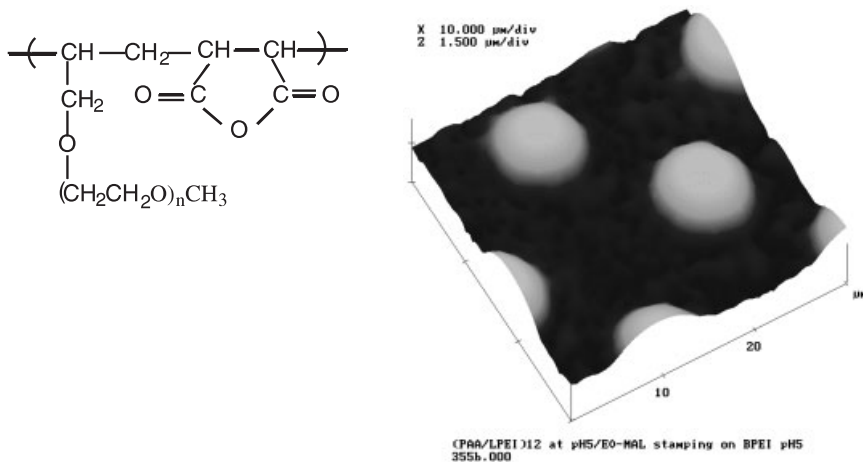
It is clear from the use of surface chemistry described above, as well as a myriad of other studies from numerous groups which utilize surface monolayer chemistry [15, 25–27], that the ability to create chemically patterned surfaces can lead to the templating of one, two or more materials systems to a surface through adsorption, polymerization, and other materials deposition methods. The use of alkanethiols on gold [4, 6] or trichloro and triethoxy silanes on glass [4] has brought with it a broad range of potential systems for surface templating; however, the use of such systems can be limiting in the numbers of commercially viable applications that are accessible using traditional chemisorbed SAMs on metal or metal oxide surfaces as substrates. There is a strong interest in the use of polymers as lightweight substrates for displays, sensors, electronic media, and other applications; however, most such surfaces are not accessible to patterning using silane or thiol chemistry. The use of thiols or silanes also often requires targeted synthesis to gain new functional systems. Finally, the ability to pattern on top of an existing polyelectrolyte multilayer can lead to the development of complex patterned 2D or 3D multilayers and hybrid materials systems, allowing the possibility of taking full advantage of the range of functional groups that can be incorporated into multilayer films for device and other applications. We have developed a new approach to the creation of chemical surface patterns which does not rely on the use of traditional chemisorbed monolayers [28], and have since begun to explore the use of functionalized polymers, polyions and low molar mass substituents which can be stamped directly onto other surfaces, particularly plastic substrates and multilayer films, by careful selection of surface chemistry [29]. Our motivations for exploring these routes are two-fold: 1. The functionalization and subsequent patterning of ionic multilayers and other materials on a broad range of substrates, including polymeric surfaces, without elaborate pretreatment; 2. the creation of complex multiple level heterostructures via stamping atop continuous or patterned polymer thin films, followed by subsequent selective adsorption or deposition steps.

Fig. 10.9 illustrates the polymer-on-polymer stamping process schematically. A polymer is transferred directly to the top surface of a polyelectrolyte multilayer thin film based on covalent and/or non-covalent interactions. For example, a polyanion can be stamped directly onto a charged polycation top multilayer surface to create alternating regions of plus and minus charge. On the other hand, block and graft copolymers can present a reactive functional group for attachment to



**Fig. 10.9** Schematic illustrating the concept of polymer-on-polymer stamping (POPS). Utilizing a PDMS stamp and a polymer “ink” to microcontact print a polyelectrolyte or block copolymer to a multilayer surface.

the surface, and a second functional group to modify the surface, as will be discussed further. We have found that even a *single* adsorbed layer of polyelectrolyte can be used as a functional surface for stamping. By creating patterned functional chemistry atop a polyelectrolyte surface, we ultimately introduce a broad approach that enables modification of any surface which can be covered with at least one surface layer of polyanion. Because a number of existing polymers may be used for this technique, many new functional surfaces can be achieved through the use of block copolymers or graft copolymers. This approach is much more commercially viable for the modification of flexible film using roll-by-roll processing than lithography or ink jet printing, and does not require a metallization or the creation of an oxide layer on the substrate, as with most SAMs.



**Fig. 10.10** An AFM image of a multilayer surface adsorbed onto a polystyrene substrate, which has been functionalized with the EO-MAL graft copolymer, followed by multilayer

adsorption of SPS/PDAC bilayers, which deposit only on the regions which did not contact the stamp [28].

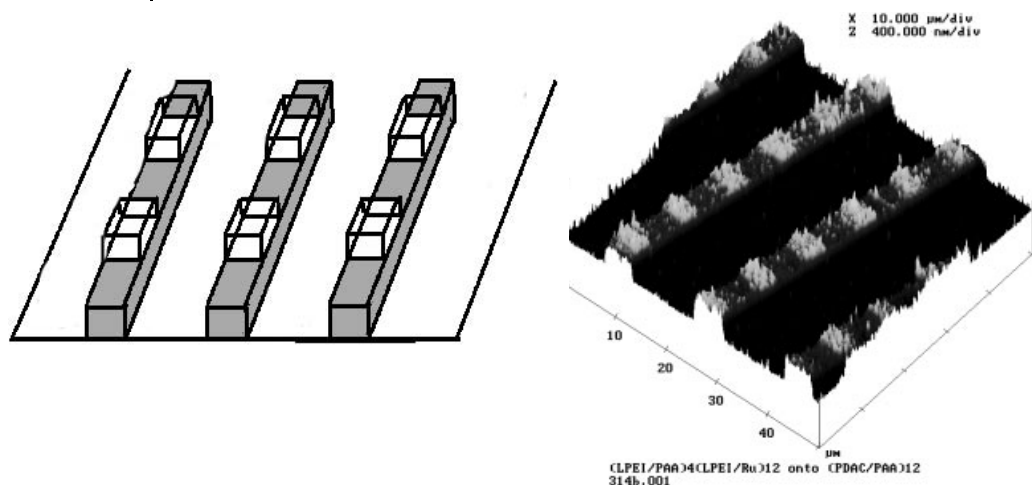


Fig. 10.11 An illustration of multiple level patterning, in which an existing patterned multilayer set of stripes is patterned with a second set of lateral stripes using EO-MAL [28].

The polymer stamping concept has been illustrated through the patterning of an oligoethylene glycol resist atop a polyelectrolyte multilayer surface. A resist layer was created by stamping an oligoethyleneoxide–maleic anhydride graft copolymer (EO-MAL) onto the top polyamine surface. Further deposition of polymer multilayers results in the formation of a patterned polymer film atop the original continuous multilayer thin film platforms as shown in Fig. 10.10. When a patterned polyelectrolyte film is used as the base layer or substrate in this process, a second pattern can be stamped atop the original patterned array. Subsequent selective adsorption of polymers yields a second level of microstructures, illustrating the concept of multiple level patterning for layer-by-layer thin films, as demonstrated in Fig. 10.11 [28].

Polymer-on-polymer stamping can be broadened to include selective deposition of numerous materials on top of multilayer polymer systems [28] and other functional surfaces. These films may then be used to template materials deposition, including other layer-by-layer thin films [28], polymers, metals [30], and colloidal particles [31].

### 10.3.1

#### Fundamental Studies of Polymer-on-Polymer Stamping

A number of issues exist for the application of polymer-on-polymer stamping. The transfer of polymers using a direct contact method requires that the polymer be applied to the PDMS stamp, and transferred in a dry or highly concentrated state after the removal of solvent. Due to the high molecular weight and lowered diffusion rate of polymers, the kinetic timescales of polymer transfer to the surface are expected to differ from those of typical alkanethiols on gold. It is also important

to consider differences in reactivity between the chemisorption of thiols or silanes, and the much less reactive groups on many polymer systems involved in ionic or hydrogen bonding interactions between the polymer and the surface. Perhaps more importantly, the nature of the transferred layer will be a function of the type of interaction used, the solvent used to create the polymer “ink”, and the wetting properties of the polymer with the stamp and the multilayer surface.

#### 10.3.1.1 Stamping of Ionic Polymers

Charged polymers can be transferred directly to a polymer surface of opposite charge using microcontact printing. This approach has been demonstrated for the transfer of strong polyelectrolytes to a polyelectrolyte multilayer platform. In the stamping process, a solution containing the polymer of interest is applied to a PDMS stamp. The excess solvent is then removed through air or nitrogen drying, and the stamp is placed on the substrate surface to be patterned. We have found that when a permanently charged polycation, PDAC is transferred to a negatively charged surface of an SPS/PDAC multilayer, a thin layer of positively charged polymer adheres to the surface even after thorough rinsing and sonication in water [32]. The thickness of the stamped layer is approximately 30 to 40 Å, close to the amount of film adsorbed from solution in the formation of multilayer thin films. A fundamental question that must be answered is whether the stamping process is analogous to the adsorption of polymers from solution. If the stamping process is comparable to adsorption from solution, then it should be possible to manipulate the thickness and the number of “free” ionic or functional groups present on the surface by varying the ionic strength or pH of the inking solution [32].

The rate at which the polymer is transferred in such processes is also of great interest; the kinetics of transfer of the polymer chains to the surface will influence the processing times for this technique. It is generally known that during the solution adsorption process used to form multilayers, more than 90–95% of the final amount adsorbed is achieved in the first few minutes of the adsorption process, making short contact times feasible for the formation of multilayers. To achieve good surface coverage during the stamping process, the kinetics of macromolecular rearrangements at the surface must be accommodated; for this reason, it is expected that stamping time will be a critical factor in polymer-on-polymer stamping. Furthermore, the solvent used, as well as temperature and other parameters, may greatly influence polymer dynamics and the required time required for contact of the stamp with the surface.

#### 10.3.1.2 Stamping of Block Copolymers

Block and graft copolymers present an opportunity to introduce long polymer chains as a means of surface modification; thus these systems are expected to be particularly effective in creating chemical patterns or templates. A second benefit of using block copolymers is the wealth of copolymer systems already in existence and commercially accessible, many of which contain charged or ionizable polymer

segments such as polyvinylpyridine, polymethacrylic acid, polyacrylic acid, sulfonated polystyrene, and many others. Further, a number of straightforward techniques are available to synthesize graft and block copolymers containing a functional group of interest.

In general, a copolymer presents two different chemical groups, one block that acts as an anchor, and interacts with the underlying surface, and a second, functional block that acts to present a new functionality on the surface, as illustrated in the left and center images of the schematic in Fig. 10.12. The stability of chemi- or physisorbed block copolymers on the surface is of critical importance, as the anchoring block must remain bound to the surface, and the polymer chains in the graft segments or second block must provide dense coverage of the exterior of the surface. Rearrangements of copolymers at interfaces can occur when the polymer is introduced to different solvent media due to minimization of interfacial free energy. For this reason, it is important to understand and control the adhesion of the first block to the surface. The stamping of polystyrene–PAA block copolymers has been examined recently [32]. The stability of the monolayer can be tested by examining the contact angle with water following stamping after a series of treatments in aqueous and organic solvents. We have found that when the surface is pretreated to obtain neutral, basic  $\text{-NH}_2$  groups, the monolayer is more stable than when stamped onto a protonated amine surface containing primarily  $\text{-NH}_3^+$  groups. Similarly, more stable films are formed at high rather than room temperature. Both of these observations suggest that the formation of covalent, as well as ionic or dipolar interactions, may be critical to the formation of a stable block copolymer monolayer.

Polymer-on-polymer stamping of block copolymers allows patterned modification of the surface properties of a film, and can be used to vary reactivity, charge, or wetting characteristics selectively. For example, a PS–PAA block copolymer stamped onto a polyamine functional surface can yield alternating hydrophobic and hydrophilic regions, as seen in Fig. 10.13. Such surfaces can act as templates for materials deposition, as will be discussed in detail below. A real advantage of this process is that it can be done on virtually any substrate onto which a multilayer can be adsorbed: polystyrene, Mylar<sup>®</sup> film, ink jet transparencies, glass surfaces, and metals of all types.

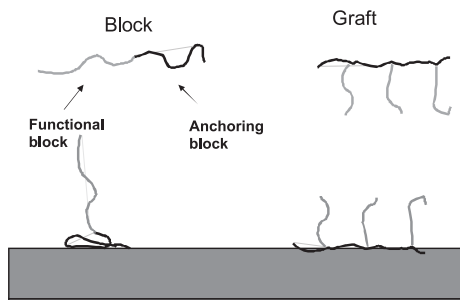
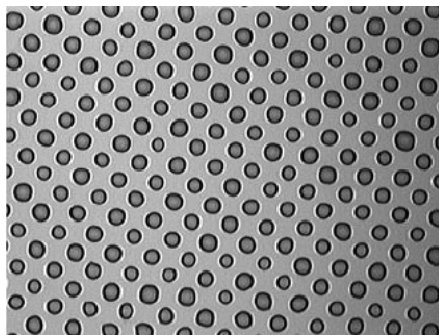


**Fig. 10.12** Illustration of surface functionalization via polymer-on-polymer stamping of block and graft copolymers and polyelectrolytes.

**Fig. 10.13** Water condensation figures are formed on an amino functional surface stamped with a PS–PAA block copolymer. The stamped hydrophobic regions are the exterior areas of the pattern, and the underlying amine functionalized hydrophilic regions are circles onto which water droplets are pinned. These results can be achieved on glass and polymer surfaces [29].



In the printing of polymers on multilayer surfaces, the composition of the multilayer surface is a critical component of the stability of the film. In particular, weak polyelectrolyte multilayers can vary a great deal in their thickness, degree of interpenetration, and surface functional density [33, 34]. In collaboration with the Rubner research group at MIT, the role of the weak polyelectrolyte multilayer is currently being examined in polymer-on-polymer stamping. Weak polyelectrolyte systems such as PAH and PAA are also being stamped directly onto multilayer surfaces to create functional amino and acid functionalized surfaces for a variety of applications.

### 10.3.2

#### **POPS as a Template for Other Materials Deposition**

The chemically templated surfaces formed using polymer-on-polymer stamping can be used to direct materials deposition onto glass, metal, semiconductor, and plastic surfaces. By selecting a block or functional polymer with a given interaction or reactivity, various materials deposition processes will be examined. One example of materials deposition is metal plating. Early investigations have shown that polymer-on-polymer stamping can be used to template electroless plating on polymer surfaces. In this work, the electroless plating chemistry developed in the groups of Rubner and Cohen for plating of continuous multilayer films [35] was applied to stamped polyelectrolyte multilayer surfaces in a collaborative effort. An oligoethylene oxide allyl ether–maleic anhydride alternating copolymer (EO–MAL) was stamped atop the PAH surface of a PAA/PAH multilayer. When the substrate is immersed in the catalyst bath, followed by the Ni plating bath, only the regions that were stamped are plated, resulting in a patterned metal film with high edge resolution and fidelity to the original pattern, as seen in Fig. 10.14 [30]; templating may also be accomplished through the use of stamped polyelectrolyte patterns utilizing strong polyelectrolytes. We have found that the metal plated onto the surface exhibits excellent adhesion to the underlying multilayer thin film. This approach provides a simple means of creating micron scale patterned metal regions for electrodes and device applications atop an existing polyelectrolyte multilayer. What is particularly attractive about this approach is that the multilayer may



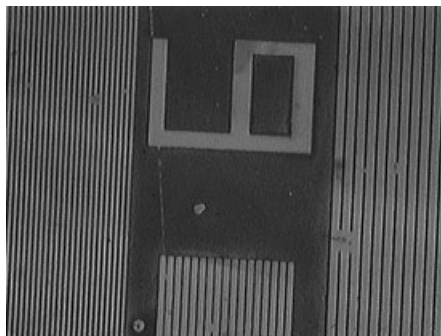


**Fig. 10.14** Electroless metal deposition on a polymer template formed by stamping EO-MAL graft copolymer atop the surface of a PAA/PAH polyelectrolyte multilayer. Dark regions are Ni metal, smallest dimensions are 2–3 microns wide [30].

contain a functional system of interest, such as chromic or luminescent films for devices. Further, simple plastic surfaces may be treated with a single or a small number of polyion bilayers, and subsequently patterned without the use of elaborate surface treatments.

A second area in which the techniques described above can be applied to practical problems is the creation of conducting polymer electrodes such as polyaniline and the transparent conducting polymer, PEDOT with micron scale dimensions. Here the real challenges involve achieving unusually high adsorption selectivity on the surface, particularly with polymer systems which can undergo multiple secondary interactions such as hydrogen bonding. Conducting polymers are of particular interest for applications in which flexibility is an issue, such as Mylar substrates. Very recent preliminary results show that we can effectively pattern polyelectrolyte multilayers containing PEDOT (Baytron P<sup>®</sup> suspension with SPS from Bayer) utilizing alternating COOH/EG functional surfaces. Similar results have been found with polyaniline (PANI) multilayer thin films. At this time, we are continuing to investigate a number of conducting polymers using selective deposition onto patterned substrates, including plastic and silicon substrates. We can also use polymer-on-polymer stamped polyelectrolyte multilayer surfaces as templates for spin cast or solvent cast films of conducting polymers. MacDiarmid and coworkers have shown that alternating hydrophobic and hydrophilic regions of a surface created by laser printing [36, 37] can be used as a means of controlling the morphology of polyaniline deposited on the surface from solution, creating many orders of magnitude difference in the conductivity of films on the hydrophobic versus hydrophilic regions of the surface [36, 38]. In this work, the resolution of patterning was in the range of millimeters. Here we can examine similar effects with micron scale resolution utilizing alternating hydrophobic/hydrophilic surfaces created by stamping of block copolymers such as the PS-PAA system described above; the resulting surfaces can be exposed to a polymerizing bath of polyaniline to create patterned conducting films.

## 10.4 Directed Assembly of Colloidal Particles

Recently, there has been strong interest in the self-assembly of particles to create ordered structures in two and three dimensions. Such systems have a range of potential applications: functional templates and catalysts for chemical and biological processes, sensor arrays, masks for non-lithographic patterning of deposited species, and novel optical materials and photonic crystal devices. Fabrication of photonic crystals that operate at visible wavelengths, for example, benefits from the sub-micron size scale accessible using self-assembled systems. Self-assembly is thus a tool of great interest based on the need for an inexpensive approach to controlling the arrangement of small objects over large areas.

The stability and adhesion of colloids adsorbed to a molecular monolayer (SAM) can vary to a large extent, depending on the specific interactions of the particle with the surface, and the nature of the monolayer. Adhesion can be improved by manipulating the film thickness, or the density of functional groups on the uppermost surface layers. Further, a number of new applications for ordered colloidal arrays may be realized by incorporating functionality into the underlying layers. An ideal approach would therefore utilize patterned layer-by-layer thin films as functional templates for the assembly of particles on the polymer surface. We recently demonstrated for the first time an approach that utilizes patterned layer-by-layer thin films as functional templates for the assembly of particles on the polymer surface, as shown in schematically in Fig. 10.15 [39], and have extended it utilizing surface chemistry, secondary interactions and confinement effects [40–43]. In this process, multilayers patterned onto alternating COOH/EG surfaces act as regions for deposition of charged particles, and the bare EG regions act as neutral regions which resist particle deposition at standard adsorption conditions. The ability to incorporate functionality in the underlying film is a novel and promising approach that takes full advantage of the layer-by-layer assembly method. The inte-

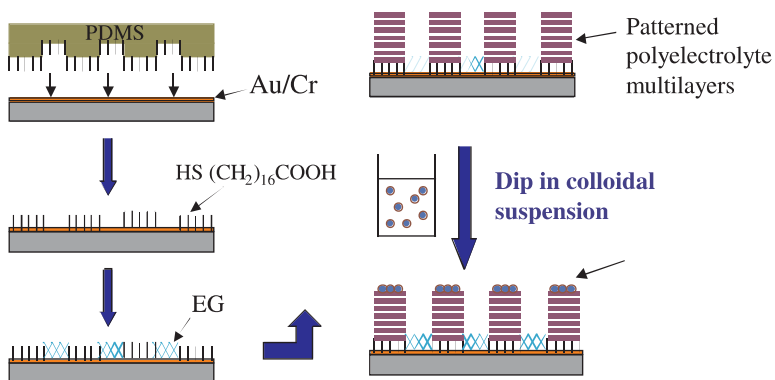


**Fig. 10.15** Schematic of approach for templating of colloidal assembly on patterned polyelectrolyte multilayers.

gration of conducting or luminescent polyelectrolyte multilayer films, nonlinear optical dyes, or electrochemical mediators with patterned colloidal assemblies can lead to components in optical or photonics devices or sensors. Further, adhesion of the particle to the surface is greatly enhanced with the use of polymer templates over self-assembled monolayer films derived from low molar mass compounds.

#### 10.4.1

##### Selective Deposition and Controlled Cluster Size on Multilayer Templates

We have demonstrated control over the density and selectivity of particle adsorption. Three mechanisms have been used to control adsorption of charged particles: 1) Adjustment of the pH of the colloid suspension, which determines the ionization of the uppermost surface of the polyelectrolyte multilayer; 2) adjustment of the ionic strength of the suspension, which determines the extent of charge screening about the colloid and polyelectrolyte; and 3) variation of the concentration of added surfactant, which introduces charge screening on the particle surface, and introduces hydrophobic interactions between the particles and the underlying surface. We have extended the concepts developed above for the selective deposition of polyelectrolyte multilayers onto micron-sized particles, demonstrating the appropriateness of the selective deposition approach for mesoscale as well as molecular scale systems. By varying these parameters, as well as the hydrophobic or hydrophilic nature of the particle surface, we can successfully template particles on the surface. These concepts were first explored in a series of studies utilizing silica particles and negatively charged latex spheres, and SPS/PDAC multilayers patterned as lines on surfaces as a template. When the area of the region of deposition is limited in width, we can direct single lines of particles onto a patterned polyelectrolyte template, as shown in Fig. 10.16(a) [39]. In more recent studies, we have extended this concept and examined the effect of confinement of the adsorbing particle by confining the size of a polyelectrolyte multilayer dot-

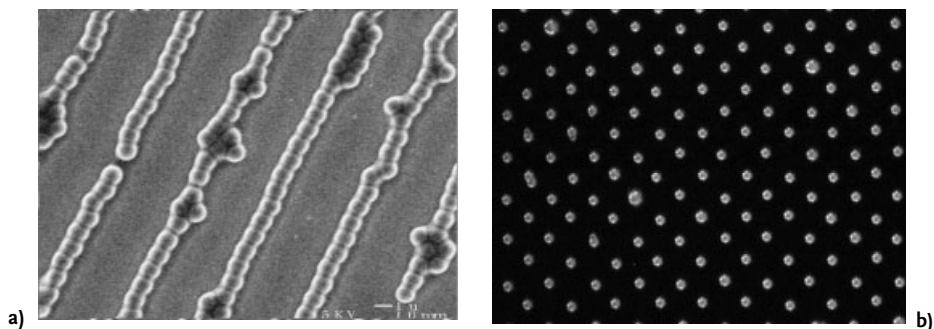


**Fig. 10.16** Colloids directed to confined regions of a surface arrange in ordered patterns. (a) one micron particles on a two mi-

cron wide stripe [39], and (b) a single particle array on a dot pattern multilayer surface [40].

shaped template to achieve a single particle array of particles, as shown in Fig. 10.16 (b) [40]. This concept allows us to direct the organization of colloidal particles and precisely control cluster size and organization on multilayer surfaces by a systematic variation in the size of the multilayer template onto which the particles can adsorb; the result of systematic changes in template size are illustrated in Fig. 10.17. The self-organization technique resulting from this work expands the possibility of fabricating complex micro- and nanostructures by the manipulation of submicron particles via an elegant, self-driven process.

Similar templating effects can also be achieved by using polymer-on-polymer stamping techniques to stamp a polyelectrolyte onto the oppositely charged top surface of a continuous, unpatterned polyelectrolyte multilayer [43]. The resulting patterning of alternating positive and negatively charged regions acts as a template for the deposition of particles, in which the oppositely charged regions attract and the like-charged regions repel the adsorbing particles. The advantages of this technique include the fact that a gold or silicon oxide is no longer needed to template the particle array; a multilayer on any surface will work effectively. It is also possible to stamp a positively charged polymer directly onto a Si oxide surface, and achieve a similar templating effect; however, the presence of the multilayer is important for enhanced adhesion to the original surface.

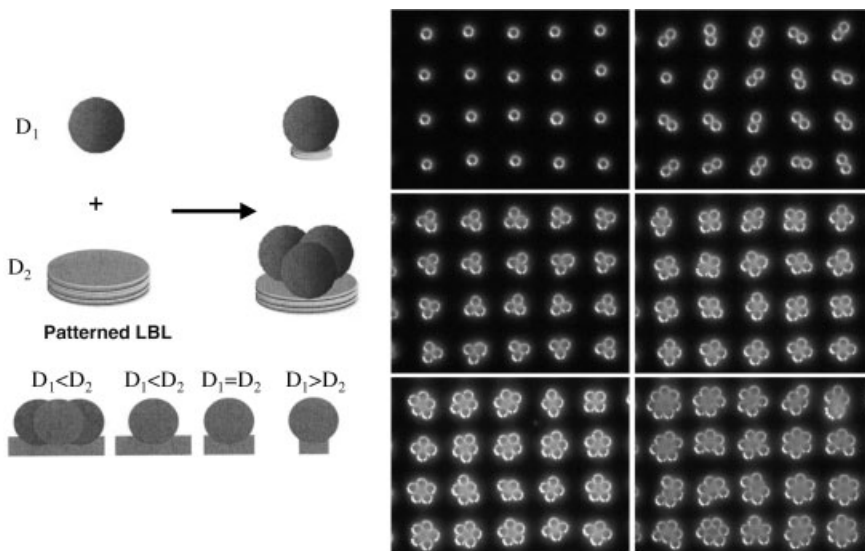


**Fig. 10.17** Left: Schematic illustrating effect of confinement in a circular patterned layer-by-layer film in which the dot pattern is varied in size. Right: Controlled colloid cluster arrays adsorbed on LBL templates of increasing size from top to bottom and left to right.

## 10.4.2

**Surface Sorting with Particles on Multilayer Surfaces**

Mesoscale objects may also be directed using the concept of surface sorting. A significant finding of the colloid adsorption studies was that by simply changing adsorption conditions such as pH and ionic strength, the preferred region of adsorption and degree of selectivity can be changed drastically [39]; these adsorption parameters can be used as tools in the construction of complex particle/polymer assemblies. A unique tool that we have found to be effective in controlling selectivity is the use of a positively charged surfactant, DTAB, added to shield the surface of a negatively charged particle. Without the addition of DTAB, the deposition of negatively charged polystyrene latex particles occurs selectively on the uppermost, positively charged PDAC surface of an SPS/PDAC multilayer via ionic interactions. Hydration and steric forces from the EG SAM resist region effectively prevent deposition of charged particles onto the EG surface. When low concentrations of DTAB are added to the colloidal suspension ( $10^{-6} \sim 10^{-5}$  M), the particles deposit primarily on the multilayer surface, but with small increases in their packing density due to favorable inter-particle hydrophobic interactions and increased ionic shielding [39]. As more DTAB, ( $10^{-4} \sim 10^{-3}$  M) is added, the surfaces of the particles become increasingly hydrophobic and the selectivity of the particles for the PDAC surface decreases sharply, resulting in little or no selectivity. Finally, at high degrees of shielding, the selectivity is reversed, and deposition occurs preferentially on the EG surface, with no deposition on the positively charged multilayer surface [39]. It was proposed that hydrophobicity is the main driving force in directing spheres to the EG surface when the degree of shielding with DTAB for 0.5  $\mu\text{m}$  spheres reaches about greater than 100% shielding due to favorable interactions between the surfactant on the particle surface and the hydrophobic ethylene groups present in the EG SAM repeat units, in much the same manner that the polyion, PAH, is attracted to the EG surface in a specific pH range. Recent measurements indicate that the sharp transition from the EG SAM as a resist to a region for deposition occurs at about 190 and 95% charge shielding for the 1.0 and 1.9  $\mu\text{m}$  PSS spheres, respectively. By taking advantage of the resulting differences in selectivity, we have successfully fabricated two component colloidal arrays on a single patterned PDAC/EG surfaces simply by varying the conditions for adsorption in each case, as shown in Fig. 10.18(a) [42].

We can also use hydrogen bond interactions in place of hydrophobic interactions to achieve two component “surface-sorting” of colloidal particles on the multilayer/EG patterned surface. For example, the amidine functional group is known to undergo strong hydrogen bonding interactions. Adsorption of amidine functionalized polystyrene latex particles on an EG/polyelectrolyte multilayer surface at moderate to high pH levels leads to adsorption of the amidine functionalized particles on the EG regions of the surface. The image shown in Fig. 10.18(b) illustrates the presence of two different sized particles on the surface. In this case, SPS/PDAC multilayers were adsorbed onto the COOH regions of a COOH/EG functionalized gold surface. Negatively charged sulfonated latex particles microns

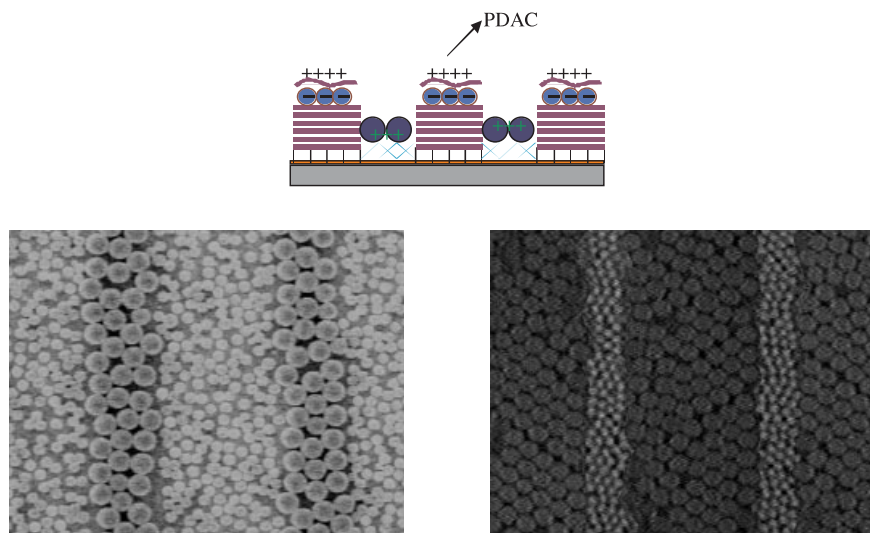


**Fig. 10.18** Two different types of particles can be adsorbed to the charged multilayer surface or the alternating oligoethylene glycol monolayer based on ionic charge interactions combined with hydrophobic (left (a) large parti-

cles are DTAB shielded) and hydrogen bonding (right (b) large particles are amidine functionalized) interactions [42]. In both cases, small particles are on the multilayer surface, large particles are on the EG surface.

were then adsorbed onto the top layer of PDAC on the polyelectrolyte multilayer films. To prevent the desorption of sulfonated particles on exposure to aqueous basic solution, a single layer of polycation was adsorbed onto the sulfonated particles. Following this adsorption step, a second set of smaller amidine functionalized spheres was then adsorbed onto the EG regions of the surface at high pH [42]. The result for each of these two examples is a patterned two-dimensional array in which particles are confined to specific regions of the surface based on surface chemistry. On both surface regions, in this case, the particles form single monolayer arrays with good edge resolution.

### 10.4.3

#### Selective Electroless Plating of Colloidal Particle Arrays

It is possible to utilize the plating chemistry adapted for multilayer thin films [35], and apply it to the selective plating of colloidal arrays. Because catalysts containing a positively or a negatively charged palladium complex can be used to direct electroless nickel plating on charged surfaces, we can utilize this approach to plate the particle without plating the underlying multilayer, or both the multilayer and the particle. Fig. 10.19 shows the results of a two-step metal plating technique for the formation of particle arrays on the surface using the patterned polyelectrolyte multilayer technique, in which metal coated particle arrays on surfaces are prepared [41]. These controlled and stable metal coated particle arrays on surfaces

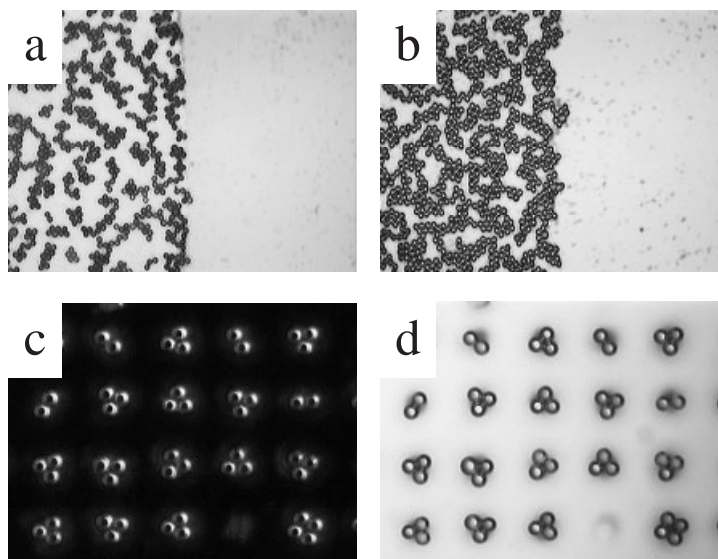


**Fig. 10.19** Selective nickel deposition in controlled particle arrays. Catalyst 1 ( $\text{Na}_2\text{PdCl}_4$ ) was used in b to plate the multilayer, EG region and particle, and catalyst 2 ( $[\text{NH}_4]_4\text{PdCl}_2$ ) in a, c, and d, to plate the particle and surrounding EG regions, but not the underlying multilayer.

have a great potential application in many areas, including opto-electronic and magnetic, sensor, photonic, and bio-chip applications. Samples of 2D colloidal arrays on patterned polyelectrolyte templates were pretreated with  $\text{Na}_2\text{PdCl}_4$  (a negatively charged Pd complex, see Fig. 10.19b) and  $[\text{NH}_4]_4\text{PdCl}_2$  (a positively charged Pd complex, see Fig. 10.19a, c, and d) at 5 mM concentration in DI water for 10 s; then the pretreated samples were dipped into a Ni bath containing nickel sulfate (Ni source). Negatively charged colloidal particles selectively adsorb on the positively charged multilayer region only, not on the EG SAM resist area, but nickel selectively plates to the positively or negatively charged surfaces depending on the charge of the catalyst. Positively charged Pd complexes also go readily to the EG SAM area.

## 10.5

### Functional Polymer Thin Films for Electrochemical Device and Systems Applications

The motivation for creating patterned thin films is, in many cases, the development of devices and sensors on the sub-micron to millimeter length scale for a number of applications, including displays. Many of the interesting functional properties of polyelectrolyte multilayer films utilize electrochemistry in their application. In this section, preliminary work involving the formation of ionically con-

ducting polyion multilayers, and work focused on the assembly of electrochromic thin films is addressed. The goal of this project has been to construct an electrochromic device using layer-by-layer (LBL) assembly. The elements of such a device are an electrochemically reactive cathode and anode, along with a solid electrolyte that separates the two electrodes and provides sufficient ionic conductivity to support a fast electrochemical reaction within the electrodes. Candidate polymers for anodes and cathodes include the electrically conducting polymers, most of which are electrochromic in the UV-Vis range, and most of which are polycations in the doped state. This class of polymers was originally assembled using layer-by-layer techniques by Rubner et al. [44–48], with a focus on the investigation of electronic conducting properties of these films; our recent studies have examined the electrochemical behavior and electrochromic response of these films on applied potential. Electrochromism and redox behavior within polyelectrolyte multilayers has also been studied by the Schlenoff's research group using polyviologens to form redox-active polymer films [49, 50].

### 10.5.1

#### **Electrochromic Polyelectrolyte Multilayer Device Construction**

In our work, we have constructed solid state electrochromic films containing PANI and poly(3,4-ethylenedioxythiophene): sulfonated poly(styrene) colloid (PEDOT:SPS, Baytron P from Bayer), colayered with several counterpolyions [51]. The redox-active properties of the LBL films containing these two electrically conducting polymers have been demonstrated and characterized by cyclic voltammetry [51]. The films show redox activity typical of the conjugated polymer contained in the film. Co-layering with different polyanions can be shown to affect the number of redox states available in PANI. The spectral electrochemical properties of these films have been also been assessed [51]. Characteristic absorption can be observed at the different redox states for each polymer. For each of the polymers, the neutral, polaron, and (in some cases) bipolaron absorptions can be observed as the polymer is progressively doped to increasing degeneracy.

As PANI is an oxidatively coloring material (anodic electrochrome) and PEDOT is a reductively coloring material (cathodic electrochrome), the two materials were combined into a complementary coloring electrochromic device. This prototype device had an anode material consisting of PANI co-layered with poly(2-acrylamido-2-methyl-1-propane sulfonic acid) (PAMPS), LbL assembled for 20 bilayers – (PANI/PAMPS)<sub>20</sub>. The PEDOT:SPS colloid was co-layered with linear poly(ethylene imine) (LPEI), also assembled for 20 bilayers – (LPEI/PEDOT:SPS)<sub>20</sub>. The electrode materials were LBL assembled atop plasma treated ITO glass with a thickness of about 2000 Å for both. The electrolyte for this first device was a gel electrolyte consisting of a solvent-cast PAMPS film. An electrochromic cell with 40-bilayer elements was also constructed. These devices performed well for first-generation devices from commercially available materials, with a switching speed less than 2 s and maximum optical contrast of 30% (see Fig. 10.20).



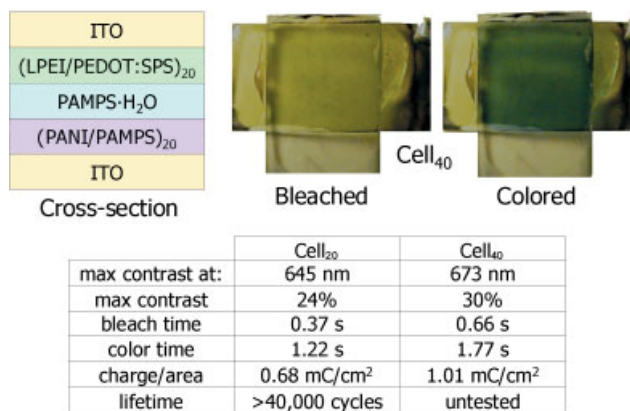


**Fig. 10.20** Demonstration of colored and bleached cell containing 40 bilayers of each chromic multilayer system. Table gives performance characteristics for 20 and 40 bilayer cell systems.

### 10.5.2

#### Ionically Conducting Multilayers for Electrochemical Device Applications

Candidate polymers for the ionically conducting solid polymer electrolyte vary widely, but include those employed as commercial gel-type polyelectrolytes, perfluorinated ionomers, and even weak polyelectrolytes with pH-dependent behavior. In all cases, the strategy in formulating solid electrolytes from LBL thin films has been to create a high dielectric constant, hydrophilic matrix in which small molecule ions (most often protons on polyacids) still contained in the LBL films can dissociate and migrate freely. The analysis of ionic conductivity in LBL thin films is currently underway, and should allow the replacement of the PAMPS gel as an ionic transport medium in the second-generation electrochromic cell with a layer-by-layer polymer system, so that the entire electrochromic cell can be assembled from the bottom up on a conductive substrate. The ionically conductive LBL films offer promise in a number of applications aside from electrochromic devices, including membranes in lithium polymer batteries and proton exchange membranes in fuel cells. Thus far, (LPEI/PAMPS), (LPEI/PAA), and (LPEI/NAFION) films have been assembled at several pH conditions and tested by impedance analysis [52, 53]. Films constructed using hydrogen bonding interactions, (PEO/PAA), (PEO/PMAA), and (PEO/NAFION), have also been tested [52, 53]. The ionic conductivity of these systems at an intermediate humidity of  $\sim 50\%$  varies by four orders of magnitude. The peak conductivity at this humidity is approximately  $10^{-8} \text{ S cm}^{-1}$ . However, we have shown that the conductivity of a single film can vary by almost 5 orders of magnitude, depending on the level of hydration as determined by relative humidity. At very high humidity conditions, the conductivity of (LPEI/PAMPS) approaches  $10^{-5} \text{ S cm}^{-1}$ , conductivity appropriate for electro-

chromic devices, but still too small for power delivery applications. Efforts continue to fully explore the response of these films to changes in humidity.

## 10.6

### Summary

Surface chemistry can be used to effectively direct the deposition of layer-by-layer thin films formed from solution. By establishing a set of rules that define the conditions required for selective deposition on specific surface regions for both strong and weak polyelectrolyte adsorption, it is possible to use this understanding for the assembly of complex, multicomponent 2D lateral and 3D film microstructures. Surface patterns can be used to assemble two or more elements of different type onto a surface in a desired arrangement. This concept of adsorption directed by chemistry is universal, in that the same sets of rules derived for polymeric systems can also be applied to meso-scale systems as, including particles, colloids, and biological elements. We have successfully expanded this understanding of polyion-surface interactions to mesoscale systems, including functionalized micron sized colloidal particles. Arrays of particles of different surface functionality can be directed to different regions of a substrate, and single particle arrays on a lattice can be assembled on surfaces using patterned polyelectrolyte multilayers as a template. This deposition is driven by the spatially-varied electrostatic and secondary interactions between the colloid and the substrate. New developments include the investigation of hydrogen bonding, and other more specific interactions, as a means of directing the deposition of polymers and other materials.

A second important area of development is the ability to pattern polymer multilayer and other functional surfaces without the use of thiol or silane coupling chemistry, which is appropriate only for metal or metal oxide surfaces. This technique of polymer-on-polymer stamping opens up a broad range of possibilities with respect to the functionalization and manipulation of polymer thin films to make multi-level three-dimensional structures using cheap and easy processing techniques. Plastic substrates may now be used in place of the silicon, metal or metal oxide surfaces needed to functionalize surfaces with alkanethiols or triethoxysilanes. Further, the use of polymer-on-polymer stamping can be used to create multiple level patterns on surfaces and build up three-dimensional microstructures on the surface, in which more than one polymer system can be selectively placed on a surface. Ongoing collaborative efforts have led to new applications using this technique, including its use to direct colloid assembly, electroless metal plating, and even the growth of cells on engineered polyelectrolyte multilayer surfaces. Finally, new approaches to the assembly of polyelectrolyte functional multilayer systems which exhibit ionic as well as electronic conductivity and/or are electrochromic will prove useful for a number of new applications. New patterning techniques, combined with functional polyelectrolyte multilayer systems, lead the way to a wide range of applications in plastic electronics, thin film power devices, electro-optic systems, and biomaterials.

## 10.7

## References

- 1 B. L. BOOTH, In *Polymers for electronic and photonic applications*; C. P. Wong, Ed., Academic Press: Boston, 1993; pp. 549–597.
- 2 E. REICHMANIS, In *Polymers for electronic and photonic applications*; C. P. Wong, Ed., Academic Press: Boston, 1993; pp. 67–111.
- 3 P. T. HAMMOND, G. M. WHITESIDES, *Macromolecules* 1995, 28, 7569–7571.
- 4 Y. XIA, M. MRKSICH, E. KIM, G. M. WHITESIDES, *J. Am. Chem. Soc.* 1995, 117, 9576–9577.
- 5 A. KUMAR, G. M. WHITESIDES, *Science* 1994, 263, 60–62.
- 6 A. KUMAR, H. A. BIEBUYCK, G. M. WHITESIDES, *Langmuir* 1994, 10, 1498–1511.
- 7 S. L. CLARK, M. MONTAGUE, P. T. HAMMOND, *Supramol. Sci.* 1997, 4, 141–146.
- 8 S. L. CLARK, M. F. MONTAGUE, P. T. HAMMOND, *Macromolecules* 1997, 30, 7237–7244.
- 9 S. L. CLARK, P. T. HAMMOND, *Langmuir* 2000, 16, 10206–10214.
- 10 S. L. CLARK, E. S. HANDY, M. F. RUBNER, P. T. HAMMOND, *ACS Polym. Prepr.* 1998, 39, 1079–1080.
- 11 P. HARDER, M. GRUNZE, R. DAHINT, G. M. WHITESIDES, P. E. LAIBINIS, *J. Phys. Chem. B* 1998, 102, 426–436.
- 12 R. L. C. WANG, H. J. KREUTZER, M. GRUNZE, *J. Phys. Chem. B* 1997, 101, 9767–9773.
- 13 S. I. JEON, J. H. LEE, J. D. ANDRADE, *J. Colloid Interface Sci.* 1991, 142, 149–158.
- 14 M. MRKSICH, G. M. WHITESIDES in *Poly(ethylene glycol)*, 1997; Vol. 680, pp. 361–373.
- 15 Y. N. XIA, G. M. WHITESIDES, *Angew. Chem.* 1998, 37, 551–575.
- 16 S. L. CLARK, M. F. MONTAGUE, P. T. HAMMOND, *ACS Symp. Ser.* 1998, 695, 206–219.
- 17 M. R. BÖHMER, O. A. EVERS, J. M. H. M. SCHEUTJENS, *Macromolecules* 1990, 23, 2288–2301.
- 18 G. DECHER, J.-D. HONG, *Ber. Bunsen-Ges. Phys. Chem.* 1991, 95, 1430–1434.
- 19 N. G. HOOGEVEEN, M. A. COHEN STUART, G. J. FLEER, *J. Colloid Interface Sci.* 1996, 182, 133–145.
- 20 Y. LVOV, G. DECHER, H. MOHWALD, *Langmuir* 1993, 9, 481–486.
- 21 H. G. M. VAN DE STEEG, M. A. COHEN STUART, A. DE KEIZER, B. H. BIJSTERBOSCH, *Langmuir* 1992, 8, 2538.
- 22 S. L. CLARK, P. T. HAMMOND, *Adv. Mater.* 1998, 10, 1515–1519.
- 23 X.-P. JIANG, C. ORTIZ, P. T. HAMMOND, *Langmuir* 2001, 18, 2607–2615.
- 24 X.-P. JIANG, S. L. CLARK, P. T. HAMMOND, *Adv. Mater.* 2001, 13, 1669–1673.
- 25 P. GHOSH, R. M. CROOKS, *J. Am. Chem. Soc.* 1999, 121, 8395–8396.
- 26 M. MRKSICH, L. E. DIKE, J. TIEN, D. E. INGBER, G. M. WHITESIDES, *Exp. Cell Res.* 1997, 235, 305–313.
- 27 T. K. WHIDDEN, D. K. FERRY, M. N. KOZICKI, E. KIM, A. KKUMAR, J. L. WILBUR, G. M. WHITESIDES, *Nanotechnology* 1996, 7, 447–451.
- 28 X.-P. JIANG, P. T. HAMMOND, *Langmuir* 2000, 16, 8501–8509.
- 29 X.-P. JIANG, H. ZHENG, S. GOURDIN, P. T. HAMMOND, *Langmuir* 2002, 18, 2607–2615.
- 30 X.-P. JIANG, H. ZHENG, J. CHOI, M. F. RUBNER, P. T. HAMMOND, *in preparation* 2002.
- 31 X. P. JIANG, K. M. CHEN, L. C. KIMERLING, P. T. HAMMOND, *Abs. Papers ACS* 2000, 220, 301–COLL.
- 32 X. P. JIANG, P. T. HAMMOND, *Abs. Papers ACS* 2001, 221, 93–PMSE.
- 33 S. SHIRATORI, M. F. RUBNER, *Macromolecules* 2000, 33, 4213–4219.
- 34 D. YOO, S. S. SHIRATORI, M. F. RUBNER, *Macromolecules* 1998, 31, 4309–4318.
- 35 T. WANG, B. CHEN, M. F. RUBNER, R. COHEN, *Langmuir* 2001, 17, 6610.
- 36 D. HOHNHOLZ, A. G. MACDIARMID, *Synth. Met.* 2001, 121, 1327–1328.
- 37 P. C. WANG, Z. HUANG, A. G. MACDIARMID, *Synth. Met.* 1999, 101, 852–853.
- 38 Z. HUANG, P. C. WANG, A. G. MACDIARMID, Y. XIA, G. M. WHITESIDES, *Langmuir* 1997, 13, 6480.

- 39 K. CHEN, X.-P. JIANG, L.C. KIMERLING, P.T. HAMMOND, *Langmuir* **2000**, *16*, 7825–7834.
- 40 I. LEE, H. ZHENG, M.F. RUBNER, P.T. HAMMOND, *Adv. Mater.* **2002**, *14*, 573–577.
- 41 I. LEE, M.F. RUBNER, P.T. HAMMOND, *in preparation* **2002**.
- 42 H. ZHENG, I. LEE, M.F. RUBNER, P.T. HAMMOND, *Adv. Mater.* **2002**, *14*, 569–572.
- 43 H. ZHENG, M.F. RUBNER, P.T. HAMMOND, *Langmuir* **2002**, *18*, 4505–4510.
- 44 J.H. CHEUNG, A.F. FOU, M.F. RUBNER, *Thin Solid Films* **1994**, *244*, 985–989.
- 45 J.H. CHEUNG, W.B. STOCKTON, M.F. RUBNER, *Macromolecules* **1997**, *30*, 2712–2716.
- 46 M. FERREIRA, J.H. CHEUNG, M.F. RUBNER, *Thin Solid Films* **1994**, *244*, 806–809.
- 47 M. FERREIRA, M.F. RUBNER, *Macromolecules* **1995**, *28*, 7107–7114.
- 48 A.C. FOU, M.F. RUBNER, *Macromolecules* **1995**, *28*, 7115.
- 49 J. STEPP, J.B. SCHLENOFF, *J. Electrochem. Soc.* **1997**, *1444*, L155.
- 50 M. LI, H. LY, J.B. SCHLENOFF, *J. Am. Chem. Soc.* **1998**, *120*, 7626.
- 51 D.M. DELONGCHAMP, P.T. HAMMOND, *Adv. Mater.* **2001**, *13*, 1455–1459.
- 52 D.M. DELONGCHAMP, P.T. HAMMOND, *Abs. Papers ACS* **2000**, *220*, 75–POLY.
- 53 D.M. DELONGCHAMP, P.T. HAMMOND, *Abs. Papers ACS* **2001**, *221*, 136–PMSE.

## 11

# Layered Nanoarchitectures Based on Electro- and Photo-active Building Blocks

XI ZHANG, JUNQI SUN and JIACONG SHEN

### Abstract

Layered multilayer assemblies based on electro- and photo-active building blocks were fabricated by the ionic self-assembly technique. It is demonstrated that this technique is a powerful way to fabricate multilayer film-based chemically modified electrodes. By incorporating electroactive materials into multilayers, chemically modified electrodes based on both single and binary active species were fabricated. This technique allows tailoring of the properties of the chemically modified electrodes by incorporating multi-component species in a designed way. By combining the ionic self-assembly technique with post photoreaction between the film, an easy way to fabricate covalently attached multilayer assemblies has been developed. This concept is applicable to building blocks containing diazonium groups and their counterparts containing sulfonate, acrylic acid and even phenol groups. The stability of the covalently attached assemblies increases dramatically when compared with those held together by electrostatic interaction or ionic bonds. It is anticipated that active components could be engineered into stable assemblies that take synergic interaction to produce new functions.

### 11.1

#### Introduction

Supramolecular chemistry at interfaces has made continuous progress [1]. When molecular assembly occurs at the liquid/solid or gas/liquid interface, the molecules are in a confined state, in contrast with molecular self-assembly in solution. This may allow fabrication of molecular assemblies with controlled composition and orientation. Many types of state-of-the-art surface and interface instruments can be used to characterize the assembling process in situ. Moreover, this may facilitate the integration of molecular architecture and functional assembly, leading to various thin-film-based devices and sensors.

There are many kinds of interfacial assembly techniques, such as the Langmuir–Blodgett (LB) technique [2], self-assembly based on interfacial chemical reaction [3], the layer-by-layer (LbL) assembly technique [4], etc. Among them, the io-

nic self-assembly technique, introduced by Decher in 1991 [5], provides an elegant way of controlling the composition of the resulting assemblies and the thickness of an individual layer on the nanometer scale. Large varieties of charged materials, including almost all kinds of polyions, dyes, organic/inorganic particles, proteins, viruses, and other biosystems have been incorporated into multilayer assemblies using this technique [6, 7]. These thin film assemblies have potential applications in nonlinear optical materials [8], conductive films [9], permselective gas membranes [10], light emitting devices [11, 12], sensors [13], etc.

Furthermore, the driving force for the layer-by-layer assembly need not be electrostatic interaction. Other forces, such as hydrogen bonding [14, 15], coordination bonding [16, 17], charge transfer [18], molecular recognition [19], etc. can also be used as the driving force for the assembly process. For example, the alternating deposition between polyelectrolyte and bolaform amphiphile bearing mesogenic groups led to the formation of multilayer assemblies with an improved interfacial structure, as shown in Fig. 11.1A [20]. The driving force for the layer buildup is electrostatic interaction as well as  $\pi$ - $\pi$  stacking. Xiong et al. fabricated a multilayer film on the basis of coordination bonds by alternate adsorption of poly(copper 4-styrene sulfonate) (PSS-Cu) with poly(4-vinylpyridine) [16]. Through in situ chemical reaction, an organic-inorganic hybrid nanocomposite can be obtained, as shown in Fig. 11.1B. Moreover, Wang et al. fabricated alternate multilayer assemblies of poly(4-vinylpyridine) and poly(acrylic acid) based on hydrogen bonding between pyridine and acrylic acid (Fig. 11.1C) [14]. Even though FTIR data have clearly revealed that hydrogen bonding is the dominant driving force for the layer-by-layer assembly, recent data of single molecular force spectroscopy have demonstrated that the force value was much larger than that of hydrogen bonding, indicating that combined interaction of different forces must be responsible for the multilayer formation. Actually, in most cases, multilayer assemblies are not based

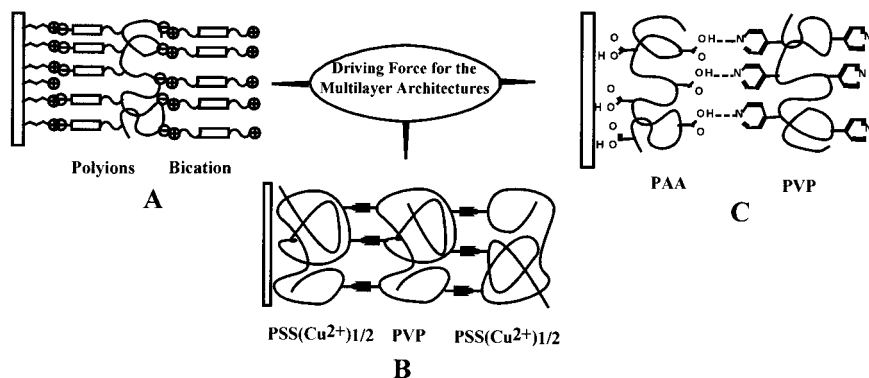


**Fig. 11.1** Attempts to fabricate layered nanoarchitectures: (A) Electrostatic multilayer assemblies of polyelectrolyte and bication bearing a mesogenic group; (B) multilayer as-

semblies of PSS(Cu<sup>2+</sup>)<sub>1/2</sub> and PVP based on coordination bonding; (C) multilayer assemblies of PAA and PVP based on hydrogen bonding.

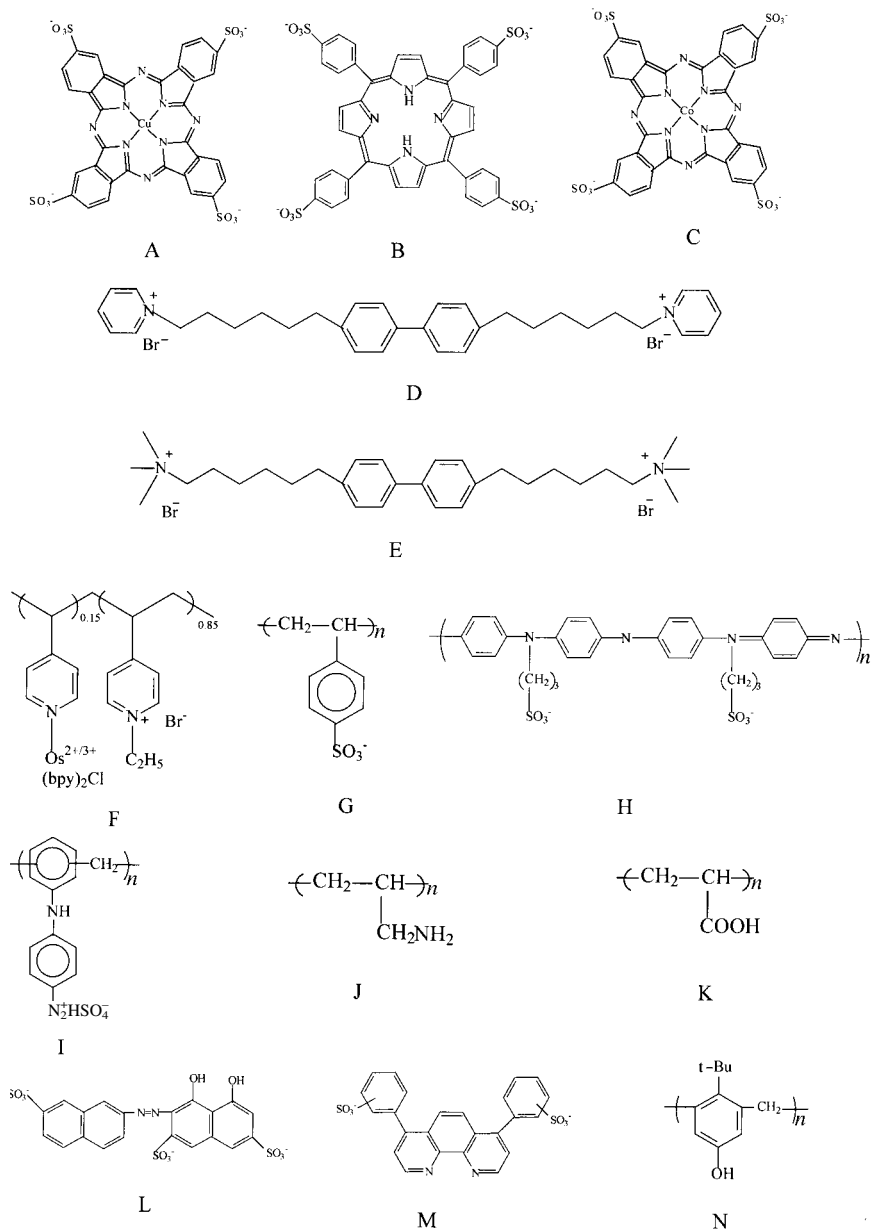


**Fig. 11.2** Building blocks for layer-by-layer assembly. (A) CuTsPc, (B) tpps<sub>4</sub>, (C) CoTsPc, (D) PyC<sub>6</sub>BPC<sub>6</sub>Py, (E) NC<sub>6</sub>BPC<sub>6</sub>N, (F) PVP-Os, (G) PSS, (H) PAPSAH, (I) DAR, (J) PAH, (K) PAA, (L) SNAN, (M) BST and (N) PR.

on a single type of driving force, but on a synergetic interaction of several kinds of forces.

Among other charged species, assemblies of electro- and photo-active materials have attracted considerable attention. On the one hand, these materials will endow the resulting assemblies with novel properties and finally realize functional assemblies due to the boundless materials with different functions that can be incorporated. On the other hand, assemblies with photo- and electro-active groups will provide models for the investigation of the relationship between nanostructures and their functions. The integration of nanoarchitecture and function in one self-assembly system is one of the ultimate goals of scientists and the best way to fabricate nanosized devices and sensors [21]. However, there is still a long way to go to bridge the gap between structural architecture and functional assemblies.

In this chapter, the assemblies of electro- and photo-active polyelectrolytes produced by the ionic self-assembly technique, based mainly on our work, will be presented and discussed in detail. All the building blocks used are shown in Fig. 11.2.

## 11.2

### Multilayer Assemblies of Electroactive Species for Chemically Modified Electrodes

The interest in chemically modified electrodes (CMEs) has increased tremendously during the last decade. To develop a general method for production of CMEs in which electroactive materials can be controlled at the molecular level and deposited in a three-dimensional manner is of importance not only in basic research but also in technical applications. It is known that there exist several strategies for fabricating high quality CMEs [22]. Covalent immobilization and self-assembly of alkanethiol-containing electroactive compounds have proved to be particularly attractive. Polymers have been coated onto electrodes by dipping, spin coating, organosilane bonding, electrochemical precipitation and polymerization, adsorption from solution, and plasma discharge polymerization, etc. However, there are also requirements to produce multilayer-based CMEs, which guarantee that both the type and quantity of electroactive materials will be loaded onto the electrode surface in a controlled way. Ionic self-assembly of charged electroactive materials may be an alternative approach to the fabrication of CMEs.

Since Sun et al. reported the first example of a chemically modified electrode fabricated by the ionic self-assembly technique in 1995 [13], the research and fabrication of CMEs or sensors based on this technique has received extensive interest. A large variety of chemically modified electrodes and sensors have been fabricated and their properties have been well studied [13, 23–30]. The ionic self-assembly technique has three main advantages over other techniques when used to fabricate CMEs: (1) It is applicable to electrodes of any material, size and topology. This is due to the self-adjusting ability of the technique, which makes the influence of the substrates on which the layers are built up decrease after several cycles of deposition. (2) It is particularly suitable for the production of chemically



modified electrodes with multi-components in a designed way. This is determined by the ability of this technique to produce three-dimensional composite multilayer assemblies. Usually, the detection of the substrates in these types of electrodes is based on a series of reactions between the substrate and the electroactive materials bound to the electrode surface. The sequence of the materials assembled on the electrode surface will play an important role in the detection of the substrate. (3) Electrodes fabricated by this technique are satisfactory with respect to their reproducibility. This originates from the ability to control the assemblies at the molecular level.

### 11.2.1

#### **Controlled Fabrication of Multilayers with a Single Active Component**

The ionic self-assembly technique can be used to fabricate layered nanoarchitectures not only for polyelectrolytes, but also for oligo-charged species, e.g., disk-shaped porphyrins and phthalocyanines containing sulfonic groups. These porphyrins and phthalocyanines are planar conjugating molecules that have unique physiochemical properties. Assembly of these molecules into multilayer assemblies can find applications in catalysis, voltaics, electrochromics and nonlinear optics, etc. Zhang et al. incorporated meso-tetra(4-sulfonylethyl)porphyrin (tpps<sub>4</sub>) or copper phthalocyanine tetrasulfonic acid, tetrasodium salt (CuTsPc) into multilayer assemblies by a method based on the ionic self-assembly technique, alternately depositing with bipolar pyridine salt (PyC<sub>6</sub>BPC<sub>6</sub>Py) [31]. Furthermore, this technique has been utilized to fabricate functional supramolecular assemblies of pure rigid porphyrin and phthalocyanine [32]. Combining the ionic self-assembly and electroanalytical chemistry, we have demonstrated a series of chemically modified electrodes of porphyrins and phthalocyanines which have the ability to detect Cu<sup>2+</sup>, I<sup>-</sup>, carbohydrates, glucose, hydrazine, etc. in solution [13, 23–25]. At the beginning of this work, single component electrodes were fabricated on which only one type of electroactive material was alternately deposited on the electrode surfaces. This method of constructing electrodes is simple, but has provided a new way to fabricate complex sensing surfaces, as summarized in Tab. 11.1.

Copper(II)-selective electrodes based on mixed copper(II) sulfide and silver(I) sulfide membranes have been reported in the past. The nature of the potential response of these kinds of electrodes is complex and their sensitivity towards copper (II) ions is lost in highly oxidizing systems or in the presence of chloride ions. Therefore the development of potentiometric copper (II) sensors with good performance remains a fascinating challenge for scientists. Herein, we discuss a new kind of copper(II)-selective electrode fabricated by alternately depositing negatively charged copper phthalocyanine tetrasulfonic acid (CuTsPc) with a bipolar pyridine salt (PyC<sub>6</sub>BPC<sub>6</sub>Py) on a gold electrode [13]. The original motivation was to characterize the multilayer assemblies of CuTsPc/PyC<sub>6</sub>BPC<sub>6</sub>Py with an electroanalytical method. We failed in this regard because of the very small redox currents. However, it shows, interestingly, a potential dependence on the copper(II) ions. Compared with conventional copper(II)-selective electrodes, it has advantages such as

Tab. 11.1 Examples of chemically modified electrodes fabricated by ionic self-assembly

Assemblies	Electrode	Detection	Comments	Ref.
CuTsPc/PyC <sub>6</sub> BPC <sub>6</sub> Py	Gold	Cu <sup>2+</sup>	1×10 <sup>-5</sup> –0.1 mol L <sup>-1</sup> , potentiometry	[13]
CoTsPc/PyC <sub>6</sub> BPC <sub>6</sub> Py	Gold	Carbohy- drates	Detection limit: 150 pmol for glu- cose, 6 pmol for maltose	[23]
CoTsPC/PyC <sub>6</sub> BPC <sub>6</sub> Py	Gold	Hydrazime	1×10 <sup>-5</sup> –1×10 <sup>3</sup> mol L	[24]
tpps <sub>4</sub> /polypyrrole	Silver	I <sup>-</sup>	1×10 <sup>-6</sup> –0.1 mol L	[25]
PVP-Os/PSS PVP-Os/PAPSAH	Gold	NO <sub>2</sub> <sup>-</sup>	PAPSAH can improve the response of the electrode	[26]
Bis-bipyridinium/Au nanoparticles	ITO	<i>p</i> -Hydroqui- none	Receptor-colloid superlattice acts as a rough interface for the precon- centration and electrochemical interface	[27]
Glucose oxidase/ferrocene derivative	Gold	Glucose	An electrical “wire” is introduced between glucose oxidase and elec- trode surface	[28]
Polyoxometalate/PVP-Os	Gold		Cyclic potential sweeps was used for the multilayer deposition	[29]
Glucose oxidase/glucoa- mylase	Gold	Maltose/ glucose	Take the co-functions of bienzyme for catalyzing	[30]

low resistance, short conditioning time, fast response and perfect operation in the presence of chloride ions.

The fabrication of CuTsPc/PyC<sub>6</sub>BPC<sub>6</sub>Py multilayer assemblies on a gold electrode is shown schematically in Fig. 11.3. A freshly cleaned gold electrode was immersed in an ethanolic solution containing 0.01 M 3-mercaptopropionic acid to get a self-assembled monolayer. Afterwards, the gold electrode with negatively charged surface was alternately immersed in aqueous solutions of PyC<sub>6</sub>BPC<sub>6</sub>Py (0.5 mg ml<sup>-1</sup>) and CuTsPc (0.1 mg ml<sup>-1</sup>), and washed with water and dried in N<sub>2</sub>. By repeating the two immersion steps in a cyclic fashion, an electrode modified with a multilayer of PyC<sub>6</sub>BPC<sub>6</sub>Py/CuTsPc can be obtained. The progressive deposition was confirmed by means of UV–Vis spectroscopy. In the experiments, a gold electrode with 6 layers of CuTsPc deposited on it was used throughout. Between measurements, the sensor was stored in a dry state at room temperature.

Fig. 11.4 shows cyclic voltammograms of a gold electrode modified with 6 layers of CuTsPc in 0.2 M acetate buffer solution (pH 4.5). It can be seen that a pair of redox peaks of CuTsPc appear in the potential range +0.8 to -0.5 V (vs. SCE) in each cyclic voltammogram. The peak current of the electrode modified with 6 bi-layers of PyC<sub>6</sub>BPC<sub>6</sub>Py/CuTsPc is proportional to the square root of the scan rate. This indicates that CuTsPc has been modified on the gold electrode and the elec-

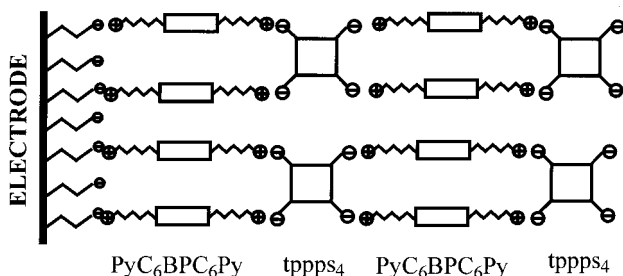


Fig. 11.3 Schematic illustration of the structure of a CuTsPc/PyC<sub>6</sub>BPC<sub>6</sub>Py modified electrode.

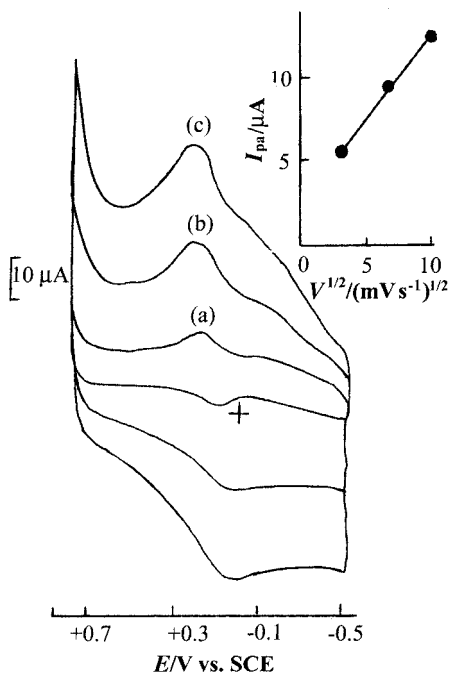


Fig. 11.4 Cyclic voltammograms of the Au electrode modified with 6 layers of CuTsPc in 0.2 M acetate buffer (pH 4.5). Scan rate: (a) 10, (b) 50, (c) 100  $\text{mV s}^{-1}$ . The inset shows anodic peak current as a function of the square root of the scan rate.

trochemical reaction in the multilayer assemblies is a diffusion-controlled redox process.

It was found that the properties of the PyC<sub>6</sub>BPC<sub>6</sub>Py/CuTsPc modified electrode were dependent on the pH of the solution. A stable response potential was obtained in a pH range of 1–5 in 0.2 M potassium nitrate in the presence of  $1 \times 10^{-3}$  M copper (II). Meanwhile, we also found that there existed a dependence of the response of the electrode on the types of buffer at the same pH value and concentration. As indicated in Fig. 11.5, the electrode has its best performance in the acetate buffer and potassium nitrate solutions, with its response slopes being 29 and 31  $\text{mV decade}^{-1}$ , respectively. In sodium dihydrogenphosphate medium, the response of the elec-

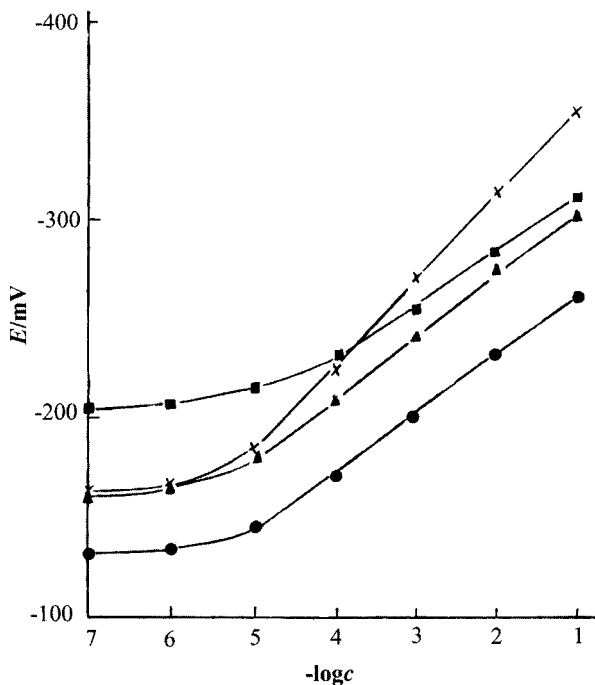


Fig. 11.5 Effects of different buffer media on the responses of the electrode to copper (II). Buffer: 0.2 M, pH 4.5, sodium dihydrogenphosphate (■); acetate (●); potassium nitrate (▲); potassium chloride (×).

trode was worst, with a response slope of 25 mV decade<sup>-1</sup> and linear range between 10<sup>-4</sup> and 10<sup>-1</sup> M. In a potassium chloride medium, the response of the electrode was good, but its response slope of 41 mV decade<sup>-1</sup> was higher than Nernstian.

From the typical calibration graph for the gold electrode modified with 6 layers of CuTsPc in an optimized condition of 0.2 M acetate buffer (pH 4.5), it can be seen that the electrode has a linear response over the range 1 × 10<sup>-5</sup> to 0.1 M with a Nernstian response slope of 29 mV decade<sup>-1</sup> and a detection limit (extrapolation of linear graph) of 7 × 10<sup>-6</sup> M. The typical dynamic response time of the electrode (*t*<sub>95</sub>) was 15–30 s with stirring. The steady state potential response after the addition of copper (II) remained constant for 60–120 s, then slowly increased in the negative direction and reached a final steady potential value.

The potential response of the electrode towards copper (II) ions has a good reproducibility. The relative standard deviation (RSD) is 1.7% for ten determinations of 1 × 10<sup>-5</sup> M Cu<sup>2+</sup> at pH 4.5 in 0.2 M acetate buffer. The selectivity of the electrode toward copper(II) is very satisfactory, as shown in Tab. 11.2. Except for Fe<sup>3+</sup>, Fe<sup>2+</sup> and Co<sup>2+</sup>, other common inorganic cations do not interfere in the determination of copper (II). The interference of Fe<sup>2+</sup> ions can be eliminated by oxidizing

**Tab. 11.2** Selectivity coefficients of CuTsPc/PyC<sub>6</sub>BPC<sub>6</sub>Py modified copper(II) selective electrode

Cation	$\log K_{ij}^{\text{pot}}$	Cation	$\log K_{ij}^{\text{pot}}$
Ca <sup>2+</sup>	-3.0	Al <sup>3+</sup>	-3.0
Mg <sup>2+</sup>	-3.0	Co <sup>2+</sup>	-1.0
Zn <sup>2+</sup>	-3.1	Mn <sup>2+</sup>	-3.0
Cd <sup>2+</sup>	-3.0	Fe <sup>3+</sup>	0
Ni <sup>2+</sup>	-3.1	Fe <sup>2+</sup>	0
Pb <sup>2+</sup>	-3.2		

them to Fe<sup>3+</sup>, which can be masked with F<sup>-</sup> ions. Anions such as NO<sub>3</sub><sup>-</sup>, Cl<sup>-</sup>, acetate and SO<sub>4</sub><sup>2-</sup> do not interfere with copper (II) during the detection.

As metallophthalocyanines and porphyrins represent a family of compounds well known for their catalytic activity for a wide range of redox processes, a similar concept can be applied to fabricate chemically modified electrodes with designed sensing properties. When CuTsPc is replaced by cobalt phthalocyanine tetrasulfonate (CoTsPc), PyC<sub>6</sub>BPC<sub>6</sub>Py/CoTsPc alternating assemblies can be fabricated similarly on gold electrodes. It was found that the gold electrode modified with 6 bilayers of PyC<sub>6</sub>BPC<sub>6</sub>Py/CoTsPc exhibited an excellent electrocatalytic response for the oxidation of hydrazine, therefore it could act as an amperometric sensor of hydrazine [24]. In combination with flow-injection analysis, hydrazine can be detected with high sensitivity using the above electrode. The linear response of the electrode towards hydrazine ranges from 1×10<sup>-3</sup> to 1×10<sup>-6</sup> M, with a detection limit of 6×10<sup>-7</sup> M. Meanwhile, this electrode also shows an electrocatalytic response for the oxidation of carbohydrates, such as glucose, fructose, sucrose and maltose, as shown in Tab. 11.1 [23]. Furthermore, tetraphenylporphine tetrasulfonic acid (tpps<sub>4</sub>) can alternately assemble with polycationic polypyrrole on a silver electrode, which can act as a potentiometric sensor for iodide ions [25]. The electrode has good selectivity compared with a poly[tetrakis(*p*-aminophenyl)porphyrin] film-modified electrode.

As mentioned, the above electrodes fabricated by the ionic self-assembly technique have many advantages. Among them, the incorporation of more than one kind of correlative electroactive species in a designed way, which may endow the electrode with novel functions by a synergetic effect of these electroactive species giving better results than any one of them alone.

### 11.2.2

#### Controlled “Cascade” Modification with Binary Active Components

The assembly of ultrathin films containing biological macromolecules such as proteins and DNA has attracted considerable interest, e.g. for the construction of bioreactors and biosensors containing enzymes and other biological catalysts. Protein can be adjusted to be anionically or cationically charged by simply changing the pH value of the solution to be higher or lower than its isoelectric point (IEP). In this sense, proteins can be treated as anionic or cationic polyelectrolytes and al-

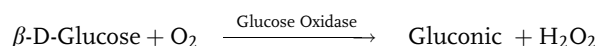
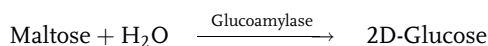
ternately assemble with oppositely charged species. Kong et al. extended the concept of Decher and immobilized glucose isomerase in a layer-by-layer fashion by alternating deposition with a bipolar amphiphile [33]. Moreover, the same concept was applied to enzyme immobilization in porous trimethylamine polystyrene [34]. To our knowledge, this is the first demonstration of ionic self-assembly on a non-flat substrate. At almost the same time, Lvov et al. constructed multilayer films containing DNA [35], biological colloids such as charged virus particles [36], and many other enzymes such as myoglobin (Mb), lysozyme (Lys), hemoglobin (Hb) and glucose oxidase (GOD), etc. [37]. The possibility of creating ordered protein layers on a solid substrate opens the way for microreactors and biosensors.

#### 11.2.2.1 Bienzyme Assemblies of Glucose Oxidase and Glucoamylase

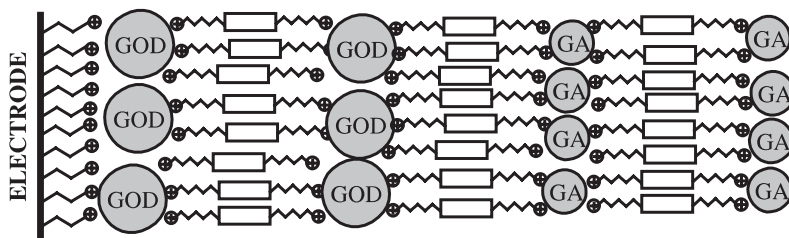
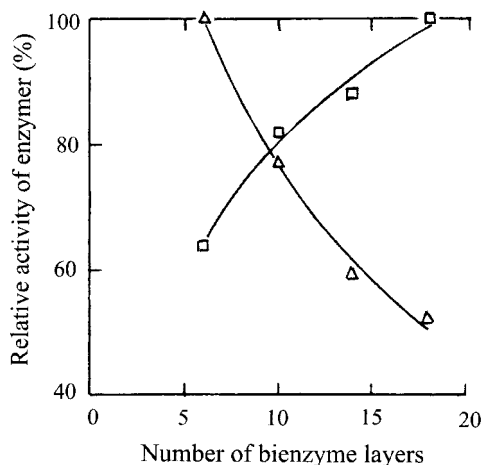
Glucose oxidase (GOD) and glucoamylase (GA) are widely used enzymes in the fields of enzyme engineering and biosensors. Sun et al. selected GOD and GA as a model system to demonstrate the possibility of incorporating these two enzymes in one-multilayer assembly. GOD and GA have IEPs of pH 4.3 and 4.2, respectively. Under a deposition condition of pH 7.0, both enzymes can become negatively charged. So a positively charged bipolar quaternary ammonium salt  $\text{NC}_6\text{BPC}_6\text{N}$  was used to alternately assemble with these two enzymes. An enzyme multilayer film was fabricated in which GOD and GA are alternately sandwiched between the bi-cationic compound  $\text{NC}_6\text{BPC}_6\text{N}$  [30]. Quartz crystal microbalance (QCM) measurements show that both GOD and GA are loosely, rather than densely packed in the film. The relatively loose packing of enzymes is favorable for the easy diffusion of the substrate in the film, which will guarantee that the reaction of the substrate with the immobilized enzyme proceeds smoothly.

Fig. 11.6 shows the change in overall activity of the bienzyme in multilayers with the number of layers. The total activity increases with the number of layers, which means the higher the number of layers deposited, the more enzyme is immobilized. On the other hand, since the diffusion of the substrate plays an important role in the determination of enzyme activity, the average activity per enzyme layer decreases with the increase in the number of layers. These results are consistent with those reported previously.

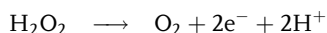
In the electrochemical experiment, two layers of GOD followed by two layers of GA were alternately deposited with  $\text{NC}_6\text{BPC}_6\text{N}$  on the surface of a 3-mercaptopropionic acid modified gold electrode. The conceptual construction of bienzyme multilayer assemblies is shown schematically in Fig. 11.7. The enzymes were arranged in this way in the multilayer film because of the coupled reaction between GOD and GA, as shown below:



**Fig. 11.6** Relationship between relative activity and the number of bienzyme layers. Total activity of bienzyme layers on the slide ( $\square$ ); average activity per bienzyme layer ( $\triangle$ ). (Total activity of 18 layers of bienzyme is defined as 100% in curve ( $\square$ ); average activity of 6 layers of bienzyme is defined as 100% for curve ( $\triangle$ )).



**Fig. 11.7** The schematical construction of a bienzyme multilayer of GOD and GA on a gold electrode surface.



The resulting multilayer can act as a maltose sensor in which maltose can first react with outside GA layers to produce glucose.  $\beta$ -D-glucose then diffuses and reacts with the inside GOD layers to produce  $\text{H}_2\text{O}_2$ , which is oxidized on the electrode surface and detected. Fig. 11.8 shows a typical maltose response curve, from which it can be seen that the time required to reach 95% of the steady-state current is less than 60 s after the addition of maltose. The calibration curve for the determination of maltose is given in Fig. 11.9. A linear relationship up to 6  $\text{mmol L}^{-1}$  was obtained between the response current and the maltose concentration. In comparison with a similar electrochemical sensor, the uppermost detection concentration of the present sensor is higher. The reason being that the multilayer limits the diffusion of the substrate and reduces the effective substrate concentration within the enzyme layer to well below the saturation threshold.

It was confirmed that only when GA and GOD are fabricated rationally on the surface of gold electrode could the sensor be used to detect maltose. The GA as-

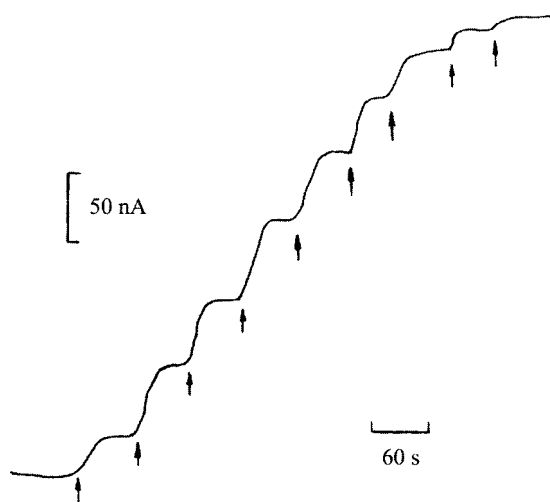


**Fig. 11.8** Typical response of the sensor to addition of maltose. Arrows indicate the addition of 0.1 mL of 0.1 M maltose to the test solution (initial solution volume 10 mL). Operating potential controlled at +0.7 V vs. SCE. 0.1 M phosphate buffer of pH 7.0 was used as the supporting electrolyte.

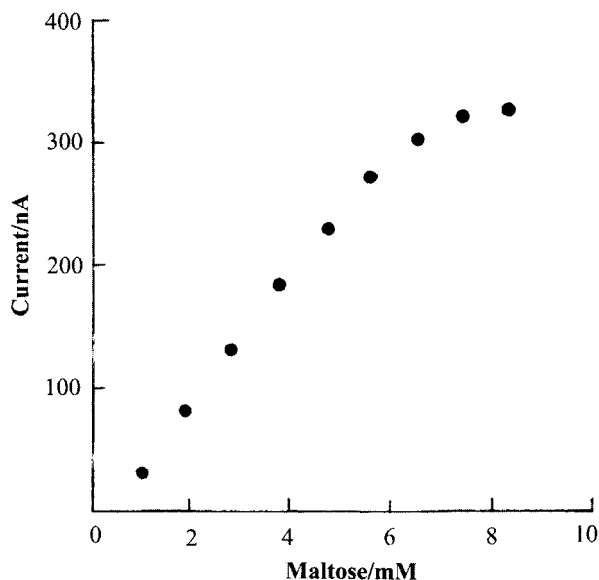


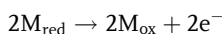
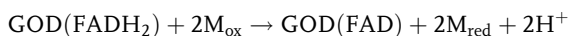
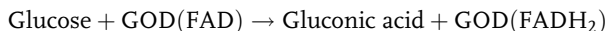
**Fig. 11.9** Relationship between steady-state current and concentration of maltose.

sembled alone on the gold electrode does not have the ability to detect maltose. This supports the idea that new functions could come from assemblies. Meanwhile, it was discovered that the gold electrode fabricated with GOD and GA can catalyze the oxidation of glucose due to the existence of the inner GOD layers. For the determination of either maltose or glucose, the current response examined was all the oxidizing current of  $H_2O_2$  that was produced in the enzymatic reactions.



### 11.2.2.2 Alternating Assemblies of Glucose Oxidase and Polycationic Electron Transfer

The redox active centers of GOD, i.e., flavin adenine dinucleotide (FAD)/hydrogenated flavin adenine dinucleotide (FADH<sub>2</sub>) are situated at the inner core of the glycoprotein, and covered by a non-conducting oligosaccharide shell. This makes direct electron transfer between GOD and the electrode surface on which it was immobilized difficult. An efficient method to solve this problem is to establish an easy electrical communication between GOD and the electrode surface by using an electron mediator. Its role can be described as follows:



Here GOD(FAD) and GOD(FADH<sub>2</sub>) represent oxidized and reduced forms of GOD, M<sub>ox</sub> and M<sub>red</sub> the oxidized and reduced forms of the mediators. The intimate contact between the GOD redox centers and the electroactive species facilitates the flow of electrons from the enzyme to the electrode surface.

Combining the enzyme assembly with the concept of electron transfer, we have realized alternating assemblies of GOD and quarternized poly(4-vinylpyridine) partially complexed with [Os(bpy)Cl]<sup>+ / 2+</sup> (PVP-Os) on the surface of a gold electrode [38, 39]. The ideal structure of PVP-Os/GOD multilayer assemblies on the surface of a gold electrode is shown in Fig. 11.10. As indicated in this figure, the adsorbed PVP-Os on the underlayer GOD could fold along the enzymes and penetrate into them, thus mediating electron transfer from the FADH<sub>2</sub> center of the enzyme to the electrodes. Fig. 11.11 shows the response of a 3-bilayer PVP-Os/GOD modified gold electrode in the presence of 40 mM glucose. In the absence

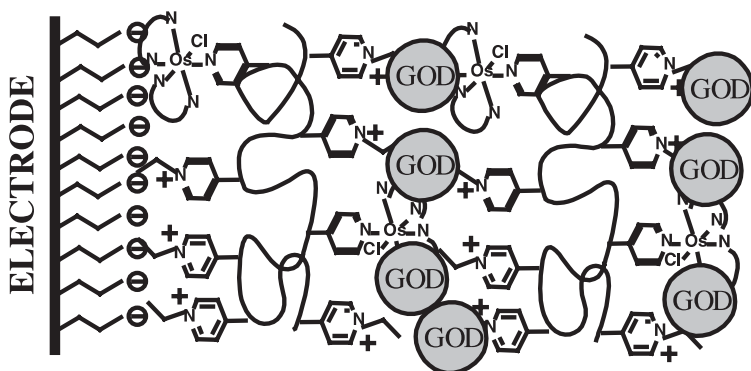


Fig. 11.10 The ideal structure of PVP-Os/GOD multilayer assemblies on the surface of a gold electrode.

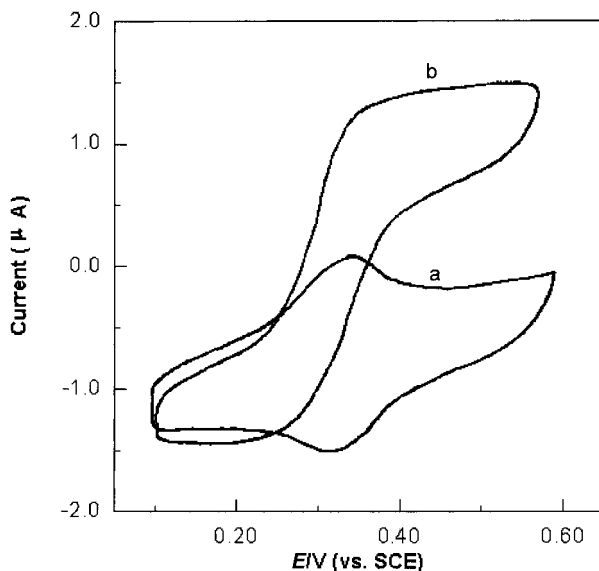


Fig. 11.11 Cyclic voltammograms of the three bilayers of a PVP-Os/GOD modified electrode (a) without glucose and (b) in the presence of  $40 \text{ mmol l}^{-1}$  of glucose. Conditions:  $0.1 \text{ mol l}^{-1}$  phosphate buffer, pH 6.4; scan rate  $5 \text{ mV s}^{-1}$ .

of glucose, a pair of cathodic/anodic peaks of almost equal magnitude could be observed over the range 0.1 to 0.6 V (vs. Ag/AgCl), which corresponds to the reversible redox reaction of PVP-Os. Upon addition of glucose, an obvious increase in the oxidative current and concomitant decrease in the reductive current were found, indicating that GOD was reduced by glucose diffusing into the assembled films, then electrons were transferred through the polymer bearing osmium complex films to the electrode surface. From the dependence of the glucose catalytic oxidation current on the electrode potential, the optimized potential for the detection of glucose could be selected as 0.35 V (vs. SCE), which is much lower than without electron transfer. At this low potential, the influence of some interfering materials, such as ascorbic acid and uric acid can be largely eliminated.

### 11.2.3

#### The Incorporation of Conductive Species to Improve the Performance of the Modified Electrodes

It thus has been proven that the ionic self-assembly technique is a very easy and efficient way to fabricate a composite film modified electrode, in which more than one kind of electroactive material can be incorporated in the normal direction of the electrode surface. The properties of the electroactive material in the multi-layer-modified electrode will depend much on the way it is assembled. It is meaningful to investigate the structure-related function in multilayer-modified electro-

des in order to find a general way to improve their performance. We have studied comparatively the molecular assemblies of PVP-Os with the conductive polyanion of poly(aniline-*co*-*N*-propanesulfonic acid aniline) (PAPSAH) [40] and the non-conductive polyanion of poly(sodium 4-styrene sulfonate) (PSS) in an attempt to find a way to improve the performance of the chemically modified electrodes fabricated by the ionic self-assembly technique [26].

Two kinds of electrodes were fabricated. The electrode modified with PVP-Os/PSS was denoted electrode I, and that modified with PVP-Os/PAPSAH was denoted electrode II. Cyclic voltammetry was employed to characterize the electrochemical properties of the modified electrodes. The resulting cyclic voltammograms (CVs) of electrode I (PVP-Os + (PSS/PVP-Os)<sub>5</sub>) and electrode II (PVP-Os + (PAPSAH/PVP-Os)<sub>5</sub>) in 0.2 M Na<sub>2</sub>SO<sub>4</sub> (pH 1.0, adjusted by H<sub>2</sub>SO<sub>4</sub>) at different scan rates are shown in Fig. 11.12(A) and (B), respectively. For electrode I, only one pair of anodic/cathodic peaks appears with formal potential ( $E_{1/2}$ ), taken as the average value of the anodic and cathodic peak potentials, of 340 mV, which is related to the Os<sup>2+</sup>/Os<sup>3+</sup> redox couple in PVP-Os. While, for electrode II, two pairs of anodic/cathodic peaks appear with  $E_{1/2}$  peaks at 150 mV and 295 mV, which correspond to those of PAPSAH and PVP-Os, respectively. As can be seen, with increasing scan rate, the anodic/cathodic peak currents of PVP-Os in both electrodes increase linearly in the range from 10 to 200 mV s<sup>-1</sup>, which indicates a surface redox process. Comparing the CVs of electrodes I and II, it is obvious that electrode II yields more symmetrical voltammograms, e.g., at a scan rate of 200 mV s<sup>-1</sup>, the peak-to-peak separation was 30 mV for electrode II and 80 mV for electrode I (with respect to the redox peak of PVP-Os on both electrodes). This shows that the electron transfer on electrode II is much easier than that on electrode I.

We further examined the dependence of the electrode response on the number of deposition layers for electrodes I and II. There exists a critical number of deposition layers (CNDL) for both electrodes, beyond which the electrode response begins to decrease. The existence of a CNDL in a multilayer-modified electrode is related to the vertical electron transfer within the film. Fig. 11.13 shows the dependence of the cathodic peak currents of both electrodes on the number of PVP-Os layers deposited, from which it can be seen that the CNDLs for electrodes I and II are 8 and 12, respectively. This confirms again that by replacing PSS with PAPSAH, electron transfer becomes much easier.

It is found that both electrodes consisting of PVP-Os have the ability to catalyze the reduction of nitrite in 0.2 M Na<sub>2</sub>SO<sub>4</sub> (pH 1.0). Catalytic currents obtained on both electrodes with an operating potential controlled at 200 mV (vs. SCE) are proportional to the concentration of nitrite as shown in Fig. 11.14(A) and (B). It is worth noting that the reduction currents of electrode II are much larger than those at electrode I.

Based on the difference in peak-to-peak separation, CNDL and the response to nitrite reduction, it has been proven that by replacing PSS with PAPSAH, the performance of the resulting PVP-Os modified electrode can be improved to some extent. The only difference between these two electrodes is the polyanions used. For electrode I, PSS is nonconductive and should act as a barrier to electron transfer

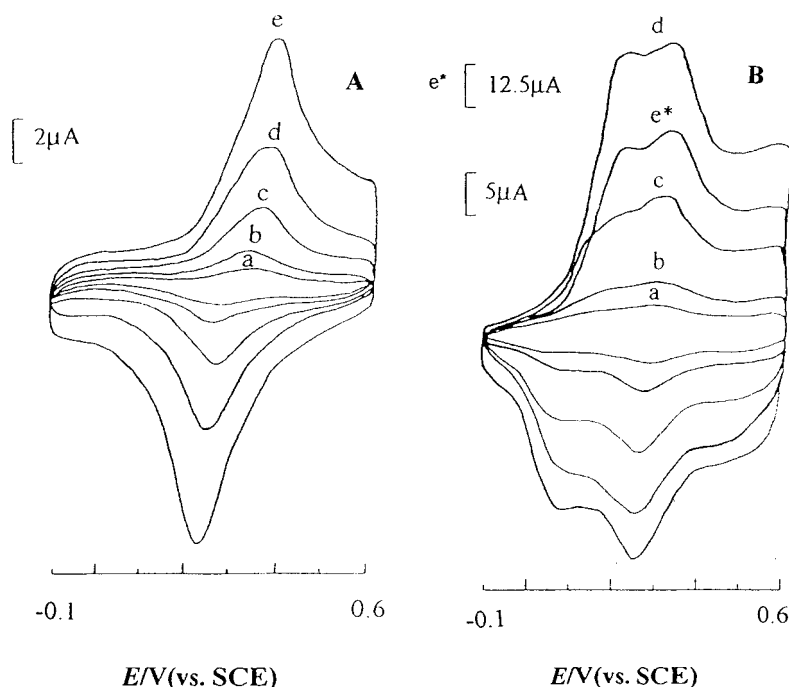


**Fig. 11.12** Cyclic voltammogram of (A) electrode I and (B) electrode II in 0.2 M  $\text{Na}_2\text{SO}_4$  at pH 1.0. Electrode I consists of 1 layer of PVP-Os and 5 bilayers of PSS/PVP-Os, while

electrode II consists of 1 layer of PVP-Os and 5 bilayers of PAPSAH/PVP-Os. Scan rates ( $\text{mV s}^{-1}$ ): (a) 10, (b) 20, (c) 50, (d) 100 and (e) 200.

within the film, whereas, for electrode II, PAPSAH is conductive and should thus facilitate the electron transfer. In our experiment, the supporting solution used was 0.2 M  $\text{Na}_2\text{SO}_4$  with pH 1.0. It is believed that the acidic condition of the solution may help to keep the PAPSAH layers more conductive. Thus, PAPSAH incorporated between PVP-Os layers may act as a conductive “wire” and decrease the ohmic film resistance, which provides a way for easy transfer of electrons.

From the view of increasing the electrical conductivity of the multilayer film to improve the performance of the electrode, it is believed that the incorporation of Au nanoparticles should have a similar effect to that of the conductive polymer PAPSAH. Au nanoparticles have good conductivity and their surface is easily modified negatively or positively making it suitable for assembling with any charged electroactive materials. Another advantage of Au particles as linker between electroactive PVP-Os or other electroactive materials is that, in general, the roughness of the particle-covered surface is greater than that of the polymers which can increase largely the area of the electrode, and thus the amount of electroactive materials immobilized. To increase the load of the electroactive materials on the electrode surface by a simple and general method is very important in practical applications because it can improve the sensitivity and detection limit of

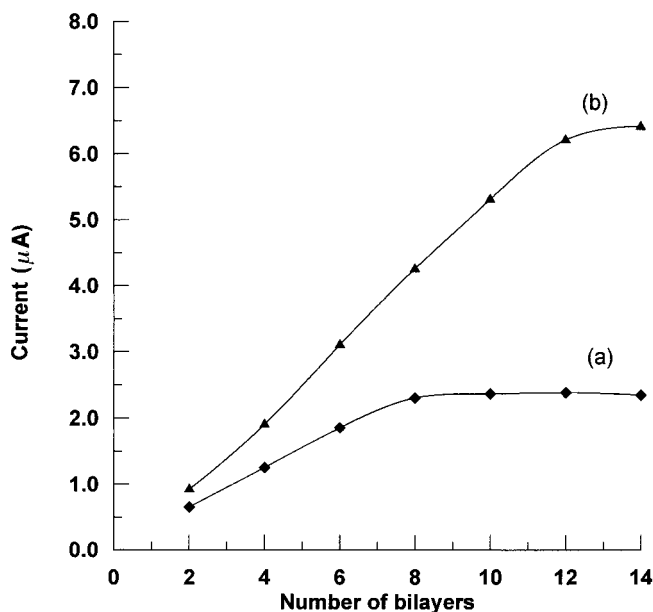


Fig. 11.13 Dependence of cathodic peak current on the number of PVP-Os layers deposited. (a) electrode I and (b) electrode II. Scan rate:  $70 \text{ mV s}^{-1}$ .

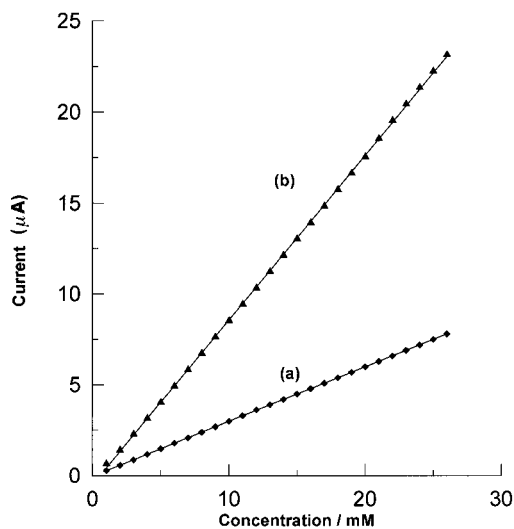


Fig. 11.14 The calibration curves of current vs. nitrate concentration (a) on electrode I and (b) on electrode II.

the resulting chemically modified electrode. Briefly, by carefully choosing the conductive species as counterpart for the construction of a multilayer-modified electrode, the performance of the resulting chemically modified electrode can be optimized to some extent.

## 11.3

## Ionic Self-assembly of Photoactive Materials and the Fabrication of "Robust" Multilayer

The neighboring layers of an ionically self-assembled multilayer are held together by electrostatic interaction or ionic bonds. The stability of this kind of multilayer assembly can be affected by the environmental conditions, e.g., the type of solvent, ionic strength, pH of the solvent, etc. In some cases, the stability of the films is particularly important. Films having the ability to resist the etching of some special solvents and to work under more severe conditions are required. Since the covalent bond is, in general, stronger than the electrostatic interaction, it is reasonable to use covalent bonds instead of electrostatic interaction to form stable multilayer assemblies. The traditional method using stepwise chemical reaction to fabricate covalently attached multilayer films is one of the choices, but suitable chemical reactions are limited and tiresome work is involved. We have considered whether or not we can make use of the simplicity of the ionic self-assembly technique in operation and the subsequently induced reaction within multilayers to get covalently attached multilayer assemblies. The possibility of achieving this hinges on the discovery of charged pair groups which can undergo reaction to form covalent bonds. It is well known that diazonium groups can undergo photoreaction with a variety of polyions containing sulfonate or acrylic acid groups under UV irradiation or by heating. By deliberately choosing a photoreactive diazo-resin (DAR) as the polycation and combining its post photoreaction with sulfonate groups induced by UV irradiation, we successfully achieved this, as shown in Fig. 11.15 [41]. The stability of the thus-fabricated multilayer assemblies improved remarkably, as expected. Till now, we have fabricated stable multilayer assemblies from polyanions containing sulfonate and carboxylic acid groups, e.g. (PSS), PAPSAH, oligo-charged organic molecules, inorganic colloids and poly(acrylic acid) (PAA) [42–46]. Along the same line of research, Bruening et al. used poly(allylamine hydrochloride) (PAH) and PAA to construct multilayer films, and the following heat treatment induced the formation of amide bonds, through which the films were crosslinked thus improving their stability greatly [47]. A variety of other crosslinked multilayer films which employed the photo-induced addi-

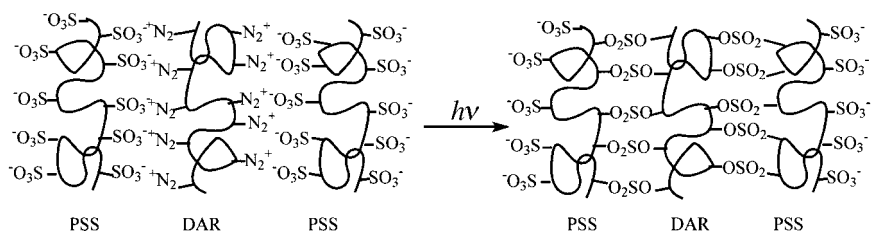


Fig. 11.15 Schematic representation for structure changes of multilayer assemblies from ionically to covalently attached upon UV irradiation.

tive reaction of oligo-molecules containing double carbon-carbon bonds within the layers have also been constructed.

### 11.3.1

#### Ways to Fabricate Covalently Attached Multilayer Assemblies

In general, the above way to fabricate covalently attached multilayer assemblies involves two steps: ionic self-assembly followed by UV irradiation. Take the fabrication of covalently attached DAR/PSS multilayer on a positively charged substrate for example [41, 42]. First, an electrostatic interaction based multilayer of DAR/PSS is obtained by alternately dipping the substrate in aqueous solutions of PSS and DAR. Next, the films are exposed to UV irradiation for a given time to ensure complete photoreaction. In this way, the covalently attached multilayer films can be obtained. It is worth noting that the ionic self-assembly step must be conducted in the dark to avoid decomposition of the DAR.

UV-Vis spectroscopy was used to follow the ionic self-assembled multilayer fabrication process. Fig. 11.16 shows the UV-Vis absorption spectra of 2, 4, 6 and 8 bilayers of DAR/PSS assembled on a quartz slide. The absorbance at 380 nm was attributed to the  $\pi-\pi^*$  transition of the diazonium group. The linear increase in absorbance at 380 nm with the number of layers indicates a progressive deposi-

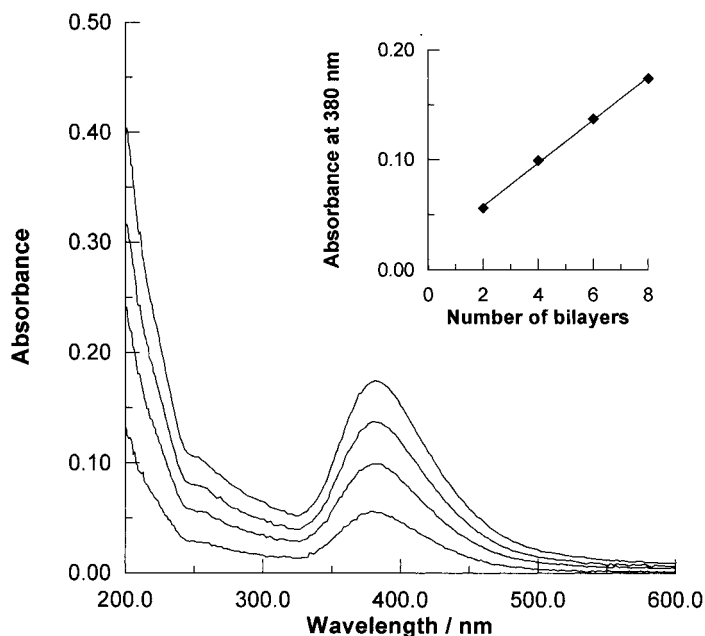
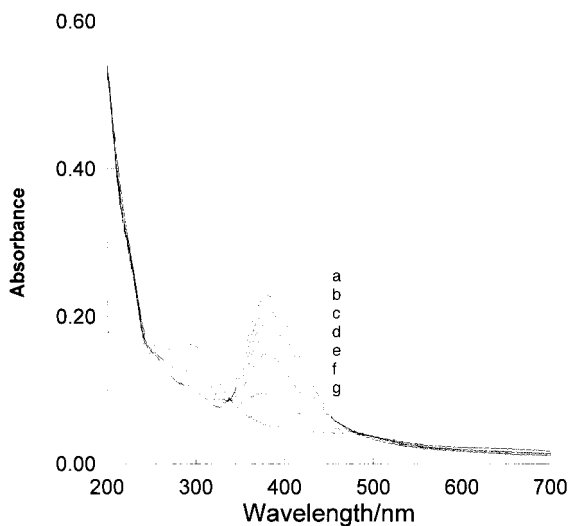


Fig. 11.16 UV-Vis absorption spectra of multilayer films of DAR/PSS. From the lower to upper, the number of bilayers is 2, 4, 6 and 8. Inset shows the absorbance at 380 nm vs. the number of bilayers.

tion with almost equal amount of deposition of the polyions in each cycle. Owing to the well known high reactivity of diazonium and sulfonate groups, the above assembled films containing 8 bilayers of DAR/PSS were irradiated with a 30 W mercury lamp at a distance of 10 cm. Fig. 11.17 shows the changes in the UV-Vis spectra of the films with irradiation time, from which we can clearly see that with UV irradiation, the diazonium groups decomposed with a dramatic decrease in the absorbance at 380 nm and a concomitant increase in the absorbance in the vicinity of 290 nm. At the same time, an isosbestic point at 332 nm appears. Throughout the experiment, it was found that the decomposition proceeded completely within 5 min. The presence of photo-induced sulfonic ester within the layers was confirmed by FTIR. The photoreaction between diazonium connected phenyl and sulfonate groups takes place, as shown in Fig. 11.18. First, DAR was converted into its phenyl cationic form after releasing  $N_2$  upon UV irradiation, then an  $S_N1$  type of nucleophilic reaction by sulfonate occurred.

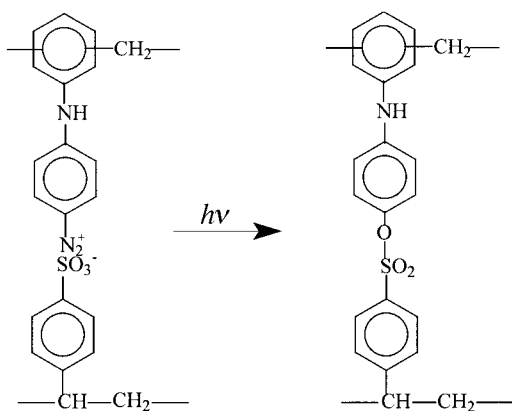
The photoreaction in between the film can also be confirmed by the improved stability of the film after UV irradiation. The ionically assembled film of DAR/PSS was etched by immersing in a ternary mixture of  $H_2O$ -DMF- $ZnCl_2$  (3:5:2, w/w/w) to test its stability. The ternary system was chosen because of the high solubility of the DAR/PSS polyelectrolyte complex in this solvent. Nearly 30% of the assembled film was dissolved after 5 min immersion, according to the decrease in absorbance at 250 and 380 nm. This result shows that this type of ionically self-assembled film is not adequately stable in the ternary solvent. As a comparison, we etched the irradiated film by sonicating it in the same ternary solvent



**Fig. 11.17** UV-Vis absorption spectra of eight bilayers of DAR/PSS upon UV irradiation for (a) 0 s, (b) 20 s, (c) 40 s, (d) 1 min, (e) 1.5 min, (f) 3 min and (g) 5 min.



**Fig. 11.18** Photoreaction between diazonium connected phenyl and sulfonated groups in DAR/PSS multilayer assemblies.



for 0.5 h. No detectable damage of the film was found, according to the absorbance at 250 nm, indicating a much greater stability of the UV irradiated film. Photoreaction changes the crosslinking structure of multilayer films from ionic to covalent bonds so that a three-dimensional network is formed which covers the whole substrate including the four side faces. This can explain why, although the interaction between the substrate and the first layer of multilayer films was not covalent, the films were stable in many solvents, like MeOH, DMSO, DMF,  $\text{CHCl}_3$ , and even the ternary solvent as described previously.

It has been observed that the thickness of an individual adsorbed polyion layer can be influenced by the ionic strength of the solution, changed by adding inorganic salt or adjusting its concentration. In our experiment, we kept the concentration of PSS at  $1.0 \text{ mg ml}^{-1}$  while changing the concentration of DAR or adding NaCl to DAR solution to realize thickness tuning of the films. Three cases were investigated, (1) DAR  $1.5 \text{ mg ml}^{-1}$  dissolved in  $0.5 \text{ M NaCl}$ ; (2) DAR  $1.5 \text{ mg ml}^{-1}$ ; (3) DAR  $0.3 \text{ mg ml}^{-1}$ . Thickness measurements by X-ray diffraction were performed on the above samples after UV irradiation. As shown in Fig. 11.19, a series of well resolved Kiessig fringes is found in all cases, which proves the homogeneousness of the films. The existence of only Kiessig fringes but no Bragg peaks was similar to typical polycation/polyanion systems based on electrostatic interaction, indicating an interpenetrating structure between the layers. For a quartz slide covered with 10 bilayers of DAR/PSS deposited from solutions of different concentration or ionic strength of DAR after UV irradiation, the total thickness of films in the cases (1), (2) and (3) was calculated to be about 23.4 nm, 16.8 nm and 15.2 nm, respectively. So the thickness of one bilayer can be tuned in the range  $15 \text{ \AA}$  to  $23 \text{ \AA}$  by simply changing the ionic strength or the concentration of DAR solution. The control of the individual layer thickness of polyion deposited is simply due to the well-known changes in the coil structure of the polyions in solutions of different ionic strength. Most importantly, all films after UV irradiation were very stable in the ternary solvent, examined in the same way as described before. This means that this method of fabricating covalently attached multilayer

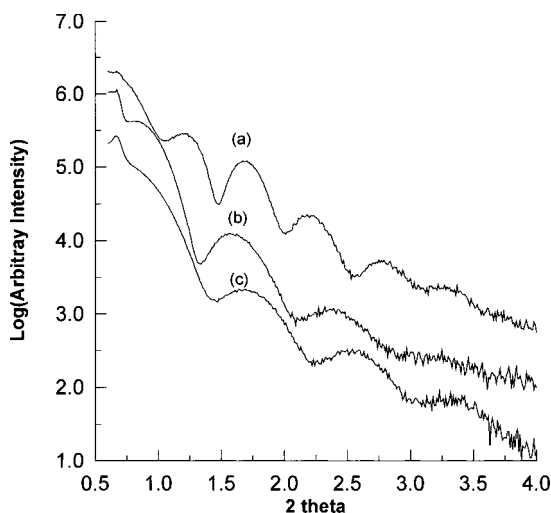


**Fig. 11.19** X-ray diffraction of 10-bilayer DAR/PSS film deposited on quartz slides. (a) DAR  $1.5 \text{ mg ml}^{-1}$  dissolved in  $0.5 \text{ M NaCl}$ ; (b) DAR  $1.5 \text{ mg ml}^{-1}$ ; (c) DAR  $0.3 \text{ mg ml}^{-1}$ .

film is applicable for multilayers whose individual layer thickness can be tuned in a wide range.

By using a heat treatment after ionic self-assembly, Bruening et al. developed a way of fabricating a kind of passivating, nylon-like coating through crosslinking ultrathin polyelectrolyte film [47]. First, multilayer assemblies of poly(allylamine hydrochloride) (PAH) and poly(acrylic acid) (PAA) were fabricated by the ionic self-assembly technique, then the film was heated at  $130^\circ\text{C}$  or  $215^\circ\text{C}$  for some time under  $\text{N}_2$  atmosphere. In this way, crosslinking between the ammonium groups of PAH and the carboxylate groups of PAA occurs through formation of an amide bond, as confirmed by FTIR spectroscopy. The change in the structure of the PAH/PAA film after heat treatment is shown in Fig. 11.20. Both cyclic voltammetry and impedance spectroscopy show that the film permeability decreases dramatically upon cross-linking and depends on the heating conditions. Crosslinking of a PAH/PAA multilayer film stabilizes the film over a wide pH range. These nylon-like, crosslinked films could find potential applications as ultrathin membranes or corrosion-resistant coatings.

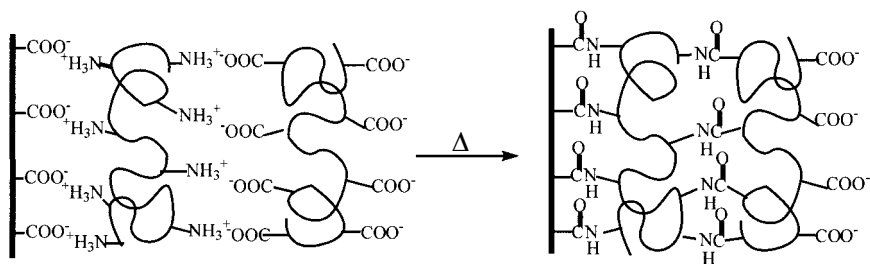


**Fig. 11.20** The chemical reaction in PAH/PAA multilayer assemblies after heat treatment.

## 11.3.2

**Stable Entrapment of Oligo-charged Molecules Bearing Sulfonate Groups in Multilayer Assemblies**

As mentioned before, the ionic self-assembly technique has provided an effective way to realize the three-dimensionally layered assembly of oligo-charged organic molecules. Compared with the polycation/polyanion assemblies, a multilayer containing small organic molecules is even less stable because the bonding sites on small organic molecules are relatively fewer. As a continuous program of work, we have further developed this method in an attempt to realize the stable entrapment of organic dyes bearing sulfonate groups [44, 46]. Covalently attached multilayer assemblies were fabricated by exposing the assemblies of DAR and a variety of organic dyes bearing sulfonate groups, ranging from 2 to 4 per molecule, such as tpps<sub>4</sub>, CuTsPc, SNAN and BST. As indicated in Tab. 11.3, the stability of the films after UV irradiation improved greatly compared with those before UV irradiation. However, it failed to stabilize each small molecule in the film because the reaction between diazonium and sulfonate in the film cannot reach 100%. By covering the DAR/dye assemblies with additional layers of photoreactive DAR/PSS or fabricating DAR/dye/DAR/PSS alternate film, the stability of dyes in the assemblies will be further improved.

The electrochemical response of Fe(CN)<sub>6</sub><sup>3-/4-</sup> on DAR/tpps<sub>4</sub> film was largely suppressed after UV irradiation. This means that the UV irradiation made the film more impermeable. As for a 6 bilayers tpps<sub>4</sub>/DAR covered ITO electrode, after UV irradiation, the electron communication between the ITO electrode and Fe(CN)<sub>6</sub><sup>3-/4-</sup> could be blocked almost completely. The impermeability of the film makes it a good candidate for corrosion prevention but not for multilayer-film-based sensors. A sensor requires the film to be both stable and permeable. How to make the film stable and permeable at the same time becomes crucially important for its applications in multilayer-film-based sensor. It was found that solvent etching the covalently attached film could make it more permeable. As shown in Fig. 11.21(a), an ITO electrode covered with 3 bilayers of DAR/tpps<sub>4</sub> film was scanned in 0.1 M KCl solution containing 1 mM Fe(CN)<sub>6</sub><sup>3-</sup>, the peak currents are very small. After sonicating this electrode

**Tab. 11.3** Stability test of small molecules bearing sulfonate groups in the multilayer assemblies of DAR/dyes

Multilayer assemblies	Fraction desorbed <sup>a)</sup>				
	a	b	c	d	Absorbance/nm
(DAR+tpps <sub>4</sub> )*8+DAR	84	91	5.6	11	426
(DAR+CuTsPc)*8+DAR	71	83	6.8	12	232
(DAR+SBT)*8+DAR	47	72	9	12	284
(DAR-SNAN)*8+DAR	70	80	7	23	535

a) a: Immersion for 5 min (before UV irradiation); b: Sonicated for 5 min (before UV irradiation); c: Immersion for 5 min (after UV irradiation); d: Sonicated for 5 min (after UV irradiation).

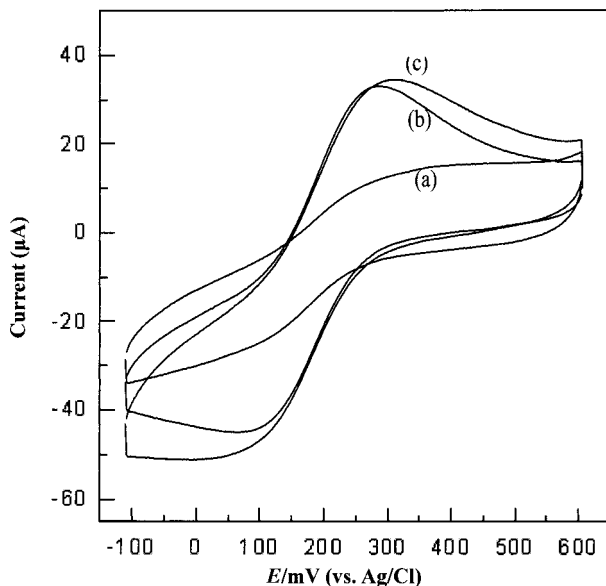


**Fig. 11.21** CVs of a (DAR+tpps<sub>4</sub>)\*3 + DAR modified ITO electrode (a) after UV irradiation, (b) after sonication for 5 min in ternary solvent and (c) after another 5 min sonication in ternary solvent. Conditions: 0.5 M KCl solution containing 1 mM Fe(CN)<sub>6</sub><sup>3-</sup>, scan rate: 100 mV s<sup>-1</sup>.

in ternary solvent for 5 min, the peak currents increase obviously (Fig. 11.21 (b)). Another 5 min sonication increased the peak currents lightly again but not as much as the first sonication did (Fig. 11.21 (c)). We would speculate that the solvent etching of the unreacted absorbates would be responsible for the increasing permeability, and the reacted tpps<sub>4</sub> in the film is stable enough to resist further solvent etching. It is believed that the permeability of the resulting film could be controlled easily by many factors, e.g., by the reaction ratio, by trapping some larger template molecules or by replacing DAR with diazonium-containing copolymers. The possibility to covalently entrap electro-active species in the multilayer assemblies, combined with the high permeability caused by solvent etching should make this technique a preferred candidate for the fabrication of stable chemically modified electrodes.

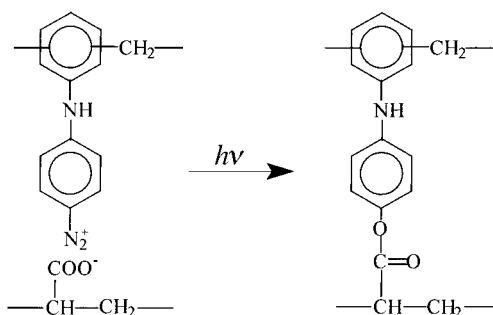
### 11.3.3

#### Covalently Attached Multilayer Assemblies of Polycationic Diazo-resins and Polyanionic Poly(Acrylic Acid)

Acrylic acid-containing materials are another kind of everyday used negatively charged species. Now it is important to know whether this new method of fabricating covalently attached multilayer film is applicable for acrylic acid-containing species. Herein, we choose poly(acrylic acid) (PAA) as a model material to investi-

gate the possibility of using this method to fabricate DAR/PAA covalently attached multilayers [45]. It was well demonstrated that DAR could alternately assemble with PAA in aqueous solution to form multilayer assemblies. Within the PAA chain, there are two kinds of groups, acrylic acid and acrylate. The ratio of these two groups is dependent on the pH of the solution. Therefore the driving force for the assembly is based on a combination of electrostatic interaction between diazonium and acrylate groups and hydrogen bonds between secondary amine and acrylic acid groups. Upon UV irradiation, a partially covalently attached multilayer of DAR/PAA can be formed, which improves the stability of the resulting film greatly compared with that without UV irradiation. The reaction in the DAR/PAA film is shown in Fig. 11.22 (A). Since PAA is a weak polyelectrolyte, the

A



B

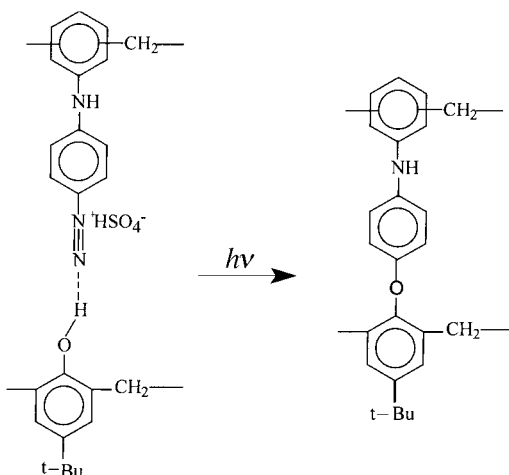


Fig. 11.22 Photoreaction of (A) DAR and PAA, (B) DAR and PR in the multilayer assemblies.

conformation of PAA chains is very sensitive to the change in pH of the solution. By changing the pH of the PAA solution, the thickness of an individual layer can be finely tuned on the nanometer scale. One more interesting example is concerned with hydrogen bonding directed self-assembly and post-chemical reaction to fabricate covalently attached films. Cao et al., reported the fabrication of alternately assembled multilayer film of DAR and phenol-formaldehyde resin (PR) based on hydrogen bonding as the driving force [48]. UV irradiation converted the hydrogen bonds into a covalently attached multilayer, as shown in Fig. 11.22(B). Its stability towards polar solvents was proved to increase dramatically. We would anticipate that the same concept might be applied to other building blocks bearing carboxylic and phenol groups.

#### 11.3.4

##### **Robust Nanoassemblies with Complex and Hybrid Structures**

The improved stability leads to these kinds of covalently attached multilayer assemblies finding applications in a wider range. When functional species were incorporated, functional assemblies with high stability could be obtained. For example, when an electroactive material was used, this technique could produce a chemically modified electrode with high stability. PAPSAH is a kind of water-soluble self-acid-doped conducting polyaniline in which the sulfonic acid groups are located in the polyaniline chain [40]. The sulfonate groups along its chain makes PAPSAH suitable for fabricating a covalently attached film with DAR [43]. Fig. 11.23 shows the cyclic voltammograms of (a) a self-assembled monolayer (SAM) of 3-mercaptopropylsulfonate (MPS) on a gold electrode, (b) a 3-bilayer-(DAR/PAPSAH) modified gold electrode and (c) a 6-bilayer-(DAR/PAPSAH) modified gold electrode (both after UV irradiation) in 0.2 M Na<sub>2</sub>SO<sub>4</sub> (pH 1.0) at a scan rate of 10 mV s<sup>-1</sup>. Within the potential range studied, -0.1 to 0.7 V, no redox peaks are observed in curve (a) for electroinactive MPS. In contrast, both the PAPSAH-containing multilayer films exhibit one minor (I-I') and one major (II-II') redox peak at ca. 0.15 and 0.44 V, respectively. These two redox peaks should be assigned to the two-step PAPSAH-based redox processes. The first redox peak corresponds to oxidation from the fully-reduced insulating leucoemeraldine salt form to the partially-oxidized conducting emeraldine salt form; the second redox peak corresponds to oxidation from emeraldine to fully-oxidized insulating permigraniline. Like the other types of polyaniline, the redox properties of PAPSAH incorporated in a covalently attached film is also pH dependent. When the pH of the solution decreases, the redox peak potentials of PAPSAH shift positively and the peak currents increase obviously. The increase in peak currents with the decrease in pH value should arise from the fact that the acidic condition of the solution is helpful in keeping the PAPSAH multilayers conductive because of the protonic doping effect. All these results show that the properties of PAPSAH still remain in the covalently attached multilayer. It is anticipated that this robust PAPSAH-containing film could find applications in chemically modified electrodes and electrochromics.

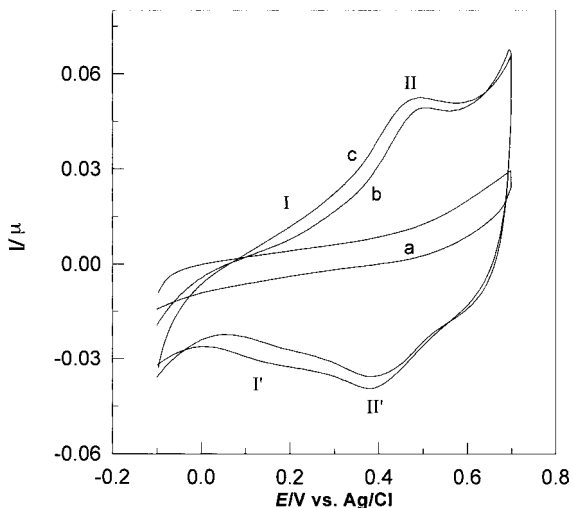


Fig. 11.23 CVs of (a) a monolayer of MPS modified gold electrode, (b) 3 bilayers of DAR/PAPSAH modified gold electrode in 0.5 M KCl solution containing 1 mM  $\text{Fe}(\text{CN})_6^{2-}$  and (c) 6 bilayers of DAR/PAPSAH modified gold electrode in 0.5 M KCl solution. Scan rates:  $50 \text{ mV s}^{-1}$ .

Organic–inorganic hybrid materials, with fascinating properties stemming from their synergic effect, have been paid increasing attention [49–52]. More recently, a robust gold nanoparticles/polymer hybrid multilayer was fabricated by alternately assembling DAR and MPS covered gold nanoparticles followed by UV irradiation [53]. The ideal structure of this covalently attached gold nanoparticles/polymer hybrid multilayer is shown schematically in Fig. 11.24. The properties of gold nanoparticles were kept in the covalently attached multilayer assemblies, meanwhile, the stability of the resulted film increased greatly. It is believed that the same concept may be applied to other particles containing sulfonate or carboxylic acid

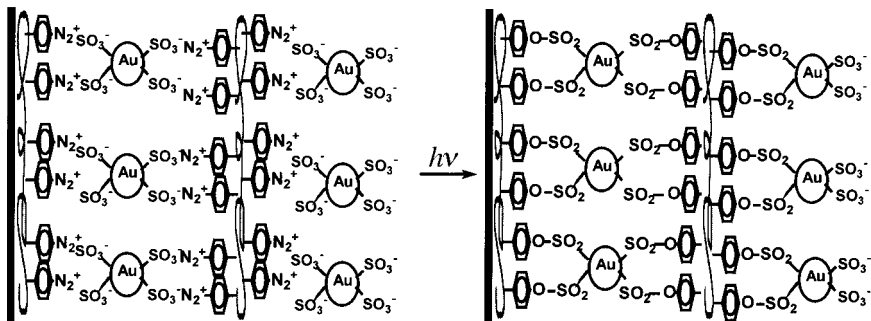


Fig. 11.24 The ideal structure of a gold nanoparticles/DAR hybrid multilayer and its change upon UV irradiation.

groups to fabricate a variety of robust hybrid multilayer assemblies with tailored properties.

## 11.4

### Summary and Outlook

We have demonstrated a variety of multilayer assemblies of electro- and photoactive species by means of the ionic self-assembly technique. By combining the ionic self-assembly technique with in situ chemical reaction in between the film, robust multilayer assemblies in which the neighboring layers are held together by covalent bonds can be easily fabricated. This technique is particularly suitable for charged building blocks containing diazonium groups and their counterparts containing sulfonate, acrylic acid and even phenol groups, but it can also be extended to other systems when pairs of appropriate reactive materials are selected. This technique to fabricate covalently attached multilayer films could be used to produce chemically modified electrodes with high stability, which guarantees the application of these electrodes under severe conditions. Because DAR or diazonium-containing polycations are photosensitive, this will also provide a new kind of surface patterning material. For example, due to the different solubility of the multilayer assemblies before and after UV irradiation, when a proper solvent is chosen which can dissolve the multilayer formed without UV irradiation but not that formed after UV irradiation, robust multilayer patterning surfaces can be produced. By incorporating electroactive materials into multilayers, chemically modified electrodes based on both single and binary active species have been fabricated. In the binary active species modified electrodes, two components can be incorporated in such a way that the function is based on their organization. In other words, multi-component active species could use their synergy to produce new functions which are unavailable for any individual species.

## 11.5

### References

- 1 H. RINGSDORF, B. SCHLARB, J. VENZMER, *Angew. Chem. Int. Ed. Engl.*, **1991**, *27*, 113–158.
- 2 K. B. BLODGETT, *J. Am. Chem. Soc.*, **1935**, *57*, 1007–1010.
- 3 A. ULMAN, *Chem. Rev.*, **1996**, *96*, 1533–1554.
- 4 G. DECHER, *Science*, **1997**, *277*, 1232–1237.
- 5 G. DECHER AND J.-D. HONG, *Makromol. Chem. Macromol. Symp.*, **1991**, *46*, 321–327.
- 6 P. BERTRAND, A. JONAS, A. LASCHEWSKY, R. LEGRAS, *Macromol. Rapid Commun.*, **2000**, *21*, 319–348.
- 7 P. T. HAMMOND, *Curr. Opin. Colloid Interface Sci.*, **2000**, *4*, 430–442.
- 8 A. LASCHEWSKY, E. WISCHERHIFF, M. KAURANEN, A. PERSOONS, *Macromolecules*, **1997**, *30*, 8304–8309.
- 9 J. H. CHEUNG, A. F. FOU, M. F. RUBNER, *Thin Solid Films*, **1994**, *244*, 985–989.
- 10 F. ACKERN, L. KRASEMANN, B. TIEKE, *Thin Solid Films*, **1998**, *327–329*, 762–766.



- 11 H. HONG, D. DAVIDOV, Y. AVNY, H. CHAYET, E. Z. FARAGGI, R. NEUMANN, *Adv. Mater.* **1995**, *7*, 846–849.
- 12 A. C. FOU, O. ONITSUKA, M. FERREIRA, M. F. RUBNER, B. R. HSIEH, *J. Appl. Phys.*, **1995**, *79*, 7501–7509.
- 13 C. Q. SUN, Y. P. SUN, X. ZHANG, H. D. XU, J. C. SHEN, *Anal. Chim. Acta*, **1995**, *312*, 207–212.
- 14 L. Y. WANG, Z. Q. WANG, X. ZHANG, J. C. SHEN, *Macromol. Rapid Commun.*, **1997**, *18*, 509–514.
- 15 W. B. STOCKTON, M. RUBNER, *Macromolecules*, **1997**, *30*, 2717–2725.
- 16 H. M. XIONG, M. H. CHEN, Z. ZHOU, X. ZHANG, J. C. SHEN, *Adv. Mater.*, **1998**, *10*, 529–532.
- 17 M. SCHÜTTE, D. G. KURTH, M. R. LINFORD, H. CÖLFEN, H. MÖHWALD, *Angew. Chem. Int. Ed. Engl.*, **1998**, *37*, 2891–2893.
- 18 Y. SHIMAZAKI, M. MITSUISHI, S. ITO, M. YAMAMOTO, *Langmuir*, **1997**, *13*, 1385–1387.
- 19 J. ANZAI, Y. KOBAYASHI, N. NAKAMURA, M. NISHIMURA, T. HOSHI, *Langmuir*, **1999**, *15*, 221–226.
- 20 X. ZHANG, Y. P. SUN, M. L. GAO, X. X. KONG, J. C. SHEN, *Macromol. Chem. Phys.*, **1996**, *197*, 509–515.
- 21 X. ZHANG, J. C. SHEN, *Adv. Mater.*, **1999**, *11*, 1139–1143.
- 22 S. J. DONG, G. L. CHE, Y. W. XIE, *Chemically Modified Electrodes*, Science Publishing House, Beijing, **1995**, p. 16–43.
- 23 C. Q. SUN, X. Y. ZHANG, D. JIANG, Q. GAO, H. D. XU, Y. P. SUN, X. ZHANG, J. C. SHEN, *J. Electroanal. Chem.*, **1996**, *411*, 73–78.
- 24 C. Q. SUN, Y. P. SUN, X. ZHANG, X. Y. ZHANG, D. JIANG, Q. GAO, H. D. XU, J. C. SHEN, *Thin Solid Films*, **1996**, *288*, 291–295.
- 25 C. Q. SUN, J. H. ZHAO, H. D. XU, Y. P. SUN, X. ZHANG, J. C. SHEN, *Talanta*, **1998**, *46*, 15–21.
- 26 J. Q. SUN, Y. P. SUN, S. ZOU, X. ZHANG, C. Q. SUN, Y. WANG, J. C. SHEN, *Macromol. Chem. Phys.*, **1999**, *200*, 840–844.
- 27 A. N. SHIPWAY, M. LAHAV, R. BLONDER, I. WILLNER, *Chem. Mater.*, **1999**, *11*, 13–15.
- 28 J. HODAK, R. ETCHENIQUE, E. J. CALVO, K. SINGHAL, P. N. BARTLETT, *Langmuir*, **1997**, *13*, 2708–2712.
- 29 L. CHENG, L. NIU, J. GONG, S. J. DONG, *Chem. Mater.*, **1999**, *11*, 1465–1475.
- 30 Y. P. SUN, X. ZHANG, C. Q. SUN, B. WANG, J. C. SHEN, *Macromol. Chem. Phys.*, **1996**, *197*, 147–153.
- 31 X. ZHANG, M. L. GAO, X. Q. KONG, Y. P. SUN, J. C. SHEN, *J. Chem. Soc., Chem. Commun.*, **1994**, 1055–1056.
- 32 Y. P. SUN, X. ZHANG, C. Q. SUN, Z. Q. WANG, J. C. SHEN, D. J. WANG, T. J. LI, *Chem. Commun.*, **1996**, 2379–2380.
- 33 W. KONG, X. ZHANG, M. L. GAO, H. ZHOU, W. LI, J. C. SHEN, *Macromol. Rapid Commun.*, **1994**, *15*, 405–409.
- 34 W. KONG, L. P. WANG, M. L. GAO, H. ZHOU, X. ZHANG, W. LI, J. C. SHEN, *Chem. Commun.*, **1994**, 1297–1298.
- 35 Y. LVOV, G. DECHER, G. SUKGORUKOV, *Macromolecules*, **1993**, *26*, 5396–5399.
- 36 Y. LVOV, H. HASS, G. DECHER, H. MÖHWALD, A. MICHAÏLOV, B. MITCHELISHVILY, E. MORGUNOVA, B. VARNISHTAIN, *Langmuir*, **1994**, *10*, 4232–4236.
- 37 Y. LVOV, K. ARIGA, I. ICHINOSE, T. KUNITAKE, *J. Am. Chem. Soc.*, **1995**, *117*, 6117–6123.
- 38 Y. P. SUN, J. Q. SUN, X. ZHANG, C. Q. SUN, Y. WANG, J. C. SHEN, *Thin Solid Films*, **1998**, *327–329*, 730–733.
- 39 J. Q. SUN, Y. P. SUN, Z. Q. WANG, C. Q. SUN, Y. WANG, X. ZHANG, J. C. SHEN, *Macromol. Chem. Phys.*, **2001**, *202*, 111–116.
- 40 S. A. CHEN, G. W. HWANG, *J. Am. Chem. Soc.*, **1994**, *116*, 7939–7940.
- 41 J. Q. SUN, T. WU, Y. P. SUN, Z. Q. WANG, X. ZHANG, J. C. SHEN, W. X. CAO, *Chem. Commun.*, **1998**, 1853–1854.
- 42 J. Q. SUN, Z. Q. WANG, L. X. WU, X. ZHANG, J. C. SHEN, S. GAO, L. F. CHI, H. FUCHS, *Macromol. Chem. Phys.*, **2001**, *202*, 961–966.
- 43 J. Q. SUN, L. CHENG, F. LIU, S. J. DONG, Z. Q. WANG, X. ZHANG, J. C. SHEN, *Colloids Surf. A*, **2000**, *169*, 209–217.
- 44 J. Q. SUN, Z. Q. WANG, Y. P. SUN, X. ZHANG, J. C. SHEN, *Chem. Commun.*, **1999**, 693–694.
- 45 J. Q. SUN, T. WU, F. LIU, Z. Q. WANG, X. ZHANG, J. C. SHEN, *Langmuir*, **2000**, *16*, 4620–4624.
- 46 J. Q. SUN, T. WU, B. ZOU, X. ZHANG, J. C. SHEN, *Langmuir*, **2001**, *17*, 4035–4041.

- 47 J. J. HARRIS, P. M. DEROSE, M. L. BRUENING, *J. Am. Chem. Soc.* **1999**, *121*, 1978–1979.
- 48 J. Y. CHEN, W. X. CAO, *Chem. Commun.*, **1999**, 1711–1712.
- 49 P. GOMEZ-ROMERO, *Adv. Mater.*, **2001**, *13*, 163–174.
- 50 M. Y. GAO, X. ZHANG, B. YANG, J. C. SHEN, *Chem. Commun.*, **1994**, 2229–2230.
- 51 M. Y. GAO, M. L. GAO, X. ZHANG, Y. YANG, B. YANG, J. C. SHEN, *Chem. Commun.*, **1994**, 2777–2778.
- 52 Y. P. SUN, E. C. HAO, X. ZHANG, B. YANG, J. C. SHEN, L. F. CHI, H. FUCHS, *Langmuir*, **1997**, *13*, 5168–5174.
- 53 Y. FU, H. XU, J. Q. SUN, Z. Q. WANG, X. ZHANG, *Macromol. Rapid Commun.*, **2002**, *23*, 256–259.

## 12

# Coated Colloids: Preparation, Characterization, Assembly and Utilization

FRANK CARUSO and GLEB SUKHORUKOV

### Abstract

The preparation of nanocomposite colloids with tailored properties, and the subsequent assembly of nanostructured materials from these particles provide new opportunities for the technological application of colloids in areas such as coatings, catalysis, sensing, separations, drug delivery, electronics and photonics. This chapter highlights a recently developed self-assembly layer-by-layer (LbL) process for the surface engineering of colloid particles at the nanoscale level. Through polymer-mediated adsorption of charged species from solution onto colloids, new classes of functional core-shell colloids are produced. The versatility of the LbL strategy is demonstrated by a number of examples of nanoengineered colloidal entities, including magnetic, fluorescent, and biocolloids. Extension of the LbL process to encapsulate a variety of biomacromolecules and low molecular weight compounds is also detailed. Additionally, the creation and potential applications of multilayered functional thin films and ordered colloidal assemblies from the core-shell colloids are described.

### 12.1

#### Introduction

Colloids are ubiquitous, present all around us. Technologically, they have been of importance for centuries, being exploited in diverse areas ranging from additives and pigments (e.g. in foods, cosmetics, inks and paints), to catalysis, as well as in the photography, agriculture and mining industries [1–5]. A prerequisite for the successful utilization of colloids for many applications is that they remain colloidally stable. The two main components of the intermolecular interactions that influence colloidal stability, namely the electrostatic repulsion and van der Waals attraction, have been intensively studied [1, 2]. These interactions can be tuned by, for example, the addition of salt and polymers to the colloidal dispersion, providing the basis for the use of optimized colloidal systems for various fundamental investigations or for the manufacture of hierarchically ordered structures. The size and type of colloids available nowadays is quite broad, varying from organic

(e.g., latexes) to inorganic (e.g., silica, gold, semiconductors). These types of colloids are routinely employed for scientific investigations and technology-driven applications [3–5]. The emerging nanotechnology and biotechnology fields, however, will require tailor-made building blocks for the construction of advanced materials and devices. Since colloid particles are useful components of such systems, the availability of colloids with unique and tailored functional properties (e.g., optical, mechanical, thermal, electrical, magnetic, catalytic, biological) is highly desired, and routes that allow their preparation have attracted considerable interest [6].

One strategy to prepare colloids with novel physical and chemical properties involves their surface modification and/or coating with a range of compounds, either organic or inorganic [6, 7]. Several techniques have been used for forming polymer coatings [7], although polymerization-based methods are the most commonly employed. These include direct polymerization of monomers adsorbed onto the particle surface [8, 9], heterocoagulation-polymerization [10], and emulsion polymerization [7, 11]. Inorganic coatings are often formed by precipitation and/or surface reactions of inorganic precursors with the particle surface [12–14] or by the sonochemical generation of nanoparticles in the presence of larger colloids [15, 16]. Such coated colloids often display improved properties over the single-component particles, thus making them attractive for use in a broader range as well as new applications. For example, coated (or core–shell) colloids have been applied in encapsulation technologies, as immobilized catalysts, in drug delivery, electronics, separations, and diagnostics, as well as in the synthesis of combinatorial libraries [7, 17–23]. Despite the widespread use of coated colloids in these areas, many of the existing coating methods do not allow nanoscale control of the coating composition and thickness, and often the particles are non-uniformly coated, thus promoting aggregation. Therefore, there is much interest in the development and implementation of new particle coating technologies, especially ones that are both flexible and facile, and that are independent of the particle surface morphology and composition to deposit multicomposite coatings.

This chapter presents an overview of a recent, new, versatile layer-by-layer self-assembly process (when applied to colloids) that permits the preparation of coated (and encapsulated) colloids of different shapes and sizes, with uniform layers of diverse composition as well as controllable thickness. Herein, the method is denoted layer-by-layer colloid templating, LbL-CT. Following some practical issues that are important for the successful coating of colloids using the LbL-CT technique, emphasis will be placed on the wide variety of layer constituents as well as core colloids that can be used in the process. This will be exemplified by presenting a number of systems, ranging from coatings comprised solely of polymers, to nanoparticle-, protein-, and phospholipid-based coatings on colloids. It will be demonstrated that the colloid cores can be varied from enzyme crystals to crystallized low molecular weight dyes to biological cells. In these cases, the LbL-CT approach is exploited for encapsulation of the cores. The nanoscale control that can be afforded over the wall thickness will also be highlighted. An alternative procedure for colloid coating, termed controlled precipitation, will also be described. This is of particular interest when thick coatings are desired. Examples

demonstrating the mesoscopic arrangement of the coated colloids will be presented, followed by the properties of various functional (e.g. catalytically, optically, etc.) core-shell colloids, along with their utilization in various areas, such as photonics and immunodiagnosics.

## 12.2

### Preparation and Characterization of Coated Colloids

Application of the LbL self-assembly to colloid templates represents a new and promising approach for the construction of coated particles. The LbL technology for “coating” *macroscopically flat* surfaces is now well established. Its origins can be traced back to the mid-1960s, when Iler showed that it was possible to deposit particles onto solid substrates in a LbL manner [24]. However, it was only after the pioneering work of Decher in the early 1990s, involving the LbL assembly of a combination of linear polycations and polyanions [25, 26], that an explosive growth occurred in the use of the LbL technology [27]. In ensuing years, the LbL technique was expanded to include, among other species, a host of inorganic nanoparticles, biomolecules, clays, and dyes in polyelectrolyte multilayer assemblies [27]. The LbL method was also applied to various *particles*, thus permitting the formation of nanocomposite core-shell particles [28, 29] and the encapsulation of various species [30–33]. For example, in the mid-1990s, Keller et al. reported the construction of alternating composite multilayers of exfoliated zirconium phosphate sheets and charged redox polymers on silane-modified silica particles [28]. Several years later, Chen and Somasunduran deposited nanosized alumina particles in alternation with poly(acrylic acid), which acts as the bridging polymer, on submicrometer-sized alumina core particles [29]. In other related studies, it was shown that the use of sequentially deposited polycation/polyanion multilayer coatings on preformed alginate-based microcapsules are effective in controlling their permeability. Vogt et al. showed that enzymes could be retained within alginate microcapsules upon coating with polycation/polyanion multilayers [30, 31]. A later study showed that one bilayer of alginate and chitosan deposited on preformed alginate-chitosan capsules only had a minor influence on the permeability of immunoglobulin G (IgG), whereas four double layers yielded a large effect in limiting the diffusion of IgG [32]. In most of these aforementioned studies [28–33], experimental evidence was provided for the formation of the coatings, however, the coatings were not characterized in detail after deposition of each layer, step-by-step. This section will deal specifically with our recent work on the LbL coating of colloids [34–39], outlining the practical considerations for coating colloids, as well as illustrating the layer-by-layer growth of various species on a host of different colloids, as assessed by a range of experimental techniques.

## 12.2.1

**Layer-by-Layer Adsorption**

The LbL-CT method allows the deposition of multiple layers on colloids in a controlled fashion [34–39]. In this strategy, depicted in Fig. 12.1, the first added species usually has an opposite charge to that on the colloids, thereby adsorbing through electrostatic interactions. An overcompensation of charge often results with adsorption of each layer, and at this stage the charge on the surface of the particles is reversed. This facilitates the alternate deposition of subsequent layers of a wide range of charged components. As is the case on planar supports [27], generally a polyelectrolyte is used to separate layers of the same or different materials. These polyelectrolyte interlayers not only act as molecular “glue”, but they can also impart enhanced colloidal stability to the coated particles via electrostatic as well as steric contributions.

Although there are various experimental parameters that need to be optimized in order to LbL coat particles uniformly (e.g., particle concentration and size, polymer type, length, and concentration, and total salt concentration in the adsorbing solution; see later), the chief issue in transferring the LbL technology from macroscopic (planar) supports to colloid particles is the effective separation of the remaining free (unadsorbed) charged species from the colloidal dispersion prior to the next deposition cycle. Here we consider the case of polyelectrolyte adsorption, although many charged species can be treated in the same way as described in the following. The LbL assembly of polyelectrolytes onto colloid particles can be performed in two main ways. Either the concentration of polyelectrolyte added at

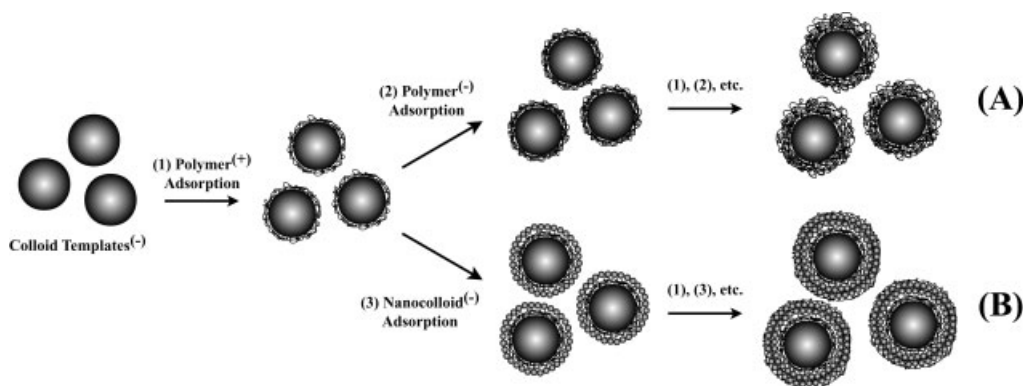


**Fig. 12.1** Schematic illustration of LbL-CT constructed colloids. The coatings can be polyelectrolytes (A), or nanocolloids such as inorganic nanoparticles or proteins (B). Dyes or lipids can also be used as layer components (see text for details). The templates can be of synthetic (latexes, metal, crystallized low molecular weight compounds etc.) or

biological origin (proteins, cells), with diameters in the nanometer to micrometer regime. The process typically involves the consecutive deposition of oppositely charged species onto the colloid particles, with repeated centrifugation or filtration and intermittent water washings between deposition of each layer.

each step is just sufficient to form a saturated layer [38], or adsorption is carried out at an excess concentration of polyelectrolyte [34–37]. Fig. 12.2 illustrates the  $\zeta$ -potential behavior of PS particles, as well as the fluorescence of the non-adsorbed oppositely charged polyelectrolyte, as a function of total concentration of added polyelectrolyte [38]. The amount of “free” fluorescently labeled polyelectrolyte was measured in the supernatant after the particles were separated by centrifugation. The  $\zeta$ -potential data show that with increasing bulk concentration of the adsorbing polyelectrolyte, recharging of the particle surface takes place. At a certain concentration, the  $\zeta$ -potential levels off and, below this concentration, the polyelectrolyte is mostly adsorbed on the particles, depleting the bulk solution from the majority of polyelectrolyte. Further increasing the bulk polyelectrolyte concentration beyond this value does not influence the  $\zeta$ -potential or the amount of polyelectrolyte on the particles. Repeating this process with optimized polyelectrolyte to particle concentrations can lead to the formation of polyelectrolyte multilayers on particles when oppositely charged polymers are employed.

In the second method, the excess, non-adsorbed polyelectrolyte is removed prior to the addition of the next polyelectrolyte (of opposite charge) in order to avoid the formation of polyelectrolyte complexes in bulk solution. The removal of excess polyelectrolyte can be achieved efficiently by performing several repeated centrifugation/washing cycles in pure water, followed by re-suspension of the particles [34–37], or by using a filtration set-up where the colloid particles are retained on the filter, but the polyelectrolytes are small enough to pass through the pores of the filter [40].

The above different approaches allow the formation of multiple layers of charged species on colloid particles, however some differences exist in the adsorbed amount of material, the number of particle aggregates, the ease of varia-

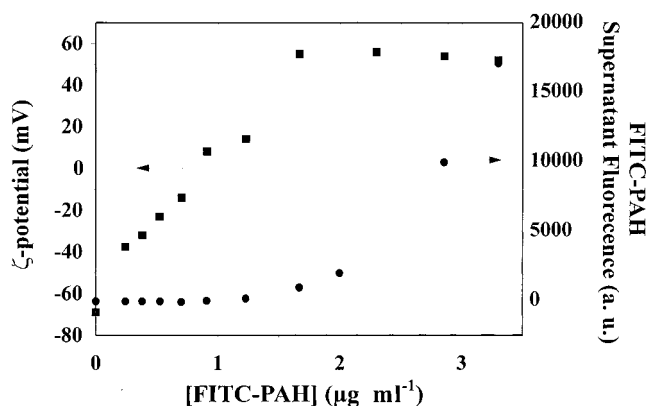


**Fig. 12.2**  $\zeta$ -potential of negatively charged 640 nm diameter PS particles and fluorescence intensity of non-adsorbed FITC-labeled PAH as a function of total concentration of

added FITC-PAH. The adsorption of FITC-PAH was performed from aqueous solutions containing 0.5 M NaCl. The particle concentration was  $2.2 \times 10^8$  particles  $\text{mL}^{-1}$  [38].

tion of the deposited substances, the degree of material loss during preparation, and the possibility to scale-up production of the coated particles [36, 38]. Regardless of the method used, typically, particle concentrations of a few (up to 10) wt.% are used in order to avoid particle aggregation upon addition of the coating species (e.g., polyelectrolyte, inorganic nanoparticles, proteins, lipids etc.).

In the following we address the main advantages and drawbacks of the aforementioned coating approaches. The main general challenge in the coating process is to suppress particle aggregation at different stages of the preparation, as it is often rather difficult (or even impossible) to resuspend strongly aggregated particles without significant modification or damage to the particle surface (e.g., due to sonochemical treatment when attempting to separate aggregated particles). The centrifugation/dispersion process can make the subsequent resuspension of the particles difficult if high centrifugal forces are applied. Other drawbacks of this strategy are the associated difficulties in centrifuging smaller particles (e.g. <50 nm) and the significant loss of particles during preparation. For instance, assembling 20 layers of polyelectrolytes on 640 nm diameter particles under typical coating conditions [36] can result in an accumulated total loss of 80% of the particles originally introduced. Washing and redispersing the particle suspension by means of centrifugation can also be rather time consuming, particularly if relatively small (<100 nm) particles are used. Nonetheless, the centrifugation approach continues to be widely used for the LbL coating of colloids, as the experimental conditions can be readily adapted for a variety of systems.

In the case of the sequential addition of polyelectrolyte at a suitable concentration to just coat the total available particle surface area, it is possible to prevent the direct formation of aggregates. In contrast to the centrifugation and filtration protocols, there is no loss of the polyelectrolytes used as layer constituents or the core particles. Further, once the conditions for the multilayer coating are determined (which may not always be straightforward), the coating process can be performed on a relatively short time scale because the adsorption of a polyelectrolyte layer (in the concentration range employed) usually takes only a few minutes. The major and highly limiting drawback of this procedure is that the probability of forming polyelectrolyte complexes and particle aggregates, as revealed by single particle light scattering (SPLS), is rather high [36]. This can, to some extent, be overcome by employing a dilute particle suspension. Notwithstanding, the concentrations of all components of the suspensions need to be accurately determined and controlled during the entire coating process; this can turn out to be laborious and highly involved. For these reasons, this method remains attractive only in a select few cases.

The filtration method is essentially the most practicable approach to scaling-up the LbL process for coating a large variety of colloid particles [40]. The particles are not subjected to intense centrifugal forces but are permanently and gently stirred. The liquid level above the filter can be exactly controlled by the interplay between the inflow and outflow of the components, including the suspension medium, and pressure applied for filtration. Since the filtrate can be recovered easily, this preparation procedure can, in principle, be readily automated. The membrane filtration unit has



adaptation capacity to meet the requirements of a variety of chemical and colloid chemical systems. Some limitations exist when dealing with smaller particles in this system, as this makes the use of filters with small pore size necessary, hence slowing down the process. This can lead to frequent replacement of filters due to clogging of the pores by the polyelectrolytes. Despite such issues, this method is the most attractive for preparing large quantities of coated particles.

The next subsections will deal with the fabrication and characterization of a range of novel core-shell materials using the LbL-CT approach. The first part will focus on the coating of colloids with multilayers of different composition and the second part on the use of different core materials. It will be shown that parameters such as shell thickness, composition and coating uniformity can be readily controlled. An alternative technique to obtain coatings on colloids via precipitation from solution onto particles will then be described.

### 12.2.1.1 Multilayered Coatings

As depicted in Fig. 12.1, colloid particles can be coated with a range of different species. These include, among other charged species, polyelectrolytes, inorganic nanoparticles, proteins, dyes and lipids. The following provides examples of such systems and data to verify their layer-by-layer preparation.

#### Polymers

Several experimental techniques can be employed to monitor the formation of each polyelectrolyte layer deposited sequentially on colloids. Microelectrophoresis provides a qualitative indication as to whether or not multilayers are deposited [34–38]. Fig. 12.3 shows the  $\zeta$ -potential as a function of polyelectrolyte layer number for negatively charged polystyrene (PS) particles coated with poly(allylamine hydrochloride) (PAH) and poly(styrenesulfonate) (PSS), or with poly(diallyldimethylammonium chloride) (PDADMAC)/PSS. As expected, the negatively charged (uncoated) PS particles show a negative  $\zeta$ -potential, ca. 65 mV. The presence of a single layer of adsorbed positively charged polyelectrolyte on the PS particles causes a reversal in  $\zeta$ -potential to positive values, and subsequent deposition of a negatively charged polyelectrolyte reverts the  $\zeta$ -potential back to negative values. Further polyelectrolyte depositions cause the  $\zeta$ -potential to alternate in sign, depending on whether the outermost layer is positively or negatively charged. This alternation in  $\zeta$ -potential qualitatively demonstrates a successful recharging of the particle surface with deposition of each polyelectrolyte layer, suggesting that step-wise layer growth occurs on the particles. Similar data have been observed for a broad range of LbL assembled polyelectrolyte coatings [35, 36, 38, 40–43].

Quantitative evidence for the sequential deposition of polyelectrolyte multilayers on particles is provided by the technique of single particle light scattering (SPLS) [41]. SPLS involves recording the light scattered from a single particle at a given moment in time, and is therefore sensitive to the amount of adsorbed material on the colloid particles. This method is capable of unambiguously identifying coated

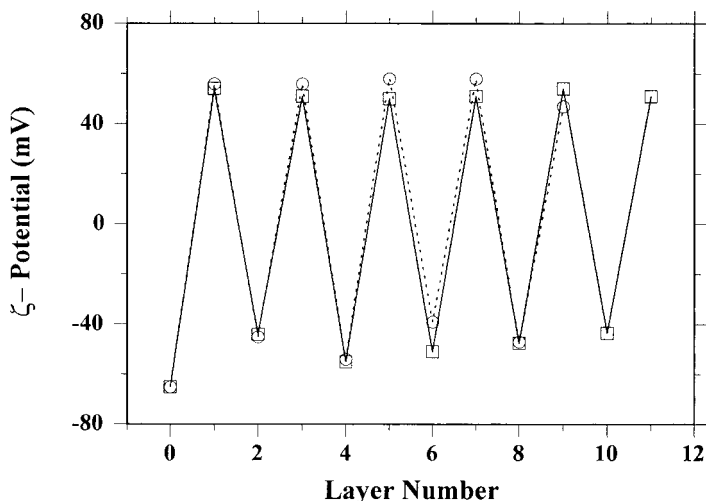


**Fig. 12.3**  $\zeta$ -potential of negatively charged 640 nm diameter PS particles as a function of polyelectrolyte layer number for (circles) PAH/PSS- and (squares) PDADMAC/PSS coatings. The odd layer numbers correspond to PAH or PDADMAC deposition and the even layer numbers to PSS adsorption. (Reproduced by permission of the American Chemical Society [41])

particles and discriminating between singlets, doublets, and triplets (as well as higher order aggregates) of particles. The layer thickness resolution of SPLS is about 1–2 nm. Currently, monodisperse particles as small as 200 nm up to about 950 nm in diameter can be investigated by SPLS. In Fig. 12.4, the intensity distribution of the control bare particles is compared with particles coated with 11 and 21 layers assembled by the filtration technique [40]. From the shift of the peak of the intensity distribution, the adsorbed mass can be derived. Given the refractive index of the polyelectrolyte layers (1.47), these data can be converted into layer thicknesses for the adsorbed polyelectrolyte multilayers. The polyelectrolyte film thickness increases proportionally with the number of layers deposited (Tab. 12.1) [41]. The mean polyelectrolyte layer thickness is approximately 1.5 nm (equivalent to approximately  $1.0 \text{ mg m}^{-2}$ ) for PAH/PSS and PDADMAC/PSS coatings assembled from 0.5 M NaCl. Similar thickness values are obtained, regardless of whether the layers are prepared by centrifugation or filtration methods [40, 41]. It should be noted that the average layer thickness of polyelectrolyte multilayers can depend strongly on the type of polyelectrolytes and especially the salt concentrations used to process the layers [44]. Typically, increasing the salt concentration in the solution from which the polyelectrolytes are adsorbed leads to thicker layers. The above SPLS data show that the coating thickness can be controlled at the nanometer level for the polyelectrolyte layers, and that step-wise growth of the layers on colloids is achieved by using the LbL strategy. The thickness values obtained are also in agreement with those from X-ray reflectivity measurements for similar polymer multilayer films formed on planar silicon substrates under the

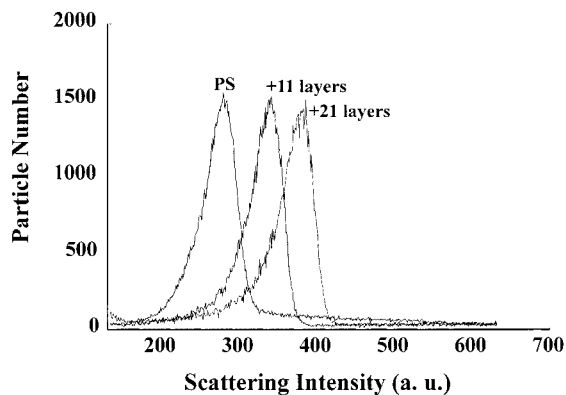


**Fig. 12.4** Normalized SPLS intensity distributions (from left to right) of bare 640 nm diameter PS particles, and the same particles

coated with a total of 11 and 21 PAH/PSS layers. (Reproduced by permission of the American Chemical Society [40].)

same ionic strength conditions [44]. The deposition of polyelectrolytes that contain strongly absorbing or fluorescing chromophores can be verified by UV-vis spectrophotometry and/or fluorescence spectroscopy, respectively [36, 42, 43].

Further confirmation for the successful nanoscale coating of colloids with polyelectrolyte multilayers is provided by transmission electron microscopy (TEM). Electron microscopy analysis of coated particles allows visualization of the increase in particle diameter with increasing layer number. Fig. 12.5 shows a TEM image of 640 nm diameter PS particles coated with 21 layers of PAH and PSS. The average diameter of the coated particles is increased to approximately 720 nm. The calculated coating thickness from TEM is in good agreement with the SPLS data (see Tab. 12.1). Uniformly coated and individual particles are seen.

**Tab. 12.1** Thickness of polyelectrolyte multilayers assembled on 640 nm diameter PS particles as a function of layer number.

Layers	Film thickness, $d$ (nm) <sup>a)</sup>	
	PAH/PSS	PDADMAC/PSS
1	1.2	1.4
3	3.4	3.3
5	5.6	6.6
7	8.4	8.5
9	11.5	11.7
11	15.0	–
15 <sup>b)</sup>	24.8	–
21 <sup>b)</sup>	33.9	–

a) Thicknesses were determined from SPLS data and using a refractive index of 1.47.

b) The layers for these samples were prepared by using filtration (instead of centrifugation) to separate excess, unadsorbed polyelectrolyte. Adapted from [41].

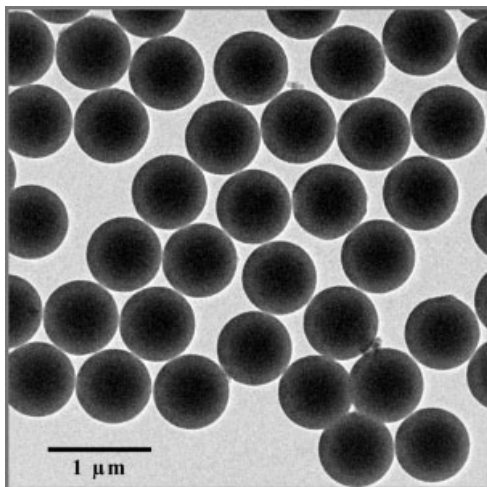


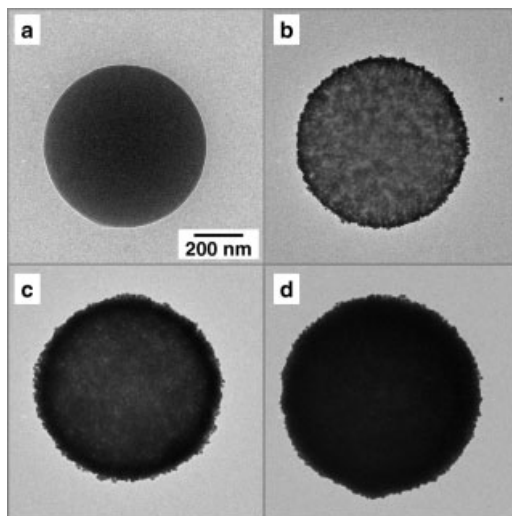
**Fig. 12.5** TEM image of 640 nm diameter PS particles coated with a total of 21 layers of PAH/PSS. The particles were prepared by the LbL-CT approach shown in Fig. 12.1. The 21-layer coating resulted in an increase in particle diameter from 640 nm to approximately 720 nm. The polyelectrolyte coating cannot be seen by TEM due to the similar electron contrast of the core and coating [6].

The internal structure of polyelectrolyte multilayers is known to consist of an overlapping network of polycations and polyanions. That is, polyelectrolytes in multilayer films do not form strictly stratified layers but show an overlap (or interpenetration) over about 4 neighboring layers [27, 45]. This is supported by experiments involving PS particles coated with PAH/PSS multilayers of varying thickness (1 to 34 nm or 1 to 21 layers) and loaded with the multivalent fluorescent dye, pyrenetetrasulfonic acid, tetrasodium salt (4-PSA) [41]. After exposure to PSS solution, the PSS displaces the dye from layers within the film, suggesting that the top polyelectrolyte layer extends at least 4 layers downwards into the film, whilst the seventh layer contacts the fourth layer from the top.

#### Polymer–inorganic particles

By substituting one of the charged polyelectrolyte components with *nanoparticles*, nanoparticle-based multilayer assemblies can be constructed on colloid particles by the LbL-CT technique. The step-wise and regular formation of a wide range of nanoparticle-based coatings, from metals to metal oxides and semiconductors, have been prepared on submicrometer-sized particles via this approach. These include silica [37, 46–48], zeolite [49], iron oxide [50, 51] titania [48, 52], clays [48], gold [53], silica-coated gold (Au/SiO<sub>2</sub>) [54], and luminescent semiconductors (CdTe) [55, 56]. The thickness of the multilayer coatings could be controlled with nanometer precision. Growth of the individual layers and morphology of the resulting coated particles were followed by electrophoresis, light scattering and electron microscopy. The representative TEM images in Fig. 12.6 show the highly uniform coatings obtained and the nanoscale control over the coating layer thickness (and hence the composite particle diameter) through simple variation of the number of deposition cycles for Au/SiO<sub>2</sub> nanoparticles (~20 nm diameter) [54]. (The nanoparticles were deposited in alternation with PDADMAC on 640 nm diameter

**Fig. 12.6** TEM micrographs of PS spheres coated with (a) PDADMAC/PSS/PDADMAC and an additional (b) one, (c) three, and (d) five Au/SiO<sub>2</sub> nanoparticle/PDADMAC multilayers. A high uniformity of the Au/SiO<sub>2</sub> nanoparticle coating on the PS spheres can be seen, as well as a systematic increase in diameter of the particles with increasing layer number [54].



PS spheres.) By using processing conditions that screen the silica surface charge on the nanoparticles sufficiently (e.g., salt-based solutions), thereby allowing them to pack closely on the particle surface, approximately one monolayer of nanoparticles was adsorbed at each deposition step. The coated particles remain as individual, unaggregated colloidal entities in solution. If the Au/SiO<sub>2</sub> nanoparticles were deposited directly from pure water solutions, only sparse nanoparticle coverage on the spheres was obtained, and particle clumping occurred. The above study, as well as others [37, 46–53, 55, 56], underscores the importance of controlling the solution conditions to achieve uniform nanoparticle coatings on larger colloids when using the LbL technique. Microelectrophoresis experiments also show a reversal of surface charge when oppositely charged nanoparticles and polyelectrolytes are deposited onto larger colloid spheres, while SPLS and scanning electron microscopy (SEM) data verify that the coatings can be tuned with a thickness precision equal to the diameter of the nanoparticles for each nanoparticle deposition step [37, 46–53]. Additionally, atomic force microscopy (AFM) can be used to reveal a uniform nanoparticle coating and a systematic increase in the diameter of the coated colloids [47].

In contrast to the pure polyelectrolyte coatings, the incorporation of nanoparticles can introduce further structural stability to the layers. This is especially important in the creation of hollow spheres (see Section 12.3.1.2 and Chapter 13).

### Polymer–proteins

The LbL-CT approach has also been shown to be suitable for the construction of protein multilayer architectures on colloid particles [57–61]. By the alternate deposition of protein and oppositely charged polymer on PS spheres, multilayer films of various proteins have been formed, including bovine serum albumin (BSA) [57], immunoglobulin G (IgG) [57], glucose oxidase (GOD) [58, 59], horse-

radish peroxidase (POD) [59],  $\beta$ -glucosidase ( $\beta$ -GLS) [60], and urease [61]. The thicknesses of the protein coatings varied from several to tens and even hundreds of nanometers [57], depending on the protein, the number of protein layers deposited, and the conditions of assembly. For example, by using the appropriate refractive indices for the protein ( $n=1.43$ )/polyelectrolyte (1.47) coatings, the average thickness of the coatings could be determined from the SPLS data. For the fluorescein isothiocyanate-labeled BSA (FITC-BSA) multilayers, the coating thickness increases linearly with the number of protein layers deposited [57]. (The thickness of the polyelectrolyte interlayers, separating FITC-BSA layers, is approximately 0.5 nm.) The calculated average layer thickness increment for the FITC-BSA layers was  $3.3 \pm 1.1$  nm when adsorbed from pure water (pH  $\sim 5.6$ ), and  $5.8 \pm 2.5$  nm when deposited from a phosphate-buffered saline solution, pH 7. This difference in thickness was largely attributed to the higher percentage of charged groups on BSA at pH 7, and hence the greater degree of electrostatic interaction with the PDADMAC surface onto which it adsorbed. For IgG coatings, individual

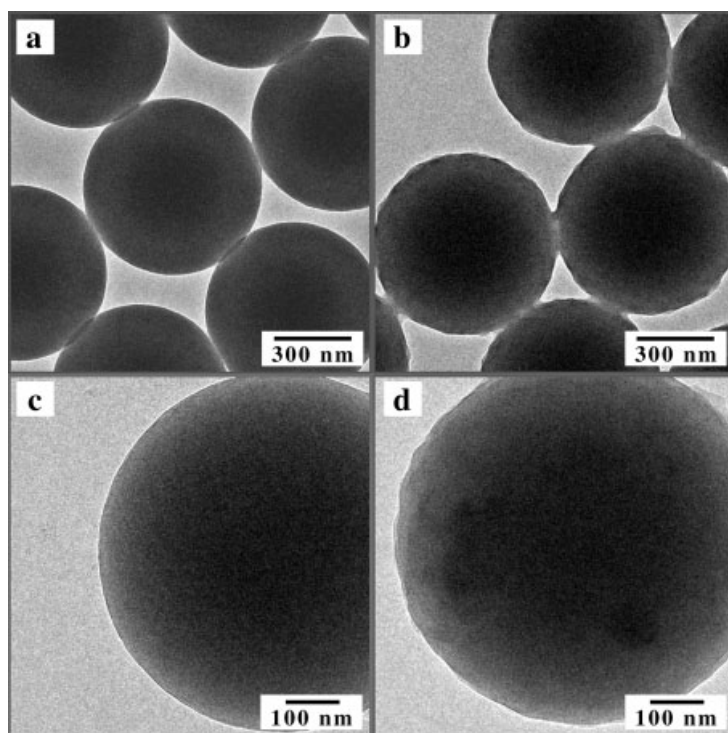


**Fig. 12.7** TEM micrographs of PDADMAC/PSS/PDADMAC-coated PS spheres (a and c) and the same spheres additionally coated with [(FITC-BSA/PDADMAC)<sub>2</sub>/FITC-BSA] (b and d). FITC-BSA was adsorbed from pure water. The presence of FITC-BSA on the sur-

face can be seen (images b and d). The “bridging” seen at the surface where the particles are in contact is due to sample drying effects. (Reproduced by permission of the American Chemical Society [57].)

layer thicknesses of up to  $\sim 37$  nm were observed, corresponding to the equivalent of several monomolecular protein layers [57].

TEM micrographs of PS particles (a and c) and those coated with three BSA multilayers (b and d) are shown in Fig. 12.7 [57]. The “control” PS particles display a smooth surface, whereas the PS particles coated with BSA multilayers show both an increase in surface roughness and an increase in diameter (compared with the “control” PS spheres). From the TEM images, the diameter increase of the particles coated with the three BSA layers is approximately 20 nm, corresponding to a coating/layer thickness increase of  $\sim 10$  nm, a value which is in accord with the SPLS data. Although there can be a tendency for protein-coated particles to aggregate during or immediately after the protein deposition step, careful selection of the processing conditions for the coatings can alleviate this. Additionally, enhanced colloidal stability can be imparted to the systems by the presence of one or more outermost polyelectrolyte layers; subsequent deposition of outer polyelectrolyte layers is typically performed prior to storage and use of the particles. The LbL-CT approach permits the preparation of biofunctional coatings on colloids with a high density of biomolecules, making them of interest in applications where the signal, as a result of biological interaction, needs to be amplified for the successful detection of various species, or where a higher efficiency of product from enzyme–substrate reactions is required [58–61]. (Examples of this will be given in Section 12.3.2.)

#### **Polymer–low molecular weight compounds**

The alternating adsorption of multivalent ions and oppositely charged polyelectrolytes on colloid particles has been investigated recently [62]. Multilayer films composed of  $Tb^{3+}$ /PSS and 4-PSA/PAH were assembled on PS and melamine formaldehyde (MF) particles. The amount of assembled material was estimated by fluorescence spectroscopy. Linear growth of the “coating amount” versus the number of layers deposited was demonstrated. These multilayers are not stable and can be decomposed by the addition of salt and by varying the temperature, providing a means of altering the stability of the layers. Extraction of the low-molecular weight compounds from the coating can also lead to the break up of the layers.

#### **Polymer–lipids**

Lipids were shown to be involved in the LbL assembly on colloid particles when alternately adsorbed with polyelectrolytes. Lipid assembly can be performed by adsorbing the lipids on the particles from methanol solution or by adsorption of lipid vesicles from aqueous solution, following spreading of the lipids on the colloid particle surface [62–65]. The conformation of the assembled lipids is presumably in the form of bilayers, as was indicated by energy transfer measurements [63], but can depend on the type of lipids used. In the particular case investigated, the charged lipids formed bilayers and the non-charged lipids formed multilamellar structures. The attractive forces between the lipids and polyelectrolytes appear to determine the final conformation of the lipids on the particles.

In the case of lipid-coated hollow polyelectrolyte shells (obtained after core removal; see Chapter 13), the lipid coating was shown to affect the permeability properties of the polyelectrolyte shells. The shell wall becomes impermeable to water-soluble dyes [64] and less permeable to ions [65]. The presence of lipid layers on a supporting skeleton of polyelectrolyte, as for the polyelectrolyte shells, makes such systems attractive models for basic biophysical studies. They have a high stability and can be prepared with a defined size and shape (see Chapter 13).

#### 12.2.1.2 Coating of Specific Cores

##### **Influence of core size**

Colloids of different sizes, shapes and composition can be employed as template particles in the LbL-CT method. Concerning organic colloid spheres, typically latex particles, both PS and MF, in the approximate range of 500 nm to 5  $\mu\text{m}$  diameter are utilized [35–41]. Reducing the size of the latex particles represents a challenge with respect to establishing the appropriate experimental methods and conditions to generate uniform coatings and stable dispersions of the coated colloids. The importance of the experimental protocol mainly resides in the effectiveness of the separation procedures; that is, separating excess polyelectrolyte from coated particles that are less than 100 nm in diameter. It was shown that conventional centrifugation, using commercial, bench-top systems, could be applied to separate latex particles down to about 70 nm in diameter [42], although the centrifugal force needed (40 000  $g$ ) was considerably higher than that required for colloids larger than 500 nm in diameter ( $\sim 10\,000\,g$ ). If latex particles of even smaller size are employed, centrifugation becomes less attractive for routine separation of polymer and particles, particularly with respect to the time required, as typically several centrifugation/water wash cycles are employed. However, inorganic colloids, especially metals, can be readily separated by centrifugation, due to their inherently high density (compared with latex particles, for example). Gold nanoparticles are especially attractive for this purpose because the optical properties of the colloids can also be used to investigate the deposition of coatings on their surface [66, 67]. Despite the fact that the separation science is quite clear for the use of metal nanoparticles, as the template particles reduce in size, issues with regard to particle curvature become important. As already mentioned in Section 12.2.1, some of the important general experimental parameters that affect the coating of particles with polyelectrolytes are the nature of the polymer, polymer length, polymer concentration, and total salt concentration in the adsorbing solution. By taking into account the polymer length, polymer stiffness and added salt (leading to finite screening lengths), suitable conditions can be established that lead to polyelectrolyte-coated *nanoparticles* [66, 67]. In agreement with theoretical predictions [68], experimental conditions of 1 mM salt and polymers in the range of about 15–20 kDa were used to LbL deposit polyelectrolyte multilayers on gold nanoparticles of 30 nm in diameter. Red shifts in the spectral position of the surface plasmon absorption band peak (with little broadening) of the gold nanoparticles were observed, confirming the uniform deposition of polyelectrolyte multilayers [66, 67].



Preliminary studies show that sub-10 nm diameter particles can also be LbL coated; the importance here lies in modulating the unique size-dependent optical properties afforded by colloids in this size range, as well as their surface characteristics.

### Enzyme particles

The LbL-CT protocol has been extended to coat, or more specifically to encapsulate, biologically significant materials in the form of biocolloids. Enzyme crystals (e.g., catalase) were encapsulated via the sequential deposition of oppositely charged polyelectrolytes onto their surface [69]. The catalase crystals, approximately 10  $\mu\text{m}$  in diameter, exhibit a positive surface charge in water at pH 5 ( $\zeta$ -potential = +20 mV, catalase isoelectric point = 5.8). This positive charge on the surface of the crystals facilitated the adsorption of FITC-PAH/PSS multilayers. As is the case for other colloidal systems, alternating  $\zeta$ -potentials were obtained depending on the outermost layer (FITC-PAH, +20 mV; PSS, 30 mV), which is characteristic of polyelectrolyte multilayer growth on colloid templates (see earlier). Since the crystals are soluble in water above pH 6 and below pH 4, the coating steps were performed at pH 5 and 4°C, and from polyelectrolyte solutions containing 1 M potassium acetate, to minimize enzyme dissolution. Fig. 12.8 shows a fluorescence micrograph of coated catalase crystals: the fluorescence originates from the surface of the polymer multilayer-coated enzyme crystals. No change in morphology of the crystals was observed as a result of coating. These particles contain an extremely high enzyme loading in each polyelectrolyte multilayer coating, and the activity of the encapsulated catalase is preserved after coating. The polymer multilayers assembled on the enzyme crystals underwent a morphology change from essentially rectangular to almost spherical upon solubilization (at pH 2) of the enzyme crystals [69]. This was attributed to the osmotic pressure build up inside the capsules as a result of solubilization of the enzyme (the coatings are permeable to small ions and water), since the enzyme was entrapped inside the polyelectrolyte

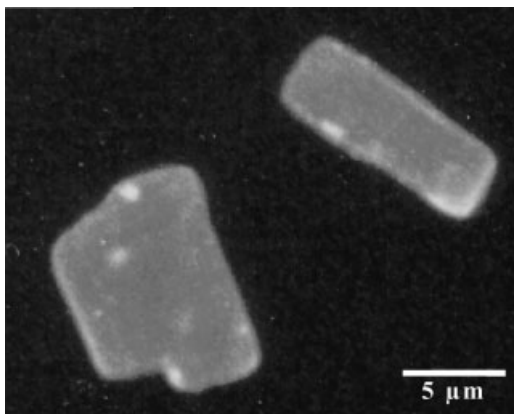


**Fig. 12.8** Fluorescence optical micrograph of micrometer-sized catalase crystals coated with eight [(PSS/FITC-PAH)<sub>4</sub>] polyelectrolyte layers, highlighting the applicability of the LbL-CT method for encapsulation. The multilayer coating does not alter the enzyme crystal morphology, or the activity of the enzyme. (Adapted from [69].)

coating. The thin coatings also act as protective layers for the catalase, shielding them from enzyme degrading substances, such as proteases [69].

Polyelectrolyte multilayer assembly can also be performed on *amorphous* particles consisting of aggregates of proteins, which are formed prior to multilayer build-up. The use of micron-sized amorphous protein aggregates as templates for polyelectrolyte multilayer assembly was demonstrated for lactate dehydrogenase [70] and chymotrypsin [71]. As for the enzyme crystals, the polyelectrolyte multilayer coating of these aggregates encapsulates them and also provides a selective barrier for the diffusion of different species (substrates, inhibitors) from the exterior. A general scheme of protein aggregate encapsulation by polyelectrolyte multilayers is presented in Fig. 12.9. The concept of polyelectrolyte multilayer formation on protein aggregates is similar to that of multilayer deposition on colloid particles. It was shown that chymotrypsin, chosen as a model protein because its activity can be easily monitored [71], could be salted out to form chymotrypsin aggregates (Fig. 12.9a,b). The precipitation of protein started immediately after mixing of the enzyme and saline solutions and was followed by an increase in turbidity of the solution. After a certain time the turbidity remained constant. Variations in the  $\alpha$ -chymotrypsin and sodium chloride concentrations used permitted optimization of the enzyme precipitation reaction. Due to the positive charge of chymotrypsin at pH 2.3, the negatively charged polyelectrolyte PSS was deposited as a first layer to begin the multilayer assembly process (Fig. 12.9c). PAH was assembled next (Fig. 12.9d). Finally, these aggregates could be covered with a defined number of polyelectrolyte layers (Fig. 12.9e). A typical SEM image of chymotrypsin aggregates coated with PSS/PAH/PSS layers is shown in Fig. 12.10. Rather amorphous aggregates of micron size were found. Each aggregate consisted of numerous, smaller protein particles, so called primary aggregates, in the shape of small spheres with a diameter of the order of 100–300 nm. This indi-

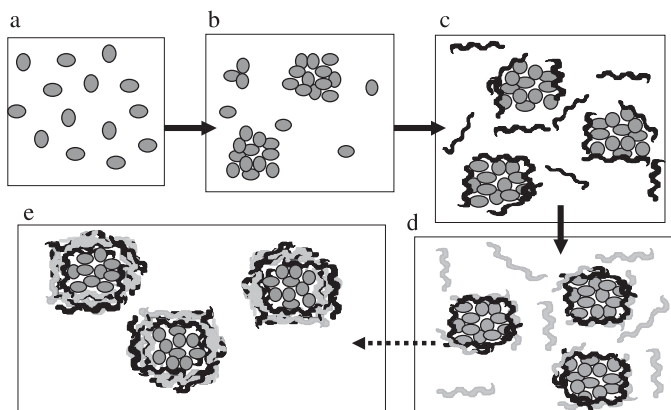
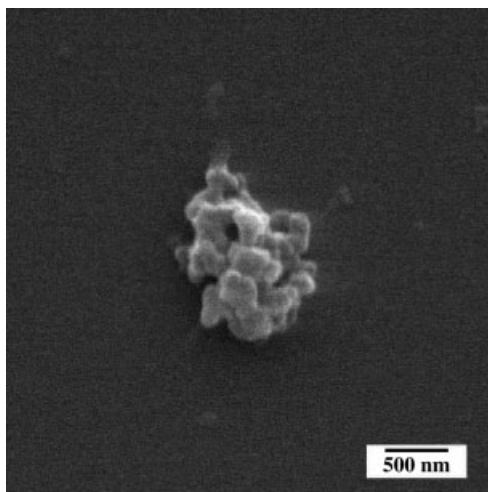


**Fig. 12.9** Schematic of the LbL adsorption of polyelectrolytes onto protein aggregates preformed in salt solutions. See text for details. (Reproduced by permission of John Wiley and Sons [71].)

**Fig. 12.10** SEM image of protein aggregates coated with PSS/PAH/PSS. (Reproduced by permission of John Wiley and Sons [71].)



icates a hierarchy in the formation of the protein aggregates. A characteristic feature of the aggregates is their large surface area, where pores within the aggregates can be observed. Such structures can be formed as a result of secondary aggregation of the primary aggregates, which is enhanced upon polyelectrolyte deposition. Further sequential polyelectrolyte layer assembling then preserves the structure of the secondary aggregates. Generally, the morphology of aggregates should depend on the preparation conditions, such as the time of aggregate growth, the nature of the polyelectrolyte used, and the number of layers deposited, which might influence the composition of aggregates. Enzymatic studies revealed that about 70% of the activity of the encapsulated chymotrypsin remained. As was the case for the enzyme crystals [69], the encapsulated enzyme is protected from high molecular weight inhibitors, which cannot penetrate the polyelectrolyte coating and influence the enzyme functionality [70]. In a related study, the assembly of three polyelectrolyte layers was performed on condensed DNA particles, with sizes of about 50–100 nm. Certain polymer compositions used for coating the DNA particles yield stable suspensions [72, 73], and facilitate the uptake of these particles by biological cells with sequential gene expression [73, 74].

### **Crystals of low molecular weight species**

Similar to the crystals comprised of enzymes, crystallized, largely water-insoluble low molecular weight substances can also be encapsulated by LbL coating [75, 76]. However, unlike latex and biocrystal particle templates, the crystals used, either pyrene or fluorescein diacetate (FDA) [75, 76], were uncharged and required a pre-charging step prior to polyelectrolyte multilayer coating. Following exposure to a solution containing amphiphilic molecules (e.g., surfactants or phospholipids), the crystals could be redispersed in aqueous solution and were then found to be amenable to coating with polyelectrolyte multilayers. The pyrene and FDA tem-

plates could then be removed by exposure of the encapsulated particles to ethanol solution, which resulted in their solubilization. The LbL-CT coating of uncharged templates represents a significant step forward in encapsulation technologies, as the process can be applied to a variety of other low molecular weight, crystallized (or amorphous) materials, such as drugs. Studies have also shown that the release rate of the encapsulated low molecular weight materials is a function of the polymer coating thickness and the nature of the precharging layer [76].

### Biological cells

Biological cells can also be utilized as cores for encapsulation. Glutaraldehyde-fixed echinocytes have been coated with polymer [77, 78] and polymer/nanoparticle [39] multilayers. The biocolloids have a jagged and highly structured surface, however the coating tends to follow the contour with nanoscale precision. Following removal of the core by treatment with a highly oxidizing solution, it was shown that the structure of the coating left behind mimics the original shape, including the secondary structure (spikes) of the biocolloid [39, 77, 78]. This is shown in Fig. 12.11 for the polymer/nanoparticle coatings [39]. Coating of biological cells in

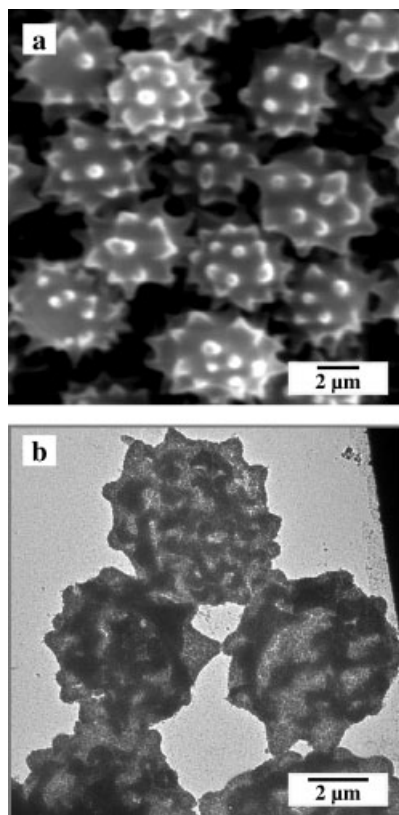


**Fig. 12.11** (a) SEM image of echinocytes and (b) TEM image of hollow composite nanoparticle/polymer structures, derived by depositing three SiO<sub>2</sub> nanoparticle/PDADMAC layer pairs on polyelectrolyte-modified echinocytes and then removing the core by using an oxidizing solution [39].

this manner can provide an attractive means to encase them in ultrathin coatings, thus protecting them from external, undesirable species. Additionally, the surface properties of the cells can be modified by simple solution self-assembly of components onto their surface.

Overall, the above examples highlight the versatility and effectiveness of the LbL-CT method for preparing core-shell colloids with unique properties (see Section 12.3) and as a novel means for the facile encapsulation of a variety of compounds.

### 12.2.2

#### Colloid Precipitation

In contrast to the LbL method, the controlled surface precipitation (CP) approach consists of forming coatings of only one component. Additionally, this method can use charged and non-charged polymers and nanoparticles as coating constituents. The idea lies in controlling the heterocoagulation process when the quality of polymer or nanoparticle solution worsens (with respect to solubility), and precipitation begins. Since a particle suspension contains a large number of colloid particles, the precipitating materials collect on the surface of the particles. It was demonstrated that the slow heterocoagulation of polymer within a suspension of colloids leads to the controlled coating of particles by polymeric films [79]. Precipitation could be caused either by non-soluble complex formation between the polyelectrolyte and multivalent ions or by mixing the polymer solution with non-solvent. The proper choice of concentration ratio between the polymers, particles, and the speed of coagulation provides a coating coverage with a defined amount of precipitated polymer on each particle. The particles harvest the coagulated polymers and their complexes with multivalent ions on the particle surface. A theoretical consideration of this heterocoagulation of polymers in the presence of collector particles has been presented [79]. Experimental observations of the formation of a smooth film on the colloid particles have also been reported [80, 81], where it was shown that coatings composed of only one component (DNA), utilizing non-charged polymers (dextran), or complexes between ions and polyelectrolytes ( $\text{Me}^{3+}/\text{PSS}$ ) [80], and coatings composed of PAH/PSS complexes formed in the solution prior to precipitation could be formed on colloid particles. The PAH/PSS complex was formed by slightly changing the solution pH from alkaline ( $\text{pH} \sim 12$ ), where there is no complex between these polymers, to pH around 8, resulting in polyelectrolyte complex formation. DNA and dextran were precipitated on the particle surface by the dropwise addition of ethanol in aqueous solution. As revealed by confocal microscopy images, the resulting coating is homogeneous for the investigated systems. The thickness of the polymeric film on colloids can be tuned down to the level of a few monomolecular layers. The CP method has an advantage in that it can be applied to compounds that cannot be deposited by means of LbL assembly. Conditions for precipitation, such as changing the solvent conditions or adding complexing ions, might be found for a wide class of polymers and nanoparticles as well. As shown by TEM, a homogeneous coating

on submicron sized latex particles can be formed from 4 nm semiconductor CdTe nanocrystals by their precipitation in ethanol (Fig. 12.12) [82]. These coatings can be formed with tunable thicknesses. Homogeneous and complete coverage of the colloid cores with a shell of luminescent nanocrystals with a thickness in the range 15–40 nm was achieved [82]. Controlling the precipitation of the solution components on the colloids implies that an adequate window is found with regard to the range of concentration of polymers, particles, and coagulation speed for each species to be deposited. Theoretical estimations of the concentration parameters in the system on the basis of a simple coagulation model give good agreement with experimentally observed optimal values [79]. Another advantage of the CP method of coating colloid particles, compared with the LbL technique, is that it is significantly less time-consuming, especially if thicker coatings (e.g. tens of monomolecular layers) are desired. By CP, the assembly is complete within minutes. The drawback of the CP approach is the crucial dependence of aggregation of the components on the diameter of the collector particles. Successful coatings by CP were obtained on particles with diameters of more than 400 nm, while the LbL-CT method has been explored for particles of diameter below 30 nm. Both the CP and LbL-CT methods complement each other. Additionally, the ordering of the monomolecular layers in the *z*-direction to the particle surface appears to be higher for coatings prepared by the LbL-CT method than those obtained by CP. While the LbL technique usually results in the formation of stable films, the CP assembled films can be easily decomposed by solubilizing the polymer again or by extracting the complexed ions. Added benefits should be brought by a combination of both of these methods, allowing the assembly of multicomposite films. LbL- and CP-processed colloid building blocks may provide solutions to diverse tasks related to the manufacture of micro- and nanostructured materials.

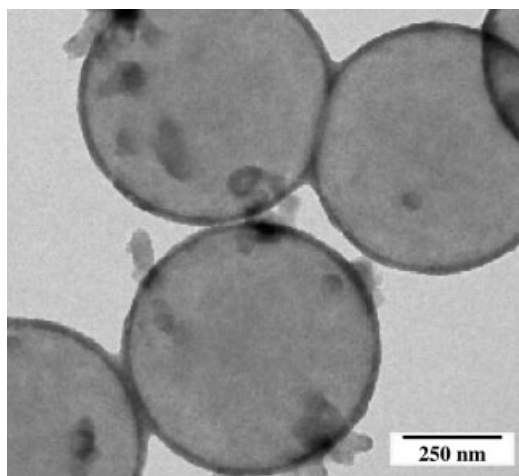


**Fig. 12.12** TEM image of PS spheres covered by CdTe nanocrystals. The coating was formed by precipitation of the nanocrystals onto the spheres by drop-wise addition of ethanol into the aqueous nanocrystal solution. The coating can be seen as a ring around the spheres. Some excess (i.e., non-adsorbed) material can also be seen [82].

## 12.3

### Assembly and Utilization of Coated Colloids

#### 12.3.1

##### Mesoscopic Arrangement

###### 12.3.1.1 Colloidal Crystals

Monodisperse colloid spheres (e.g., silica or polystyrene) can spontaneously self-organize into crystal structures at optical wavelength scales with long-range periodicity [83–88]. These ordered colloidal assemblies, otherwise known as colloidal crystals, can possess an optical stop band in the visible and near-IR spectral ranges when the spheres are in the micron- and submicron-size regime. Although numerous studies exist on the formation of photonic materials from colloids, few have exploited the use of *coated colloids* as building blocks [89, 90]. The employment of LbL coated colloids in the formation of these crystals, with independent control over the size of the core, as well as thickness and composition of the coating, opens up a versatile and attractive route to tailoring their optical properties. Recently, via LbL control of the coating thickness and coating composition, colloidal crystals with tunable optical properties have been constructed [56, 91, 92]. Coatings comprised of pure polyelectrolyte multilayer [91, 92], semiconductor nanoparticle/polyelectrolyte [56], and gold nanoparticle/polyelectrolyte [92] coatings have been formed on submicron-sized PS spheres, and the resulting coated colloids have been assembled into ordered arrays by either sedimentation of the colloids or by using a specially designed filtration-flow cell. Fig. 12.13 shows a representative example of the utilization of CdTe(S)/polyelectrolyte-coated PS particles to form colloidal crystals. Such LbL-CT processed colloids can be crystallized [56], although optimized coating conditions should be employed to prepare uniformly coated, isolated particles in solution since the presence of even a small number of aggregates can significantly influence or prevent their crystallization. The position of the optical stop band of colloidal crystals prepared from LbL coated colloids can be tuned with nanoscale precision, through variation of the coating thickness and/or by the composition of the coating [91, 92]. The above investigations into the formation of colloidal crystals from LbL-CT prepared colloids are very recent. It is anticipated that following further elaborate studies into the crystallization behavior of multilayer-coated particles, considerable progress will be made with the formation of novel colloidal crystals with unique optical properties.

###### 12.3.1.2 Macro- and Mesoporous Materials

Colloid particles have also found wide use in the formation of a broad range of three-dimensional macroporous materials. These materials are generally comprised of highly ordered air spheres interconnected by small channels [93, 94]. They can be produced by using colloidal crystals as a three-dimensional ordered scaffold, around which other materials can be infiltrated or synthesized using wet chemistry techniques, such as sol-gel processes. The templates are then removed

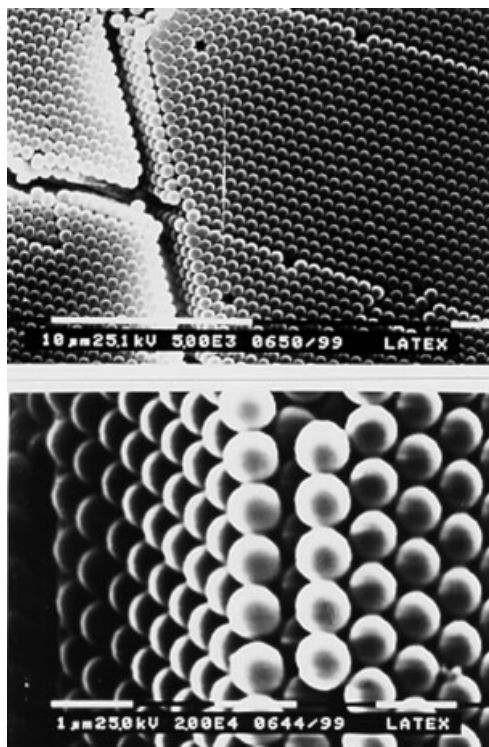
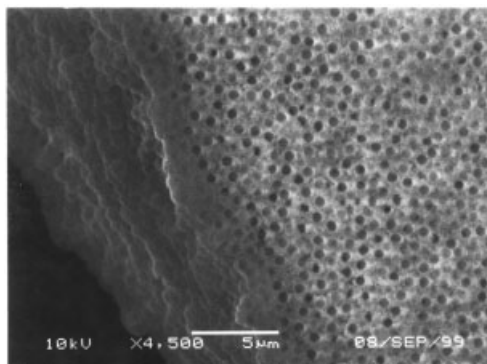


**Fig. 12.13** SEM images of 3D colloidal crystals of 640 nm diameter PS spheres coated with polyelectrolyte/CdTe(S) nanocrystals. The coating thickness is 5–8 nm [56].

by calcination or decomposition with a solvent, leaving a periodic and open pore structure in the dielectric matrix, also known as “inverse opals”. Inverse opals of metals [95, 96], metal oxides [97, 98], semiconductors [99], carbon and silicon [100, 101], and polymers [102–105], have been fabricated by using a variety of colloidal crystal templates. LbL-CT constructed colloids have also been used to prepare macroporous inorganic and inorganic-composite materials [49, 106]. It was shown that an ordered silicalite (zeolite) macroporous monolith was formed by gravity sedimenting prefabricated PS sphere–silicalite nanoparticle/polyelectrolyte core-shell particles into close-packed assemblies, followed by calcination (Fig. 12.14) [49]. The wall thickness and pore diameters of the hierarchically ordered monolith were controlled by the coating thickness and template diameter, respectively. In a related study, macroporous  $\text{TiO}_2$  and inorganic-composite structures were produced by infiltrating a titanium dioxide precursor into templates of sedimented, close-packed coated colloid spheres, followed by removal of the organic material by calcination [106]. The pore morphology of the resulting macroporous structures was controlled by the nature of the multilayers deposited on the colloid particles: open and closed pore structures were observed for spheres coated with polyelectrolyte multilayers and silica nanoparticle/polyelectrolyte multilayers, respectively. The wall thickness of the pores was tuned on the nanometer scale by



**Fig. 12.14.** SEM image of an ordered macroporous monolith, formed by assembling PS spheres coated with five silicalite nanoparticle/polyelectrolyte layer pairs into a close-packed arrangement, and subsequently calcining. (Reproduced by permission of the American Chemical Society [49].)



varying the number of deposited multilayers (e.g., from about 10 to 40 nm for PS spheres coated with 5 and 21 polyelectrolyte multilayers, respectively). In a further study, regularly spaced, linear chains of up to 600  $\mu\text{m}$  of core-shell particles comprising latex cores and iron oxide nanoparticle shells have been formed under the influence of an external magnetic field [107]. The separation and the length of the individual chains can be tuned by the magnetic field strength and the concentration of the particle solution. This opens new avenues for the creation of organized structures from magnetic core-shell building blocks.

Coated colloids can also be used as precursors to the formation of hollow colloids (or hollow capsules), which are of immense interest in a range of areas, including drug delivery, catalysis, waste removal, piezoelectric transducers, and functional materials processing [39]. The hollow colloids can be derived from the coated colloids upon removal of the core by either chemical or thermal means (see Chapter 13). Since the coatings are semi-permeable, the core can be removed, leaving behind a “shell”, that is, the coating. Hollow polymer [34, 38, 42, 66, 108, 109], inorganic [37, 48, 49, 51, 52, 54], and organic-inorganic composite [37, 39] colloids have been prepared. The hollow polyelectrolyte colloids are usually generated by using a solvent-decomposable colloid, which acts as the template for coating. When hollow inorganic colloids are formed, the nanoparticles in the coating are sintered through the high temperature treatment used to generate them, providing structural integrity for the hollow colloids. The hollow capsules can be LbL engineered to be robust, biocompatible, decomposable, and with tuned permeability. Additionally, they can exhibit macropores, mesopores and/or micropores in their walls. Chapter 13 deals specifically with the formation of hollow capsules and their application.

## 12.3.2

**Enzymatic Catalysis**12.3.2.1 **Dispersions**

Enzyme multilayer-coated colloids are attractive enzyme reactors. This is mainly due to the inherently high surface area of colloids, which provides the potential to yield higher enzymatic reaction efficiencies than their planar film counterparts. It was shown that by using the LbL-CT approach, control could be exerted over both the total amount of enzyme deposited on colloid particles and the architecture of the enzyme film [58–61]. Glucose oxidase (GOD), horseradish peroxidase (POD), or preformed enzyme–polyelectrolyte complexes were assembled in alternation with oppositely charged polyelectrolytes onto PS particles [58, 59]. It was found that deposition of polyelectrolyte onto particles with GOD or POD forming the outermost layers resulted in partial removal of the adsorbed enzyme layer, whereas no such enzyme removal was observed with subsequent polyelectrolyte deposition onto coated particles when the enzyme was pre-complexed with polyelectrolyte prior to adsorption. The latex carrier particles coated with the enzyme multilayers such as GOD and/or POD were exploited as specific enzyme reactors [58, 59]. Use of the colloidal biocatalysts for enzymatic catalysis showed that the enzymatic activity (per particle) increased with the number of enzyme layers immobilized, irrespective of whether or not the enzyme was pre-complexed. Particles coated with preformed enzyme–polyelectrolyte complexes, however, displayed a significantly lower enzymatic activity (about 10 times less) than those prepared by the direct adsorption of free enzyme. Fig. 12.15 shows the rate of change of absorbance at 500 nm (i.e., a direct measure of the enzymatic activity) for PS particles coated with one to four PEI/GOD layers, and with one to five PSS/POD layers [59]. (Here, the enzyme and polyelectrolytes were not pre-complexed before deposition.) The differences in the relative increase in activity with layer number for the two systems was attributed to differences in the enzyme/polymer layer structure. These studies demonstrate that enzyme multilayer-coated particles with tailored enzymatic yields could be prepared. Multi-component enzyme multilayer films on colloids were also prepared and exploited in sequential enzymatic catalysis. In addition, particles pre-modified with an electrostatically deposited layer of magnetic nanoparticles and subsequently coated with enzyme multilayers were repeatedly used as catalysts [59, 61]. These particles were fabricated by using the LbL approach, beginning with the magnetic nanoparticles, followed by the enzyme multilayers. They were rapidly and easily separated with a magnet after the enzymatic reactions were performed. These colloidal systems are of major significance because of their inherently high surface area for reaction, their ability to increase the catalytic output in relation to the number of immobilized enzyme layers, their complex and multiple catalytic functions, and because the particles can be easily separated and reused multiple times.

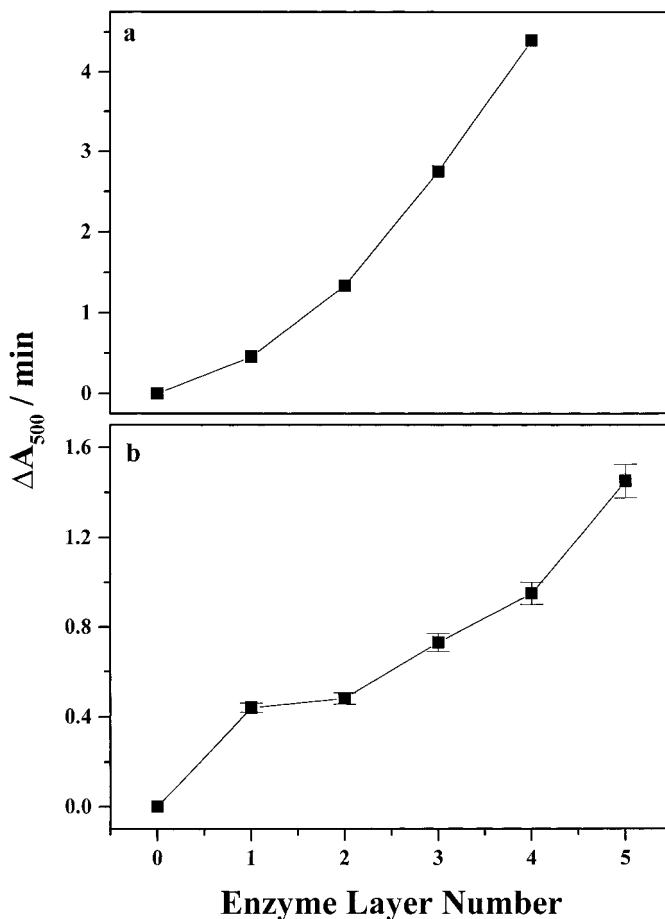


**Fig. 12.15** Activity ( $\Delta A_{500}/\text{min}$ ) of colloidal catalysts-PS particles coated with enzyme multilayers: (a) PEI/GOD bilayers and (b) PSS/POD bilayers. The data is normalized for particle number. (Adapted from [59].)

### 12.3.2.2 Thin Films

As outlined in Section 12.2.1.2 enzyme particles, the LbL-CT encapsulation of crystallized enzymes yields a high loading of encapsulated biomaterial within a very thin coating of polyelectrolytes [69]. Such encapsulated enzyme microcrystals are attractive for use as immobilized catalysts. This was achieved by employing them as building blocks in the preparation of novel enzyme multilayer films. They were LbL assembled on planar supports with an oppositely charged polymer to create stable, relatively thin (few micrometers), high enzyme content multilayer films for biocatalysis applications [110]. Through the number of layers deposited, thin films of controllable thickness and biocomponent content were prepared. The formation of the films was monitored by using a quartz crystal microbalance,

which showed that each enzyme layer formed from polyelectrolyte-encapsulated catalase crystals had a mass of about 3870 ng (equivalent to 120 mg m<sup>-2</sup>), compared with 378 ng for uncoated catalase crystals and about 100 ng for solubilized catalase. This highlights the fact that the polyelectrolyte coating facilitated film growth with regard to higher enzyme loadings. The thin films were found to be highly bioactive, exhibiting biocatalytic activities of up to 50 times higher than those prepared by conventional LbL deposition of solubilized enzyme. Even films formed by the deposition of the encapsulated catalase crystals for only 10–30 s (adsorption equilibrium was reached after 60 min) showed enzymatic activities 20–30 times higher than corresponding films formed from solubilized enzyme. These films can also be used as biosensors: since they are very thin, they can provide fast response times [111]. Additionally, multicomponent films can be prepared simply by depositing polyelectrolyte-encapsulated colloids of different enzymes. These films form attractive candidates for use in various biotechnological applications.

### 12.3.3

#### Tailored Optical Properties

Coating colloids with optically functional materials such as dye-labeled polymers and metal nanoparticles permits the creation of colloids with unique optical properties [53, 54, 112]. Fluorescent microspheres were prepared by the LbL assembly of dye-labeled PAH and PSS onto PS particles [112]. By selecting different fluorescent dyes (FITC, RhBITC, Cy5) to conjugate with PAH, 640 nm diameter particles with three different emission maxima were prepared. As shown in Fig. 12.16, the emission maxima of FITC–PAH, RhBITC–PAH and Cy5–PAH coated PS particles were 526 nm, 586 nm, and 665 nm, respectively, showing that particles with predetermined emission wavelengths can be readily prepared. Equally important is that the fluorescence intensity of LbL-CT prepared particles can be tuned, depending on the number of dye-labeled polyelectrolyte deposition cycles. Fluorescence microscopy image (FMI) analysis of individual particles showed that the fluorescence intensity of the coated particles increases linearly with increasing number of FITC–PAH layers [112]. The LbL-CT approach represents a promising method to fabricate powerful fluorescent particles, which may be utilized in immunoassays (see Section 12.3.4).

The deposition of metal nanoparticles on larger spheres provides a new class of micron-scale colloidal entities with optical properties that can be tailored by changing the hierarchical assembly of the nanoparticles [53, 54]. It was shown that the optical properties of PS–Au/SiO<sub>2</sub>/PDADMAC core–shell particles, prepared by LbL-CT (e.g., see Fig. 12.6), can be modulated via altering the thickness of the nanoparticle-based multilayer shell [54]: the spectral position of the surface plasmon absorption band maximum,  $\lambda_{\text{max}}$ , due to the core of Au/SiO<sub>2</sub> nanoparticles, red-shifted with increasing shell thickness.  $\lambda_{\text{max}}$  for the particles coated with one, three, and five Au/SiO<sub>2</sub> nanoparticle/PDADMAC multilayers shifted from 588 ± 2 to 618 ± 2 to 642 ± 2 nm, respectively. This red shift in  $\lambda_{\text{max}}$  is due to the coupling of the surface

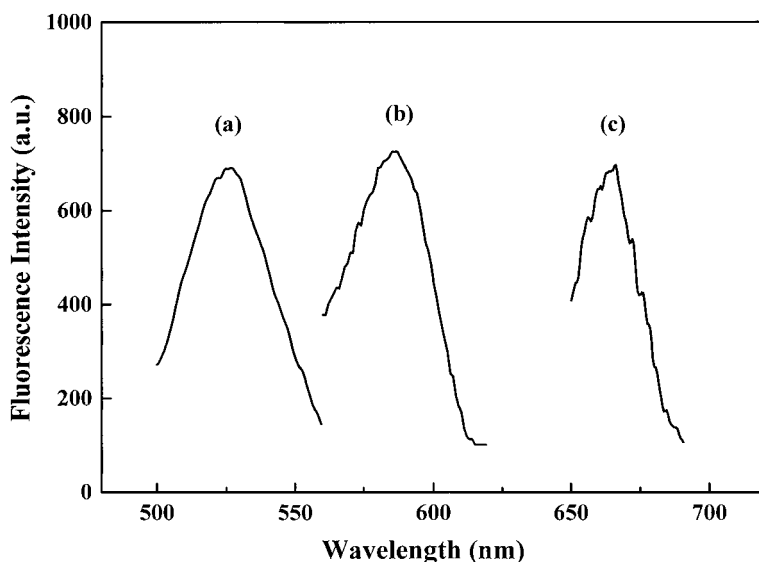


**Fig. 12.16** Normalized fluorescence spectra of  $\sim 640$  nm diameter PS particles LbL coated with dye-labeled PAH. The unlabeled polyelectrolyte PSS was used as the interlayer. (a) PS/(FITC-PAH/PSS); (b) PS/(RhBITC-PAH/PSS);

(c) PS/(Cy5-PAH/PSS). The morphology of the coated particles is similar to that of the particles shown in Fig. 12.5. (Reproduced by permission of Academic Press [112].)

plasmons in neighboring particles. ( $\lambda_{\max}$  of the Au/SiO<sub>2</sub> nanoparticles in aqueous solution is at  $520 \pm 1$  nm.) However, the gold nanoparticles behave as discrete but coupled particles and not as a thin, continuous metal shell.

Colloids coated with CdTe nanoparticle/polyelectrolyte multilayers were also prepared and used to form colloidal crystals (as mentioned in Section 12.3.1.1; see Fig. 12.13) [56]. These particles display luminescence properties due to the nanoparticles embedded in the polymer coatings. The luminescence maximum red-shifted from 590 nm for CdTe(S) nanoparticles in aqueous solution to 595 nm for the nanoparticles in the colloidal crystal. This difference was attributed to the close packing of the CdTe(S) nanoparticles in the polyelectrolyte layers and the change in the environment for the semiconductor nanoparticles from water to polymer. Designing colloidal crystal systems where the emission spectrum of, say the nanocrystals in the coating, overlaps with the photonic stop band of the colloidal crystal provides the opportunity to control the spontaneous emission using both the electronic (semiconductor nanoparticles) and photonic (artificial opals) states.

#### 12.3.4

#### Other Applications

Biologically-modified particles are widely used in immunodiagnostics. Such particles are commonly fluorescent with specific immunoreagents adsorbed onto their

surfaces. Biofunctional fluorescent microparticles for application in immunoassays were prepared by the LbL-CT method: multiple layers of fluorescently labeled polyelectrolytes were deposited onto colloid particles, followed by deposition of the protein [112]. The suitability of the mouse immunoglobulin G (IgG)-coated fluorescent PS particles for immunodetection was investigated by a solid-phase immunoassay. Goat anti-mouse IgG adsorbed on the polystyrene culture dish surface acted as the capture antibody to recognize mouse IgG. Strong binding between anti-mouse IgG and mouse IgG immobilized on the fluorescent PS microparticles was observed, leading to fluorescence from the dish. Control experiments verified the specific interaction between passively adsorbed immunospecies on the particles and the immobilized antibodies or antigens on the dish. Similar studies were conducted with smaller particles (<100 nm) as templates in order to compare the sensitivity of the biofunctional particles with conventional immunoprobes. The preliminary data of the sandwich microplate assay showed this to be a promising approach to increase the sensitivity of fluorescent immunoassays.

When low molecular weight uncharged model drugs in crystalline form are encapsulated in polyelectrolyte multilayers (see Section 12.2.1.2 Crystals of low molecular weight species), the drug release rate, after solubilization of the drugs, can be tuned by varying the number of layers deposited and the nature of the precharging species [76]. This, and similar systems [113], are highly attractive for the sustained release of drugs (also see Chapter 13). They are also appealing for immunoassay applications when the low molecular weight compounds are fluorescent and when receptor molecules are attached to the surface of these coated particles. Biomodified, polyelectrolyte-encapsulated crystals of low molecular weight, fluorescent compounds have recently been utilized in immunoassays [114]. After interaction of these particles with the immobilized biomolecules in the immunoassays and exposure to ethanol to solubilize the uncharged core molecules, extremely high fluorescent signals are obtained, providing a novel means to conduct highly sensitive immunoassays.

Core-shell microspheres containing catalytically active complexes [115] or metal nanoparticles [116] have also been prepared for catalysis investigations. These studies make use of the LbL-CT protocol to prepare multilayer-coated colloids.

## 12.4

### Summary and Outlook

The examples presented in this chapter demonstrate the wide range of coated colloids that can be nanoengineered through application of the LbL technique to colloids. The inherent flexibility and unparalleled simplicity of the LbL method, demonstrated for over a decade on planar supports, can be equally well adapted to colloids, provided that parameters such as the concentration, and the nature and size of the core particles are considered along with the appropriate conditions to deposit the coating layers; for example, polymer type, length, and concentration for polyelectrolyte coatings, and nanoparticle type and size for nanoparticle coatings.

As documented in studies involving the formation of planar thin films, the role of salt in the adsorption solutions is important in determining the final structure and thickness of the layers; however, the influence of salt on the interaction between the template particles and the coating species needs also to be considered when LbL coating colloids, as it can lead to aggregation of the particles. Use of “suitable” salt concentrations can make the polyelectrolyte more flexible so that it coats more effectively, and can screen the charges between the nanoparticles being deposited to make them pack closer to each other and give more uniform nanoparticle coatings. These conditions need to be determined and optimized for specific systems and become more important as the size of particles to be coated is decreased into the nanometer regime. The control that has been available for processing thin films on planar supports has also been shown to apply to coatings on particles: the coating thickness can be modulated with nanometer precision, and the coating composition is defined by the step-by-step deposition of each species. The LbL-CT approach not only allows the creation of novel core-shell colloids with various functions (e.g. catalytic, optical, chemical magnetic etc.) but it provides a facile means to encapsulate a variety of significant compounds. Examples given of the utilization of LbL processed coated/encapsulated colloids emphasize the enormous technological relevance of such colloids. When used as building blocks, complex, hierarchical structures with predefined functions can be constructed. This opens new, exciting opportunities for the application of these colloids in various applications in the physical and life sciences, including photonics, catalysis, sensing, diagnostics, and drug delivery.

### Acknowledgements

We thank our many outstanding colleagues from around the world, whose names are listed in the bibliography, for their excellent contributions to the research and for their fruitful collaboration. We also thank H. Möhwald for support of this work. We acknowledge funding from the BMBF under the BioFuture, Functional Supramolecular Systems, and Sofia Kovalevskaja programs, the Volkswagen Foundation, the DFG, the DAAD, the Alexander von Humboldt Foundation, and the companies Bayer, BASF, and Henkel.

## 12.5

### References

- 1 J. N. ISRAELACHVILI, *Intermolecular and Surface Forces*, Academic Press, New York, 2nd edn., 1991.
- 2 P. M. CLAESSON, T. EDERTH, V. BERGERON, M. W. RUTLAND, *Adv. Colloid Interface Sci.* **1996**, 67, 119.
- 3 D. C. BLACKLEY, *Polymer Latices: Science and Technology*, Chapman and Hall, London, 2nd edn., 1997, vol. 2.
- 4 *Colloidal Gold: Principles, Methods and Applications*, Ed. M. A. HAYAT, Academic Press, New York, 1989, vol. 1.
- 5 E. MATIJEVIC, *Chem. Mater.* **1993**, 5, 412.

- 6 For a review, see: F. CARUSO, *Adv. Mater.* **2001**, *13*, 11, and references therein.
- 7 C.H.M. HOFMAN-CARIS, *New J. Chem.* **1994**, *18*, 1087, and references therein.
- 8 S.M. MARINAKOS, J.P. NOVAK, L.C. BROUSSEAU, A.B. HOUSE, E.M. EDEKI, J.C. FELDHAUS, D.L. FELDHEIM, *J. Am. Chem. Soc.* **1999**, *121*, 8518.
- 9 C.L. HUANG, E. MATIJEVIC, *J. Mater. Res.* **1995**, *10*, 1327.
- 10 R.H. OTTEWILL, A.B. SCHOFIELD, J.A. WATERS, N.ST.J. WILLIAMS, *Colloid Polym. Sci.* **1997**, *275*, 274.
- 11 L. QUARONI, G. CHUMANOV, *J. Am. Chem. Soc.* **1999**, *121*, 10642.
- 12 R.K. ILER, *U.S. Pat.*, 2,885,366, 1959.
- 13 N. KAWAHASHI, E. MATIJEVIC, *J. Colloid Interface Sci.* **1991**, *143*, 103.
- 14 L.M. LIZ-MARZAN, M. GIERSIG, P. MULVANEY, *Langmuir* **1996**, *12*, 4329.
- 15 S. RAMESH, Y. COHEN, R. PROSOROV, K.V.P.M. SHAFI, D. AURBACH, A. GEDANKEN, *J. Phys. Chem. B* **1998**, *102*, 10234.
- 16 N. ARUL DHAS, A. ZABAN, A. GEDANKEN, *Chem. Mater.* **1999**, *11*, 806.
- 17 F. LIM, A.M. SUN, *Science* **1980**, *210*, 908.
- 18 *Hollow and Solid Spheres and Microspheres: Science and Technology Associated With Their Fabrication and Application*, Eds. D.L. WILCOX, M. BERG, T. BERNAT, D. KELLERMAN, J.K. COCHRAN, Materials Research Society, Pittsburgh, **1995**.
- 19 E. MATIJEVIC, in *Fine Particle Science and Technology*, Ed. E. Pelizzetti, Kluwer, Dordrecht, **1996**, pp. 1–16.
- 20 S.J. SHUTTLEWORTH, S.M. ALLIN, P.K. SHARMA, *Synthesis* **1997**, *11*, 1217.
- 21 R. PARTCH, in *Materials Synthesis and Characterization*, Ed. D. Perry, Plenum Press, New York, **1997**, pp. 1–17.
- 22 R. DAVIES, G.A. SCHURR, P. MEENAN, R.D. NELSON, H.E. BERGNA, C.A.S. BREVETT, R.H. GOLDBAUM, *Adv. Mater.* **1998**, *10*, 1264.
- 23 R. LANGER, *Acc. Chem. Res.* **2000**, *33*, 94.
- 24 R.K. ILER, *J. Colloid Interface Sci.* **1966**, *21*, 569.
- 25 G. DECHER, J.-D. HONG, *Ber. Bunsen-Ges. Phys. Chem.* **1991**, *95*, 1430.
- 26 DECHER, G., HONG, J.-D. *Makromol. Chem., Macromol. Symp.* **1991**, *46*, 321.
- 27 For reviews, see: (a) G. DECHER, *Science* **1997**, *277*, 123, and references therein; (b) G. DECHER, in *Templating, Self Assembly and Self-Organisation*, Eds. J.-P. SAUVAGE, M.W. HOSSEINI, Pergamon Press, Oxford, **1996**, vol. 9, pp. 507–528.
- 28 S.W. KELLER, S.A. JOHNSON, E.S. BRIGHAM, E.H. YONEMOTO, T.E. MALLOUK, *J. Am. Chem. Soc.* **1995**, *117*, 12879.
- 29 T. CHEN, P. SOMASUNDARAN, *J. Am. Ceram. Soc.* **1998**, *81*, 140.
- 30 R. POMMERSHEIM, J. SCHREZENMEIR, W. VOGT, *Macromol. Chem. Phys.* **1994**, *195*, 1557.
- 31 P. RILLING, T. WALTER, R. POMMERSHEIM, W. VOGT, *J. Membr. Sci.* **1997**, *129*, 283.
- 32 O. GASEROD, A. SANNES, G. SKJAK-BRAEK, *Biomaterials*, **1999**, *20*, 773.
- 33 A. BARTKOWIAK, D. HUNKELER, *Chem. Mater.* **2000**, *12*, 206.
- 34 E. DONATH, G.B. SUKHORUKOV, F. CARUSO, S.A. DAVIS, H. MÖHWALD, *Angew. Chem. Int. Ed. Engl.* **1998**, *37*, 2201.
- 35 F. CARUSO, E. DONATH, H. MÖHWALD, *J. Phys. Chem. B* **1998**, *102*, 2011.
- 36 G.B. SUKHORUKOV, E. DONATH, H. LICHTENFELD, E. KNIPPEL, M. KNIPPEL, H. MÖHWALD, *Colloids Surf A* **1998**, *137*, 253.
- 37 F. CARUSO, R.A. CARUSO, H. MÖHWALD, *Science* **1998**, *282*, 1111.
- 38 G.B. SUKHORUKOV, E. DONATH, S. DAVIS, H. LICHTENFELD, F. CARUSO, V.I. POPOV, H. MÖHWALD, *Polym. Adv. Technol.*, **1998**, *9*, 759.
- 39 For a review see: (a) F. CARUSO, *Chem. Eur. J.* **2000**, *6*, 413, and references therein.
- 40 A. VOIGT, H. LICHTENFELD, G.B. SUKHORUKOV, H. ZASTROW, E. DONATH, H. BAÜMLER, H. MÖHWALD, *Ind. Eng. Chem. Res.* **1999**, *38*, 4037.
- 41 F. CARUSO, H. LICHTENFELD, E. DONATH, H. MÖHWALD, *Macromolecules* **1999**, *32*, 2317.
- 42 F. CARUSO, C. SCHÜLER, D.G. KURTH, *Chem. Mater.* **1999**, *11*, 3394.
- 43 D.G. KURTH, F. CARUSO, C. SCHÜLER, *Chem. Commun.* **1999**, 1579.
- 44 G.B., SUKHORUKOV, J. SCHMITT, G. DECHER, *Ber. Bunsen-Ges. Phys. Chem.* **1996**, *100*, 948.



- 45 HSIEH, M.C. FARRIS, R.J., MCCARTHY, T.J. *Macromolecules* **1997**, *30*, 8453.
- 46 F. CARUSO, H. LICHTENFELD, H. MÖHWALD, M. GIERSIG, *J. Am. Chem. Soc.* **1998**, *120*, 8523.
- 47 F. CARUSO, H. MÖHWALD, *Langmuir* **1999**, *15*, 8276.
- 48 R.A. CARUSO, A. SUSHA, F. CARUSO, *Chem. Mater.* **2001**, *13*, 400.
- 49 K. RHODES, S.A. DAVIS, F. CARUSO, B. ZHANG, S. MANN, *Chem. Mater.* **2000**, *12*, 2832.
- 50 F. CARUSO, A.S. SUSHA, M. GIERSIG, H. MÖHWALD, *Adv. Mater.* **1999**, *11*, 950.
- 51 F. CARUSO, M. SPASOVA, A. SUSHA, M. GIERSIG, R.A. CARUSO, *Chem. Mater.* **2001**, *13*, 109.
- 52 F. CARUSO, X. SHI, R.A. CARUSO, A. SUSHA, *Adv. Mater.* **2001**, *13*, 740.
- 53 D.I. GITTINS, A.S. SUSHA, B. SCHÖLER, F. CARUSO, *Adv. Mater.* **2002**, *14*, 508.
- 54 F. CARUSO, M. SPASOVA, V. SALGUEIRO-MACEIRA, L.M. LIZ-MARZÁN, *Adv. Mater.* **2001**, *13*, 1090.
- 55 A. SUSHA, F. CARUSO, A. L. ROGACH, G.B. SUKHORUKOV, A. KORNOWSKI, H. MÖHWALD, M. GIERSIG, A. EYCHMÜLLER, H. WELLER, *Colloids Surf. A* **2000**, *163*, 39.
- 56 A. ROGACH, A. SUSHA, F. CARUSO, G. SUKHORUKOV, A. KORNOWSKI, S. KERSHAW, H. MÖHWALD, A. EYCHMÜLLER, H. WELLER, *Adv. Mater.* **2000**, *12*, 333.
- 57 F. CARUSO, H. MÖHWALD, *J. Am. Chem. Soc.* **1999**, *121*, 6039.
- 58 C. SCHÜLER, F. CARUSO, *Macromol. Rapid Commun.* **2000**, *21*, 750.
- 59 F. CARUSO, C. SCHÜLER, *Langmuir* **2000**, *16*, 9595.
- 60 F. CARUSO, H. FIEDLER, K. HAAGE, *Colloids Surf. A* **2000**, *169*, 287.
- 61 Y. LVOV, F. CARUSO, *Anal. Chem.* **2001**, *73*, 4212.
- 62 I. L. RADTCHENKO, G. B. SUKHORUKOV, S. LEPORATTI, G. B. KHOMUTOV, E. DONATH, H. MÖHWALD, *J. Colloid Interface Sci.* **2000**, *230*, 272.
- 63 S. MOYA, E. DONATH, G. B. SUKHORUKOV, M. AUCH, H. BÄUMLER, H. LICHTENFELD, H. MÖHWALD, *Macromolecules* **2000**, *33*, 4538.
- 64 G. B. SUKHORUKOV, E. DONATH, S. MOYA, A. S. SUSHA, A. VOIGT, J. HARTMANN, H. MÖHWALD, *J. Microencapsulation* **2000**, *17*, 177.
- 65 R. GEORGIEVA, S. MOYA, S. LEPORATTI, B. NEU, H. BÄUMLER, C. REICHLE, E. DONATH, H. MÖHWALD, *Langmuir* **2000**, *16*, 7075.
- 66 D. I. GITTINS, F. CARUSO, *Adv. Mater.* **2000**, *12*, 1947.
- 67 D. I. GITTINS, F. CARUSO, *J. Phys. Chem. B* **2001**, *105*, 6846.
- 68 K.-K. KUNZE, R.R. NETZ, *Phys. Rev. Lett.* **2000**, *85*, 4389.
- 69 F. CARUSO, D. TRAU, H. MÖHWALD, R. RENNEBERG, *Langmuir* **2000**, *16*, 1485.
- 70 M. E. BOBRESHOVA, G. B. SUKHORUKOV, E. A. SABUROVA, L. I. ELFIMOVA, B. I. SUKHORUKOV, L. I. SHARABCHINA, *Biophysics* **1999**, *44*, 813.
- 71 N.G. BALABUSHEVITCH, G. B. SUKHORUKOV, N. A. MOROZ, D. V. VOLODKIN, N. I. LARIONOVA, E. DONATH, H. MÖHWALD, *Biotechnol. Bioeng.* **2001**, *76*, 207.
- 72 V. S. TRUBETSKOY, A. LOOMIS, J. E. HAGSTROM, V. G. BUDKER, J. A. WOLFF, *Nucleic Acids Res.* **1999**, *27*, 3090.
- 73 D. FINSINGER, J. S. REMY, P. ERBACHER, C. KOCH, C. PLANK, *Gene Therapy* **2000**, *7*, 1183.
- 74 R. DALLÜGE, A. HABERLAND, S. ZAITSEV, M. SCHNEIDER, H. ZASTROW, G. B. SUKHORUKOV, M. BÖTTGER, *Gene Str. Express. BRA*, **2002**, *1576*, 45.
- 75 F. CARUSO, W. YANG, D. TRAU, R. RENNEBERG, *Langmuir* **2000**, *16*, 8932.
- 76 X. SHI, F. CARUSO, *Langmuir* **2001**, *17*, 2036.
- 77 E. DONATH, G. B. SUKHORUKOV, H. MÖHWALD, *Nach. Chem. Tech. Labor.* **1999**, *47*, 400.
- 78 B. NEU, A. VOIGT, R. MITLÖHNER, S. LEPORATTI, E. DONATH, C. Y. GAO, H. KIESEWETTER, H. MÖHWALD, H. J. MEISELMAN, H. BÄUMLER, *J. Microencapsulation* **2001**, *18*, 385.
- 79 V. DUDNIK, G. B. SUKHORUKOV, I. L. RADTCHENKO, H. MÖHWALD, *Macromolecules* **2001**, *34*, 2329.
- 80 I. L. RADTCHENKO, G. B. SUKHORUKOV, H. MÖHWALD, *Colloids Surf. A* **2002**, *202*, 127.
- 81 A. VOIGT, E. DONATH, H. MÖHWALD, *Macromol. Mater. Eng.* **2000**, *282*, 13.

- 82 I. L. RADTCHENKO, G. B. SUKHORUKOV, A. L. ROGACH, A. KORNOWSKI, H. MÖHWALD, *Adv. Mater.* **2001**, *13*, 1684.
- 83 S. H. PARK, Y. XIA, *Langmuir* **1999**, *15*, 266.
- 84 P. JIANG, J. F. BERTONE, K. S. HWANG, V. L. COLVIN, *Chem. Mater.* **1999**, *11*, 2132.
- 85 S. A. ASHER, J. HOLTZ, J. WEISSMAN, G. PAN, *MRS Bull.* **1998**, *October*, 44.
- 86 W. L. VOS, M. MEGENS, C. M. VAN KATS, P. BOESECHE, *Langmuir* **1997**, *13*, 6004.
- 87 A. VAN BLAADEREN, R. RUEL, P. WILTZIUS, *Nature* **1997**, *385*, 321.
- 88 O. D. VELEV, A. M. LENHOFF, E. W. KALER, *Science* **2000**, *287*, 2240.
- 89 M. L. BREEN, A. D. DINSMORE, R. H. PINK, S. B. QADRI, B. R. RATNA, *Langmuir* **2001**, *17*, 903.
- 90 K. P. VELIKOV, A. VAN BLAADEREN, *Langmuir* **2001**, *17*, 4779.
- 91 G. KUMARASWAMY, A. M. DIBAJ, F. CARUSO, *Langmuir* **2002**, *18*, 4150.
- 92 Z. LIANG, A. S. SUSHI, F. CARUSO, *Adv. Mater.* **2002**, in press.
- 93 O. D. VELEV AND E. W. KALER, *Adv. Mater.* **2000**, *12*, 531.
- 94 Y. XIA, B. GATES, Y. YIN, Y. LIU, *Adv. Mater.* **2000**, *12*, 693.
- 95 O. D. VELEV, P. M. TESSIER, A. M. LENHOFF, E. W. KALER, *Nature* **1999**, *401*, 548.
- 96 K. M. KULINOWSKI, P. JIANG, H. VASWANI AND V. L. COLVIN, *Adv. Mater.* **2000**, *12*, 833.
- 97 J. E. G. J. WIJNHOFEN, W. L. VOS, *Science* **1998**, *281*, 802.
- 98 B. T. HOLLAND, C. F. BLANFORD, A. STEIN, *Science* **1998**, *281*, 538.
- 99 Y. A. VLASOV, N. YAO, D. J. NORRIS, *Adv. Mater.* **1999**, *11*, 165.
- 100 A. A. ZAKHIDOV, R. H. BAUGHMAN, Z. IQBAL, C. X. CUI, I. KHAYRULLIN, S. O. DANTAS, I. MARTI, V. G. RALCHENKO, *Science* **1998**, *282*, 897.
- 101 A. BLANCO, E. CHOMSKI, S. GRABTCHAK, M. IBISATE, S. JOHN, S. W. LEONARD, C. LOPEZ, F. MESEGUER, H. MIGUEZ, J. P. MONDIA, G. A. OZIN, O. TOADER, H. M. VAN DRIEL, *Nature* **2000**, *405*, 437.
- 102 B. GATES, Y. YIN, Y. XIA, *Chem. Mater.* **1999**, *11*, 2827.
- 103 S. A. JOHNSON, P. J. OLIVIER, T. E. MALLOUK, *Science* **1999**, *283*, 963.
- 104 P. JIANG, J. CIZERON, J. F. BERTONE, V. L. COLVIN, *J. Am. Chem. Soc.* **1999**, *121*, 11630.
- 105 WANG, D., CARUSO, F. *Adv. Mater.* **2001**, *13*, 350.
- 106 D. WANG, R. A. CARUSO, F. CARUSO, *Chem. Mater.* **2001**, *13*, 364.
- 107 E. L. BIZDOACA, M. SPASOVA, M. FARLE, M. HILGENDORFF, F. CARUSO, *J. Magn. Magn. Mater.* **2002**, *240*, 44.
- 108 I. PASTORIZA-SANTOS, I., B. SCHÖLER, F. CARUSO, *Adv. Functional Mater.* **2001**, *11*, 122.
- 109 C. SCHÜLER, F. CARUSO, *Biomacromolecules* **2001**, *2*, 921.
- 110 W. JIN, X. SHI, F. CARUSO, *J. Am. Chem. Soc.* **2001**, *123*, 8121.
- 111 D. TRAU, R. RENNEBERG, F. CARUSO, in preparation.
- 112 W. YANG, D. TRAU, R. RENNEBERG, N. T. YU, F. CARUSO, *J. Colloid Interface Sci.* **2001**, *234*, 356.
- 113 A. A. ANTIPOV, G. B. SUKHORUKOV, E. DONATH, H. MÖHWALD, *J. Phys. Chem. B* **2001**, *105*, 2281.
- 114 W. YANG, D. TRAU, M. LEHMANN, F. CARUSO, N. T. YU, R. RENNEBERG, *Anal. Chem.* **2002**, in press.
- 115 S. MECKING, R. THOMANN, *Adv. Mater.* **2000**, *12*, 953.
- 116 A. DOKOUTCHAEV, J. T. JAMES, S. C. KOENE, S. PATHAK, G. K. S. PRAKASH, M. E. THOMPSON, *Chem. Mater.* **1999**, *11*, 2389.

## 13

### Smart Capsules

HELMUTH MÖHWALD, EDWIN DONATH and GLEB SUKHORUKOV

#### Abstract

A procedure to produce hollow capsules with equally defined walls from a defined polyelectrolyte multilayer is described. Decomposable colloid particles are coated by the layer by layer technique, the core is then dissolved and low molecular weight residuals permeate through the wall. The core may consist of inorganic, organic or biological materials, polymers, or cells, consequently the removal chemistry is highly varied. The walls can consist of the whole diversity of materials that have been used for planar multilayers. Because of the great diversity and modularity permeation can be controlled by pH, ionic strength or temperature, and there are also prospects for control via light. The stability and mechanical properties can be optimized via material selection but also via additional chemical treatment, e.g. crosslinking. One may make use of specific physical and chemical processes inside the wall, in particular

- precipitation and crystallization
- polymerization and polymer functionalization
- enzymatic and heterogeneous catalysis
- photocatalysis and crosslinking

Use is made of the specific wall features, selective permeability, and controlled composition of inner and outer surface. The rapid progress in the field has been achieved by building on the knowledge of the preparation and characterization of planar multilayers with the addition of newly developed techniques of colloid characterization such as scanning force microscopy, confocal microscopy and single particle light scattering, in combination with traditional methods. Thus a system is described with many application perspectives in materials and life sciences but also with new features for additional film characterization by techniques requiring much surface.

## 13.1

### Preparation and Structure

#### 13.1.1

##### General Aspects

###### 13.1.1.1 Core materials

In Chapter 12 the coating of different core materials by polyelectrolyte multilayers was discussed. This will not be reiterated here. Instead the special issues that concern removal of the core to obtain a hollow capsule or a capsule with a specific function inside will be addressed.

The first hollow capsules were made from a polymeric core, in this case weakly crosslinked melamine formaldehyde [1, 2]. For this core, methods of preparation were established to obtain very uniform core diameters between 100 nm and 10  $\mu\text{m}$ , spherical shapes and low surface roughness and it was also known that the core could be destroyed by going to a  $\text{pH} < 1.6$  or by treatment with dimethylformamide. In addition, techniques to fabricate lattices are very well developed and hence are presumably economical. One may also envisage other ways to destroy the polymer e.g. by light, heat or enzymes. However, there may also arise polymer-specific problems like unspecific side reactions or residual oligomers sticking to or inside the walls. These aspects will be considered in detail in Section 13.1.2.

The problem of product removal after core destruction is less severe if the core is an inorganic colloid. Also one does not need to worry about toxic side effects if the core is e.g.  $\text{CaCO}_3$ , which in addition is very cheap. The kinetic hindrance of a reaction induced by a  $\text{pH}$  change or by a complexing agent like EDTA is also a less severe problem than with polyelectrolytes. However, techniques to obtain inorganic particles of uniform sizes in the  $\mu\text{m}$  range are not yet well developed for most candidate materials. Depending on the demands for a certain application, inorganic cores are a promising alternative. A special case of an inorganic, rather low-cost, sufficiently monodisperse core is silica. It can be easily coated and the silica can be removed afterwards by treatment with hydrofluoric acid. The disadvantage of silica is that the core removal procedure involves a dangerous step when the hydrofluoric acid is applied. The polyelectrolyte coat was found to be rather stable in hydrofluoric acid.

Other alternatives are organic particles of low molecular weight compounds [3, 4]. They often have the problem of being soluble in solvents different from those for polyelectrolytes. This may be overcome by using surfactants or polymeric amphiphiles covering the particle surface, thus rendering them water soluble and/or charged. However, one thus obtains a multicomponent system and some of these surfactants remaining in solution may undergo unwanted reactions, or complexation, during further coating processes. Also the techniques to prepare organic particles of uniform size and shape in the  $\mu\text{m}$  range do not exist, and one typically has to use organic solvents which are undesirable from many other, e.g. environmental aspects.

Special types of core are precipitates of enzymes [5] or of DNA [6]. They are not meant to be destroyed but to function while being protected by the shell that may

later be destroyed, e.g. after attaching to a cell nucleus. To this class also belong cores of inorganic/organic composites where later the organic component is removed and the inorganic one remains inside as a particulate catalyst, fluorophore or magnetic tag.

Compared to the solid core, liquid cores are more difficult to handle due to their higher flexibility and mobility. However, it has been possible to freeze this flexibility by coating oil droplets with polyelectrolytes. For this the oil did not have to be coated and charged by an ionic surfactant since even charged polyelectrolytes like PSS are somewhat enriched at the oil/water interface and are then amenable to further coating by oppositely charged polyelectrolyte. It is desirable to use polymeric amphiphiles with higher interfacial activity because polymers not residing at the interface may complex with oppositely charged ones on further coating and the resulting unwanted structures may have to be removed. In any case, coating of oils is technically very promising since it yields a new type of emulsion with low dynamics and stabilized by Coulombic forces, for use e.g. in cosmetics, the food industry or pharmacy.

Early in the development of the subject, erythrocytes or yeast cells were successfully coated [7]. Here the coat may be useful as a protective surface or as a way to target the cell to a specific location. On the other hand many cells have very peculiar shapes and one may obtain hollow capsules with anisometric shapes. Red blood cells have been fixed in shape by glutardialdehyde crosslinking (thus losing their function). Although the charge pattern on a cell surface is very nonuniform it was possible to obtain alternating overall surface charge patterns after four coating cycles. Methods to destroy cell material have also been developed, e.g. treatment with NaOCl, called a deproteinizer. It has been possible thus to obtain hollow capsules with templated shapes (see Fig. 13.1). However, the treatment is very harsh and in Section 13.1.2 various side reactions will be discussed.

### 13.1.1.2 Wall materials

First we set technical limits to the selection of wall materials:

- The coating process includes the bending of a polymer on a curved surface. This is not a problem for micron-sized colloids but becomes an issue for dimensions below 100 nm when the particle size approaches the length of the polymer. As an important example DNA wrapping a histon protein has also been studied theoretically, where the competition between electrostatic interaction and bending yields an ionic strength window where coating is possible.
- For smaller particles at reasonable concentration (100 nm, (1% v/v)) stability against flocculation becomes a problem because the time between particle collisions due to thermal motion and that of charge reversal becomes comparable. Acceleration of charge reversal is possible using smaller polymers or oligomers.
- Another problem associated with the smaller size is that at particle concentrations as low as 1–3% it becomes increasingly difficult to adjust the polyelectrolyte concentration in such a way that polymer is present in sufficient excess in

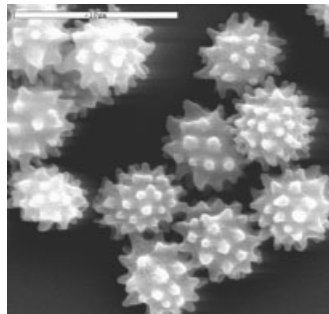
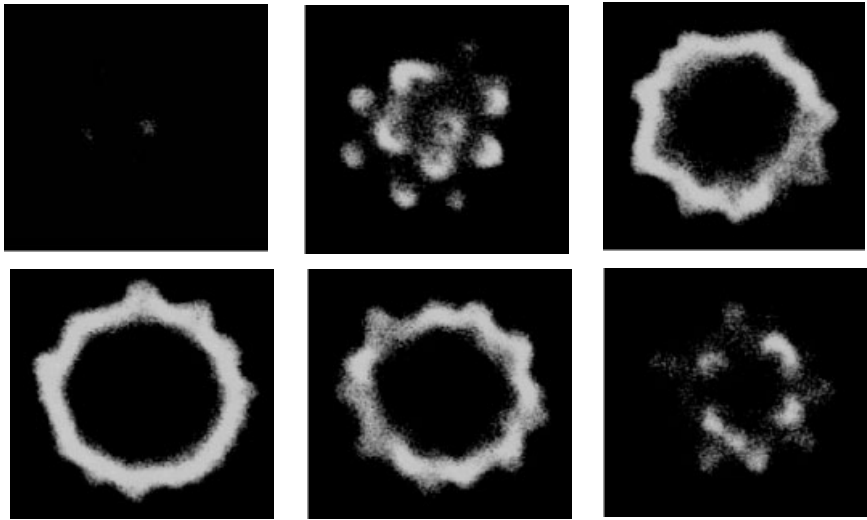


**Fig. 13.1** Confocal microscopy scans of a polyelectrolyte shell consisting of 11 layers of PSS/PAH templated on an echinocyte. The outer layer is FITC labelled PAH. The width of the images is  $7\ \mu\text{m}$ . The scans (left-right, top-

bottom) were made in two planes separated by a distance of  $1\ \mu\text{m}$ . Scan runs through the upper part of the shell. The SEM image on the bottom shows the initial echinocyte cells.

the aqueous solution. The total surface area of the particles at the same volume fraction increases with  $r^{-1}$  while the polyelectrolyte concentration has a practical limit due to solubility and the viscosity of the solution.

The first wall materials used were polyelectrolytes poly(styrene sulfonate) (PSS) and poly(allylamine hydrochloride) (PAH). Since then a variety of polymers have been used and there is virtually no restriction if the polymer contains multiple charges. Depending on some specific requirement chitosane, chitosanesulfate and a variety of other modified polysaccharides have been used as biocompatible and

biodegradable polymers, DNA was used as a stiff polymer that later may offer some function like gene therapy. Co-polymers with another functionality, e.g. thermal responsiveness were used successfully where the second uncharged component could be in fractions close to 90%. Also other building principles than electrostatics like biospecific ligand binding, hydrogen bonding and metal coordination were applied successfully to the preparation of shells. In these latter cases special care had to be taken to ensure colloid stability, because Coulomb repulsion as a stabilizing mechanism is at least reduced.

Inorganic particles could be used as a wall material in combination with an oppositely charged polyelectrolyte to render the wall magnetic [8], luminescent or simply to change the elastic properties of the wall. As an extreme into the latter direction  $\text{SiO}_2$  particles could be calcined, leading to sintering and thus building of solid bridges between the particles [9]. This leads to porous inorganic hollow capsules. Another promising route may be metal particle incorporation to give a conducting wall and/or to have an efficient microwave absorber.

It is also possible to build up the walls from a combination of multiply charged low molecular weight molecules or metal ions [10]. This is attractive if the wall is supposed to absorb or to emit light and if the chromophore is arranged at a specific location along the surface normal. This may be required, e.g. to build an electron transfer chain through the wall, to study the accessibility to quenchers and thus their diffusion or to generate a charge separation by light at a specific location inside the wall. In many of these cases, however, it is simpler to incorporate a polyelectrolyte with a dye covalently coupled to it. A special advantage of using low molecular weight compounds may be that their coupling is not very stable. Thus the wall can be destroyed again, e.g. by adding high salt concentrations ( $\sim 1$  M).

In order to achieve specific functions it has also been possible to incorporate proteins as a structural material. Because the build-up defines a position along the normal it is thus possible to design enzyme cascades whilst still protecting the enzymes against proteases. Of course, in this case one has to be careful that the core removal chemistry does not destroy the enzymes. For the purposes of targeting one may envision attaching antibodies or other specific ligands at the outer surface. These attempts, however, are far from being optimized.

The more biomimetic approach would be to adsorb a lipid monolayer or bilayer at the outer surface. In this case the capsules become soluble in hydrophobic solvents or impermeable to hydrophilic components [11]. In these attempts binding occurred through Coulombic interactions, but these could be reduced by e.g. using mixtures of charged lipids. In the latter case the problem of having exclusively bilayers has not yet been solved, but the coupling was low enough to keep liquid crystalline and solid phases as observed for free bilayers. In Section 13.2.1 we will also discuss the problem of controlling defects in the bilayers which dramatically affect their ion permeability such that we are far from the insulating properties of a black lipid membrane. Still, at this stage, the bilayer coating is sufficiently homogeneous and perfect that studies with incorporated ion channels and receptors become meaningful.

### 13.1.1.3 Molecular Dynamics

Obviously the dynamics of molecules is of high relevance for the control of wall properties, e.g. permeability, but the shells also provide a unique possibility of studying this dynamics: because of their large specific surface area they enable the application of typical bulk techniques like NMR and flash spectroscopy. For typical diameters near 1  $\mu\text{m}$  they may be considered as free standing film which can be made asymmetric at will, and for smaller dimensions curvature effects may come into play. These features are just beginning to be explored, and therefore this section does not contain many hard facts. Dynamics usually involves many motional modes, length and time scales. There are not yet any data available on time scales below 1  $\mu\text{s}$  and the segment mobility also could not be elucidated. A way to get access to this could be  $^2\text{D}$  NMR for highly swollen walls, but this is demanding as regards technique, deuterated material and preparation with the proper degree of swelling. The translational motion of polymer melts is generally described by the reptation model, where a polymer moves in a tube with diameter equivalent to its cross section. For polyelectrolyte multilayers one expects electrostatic coupling with neighboring molecules, and it is thus not surprising that one could not measure any lateral polyelectrolyte mobility in planar films, i.e. the diffusion coefficient is below  $10^{-15} \text{ cm}^2 \text{ s}^{-1}$  as measured by fluorescence recovery after photobleaching (FRAP). One also expects similarly small values for capsules.

More interesting, and also quantitatively measurable, is the translational mobility of small molecules and ions. This process is generally described by a free volume model, i.e. in order for a species to move a free volume  $V_f$  has to be created thermally and the molecule can then jump into this vacancy. The free energy of this hole depends exponentially on the necessary free volume and the compressibility and one therefore expects a drastic dependence on these parameters. This has been verified for polymeric glasses, and also for polyelectrolyte multilayers by studying the fluorescence quenching by molecules of different sizes. In the latter cases diffusion coefficients between  $10^{-15}$  and  $10^{-12} \text{ cm}^2 \text{ s}^{-1}$  were determined, and modeling of the data also revealed that the mobility was up to two orders of magnitude larger in the top 10 nm of the multilayer adjacent to water. This has been ascribed to swelling of the film adjacent to water and one may expect even ten orders of magnitude faster diffusion if one has a completely swollen film. This has not yet been verified for planar films, and also the equivalent experiments have not yet been performed for capsules. One could principally learn about diffusion from the permeation experiments described in Section 13.2.1 if the latter were due to diffusion through the matrix, not through the pores. In this case values of  $D \approx 10^{-11} \text{ cm}^2 \text{ s}^{-1}$  were derived. These might be attributed to a different preparation protocol of capsules (always in water) compared to planar films (dried after each adsorption step) but more probably it is due to the fact that diffusion is not the permeation mechanism.

Obtaining more quantitative information on diffusion has been inhibited by the fact that there are slow aging mechanisms (see Section 13.2.2). These may be related to the internal dynamics of the polyelectrolyte complex which is basically



due to the low stability of the Coulomb interaction in an aqueous environment. As a simple estimate the attractive energy  $E$  of two opposite charges a distance  $R=2.5 \text{ \AA}$  apart in matter ( $\epsilon=80$ ) amounts to  $E = \frac{e_0^2}{4\pi\epsilon\epsilon_0 r} = 2.8 kT$ , where  $k$  is Boltzmann's constant and  $T$  the absolute temperature.

The lifetime  $\tau$  of the bond would thus be  $\tau = \tau_0 \exp(nE/kT)$ , where  $n$  is the number of bonds, and with  $\tau_0 \sim 10^{-13} \text{ s}$ , a typical inverse vibration frequency, one obtains  $\tau = 2.5 \text{ \mu s}$  for six simultaneous bonds. Thus individual bonds would reform much faster than  $1 \text{ \mu s}$  if they were not stabilized by lower water content in the film and by neighboring bonds. These effects, however, depend strongly on the individual polymers and one should not be surprised to find drastic differences in the internal dynamics when comparing different systems.

Indirect information on the dynamics of water in the shells can be obtained from  $^1\text{H-NMR}$  relaxation experiments. There one basically determines the fraction of water immobilized multiplied by its "immobilization strength". One thus finds that water is immobilized in the film, even in the inner layers, but the amount depends drastically on the charge of the outer layer, as if the latter either compresses or expands the total film to remove or create water pockets. Recently the swelling kinetics of films brought into contact with water or with air of different humidity were analyzed in terms of two processes, the faster one (100 s) ascribed to permeation of water into the films and the slower one to reorganization of the matrix. Such a slow water diffusion (100 s) would be very surprising since, judging from experiments with dye probes, one would expect diffusion of water, metal ions, protons, and other small solvent molecules to penetrate in less than 1 ms.

### 13.1.2

#### Physics and Chemistry of Core Removal

The above, mostly qualitative, remarks on dynamics were necessary to conceive that small molecules can permeate the walls and that the multilayers possess viscosity and possibly also elasticity. Hence to remove the core one first has to break it into small entities that can diffuse through the wall. Consequently, we will first discuss the process of core destruction and then removal of core material and concomitant changes of the wall.

#### 13.1.2.1 Core Destruction

##### Depolymerization

The first core material used was melamine formaldehyde. It is prepared by polymerization from a precondensate solution. The particle formation involves kinetic control of droplet growth as well as crosslinking. This leads to uniform size distribution with polydispersities of less than 5%. The crosslinking reaction is acid catalyzed and proceeds more slowly than particle formation. It can be stopped at an early stage. In this way melamine resin particles are fabricated which can easily be dissolved afterwards in 0.1 M hydrochloric acid.

The decomposition process of the melamine formaldehyde cores has been studied in detail [12]. The melamine resin represents a network of melamine formaldehyde crosslinked either by ether linkages or methylene bridges. Primary hydroxy and amino groups not utilized for crosslinking are also present. Upon treatment with hydrochloric acid the ether linkages are hydrolyzed, while the methylene bridges remain intact; as a result the core is decomposed into oligo- as well as polymeric units. In parallel with the hydrolysis of the ether bridges, melamine is hydrolyzed to ammeline, as was evidenced by the appearance of a characteristic amide group.

It is remarkable that in parallel with hydrolysis a second acid catalyzed re-polymerization reaction occurs which results in the formation of C–N–C linkages. If this reaction is faster than the hydrolysis the core will be converted to an insoluble resin. It is hence a subtle balance which should be obeyed, otherwise hollow shells cannot be produced. This occurs frequently if the pH is either too large or too small. A mild acid pretreatment will typically produce insoluble cores. If the hydrochloric acid is too strong ( $>0.1$  M) the re-polymerization becomes increasingly faster than the hydrolysis.

The size of the degradation products was estimated from diffusion coefficient measurements which were conducted by means of fluorescence correlation spectroscopy. It was concluded that the products of hydrolysis were on average composed of melamine formaldehyde polymers consisting of about 60 monomers. If, however, the core was dissolved in dimethyl formamide, a good solvent for melamine formaldehyde, polymeric products composed of about 4000 monomers were obtained. The hydrodynamic radius of the melamine formaldehyde polymer obtained by means of hydrolysis is about 3–4 nm. This is too large for fast diffusion through the shell walls. The increase in osmotic pressure is currently thought to be responsible for widening the pre-existing pores or for the formation of new pores which then allow passage of the melamine resin degradation products. The physico-chemical aspects of this process will be discussed later. The osmotically induced stretching of the wall is clearly visible when the degradation is followed under the confocal microscope. In parallel with a remarkable diameter increase the core products are released. If the layer is too thick this pore widening is impossible. As a result of the increased osmotic pressure the shells will break. This occurs typically if, for example, more than 8 pairs of PAH and PSS are assembled onto a micron sized core. Other shell wall materials may be less suitable for shell formation due to their different mechanical and permeability properties.

The polymeric nature of the degradation products has another less favorable consequence. Some core material almost always remains inside the shells. As soon as the driving force for release disappears, which takes place toward the end of release, the pores will close and some core material is captured inside. Various fluorescence techniques such as confocal microscopy and Förster energy transfer have revealed that most of the remaining material is adsorbed on the wall. Since the melamine formaldehyde degradation products are positively charged they preferentially interact with the polyanion in the multilayer. This may lead to a modification of the layer properties and has to be taken into account if the shells are used afterwards.

Another alternative core could be protein precipitates or cells. For their destruction a treatment with NaOCl, called deproteinizer, is well established [7]. Hypochlorite is widely used as a strong disinfecting and cleaning agent. Its function is based on its reductive potential, +0.89 mV, as a result of electron release when the compound is hydrolyzed. It is interesting to recall that hypochlorite is an agent released in the human body by neutrophils during their immune reaction against bacteria. It destroys the proteins of the invading microorganism by oxidation in very much the same way that an erythrocyte core can be destroyed inside a polyelectrolyte multilayer adsorbed on top of it. The proteins are broken into smaller pieces which can leave the shell. However, a deeper analysis showed that, for example, PSS is also degraded. It was found that as much as 90% of the originally present PSS was lost during the deproteinizer treatment. PAH is also degraded. A large variety of oxidation reactions occur which convert the amino groups into nitrile, nitro and nitroso groups. Aldehydes and carboxylic acid groups are also produced. Secondary reactions may then cross-link these entities forming azo, azo-methine and azoxy-bridges.

Hence it can be concluded that the deproteinizer treatment finally produces a loose polymer network which is completely different from the original multilayer structure. It does not have any cationic groups. The nature of the obviously present anionic groups is still uncertain, the negative charge may result from some remaining sulfonic acid groups.

It is worth mentioning that successful shell formation is closely connected with the presence of the PAH. With other polycations the process of shell fabrication does not yet work properly. For example pure polysaccharide multilayers were completely degraded during core decomposition.

### **Core dissolution**

If the core is made of precipitates of low molecular weight compounds destruction requires merely change of the solubility product. This can be achieved by changing the pH, as exemplified for an organic molecule by adding a strongly complexing agent, e.g. EDTA in the case of  $\text{CaCO}_3$  or  $\text{CdCO}_3$  [13]. In these cases one does not expect any side reactions. There are problems related to the attraction of divalent ions or EDTA to the polyelectrolyte but these problems are not major. The limiting factor lies more in obtaining inorganic cores of the desired size and dispersity and free of stabilizing polymer.

Since techniques to prepare  $\text{SiO}_2$  particles of defined dimensions have been well developed it is desirable to develop these techniques to induce core removal. It has been possible to dissolve these cores in HF, a standard method for dissolving glass and applicable here, too.

### **Other techniques of core destruction**

In principle, it should also be possible to destroy cores with light, but this has not yet been attempted successfully. Another way is heat treatment and the extreme of this is calcination [9]. For this case protocols have been developed to destroy

thermally a polymeric core while leaving an inorganic shell largely intact, although porous. Such a treatment was elaborated for cores coated with a  $\text{SiO}_2$ / polyelectrolyte composite. In this case the organic components were destroyed, the  $\text{SiO}_2$  particles at the walls were sintered, i.e. bridges were built between individual particles. This enabled the formation of porous hollow  $\text{SiO}_2$  spheres. These shells are stable even after calcination from walls with one monolayer  $\text{SiO}_2$ , but of course they are much more stable if prepared from  $\text{SiO}_2$  in many multilayers.

### 13.1.2.2 Core Material Release

As has become clear above, different core materials require different destruction processes, and this in turn will affect material removal and its optimization. The process has been investigated in detail for MF cores [12] and these will now be considered in detail here. In this way it will become clear that there are many features to be optimized for a successful preparation, and these may depend drastically on the system.

Fig. 13.2 shows a confocal microscopy sequence of the removal of fluorescently labeled MF. One clearly observes the removal of the material first from the outer parts and this process takes of the order of 1000 s. One also sees an increase in the capsule diameter followed later by a decrease. This indicates an increase in osmotic pressure that is later relaxed due to material permeation into the external medium. The shells are apparently elastic, the degree depending on the material.

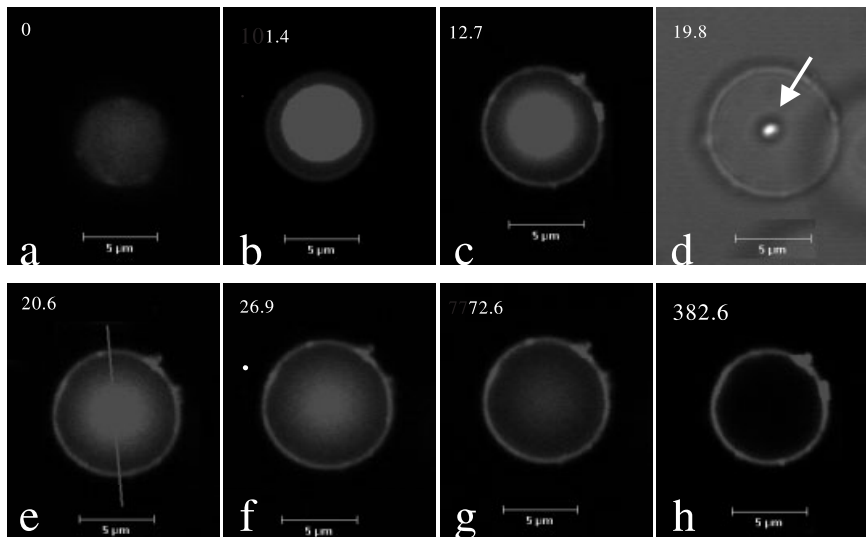


**Fig. 13.2** CLSM images of the core decomposition process as a function of time. Rd-labeled MF colloids with a diameter of  $6.4 \mu\text{m}$  deposited with  $(\text{PSS}/\text{PAH})_8$ . The arrow in

(d) indicates the residue of the core. 13.2d corresponds to transmission light microscopy. The numbers in the insets indicate the core decomposition time.

E.g. for PSS/PAH we observe full recovery of the initial diameter after a long time but for PSS/PDADMAC there is only partial recovery.

The osmotic pressure release may also lead to shell rupture, and this again depends sensitively on the preparation conditions. Thus Fig. 13.2 shows for the specific system MF coated with 8 layers PSS/PAH that there is a narrow optimum of pH at which the preparation is successful. Then one obtains more than 90% intact capsules. Next we present some estimate of important numbers to demonstrate which parameters are crucial and where one does expect limits.

Let us first estimate the maximum osmotic pressure that might be built up if the core material were not released. If we assume that it breaks up into small entities of molecular weight  $200 \text{ g mol}^{-1}$  this would correspond to a density of about  $\nu = 5 \text{ mol l}^{-1}$  and according to van't Hoff's law  $\mu_{\max} = RT\nu$  to 10 MPa. This very high value may be reduced by up to an order of magnitude due to volume increase, it may also be reduced if the fragments are larger. However, if the fragments are ionic the counter ions will dominate the osmotic pressure. Hence values of 10 MPa are realistic upper limits. The case of inorganic particle dissolution is less relevant for the estimate since the resulting ions may quickly diffuse through the wall.

The next question to be asked is: Is this pressure  $\pi_{\max}$  ever reached? For this we consider a capsule of volume  $\frac{4\pi}{3}r^3$ , surface  $4\pi r^2$ , permeability  $P$  and solute concentration  $c_1 (c_1 \ll c_{\text{external}})$ .

From  $\frac{-dc_1}{dt} \cdot \frac{4\pi}{3}r^3 = P \cdot 4\pi r^2 \cdot c_1$  we obtain

$$c_1 = c_1^0 \exp\left(\frac{-3P}{r}t\right) \quad (1)$$

From permeability studies (Section 13.2.1) we derive for typical organic dyes  $P = 2\text{--}7 \times 10^{-9} \text{ m s}^{-1}$ , hence for a typical radius  $r = 1 \mu\text{m}$  we obtain  $\left(\frac{3P}{r}\right) = (6\text{--}21) \times 10^{-3} \text{ s}^{-1}$  with the lower values for the thicker walls. In the experiment of Fig. 13.2 we saw that core removal takes some  $10^2 \text{ s}$ . Consequently the maximum osmotic pressure may be reached.

Inspecting Eq. (1) one also realizes that release slows down with  $r$ , i.e. because of the lower surface to volume ratio a larger osmotic pressure may build up. We should also remark that with diffusion coefficients measured for planar films a three orders of magnitude lower permeability would be obtained, hence the maximum osmotic pressure would be reached. This indicates that during core removal the osmotic pressure of 10 MPa leads to a tension of  $10 \text{ N m}^{-1}$  in the wall of a particle of  $1 \mu\text{m}$  in radius. This tension is rather large given the very small thickness of the layer. It exceeds, for example, the known limit of stability of a lipid bilayer by a factor of 100. Pores are created in the shell through which material may escape. Consequently we expect that pores are formed by templating from polymeric cores and there remains an open question whether these pores may anneal with time.

Altogether we conclude that to template a capsule from a polymeric core the shell has to sustain osmotic pressures of the order of 10 MPa, templating is easier for smaller cores, since the tension responsible for rupture is proportional to the particle radius. As regards the dependence on wall thickness  $d$ , the permeability decreases with  $d$  leading to an increase in  $\pi$ , but the rupture strength is also expected to increase with  $d$ . Since both features are nonlinear and opposite one cannot yet make a prediction as to the dominating effect. Experimentally, however, it was observed that there is an optimum thickness corresponding to a minimum of broken shell fraction. For the example of PSS/PAH this is close to 10 layers.

Another question on core removal concerns sticking of core material to the wall. The fluorescence micrographs in Fig. 13.2 show enhanced intensity from the walls. Obviously there were also fluorescent oligomers produced which were sticking to the walls. In order to quantify this amount single particle light scattering may contribute. Fig. 13.3 shows the distribution of scattering intensities before and after core removal. Also shown is the distribution expected theoretically if all core material is removed. From the comparison one may deduce that about 1% of the core material remains in the wall. This may not only be problematic for medical and pharmaceutical applications but it may also affect the physico-chemical properties of the wall. E.g. for a typical wall thickness of 10 nm and a core radius of 2  $\mu\text{m}$  the volume ratios of wall and core are:

$$\frac{V_{\text{wall}}}{V_{\text{core}}} = \frac{r^2 \times 10 \text{ nm}}{3r^2} = 1.5\% \quad (2)$$

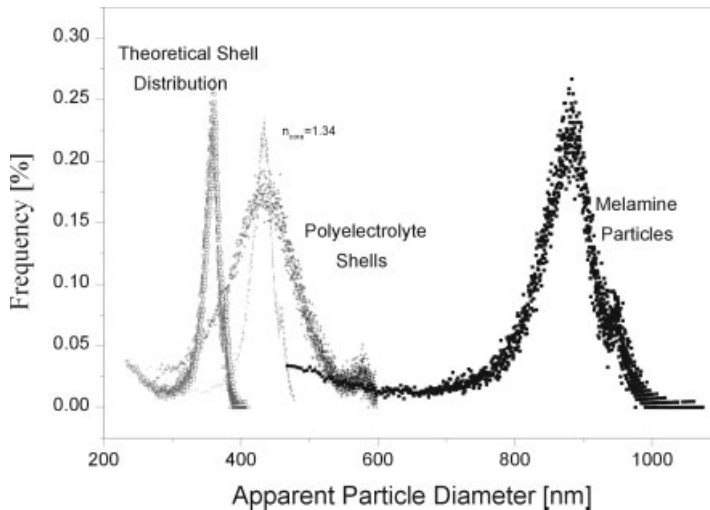


Fig. 13.3 Experimental and theoretical single particle light scattering distribution as a function of capsule radius.

Hence in the example above almost half of the wall material consists of oligomers from the unremoved core.

Finally some remarks on inorganic templates. One expects diffusion through the walls to be fast, hence there is no osmotic pressure build-up and no mechanical stress. This is certainly the case if the water permeability is of the order of the ion permeability. While current experience supports this assumption it may not generally be the case. Sticking to the wall may also be less of a problem. The remaining task then is to have cores with the desired dimensions.

### 13.1.3

#### Modification of walls

The last section on core removal already hinted at a process that may become useful if performed in a dedicated way: The covalent cross-linking of polyanion and polycation, for the special case of amino and sulfonate groups.

For steric reasons one does not expect it to proceed quantitatively, but even so the cross-linking may lead to an elastic network. This should not necessarily give a higher elastic modulus but a lower loss modulus and a shape memory, which have not yet been tested. Also, having in mind the network of an elastomer, controlling the mesh size should yield selective permeability for nanometer-sized entities.

Another method of wall modification results if homopolymers are grafted from the walls. This was achieved by incorporating polymers with benzophenone side groups into the shell. These side groups then serve as photoinitiator for the light-induced polymerization of styrene sulfonic acid. Thus an additional (anionic) PSS shell could be built up with thickness and density depending on the polymerization parameters. This should lead to ion selective permeability and it was indeed shown that the wall was impermeable to low molecular weight anions [14].

Another way to control the wall permeability might be through a photoreaction in the wall. It was shown that the photoisomerization of azobenzenes as main chains and as side chains is possible, presumably due to a sufficiently large free volume inside the wall, however a change of properties has not yet been established.

In recent years much progress has been achieved in enriching polymer matrices by inorganic ions that later were reacted to form inorganic particles [15]. This should also be possible in a polyelectrolyte multilayer since there are many polar groups available for metal coordination. Moreover one may use the fact that metal organic precursors are more soluble in the wall than in the water surroundings. Thus  $\text{Ti}\cdot\text{org}$  was dissolved in the wall, then reacted to give  $\text{TiO}_2$  particles causing the wall to have a higher refractive index [16]. This may become useful if the shells are to be arranged periodically to become a photonic crystal. As another example  $\text{Ag}^+$  ions were used to construct shells. These could then be reduced by light to form metallic silver particles. Because they absorb light they can be visualized by confocal microscopy, and hence the process may be used to label individual shells (Fig. 13.4) [17]. On the other hand the process may be used to form con-

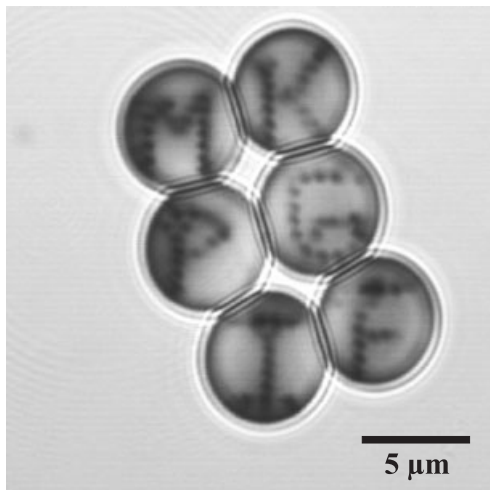


**Fig. 13.4** Silver-painting on colloidal particles.  $\text{Ag}^+/\text{PSS}^-$  multilayer films were assembled on 5  $\mu\text{m}$  MF particles. Silver ions were reduced to the metallic state by the laser of the confocal microscope. The letters MPIKGF in the painting stand for Max Planck Institut für Kolloid und Grenzflächen-Forschung (Colloid and Interface Research).

ductive shells, at least to form wires on the wall. This may become useful in sensor applications where a reaction inside the capsule is detected electrically by an electrode. Another perspective of metallized shells results from their increased microwave absorbance by the conducting electrons. This may be used for local heating, e.g. in controlled drug release. The latter process may be less efficient if the wall is made conducting by organic polymers like polyanilines [17].

Concluding this section on wall modification, we have demonstrated the feasibility of many different processes, in one case also one resulting property, but the concomitant structural changes have not yet been studied. These, however, are to be expected if local bonds are changed or due to the aggregation tendency of metal particles. Hence each direction will require elaborate structural studies, and some of them will also have to be performed with planar films because they are more suitable for some techniques like X-ray, neutron reflectivity or ellipsometry.

## 13.2

### Properties and Utilization

#### 13.2.1

##### Permeability Control

The large variability of wall materials in principle also leads to many ways of controlling capsule permeability. This is one of the salient features of these systems, which is therefore described in detail. By means of specific examples we discuss possible mechanisms and methods. Subsequently we will pinpoint ways to control and switch permeability. We will concentrate first on the transport of molecules and then briefly consider transport of charges and small ions.



### 13.2.1.1 Permeation Mechanisms

In Section 13.1.1 we described a diffusion model that is established for polymeric glasses and for solutes of molecular weight between 100 u and 1000 u. Within this model fluctuations create transient voids into which the solute can jump. Since void formation depends drastically on the energy to create a sufficiently large free volume one thus expects a drastic dependence on solute dimensions and compressibility. Hence for an ultrathin film that is more swollen towards the water phase this should result in a spatially dependent diffusion coefficient. Since experiments are generally not sufficiently precise to resolve this distribution one may simplify the analysis by assuming two different diffusion coefficients  $D$ . This was done by analysing experiments with planar multilayers, and a data fit yielded a two orders of magnitude higher value of  $D$  for the outer 10 nm of the film adjacent to water [18]. As a more crude estimate, with only one diffusion coefficient one may assume this to increase with film thickness.

For the experiment to be analyzed we assume for simplicity a uniform value of  $D$ . The experiment is a typical release situation where a drug crystal is contained inside the capsule. Changing the pH leads to a saturation concentration  $c_s$  inside the capsule. The concentration gradient drives the drug to the outside yielding a time dependent concentration  $c_0 \ll c_s$  there.  $c_0(t)$  is measured by fluorescence spectroscopy since the drug crystals do not fluoresce and since the volume is much larger outside than inside. This stationary state is established when  $c_s$  is reached after the pH jump until the whole crystal is dissolved and  $c_s$  decreases again.

With the capsule permeability  $P=D \times \text{thickness}$ , solution volume  $V_0$  and capsule surface  $s$  one then obtains for the flux  $J$

$$J = \frac{dc_0}{dt} V_0 = P c_s s \quad (3)$$

Hence one expects a linear time dependence of  $c_0$  and from measurement of  $\frac{dc_0}{dt} P$  can be derived. The time dependent release measured by fluorescence spectroscopy is indeed linear over a large time interval. One can understand the deviation at the beginning because  $c_s$  first has to be established and the later almost exponential approach to a saturation value is also expected because now all the crystals are dissolved. For the latter interval one expects a time dependence according to

$$c_0(t) \sim (1 - \exp(-Ps/V)t)$$

with  $V$  the capsule volume. This yields another way to determine  $P$  but it is less accurate if the capsules are not sufficiently monodisperse.

From the slope in the linear regime (see Fig. 13.5) we can calculate the diffusion coefficient  $D$ , and the thickness dependence is as expected qualitatively.  $D$  is large for small thickness, then decreases and becomes constant at large thickness. However, the absolute values of  $D$  are more than 3 orders of magnitude larger than those measured for flat films [4]. There may be two reasons for this discrepancy:

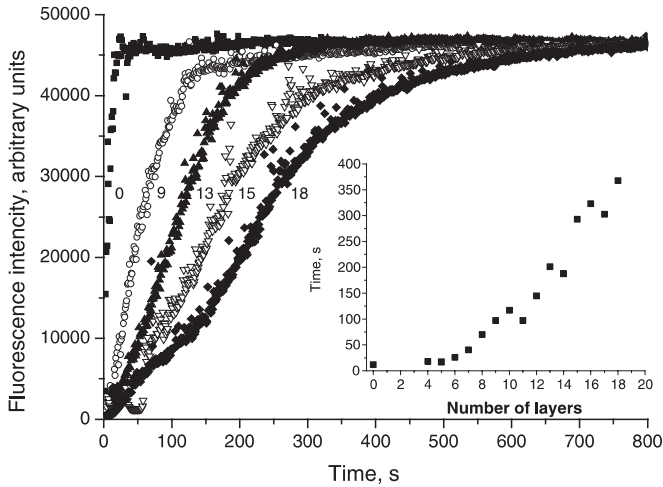


**Fig. 13.5** Fluorescence increase with time, obtained by dissolving fluorescein particles covered with shells of different thickness (9, 13, 15, and 18 layers), compared with naked (0) fluorescein particles. Insert: Time-dependence of core-decomposition time on the number of layers in the shells

1. The preparation conditions for flat film and hollow capsule are different. E.g. the hollow capsules, in contrast to planar films, are prepared without any drying step between adsorption cycles and also core removal involves chemistry.
2. The capsule may exhibit transient or permanent pores through which molecules could permeate. The constant value of  $D = P \times \text{thickness}$  for large thickness could then be explained if the fraction of these pores or their conductivity decrease with thickness.

Experiments are under way to distinguish which of these mechanisms dominates. The difficulty in obtaining quantitative information results from the fact that there is material and preparation specific aging leading to a reduced permeability.

### 13.2.1.2 Controlled Release Profiles

In most practical applications one aims for either release to establish a constant concentration over a long time or a burst release. For a time independent concentration one has to adapt the release to a drain term related to drug removal or decomposition. The discussion above has shown that the release time can be varied by more than an order of magnitude with feasible thickness changes. More dramatic changes are possible by varying  $c_s$  via the pH ( $\sim 10^3$ ), but this is often not a freely variable parameter. One may also imagine that  $P$  can be fine tuned via other parameters but quantitative data on this are still missing (see Section 13.2.1.3).

Achieving a burst release is, in principle, easier since processes can be irreversible and without detailed control of local structure. Proven examples are:

- Inclusion of osmotically active compounds like polyelectrolytes or proteins. Then via dissolving a protein crystal inside or changing the external ion content an osmotic pressure is established leading to wall rupture.
- Build-up of the wall by a low and a high molecular weight polyelectrolyte. The electrostatic bond can then be weakened by high salt concentration leading to capsule decomposition. Less drastic changes can be effected by salt acting on otherwise stable systems. Then only a sustained release without decomposition may occur.
- Build-up of the wall of heat, light or pressure sensitive materials. The burst has been demonstrated up to now only for heating to 40°C for specially selected materials. The very steep temperature dependence is probably due to the high cooperativity of adjacent electrostatic bonds.

### 13.2.1.3 Switchable release

One may envisage many reversible reactions which may lead to reversible structural and hence permeability changes. However, since the multilayer is essentially a non-equilibrium system, reversibility is a critical issue. To switch permeation of small molecules and inorganic ions one may insert selective or gated ion channels as used in biology, but examples on this are lacking. Permeation of large molecules could, however, be switched via pH, and the example discussed below may also be extended to other situations.

In the example PSS/PAH capsules were prepared and kept at  $\text{pH} \approx 8$ . Then fluorescently labeled proteins or sugars were added and by confocal fluorescence microscopy it was shown that these molecules did not penetrate the shell (see Fig. 13.6) [19]. Then on reducing the pH to below 6 the wall becomes permeable and one observes fluorescence of the macromolecules from inside the capsules. Returning to pH 8 and removing molecules from outside (by centrifugation) the remaining emission exclusively from inside proves that the fluorophores have been entrapped [19]. This experiment thus shows reversible switching of the permeability via pH with a threshold near pH 7 (Fig. 13.6).

The pH induced structure change can be understood as follows: The multilayer consists of the strong polyelectrolyte PSS and the weak polyelectrolyte PAH. Thus at the conditions of preparation ( $\text{pH} \sim 7.5$ ) some side groups of PAH are charged and others are not. Since only the charged side groups compensate the PSS negative charges the film interior contains additional uncharged side groups from PAH. Now on reducing the pH some of these are protonated, the film interior becomes altogether charged, and Coulombic repulsion tends to destabilize the film. This is partly compensated by counter ions penetrating the film, but this results in an osmotic pressure with, qualitatively, the same destabilization.

The above discussion reveals that one expects structural changes of the film if one component is a weak polyelectrolyte. The effect should be most pronounced if the film is prepared at pH values near the apparent  $\text{p}K$ , but it should exist also at other pH values since, for weak polyelectrolytes, the degree of dissociation typically depends only weakly on pH. Because the force is due to osmotic pressure

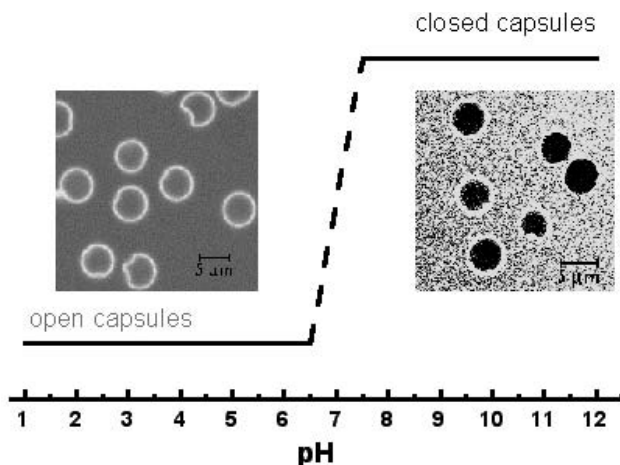


**Fig. 13.6** Schematic representation of open and closed state of the capsules composed of 8 PSS/PAH layers assembled at neutral pH. Labeled penetrant is dextran-FITC ( $M_w=70\,000$ ).

from counter ions it should decrease with ionic strength. However, this dependence is expected to be more complex since counter ions also screen the electrostatic interactions responsible for film stability. We also would not be able to predict whether a pH change causes pores to form, as in this example, if the forces are too small to effect any change or too large leading to total destruction of the film. Hence this opens a large area for research relating structure and permeability. The discussion also suggests that the threshold of permeability could be shifted by preparation conditions and dissociable side groups, hence yielding perspectives to tailor the threshold.

We also would not have predicted a reversible change. This is presumably not the case concerning the total structure, but pores seem to close again, and annealing processes will be discussed in the next section.

### 13.2.2

#### Stability and Mechanical Properties

The polyelectrolyte film possesses a defined structure along the surface normal with only nanometer precision and no order in the plane. The preparation from sheet or blob-like polyelectrolytes is also not expected to yield an equilibrium structure, therefore we foresee many features in analogy to polymeric glasses. There, relaxation processes are known to occur over time scales from seconds to centuries, and it is difficult to assess especially long times which may become relevant for applications. It has become useful to extrapolate long times from measurements at high temperatures and quantitative relations for this extrapolation are known as the time/temperature superposition principle. The parameters entering into the relevant equations have not been established for our systems, and

therefore we do not include mathematical details. Instead we will discuss first special features observed at elevated temperatures and then conclude on stability before considering mechanical studies.

### 13.2.2.1 Temperature Dependent Structures

Fig. 13.7 shows capsules of PSS/PAH before and after heating to 70 °C [20]. Obviously heating caused a shrinking of the surface area, in this case by 20%. In scanning force microscopy measurements (with dried samples) we observe that this is accompanied by a wall thickness increase by about 20%. Hence the three-dimensional arrangement is temperature independent, the initially stratified polyelectrolytes become more coiled. This increases the film thickness and hence reduces the area. The alternative might be that the film is no longer planar and consists of blobs. These can also be observed at higher resolution with characteristic lateral dimensions around 100 nm. However the blobs are connected, and we do not encounter increased permeability.

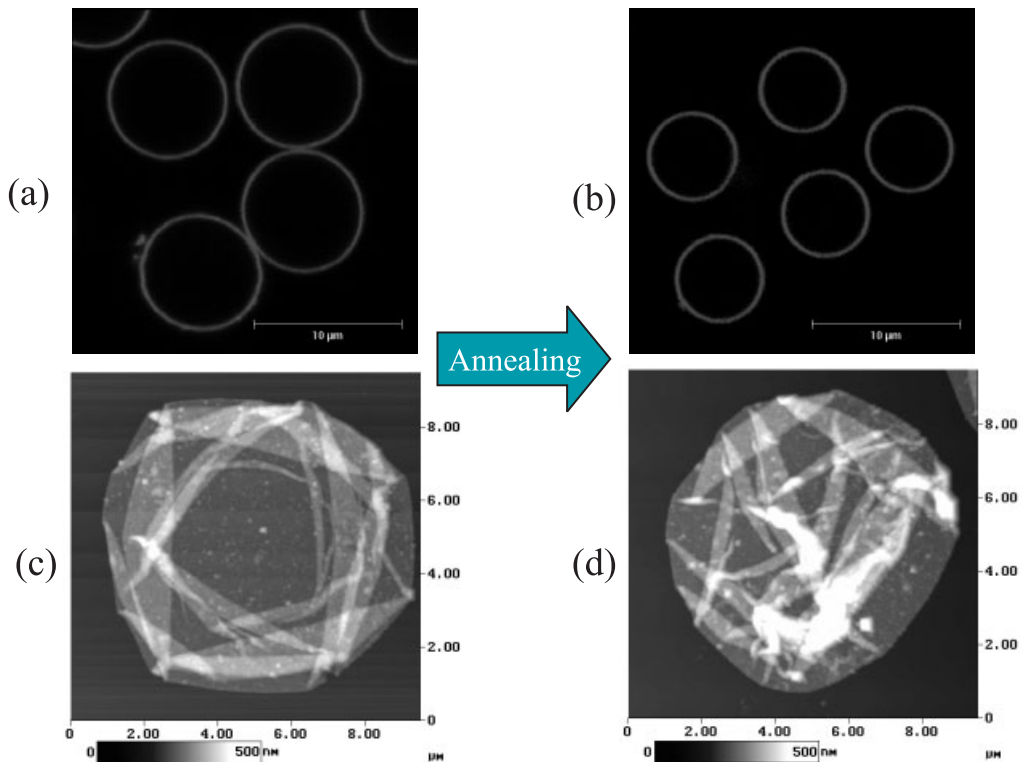


**Fig. 13.7** CLSM images (a), (b), and SFM (contact mode) topview images (c), (d) of 10-layer (PSS/PAH)<sub>5</sub> polyelectrolyte capsules pre-

pared on melamine formaldehyde resin latex ( $\varphi = 8. \mu\text{m}$ ) solution, (a), (c) before and (b), (d) after annealing at 70 °C for 2 h.

In order to understand qualitatively that a change from 290 K to 340 K can allow for these structural rearrangements we can estimate the energy barrier that has to be overcome for this change. For this we assume that to change the structure  $n$  electrostatic bonds with energy  $E$  (see Section 13.1.2) have to be broken.  $n$  corresponds to a persistence length and we may thus estimate the lifetime  $\tau$  of the bound state

$$\tau = \tau_0 \exp\left(\frac{nE}{kT}\right) \quad (4)$$

With reasonable values  $n=14$ ,  $\varepsilon=45$ ,  $d=2.5 \text{ \AA}$  Eq. (4) yields values in agreement with experiment :  $\tau (290 \text{ K})=2 \times 10^6 \text{ s}$  ,  $\tau (340 \text{ K})=4.3 \times 10^3 \text{ s}$ . However, one has to keep in mind that due to the high value of the activation energy  $nE$  small changes have a tremendous influence on  $\tau$ , similar to the effect of changing the temperature by 20%. This estimate leads to the following conclusions:

- For low water content, i.e. dry films when  $\varepsilon < 5$  the multilayer is expected to be stable.
- For high water content ( $5 < \varepsilon < 80$ ) stability is critical and depends also on persistence length and charge–charge distance  $d$ . Hence one expects capsules of swellable polymers to be less stable and also those where e.g. methyl groups shield the tertiary amine group against electrostatic binding (PDADMAC see below) to decompose more easily.
- In any case one expects a very steep temperature dependence of all properties, which again can be tuned via molecular parameters.

Altogether this means that there are qualitative guide lines to control stability but each system will require a dedicated treatment

Again, in analogy with classical systems, temperature treatment may have different consequences:

1. Mild treatment may help the annealing of defects and thus improve the structure
2. Going to higher temperatures may destroy the capsules completely.

The latter was observed for the system PSS/PAH above  $100^\circ\text{C}$  and PSS/PDAMAC above  $40^\circ\text{C}$ . The former case was encountered for PSS/PAH on heating below  $70^\circ\text{C}$ . Then a reduction in permeability was observed, as expected for a reduced defect density. The latter is also expected if the capsules are stored over months, and indeed one observes that aged capsules are less permeable. Consequently process 1. is essentially an acceleration of processes that at room temperature take months, but at higher temperature only hours.

### 13.2.2.2 Capsule Elasticity

One of the important features of the hollow capsules is that their elasticity can be tuned from that of ultrathin flexible polymer films to polymer/inorganic compo-

sites to totally inorganic sintered films and it can additionally be controlled via reactions within the wall. This potential, however, requires measurement of these properties and the large variety will need different methods. Up to now only the pipette and the osmotic pressure technique have been applied, and first results obtained with these will be described.

With the osmotic pressure technique one uses the fact that the capsules are generally impermeable to large molecules like polyelectrolytes [21]. Hence adding polyelectrolytes to the outside medium causes a concentration gradient and thus an osmotic pressure difference predominantly due to the associated counter ions. Increasing the osmotic pressure leads initially to an affine compression and then to a deformation (Fig. 13.8). This can be observed microscopically and the critical pressure  $p_c$  can be determined [21]. Over the short measurement times viscous effects can be neglected and one can model the capsule as a spherical shell with radius  $R$  and wall thickness  $\delta$ . With the elastic modulus  $\mu$  the critical pressure is then given as

$$p_c = 4\mu \frac{\delta^2}{R^2} \quad (5)$$

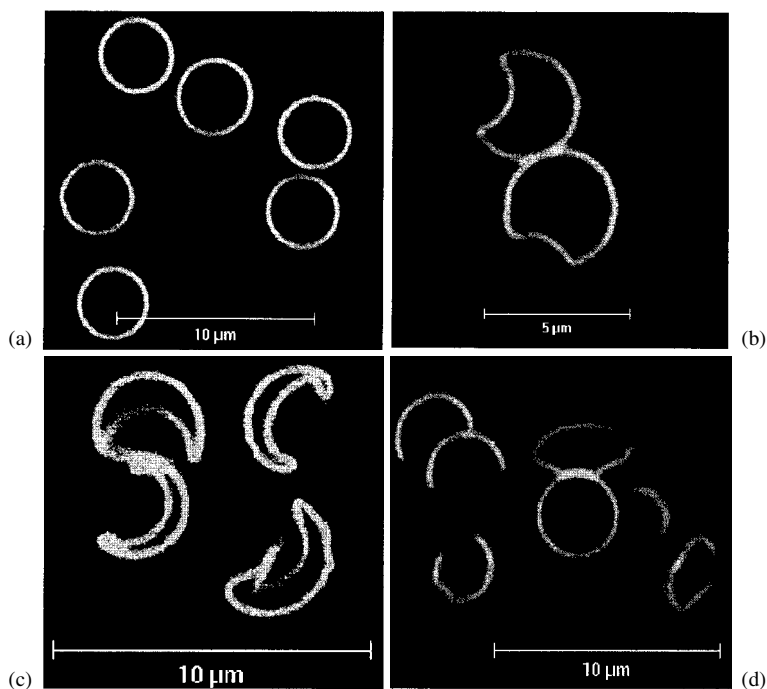


**Fig. 13.8** The deformation of polyelectrolyte capsules consisting of 10 layers of PSS/PAH as a function of the PSS ( $M_w = 70000$ ) bulk

concentration. (a) control, (b) 2.5 wt.% PSS, (c) 5 wt.% PSS, and (d) 10 wt.% PSS. Capsule radius  $2 \mu\text{m}$ .

$\mu$  denotes here the shear elastic modulus. Eq. (5) was obtained assuming  $K \gg \mu$ , where  $K$  is the compression modulus. Hence  $\mu$  is related to Young's modulus by  $E = 3\mu$ , with the Poisson ratio equal to  $\frac{1}{2}$ .

The dependence on  $\delta^2$  and  $R^{-2}$  could be experimentally verified and one therefore obtains  $\mu$  from the measurement of  $p_c$ . For PSS/PAH capsules containing PAH with a molecular weight of 8–15 kDa one obtains values of  $\mu \sim 500$  MPa. For PAH with  $M_w = 50\text{--}65$  kDa  $\mu$  increases to 750 MPa. In both situations the  $M_w$  of PSS was 70 kDa. The dependence on molecular weight is as expected qualitatively. These values are very similar to those of plastic bulk materials, where, for example, polyvinyl chloride has an elasticity modulus of 560 MPa. One might argue against the simple model to analyze the measurements, since a continuum model was used while the thickness of the polyelectrolyte multilayer is considerably smaller than the contour length of a polyelectrolyte molecule. The wall is also not uniformly thick and  $\mu$  may vary locally. However the functional dependence of Eq. (5) has been verified, which is a strong argument for the applicability of the simple continuum elastic theory approach.

Application of the above technique to PSS/PDADMAC capsules leads to considerably lower values of  $\mu$  ( $\mu = 140$  MPa). This is in agreement with qualitative observations and can be explained by the fact that the repeat distances of the charged groups of PSS in a helical arrangement along the chain ( $d_{\text{rep}} = 0.62$  nm) [22] and PDADMAC ( $d_{\text{rep}} = 0.91$  nm) [23] are different, in contrast to the situation with PSS/PAH. In addition PDADMAC does not have a regular conformation, and furthermore, the quarternary amino groups are shielded by methylene groups, thus increasing the distance of closest mutual charge approach. This mismatch must reduce cohesion between the oppositely charged polyelectrolyte pair PDADMAC/PSS compared with PAH/PSS.

Attempts to measure the elastic properties of polyelectrolyte multilayer capsules templated on melamine resin cores with the micropipette aspiration technique failed. Upon touching the capsule with the pipette plastic deformations occurred, which increased further upon releasing the capsule. The adhesion to the pipette mouth was probably too strong. Furthermore, when the sucking pressure was increased, instead of gradually sucking in the capsule a crumpling transition occurred, which prevented any further interpretation. The volume of these capsules is not defined. Hence, it seems to be difficult to prevent shape changes where the local bending is small. The resistance toward bending is obviously not large. This is understandable since the layer is very thin, and, consequently,  $E \cdot \int \xi^2 d_s$  which describes the resistance toward elastic bending out of plane (small deformations) is a rather small value, even if Young's modulus is large. Here  $s$  is the cross section and  $\xi$  the distance to the neutral plane. Interestingly, when, however, the layer was a composite consisting of polyelectrolytes and a lipid bilayer the bending was completely inhibited in the range of pressures applicable with the aspiration technique ( $p < 10^4$  Pa). This result is not fully understood. It might have been caused by the fact that the lipids were in the condensed state. It is also possible that the limited water permeability contributed to the remarkably decreased bend-



ing deformability, preventing volume changes from occurring. Only when rather large pressures generated by osmotic pressure differences were applied did the capsules respond with an irreversible shrinking.

When, however, capsules prepared by templating red blood cells were investigated by the aspiration technique it was possible to successfully suck in the capsules. An interesting behavior was observed: when the deformation was applied for a longer time, of the order of minutes, it was irreversible, but applied forces of the order of seconds demonstrated an elastic behavior. The polyelectrolyte network is apparently much softer than the original multilayer, however, it has a shape memory over a shorter period of time.

### 13.2.2.3

#### **Plasticity, viscosity and rupture strength**

Due to a lack of dedicated experiments we list below only some observations pertinent to this topic. By releasing polyelectrolytes from the inner wall or synthesizing them inside (see Section 13.2.3) one may establish an osmotic pressure gradient from inside to outside. This may cause an increase in capsule size or, at high tensions, rupture. In Section 13.1.2 we have already argued that rupture occurs for tensions exceeding  $10 \text{ N m}^{-1}$ . For smaller tensions we observe reversible size changes if the pressure is relaxed after some 100 s, for PSS/PAH, but for PSS/PDADMAC most of the change is irreversible. Maintaining the pressure over longer times we observe a size increase by up to a factor of 2 (area change factor 4!), and this is obviously due to plastic deformation.

### 13.2.3

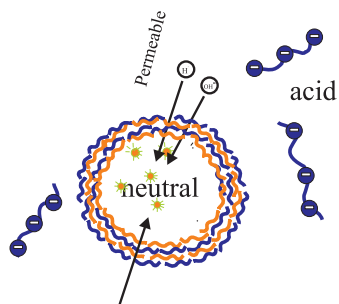
#### **Chemistry and Physics in Nanovolumes**

Various applications of capsules may be derived from the fact that the inner volume is loaded via a chemical or a physical process. Combinatorial chemistry also makes use of the fact that reactions can be followed in small volumes, hence many processes can be run parallel. The interesting basic science in this field is that the wall influence becomes dominant and that one deals with small numbers, limiting thermodynamics. E.g. a typical enzyme concentration of  $10 \text{ nM}$  yields 6 molecules in a volume of  $1 \mu\text{m}^3$ . Hence the capsules should enable observation of the action of an individual catalyst while small molecules are exchanged with the outside medium. These possibilities have not yet been made use of, but we can cite quite a few interesting routes along this line. We first consider experiments to create a specific chemical composition inside the capsule to enable processes to occur exclusively there. Then we consider physical and chemical processes.

### 13.2.3.1 Chemical Gradients from Inside to Outside

Various strategies have been successful in achieving a chemical environment inside a capsule that is different from the environment outside:

1. A Donnan equilibrium was established making use of the fact that generally the wall is impermeable to polyelectrolytes. Thus by adding a polyacid to the outside the dissociated protons could penetrate the wall but if they dominate the ionic content of the solution this would create a charge imbalance. Consequently the proton concentration outside will be larger than inside (Fig. 13.9). The resulting pH difference has been verified experimentally using pH sensitive fluorescent probes in the capsules [24]. In this way pH differences of about 1 unit, or if the polyelectrolyte is deposited inside even up to 4 units, could be established. This is in agreement with theoretical calculations of the Donnan equilibrium taking into account the finite volume and compressibility of the container. Also in agreement with calculations the pH difference decreases with adding salt. This gives a handle to control the pH but it is also a problem if one has to work at high salt content.
2. A particulate, a polymeric catalyst or an enzyme may be caged inside. This can be achieved by either adsorbing it to the template before polyelectrolyte coating or depositing with decomposable components in the inner layers [25]. This process, however, may often be critical if core decomposition requires harsh conditions causing deterioration of the catalysts. Hence a milder way that makes use of the fact that wall permeability for large molecules can be reversibly switched near neutral pH (see Section 13.2) may be used. This allows incorporation after capsule formation. However, since typically the inner volume fraction of the solution is of the order of per cent the encapsulation efficiency may be low. That it was observed to be nearly 1 may be ascribed to the fact that there is a specific affinity between catalyst and material in the wall or inside. A detailed control and understanding of this process is still pending.



Fluorescent marker

Electroneutrality ( $C_{OH} = C_H$ )  
yields  $pH=7$

**Fig. 13.9** Schematic representation of the Donnan equilibrium developing in the presence of bulk polymeric acid not capable of penetrating the wall of the hollow polyelectrolyte capsule.

3. Preparing the inner wall such that the catalysts or solvents are enriched inside. Verified examples are excess charges at the inner wall where an initiator or catalyst of opposite charge is enriched or preparing the inner (or outer) wall with an amphiphilic polymer. Thus e.g. hydrophobic solvents can be entrapped inside. This leads essentially to stable emulsions where many selective reactions have been established. One obviously imagines the inner wall to be composed of a co-polymer with components of different hydrophilicity and yet oil encapsulation was achieved even with PSS as the inner wall material. Apparently even this polyelectrolyte is sufficiently amphiphilic.

### 13.2.3.2 Precipitation and Dissolution

Selective precipitation inside a capsule is an efficient method of loading. On the other hand the capsule environment may be chosen so as to achieve a desired shape, size and morphology. These possibilities have been demonstrated for organic precipitates using all four principal ways to establish chemical disequilibrium:

- The negatively charged dye carboxyfluorescein (CF) precipitates at pH lower than 3. Hence incorporation of a strong polyanion, like PSS, in the capsule interior establishes a Donnan equilibrium with lower pH inside and dye precipitation will commence inside. Thus more monomeric CF will be sucked inside until the capsule is filled with dye precipitates (Fig. 13.10).

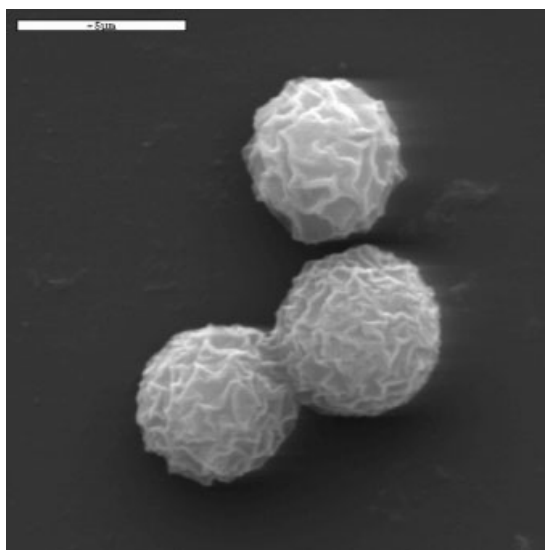


**Fig. 13.10** Scanning electron microscopy image of CF precipitates formed in the capsule loaded with PSS due to the lower pH inside the capsule.

- Inserting a polymeric crystallization promoter inside also causes exclusive precipitation there.
- Forming the inner wall from the positively charged PAH the dye CF is enriched there. Hence precipitation starts from there to the inside and hence the shape of the inner volume is templated [26]. This way even the discoid shapes of erythrocytes could be obtained as dye aggregates.
- Establishing polarity gradient by encapsulation of hydrophilic polymers. These capsules being immersed in water/organic solvent mixture keep higher water content inside the capsules than outside (Fig. 13.11). On evaporation of organic solvent the molecules that are poorly soluble in water are collected in the capsule interior due to the lower solubility there. Finally one has an aqueous suspension of capsules containing precipitates of organic molecules [27].

We found that the precipitates formed inside capsules did not show any X-ray diffraction signals unless later annealed. Hence they are either amorphous or consist of nanocrystallites. This is a highly desirable feature for many drug applications since it facilitates dissolution and hence release. However, the time dependence and control of dissolution processes as well as their mechanisms have not yet been studied.

In order to synthesize inorganic particles exclusively inside the capsule one could again make use of the Donnan equilibrium establishing also a different potential inside. The capsules loaded with polycation are at a more basic pH inside than outside [28]. Thus  $\text{Fe}_2\text{O}_3$  particles of very uniform ellipsoidal shape were formed from iron chloride solution exclusively in the capsule interior (Fig. 13.12).

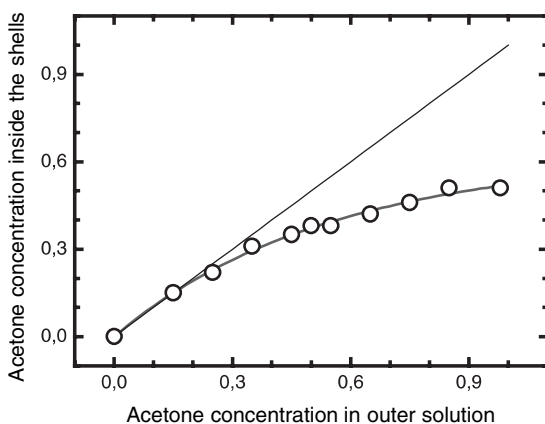


**Fig. 13.11** Diagram demonstrating the polarity variation (acetone/water ratio) in the capsules filled with hydrophilic polymer bearing fluorescent markers. Polarity outside the capsules is given by the acetone/water mixture [27].

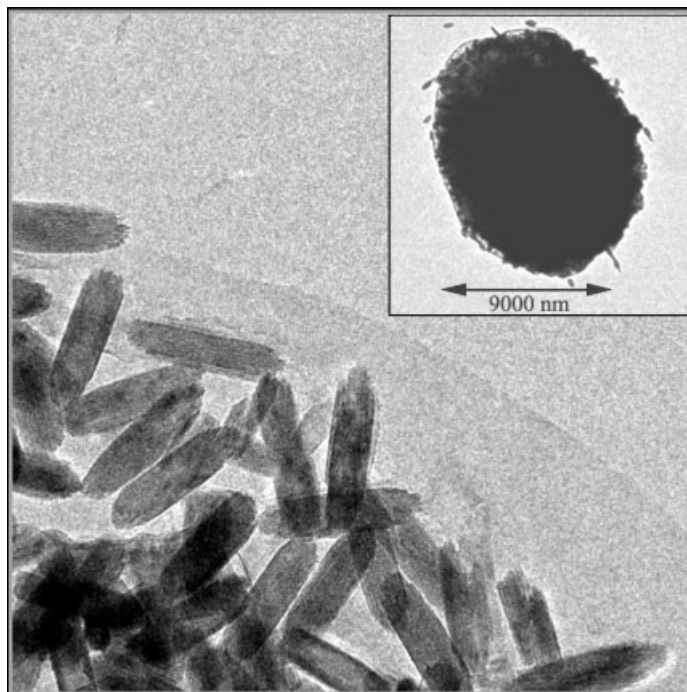


**Fig. 13.12** Transmission electron microscopy images of iron oxide particles synthesized inside a polyelectrolyte capsule filled with PAH. Since these capsules, are immersed in iron chloride solution the iron oxide particles are formed due to the higher pH in the capsule

interior. The insert shows a general view of a capsule filled with iron oxide particles. Detailed view of these elongated particles taken close to the capsule edge for better resolution [28].

### 13.1.3.3 Chemistry in Capsules

Chemical processes within capsules have previously been discussed in conjunction with core removal, and also reactions within the wall have already been considered. Thus below we will concentrate on processes making use of or being useful for the micro- or nanocontainer.

An obvious advantage of the system is that in general large molecules do not penetrate the wall but small molecules do. Hence enzymes can be entrapped and protected against proteases and high molecular weight inhibitors. Small substrates can penetrate to react inside and products can be released. These possibilities have been established for model enzymes like chymotrypsin [29] and horseradish peroxidase. There the protection was quantitative but encapsulation was accompanied by activity losses. Future optimization for each individual enzyme and application will be necessary. No use has yet been made of the fact that inside the capsule one may prepare a suitable microenvironment, arrange neighborhood or co-factors and co-enzymes and organize the capsules on e.g. sensor surfaces or via magnetic/electric fields.

For optical or sensing applications it may also be attractive to prepare functional polymers inside the capsule. They may also serve as nucleation sites for subsequent precipitation or as adsorption sites for various materials. This has been realized with quite a number of polymers. With a water soluble initiator and a soluble monomer, for example, monomeric styrene sulfonate, then synthesis will start both in the bulk phase and in the capsule interior. The polymer produced outside can very easily be removed afterwards and polymer filled capsules are obtained [14]. This idea can also be transferred to the synthesis of nanoparticles. The principle of synthesis in cages is quite promising. By controlling the diffusion of the substrate through the wall one gets a new means of controlling the polymerization reaction. Among the various applications we mention here only the case where a dye/PSS co-polymer was fabricated inside. These capsules worked well as pH-sensors based on the functionality of the particular dye. By bleaching the interior, individual capsules can be optically addressed. The situation when a weak polyelectrolyte was included by synthesis is also quite interesting. By changing the external ionic conditions reversible volume changes occurred. This should allow manufacture of osmotic pumps with nanodimensions.

Being able to prepare functional polymers inside a capsule yields perspectives for further reactions, e.g. photocrosslinking and photobleaching [30].

These examples point to future applications where small volumes are required, the most popular at the time concern combinatorial chemistry and DNA/RNA replication schemes. They are important, but one should not forget that especially interesting basic science at the single molecule and nanovolume level has not yet been addressed.

### 13.3

#### Summary and Outlook

In this contribution we have gone from a defined multilayer on a colloidal template to a hollow capsule. The shell of the capsule can be varied in many different ways depending on the desired properties. Of these the most important are permeability, stability and mechanical properties. Finally physics and chemistry in nano- and micro-containers have been considered. The system was shown to be extremely modular involving inorganic and organic molecules and particles, polymers, proteins and biomolecules such as DNA. Consequently the research involves many disciplines, and the applications are highly varied. Many aspects have only been considered qualitatively since we only have a quantitative understanding in some cases. Also most examples are from the work of our group since there are not yet many others active in this emerging field. This chapter is also meant to change this situation, since not only are the application perspectives broad but also there is too much to be done to understand most of the basic aspects. If this chapter stimulates and motivates more groups to join this endeavour then it has been worth writing!

## Acknowledgements

We express our gratitude to members of our group at the MPI working on this topic: Dr. A. Voigt, Dr. L. Dähne (now both at Capsulation NanoScience AG), Dr. H. Lichtenfeld, Dr. M. Schönhoff, Dr. S. Loporatti, Dr. S. Moya, Dr. O. Tiourina, H. Zastrow, A.A. Antipov, I.L. Radtchenko and G. Ibarz. Dr. M. Giersig (Hahn-Meitner Institute) is acknowledged for providing TEM measurements. We appreciate BMBF, DFG and the companies Bayer, BASF and Henkel for financing this work. G.S. greatly thanks the Sofia Kovalevskaja Program of the Alexander von Humboldt Foundation and the German Ministry of Education and Research.

## 13.4

### References

- 1 E. DONATH, G. B. SUKHORUKOV, F. CARUSO, S. A. DAVIS, H. MÖHWALD, *Angew. Chem. Int. Ed. Engl.* **1998**, *37*, 2202.
- 2 G. B. SUKHORUKOV, E. DONATH, S. A. DAVIS, H. LICHTENFELD, F. CARUSO, VI. POPOV, H. MÖHWALD, *Polym. Adv. Technol.* **1998**, *9*, 759.
- 3 F. CARUSO, W. YANG, D. TRAU, R. RENNEBERG, *Langmuir* **2000**, *16*, 8932.
- 4 A. A. ANTIPOV, B. B. SUKHORUKOV, E. DONATH, H. MÖHWALD, *J. Phys. Chem. B* **2001**, *105*, 2281.
- 5 N. G. BALABUSHEVITCH, G. B. SUKHORUKOV, N. A. MOROZ, D. V. VOLODKIN, N. L. LARIONOVA, E. DONATH, H. MÖHWALD, *Biotechnol. Bioeng.* **2001**, *76*, 207.
- 6 V. S. TRUBETSKOY, A. LOOMIS, J. E. HAGSTROM, V. G. BUDKER, J. A. WOLFF, *Nucleic Acids Res.* **1999**, *27*, 3090.
- 7 B. NEU, A. VOIGT, R. MITLÖHNER, S. LEPORATTI, C. Y. GAO, E. DONATH, H. KIESEWETTER, H. MÖHWALD, H. J. MEISELMAN, H. BÄUMLER, *J. Microencapsulation* **2001**, *18*, 385.
- 8 A. VOIGT, N. BUSKE, G. B. SUKHORUKOV, A. A. ANTIPOV, S. LEPORATTI, H. LICHTENFELD, H. BÄUMLER, E. DONATH, H. MÖHWALD, *J. Magn. Mater. Magn.* **2001**, *225*, 59.
- 9 F. CARUSO, R. A. CARUSO, H. MÖHWALD, *Science*, **1998**, *282*, 1111.
- 10 I. L. RADTCHENKO, G. B. SUKHORUKOV, S. LEPORATTI, G. B. KHOMUTOV, E. DONATH, H. MÖHWALD, *J. Colloid Interface Sci.* **2000**, *230*, 272.
- 11 S. MOYA, E. DONATH, G. B. SUKHORUKOV, M. AUCH, H. BÄUMLER, H. LICHTENFELD, H. MÖHWALD, *Macromolecules* **2000**, *33*, 4538.
- 12 C. GAO, S. MOYA, H. LICHTENFELD, A. CASOLI, H. FIEDLER, E. DONATH, H. MÖHWALD, *Macromol. Mater. Eng.* **2001**, *286*, 355.
- 13 A. A. ANTIPOV, G. B. SUKHORUKOV, S. LEPORATTI, I. L. RADTCHENKO, E. DONATH, H. MÖHWALD, *Colloids Surf. A* **2002**, *198–200*, 535.
- 14 L. DÄHNE, S. LEPORATTI, E. DONATH, H. MÖHWALD, *J. Am. Chem. Soc.* **2001**, *123*, 5431.
- 15 H. CÖLFEN, M. ANTONIETTI, *Adv. Polym. Sci.* **2000**, *150*, 67.
- 16 D. WANG, R. A. CARUSO, F. CARUSO, *Chem. Mater.* **2001**, *13*, 364.
- 17 A. A. ANTIPOV, G. B. SUKHORUKOV, J. HARTMANN, M. GIERSIG, H. MÖHWALD, *Langmuir*, in press.
- 18 R. VON KLITZING, H. MÖHWALD, *Macromolecules*, **1996**, *21*, 6901.
- 19 G. B. SUKHORUKOV, A. A. ANTIPOV, A. VOIGT, E. DONATH, H. MÖHWALD, *Macromol. Rapid. Commun.* **2001**, *22*, 44.
- 20 S. LEPORATTI, C. GAO, A. VOIGT, E. DONATH, H. MÖHWALD, *Eur. Phys. J. E* **2001**, *5*, 13.
- 21 C. GAO, E. DONATH, S. MOYA, V. DUDNIK, H. MÖHWALD, *Eur. Phys. J. E* **2001**, *5*, 21.
- 22 E. DONATH, D. WALTHER, V. N. SHILOV, E. KNIPPEL, A. BUDDE, K. LOWACK, C. A.

- HELM, H. MÖHWALD, *Langmuir* **1997**, *13*, 5294.
- 23 K. DE MEIJERE, R. NETZ, J. F. JOANNY, E. DONATH, T. PFOHL, H. MÖHWALD, G. BREZESINSKI *Langmuir*, submitted.
- 24 G. B. SUKHORUKOV, M. BRUMEN, E. DONATH, H. MÖHWALD, *J. Phys. Chem. B* **1999** *31*, 6434.
- 25 I. L. RADTCHENKO, G. B. SUKHORUKOV, H. MÖHWALD, *Colloids Surf. A* **2002**, *202*, 127.
- 26 G. B. SUKHORUKOV, L. DÄHNE, J. HARTMANN, E. DONATH, H. MÖHWALD. *Adv. Mater.* **2000**, *12*, 112.
- 27 I. L. RADTCHENKO, G. B. SUKHORUKOV, unpublished results,
- 28 I. L. RADTCHENKO, M. GIERSIG, G. B. SUKHORUKOV, *Langmuir*, in press.
- 29 O. TIOURINA, A. A. ANTIPOV, G. B. SUKHORUKOV, N. I. LARIONOVA, Y. LVOV, H. MÖHWALD, *Macromol Biosci.* **2001**, *1* 209.
- 30 I. PASTORIZA-SAUTOS, B. SCHÖLER, F. CARUSO, *Adv. Funct. Mater.* **2001**, *11*, 122.



## 14

### **Multilayers on Solid Planar Substrates: From Structure to Function**

D. G. KURTH, D. VOLKMER, and R. V. KLITZING

#### **Abstract**

Electrostatic layer-by-layer self-assembly (ELSA) to fabricate thin multilayers on a solid planar surface is discussed. The fundamental parameters that govern multilayer formation and structure as well as adsorption kinetics are discussed in detail. Most importantly, the ionic strength of the polyelectrolyte dipping solution has a profound impact on the formation and structure of these layers. Clearly, electrostatic interactions are identified as a primary driving force for multilayer formation in the case of strong polyelectrolytes. These multilayers are very smooth and homogeneous, as indicated by X-ray and neutron reflectometry. Generally, ELSA multilayers are not strictly stratified because adjacent polyelectrolyte layers can interdigitate. Fluorescence measurements indicate that the interfacial region is more permeable and more loosely packed than the inner part of the multilayers. Implementing functional components based on metallosupramolecular coordination polyelectrolytes (MEPEs) or polyoxometalate clusters (POMs) gives rise to materials with tailored properties, such as electrochromic windows. The structure and function of these novel layers is presented in detail. The intrinsic properties of these functional devices offer novel opportunities to implement value-adding functions in multilayers as well as to address fundamental questions concerning the formation, structure, and microenvironmental effects in such multilayers.

#### **14.1**

##### **Introduction**

From nature we learn that self-organization through weak non-covalent interactions represents an efficient and elegant way to combine, position, and orient molecular components in a well-defined supramolecular architecture. The progression of the structural hierarchy from the atom to the molecule, the supermolecule, and the supramolecular assembly is paralleled by an increase in diversity and complexity. At each level of the hierarchy, characteristic functions emerge that do not exist at lower levels. The final supramolecular entity evolves spontaneously from suitably instructed components through a sequence of recognition, growth,

and termination steps [1]. Discrete nano-sized supramolecular assemblies have been prepared exploiting ligand–metal ion interactions [2],  $\pi$ - $\pi$  interactions [3] or hydrogen-bonding [4]. The applications of such systems are intriguingly diverse, including information storage, signal transduction and amplification, as well as host–guest recognition [5]. However, the realization of molecular based devices faces two entirely different challenges: First, components possessing suitable physical properties have to be identified and synthesized. Second, the active components have to be combined and positioned in a pre-defined way into the architecture of the final device. The ability of supramolecular species to spontaneously form from their components, bypassing microfabrication, and to accomplish intricate functions provides opportunities that go far beyond current silicon-based technology [6]. The ultimate goal is, therefore, to exploit the principles of molecular self-organization in device fabrication in order to overcome some of the problems associated with conventional technologies: i.e. parallel fabrication, (molecular) dimension control, component alignment, and thermodynamically driven mechanisms for self-repair. In order to support, handle, manipulate, and operate such devices, it will be necessary to collect and arrange the components in surface structures, however, until now there have been no generic methodologies available to achieve this goal [7].

A favorable possibility to fabricate ultrathin films is the so-called electrostatic layer-by-layer self-assembly (ELSA) method, where polyanions and polycations are alternately adsorbed onto a substrate [8]. This method is of great versatility, provides nm thickness control, can easily be adapted for automated fabrication, and is applicable to any substrate shape. Typically, the thickness of ELSA films increases linearly with the number of dipping cycles [9]. The thickness of a single polyelectrolyte layer is of the order of several Angstroms and, therefore, the total film thickness can be precisely controlled by the number of adsorbed layers. In general, ELSA multilayers are not strictly stratified because adjacent polyelectrolyte layers partially interdigitate and are also less ordered than self-assembled monolayers or Langmuir–Blodgett (LB) films [10, 11].

Two kinds of driving forces for multilayer formation are discussed in the literature: electrostatic interactions [12] and hydrogen bonds [13]. Other interactions like hydrophobic ones can also play a role. This review focuses on multilayers which form primarily through electrostatic interactions. The electrostatic interactions can be tailored by modifying the degree of polymer charge, which is achieved by changing the pH of the dipping solution in the case of weak polyelectrolytes or by using copolymers containing different ratios of ionic groups. Moreover, an increase in salt concentration of the dipping solution screens the electrostatic interactions. At high salt concentration or at low polymer charge density, the electrostatic repulsion between different polyelectrolyte segments is reduced, thereby favoring adsorption. On the other hand, the electrostatic attraction between the polyelectrolyte and the oppositely charged surface is reduced, which counteracts polyelectrolyte adsorption. This balance between the polyelectrolyte segment–segment and the polyelectrolyte segment–surface interactions governs layer growth and thickness.

During the adsorption process, complexation of polyanions and polycations occurs, which is associated with an exchange of counter ions. The formation of complexes may also lead to interdigitation between adjacent polyelectrolyte layers. Nevertheless it is possible to establish a property gradient perpendicular to the interface within the multilayer. Gradients are required for sequential reactions, which need a separation of reaction space, like the conversion of biomolecules [14] by enzymes, or vectorial transport processes, including charge separation. The permeability properties are also important with respect to the selectivity of ions or molecules. ELSA multilayers have been employed as selective membranes for the separation of gases [15] and dissolved compounds [16]. Depending on the chemical nature of the polyelectrolytes, coatings with diverse functions can be prepared, including thermosensitive materials [17]. Therefore, understanding and developing methods to control the structure and the properties of ELSA multilayers is a major concern.

The first part of this chapter deals with basic questions concerning multilayer formation and the structure of simple synthetic polyelectrolytes at planar interfaces. In the second part, composite systems based on metallosupramolecular devices are presented, which may lead to novel functional materials.

## 14.2 Formation and Structure of Multilayers

### 14.2.1 Adsorption Kinetics of Polyelectrolytes

The adsorption kinetics at solid interfaces has been investigated by several methods, including optical and scattering techniques, and they all show that the adsorption process is complete within 20–30 min. In situ investigations are possible with surface plasmon resonance spectroscopy (SPR). Under attenuated total reflection (ATR) conditions, the adsorption of the polyelectrolyte at the surface can be detected with high sensitivity and time resolution by monitoring the shift of the plasmon absorption. The thickness and the refractive index of the layer can be calculated from standard electrodynamic theory [18]. Other related methods for in situ measurements include optical ellipsometry [12] and reflectometry [19]. An alternative method to study adsorption kinetics with high time resolution and great precision is the quartz crystal microbalance (QCM) [20] where a decrease in crystal resonance frequency is detected during adsorption. Plech and coworkers investigated the adsorption process of sodium poly(styrene sulfonate) (PSS) onto poly(ethylenimine) (PEI) by X-ray reflectivity in an energy dispersive mode with a time resolution lower than 1 min [21].

The influence of polyelectrolyte concentration on the adsorption time and the amount adsorbed can be studied by total internal reflection fluorescence (TIRF). In a TIRF apparatus a laser beam is coupled into the glass substrate, which serves also as the top of a flow cell. For the adsorption experiments, the substrate is first

coated with polyelectrolytes, then an aqueous solution of an oppositely charged dye-labeled polyelectrolyte is flushed into the cell. The evanescent field, induced by the totally reflected laser beam, excites the dye near the substrate surface, and the fluorescence intensity is measured by an optical multichannel spectrometer.

The adsorption process of small molecules is governed by their transport to the surface and by their adsorption kinetics. In contrast to small molecules, polymers are able to change their conformation during adsorption with an associated rearrangement of the polymer chains at the surface. The adsorbed chain can be divided into three parts depending on their contact with the surface: Those parts of a polymer chain, which are adsorbed with all segments at the surface are called *trains*. A *loop* connects two trains and its segments are not adsorbed at the interface. The *tails* are the free ends of a polymer chain, directed towards the solution.

The concentration of additional salt in the polyelectrolyte dipping solution has a profound influence on the adsorbed amount and the adsorption kinetics. Fig. 14.1 shows the adsorbed amount of fluorescein-labeled poly(allyl amine hydrochloride) (FITC-PAH) as a function of the incubation time at different ionic strengths. At any fixed adsorption time, the adsorbed amount increases with increasing ionic strength, which is rationalized in terms of chain conformation: In solutions of low ionic strength the charges along the polyelectrolyte chain repel each other and the polyelectrolytes are stretched (large radius of gyration). After adsorption the chains form trains or long tails. With increasing ionic strength the charges along the polyelectrolyte are screened (*intrachain* screening) and the polyelectrolytes become more flexible and coiled (decrease in persistence length and in radius of gyration). Adsorption of the randomly coiled chains leads to an increased number of loops and, therefore, thicker layers. In addition, salt reduces the interchain repulsion (*interchain* screening), which also favors adsorption. Another interesting feature becomes obvious within the first few minutes of adsorption. While at low salt concentrations the fluorescence intensity increases with time in a monotonic way, at high ionic strength and high polyelectrolyte concentration an overshoot that is adsorption followed by partial desorption of adsorbed material is

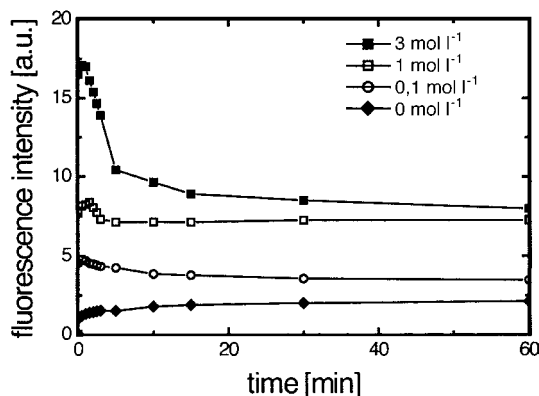


**Fig. 14.1** Change in TIR-fluorescence intensity during adsorption process as a function of the ionic strength. The point  $t=0$  corresponds to the time when FITC-PAH ( $10^{-2}$  monomol  $L^{-1}$ ) solution is flushed into the cell.

observed. This leads to the conclusion that some polyelectrolytes bind more strongly than others. A polyelectrolyte with many surface interactions can form additional interactions with the surface at the expense of chains with fewer adsorption interactions. This is due to entropic reasons: For a polyelectrolyte with many surface interactions, the formation of additional adsorption interactions results in a smaller loss of translational entropy compared to chains attached with fewer binding sites. The replacement of chains with few interactions sites during layer formation results in an apparent loss of material from the surface. On the other hand, the adsorption energy of a polymer segment is independent of the polymer chain length and, therefore, independent of the number of segments, which are already adsorbed. The fact that the overshoot does not occur at low polyelectrolyte concentration is trivial with respect to the explanation given above. At low ionic strength the stiffness of the chain can counteract the conformational rearrangement of the polyelectrolyte. Likewise, a decrease in the polyelectrolyte concentration of the dipping solution reduces the adsorbed amount and increases the time scale of the adsorption process, while increasing the polyelectrolyte concentration enhances adsorption. This is due to the fact that a change in the polyelectrolyte concentration also affects the ionic strength of the solution and, therefore, the polyelectrolyte conformation.

#### 14.2.2

##### **Multilayer Formation**

ELSA multilayers are prepared by successive adsorption of polycations and polyanions from aqueous solutions and intermittent washing steps. After the substrate (*e.g.* glass, silicon) is cleaned, it is typically dipped in the polyelectrolyte dipping solution for 20 min. It is then rinsed with water followed by a dip in the solution of the oppositely charged polyelectrolyte. After rinsing with water the process is repeated. One polycation/polyanion layer is called a *double layer*. The films are either dried after certain adsorption steps or only at the end of the preparation in a gas stream. This can be important since the drying process is assumed to change the conformation and the interdigitation of the polyelectrolyte chains.

In many cases, the first few double layers, which are directly adsorbed onto the substrate, are somewhat thinner than the following layers. This has been confirmed by UV-vis spectroscopy [9], quartz crystal microbalance [20] measurements, X-ray reflectometry [22], surface force microscopy (SFM) [23] and ellipsometry. The thickness increment (adsorbed amount) per double layer increases and stabilizes to a final constant value after approximately three double layers. This formation behavior can be explained by a change in surface roughness, which is calculated from SFM measurements [23]. The roughness increases for the first few layers and becomes constant after a certain number of layers are deposited. In comparison to a smooth surface a rougher one has a larger surface area *i.e.* more charges, which in turn require a larger amount of oppositely charged polyelectrolytes for charge compensation.

## 14.2.3

 **$\zeta$ -potential**

The constant increment in film thickness gives a hint for the reproducibility of the surface properties after each double layer deposition. In the case of electrostatically driven multilayer formation, not only the roughness, but also the surface potential remains the same after a complete polyanion/polycation deposition cycle. Typically, the surface potential is not accessible, but the  $\zeta$ -potential is, which also takes into account the adsorbed counter ions [24]. In general, the  $\zeta$ -potential changes sign after deposition of a polyelectrolyte layer, indicating a reversal of surface charge [25]. For example, after adsorption of PSS on positively charged melamine formaldehyde particles, the surface potential amounts to  $(-40 \pm 10)$  mV and after adsorption of PAH it is  $(+30 \pm 10)$  mV [26]. The same experiments on negatively charged polystyrene latex particles result in a surface potential of about +50 mV after PAH and  $-40$  mV after PSS deposition, respectively [27]. Streaming potential measurements on PAH and PSS solutions through a silica capillary result in a  $\zeta$ -potential of +20 mV and  $-20$  mV, respectively [28]. Similarly, force measurements in a surface force apparatus (SFA) between two PAH/PSS covered mica surfaces result in a potential of 50 mV [29]. However, the sign of the potential cannot be determined by this method.

In TIRF experiments the electrostatic properties are measured via the proton distribution within the film [30]. A pH sensitive fluorescent dye (fluorescein) is positioned at different defined distances from the surface in the multilayer by adsorbing a different number of layers on top of the dye-containing layer (FITC-PAH). Titration of the dye shows that the  $pK_a$  value depends on the position of the dye inside the film.

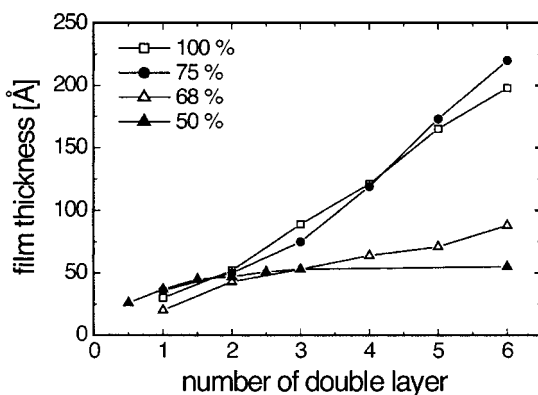
The presented methods measure the potential at different positions within the interfacial region of the multilayer, which should be taken into account if potential values determined by different techniques are compared. In SFA measurements, the surface potential is determined at a distance from the film surface where a transition from purely electrostatic to steric/entropic interactions occurs. Here, the forces are dominated by tails. Also, in the electrokinetic experiments, the shear forces act predominantly in the tail region, i.e. the outer part of the surface. TIRF provides information about the inner part of the multilayer where the polymer density is higher and the structure is determined by loops [31].

## 14.2.4

**Effect of Polymer Charge**

The polymer charge density is the predominant quantity, which determines whether multilayer formation can take place or not. Fig. 14.2 shows the film thickness as a function of the number of double layers as a function of polymer charge density. The polyanion is PSS and the polycation is a copolymer consisting of cationic DADMAC [32] and neutral NMVA [33] monomers, respectively. When the ratio of charged to neutral groups in the polycation exceeds 68%, a multilayer

**Fig. 14.2** Thickness of PSS/P(DADMAC-stat-NMVA) films as a function of the number of deposited double layers at different charge densities of the polycation. The aqueous polyelectrolyte dipping solutions contain  $10^{-2}$  monomol  $L^{-1}$  and  $0.1$  mol  $L^{-1}$  NaCl. The experimental error is within the size of the symbols.



of PSS and P(DADMAC-stat-NMVA) can be formed. By increasing the charge density from 75% to 100% (fully charged chain) the film thickness decreases slightly. This is due to a difference in chain conformation: At a charge ratio of 75% the chains can adsorb in a coiled conformation (reduces intrachain repulsion) whereas the fully charged chain (100%) is more stretched (full intrachain repulsion). The change in conformation is reflected by a decreased surface roughness from 40 Å (75%) to 15 Å (100%), determined by X-ray reflectivity data using a box model with Gaussian roughness. The larger roughness is due to loops at the surface whereas chains with flat segments lead to a smoother surface. This increase in roughness is also confirmed by SFM images. At a charge ratio below 68% the adsorption stops after the second double layer. In the case of neutral PNMVA no layer formation is observed, demonstrating the importance of electrostatic interactions. It can be concluded that electrostatically driven multilayer formation requires a minimum charge density of both the surface and the polyelectrolyte [34].

A sharp maximum in film thickness at intermediate charge density, as found for multilayers of weak polyelectrolytes, is not observed in the present case [35–37]. This can be explained by the fact that, in the case of weak polyelectrolytes, the polyanion is charged at high pH and uncharged at low pH, and vice versa for the polycation [38]. Therefore, an intermediate pH, where both polycation and polyanion are partially charged, is favorable for the formation of multilayers with weak polyelectrolytes.

If charge overcompensation after each adsorption step is insufficient for the formation of the multilayer, salt has little influence on the film thickness [34]. Above the charge reversal threshold the thickness can be fine-tuned by the salt concentration of the dipping solution. This leads to the conclusion that surface/polyelectrolyte interactions play the most important role for polyelectrolyte deposition. Interactions between the polymer segments (influenced by ionic strength and also by charge density) affect only the thickness but do not determine whether adsorption takes place or not.

## 14.2.5

**Influence of Ionic Strength**

It has already been mentioned that the adsorbed amount increases with increasing salt concentration in the polyelectrolyte dipping solution. Due to charge screening at high ionic strength, there are fewer binding sites per chain and, therefore, more polyelectrolytes can adsorb at the surface. The increased polyelectrolyte coiling is reflected in the interfacial roughness. SFM images show a more irregular interfacial structure with deeper ridges at higher ionic strength, implying that more loops are present at the surface [23].

The dependence of the film thickness on the ionic strength is discussed controversially in the literature. While some data suggest that the film thickness is linearly dependent on the ionic strength, others show that the former is proportional to the square root of the latter. For the system PSS/PAH at the air/solid interface, it is shown by UV-vis spectroscopy, TIRF, X-ray and neutron reflectometry that, at low salt concentration (below  $0.5 \text{ mol L}^{-1}$ ), the thickness increases with the ionic strength as  $I^{0.5}$ . The same dependence is found for solvent-swollen PSS/PAH multilayers at the solid/liquid interface by neutron reflectometry [39] (Fig. 14.3) and also for PAH/PSS multilayers at the air/liquid interface by ellipsometry [40]. The fact that both, wet and dried film show a  $I^{0.5}$  dependence of the thickness on the ionic strength leads to the conclusion that the water content in the film should also increase with  $I^{0.5}$ . Consequently, the number of water molecules per polyelectrolyte should be independent of the ionic strength. This assumption was confirmed by neutron reflectivity measurements against  $\text{D}_2\text{O}$ , which resulted in a constant density of the films, independent of the salt concentration. In a concentration range between 0.5 and 3 M NaCl, Lösche and co-workers showed by neutron reflectivity that the thickness of a non-deuterated PSS/PAH multilayer at the

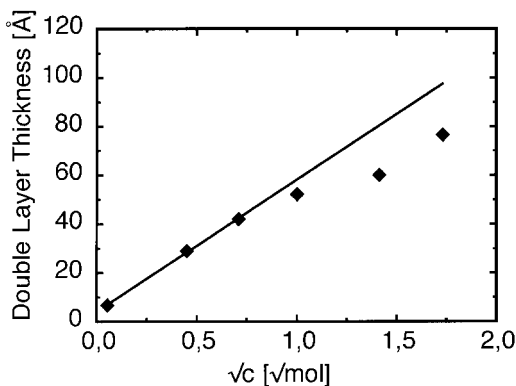


**Fig. 14.3** Thickness of PSS/PAH double layer versus the square root of the total counter ion concentration. The straight line is a guide for the eye to reveal the deviation from a lin-

ear relationship at higher counter ion concentrations. The experimental error is within the size of the symbols.



solid/air interface (100% relative humidity) varied linearly with the ionic strength of the dipping solutions [41].

The molecular architecture of the polyelectrolyte also has to be considered as the following example illustrates. In the case of commercially available branched PDADMAC a linear dependence of film thickness on the ionic strength is found for PSS/PDADMAC multilayers [23, 42]. In contrast, custom made linear PDADMAC shows an  $I^{0.5}$  dependence of the thickness of the PSS/PDDAMAC multilayers on the ionic strength, as indicated by X-ray reflectivity [34] and ellipsometry. Apparently, branching has a profound effect on the conformation and the structure of the polyelectrolyte in solution, therefore also affecting multilayer formation.

A common feature encountered in all these studies is an increase in the film thickness with increasing salt concentration of the dipping solutions. This effect even continues above an ionic strength of  $1 \text{ mol L}^{-1}$  (see Fig. 14.3). The Debye length at this ionic strength is about  $3 \text{ \AA}$ , which is less than the diameter of the hydrated ions. Under this condition, the surface potential and the charge of the polyelectrolyte chain should be completely screened. Hence, a decrease, or at least a plateau, in the adsorbed amount would be expected at this ionic strength. However, experimentally the adsorbed amount is found to increase up to an ionic strength of  $3 \text{ mol L}^{-1}$  [43]. A possible explanation could be that a mean field approximation like the Gouy–Chapman model does not adequately describe the multilayer formation under these conditions. Local charge fluctuations may also have to be taken into account. These fluctuations could lead to a temporary attraction between the polyelectrolytes and the surface, which could be sufficient for irreversible adsorption. Finally, it should be noted that both ionic strength and polymer charge density have only little effect on the polymer density in the multilayer [44].

#### 14.2.6

##### Permeability of Polyelectrolyte Multilayer

The permeability of polyelectrolyte multilayers has been measured for different compounds using TIRF [45]. A fluorescent dye is embedded into the film at a certain distance from the surface. For this purpose, FITC-PAH is adsorbed onto a PSS-coated glass substrate and a different number of PSS/PAH layers is deposited onto this sensing layer. The fluorescein fluorescence is quenched by penetrating probe molecules, such as Rhodamine or 2,2,6,6-tetramethyl-4-piperidinol 1-oxide (TEMPO). While Rhodamine is much smaller than TEMPO, both molecules also show different quenching mechanisms. In the case of Rhodamine, energy transfer occurs from fluorescein to Rhodamine via dipole–dipole interaction with an interaction radius of about  $60 \text{ \AA}$  (Förster energy transfer). The spin label TEMPO enhances the spin–orbit coupling in fluorescein with an interaction radius of about  $6 \text{ \AA}$  (paramagnetic quenching). Fig. 14.4 shows the fluorescence of fluorescein as a function of the incubation time of the Rhodamine solution for different distances of FITC-PAH from the film/liquid interface. Obviously, the fluorescence decreases faster if the FITC is closer to the film/liquid interface. If the distance of FITC to the interface

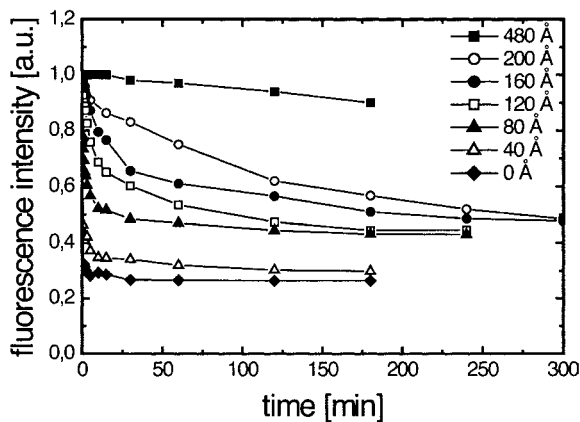


**Fig. 14.4** Change in TIR-fluorescence intensity of FITC, deposited at different distances away from the film/liquid interface, as a function of the incubation time in an aqueous Rhodamine solution. The fluorescence inten-

sity is normalized with respect to FITC fluorescence before flushing in the Rhodamine solution ( $I_0$ ). The multilayer is prepared at a NaCl concentration of  $1 \text{ mol L}^{-1}$ .

is smaller than  $80 \text{ \AA}$ , quenching is due to Rhodamine either adsorbed at the film surface or in solution with a distance from the surface smaller than the Förster radius. A quantitative analysis shows that the diffusion coefficient within the multilayer amounts to  $10^{-14} \text{ cm}^2 \text{ s}^{-1}$ . In contrast, in the interfacial region of the multilayer (distance to the film/liquid interface  $\leq 100 \text{ \AA}$ ) the diffusion coefficient is found to be higher by a factor of 50 compared to the inner part of the multilayer. Hence, the Rhodamine permeability in the interfacial region is higher than within the multilayer. Apparently, the outer layers are more loosely packed. It is interesting to note that the diffusion coefficient of multilayers, which are prepared without additional salt, is higher by a factor of two than that of multilayers prepared with a NaCl concentration of  $1 \text{ mol L}^{-1}$ . In this case, the number of deposited layers has been chosen in such a way that the distance between the dye and the surface is the same at both ionic strengths. The difference in the permeability is explained by the size distribution of defects in the multilayers, from a few large defects at low ionic strength to many small ones at high ionic strength.

The transport velocity of Rhodamine molecules can be reduced by the deposition of amphiphilic dioctadecyl dimethyl ammonium bromide (DODAB) layers within the multilayer because hydrophobic areas present a barrier for the hydrophilic Rhodamine molecules. This lowers the diffusion coefficient by a factor of two. In all cases, the diffusion coefficient of the first  $100 \text{ \AA}$  is between 1 and 2 orders of magnitude higher than that of the inner part of the multilayer.

The permeability of TEMPOL is much higher due to its smaller size. The diffusion is estimated to be two orders of magnitude higher than that of Rhodamine. Obviously, the large difference in the permeability cannot be explained solely on the basis of molecular size. It is assumed that Rhodamine transport requires slow

conformational changes of the polyelectrolyte chains while TEMPOL may diffuse directly through the (water filled) defects and cavities formed by the interdigitated polyelectrolyte chains.

#### 14.2.7

##### Internal Structure

X-ray reflectivity measurements on multilayers on solid surfaces as a function of the number of dipping cycles provide direct evidence for the sequential nature of the layer-by-layer deposition process. Typically, the polyelectrolyte adsorbs as individual layers at a time. However, the internal structure of the systems remains inaccessible by X-ray reflectometry due to the lack of contrast between adjacent layers. The question concerning the internal film structure was addressed for the first time in 1993 by Schmitt *et al.* [10], who investigated multilayers of protonated and deuterated polymers, H-PSS, D-PSS and PAH, in a combined X-ray and neutron reflectivity study. While there is no indication of Bragg peaks in the X-ray reflectivity of a 48 layer sample where every sixth layer is deuterated, the corresponding neutron reflectivity curve shows two pronounced Bragg peaks. This is due to the superlattice introduced in the film by the selective isotopic labeling. Korneev showed that the maximum repetition rate of labeled layers to observe Bragg peaks is one out of four [46]. At a higher repetition rate (e.g. 1/2) no Bragg peak could be observed due to the lack of contrast. This leads to the conclusion that adjacent polyelectrolyte layers interdigitate, that is these multilayers are not strictly stratified. Moreover, interpenetration also depends on the polyelectrolytes used [47]. For simple flexible polyelectrolytes that can form 1:1 complexes, like PAH and PSS, the roughness of the internal interfaces can be of the order of the thickness of a single layer [48, 49]. More rigid building blocks like lipid bilayers [50], inorganic platelets [51] or polymers with a stabilized conformation [11] can have a smaller interfacial roughness due to decreased overlap of adjacent layers. The improved stratification in these multilayers is discernible by the appearance of several Bragg peaks in reflectometry [52, 53]. A possible explanation of the pronounced interdigitation could be the formation of complexes between polyanions and polycations. Farhat *et al.* [54] showed by FTIR spectroscopy that complexes in multilayers are similar to those in aqueous polyanion/polycation solutions. The exchange of counter ions during complexation explains the low counter ion concentration typically found in ELSA multilayers [30, 54, 55].

Most of the structural investigations have been performed on 'dry' films at the *solid/air interface* because many methods can be applied under these conditions such as X-ray and neutron reflectivity, SFM, UV-vis and FTIR-spectroscopy as well as ellipsometry. In situ studies on adsorption kinetics and transport properties are usually carried out at the *solid/liquid interface*. Since it is assumed that the multilayer structure is different under ambient conditions and in an aqueous environment, investigations of the internal structure at the *solid/liquid interface* are very important.

In neutron reflectivity measurements at the solid/liquid interface a silicon single crystal is used as a solid substrate, which is also part of a flow cell. Silicon is transparent for neutrons, and, therefore, the sample can be irradiated from the back [56]. The neutron reflectivity data is analyzed by applying classical electrodynamic theory [57–59]. Neutron reflectivity studies of protonated polyelectrolytes against  $D_2O$  usually show Kiessig fringes [60] due to coherent interference of the beams from the film/ $D_2O$  and film/substrate interface. The occurrence of Kiessig fringes indicates that the films are very smooth and homogeneous. Typically, no Bragg peaks are observed because the difference in scattering length density between individual layers is too low and because of interdigitation of adjacent layers. Steitz et al. found that the corresponding density profile retrieved from the reflectivity data shows a decrease in polymer density towards the film/ $D_2O$  interface [39]. This result is in agreement with the permeability experiments discussed above.

After drying, the film thickness is reduced by 30% and the reflectivity curves can be fitted with a homogeneous density. This means that the outer layers (towards air) lose more water than the inner layers in the drying process. After re-swelling in water the scattering curve is the same as before drying, suggesting fully reversible swelling [43]. Apparently, uptake and loss of water does not affect the binding sites within the multilayer. These experiments reveal that the average water content inside fully hydrated films (100% relative humidity) is larger than 40% by volume with twice as much water associated with PSS than with PAH [41]. This corresponds to 8 water molecules associated with one ion pair in a polyanion/polycation complex. Farhat et al. [61] found a similar hydration number of 6 water molecules for the system PSS/PDADMAC by infrared spectroscopy.

While the effect of ionic strength of the dipping solution on the film structure is well documented, the ionic strength of the swelling solution has no influence on the multilayer structure. Fig. 14.5 shows X-ray reflectivity results for a multilayer prepared without additional salt. First, the film was measured against  $D_2O$  and subsequently against a solution of  $0.5 \text{ mol L}^{-1} \text{ NaCl}$  in  $D_2O$ . The identical reflectivity curves shown in Fig. 14.5 demonstrate that the film structure is not affected. This is due to the irreversible formation of complexes between the poly-

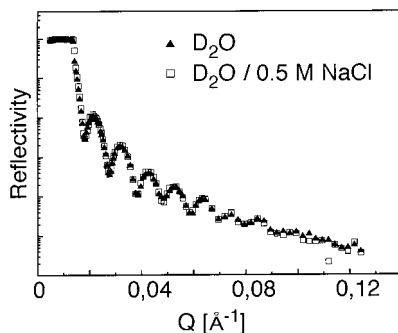


Fig. 14.5 Neutron reflectivity curves of PEI(PSS/PAH)<sub>6</sub> prepared without additional salt, measured against  $D_2O$  and ( $D_2O + 0.5 \text{ M NaCl}$ ).

electrolytes upon adsorption. The replacement of a polyelectrolyte charge by a salt ion of equal charge and, in consequence, desorption of the polyelectrolyte chain from the surface is entropically unfavorable. Therefore, the film structure is determined by the adsorption conditions and cannot be changed afterwards.

### 14.3

#### Metallosupramolecular Devices in Thin Layered Films

##### 14.3.1

##### Introduction

Metal ion induced self-assembly involves the generation of well-defined discrete [62] and extended [63] metallosupramolecular architectures, either in solution or in the solid state [64]. Metal ions have properties of special interest as functional components in supramolecular devices and materials [65]. They provide a set of variable coordination geometries, a range of different binding strengths, and ligand exchange kinetics that allow reversible assembly–disassembly of supramolecular architectures, including switchable interaction sites, e.g. electrochemical interconversion between redox states leading to different coordination geometries.

Metallosupramolecular assemblies based on organic ligands and metal ions offer a wide range of properties (Fig. 14.6). Through the judicious choice of metal ions and ligands it is, in principle, possible to tailor their thermodynamic, kinetic, and functional properties. Strong optical absorption, high quantum yields, suitable excited state life times, and luminescence make metallosupramolecular structures promising components for photonic devices. The optical absorption bands are often associated with large optical non-linearities [66]. Through the coordination geometry of the central metal ion, it is possible to introduce chirality into the final metallosupramolecular architecture, that in turn may be utilized in molecular recognition or to generate materials with non-centrosymmetric space groups. Photo-induced charge separation in polynuclear coordination compounds has been studied extensively with ligands such as bipyridines and second or third row transition metal ions such as Ru(II) and Os(II) because they possess suitable excited-state and redox properties [67]. While photo-induced charge separation has been studied in terms of artificial photosynthesis, such systems are also interesting for information processing devices. But also first row transition metal ions, especially Fe(II), show exciting possibilities due to spin-transitions [68]. The importance of transition metal complexes for constructing molecular based, photo-reactive devices and materials becomes apparent in effects like light-induced excited spin-state trapping (LIESST) [69], reverse LIESST [70] and low spin (LS) LIESST [71] effects, metal-to-ligand charge transfer in nitroprusside [72], metal-to-metal charge transfer as in Prussian Blue analogues [73], valence tautomerism [74], as well as ligand driven light-induced spin-state change (LD-LISC) [75].

Polyoxometalates (POMs) represent another interesting class of metallosupramolecular structures with a wide range of applications in fundamental and ap-

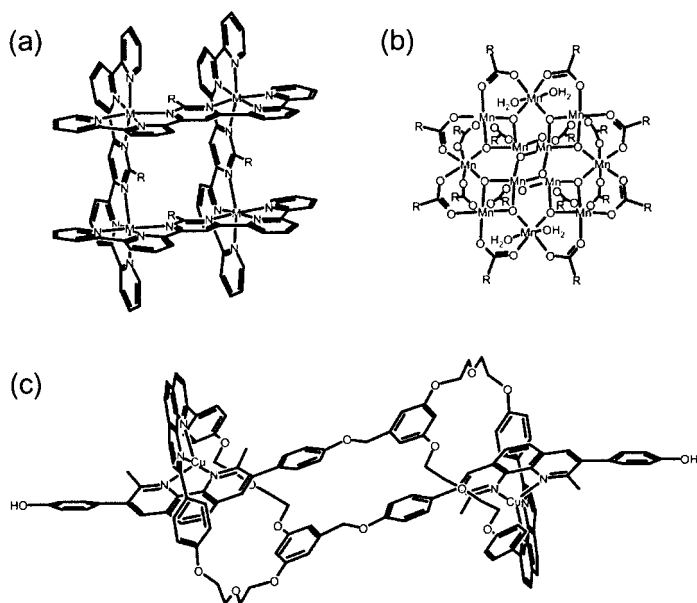


**Fig. 14.6** Representative examples of functional metallosupramolecular assemblies. (a) Supramolecular  $M_4$ -[2×2] grid ( $M = \text{Co}^{\text{II}}$ ,  $\text{Fe}^{\text{II}}$ ;  $R = \text{Ph}$  or  $\text{Me}$ ) displaying reversible thermal- or light-induced spin cross-over. [120].

(b)  $[\text{Mn}^{\text{IV}}\text{Mn}^{\text{II}}\text{O}_{12}(\text{RCOO})_{16}(\text{H}_2\text{O})_4]$  ( $R = \text{Ph}$  or  $\text{Me}$ ), a single molecule magnet [121]. (c) Doubly threaded (hermaphrodite-type) dinuclear  $\text{Cu}^{\text{I}}$  assembly as part of a unimolecular synthetic “muscle” [122].

plied science such as catalysis, [76] electrochemistry, [77] electrooptics, [78] medicine, [79] corrosion protection, dyes/pigments, dopants, bleaching of pulp, and analytical chemistry. [80]. In contrast to many semiconductor nanoparticles and quantum dots, POMs are discrete, molecularly defined monodisperse transition metal-oxide clusters with a broad range of structures and properties that form through sequential self-assembly processes of metal–oxygen building blocks (Fig. 14.7). An attractive feature of POM clusters is the size-dependence of their physicochemical properties, such as the ability of the metal–oxygen framework to accommodate excess electrons [81]. This reduction is reversible and occurs with marginal structural rearrangement. The electron storage capacity increases with cluster size: Thus, small *α*-Keggin-type POMs,  $[\text{XM}_{12}\text{O}_{40}]^{n-}$  ( $\text{X} = \text{Al}^{3+}$ ,  $\text{Si}^{4+}$ ,  $\text{P}^{5+}$ ,  $\text{M} = \text{Mo}^{6+}$  or  $\text{W}^{6+}$ ) display reversible one- or two-electron reduction steps, while larger ones (e.g. Preyssler-type POMs  $[\text{XW}_{30}\text{O}_{110}]^{n-}$ , where  $\text{X} = \text{Na}^+$ ,  $\text{Eu}^{3+}$ ) support multi-electron reduction. The reduced POMs frequently display a deep blue color. The ability to accept electrons under alteration of the light-absorbing properties is perhaps the most promising effect for the construction of functional devices and materials. The extinction coefficient of the colored POM state is comparable to that of organic dyes, however, the photochemical stability of POMs is far superior to that of organic molecules. Photochromic properties arise in the presence of cer-

tain counter ions, such as alkylammonium, anilinium and pyridinium, that can undergo photoinduced proton transfer to the POM framework. The reduction of the POM cluster results in accumulation of negative charge, which increases the basicity of the POM anion. The reduction process may be accompanied by protonation steps and, therefore, the redox properties of POMs are markedly pH sensitive. Their valuable physicochemical properties suggest using POMs as functional components in advanced materials [82]. With the recent discovery of self-assembling, discrete and nano-sized polyoxomolybdates (*giant wheels*, *Keplerates*) [83] novel inorganic components are now available that open access to constructing nano-reactors for transformation (catalysis) and molecular recognition (sensing) (Fig. 14.7).

In summary, metallosupramolecular assemblies offer intriguing prospects for the construction of technological devices. While through crystal engineering, extended 2- and 3-dimensional solid-state arrays may be constructed using either interaction of metal ions with multitopic ligands [84] or by using other weak intermolecular forces to organize metallo-units [85] the exploitation and the encoding of *value-adding* properties of metallo-units as functional components of advanced materials remains elusive, mainly due to the fact that these materials are obtained

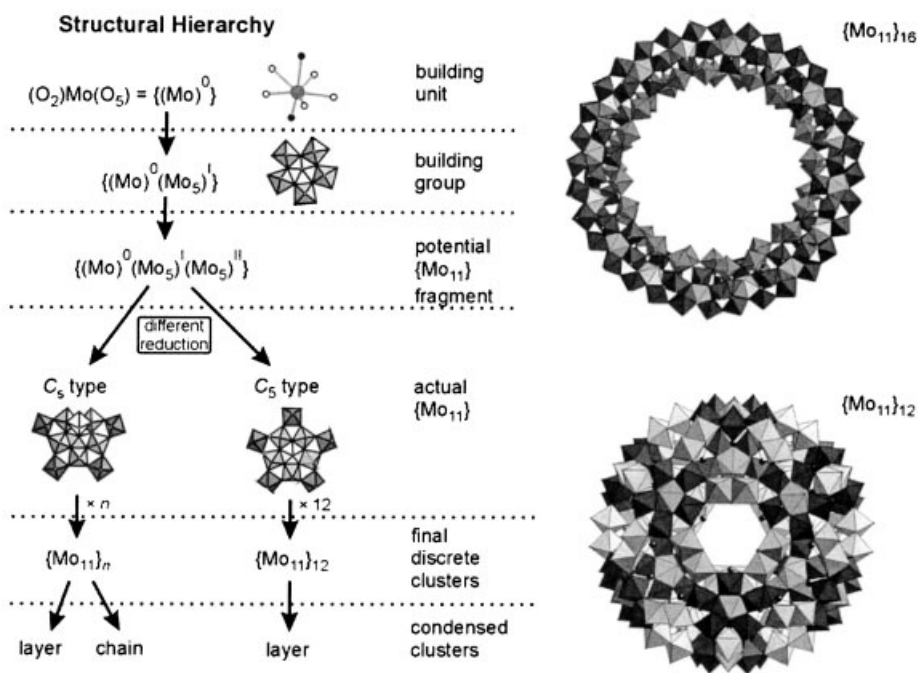


**Fig. 14.7** The emergence of structural hierarchy in polyoxometalate clusters. Left: Fundamental building units. Right: Selected examples of giant POMs emerging from self-as-

sembly:  $\{Mo_{11}\}_{16} = [Mo_{176}O_{528}H_{16}(H_2O)_{80}]^{16-}$ ;  $\{Mo_{11}\}_{12} = [Mo_{132}O_{372}(CH_3COO)_{30}(H_2O)_{72}]^{12-}$ , an inorganic superfullerene (*Keplerate*) (Adapted from [83 a] with kind permission).

as crystalline solids that are hard to process. Due to the high lattice energies associated with crystallization, the occurrence of distinct supramolecular architectures, such as liquid crystalline phases, is rarely observed [86]. The encoding of new properties and the exploitation of a material's potential will depend on developing methods to combine, position, and orient the components in the final device architecture. For these reasons, we have explored layer-by-layer self-assembly as a means to implement functional metallo-units into thin layered films.

### 14.3.2

#### **Metallosupramolecular Coordination Polyelectrolytes**

Currently, polypyridine ligands attract considerable attention as synthons in metallosupramolecular chemistry because of their interesting photo- and electrochemical properties [87]. Bipyridine ligands in combination with second and third row transition metal ions, in particular Ru(II) and Os(II), have favorable excited-state redox properties and first row transition metal ions, such as Fe(II), show interesting spin-transitions. However, in terms of structure, bipyridine is not an ideal synthon because bidentate ligands give rise to isomers in an octahedral coordination geometry [88]. The tridentate terpyridine ligand is much more convenient in this regard because metal ion coordination leads to stereochemically defined octahedral complexes. Also, substitution in the 4'-position does not cause isomerism and offers a possibility to align the substituents in a pre-defined direction.

Based on the structural advantage of the terpyridine group, we have investigated polynuclear metallosupramolecular assemblies utilizing the ditopic ligand 1,4-bis(2,2':6',2''-terpyridine-4'-yl)benzene and related ligands (Fig. 14.8). The design of the ligand with back-to-back metal ion receptors and the high directionality of the terpyridine metal ion interaction lead to linear, rod-like polynuclear structures. We refer to these assemblies as metallosupramolecular coordination polyelectrolytes (MEPE) because of the overall positive charge.

The high positive charge of MEPE opens a route to assemble these units on interfaces through electrostatic interactions using the ELSA deposition protocol (Fig. 14.9) [89]. First, the substrate is covered by a layer of PEI followed by a layer of PSS to render the interface negatively charged. Film formation is carried out by alternate immersion of the substrate in solutions containing MEPE and an oppositely charged polyelectrolyte such as PSS and intermittent washing steps.

The strong and characteristic absorbance of MEPE provides a means to follow ELSA deposition by UV-vis absorption spectroscopy. The occurrence of characteristic MLCT bands demonstrates that metal ion coordination is not affected by multilayer assembly. X-ray photoelectron spectroscopy confirms that the expected elements are present. Qualitative analysis reveals a metal to nitrogen atomic ratio of 1:6, as expected for octahedral complexes. In all cases that we have investigated so far, we observe linear growth of film thickness as a function of deposition cycles. This indicates that in every deposition step an equal amount of material is adsorbed at the interface.



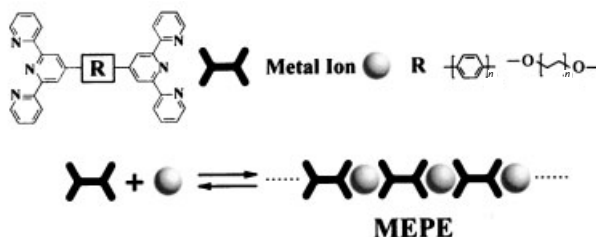


**Fig. 14.8** Metal ion induced self-assembly of ditopic bis-terpyridine ligands results in metallosupramolecular coordination polyelectrolytes (MEPE). Different structural and functional components, R, can be introduced in

the ligand, including (rigid) phenyl- or (flexible) alkyl-spacers. The availability of ligands and the diversity of terpyridine coordination chemistry provide a high degree of modularity.

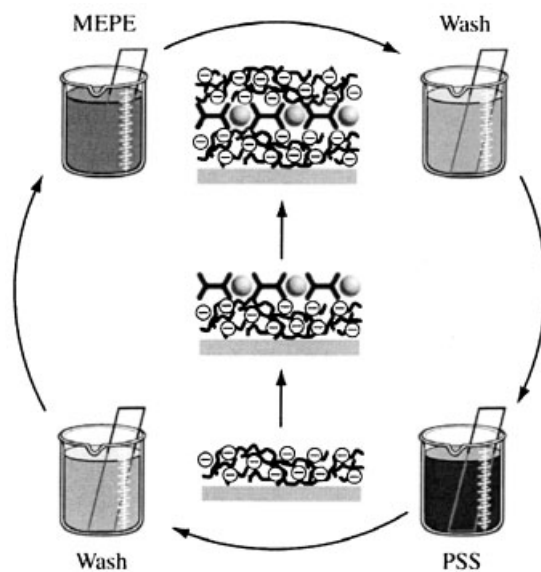


**Fig. 14.9** Due to the positive charge, MEPE adsorbs irreversibly on negatively charged interfaces. Repeated immersion of the substrate in solutions containing MEPE and PSS and intermittent washing steps result in multilayers.

From the UV-vis absorption spectra of the multilayers, we can calculate the surface coverage,  $\Gamma$ , according to Lambert-Beer's law  $\Gamma = (A_\lambda \cdot N) / 2\epsilon_\lambda$ , where  $\epsilon_\lambda$  is the isotropic molar extinction coefficient ( $\text{M}^{-1} \text{cm}^{-1}$ ),  $N$  is Avogadro's number, and  $A_\lambda$  is the absorbance at a specified wavelength. Typically, we find that approximately two MEPE monolayers adsorb per deposition step. Linear growth of the film thickness is independently confirmed by additional techniques including optical ellipsometry, QCM studies and SPR spectroscopy (Fig. 14.10). That the layers are smooth and homogeneous is indicated by the appearance of Kiessig fringes in X-ray reflectometry of (PSS/Fe-MEPE) multilayers deposited on silicon wafers. The solid lines in Fig. 14.10 (II) represent the corresponding calculated reflectance curves and reveal a layer thickness of 17 Å for Fe-MEPE and an overall interfacial

roughness of less than 1 nm. The absence of Bragg reflexes in the X-ray reflectometry, which would indicate an internal structure, could have two reasons: Either the quality of stratification within the multilayers is not sufficient for adjacent layers to interdigitate, or the electron density contrast between PSS and MEPE is not large enough.

Microgravimetry allows direct weighing of the adsorbate with a very high sensitivity and complements UV–vis spectroscopic measurements [90]. The gold electrodes of the QCM are first coated with a monolayer of mercaptopropionic acid (MPA) to provide a permanently charged electrode surface suitable for subsequent ELSA deposition. Then a layer of poly-(ethylenimine) (PEI) is adsorbed on the MPA derivatized gold surface. The QCM is coated on both sides with a (PSS/MEPE) multilayer. The change in resonance frequency after each deposition is measured *ex situ*. Each deposition step is associated with a decrease in the resonance frequency, indicating an increase in the total mass on the electrodes. In the case of Fe-MEPE, the frequency change caused by a single layer is 87 Hz or  $237 \text{ ng cm}^{-2}$ . Similarly, deposition of a single PSS layer gives rise to a frequency change of 83 Hz, corresponding to a mass of  $227 \text{ ng cm}^{-2}$ . The mass loading can be converted into a layer thickness if the density of the layer is known. As an approximation for the density of the layers we use the bulk densities. With a density of  $1.5 \text{ g cm}^{-3}$  the thickness of a single MEPE layer is 2.0 nm. Likewise, the PSS layer thickness is 1.5 nm (density  $1.2 \text{ g cm}^{-3}$ ) [91]. Very similar results are obtained with Co-MEPE, indicating reproducible coating characteristics.

The QCM also allows determination of the up-take and loss of water in these films. If the QCM crystal, coated with a (PSS/MEPE) multilayer, is exposed to

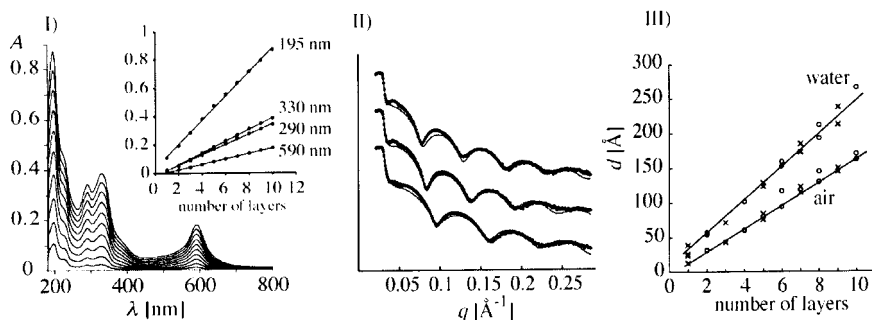


**Fig. 14.10** (I) Representative UV–vis spectra of (PSS/Fe-MEPE) multilayers deposited on quartz wafers. The MLCT band at 590 nm is characteristic for bis-terpyridine complexes of Fe(II). Plotting the absorbance at selected wavelengths versus the number of layers results in straight lines, indicating linear growth (insert). (II) X-ray reflectometry of (PSS/Fe-MEPE)<sub>3</sub>PSS, (PSS/Fe-MEPE)<sub>4</sub>, (PSS/Fe-MEPE)<sub>4</sub>PSS on silicon substrates. The appear-

ance of Kiessig fringes indicates that the multilayers are homogeneous and very smooth. The solid lines represent calculated reflectance curves. The film thickness for a single Fe-MEPE layer amounts to 17 Å and the total roughness to approximately 8 Å. (III) Film thickness determined by SPR spectroscopy versus the number of layers in air and in water. The average layer thickness is approximately 17 Å (dry) and 25 Å (water).

water vapor the frequency drops as a result of water adsorption and reaches a plateau within a few minutes. Likewise, exposure to dry air results in a frequency increase in the QCM resonator due to desorption of water. The frequency change is completely reversible. The total uptake of water is approximately 20% of the total mass loading. Swelling of the layers is also confirmed by thickness measurements using SPR spectroscopy.

Linear multilayer growth is also confirmed by IR spectroscopy. For experimental considerations, the multilayers are assembled on gold surfaces and IR-spectra are recorded in reflection mode [92]. In Fig. 14.11, reflection-absorption infrared (RAIR) spectra of a series of multilayers (PSS/MEPE)<sub>n</sub> ( $n=1, 2, 3, 4, 5, 10$ ) are shown. First we note that the characteristic strong IR absorption bands corresponding to acetate anions are absent. Apparently, the counter ions are exchanged during ELSA deposition. From the position of the sulfonate group in the RAIR spectrum we can draw conclusions about the nature of the counter ion [93]. Formation of sulfonic acid during layer build-up can be ruled out because the characteristic vibrational modes of the  $-\text{SO}_3\text{H}$  group at 1097, 1350, 1172  $\text{cm}^{-1}$  are clearly absent in the spectra. The splitting of the S–O stretching modes located at around 1200  $\text{cm}^{-1}$  provides information about the counter ion. Typically, the splitting increases with the strength of the electric field generated by the cation. For  $\text{Na}^+$  the splitting is 38, for  $\text{Co}^{2+}$  77, and for  $\text{Fe}^{3+}$  130  $\text{cm}^{-1}$ , respectively. In (PSS/MEPE) multilayers the sulfonate bands are located at 1197 and 1223  $\text{cm}^{-1}$ . The small splitting of 26  $\text{cm}^{-1}$  is attributed to the presence of the MEPE polycation. Apparently, the bulky terpyridine groups that coordinate around  $\text{Fe}^{2+}$  in an octahedral fashion shield the charge of the central cation.

Using SPR spectroscopy we can monitor (PSS/MEPE) multilayer deposition *in situ* [94]. A quantitative analysis of SPR scans indicates that initially up to three PSS layers adsorb at the interface while only two Fe-MEPE layers are deposited under similar conditions. If one takes into account that PSS can tail and loop into

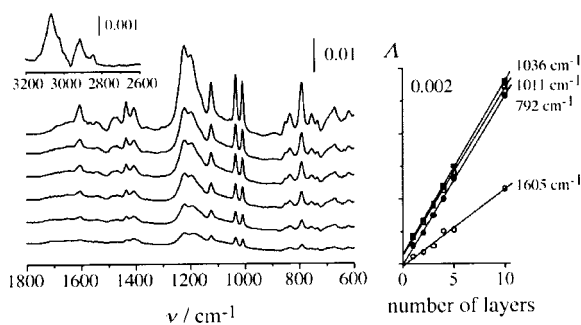


**Fig. 14.11** Reflection-absorption infrared spectra of MPA/PEI(PSS/MEPE)<sub>n</sub> ( $n=1, 2, 3, 4, 5, 10$ ) multilayers on gold coated substrates (reported in absorbance). The graph on the right shows the absorbance at selected

wavelengths as a function of the number of layers demonstrating linear film growth. The water absorbance and the CH-stretching modes are shown in the inset on the left ( $n=10$ ).

the aqueous phase and that an entangled multilayer can form at the interface, one would expect an excess of polymer at the interface. In contrast to PSS, Fe-MEPE has many fewer degrees of freedom due to the rigid-rod-like structure. The possibilities for Fe-MEPE to form tails, loops or entangled multilayers are thus diminished. We, therefore, conclude that Fe-MEPE adsorbs flat on the surface with few tails and loops. Loosely bound excess polyelectrolyte is removed from the surface during washing steps. The adsorption kinetics is described by two processes. In the beginning, adsorption obeys a  $t$  dependence. According to Fick's second law this observation implies that every molecule that reaches the surface is immediately adsorbed. We can conclude that in the early stages, adsorption is a diffusion-controlled transport process. To get a higher surface coverage, penetration of the molecules through the existing layer combined with conformational changes has to take place, which can be described by a (slower) first order rate law [95]. Both processes occur at widely separated time scales, resulting in a distinct crossover in the SPR scans.

The reversibility of the metal ion–ligand interaction offers an opportunity to modify the (PSS/MEPE) multilayers. While MEPEs readily exchange metal ions in solution, a direct exchange of metal ions in multilayers is not observed. Apparently, electrostatic interactions between MEPE and PSS slow down the metal ion exchange considerably. However, metal ions can be removed from the multilayer with a competing complexing agent such as ethylenediamine (*en*) [96]. The (PSS/Co-MEPE) multilayers are first subjected to *en* in order to remove the Co(II) ions from the multilayer. It should be noted that the layer is not decomposed in this step. Then, the vacant metal ion receptors are filled with Fe(II), which is readily detected by the occurrence of the characteristic MLCT bands. Quantitative analysis via UV–vis spectra indicates that approximately 50% of the Co(II) ions are replaced by Fe(II) ions.

The Co-MEPE has a suitable potential window in order to investigate the electrochemical properties [97]. In solution, Co-MEPE shows a pair of current waves with a redox half-wave potential of 87 mV, which is independent of the scan rate, and consistent with mononuclear Co-bis-terpyridine complexes [98]. The appearance of only one pair of current waves indicates electrochemically isolated subunits in Co-MEPE [99]. The anodic and cathodic currents are proportional to the scan velocity. The proportionality between the current and the scan velocity reflects the reversibility of the redox process. The potential difference between the two current peaks  $\Delta E_p$  is 74 mV and remains constant during the variation of the scan velocity, indicating fast electron transfer. The redox potential  $E_{1/2}$  of a (PSS/Co-MEPE) multilayer is slightly shifted to 128 mV. In this case, the anodic and cathodic current peaks are proportional to the square root of the scan velocity. This behavior is consistent with electron self-exchange reactions within the electrochemical sites in the film, in which a semi-infinite electrochemical charge diffusion condition prevails [100]. The current peak difference  $\Delta E_p$  increased to approximately 123 mV in the film, which may reflect a higher ohmic resistance of the multilayer, presumably caused by the intermittent PSS layers. These results indicate that the electrochemical properties of MEPE are fully maintained in the corresponding multilayers.

Using  $K_3[Fe(CN)_6]$  as electroactive probe we investigated the permeability of these multilayers. We note a significant difference in permeability if we compared (PSS/PAH) and (PSS/Co-MEPE) multilayers. Deposition of two PAH/PSS layers on the electrode reduces the current by an order of magnitude. However, in (PSS/PAH) multilayers the electrochemical signature of the  $Fe(CN)_6^{3-}/Fe(CN)_6^{4-}$  couple remains discernible, indicating that the redox active probe diffuses through the multilayers and undergoes electron transfer reactions at the underlying Au-electrode. Similarly, (PSS/Co-MEPE) $_n$  multilayers show a reduction in the peak current ( $n=1, 2, 3$ ). But (PSS/Co-MEPE) $_5$  multilayers show only a capacitive current and no electroactivity of the redox probe, indicating that the electrode is completely blocked at this stage.

Deposition of MEPE is not restricted to planar substrates but also works for charged nanoparticles [101]. Consecutive adsorption of PSS and Fe-MEPE on cetyltrimethyl ammonium-stabilized, positively charged polystyrene (PS) latices with an average diameter of  $73 \pm 14$  nm results in multilayers.

Evidence for the deposition of PSS/Fe-MEPE multilayers on PS-latices is obtained by visual inspection: Upon deposition, the PS-latices turn blue, the characteristic color of Fe-MEPE. Layer-by-layer growth is confirmed by recharging the particle surface with each deposition cycle. The neat PS-latices have a positive  $\zeta$ -potential of +60 mV. Deposition of PSS reverses the sign of the  $\zeta$ -potential (approximately -42 mV); subsequent deposition of Fe-MEPE results in a positive  $\zeta$ -potential (approximately +18 mV) [102]. While no quantitative conclusions can be drawn from  $\zeta$ -potential values, alternating  $\zeta$ -potentials are characteristic of regular multilayer growth on colloidal templates [103]. Additional evidence for the adsorption of Fe-MEPE on the particles is provided by energy dispersive X-ray analysis, which clearly shows the presence of Fe(II) on the PSS/Fe-MEPE-coated particles.

Using decomposable colloidal templates, such as weakly crosslinked melamine-formaldehyde particles, it is possible to generate hollow (PSS/MEPE) shells. [104]. These results demonstrate that it is possible to assemble MEPes on colloidal particles of micro- and nanometer size, thereby creating particles with tailored properties. In contrast to planar surfaces, these particles can be dispersed in solution, allowing investigations of structure and properties with solution based methods, such as nuclear magnetic resonance. These assemblies bridge the gap between discrete metallosupramolecular assemblies comprising a small number of components (metal ions and ligands) and extended solid-state structures with an infinite number of components. These particles are expected to have potential applications in electronics, photonics and catalysis. The functional and stable hollow shells consisting of (PSS/MEPE) multilayers are potentially useful as micro-reactors.

This approach can also be extended to the deposition of discrete transition metal ion complexes if we introduce secondary interactions to stabilize the metallo-units at the interface (Fig. 14.12). [105]. The low charge of these units typically does not provide sufficient interactions for irreversible adsorption. Previously, it has been demonstrated that aryl tails can be used to control the aggregation of metallo-units through  $\pi$ - $\pi$  interactions [85]. Such arrays afford several advantages over conventional coordination polymers: facile ligand synthesis, reversible assem-

bly even with kinetically inert metal ions, good solubility and straightforward characterization. We selected pyrene as the aryl moiety to control the supramolecular organization. Pyrene has a strong propensity to form coplanar pyrene stacks. In addition, stacking is associated with excimer absorption and emission bands, which allows monitoring stack formation spectroscopically. Reaction of 4'-(1-pyrenyl)-2,2':6',2''-terpyridine (Pyr-tpy) with divalent transition metal cations affords the  $[ML_2]^{2+}$  complexes as anticipated from the coordination chemistry of unsubstituted tpy. Crystallographic analysis of the iron(II) complex confirms the anticipated pyrene–pyrene stacking motif. The structure contains six-coordinate iron bis-terpyridyl units linked into a linear array through pyrene–pyrene  $\pi$ -stacks. Using PSS as counter polyelectrolyte we observe multilayer formation for  $[M(\text{Pyr-tpy})_2]^{2+}$  complexes ( $M = \text{Zn}, \text{Fe}$ ). UV–vis absorption spectroscopy, X-ray reflectometry, and optical ellipsometry confirm linear layer growth. Quantitative analysis shows that the surface coverage is approximately 1.1 metallo-units per  $\text{nm}^2$  or  $0.9 \text{ nm}^2$  per metallo-unit. The dimensions of the metallo-unit can be estimated from the crystal structure. The metal–metal distance is  $\sim 1.7 \text{ nm}$  and the width of the terpyridine unit is  $\sim 1.1 \text{ nm}$ . The occupied surface area of a single unit is, thus, estimated to be  $\sim 1.9 \text{ nm}^2$  if we assume that the metallo-units are oriented with the long axis parallel to the substrate. The experimentally determined value, therefore, corresponds approximately to one to two molecular layers. The multilayers are very smooth, as demonstrated by the occurrence of Kiessig interference fringes in X-ray reflectometry. The surface roughness of the layer is below 1 nm and the thickness of a layer pair is 2.5 nm, respectively. The thickness measurements suggest that the multilayers are composed approximately of molecular layers in agreement with the UV–vis data. A solution of the  $[\text{Zn}(\text{Pyr-tpy})_2]^{2+}$  complex in methanol shows a characteristic fluorescence emission band at 455 nm attributed to the luminescence of the molecular units (no stacking). In contrast,  $(\text{PSS}/[\text{Zn}(\text{Pyr-tpy})_2]^{2+})$  multilayers exhibit a broad emission band centered around 520 nm. The band is characteristic of excimer or excimer-like pyrene emission [106], attributed to the  $\pi$ -stacked pyrene units. The excimer emission clearly demonstrates that the pyrene tails are stacked in the multilayer adopting the same structural motif as in the solid state. The absence of any detectable 455 nm fluorescence in multilayers of  $[\text{Zn}(\text{Pyr-tpy})_2]^{2+}$  implies that virtually all metallo-units engage in  $\pi$ -stacking in each layer (as in the crystal). In contrast, simple bis-terpy-

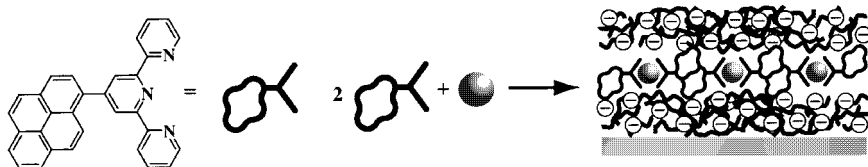


**Fig. 14.12** Immobilization of discrete metallo-units in thin films is achieved by combining electrostatic interactions of oppositely

charged species and aryl aggregation within the metallo-units as secondary interactions.

ridine complexes  $[M(\text{tpy})_2]^{2+}$ , which do not bear aryl tails do not form layers under these conditions. From this it is clear that the aryl tails play a vital role in the ELSA deposition process.

### 14.3.3

#### Polyoxometalate Clusters

The negative charge and the water solubility of polyoxometalate (POM) clusters permit us to implement these functional units in layered materials using ELSA deposition. In the first step, a (PEI/PSS/PAH) multilayer is assembled on the substrate forming the base for subsequent POM deposition. Alternate adsorption of POM anions and PAH results in multilayer formation. The largest POM cluster assembled in multilayers so far in our laboratories is the novel giant Keplerate with the chemical formula  $[\text{Mo}_{132}\text{O}_{372}(\text{CH}_3\text{COO})_{30}(\text{H}_2\text{O})_{72}]$  (Mo132) (Fig. 14.13) [107]. The nearly spherical Mo132 cluster shows promising perspectives in host-guest chemistry and size-selective catalysis because it possesses an open Mo–O framework architecture that encloses a central cavity with an approximate inner diameter of 1.7 nm. The Mo132 framework spans (Mo–O) 9-ring openings with an average ring aperture of 0.43 nm, which is comparable in size to the pores in zeolitic architectures.

The ELSA method appears most promising for the fabrication of permeable coatings in order to exploit Keplerates in catalytic and sensing applications. Due to the dark-brown color of Mo132, UV–vis spectroscopy permits facile evaluation of the deposition process. The constant increase in the absorbance confirms adsorption of Mo132 anions and is in agreement with linear multilayer growth. Apparently, the 42 negative charges provide sufficient electrostatic interactions for irreversible adsorption. We notice that for the first layer, a significantly larger amount of Mo132 is immobilized on the PEI/PAH precursor film. This is possibly due to penetration of Mo132 anions into the underlying precursor layer. Based on the absorbance data the average surface concentration of Mo132 per layer is  $(4.4 \pm 0.2) \times 10^{12}$  clusters  $\text{cm}^{-2}$  or  $(7.3 \pm 0.3) \times 10^{-12}$  mol  $\text{cm}^{-2}$ . This corresponds to an average area of  $(22.7 \pm 1.0) \text{ nm}^2$  cluster $^{-1}$ . In the crystal structure of  $(\text{NH}_4)_{42}[\text{Mo}_{132}\text{O}_{372}(\text{CH}_3\text{COO})_{30}(\text{H}_2\text{O})_{72}] \cdot \text{ca. } 300 \text{ H}_2\text{O} \cdot \text{ca. } 10 \text{ CH}_3\text{COONH}_4$  the packing density is  $9.1 \text{ nm}^2$  cluster $^{-1}$  in the (111) plane and  $10.6 \text{ nm}^2$  cluster $^{-1}$  in the (100) plane. The Mo132 packing density in the multilayer is, therefore, approximately 50% of that of the crystalline material. Most likely, the repulsive electrostatic and dipolar interactions are not compensated as efficiently in a two-dimensional film as in the solid state.

Film growth was monitored with the quartz crystal microbalance. The change in resonance frequency after rinsing and drying the film shows that the deposited quantity of Mo132 anions for a single layer amounts to  $(3300 \pm 150) \text{ ng cm}^{-2}$ . For a Mo132 monolayer we would expect a mass change of  $158 \text{ ng cm}^{-2}$ . Hence, the experimentally determined mass corresponds to many Mo132 layers. If PAH is adsorbed on top of the Mo132 layer the total mass on the QCM crystal decreases. The mass for the Mo132/PAH layer pair amounts to  $(375 \pm 18) \text{ ng cm}^{-2}$ . The de-

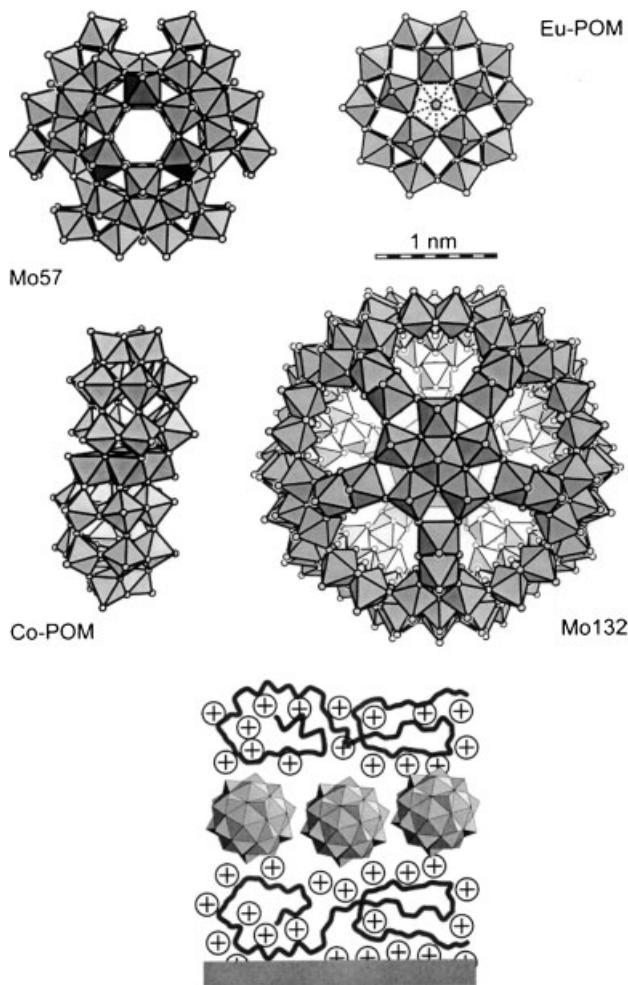
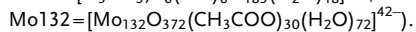
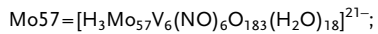
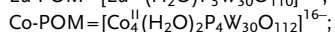
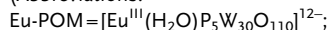


**Fig. 14.13** Polyhedral representations of POMs used in ELSA thin film formation.

(Abbreviations:



The bottom illustration shows a scheme of the resulting POM-based ELSA multilayers.

crease in mass loading can be rationalized as follows: Weakly adsorbed Mo132 anions are extracted from the surface during PAH deposition. Possibly, the Mo132 can form a complex with PAH in solution. In contrast, electrostatically immobilized Mo132 cluster anions, directly adsorbed on the underlying PAH layer, can form a surface confined Mo132/PAH complex. For this reason it is not possible to determine the individual weight contribution of each component by microgravimetric measurements because adsorption of PAH on, and extraction of Mo132



cluster anions from the interface occur simultaneously. Based on the surface coverage determined by UV-vis absorption, a single layer of Mo132 would have a mass of  $158 \text{ ng cm}^{-2}$ . The remaining  $217 \text{ ng cm}^{-2}$  are attributed to the PAH layer and water, which is always present in these multilayers. For comparison, a single PAH layer with a thickness of  $1.2 \text{ nm}$  and a density of  $1.2 \text{ g cm}^{-3}$  is expected to have a mass of  $150 \text{ ng cm}^{-2}$ . The mass loading in both cases is consistent with one to two molecular layers.

The appearance of Kiessig interference fringes in X-ray reflectance curves indicates that the multilayers are uniform and homogeneous. The average film thickness for a Mo132/PAH layer pair is  $2.2 \pm 0.2 \text{ nm}$  and the total roughness of the interface is typically below  $1 \text{ nm}$ . No Bragg reflections are observed that would indicate an internal structure. The reason for this could be that due to the low Mo132 surface coverage the electron density contrast is (a) reduced and (b) smeared out.

The next smaller POM anion that we investigated is the  $[\text{H}_3\text{Mo}_5\text{V}_6(\text{NO})_6\text{O}_{183}(\text{H}_2\text{O})_{18}]$  cluster (Mo57), which has approx. 21 negative charges (Fig. 14.13) [108]. The external form of the Mo57 cluster resembles a flattened ellipsoid with dimensions  $1.6 \times 2.4 \text{ nm}^2$  (determined by X-ray crystallography). The wide-spread application of the Keggin type POM in solid state devices, catalysis, biochemistry and medicine provides further impetus for investigation of this new class of molybdenum polyoxometalate clusters. As shown in the previous example, we observe linear film growth as determined by UV-vis absorbance, ellipsometry, and X-ray reflectometry. We notice that deposition of PAH always causes some loss of cluster from the interface, which is attributed to weakly bound material and complex formation in solution as discussed above. The surface density of Mo57 in PEI/PSS/PAH(Mo57/PAH) $_n$  films amounts to  $(1.4 \pm 0.4) \times 10^{13} \text{ clusters cm}^{-2}$  for  $n > 1$ . This corresponds to an average area of  $7.1 \pm 2.0 \text{ nm}^2$  per Mo57 anion. Hence, assuming that a single Mo57 anion occupies an area of approximately  $3.2\text{--}4.8 \text{ nm}^2$ , depending on its relative orientation, the average surface coverage is  $56 \pm 12\%$ . The average surface density for the first layer of Mo57 deposited onto the PEI/PSS/PAH precursor film is approximately twice as large, indicating that the anions penetrate the underlying PEI/PSS/PAH layer. X-ray reflectometry shows Kiessig fringes, indicating that the layers are homogeneous and even. As in the previous example, we do not observe Bragg peaks in the reflectance curves. The average thickness for the Mo57/PAH layer pair (for films with  $n > 1$ ) is  $0.8 \pm 0.1 \text{ nm}$  and the interfacial roughness is approximately  $1 \text{ nm}$ . Due to concomitant removal of Mo57 and deposition of PAH the thickness of an individual layer cannot be derived from these measurements.

The next smaller POM anion in this series of clusters is the sandwich type cobalt(II)-substituted POM compound  $[\text{Co}^{\text{II}}_4(\text{H}_2\text{O})_2\text{P}_4\text{W}_{30}\text{O}_{112}]^{16-}$  (Co-POM) [109]. This cluster with 16 negative charges is approximately  $2.3 \text{ nm}$  in length and  $1.4 \text{ nm}$  in width (Fig. 14.13). As in the previous examples we observe linear and regular growth, indicating irreversible adsorption of the POM anion. However, it should be noted that X-ray reflectometry of these layers did not produce well-resolved Kiessig fringes. Obviously, the interfacial roughness is too large to provide coherent interference of the rays from the top and bottom of the layer. Kiessig

fringes become apparent if we place an additional PAH/PSS layer pair on top of the multilayer.

Cyclic voltammetry of the Co-POM in solution indicates two  $2e^-/2H^+$  redox processes. In ELSA multilayers, such as  $(\text{Co-POM/PAH})_n$  and  $(\text{PSS/PAH/Co-POM/PAH})_n$  ( $n < 20$ ), the cathodic peak potentials shift slightly towards negative and the anodic peak potentials shift slightly towards positive potential values. The peak current increases linearly with the number of layers, confirming that the assembly process is highly regular. Moreover, the CVs of the modified electrodes show the characteristics of reversible surface redox electrochemistry. A plot of the cathodic ( $i_{pc}$ ) and anodic ( $i_{pa}$ ) peak currents as a function of scan rate,  $v$ , is linear with zero intercept, and the ratio  $i_{pc}/i_{pa}$  is unity at all scan rates, which implies that the redox processes of surface confined Co-POM anions are fast and not diffusion limited [110]. These results demonstrate that the electrochemical property of Co-POM is fully maintained in the multilayer.

It is interesting to note that the details of the electrochemical response of Co-POM-containing multilayers depend on the layer architecture. The CVs of  $(\text{PSS/PAH/Co-POM/PAH})_{10}$  and  $(\text{Co-POM/PAH})_{10}$  modified electrodes are shown in Fig. 14.14. The  $(\text{PSS/PAH/Co-POM/PAH})_{10}$  modified ITO electrode assembled from salt-free PAH solution (solid line) shows redox waves with peaks at  $-0.574$  V (C1) and  $0.73$  V (C2) and  $0.52$  (A1). A different electrochemical response is observed if the film is assembled with a PAH solution containing NaCl (0.5 M). During the cathodic sweep, only one reduction peak appears at a potential of  $-0.744$  V (C3), and during the anodic sweep two peaks appear at  $-0.563$  (A1) and  $-0.687$  (A2). Apparently, the two two-electron reduction steps merge into one four-electron process. Yet a different response is observed if the layer sequence is altered. The CV of a  $(\text{Co-POM/PAH})_{10}$  multilayer (dotted line) assembled with PAH containing NaCl (0.5 M) exhibits two peaks at potentials of  $-0.643$  (C1) and  $-0.731$

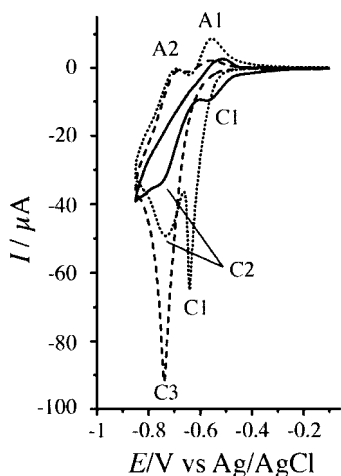


**Fig. 14.14** Representative CVs of  $(\text{PSS/PAH/Co-POM/PAH})_{10}$  assembled with salt-free solutions (solid line) and PAH solution containing NaCl (0.5 M) (dashed line) and of  $(\text{Co-POM/PAH})_{10}$  (dotted) assembled with PAH solution containing NaCl (0.5 M). (Adapted from [109]).

(C2) during the cathodic sweep, and two peaks at  $-0.554$  (A1) and  $-0.69$  (A2) during the anodic sweep, respectively. These examples demonstrate that the redox properties of the immobilized Co-POM can reveal subtle variations in film structure and composition [111]. This property suggests the use of POM anions as an electroactive probe to study microenvironmental effects in ELSA multilayers. It is interesting to note the accumulation of electrons on the Co-POMs in the combined reduction wave (C3) because it may give rise to novel chemical and catalytic effects.

The electrochemical response of ELSA-based Co-POM multilayers is also pH-dependent. The reason for this behavior is that reduction of the POM changes the basicity of the anion and may, therefore, be accompanied by protonation of the cluster. The overall redox process can be formulated as



where  $m$  is the number of protons and  $n$  the number of electrons participating in the redox process. Representative CVs of a (Co-POM/PAH)<sub>10</sub> multilayer assembled with a PAH solution containing 0.5 M NaCl are shown in Fig. 14.15. The relationship between the redox potential and pH is shown in the insert. With decreasing pH, the redox potentials shift to positive potentials. This property suggests that electroactive POMs in ELSA films may be used as pH sensors.

These findings demonstrate two new important features of POM-based ELSA films. First, Co-POM can be used to probe microenvironmental effects in multilayers. Second, the electrochemistry of Co-POM functionalized multilayers is remarkably pH-dependent. This feature makes Co-POM based multilayers potential candidates for pH microsensors, e.g. in physiological media. Our approach has sev-

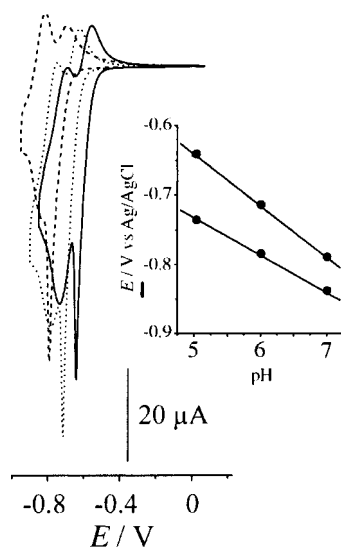


**Fig. 14.15** Representative CVs of (Co-POM/PAH)<sub>10</sub> assembled with PAH solution containing NaCl (0.5 M). Solid line: pH 5.0, dotted line: pH 6.0, dashed line: pH 7.0. The inset shows the dependence of redox potentials on pH (ITO electrode, supporting electrolyte: 0.2 M PBS, scan rate:  $10 \text{ mV s}^{-1}$ , potential  $E$  vs. Ag/AgCl). (Adapted from [109]).

eral advantages over other pH sensors [112]: it is simple and inexpensive to fabricate, operates reversibly, possesses long-term stability and, in addition, the electrochemical response characteristic, such as sensitivity and response time, can be adjusted by the structure and composition of the sensing layer.

The cluster with the smallest number of charges in this series is the Eu(III) derivative of the Preyssler-type [113] heteropolytungstate  $[\text{Eu}(\text{H}_2\text{O})\text{P}_5\text{W}_{30}\text{O}_{110}]^{12-}$  (Eu-POM, Fig. 14.13) [114]. This cluster exhibits reversible electrochemical behavior accompanied by a large electrochromic response [115]. As can be seen in Fig. 14.16, the oxidized form of Eu-POM is completely transparent in the visible region, while the reduced Eu-POM exhibits a broad adsorption band at approximately 700 nm. Each individual redox step is accompanied by an increasing coloration of the solution.

An electrochromic device is fabricated by ELSA deposition of Eu-POM, PAH, and PSS on indium tin oxide (ITO)-coated glass slides. In order to achieve a high surface coverage the dipping solutions contain NaCl. The CV of the (PSS/PAH/Eu-POM/PAH)<sub>20</sub> modified ITO electrode indicates three peaks at potentials of  $-0.384$  (C1),  $-0.466$  (C2) and  $-0.522$  (C3) V during the cathodic sweep, and three peaks at  $-0.371$  (A1),  $-0.453$  (A2) and  $-0.508$  (A3) V during the anodic sweep, respectively. The CV demonstrates that the electrochemical property of Eu-POM is fully maintained in the multilayer. A visually noticeable optical contrast (transparent to blue) during potential scanning between 0.2 and  $-0.6$  V demonstrates that the film is electrochromic. The UV-vis spectrum of the (PSS/PAH/Eu-POM/PAH)<sub>20</sub> modified ITO electrode shown in Fig. 14.16 is recorded during cyclic voltammetry. The absorbance at 700 nm  $A_{700\text{ nm}}$  increases to 0.12 at  $-1.75$  V. For a (PSS/PAH/Eu-POM/PAH)<sub>100</sub> modified ITO electrode,  $A_{700\text{ nm}}$  becomes as large as 0.7 at  $-1.85$  V. A single PSS/PAH/Eu-POM/PAH layer generates an optical density of 0.006 in the reduced state. A film less than 1  $\mu\text{m}$  thick would create an optical density of approximately 1, which is sufficient to lead towards practical device applications.

To evaluate device performance, a double potential step chronoamperometric experiment was undertaken by simultaneously recording the absorbance of the film. Fig. 14.16 shows the applied potential, the current, and the absorbance of a (PSS/PAH/Eu-POM/PAH)<sub>20</sub> multilayer at 700 nm. We observe a charging current, which decays rapidly to zero (during bleaching) or to a residual leakage current (during coloration). The residual leakage current may result from reduction of buffer solution. Both current and absorbance respond within seconds during coloration and bleaching. The stability and reversibility of the multilayer was evaluated by performing repetitive double potential steps. The CVs, the response times for coloration and bleaching, and the optical density do not change noticeably after 500 cycles. The multilayers also show a considerable optical memory, that is, after reduction the layer remains in the colored state even if the potential is removed. Therefore, it is possible to display information with this device without power consumption.

In conclusion, we have identified the Preyssler ion as a technically attractive component for electrochromic devices. Device fabrication rests on principles of molecular self-organization involving sequential adsorption of the POM and an

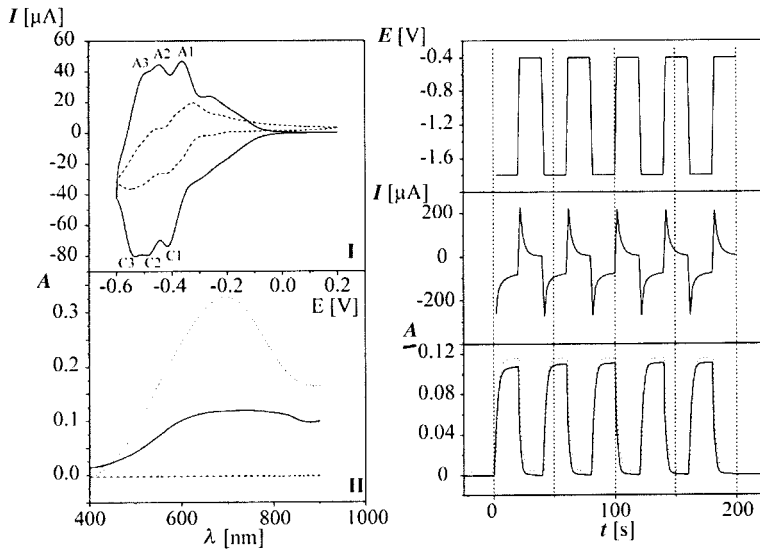


**Fig. 14.16** Left: (I) Representative CVs (vs. Ag/AgCl) of Eu-POM in solution (dashed line, ITO electrode, 0.25 mM, ordinate magnified 5 $\times$ ) and a (PSS/PAH/Eu-POM/PAH)<sub>20</sub> multilayer (solid line). Corresponding UV-vis spectra of oxidized (dashed line) and reduced (dotted line, -0.65 V vs. Ag/AgCl) Eu-POM in solution and a reduced (PSS/PAH/Eu-POM/PAH)<sub>20</sub> multilayer (solid line). Right: Potential

(vs. Pt electrode), current, and absorbance at 700 nm of the (PSS/PAH/Eu-POM/PAH)<sub>20</sub> coated ITO electrode during subsequent double potential steps between -0.4 and -1.8 V. Bottom: solid line 1st cycle, dashed line 500th cycle (traces offset for clarity). The response times for coloration and bleaching are 4.2 s and 4.4 s, respectively. (Adapted from [114a])

oppositely charged polyelectrolyte on the conducting and transparent substrate from aqueous solution. The method is readily extended to patterned substrates, so films can be prepared on predefined areas. The device operates reversibly with suitable response times, which may be reduced further by optimizing the polyelectrolyte matrix. Low operation voltage and low power consumption are additional advantages of this device. Power is required only for switching and leakage currents can be minimized by operating the device under open circuit conditions. Finally, sufficiently high optical contrast can be achieved even for thin films.

## 14.4

### Conclusions

Without doubt, layer-by-layer self-assembly of oppositely charged polyelectrolytes has become a buoyant procedure to fabricate thin film, which provides numerous opportunities in fundamental and applied science alike. The popularity of this method originates from the simplicity of layer formation, the excellent thickness

control, the stability of the multilayers, and its broad applicability. While earlier work focused on planar substrates, recent developments include particle coatings and patterned surfaces.

A particularly attractive feature of this method is that the electrostatic interactions that govern multilayer assembly can be easily changed, for instance through the ionic strength of the dipping solution, thus allowing control of polyelectrolyte conformation, film thickness, and surface coverage. This simple measure provides extensive control over the structure and function of the resulting multilayers, thus giving rise to tailored properties.

For these reasons, it is safe to predict that the realization of thin film devices will be the future trend both in fundamental and applied research. As charge is the chief requirement for successful ELSA-processing an almost unlimited range of functional components lies ahead to be implemented into ELSA structures; examples include nanoparticles for light emitting diodes [116], electroluminescent heterostructures [117], enzyme electrodes for sensing [118], composite membranes for separation [119], polyoxometalate clusters for display and sensing devices as well as nanoreactors, to name just a few examples.

### Acknowledgements

Helmuth Möhwald is acknowledged for valuable discussions. DGK, DV and RvK thank the BMBF and DFG for financial support. RvK is grateful to Roland Steitz for neutron- and X-ray reflectivity measurements and to Werner Jaeger and co-workers for the synthesis of P(DADMAC-NMVA) and P(DADMAC). Furthermore, we thank Thomas Hellweg, Mario Rodrigez, Claire S. Peyratout and John Wong for proofreading parts of the manuscript.

### Abbreviations

ELSA	Electrostatic layer-by-layer self-assembly
FITC-PAH:	Fluorescein isothiocyanate labeled poly(allylamine hydrochloride)
ITO:	Indium tin oxide
LD-LSC:	Ligand driven light-induced spin-state change (LD-LISC)
LIESST:	Light-induced excited spin-state trapping
MEPE:	Metallosupramolecular coordination polyelectrolytes
MLCT:	Metal-to-ligand charge transfer
MPA:	Mercaptopropionic acid
PAH:	Poly (allylamine hydrochloride)
PDADMAC:	Poly (diallyl dimethyl ammonium chloride)
PEI:	Poly(ethyleneimine)
PNMVA:	Poly( <i>N</i> -methyl- <i>N</i> -vinylacetamide)
POM:	Polyoxometalate

PSS:	Poly (styrene sulfonate)
QCM:	Quartz crystal microbalance
SFM:	Scanning force microscope
SPR spectroscopy:	Surface plasmon resonance spectroscopy
TEMPOL:	2,2,6,6-Tetramethyl-4-piperidinol 1-oxide
TIRF:	Total internal reflection fluorescence
TIR:	Total internal reflection

## 14.5

### References

- 1 J.-M. LEHN *Supramolecular Chemistry – Concepts and Perspectives*, VCH Wiley, Weinheim (1995).
- 2 P. J. STANG, B. OLENYUK *Acc. Chem. Res.* **30** (1997) 502.
- 3 C. G. CLAESSENS, J. F. STODDART *J. Phys. Org. Chem.* **10** (1997) 254.
- 4 (a) G. M. WHITESIDES, E. E. SIMANEK, J. P. MATHIAS, C. T. SETO, D. N. CHIN, M. MAMMEN, D. M. GORDON, *Acc. Chem. Res.* **28** (1995) 37; (b) J. REBEK *Acc. Chem. Res.* **32** (1999) 278.
- 5 V. BALZANI, A. CREDI, F. M. RAYMO, J. F. STODDART *Angew. Chem. Int. Ed. Engl.* **39** (2000) 3349.
- 6 D. G. KURTH *Ann. N. Y. Acad. Sci.* **960** (2002) 29.
- 7 J. D. SWALEN, D. L. ALLARA, J. D. ANDRADE, E. A. CHANDROSS, S. GAROFF, J. ISRAELACHVILI, T. J. MCCARTHY, R. MURRAY, R. F. PEASE, J. F. RABOLT, K. J. WYNNE, H. YU *Langmuir* **3** (1987) 932.
- 8 G. DECHER, J. D. HONG, J. SCHMITT *Thin Solid Films* **210/211** (1992) 831.
- 9 G. DECHER, J. SCHMITT *Prog. Colloid Polym. Sci.* **89** (1992) 160.
- 10 J. SCHMITT, T. GRÜNEWALD, G. DECHER, P. S. PERSHAN, K. KJAER, M. LÖSCHE *Macromolecules* **26** (1993) 7058.
- 11 M. TARABIA, H. HONG, D. DAVIDOV, S. KIRSTEIN, R. STEITZ, R. NEUMANN, Y. AVNY *J. Appl. Phys.* **83** (1998) 725.
- 12 P. BERTRAND, A. JONAS, A. LASCHEWSKY, R. LEGRAS *Macromol. Rapid Commun.* **21** (2000) 319 and references therein.
- 13 W. STOCKTON, M. RUBNER *Macromolecules* **30** (1997) 2717.
- 14 M. ONDA, Y. LVOV, K. ARIGA, T. KUNITAKE *J. Ferment. Bioeng.* **82** (1996) 502.
- 15 P. STROEVE, V. VASQUEZ, M. A. N. COELHO, J. F. RABOLT, *Thin Solid Films* **284** (1996) 708.
- 16 L. KRAEMANN, B. TIEKE *Chem. Eng. Technol.* **23** (2000) 211.
- 17 R. STEITZ, V. LEINER, K. TAUER, V. KHRENOV, R. v. KLITZING *Appl. Phys. A*, in press.
- 18 R. ADVINCULA, E. AUST, W. MEYER, W. KNOLL *Langmuir* **12** (1996) 3536.
- 19 N. G. HOOGEVEEN, M. A. COHEN STUART, G. J. FLEER *Langmuir* **12** (1996) 3675.
- 20 F. CARUSO, E. RODDA, D. FURLONG, K. NIJKURA, Y. OKAHATA *Anal. Chem.* **69** (1997) 2043.
- 21 PLECH, T. SALDITT, C. MÜNSTER, J. PEISL *J. Colloid Interface Sci.* **74** (2000) 223.
- 22 Y. LVOV, G. DECHER, H. MÖHWALD *Langmuir* **9** (1993) 481.
- 23 R. A. MCALONEY, M. SINOYR, V. DUDNIK, M. C. GOH *Langmuir* **17** (2001) 6655.
- 24 R. J. HUNTER, *Foundations of Colloid Science*, Clarendon Press, Oxford 1997.
- 25 G. B. SUKHORUKOV, E. DONATH, H. LICHTENFELD, E. KNIPPEL, M. KNIPPEL, A. BUDE, H. MÖHWALD, *Colloids Surf. A* **137** (1998) 253.
- 26 F. CARUSO, E. DONATH, H. MÖHWALD *J. Phys. Chem. B* **102**, (1998) 2011.
- 27 F. CARUSO, H. LICHTENFELD, E. DONATH, H. MÖHWALD *Macromolecules* **32** (1999) 2317.
- 28 G. LADAM, P. SCHAAD, J. C. VOEGEL, P. SCHAAF, G. DECHER, F. CUISINIER *Langmuir* **16** (2000) 1249.
- 29 K. LOWACK, C. HELM *Macromolecules* **31** (1998) 823.
- 30 R. v. KLITZING, H. MÖHWALD *Langmuir* **11** (1995) 3554.

- 31 G. J. FLEER, M. A. COHEN STUART, J. M. H. M. SCHEUTJENS, T. COSGROVE, B. VINCENT, *Polyelectrolytes at Interfaces*, Chapman & Hall, London (1993).
- 32 H. DAUTZENBERG, E. GÖRNITZ, W. JAEGER *Macromol. Chem. Phys.* **199** (1998) 1561.
- 33 D. RUPPELT, J. KÖTZ, W. JAEGER, S. E. FRIBERG, R. A. MACKAY *Langmuir* **13** (1997) 3316.
- 34 R. STEITZ, W. JAEGER, R. V. KLITZING *Langmuir* **17** (2001) 4471.
- 35 D. YOO, S. S. SHIRATORI, M. F. RUBNER *Macromolecules* **31** (1998) 4309.
- 36 S. S. SHIRATORI, M. F. RUBNER *Macromolecules* **33** (2000) 4213.
- 37 S. Y. PARK, C. J. BARRETT, M. F. RUBNER, A. M. MAYES *Macromolecules* **34** (2001) 3384.
- 38 J. HODAK, R. ETCHENIQUE, E. J. CALVO, K. SINGHAL, P. N. BARTLETT *Langmuir* **13** (1997) 2708.
- 39 R. STEITZ, V. LEINER, R. SIEBRECHT, R. V. KLITZING *Colloid Surf. A* **163** (2000) 63.
- 40 J. RUTHS, F. ESSLER, G. DECHER, H. RIEGLER *Langmuir* **16** (2000) 8871.
- 41 M. LÖSCHE, J. SCHMITT, G. DECHER, W. G. BOUWMAN, K. KJAER *Macromolecules* **31** (1998) 8893.
- 42 S. DUBAS, J. SCHLENOFF *Macromolecules* **32** (1999) 8153.
- 43 R. V. KLITZING, V. LEINER, R. STEITZ, *ILL Millennium Symposium & European User Meeting, Proceedings* **73** (2001).
- 44 R. STEITZ, W. JAEGER, R. V. KLITZING *Langmuir* **17** (2001) 4471.
- 45 R. V. KLITZING, H. MÖHWALD *Macromolecules* **29** (1996) 6901.
- 46 D. KORNEEV, Y. LVOV, G. DECHER, J. SCHMITT, S. YARADAIKIN *Physica B* **213/214** (1995) 954.
- 47 G. DECHER, *Science* **277** (1997) 1232 and references therein.
- 48 J. SCHMITT, T. GRÜNEWALD, G. DECHER, P. S. PERSHAN, K. KJAER, M. LÖSCHE *Macromolecules* **26** (1993) 7058.
- 49 G. DECHER, M. ECKLE, J. SCHMITT, B. STRUTH *Curr. Opin. Colloid Interface Sci.* **3** (1998) 32.
- 50 Y. LVOV, F. ESSLER, G. DECHER *J. Phys. Chem.* **97** (1993) 13773.
- 51 S. W. KELLER, H.-N. KIM, T. E. MALLOUK *J. Am. Chem. Soc.* **116** (1994) 8817.
- 52 H. HONG, R. STEITZ, S. KIRSTEIN, D. DAVIDOV *Adv. Mater.* **10** (1998) 1104.
- 53 S. KIRSTEIN, H. HONG, R. STEITZ, D. DAVIDOV *Synth. Met.* **102** (1999) 1067.
- 54 J. B. SCHLENOFF, H. LY, M. LI *J. Am. Chem. Soc.* **120** (1998) 7626.
- 55 T. FARHAT, J. B. SCHLENOFF *Langmuir* **17** (2001) 1184.
- 56 R. V. KLITZING, R. SIEBRECHT, V. LEINER, R. STEITZ *ILL Highlight* **98** (1999) 38.
- 57 L. G. PARRAT *Phys. Rev.* **95** (1954) 359.
- 58 L. NÉVOT, P. CROCE *Rev. Phys. Appl.* **15** (1980) 761.
- 59 T. P. RUSSEL *Mater. Sci. Rep.* **5** (1990) 171.
- 60 H. KIESSIG, *Ann. Phys.* **10** (1931) 769.
- 61 T. FARHAT, G. YASSIN, S. T. DUBAS, J. B. SCHLENOFF *Langmuir* **15** (1999) 6621.
- 62 V. G. MUCHADO, P. N. W. BAXTER, J.-M. LEHN *J. Braz. Chem. Soc.* **12** (2001) 431.
- 63 S. R. BATTEN, R. ROBSON *Angew. Chem. Int. Ed. Engl.* **37** (1998) 1461.
- 64 (a) A. D. BURROWS, C. W. CHAN, M. M. CHOWDHRY, J. E. MCGRADY, D. M. P. MINOGOS *Chem. Soc. Rev.* **24** (1995) 329; (b) M. D. WARD, C. M. WHITE, F. BARIGELLETTI, N. ARMAROLI, G. CALOGERO, L. FLAMIGNI *Coord. Chem. Rev.* **171** (1998) 481; (c) D. G. KURTH, K. FROMM, J.-M. LEHN *Eur. J. Inorg. Chem.* **6** (2001) 1523.
- 65 B. J. HOLLIDAY, C. A. MIRKIN, *Angew. Chem. Int. Ed. Engl.* **40** (2001) 2022.
- 66 N. J. LONG, *Angew. Chem. Int. Ed. Engl.* **34** (1995) 21.
- 67 R. ZIESSEL, M. HISSLER, A. EL-GHAYOURY, A. HARRIMAN *Coord. Chem. Rev.* **178–180** (1998) 1251.
- 68 P. GÜTLICH, A. HAUSER, H. SPIERING *Angew. Chem. Int. Ed. Engl.* **33** (1994) 2024.
- 69 S. DECURTINS, P. GÜTLICH, C. P. KOHLER, H. SPIERING, A. HAUSER *Chem. Phys. Lett.* **105** (1984) 1.
- 70 S. DECURTINS, P. GÜTLICH, K. M. HASSELBACH, A. HAUSER, H. SPIERING *Inorg. Chem.* **24** (1985) 2174.
- 71 F. RENZ, H. OSIO, V. KSENOFONTOV, M. WALDECK, H. SPIERING, P. GÜTLICH, *Angew. Chem. Int. Ed. Engl.* **39** (2000) 3699.
- 72 Z. Z. GU, O. SATO, T. IYODA, K. HASHIMOTO, A. FUJISHIMA, *J. Phys. Chem.* **100** (1996) 18289.
- 73 O. SATO, A. IYOTA, A. FUJISHIMA, K. HASHIMOTO *Science* **272** (1996) 704.



- 74 A. S. ATTIA, O. S. JUNG, C. G. PIERPONT *Inorg. Chim. Acta.* **226** (1994) 91.
- 75 M.-L. BOILLLOT, C. ROUX, J.-P. AUDIERE, A. DAUSSE, J. ZAREMBOWITCH *Inorg. Chem.* **35** (1996) 3975.
- 76 (a) I. V. KOZHEVNIKOV, *Chem. Rev.* **98** (1998) 171; (b) N. MIZUNO, M. MISONO *Chem. Rev.* **98** (1998) 199.
- 77 (a) I. A. WEINSTOCK *Chem. Rev.* **98** (1998) 113; (b) M. SADAKANE, E. STECKHAN *Chem. Rev.* **98** (1998) 219.
- 78 T. YAMASE *Chem. Rev.* **98** (1998) 307.
- 79 J. T. RHULE, C. L. HILL, D. A. JUDD, R. F. SCHINAZI *Chem. Rev.* **98** (1998) 327.
- 80 D. E. KATSOUKIS *Chem. Rev.* **98** (1998) 359.
- 81 (a) M. T. POPE in *Mixed Valence Compounds*, ed. D. B. Brown, Reidel, Dordrecht, (1980) p. 365; (b) M. T. POPE *Prog. Inorg. Chem.* **39** (1991) 181
- 82 D. G. KURTH, D. VOLKMER in *Polyoxometalate Chemistry*, eds. M. T. POPE, A. MÜLLER, Kluwer, Dordrecht (2001) p. 301.
- 83 (a) A. MÜLLER, P. KÖGERLER, C. KUHLMANN *Chem. Commun.* **15** (1999) 1347; (b) A. MÜLLER, E. KRICKEMEYER, H. BÖGGE, M. SCHMIDTMANN, F. PETERS *Angew. Chem. Int. Ed. Engl.* **37** (1998) 3360.
- 84 See for example M. J. ZAWOROTKO, *Chem. Commun.* (2001) 1; R. ROBSON *J. Chem. Soc., Dalton Trans.* (2000) 3735.
- 85 N. W. ALCOCK, P. R. BARKER, J. M. HAIDER, M. J. HANNON, C. L. PAINTING, Z. PIKRAMENOU, E. A. PLUMMER, K. RISSANEN, P. SAARENKETO *J. Chem. Soc., Dalton Trans.* (2000) 1447.
- 86 (a) J. P. GABRIEL, P. DAVIDSON *Adv. Mater.* **12** (2000) 9; (b) A. S. SONIN, *Colloid J.* **60** (1998) 129; (c) P. DAVIDSON, P. BATAIL, J. C. P. GABRIEL, J. LIVAGE, C. SANCHEZ, C. BOURGAUX *Prog. Polym. Sci.* **22** (1997) 913.
- 87 V. BALZANI, F. SCANDOLA, *Supramolecular Photochemistry*, Ellis Horwood, West Sussex, (1991).
- 88 R. KNAPP, A. SCHOTT, M. REHAHN *Macromolecules* **29** (1996) 479.
- 89 M. SCHÜTTE, D. G. KURTH, M. R. LINFORD, H. CÖLFEN, H. MÖHWALD *Angew. Chem. Int. Ed. Engl.* **37** (1998) 2891.
- 90 D. G. KURTH, M. SCHÜTTE *Macromol. Symp.* **164** (2001) 167.
- 91 Y. LVOV, K. ARIGA, M. ONDA, I. ICHINOSE, T. KUNITAKE *Colloid Surf. A.* **146**, (1999) 337.
- 92 D. G. KURTH *Langmuir* **14** (1998) 6987.
- 93 H. WANG, C. K. MANN, J. T. VICKERS *Appl. Spectrosc.* **49**, 127 (1995).
- 94 D. G. KURTH, R. E. OSTERHOUT, *Langmuir* **15** (1999) 4842.
- 95 H. MOTSCHMANN, M. STAMM, C. TOPRAKCIOGLU *Macromolecules* **24** (1991) 3681.
- 96 D. H. WILKINS, G. F. SMITH *Anal. Chim. Acta* **9** (1953) 338.
- 97 D. G. KURTH, M. SCHÜTTE, J. WEN, *Colloid Surf. A* **198–200** (2002) 633.
- 98 (a) J. M. RAO, M. C. HUGHES, D. J. MACCERO *Inorg. Chim. Acta* **16** (1976) 231; (b) M. MASKUS, H. D. ABRUNA *Langmuir* **12** (1996) 4455.
- 99 (a) J. P. COLLINS, P. LAINE, J.-P. LAUNAY, J.-P. SAUVAGE, A. SOUR, *Chem. Commun.* (1993) 434; (b) E. C. CONSTABLE, A. M. W. C. THOMPSON, *J. Chem. Soc. Dalton Trans.* (1995) 1615.
- 100 R. W. MURRAY, in *Electroanalytical Chemistry*, ed. A. J. Bard, Marcel Dekker, New York, (1984) vol. 13, p. 191.
- 101 D. G. KURTH, F. CARUSO, C. SCHÜLER *Chem. Commun.* (1999) 1579.
- 102 F. CARUSO, E. DONATH, H. MÖHWALD *J. Phys. Chem. B* **102** (1998) 2011.
- 103 (a) F. CARUSO, H. LICHTENFELD, E. DONATH, H. MÖHWALD *Macromolecules*, **32** (1999) 2317; (b) G. B. SUKHORUKOV, E. DONATH, H. LICHTENFELD, E. KNIPPEL, M. KNIPPEL, H. MÖHWALD *Colloids Surf. A* **137** (1998) 253.
- 104 F. CARUSO, C. SCHÜLER, D. G. KURTH *Chem. Mater.* **11** (1999) 3394.
- 105 H. KRASS, E. A. PLUMMER, J. M. HAIDER, P. R. BARKER, N. W. ALCOCK, Z. PIKRAMENOU, M. J. HANNON, D. G. KURTH *Angew. Chem. Int. Ed. Engl.* **40** (2001) 3862
- 106 F. M. WINNIK *Chem. Rev.* **93** (1993) 587.
- 107 D. G. KURTH, D. VOLKMER, M. RUTTORE, B. RICHTER, A. MÜLLER *Chem. Mater.* **12** (2000) 2829.
- 108 F. CARUSO, D. G. KURTH, D. VOLKMER, M. J. KOOP, A. MÜLLER *Langmuir* **14** (1998) 3462.
- 109 S. LIU, D. G. KURTH, D. VOLKMER *Chem. Commun.*, (2002).

- 110 (a) K. B. OLDHAM *J. Electroanal. Chem.* **121** (1981) 341; (b) P. DAUM, J. R. LENDHARD, D. ROLISAN, R. W. MURRAY *J. Am. Chem. Soc.* **102** (1980) 4649.
- 111 A. MAHMOUD, B. KEITA, L. NADJO, O. OUNG, R. CONTANT, S. BROWN, Y. DE KOUCHKOVSKY *J. Electroanal. Chem.* **463** (1999) 129.
- 112 J. LIN, *Trends Anal. Chem.* **19** (2000) 541.
- 113 (a) C. PREYSSLER *C. Bull. Soc. Chim. Fr.* **1970**, 30; (b) M. H. ALIZADEH, S. P. HARMALKER, Y. JEANNIN, J. MARTIN-FRÈRE, M. T. POPE, *J. Am. Chem. Soc.* **107** (1985) 2662.
- 114 (a) S. LIU, D. G. KURTH, H. MÖHWALD, D. VOLKMER *Adv. Mater.* **14** (2002) 225; (b) L. XU, E. WANG, H. ZHANG, D. G. KURTH, Z. LI *J. Mater. Chem.* **12** (2002) 654.
- 115 M. R. ANTONIO, L. SODERHOLM *J. Alloys Compd.* **250** (1997) 541.
- 116 M. Y. GAO, B. RICHTER, S. KIRSTEIN *Adv. Mater.* **9** (1997) 802.
- 117 O. ONITSUKA, A. C. FOU, M. FERREIRA, B. R. HSIEH, M. F. RUBNER *J. Appl. Phys.* **80** (1996) 4067.
- 118 N. ANICET, C. BOURDILLON, J. MOIROUX, J. M. SAVENANT *J. Phys. Chem. B* **102** (1998) 9844.
- 119 L. KRASEMAN, B. TIEKE *Langmuir* **16** (2000) 287.
- 120 (a) E. BREUNING, M. RUBEN, J.-M. LEHN, F. RENZ, Y. GARCIA, V. KSENOVONTOF, P. GÜTLICH, E. WEGELIUS, K. RISSANEN *Angew. Chem. Int. Ed. Engl.* **39** (2000) 2504; (b) O. WALDMANN, J. HASSMANN, P. MÜLLER, G. S. HANAN, D. VOLKMER, U. S. SCHUBERT, J.-M. LEHN *Phys. Rev. Lett.* **78** (1997) 3390.
- 121 R. SESSOLI, D. GATTESCHI, A. CANESCHI, M. A. NOVAK *Nature (London)* **365** (1993) 141.
- 122 M. C. JIMÉNEZ, C. DIETRICH-BUCHECKER, J.-P. SAUVAGE, A. DE CIAN *Angew. Chem. Int. Ed. Engl.* **39** (2000) 1295.

15

## **Functional Layer-by-layer Assemblies with Photo- and Electrochemical Response and Selective Transport of Small Molecules and Ions**

B. TIEKE, M. PYRASCH, and A. TOUTIANOUSH

### **Abstract**

Our recent research activities in the field of functional ultrathin films prepared by alternating electrostatic adsorption of polycationic and polyanionic compounds on solid supports are reviewed. Films of polyelectrolytes, bolaamphiphiles, organic–inorganic hybrid polymers, inorganic mixed valence complex salts, and latex particles are described. Functional properties such as photo- and electroactive behaviour, intense absorption in the visible and near-infrared, selective permeation of small molecules and ions are reported.

### **15.1**

#### **Introduction**

The purpose of this contribution is to review recent activities of our research group in the field of functional ultrathin films prepared by layer-by-layer (LBL) assembly on solid supports. For several years ultrathin organised films have been receiving much attention for both fundamental scientific and practical reasons. Scientific interest is based on the possibility of designing and manipulating molecular architectures and studying physical phenomena on a molecular level, while practical interest arises from the possible application in microelectronics, photonics, materials separation and sensing. Ultrathin films of controlled thickness and molecular arrangement can either be prepared by the Langmuir–Blodgett (LB) deposition method, or by self-assembly techniques [1–4]. While functional LB-films were subject to intense research in the 1980s, self-assembled films became more and more popular in the 1990s and now dominate over LB-films, mainly because of their easier preparation and higher stability. Among the self-assembly techniques, physisorption methods based on electrostatic interaction have been proven to be a very powerful tool for regular growth of ultrathin films. Electrostatic layer-by-layer deposition of organic polyions was first investigated by Decher and co-workers [5–9]. The method is based on the dipping of a charged substrate into a solution of an oppositely charged polyionic compound so that the compound is adsorbed and the surface charge is reversed. After careful washing, the substrate

is again dipped into a solution of an oppositely charged compound so that it is adsorbed and the surface charge is reversed again. Multiple repetition of the adsorption steps leads to multilayer films in a simple, yet elegant manner. Various compounds such as organic di- or polyions, polyelectrolytes, charged particles, inorganic complex ions etc. are suitable for adsorption and by a careful choice of the compounds to be adsorbed a variety of films with interesting functional properties become accessible. The progress in the field has recently been reviewed [10–15].

Having studied functional LB-films for several years [16, 17], our research group became interested in self-assembled films as soon as the first reports on functional LBL assemblies appeared [18–21]. Since 1994, we have studied a number of assemblies with

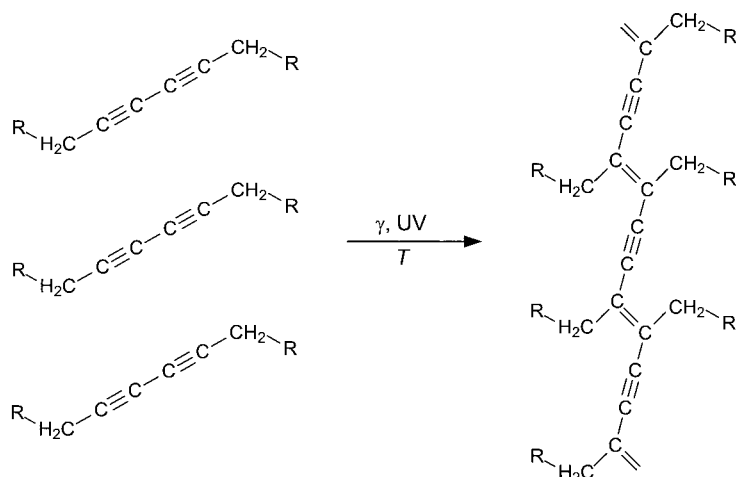
- photochemical reactivity,
- intense coloration,
- electroactive properties,
- selective transport of small molecules under pervaporation conditions,
- selective transport of ions,
- and selective uptake of ions.

Moreover, the electrostatic self-assembly of charged latex particles at oppositely charged interfaces has been investigated [22, 23]. The studies on the latex particles have recently been reviewed [24] and will not be treated further here. The purpose of this article is to review our recent research activities in the field of self-assembled functional multilayer films obtained by alternate adsorption of charged organic and/or inorganic molecular compounds.

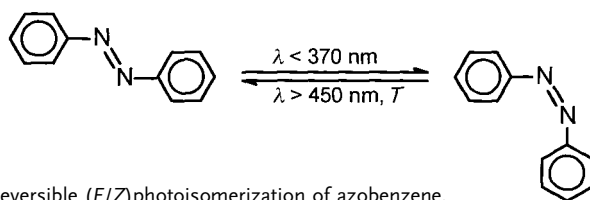
## 15.2

### Photoreactive Assemblies

Photochemical processes in the solid state are quite often restricted to a specific state of order of the system. A typical example is the diacetylene derivatives, which undergo a radiation induced 1,4-addition polymerization of the unsaturated units only, if the molecules attain a dense packing and a distinct mutual orientation (Scheme 1) [25–27]. Another example is the azobenzene derivatives, which undergo *E/Z*-photoisomerization, if irradiated with UV light (Scheme 2) [28]. The reaction only takes place in a partially disordered environment providing a certain free volume, because the cross-sectional area of the *Z* isomer is much larger than that of the *E* isomer. Thus a study of these photoreactions in LBL assemblies is of interest because the reactions can be used to probe the structure of the films. Moreover, if the reaction takes place, the films might be applicable in photopatterning and optical data storage, for example. In the following, our recent studies on the photoreactivity of diacetylene and azobenzene derivatives in LBL assemblies are described.



Scheme 15.1 Topochemical polymerization of diacetylene derivatives.



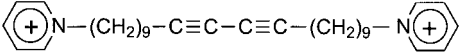
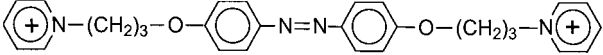
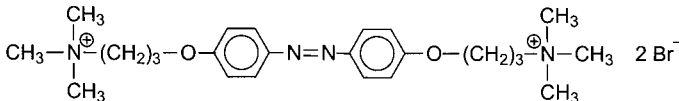
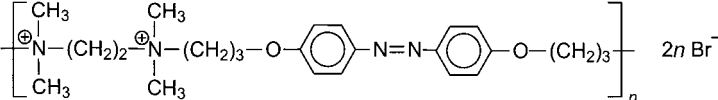
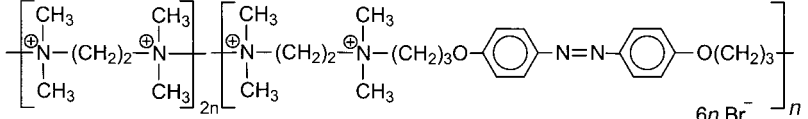
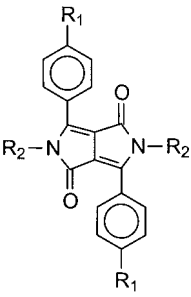
Scheme 15.2 Reversible (*E/Z*) photoisomerization of azobenzene.

### 15.2.1

#### Diacetylene Derivatives

In order to study the photopolymerization of diacetylenes in LBL assemblies, a variety of bolaamphiphiles 1–5 carrying the diacetylene unit in the mid position of the alkyl chain were synthesized (Tab. 15.1). A first study of the photoreaction was carried out on LBL assemblies containing the disodium 10,12-docosadiyne-1,22-disulfate **1** (Tab. 15.1), a dianionic bolaamphiphile, and polyallylamine hydrochloride (PAH) as a cationic polyelectrolyte [29]. Upon UV-irradiation, compound **1** was highly photoreactive. Already after short irradiation times, the PAH/**1**-film turned red and an intense absorption band with a maximum at about 536 nm occurred indicating the formation of the fully conjugated polydiacetylene backbone (Fig. 15.1). However, the increase in the absorbance was not perfectly linear with respect to the number of deposited layers (see the inset of Fig. 15.1). The low absorption of the first four layers was ascribed to some disorder in the packing of the bolaamphiphiles partially preventing the topochemical polymerization. The strong absorbance in the subsequent layers was either ascribed to improved ordering of the bolaamphiphiles, or to the adsorption of a larger number of molecules of **1** per dipping process, perhaps due to occasional adsorption of bi- or trilayers

Tab. 15.1 List of compounds used for preparation of functional LBL assemblies

Compound	No.						
${}^{-}\text{O}_3\text{SO}-(\text{CH}_2)_n-\text{C}\equiv\text{C}-\text{C}\equiv\text{C}-(\text{CH}_2)_n-\text{OSO}_3^{-}$ $2 \text{ Na}^+$	$n=9$ 1 $n=4$ 2 $n=1$ 3						
${}^{2-}\text{O}_3\text{PO}-(\text{CH}_2)_9-\text{C}\equiv\text{C}-\text{C}\equiv\text{C}-(\text{CH}_2)_9-\text{OPO}_3^{2-}$ $4 \text{ Na}^+$	4						
 $2 \text{ Br}^{-}$	5						
${}^{-}\text{O}_3\text{SO}-(\text{CH}_2)_6-\text{O}-\text{C}_6\text{H}_4-\text{N}=\text{N}-\text{C}_6\text{H}_4-\text{O}-(\text{CH}_2)_6-\text{OSO}_3^{-}$ $2 \text{ Na}^+$	6						
 $2 \text{ Br}^{-}$	7						
 $2 \text{ Br}^{-}$	8						
 $2n \text{ Br}^{-}$	9						
 $6n \text{ Br}^{-}$	10						
	<table border="1" data-bbox="645 1011 954 1148"> <thead> <tr> <th>R<sub>1</sub></th> <th>R<sub>2</sub></th> </tr> </thead> <tbody> <tr> <td><math>-\text{SO}_3\text{H}</math></td> <td><math>-\text{H}</math></td> </tr> <tr> <td><math>-\text{H}</math></td> <td><math>-(\text{CH}_2)_6-\text{OSO}_3^{-} \text{ Na}^+</math></td> </tr> </tbody> </table>	R <sub>1</sub>	R <sub>2</sub>	$-\text{SO}_3\text{H}$	$-\text{H}$	$-\text{H}$	$-(\text{CH}_2)_6-\text{OSO}_3^{-} \text{ Na}^+$
R <sub>1</sub>	R <sub>2</sub>						
$-\text{SO}_3\text{H}$	$-\text{H}$						
$-\text{H}$	$-(\text{CH}_2)_6-\text{OSO}_3^{-} \text{ Na}^+$						
	11 12						

instead of monolayers. A model illustrating the polymerization process within the LBL assembly is shown in Scheme 3. In a more comprehensive study [30], the PAH/1 system was investigated with respect to its structure and morphology using X-ray diffraction and scanning force microscopy (SFM). X-ray diagrams showed Bragg (00l)-reflections from which a layer spacing of 2.7 nm could be determined. This allowed us to develop a model structure, in which the bolaamphi-

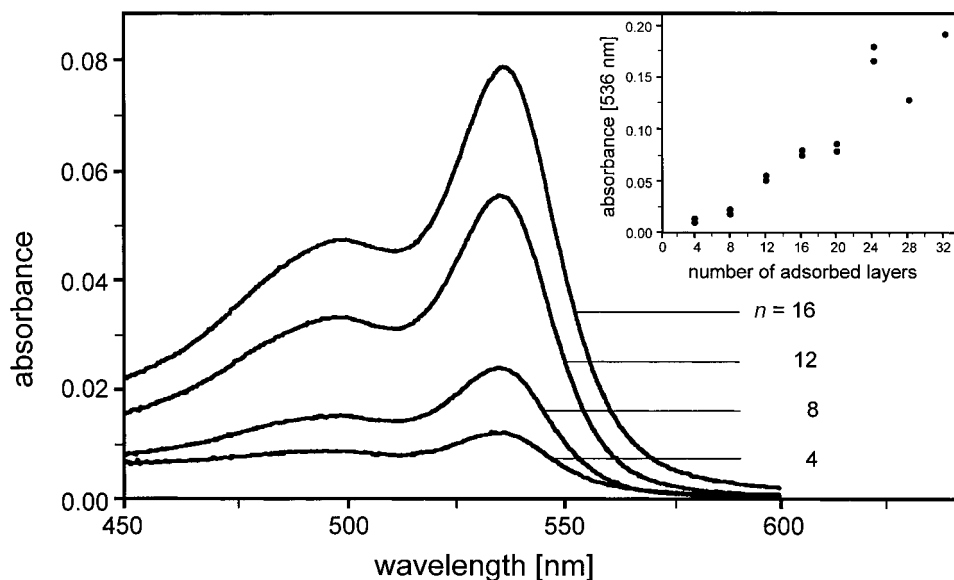
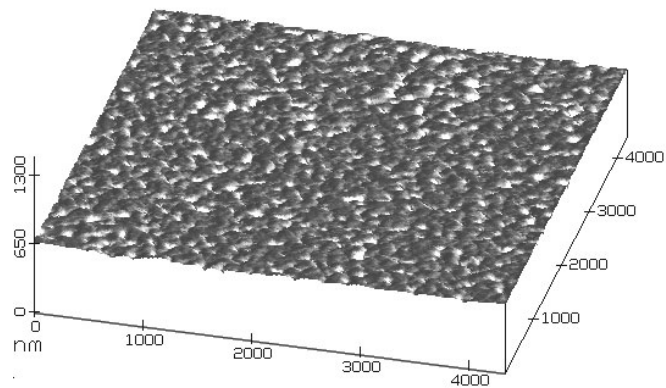


Fig. 15.1 Optical absorption spectra of LBL assemblies of PAH/1 measured after 8 min UV irradiation. Samples differ in the number  $n$  of dipping cycles applied. The inset shows a plot of the polymer absorbance at 536 nm versus  $n$ .

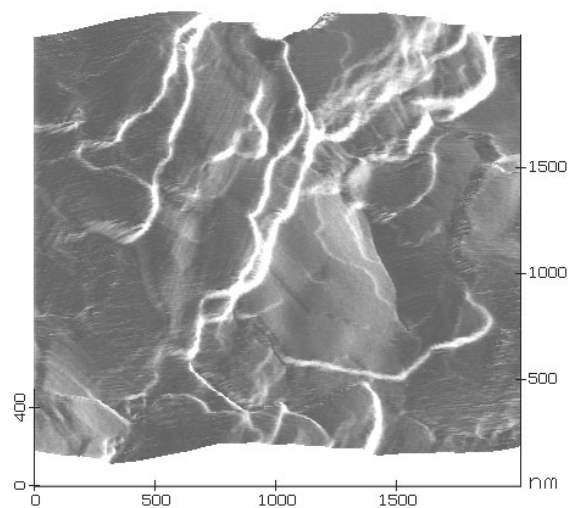
phile monolayers are sandwiched between the polyelectrolyte layers, the individual amphiphiles attaining a crystal-like arrangement with their longest molecular axis being tilted with regard to the layer plane by an angle of about  $38^\circ$  [30]. Due to the tilting, the mutual arrangement of the monomers was favourable for the topochemical reaction. The surface topology of the polymerised samples was studied using SFM [30]. As shown in Fig. 15.2(a), an assembly of 12 layer pairs of PAH/1 consists of a multitude of small, isolated domains of a few hundred nanometers in diameter. Individual domains are between 100 and 200 nm apart from each other. The height of the domains was slightly different, which can be ascribed to the occasional adsorption of bi- or trilayers of the bolaamphiphiles, as mentioned above.

Compounds 2 and 3 (Tab. 15.1) with shorter alkylene spacers between the diacetylene unit and the polar head groups were photoinactive in the solid state and in multilayer assemblies and thus were not investigated further [30]. Alternating multilayers of the diphosphate 4 and PAH were only slightly photoreactive [31]. This could be derived from the low polymer absorbance per layer reached after prolonged irradiation time. The reason is most likely that the mutual arrangement of the monomer molecules 4 is unfavourable for the photoreaction to take place, a phenomenon that quite often limits the conversion of a lattice-controlled reaction [32]. Probably for the same reason, the multilayer assemblies of the cationic bolaamphiphile 5 and poly(2-acrylamido-2-methyl-1-propanesulfonic acid) (PAMPS) were completely photoinactive [31]. Besides the polyelectrolyte/bolaam-

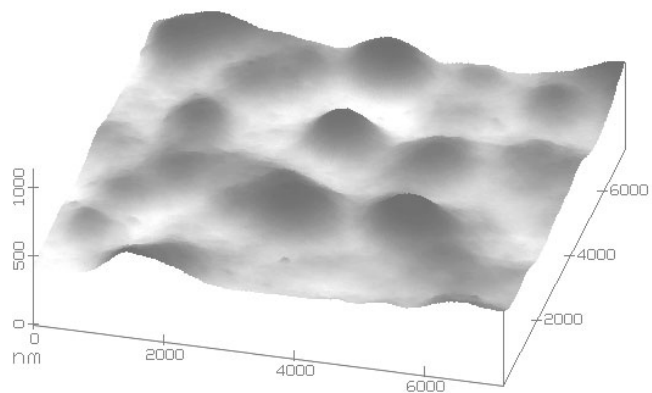
(a)



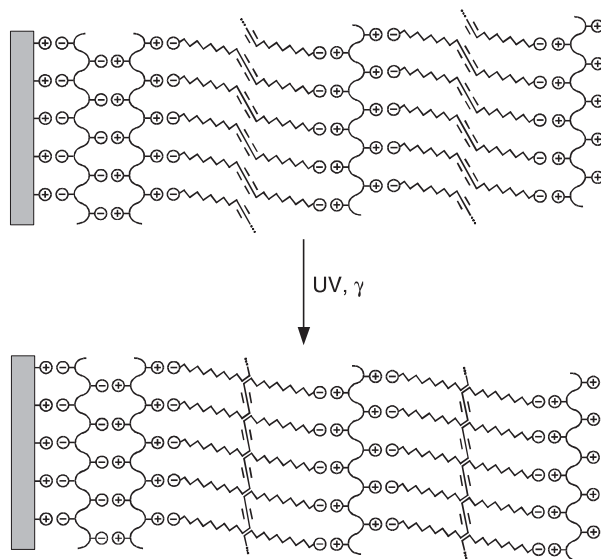
(b)



(c)







**Scheme 15.3** Diacetylene UV polymerization in the self-assembled multilayer (adapted from [29, 30]).

phiphile systems, systems composed exclusively of oppositely charged bolaamphiphiles were also investigated [31]. A system composed of the compounds **1** and **5** in alternating sequence was highly photoreactive, as indicated by the deep red coloration of the polydiacetylene backbone already appearing after very short UV irradiation times. However, a view of the polymerised samples in a microscope indicated a very inhomogeneous coloration. Some deeply colored islands were distributed over large areas of less intense color. A closer inspection by SFM showed a very inhomogeneous surface structure with phase boundaries and edges of crystallites (Fig. 15.2 (b)). It was concluded that parts of the monomeric sample crystallized and formed perfectly ordered microcrystals with strongly enhanced photoreactivity, while the non-rearranged parts were less photoreactive and thus less intensely coloured.

In the same publication [31], the preparation of LBL assemblies upon alternate adsorption of PAH and the water-soluble, anionic polymer of **1** (poly-**1**) was reported. Poly-**1** had previously been prepared by  $\gamma$ -irradiation of crystals of **1**. While

**Fig. 15.2** SFM surface views of LBL assemblies of PAH/**1** (12 dipping cycles), scan area  $4 \times 4 \mu\text{m}^2$  (a); **5**/**1** (6 dipping cycles), scan area  $2 \times 2 \mu\text{m}^2$  (b); and PAH/poly-**1** (42 dipping cycles), scan area  $7 \times 7 \mu\text{m}^2$  (c). Substrates: Pretreated quartz plates. Samples (a) and (b) contained diacetylene derivatives,

which were polymerised on the substrate subsequent to adsorption of the monomer, while sample (c) contained the polymer of **1**, which was directly adsorbed from aqueous solution (a) reproduced with permission from American Chemical Society; (b),(c) reproduced with permission from Elsevier, Amsterdam).

the solid polymer was red, the aqueous solution as well as the multilayer samples were orange with an absorption maximum at 460 nm. Different colours of  $\pi$ -conjugated polymer chains are known to originate from different conformations of the backbone [33–35]. Yellow and orange colors of polydiacetylenes are usually ascribed to a coil conformation with short conjugation length occurring in solution, while the red colour indicates extended chains with large conjugation length, as formed by UV irradiation in the crystalline state. Thus the orange color of the adsorbed polymer was taken as an indication that the polymer chains were adsorbed as coils and did not change their conformation on the substrate subsequently. SFM-pictures indicated that the direct adsorption of the polymer led to a smooth surface structure, much smoother than the adsorption of monomeric bolaamphiphiles followed by polymerization on the substrate (Fig. 15.2(c)). The reason is that the polymer chains cover a larger substrate surface than the bolaamphiphiles. Consequently, substrate areas of only low charge concentration are more easily covered and charge defects in the surface structure are more easily healed, if polyelectrolytes instead of the much smaller bolaamphiphiles are adsorbed.

### 15.2.2

#### Azobenzene Derivatives

Azobenzene and its derivatives are known to undergo a transition from the thermodynamically more stable *trans* (*E*) to the *cis* (*Z*) configuration upon irradiation with UV light ( $\lambda_1 < 370$  nm) [28] (Scheme 2). The reaction can be reversed upon heating or irradiation with visible light ( $\lambda_2 > 450$  nm). However, the isomerisation only occurs in systems providing the necessary free volume. In order to study the photoisomerisation in LBL assemblies, the dipolar amphiphiles **6–8** (Tab. 15.1), carrying the azobenzene unit in the mid position of the molecule, and the ionenes **9** and **10** (Tab. 15.1), with the reactive unit in the main chain, were prepared. In a first study [36], alternating multilayers of bolaamphiphile **6** and the cationic polyelectrolytes PAH, polyethyleneimine (PEI), polydiallyldimethylammonium chloride (PDADMAC) and chitosan (CHI) were investigated. The samples showed characteristic differences in their absorption spectra (Fig. 15.3(a) and (b)). Samples of PAH/**6** and PEI/**6** had a strong and narrow absorption band with a maximum at 314 nm, which could be ascribed to densely packed, H-aggregated chromophores in parallel alignment, in agreement with previous studies on the aggregation behaviour of azobenzene-containing amphiphiles [37, 38]. The other samples showed a broad absorption with a maximum at 340 nm, indicating less ordered dimeric chromophores in smectic layers above the phase transition temperature. The H-aggregated chromophores were photoinactive, while the less ordered chromophores could be readily switched between the *E*- and *Z*-rich photostationary state (Fig. 15.4(a) and (b)). Quite obviously the molecular structure of the polyelectrolytes is important for the arrangement of the bolaamphiphiles in the adjacent layers. As known from polyelectrolyte-surfactant complexes [39, 40], the highly charged polyelectrolytes induce a tightly packed structure, while the less charged polyions force the bolaamphiphiles into a smectic arrangement leaving enough free volume for the photoreaction to take

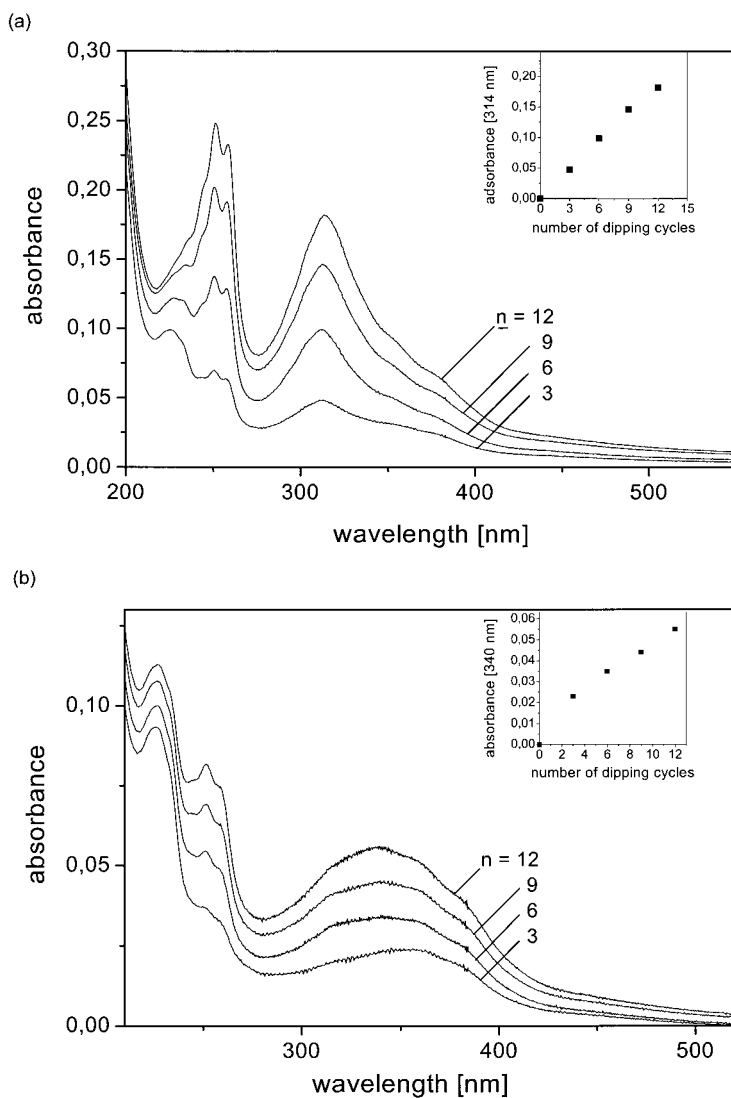


**Fig. 15.3** Optical absorption spectra of LBL assemblies of PAH/**6** (a) and PDADMAC/**6** (b). Samples differ in the number  $n$  of dipping cycles applied. In the insets, the maxi-

um absorbance of **6** in the respective assembly is plotted versus  $n$  (adapted from [36]).

place (see also the structure models in Fig. 15.5). In a subsequent study [41], LBL assemblies of the ionenes **9** and **10** and PSS or PAMPS as polymeric counterions were investigated. Two types of films were prepared by adsorbing the ionenes either as *Z*- or *E*-isomers. In both cases, a reversible photoisomerisation was found. The films only differed in the optical density, which was three times higher for the sam-

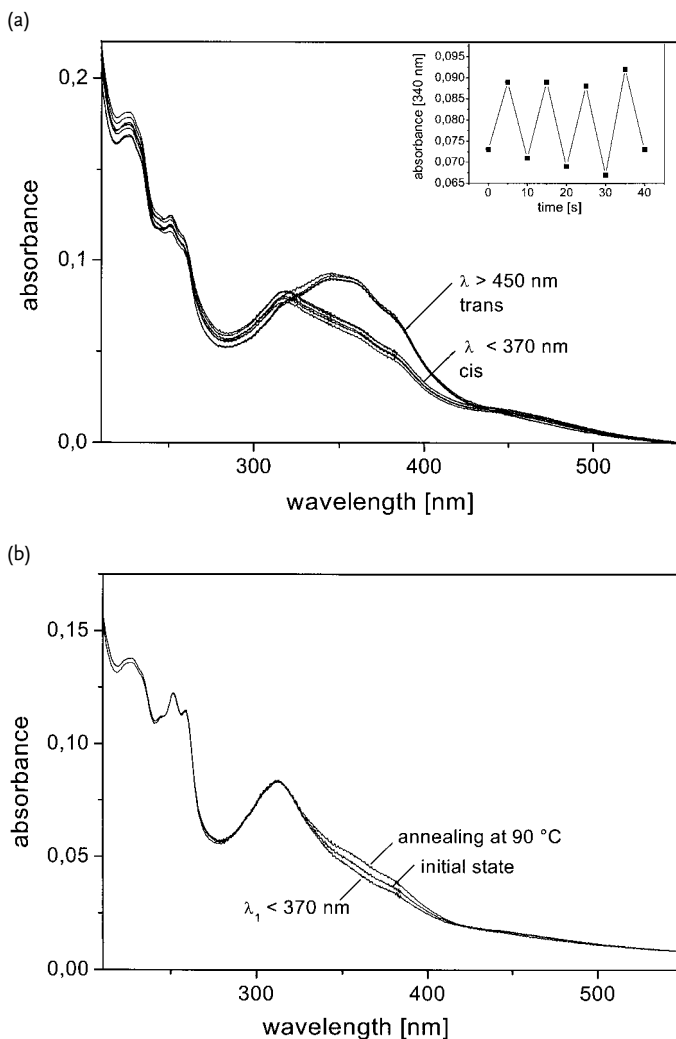


**Fig. 15.4** Photoinduced switching between the *trans* isomer and the *cis*-rich photostationary state in the self-assembled multilayer of PDADMAC/**6** (36 bilayers) (a). The inset shows the change of the maximum absor-

bance at 340 nm upon alternate irradiation at  $\lambda_1 < 370$  nm and  $\lambda_2 > 450$  nm. Sample (b) consisting of PEI/**6** is nearly photoinactive due to the formation of H-aggregates of **6** (adapted from [36]).

ple adsorbed as the *Z*-isomer. The difference was explained by orientational effects of the chromophores. The photoisomerisation of the cationic bolaamphiphiles **7** and **8** was studied in LBL assemblies with PSS as counterion [42]. Both compounds were photoreactive, no matter whether they were adsorbed as *Z*- or *E*-isomers. Again, the optical absorption of the *E*- and *Z*-rich state was significantly higher, when the samples were prepared by direct adsorption of the *Z*-isomer.

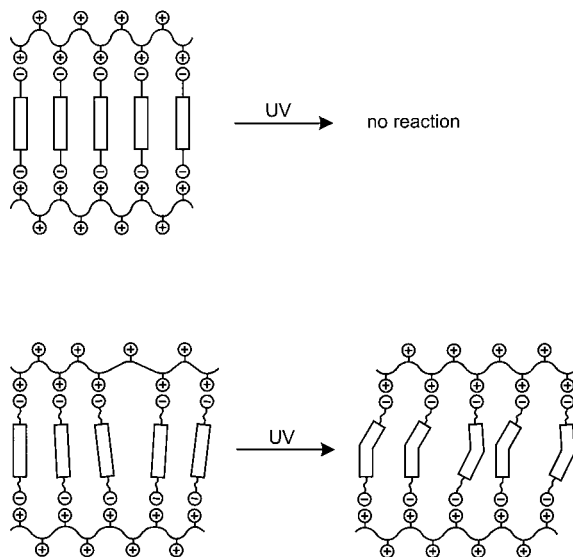


**Fig. 15.5** Proposed orientation of dianions of **6** in non-photoreactive, H-aggregated assemblies with PAH or PEI as counterion (upper part), and in photoreactive, smectic-like assemblies with PDADMAC or chitosan as counterion (lower part).

The interaction of linearly polarized light with azobenzene moieties offers the opportunity to orient these groups in thin films and thereby to generate an optical anisotropy [43–45]. The photoorientation is based on the fact that only those molecules undergo a *Z/E* isomerisation in polarized light, whose chromophore axis is parallel to the electric field vector, and that the subsequent reverse photoreaction leads to any possible molecular orientation of the *E*-isomer (provided that the molecules are not forced into their original position by steric restrictions). Hence a repeated photocycling in polarized light at a wavelength of about 457 nm, where the *Z*-rich photostationary state and the *E*-state are almost equally likely, induces a preferential orientation of the chromophoric units with the molecular axes being oriented perpendicular to the incident light vector. The photoorientation of compounds **6** to **10** in LBL assemblies has recently been studied [46]. Except for the H-aggregated systems of PEI/**6** and PAH/**6**, a significant azimuthal dichroism could be induced in all cases. The dichroism induced in the originally isotropic samples of PDADMAC/**6** or PAH/**9** was 0.34 and 0.17, respectively (Fig. 15.6). These values were lower than for LB films of photochromic side chain polymers and spin coated films of the same type of polymers [45, 47, 48]. This originates from a restricted mobility of the azobenzene moieties in the LBL assemblies caused by the strong electrostatic interactions of the cationic groups with the oppositely charged polyelectrolyte matrix. The reduced mobility was especially pronounced for the ionenes **9** and **10** and the bolaamphiphiles **7** and **8** with short spacer units of only three  $\text{CH}_2$  groups.

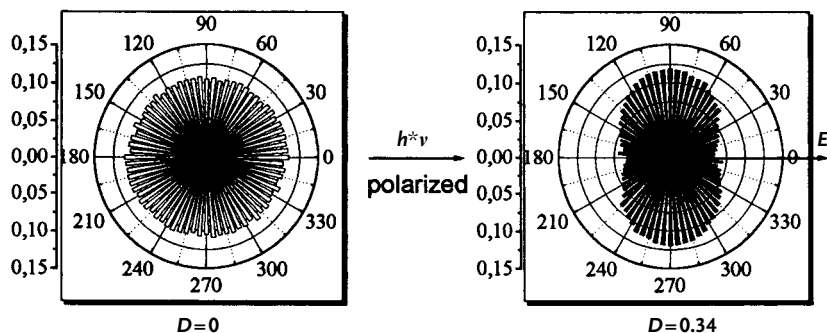


Fig. 15.6 Polar plots of angular-dependent absorbance at 367 nm prior and subsequent to irradiation with linearly polarized light (wavelength: 460 nm, power:  $100 \text{ mW cm}^{-2}$ ).

Sample: Self-assembled multilayer (12 layer pairs) of PDADMAC/6 on pretreated quartz (adapted from [46]).

### 15.3

#### Diphenyldiketopyrrolopyrrole Derivatives

Besides the diacetylene and azobenzene systems discussed above, other chromophoric units also display interesting absorption behaviour and are suitable for probing the molecular organisation in LBL-assemblies. A relevant example is the diphenyldiketopyrrolopyrrole (DPP) chromophore, which is known as a bright red pigment [49–51] showing interesting color effects [52]. For the preparation of LBL assemblies, the water-soluble DPP derivatives **11** and **12** (Tab. 15.1) were used [53, 54]. Multilayers consisting of dye **11** [53] with the sulfonic acid units attached to the phenyl rings and PAH or poly-L-lysine as counter-polyions were deep red in color, while the corresponding multilayers containing **12** were orange. Gelatine was also suitable as a cationic counterpart, but the resulting films were only weakly colored because of the low charge concentration along the polymer backbone allowing poor dye adsorption in the next layer. **11** mainly differs from the *N*-substituted derivative **12** in the ability to form aggregates via hydrogen bonding of the lactam units (Scheme 4). As a consequence, the maximum absorption of **12** in LBL assemblies is hypsochromically shifted by about 50 nm compared to **11** (Fig. 15.7(a) and (b)). From the optical spectra it is also evident that the absorbance of multilayer films containing **12** is much higher than for those containing **11**, although the extinction coefficient of **11** in solution is much higher than that of **12**. This can be ascribed to different chromophore orientations in the films as illustrated in Fig. 15.7(a) and (b). If the longest chromophore axis of **11** is more or less oriented parallel to the incident light vector, the absorption must be low, while a preferentially perpendicular alignment of the molecular axis of **12** will favor a strong absorption. LBL assemblies of PAH/**11** showed absorption bands at 534, 488 and 466 nm. The two bands at the shorter wavelengths also appear in the solution spectra, but the band at 534 nm originates from intense  $\pi$ - $\pi$ -interactions in the stack direction perpendicular to the  $\pi$ -planes of the chromophoric

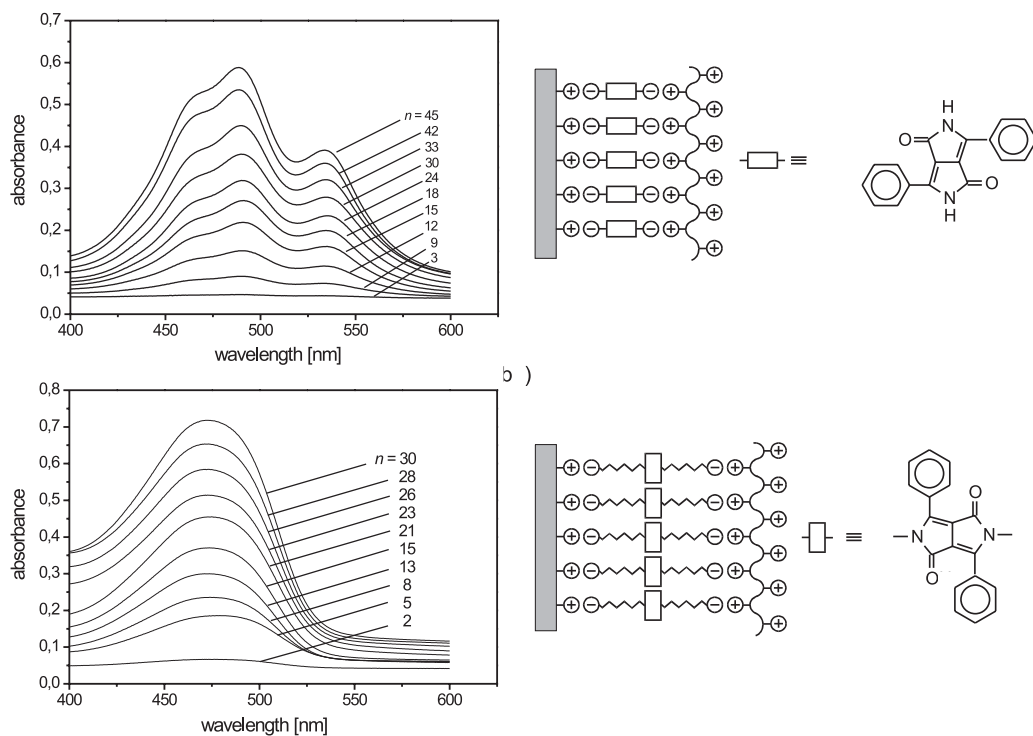
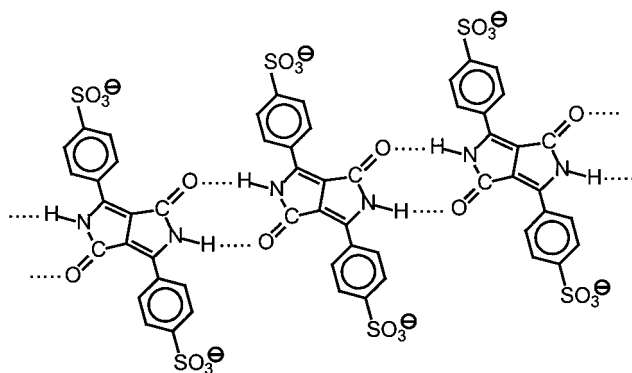


**Fig. 15.7** Optical absorption spectra of LBL assemblies of PAH/11 (a) and PAH/12

(b) (left), and proposed orientation of the chromophores (right) (adapted from [54]).



**Scheme 15.4** Hydrogen bonding of lactam units in diphenyldiketopyrrolopyrrole (from [54]).

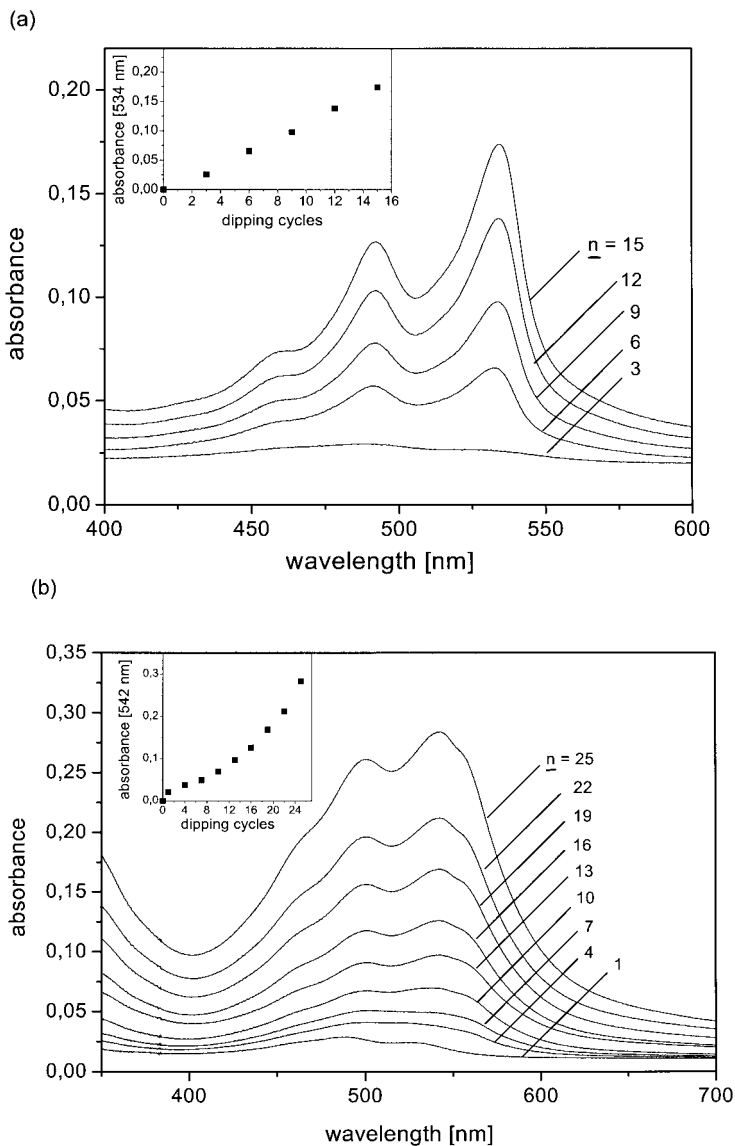


**Fig. 15.8** Optical absorption spectra of LBL assemblies of 5/11 (a), and  $\text{Ba}^{2+}/11$  (b). Differences in the spectra are due to different  $\pi$ - $\pi$ -interactions of the chromophores (adapted from [56]).

units and is only found in crystalline DPP [55]. The occurrence of this band in LBL assemblies is therefore a clear indication for a crystal-like arrangement of the chromophoric units within the layer planes. If the counterions in the LBL assemblies are varied, the position of the long wavelength absorption band is also



changed. This is shown in the absorption spectra of the multilayer samples of 5/11 and Ba<sup>2+</sup>/11 in Fig. 15.8 (a) and (b), which are significantly different from each other and from PAH/11 [56]. The reason is that the counterion variation changes the distance between the chromophores so that the  $\pi$ - $\pi$ -interactions responsible for the long wavelength absorption band are also changed.

## 15.4

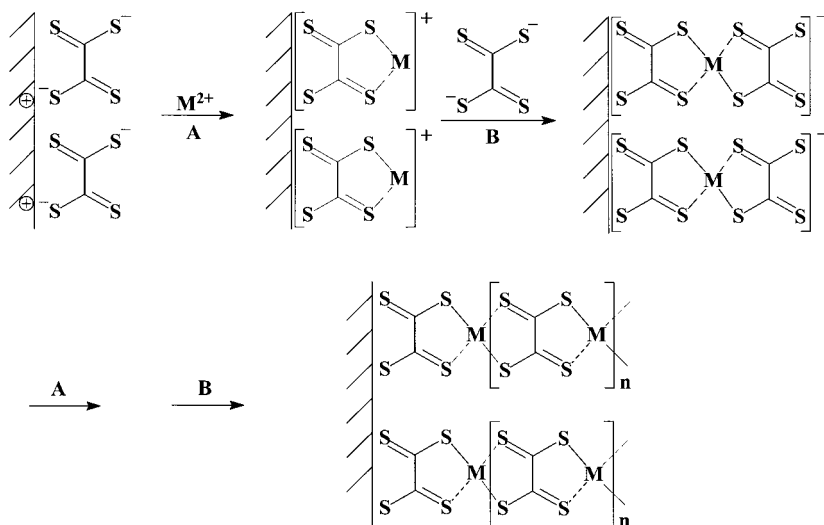
### Electroactive Assemblies

Besides organic di- or polyionic compounds, inorganic ions are also suitable as building blocks for the preparation of LBL assemblies. This was demonstrated in the previous section for the example of the Ba<sup>2+</sup>/11 multilayer, and is also known from studies in the literature [57–63]. Using divalent metal cations, we prepared novel self-assembled films of organic–inorganic hybrid polymers such as poly-(metal tetrathiooxalates) [64, 65] and completely inorganic mixed-valence complex salts such as iron hexacyanoferrate (also denoted as Prussian blue) [66–68] displaying interesting electroactive properties. Due to the formation of intense coordinative interactions between the transition metal ions and the counterions the adsorption process is not merely driven by electrostatic forces, but can be looked at as a mixture of physisorption and chemisorption, and may be called ‘reactive self-assembly’ [69]. In the following two sections, the films are characterised in more detail.

#### 15.4.1

##### Poly(metal tetrathiooxalates)

The self-assembled films of poly(metal tetrathiooxalates), [MTTO]<sub>n</sub>, were prepared by alternate adsorption of divalent transition metal cations such as palladium, cobalt, nickel or copper, and the tetrathiooxalate (TTO<sup>2-</sup>) dianion from aqueous solution onto charged substrates [70, 71]. While the starting compounds were only weakly colored, the adsorbed films immediately showed a deep coloration and intense metallic reflection; a clear indication that the film formation was accompanied by coordinative d<sub>π</sub>-p<sub>π</sub> interactions between the compounds. A corresponding scheme illustrating the self-assembly process is represented in Scheme 5. The reaction scheme indicates that the self-assembly can be looked at as a grafting-from polyaddition reaction. UV–visible absorption spectra of films with M being nickel and palladium are shown in Fig. 15.9 (a) and (b). They indicate a broad absorption in the visible and near-infrared. In the case of the [PdTTO]<sub>n</sub> films, back donation of the d electrons from the Pd to the sulfur atoms of TTO is responsible for a particularly strong absorption. The coordinative interaction between the metal and sulfur atoms was also indicated in the infrared by a characteristic shift of the C–S stretching mode to higher wavenumbers. An interesting property of bulk [MTTO]<sub>n</sub> samples is their high specific conductivity  $\sigma$ , which is about 30 S cm<sup>-1</sup> for [NiTTO]<sub>n</sub>, for example [64]. The conductivity of the self-assembled films was



**Scheme 15.5** Preparation of a poly(metal tetrathiooxalate) film via  $(n + 1)$  fold alternate adsorption of  $C_2S_4^{2-}$  ligand anions and the  $M^{2+}$

center (M: Cu, Co, Ni, Pd). The tilt angle between polymer chains and substrate surface is unknown (from [71]).

lower, but  $\sigma$ -values measured parallel and perpendicular to the layer plane were still as high as  $3 \times 10^{-3} \text{ S cm}^{-1}$ , the anisotropy being very small [71]. The lower  $\sigma$ -values might be caused by a partial substitution of the sulfur atoms by oxygen while the TTO dianions were dissolved in an aqueous medium. A partial hydrolysis was evident from the infrared spectra of self-assembled  $[\text{NiTTO}]_n$  films showing the C=O stretching mode in addition to the C=S mode.

#### 15.4.2

##### Prussian Blue and Analogues

Prussian blue (PB) and related mixed valence hexacyanometalate salts are known for their interesting electrochemical [66], electrochromic [68], photophysical [72] and magnetic properties [73]. The insoluble PB complex salt of composition  $\text{Fe}_4[\text{Fe}(\text{CN})_6]$  is obtained as a deep-blue precipitate, if aqueous solutions of  $\text{Fe}^{3+}$  and  $[\text{Fe}(\text{CN})_6]^{4-}$  ions or  $\text{Fe}^{2+}$  and  $[\text{Fe}(\text{CN})_6]^{3-}$  ions are mixed together. As recently demonstrated [74], the multiple alternating dipping of a charged substrate into solutions containing  $\text{Fe}^{2+}$  and hexacyanoferrate(III) ions is a useful method to prepare ultrathin PB films of variable thickness on the substrate. Upon dipping into the two solutions, the substrate immediately turned deep blue. This is a clear indication that the electrostatic adsorption was accompanied by the simultaneous formation of  $\text{Fe}^{\text{III}}\text{-C-N-Fe}^{\text{II}}$  sequences exhibiting intense charge transfer between the di- and trivalent iron atoms. As shown in Fig. 15.10, the charge transfer band at 700 nm increases nearly linearly with the number of dipping cycles. The alter-

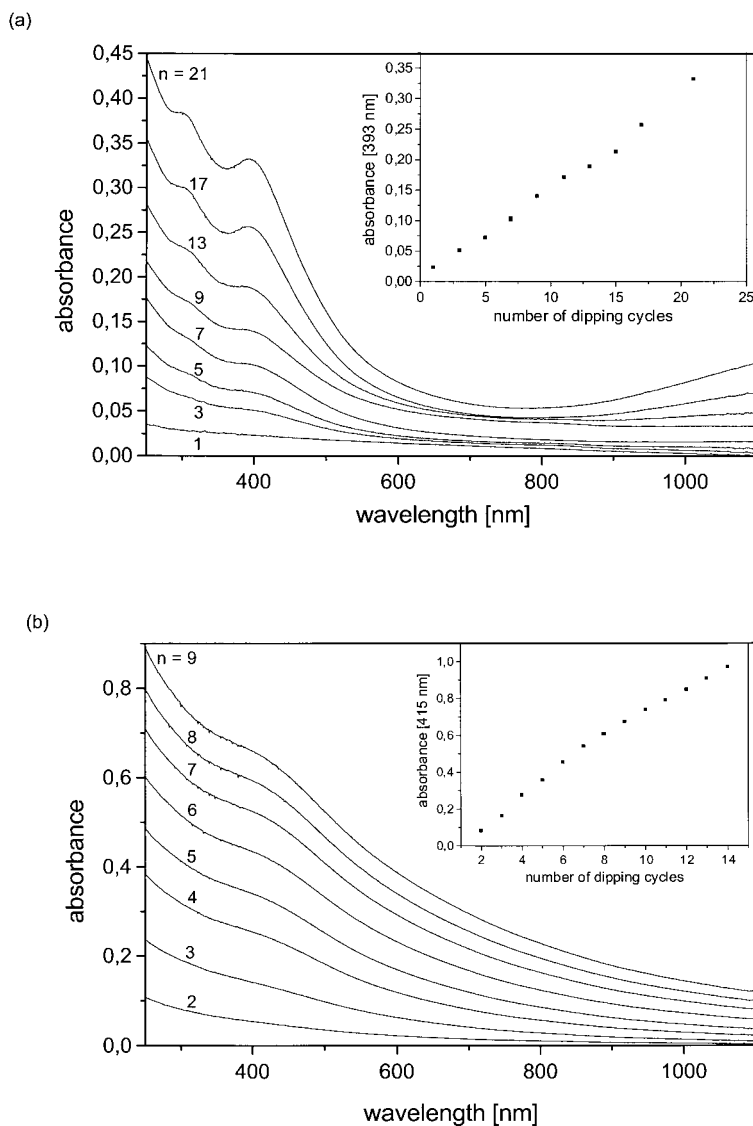


**Fig. 15.9** Optical absorption of poly(metal tetrathiooxalate) films with M being nickel (a) and palladium (b) after various dipping cycles  $n$ . The insets show plots of the absorbance at

distinct wavelengths versus  $n$ . Substrates: quartz plates precoated with three layer pairs PSS/PAH (adapted from [70, 71]).

native preparation route via dipping of the substrate into solutions of  $\text{Fe}^{3+}$  and  $[\text{Fe}(\text{CN})_6]^{4-}$  also results in the formation of deep blue films. The absorbance of these films was always three times higher than for the previous ones. This was ascribed to the higher charge density of the  $\text{Fe}^{3+}$  and hexacyanoferrate(II) ions.

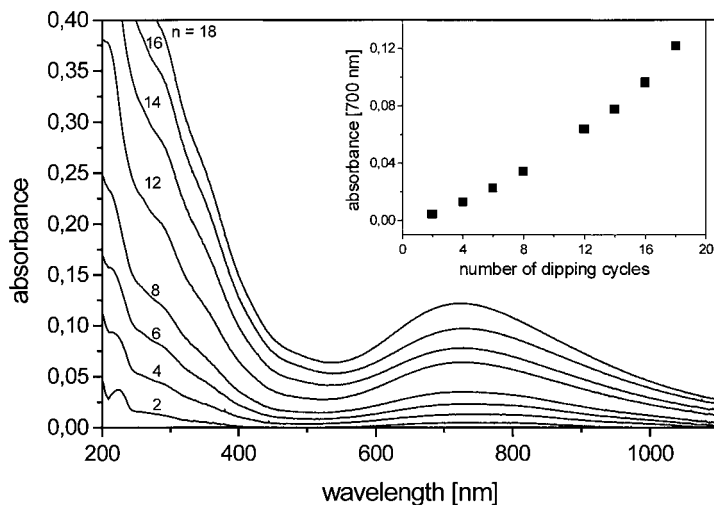


**Fig. 15.10** UV/visible absorption spectra of self-assembled PB films after various dipping cycles  $n$ , the aqueous solutions containing hexacyanoferrate (III) and iron(II) ions. The inset shows the plot of the absorbance at 700 nm versus  $n$ . Substrates: quartz plates precoated with three layer pairs PSS/PAH (adapted from [74]).

Upon adsorption of these ions, the surface charge is more effectively reversed so that in the next deposition step more ions can be adsorbed. The self-assembled films show the typical reversible redox behaviour of PB with cyclic voltammetric peaks for the oxidation to Prussian Green at 830 mV (vs. SCE) and reduction to Everitt's salt at 160 mV. Simultaneously the color of the films changes from blue to green or colourless, respectively, making the films attractive for applications in electrochromic devices. The peak intensities increased linearly with the number of dipping cycles. This is demonstrated for the potential range from  $-200$  to  $700$  mV vs. SCE in Fig. 15.11 (a). The self-assembled PB films also showed interesting photoelectrochemical behaviour, similar to observations reported previously for LB films containing PB [75]. Switching polychromatic light on and off at an applied potential of  $1$  V is accompanied by a repeated generation and disappearance of a photocurrent (Fig. 15.11 (b)). The self-assembly route is also useful to prepare films of PB analogues containing other transition metal ions such as cobalt, indium or copper. With other metal ions, charge transfer interactions, peak potentials and electrochromism are decisively altered [76].

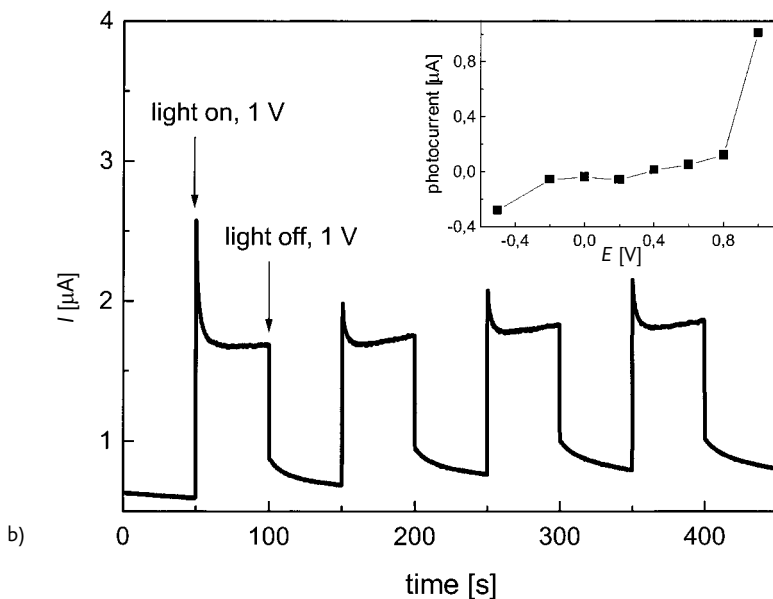
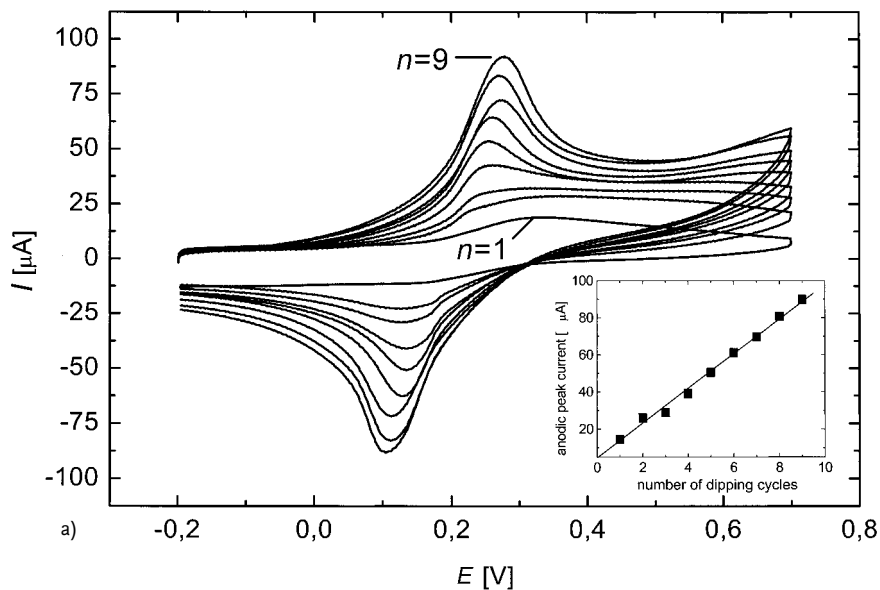


**Fig. 15.11** Electro- and photoresponsive properties of self-assembled PB films on ITO-coated quartz supports. (a) Cyclic voltammograms after different numbers  $n$  of dipping cycles using a potential range from  $-200$  to  $700$  mV vs. SCE (scan rate:  $5 \text{ mV s}^{-1}$ ,  $T=20^\circ\text{C}$ ); the inset shows a plot of the anodic peak current vs.  $n$ . (b) Current changes

induced by switching on and off the irradiation of a PB film (16 dipping cycles) with white light from a  $500 \text{ W}$  lamp. Applied potential:  $1 \text{ V}$  vs. SCE. The inset shows the dependence of the photocurrent on the applied potential. Supporting electrolyte:  $0.5 \text{ M KCl}$  (adapted from [74]).

## 15.5

## Transport of Small Molecules and Ions across Polyelectrolyte Multilayers

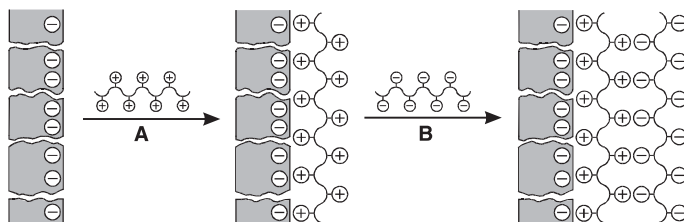
## 15.5.1

## Transport of Small Molecules

The use of polyelectrolytes for the preparation of separating membranes of macroscopic thickness was already demonstrated several years ago. From these studies [77–80] it is known that solution-cast membranes exhibit favorable properties in alcohol/water separation and the dehydration of organic solvents. Thus it was also interesting to study LBL assemblies of polyelectrolytes with respect to their transport behavior and potential use as ultrathin separating membranes. Our activities in this field have recently been reviewed [81, 82], the important aspects are described in the following. For the studies of transport behaviour [81], we always used highly porous polyacrylonitrile-based supporting membranes treated with oxygen plasma in order to increase the surface charge. The porous supports were alternately dipped into the solutions of the two oppositely charged polyelectrolytes, the polyelectrolytes were adsorbed on the substrate surface and formed a multilayer membrane of thickness in the nanometer range (Scheme 6). The pore sizes of the support were between 20 and 200 nm. Porous supports were chosen because they did not influence the permeation, so that any separation achieved could be exclusively ascribed to the polyelectrolyte multilayer membrane.

## 15.5.1.1 Gas permeation

In a first study [83] it was tested, whether the layer-by-layer adsorption of polyelectrolytes enables the pores of the substructure to close, and whether a dense separating layer can be prepared. For this purpose, the flow of nitrogen, oxygen, argon and carbon dioxide across a PAH/PSS complex membrane was studied as a function of the number of deposited layer pairs. It was found that the flux of the support could be reduced by 90%, if 20 layer pairs were adsorbed. If 60 layer pairs



**Scheme 15.6** Layer-by-layer adsorption of polyelectrolytes on plasma-treated porous supporting membrane. Multiple repetition of steps A and B leads to the ultrathin separating layer. In reality the pore diameter is 20–

200 nm, i.e. much larger than the size of the polyelectrolyte chains, the individual polymer chains are less ordered and partially overlapping (adapted from [88, 90]).

were deposited, the flux was reduced by more than 99.9%. Obviously, the layer-by-layer approach was suitable for closing the pores of the substrate. The studies also indicated that the permeation rates of  $N_2$ ,  $O_2$  and argon were nearly identical, while for carbon dioxide a higher value was found, probably due to a higher solubility of  $CO_2$  in the polyelectrolyte multilayer. Our results on gas permeation were in good agreement with those of another research group, who also found poor or no separation when they used LBL assemblies on porous substructures [84].

#### 15.5.1.2 Pervaporation separation of alcohol/water mixtures

In order to study the transport of small liquid molecules, alcohol/water mixtures were chosen and their separation under pervaporation conditions was investigated [81–86]. Pervaporation was used, because it represents a promising new technique for industrial separation of liquid mixtures [85], and because good results on alcohol/water pervaporation separation already existed for solution-cast polyelectrolyte complex membranes of micrometer thickness [78, 79]. In the first studies, ethanol/water separation using PAH/PSS multilayer membranes was investigated [83, 86]. A preferential transport of water was found, but the separation was only rather poor. Moreover, the PAH/PSS membrane was only stable up to a water content of the feed solution of about 20%. At higher concentration, the network structure was hydrolyzed and the membrane destroyed.

Further experiments were aimed at improving the separation capability. Before these studies are described, it is useful to briefly discuss the microstructure of the membrane. The LBL assemblies of cationic and anionic polyelectrolytes exhibit a physically cross-linked network structure [87], the ion pairs representing the cross-linking units of the network. An idealized model of the network structure is shown in Fig. 15.12. Molecules permeating across the films have to pass the pores of the network, i.e. the permeability will depend on the size and hydrophilicity of the individual pores. In other words, the charge density of the polyelectrolytes is

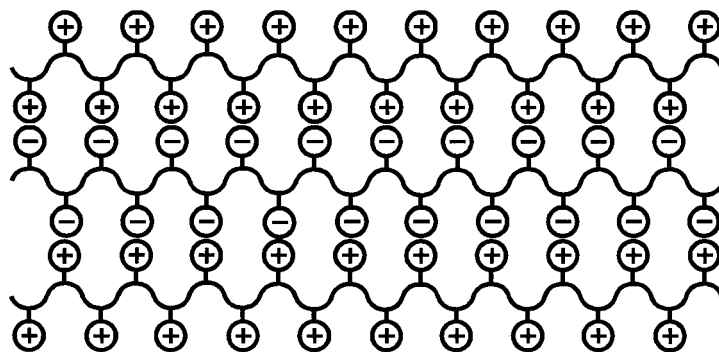
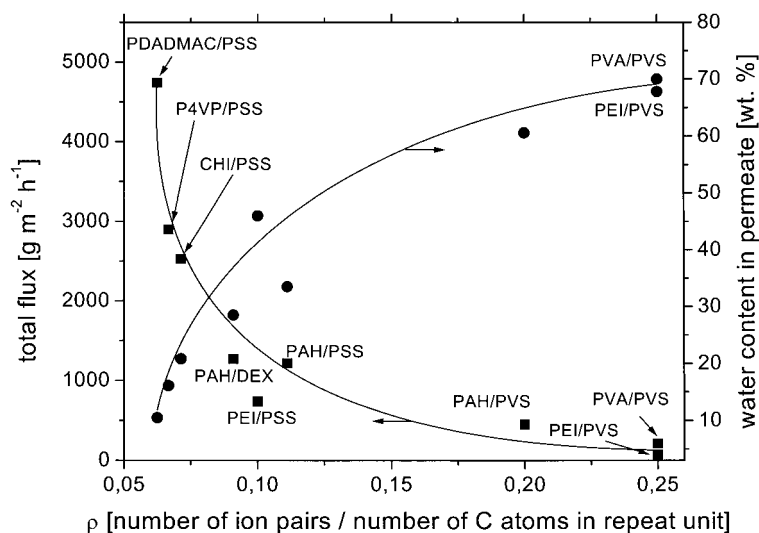


Fig. 15.12 Idealized structure of the polyelectrolyte complex membrane with the polyelectrolytes being completely ionized. In reality the individual polymer chains are less ordered and partially overlapping.

an important structural parameter controlling the permeability of the individual compounds. To prove this model, a variety of multilayer membranes with different charge density  $\rho_c$  of the polyelectrolyte complex was prepared under identical conditions, and the separation characteristics were determined as a function of the structure [88–90]. The charge density  $\rho_c$  was defined as the number of ion pairs per number of carbon atoms in the repeat unit of the polyelectrolyte complex. As shown in the plot of Fig. 15.13, the total flux was inversely proportional to  $\rho_c$ , while the water content in the permeate increased with  $\rho_c$ . The clarity of this correlation was surprising, especially because, in the definition of  $\rho_c$ , any contribution from specific structural elements such as the nature of the ionic groups, branching of the polymer, flexibility of the main chain and the side groups, presence of aromatic units etc. had been completely neglected. To a first approximation, only the charge density controls the flux and separation capability of the membrane. The main result of this study was that membranes with improved ethanol/water separation could now be tailored, if polyelectrolytes of high charge density such as PEI, polyvinylamine (PVA), polyvinylsulfate (PVS), polyvinylsulfonate (PVSu) and polyacrylate (PAA) were used.

As a first example, the PEI/PVS membrane was studied [89]. Compared with the PAH/PSS membrane, the ethanol/water separation could be highly improved. For 20% (w/w) water in the feed solution, a water content of 99.6% in the permeate was reached, which corresponds to a separation factor of nearly  $10^3$ . The flux



**Fig. 15.13** Ethanol/water pervaporation separation of various polyelectrolyte complex membranes (60 layer pairs). Dependence of total flux (a) and composition of the permeate (b) on the charge density of the polyelectrolyte complex. Feed solution: 6.2 wt.%

water. All membranes were prepared under the same conditions i.e. from NaCl-free aqueous polyelectrolyte solutions (concentration:  $10^{-2}$  monomol  $L^{-1}$ ) at pH 1.7 (adapted from [82, 89, 90]).



was about  $600 \text{ g}^{-2} \text{ h}^{-1}$ . However, the good separation characteristics could only be achieved after annealing the membrane at  $90^\circ\text{C}$  for 1 h. The post-treatment was necessary in order to increase the cross-linking density, because the branching and low backbone flexibility of PEI were unfavorable for the direct preparation of a defect-free, regular network structure similar to the one in Fig. 15.12. In order to further improve the separation, PEI was replaced by the more regular, flexible PVA. The resulting PVA/PVS membranes showed improved separation characteristics in ethanol/water pervaporation compared with PEI/PVS [90]. It was no longer necessary to anneal the membranes before use, but now a good separation was only obtained if the polyelectrolytes were adsorbed from aqueous solutions containing an additional supporting electrolyte such as NaCl. In the presence of NaCl, the diameters of the polymer coils are smaller, and the tendency of the coils to unfold during adsorption is much lower. Consequently, the thickness of the adsorbed layers is larger, and with increasing thickness the flux becomes lower, while the separation factor becomes higher.

Besides ethanol/water separation, the separation of other alcohol/water mixtures was also studied [81, 91]. It was found that *tert*-butanol/water mixtures are more efficiently separated than propanol/water or ethanol/water mixtures (Fig. 15.14(a)). Except for a feed composition with less than 5 wt.% water, the permeate always contained nearly pure water, i.e. the water concentration was 99.9 wt.% or higher. The highest flux was found for *tert*-butanol/water mixtures, i.e. with decreasing hydrophilicity of the alcohol the flux increased (Fig. 15.14(b)). The excellent results for the dehydration of the less hydrophilic alcohols were firstly due to the weaker hydrogen bonding between these alcohol molecules and water. In addition, the close, hydrophilic pores of the PVA/PVS membrane favored the water permeation and rejected the less polar alcohol molecules. From the flux  $J$  and the separation factor  $\alpha$ , the separation efficiency  $\alpha J$ , also denoted as 'pervaporation separation index' (PSI), was calculated. Highest values of more than  $3 \times 10^4$  were found for the *tert*-butanol/water mixtures. With increasing hydrophilicity of the alcohol, the PSI decreased and the maximum value shifted towards a higher water content in the feed.

As described above, the suitability of polyelectrolyte multilayer assemblies for alcohol/water separation is decisively influenced by the charge density of the polymers. The charge density not only depends on the molecular structure of the polyelectrolytes, but is also a function of the degree of ionisation of the polar groups, which is controlled by the pH of the polyelectrolyte solutions used for membrane preparation. The effect of a pH variation on flux and separation of the polyelectrolyte membrane is very strong. In the small pH region from 1.8 to 2.4, the total flux of an ethanol/water mixture across a PAH/PSS membrane varied by a factor of 4.5; the water content in the permeate was also affected [90]. Even stronger effects were found, if the pH was raised to 6.8 [92]. In Tab. 15.2, flux and separation of three membranes of high charge density prepared at pH 6.8 are compared with membranes prepared at pH 1.7 with or without salt added to the dipping solution. By far the best separation is found for the PVA/PVSu membrane prepared at pH 6.8. The separation factor is 3010, while for the same membrane prepared

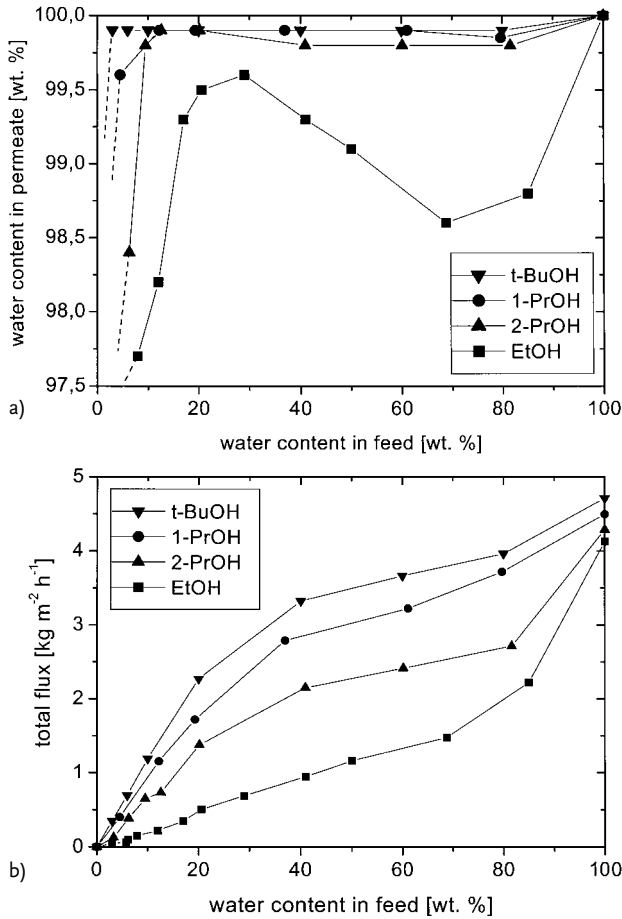


**Fig. 15.14** Dependence of water content in permeate (a) and total flux (b) on water content in the feed solution for various alcohol/water mixtures. Samples: 60 layer pairs PVA/

PVS. Polyelectrolytes were adsorbed from aqueous solutions containing NaCl as supporting electrolyte in a concentration of  $0.1 \text{ mol L}^{-1}$  (adapted from [81]).

from salt-free or salt-containing dipping solutions at pH 1.7 only  $\alpha$ -values of 45 and 345, respectively, were obtained. The very good separation can be ascribed to a high cross-linking density of the membrane caused by the use of polymers of high charge density, and by a flat adsorption of the polymer chains under the pH conditions applied [93] so that the structure resembles the model depicted in Fig. 15.12.

**Tab. 15.2** Ethanol/water pervaporation separation of polyelectrolyte multilayer membranes (60 layer pairs) of high charge density as a function of the preparation conditions (feed: 6.2 wt.% water)

Separating membrane	Prepared from polyelectrolyte solution		Total flux [g m <sup>2</sup> h <sup>-1</sup> ]	Water content in permeate [wt.%]	$\alpha$
	of pH	in presence of 0.1 M NaCl			
PVA/PVStu	1.7	–	483	74.8	45
	1.7	+	226	95.8	345
	6.8	–	104	99.5	3010
PVA/PVS	1.7	–	431	70.0	35
	1.7	+	63	94.9	282
	6.8	–	88	99.1	1666
PVA/PAA	6.8	–	75	97.1	507

## 15.5.2

**Transport of Ions**

If aqueous solutions of oppositely charged polyelectrolytes are cast on top of each other, a so-called bipolar membrane with bilayer structure is obtained. The ion permeation through bipolar polyelectrolyte membranes of macroscopic thickness was already investigated several years ago [94, 95]. It was found that divalent cations receive a much stronger repulsive force from the positively charged layers than monovalent ones. The same holds for the divalent anions, which are rejected by the negatively charged layers. Consequently, the bipolar membranes represent barriers for divalent ions in general and can be used for ion separation [94, 95]. The self-assembled polyelectrolyte multilayers consist of cationic and anionic polyelectrolytes in alternating fashion and thus can be looked at as a multi-bipolar membrane on a molecular level, which likewise should be able to separate mono- and divalent ions. In Fig. 15.15, a model of the ion rejection by a multi-bipolar membrane is represented [96]. The model implies that the ion separation becomes progressively more effective if the number of adsorbed polyelectrolyte layers is increased, and that the separation achieved is independent of the surface charge of the membrane. In a first study [88], the permeation of aqueous NaCl and MgCl<sub>2</sub> solutions across PAH/PSS membranes was investigated. A permeation rate  $P_R$  for NaCl 15 times higher than that for MgCl<sub>2</sub> was found. In a subsequent, more comprehensive study, the transport of NaCl, MgCl<sub>2</sub> and Na<sub>2</sub>SO<sub>4</sub> was investigated [96]. It turned out that the  $P_R$  values of the three salts were significantly different so that theoretical separation factors  $\alpha$  for Na<sup>+</sup>/Mg<sup>2+</sup> of up to 112.5 and for Cl<sup>-</sup>/SO<sub>4</sub><sup>2-</sup> of up to 45.0 could be determined. Numerous parameters were found to influence the  $P_R$  values and the separation factor  $\alpha$ . Among them are the number of adsorbed layer pairs, the charge density of the polyelectrolytes, pH and the presence of NaCl in the polyelectrolyte solution used for membrane preparation. As expected from the rejection model, the  $P_R$  values decreased and

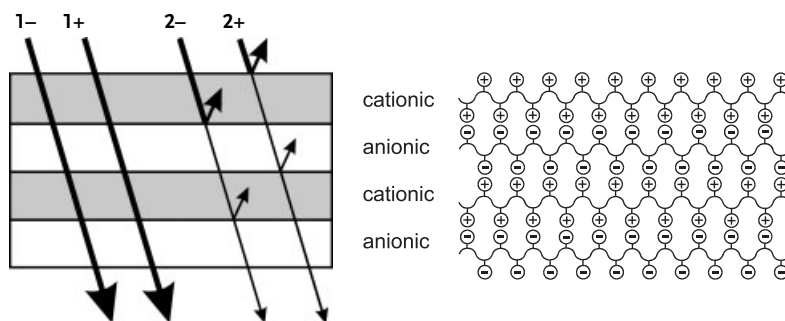
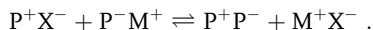
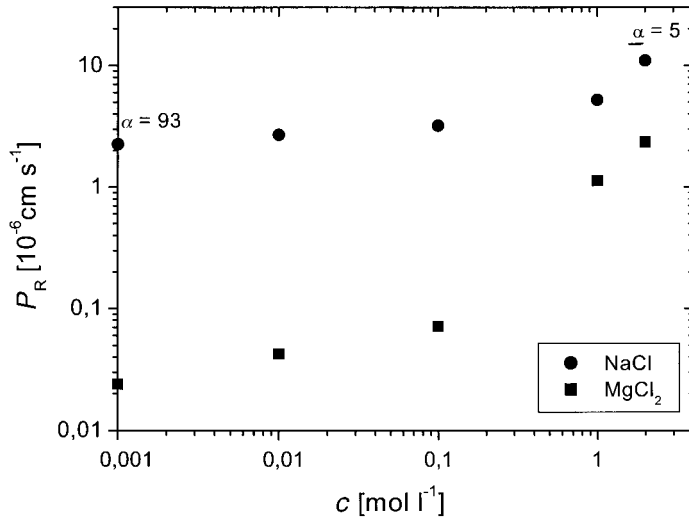


Fig. 15.15 Model of ion rejection by a multi-bipolar membrane (left) and idealized multi-bipolar structure of the polyelectrolyte LBL assembly (right) (adapted from [96, 97]).

the  $\alpha$  values increased when the number of adsorbed layer pairs was increased. If polyelectrolyte complexes of progressively higher charge density were used for membrane preparation, the network became more and more polar and the pore size was reduced. As a consequence, the  $P_R$  values decreased, but for ions of high charge density the change was much stronger than for the monovalent ions; consequently, higher  $\alpha$ -values were obtained. In a subsequent study [97], the ion permeation across PVA/PVS membranes was investigated. Because of the high charge density, the membranes exhibited very good separation properties. For the series of alkali and alkaline earth metal chlorides, the  $P_R$  values increased from LiCl to KCl, and from  $\text{MgCl}_2$  to  $\text{BaCl}_2$ , i.e. in the direction of decreasing charge density of the cations. When the salt concentration of the permeating aqueous NaCl and  $\text{MgCl}_2$  solutions was increased, the  $P_R$  values were little affected until a concentration of about  $0.3 \text{ mol L}^{-1}$  was reached (Fig. 5.16). At higher salt concentration the permeation rates increased strongly, while the separation factor dropped. The effect can be explained by considering the equilibrium of the polyelectrolyte complex formation (with  $\text{P}^+$  and  $\text{P}^-$  being charged segments of the cationic and anionic polyelectrolytes),



Upon addition of  $\text{M}^+\text{X}^-$  the equilibrium is gradually pushed to the left side, i.e. the ion pairs representing the cross-linking units of the network are partially dissociated. Larger pores are formed, the permeation rates are increased and the selectivity of the membrane is decreased. In order to study the possible influence of the surface charge of the membrane on the ion rejection, PVA/PVS membranes with alternate positive and negative surface charge were prepared, i.e. either PVA or PVS was adsorbed as the uppermost layer [97]. In Fig. 15.17, the permeation rates of NaCl,  $\text{MgCl}_2$ ,  $\text{Na}_2\text{SO}_4$  and  $\text{MgSO}_4$  are plotted as a function of number and surface charge of the deposited layers. Clearly there is no influence of the surface charge, i.e. the charged groups in the bulk volume of the membrane contribute to the ion rejection as suggested by the model of Fig. 15.15. Fig. 15.17 also



**Fig. 15.16** Plot of permeation rates  $P_R$  of NaCl and MgCl<sub>2</sub> versus the concentration  $c$  of the aqueous salt solution. Separating membrane: 60 layer pairs of PVA/PVS adsorbed from aqueous polyelectrolyte solution at pH 1.7 containing NaCl as supporting electrolyte (concentration: 0.1 mol L<sup>-1</sup>) (adapted from [97]).

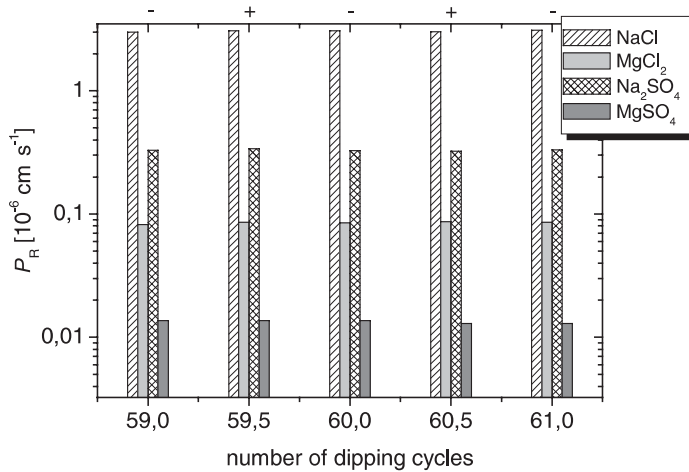


**Fig. 15.17** Effect of the surface charge of the separating membrane on the permeation rates  $P_R$  of NaCl, MgCl<sub>2</sub>, Na<sub>2</sub>SO<sub>4</sub> and MgSO<sub>4</sub>. Separating membrane: 59 to 61 layer pairs of PVA/PVS, for preparation conditions see caption to Fig. 15.18 (adapted from [97]).

shows that the permeation rates of the four electrolytes decrease in the sequence  $P_R(\text{NaCl}) > P_R(\text{Na}_2\text{SO}_4) \geq P_R(\text{MgCl}_2) > P_R(\text{MgSO}_4)$ , i.e. in the direction of increasing charge density of the ions.

### 15.5.2.1 Uptake of Ions

Using a PVA/PVS membrane, the transport of various metal chlorides including heavy metal chlorides such as  $\text{ZnCl}_2$ ,  $\text{CuCl}_2$  or  $\text{LaCl}_3$  was studied [98]. In Fig. 15.18, the permeation rates of the various metal chlorides are plotted versus the surface charge density  $z^+r^{-2}$  ( $z^+$ : charge number,  $r$ : radius of non-hydrated ions) of the corresponding cations. As expected, the  $P_R$  values were inversely proportional to the surface charge density, but some of the heavy metal chlorides and barium chloride showed exceptionally low  $P_R$  values. This indicates that effects other than the charge density may also play a role. As recently shown [98], an important effect on  $P_R$  originates from selective incorporation of specific metal ions into the membrane. For example, the incorporation of copper ions is apparent from the blue color of the PVA/PVS membrane after the permeation of aqueous copper chloride. From the absorption maximum at about 700 nm a complex formation between copper and the amino groups of PVA according to

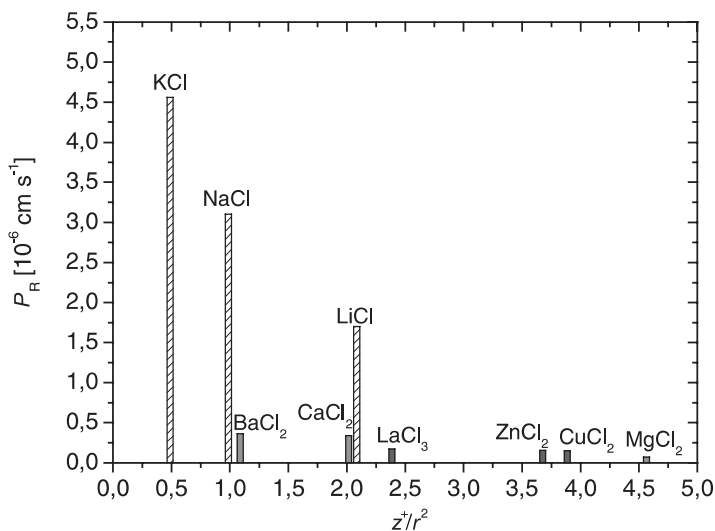
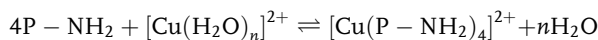


**Fig. 15.18** Plot of the permeation rates  $P_R$  of various metal chlorides in aqueous solution (concentration:  $0.1 \text{ mol L}^{-1}$ ) as a function of the charge density  $z^+r^{-2}$  of the metal cation

( $z^+$ : charge number,  $r$ : radius of metal ion). Separating membrane: 60 layer pairs of PVA/PVS, for preparation conditions see caption to Fig. 15.18 (adapted from [97]).

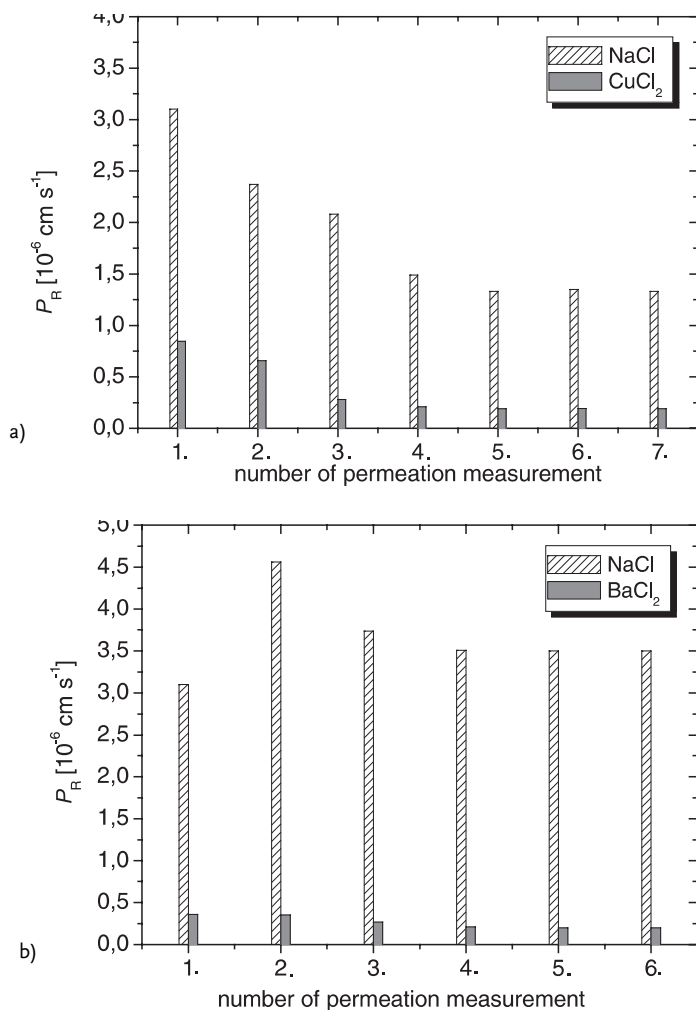
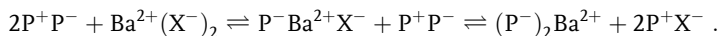


**Fig. 15.19** Effect of selective uptake of metal ions incorporation on the ion permeation of polyelectrolyte LBL assemblies. The permeation rates  $P_R$  of (a) NaCl and  $\text{CuCl}_2$ , and (b) NaCl and  $\text{BaCl}_2$  across a PVA/PVS mem-

brane (60 layer pairs) obtained upon successive permeation of the two salt solutions are shown. For preparation conditions of the membrane see caption to Fig. 15.18 (adapted from [98]).

was evident. The complex formation increases the network density of the membrane and consequently the permeability is generally decreased. This is demonstrated in Fig. 15.19(a) for a repeated alternating permeation of aqueous NaCl and CuCl<sub>2</sub> solutions across a PVA/PVS membrane. Upon repeated permeation, the  $P_R$  values of the two salts decrease until a constant rate is obtained, when the membrane is saturated with copper ions. With aqueous barium chloride, a different kind of interaction with the polyelectrolyte complex was observed. Repeated alternate permeation of aqueous NaCl and BaCl<sub>2</sub> is accompanied by an initial increase in the  $P_R$  values until they finally decrease again (Fig. 15.19(b)). The behavior was explained by considering that the barium salt of PVS is less soluble in water than the P<sup>+</sup>P<sup>-</sup> ion pairs of the PVA/PVS membrane. Consequently the barium ions react with P<sup>+</sup>P<sup>-</sup> according to the equilibria



The initial increase in the permeation rates can be ascribed to the formation of P<sup>-</sup>Ba<sup>2+</sup>X<sup>-</sup>, which is accompanied by a decrease in the cross-linking density, while the final decrease in the  $P_R$  values results from the gradual formation of (P<sup>-</sup>)<sub>2</sub>Ba<sup>2+</sup> units representing new cross-linking sites in the membrane.

## 15.6

### Summary and Conclusions

Our studies indicate that the layer-by-layer assembly of oppositely charged di- or polyionic compounds is a versatile method for the preparation of ultrathin functional films. Photoreactive films can be prepared, for example, by self-assembly of bolaamphiphiles or ionenes carrying photosensitive azobenzene or diacetylene moieties. However, the photoreactivity of these groups is strongly dependent on the nature of the polymeric counterion used for the preparation of the LBL assembly. Polyelectrolytes of high charge density such as PAH and PEI favor a crystal-like dense packing of the bolaamphiphiles, while weakly charged polyelectrolytes such as chitosan may induce a less ordered, smectic arrangement. The study of the diketopyrrolopyrrole derivatives shows that even in a densely packed, aggregated monolayer the mutual orientation of the bolaamphiphiles is determined by the nature of the counterions. The attempts to orient the azobenzene moieties uniquely in polarized light were only partially successful owing to the limited flexibility of the compounds caused by the electrostatic interactions in the film. SFM-studies indicate that the surface structure of the self-assembled films is strongly dependent on the nature of the adsorbed compounds. Indeed, bolaamphiphiles and divalent inorganic ions are suitable for construction of LBL-assemblies, but they are not able to increase the charge density or to homogenise the charge distribution at the surface. Therefore, the surface structures of films containing these compounds are always rather inhomogeneous, while polyelectrolyte films or films containing polyionic inorganic compounds usually exhibit a smoother surface. The use of transition metal ions might have the consequence that the self-as-



sembly process is not merely driven by electrostatic forces, but coordinative interactions between the d-electrons of the metal ions and p- or d-electrons of the counterions also play a role. This allowed us to prepare films of organic–inorganic hybrid polymers such as conducting poly(metal tetrathiooxalate), and of purely inorganic polymeric complex salts such as redoxactive, electrochromic Prussian blue by simple alternate dipping of the substrate into solutions of the ionic species constituting the polymers. By variation of the metal cations, or the anions, films of other hybrid polymers such as poly(metal tetrathiosquarate), poly(metal benzene-1,2,4,5-tetrathiolate), or PB analogs showing other colors and redox potentials may become accessible.

Our studies also indicate that the LBL approach allows one to prepare dense polyelectrolyte multilayers of thickness in the nanometer range, which are suitable as separating membranes. When the polyelectrolytes are adsorbed on a porous substructure, a new type of composite membrane is obtained. Due to the charge neutralisation of the cationic and anionic polyelectrolyte substituent groups, a highly crosslinked polyelectrolyte complex membrane with defined pore sizes of less than a nanometer in diameter is formed. If polyelectrolytes with high charge density are used, membranes with small, hydrophilic pores become accessible. These are highly permeable for water molecules, and only little permeable for organic solvent molecules such as alcohols. The less hydrophilic the compound, the lower the permeability across the membrane. Besides the charge density, the nature and the ionization of the polar groups and the regularity of the polymer structure are other important criteria for a good alcohol/water separation. Branched PEI is less suitable than polymers with more regular, flexible structure such as PAA or PVSu, which are prepared directly from the corresponding monomers. Moreover, the membranes should be prepared at the pH of the polyelectrolyte solution, permitting a complete ionisation of the polar groups. If all parameters are optimised, polyelectrolyte complex membranes with separation factors and efficiencies comparable to zeolite membranes can be prepared. The reason is that the polyelectrolyte and zeolite membranes exhibit similar pore sizes with diameters in the range 0.5 to 0.9 nm. Thus the polyelectrolyte complex membranes may also be denoted as ‘organic zeolite’ membranes.

Due to the alternating sequence of cationic and anionic layers, the polyelectrolyte multilayer membranes exhibit a multi-bipolar character. As a consequence, the permeating ions receive a strong Donnan rejection at equally charged layers, especially when the charge density is high. Thus the membranes are suitable for separation of ions of different charge density, as for example  $\text{Na}^+$  and  $\text{Mg}^{2+}$ , or  $\text{Cl}^-$  and  $\text{SO}_4^{2-}$ . Our studies also show that some transition metal ions, as for example  $\text{Cu}^{2+}$ , or ions of high charge density, are strongly bound to the membrane.  $\text{Cu}^{2+}$  ions are complexed by amino groups of PVA, for example, while  $\text{Ba}^{2+}$  ions are able to form insoluble salts with the sulfate groups of PVS. As a consequence, the cross-linking density of the membrane is varied and the permeation rates of all ions are changed. The selective transport of small molecules according to their hydrophilicity, and of ions according to their charge density, is certainly one of the most interesting properties of the polyelectrolyte LBL assemblies. Incorporation of

ion-selective compounds in the polyelectrolyte multilayers, as for example potassium-selective Prussian-blue layers, may further allow one to improve the selectivity and to use the LBL assemblies in specific sensor applications.

### Acknowledgement

The authors are grateful to Mrs. Burgunde Feist for valuable technical assistance in the preparation of the figures and schemes. Financial support by the Deutsche Forschungsgemeinschaft (projects TI219/3-1 to 3-4 and 6-1) is also gratefully acknowledged.

### 15.7

#### References

- 1 G. G. ROBERTS, *Langmuir Blodgett Films*, Plenum Press, New York, 1990.
- 2 A. ULMAN, *An Introduction to Ultrathin Organic Films*, Academic Press, Boston, 1991.
- 3 R. H. TREDGOLD, *Order in Thin Organic Films*, Cambridge University Press, Cambridge, 1994.
- 4 *Novel Methods to Study Interfacial Layers, Studies in Surface Science Series*, Eds. D. MOEBIUS, R. MILLER, Elsevier, Amsterdam, 2001, to be published.
- 5 G. DECHER, J.-D. HONG, *Makromol. Chem. Macromol. Symp.* **1991**, *46*, 321.
- 6 G. DECHER, J.-D. HONG, *Ber. Bunsen-Ges. Phys. Chem.* **1991**, *95*, 1430.
- 7 G. DECHER, J.-D. HONG, J. SCHMITT, *Thin Solid Films* **1992**, *210/211*, 831.
- 8 G. DECHER, J. SCHMITT, *Prog. Colloid Polym. Sci.* **1992**, *89*, 160.
- 9 G. DECHER, *Science* **1997**, *277*, 1232.
- 10 G. DECHER in *Templating, Self-Assembly and Self-Organization, Comprehensive Supramolecular Chemistry*, Eds. J.-P. SAUVAGE, M. W. HOSSEINI, Pergamon, Oxford, 1996, vol. 9, p. 507.
- 11 W. KNOLL, *Curr. Opin. Colloid Interface Sci.* **1996**, *1*, 137.
- 12 M. SANO, Y. LVOV, T. KUNITAKE, *Annu. Rev. Mater. Sci.* **1996**, *26*, 153.
- 13 V. V. TSUKRUK, *Progr. Polym. Sci.* **1997**, *22*, 247.
- 14 P. BERTRAND, A. JONAS, A. LASCHEWSKY, R. LEGRAS, *Macromol. Rapid Commun.* **2000**, *21*, 319.
- 15 P. T. HAMMOND, *Curr. Opin. Colloid Interface Sci.* **2000**, *4*, 430.
- 16 B. TIEKE, *Adv. Polym. Sci.* **1985**, *71*, 79.
- 17 B. TIEKE, *Adv. Mater.* **1990**, *2*, 222.
- 18 G. MAO, Y. TSAO, M. TIRRELL, H. T. DAVIS, V. HESSEL, H. RINGSDORF, *Langmuir* **1993**, *9*, 3461.
- 19 J.-D. HONG, K. LOWACK, J. SCHMITT, G. DECHER, *Progr. Colloid Polym. Sci.* **1993**, *93*, 98.
- 20 J. H. CHENG, A. F. FOU, M. F. RUBNER, *Thin Solid Films* **1994**, *244*, 985.
- 21 W. KONG, X. ZHANG, M. L. GAO, H. ZHOU, W. LI, J. C. SHEN, *Macromol. Rapid Commun.* **1994**, *15*, 405.
- 22 K.-U. FULDA, A. KAMPES, L. KRASEMANN, B. TIEKE, *Thin Solid Films* **1998**, *752*, 327–329.
- 23 A. KAMPES, B. TIEKE, *Mater. Sci. Eng. C* **1999**, *8–9*, 195.
- 24 B. TIEKE, K.-U. FULDA, A. KAMPES in *Nano-Surface Chemistry*, Ed.: M. Rosoff, Marcel Dekker, New York, 2001, p. 213.
- 25 *Polydiacetylenes*, Ed.: H.-J. CANTOW, in *Advances in Polymer Science*, vol. 63, Springer-Verlag, New York, 1984.
- 26 D. J. SANDMAN in *Polymeric Materials Encyclopedia*, Ed.: J. C. SALAMONE, CRC Press, Boca Raton, FL, 1996, p. 8393.

- 27 H. NAKANISHI in *Polymeric Materials Encyclopedia*, Ed.: J.C. SALAMONE, CRC Press, Boca Raton, FL, 1996, p. 8393.
- 28 H. RAU, in *Photochemistry and Photophysics*, Ed.: J.F. RABECK, CRC Press, Boca Raton, FL 1990, vol. 2, p. 119.
- 29 F. SAREMI, B. TIEKE, *Adv. Mater.* **1995**, *7*, 378.
- 30 F. SAREMI, E. MAASSEN, B. TIEKE, G. JORDAN, W. RAMMENSEE, *Langmuir* **1995**, *11*, 1068.
- 31 F. SAREMI, B. TIEKE, G. JORDAN, W. RAMMENSEE, *Supramol. Sci.* **1997**, *4*, 471.
- 32 G. WEGNER, *Pure Appl. Chem.* **1977**, *49*, 443.
- 33 K.C. LIM, L.H. FINCHER, A.J. HEEGER, *Phys. Rev. Lett.* **1983**, *50*, 1934.
- 34 M.A. MÜLLER, M. SCHMIDT, G. WEGNER, *Makromol. Chem., Rapid Commun.* **1984**, *5*, 83.
- 35 B. TIEKE, *Makromol. Chem.* **1984**, *185*, 1455.
- 36 F. SAREMI, B. TIEKE, *Adv. Mater.* **1998**, *10*, 388.
- 37 M. SHIMOMURA, R. ANDO, T. KUNITAKE, *Ber. Bunsen-Ges. Phys. Chem.* **1983**, *87*, 1134.
- 38 T. KUNITAKE, Y. OKAHATA, M. SHIMOMURA, S. YASUNANNI, K. TAKARAKE, *J. Am. Chem. Soc.* **1981**, *103*, 5401.
- 39 C.K. OBER, G. WEGNER, *Adv. Mater.* **1997**, *9*, 17.
- 40 S. ZHOU, B. CHU, *Adv. Mater.* **2000**, *12*, 545.
- 41 A. TOUTIANOUSH, B. TIEKE, *Macromol. Rapid Commun.* **1998**, *19*, 591.
- 42 A. TOUTIANOUSH, F. SAREMI, B. TIEKE, *Mater. Sci. Eng. C* **1999**, *8–9*, 343.
- 43 T. TODOROV, L. NIKOLOVA, N. TOMOVA, *Appl. Opt.* **1984**, *23*, 4309.
- 44 M.I. BARNIK, V.M. KOZENKOV, N.M. SHTYKOV, S.P. PALTO, S. G. YUDIN, *J. Mol. Electron.* **1989**, *5*, 53.
- 45 T. FISCHER, L. LÄSKER, J. STUMPE, S. KOSTROMIN, *J. Photochem. Photobiol. A: Chem.* **1994**, *80*, 4531.
- 46 A. ZIEGLER, J. STUMPE, A. TOUTIANOUSH, B. TIEKE, *Colloids Surf. A*, **2001**, *198–200*, 777.
- 47 L. LÄSKER, T. FISCHER, J. STUMPE, S. KOSTROMIN, S. IVANOV, R. SHIBAEV, R. RUHMANN, *Mol. Cryst. Liq. Cryst.* **1994**, *246*, 347.
- 48 T. FISCHER, H. MENZEL, J. STUMPE, *Supramolec. Sci.* **1997**, *4*, 543
- 49 A. IQBAL, L. CASSAR, A.C. ROCHAT, J. PFENNINGER, O. WALLQUIST, *J. Coat. Technol.* **1988**, *60*, 37.
- 50 A. IQBAL, M. JOST, R. KIRCHMAYR, J. PFENNINGER, A. ROCHAT, O. WALLQUIST, *Bull. Soc. Chem. Belg.* **1988**, *97*, 615.
- 51 Z. HAO, A. IQBAL, *Chem. Soc. Rev.* **1997**, *26*, 203.
- 52 J. MIZUGUCHI, G. WOODEN, *Ber. Bunsen-Ges. Phys. Chem.* **1991**, *95*, 1264.
- 53 M. JOST, A. IQBAL, A.C. ROCHAT (Ciba-Geigy Corp.), *Eur. Pat. Appl.* 0,224,445 (June 3, 1987).
- 54 F. SAREMI, G. LANGE, B. TIEKE, *Adv. Mater.* **1996**, *8*, 923.
- 55 J. MIZUGUCHI, G. RIHS, *Ber. Bunsen-Ges. Phys. Chem.* **1992**, *96*, 597.
- 56 F. SAREMI; Dissertation, Universität zu Köln, 1998.
- 57 G. CAO, H. HONG, T.E. MALLOUK, *Acc. Chem. Res.* **1992**, *25*, 420.
- 58 C.M. BELL, S.W. KELLER, V.M. LYNCH, T.E. MALLOUK, *Mater. Chem. Phys.* **1993**, *35*, 225.
- 59 S.D. EVANS, A. ULMAN, K.E. GOPPERT-BERARDUCCI, L.J. GERENSER, *J. Am. Chem. Soc.* **1991**, *113*, 5866.
- 60 P. KOHLI, G.J. BLANCHARD, *Langmuir* **2000**, *16*, 8518.
- 61 M.A. ANSELL, E.B. COGAN, C.J. PAGE, *Langmuir* **2000**, *16*, 1172.
- 62 H. BYRD, C.E. HOLLOWAY, J. POGUE, *ACS Polym. Prepr.* **1999**, *40(1)*, 167.
- 63 D.L. THOMSEN, T. PHELY-BOBIN, F. PAPA-DIMITRAKOPOULOS, *J. Am. Chem. Soc.* **1998**, *120*, 6177.
- 64 J.R. REYNOLDS, C. P. LILLYA, J.C.W. CHIEN, *Macromolecules* **1987**, *20*, 1184.
- 65 J.R. REYNOLDS, C.A. JOLLY, S. KRICHENE, P. CASSOUX, C. FAULMANN, *Synth. Met.* **1989**, *31*, 109.
- 66 K. HAYA, I. UCHIDA, V.D. NEFF, *Acc. Chem. Res.* **1986**, *19*, 162.
- 67 A. LUDI, *Chemie in unserer Zeit* **1988**, *23*, 123.
- 68 R.J. MORTIMER, *Chem. Soc. Rev.* **1993**, *26*, 147.
- 69 D.L. THOMSEN, F. PAPA-DIMITRAKOPOULOS, *ACS Polym. Prepr.* **1997**, *38*, 398.
- 70 M. PYRASCH, D. AMIRBEYKI, B. TIEKE, *Colloids Surf. A*, **2001**, *198–200*, 425.

- 71 M. PYRASCH, D. AMIRBEYKI, B. TIEKE, *Adv. Mater.* **2001**, *13*, 1188.
- 72 M. KANEKO, S. HARA, A. YAMADA, *J. Electroanal. Chem.* **1985**, *194*, 165.
- 73 M. VERDAGUER, *Science* **1996**, *272*, 698.
- 74 M. PYRASCH, B. TIEKE, *Langmuir* **2001**, *17*, 7706.
- 75 S. RAVAINÉ, C. LAFUENTE, C. MINGO-TAUD, *Langmuir* **1998**, *14*, 6347.
- 76 M. PYRASCH, A. TOUTIANOUSH, W. JIN, B. TIEKE, *Chem. Mater.* **2003**, accepted.
- 77 H. KARAKANE, M. TSUYUMOTO, Y. MAEDA, Z. HONDA, *J. Appl. Polym. Sci.* **1991**, *42*, 3229.
- 78 J. LUKÁS, K. RICHAU, H.-H. SCHWARZ, D. PAUL, *J. Membr. Sci.* **1995**, *106*, 281.
- 79 K. RICHAU, H.-H. SCHWARZ, R. APOSTEL, D. PAUL, *J. Membr. Sci.* **1996**, *113*, 31.
- 80 X.-P. WANG, Z.-Q. SHEN, F.-Y. ZHANG, Y.-F. ZHANG, *J. Membr. Sci.* **1996**, *119*, 191.
- 81 B. TIEKE, F.V. ACKERN, L. KRASEMANN, A. TOUTIANOUSH, *Eur. Phys. J. E* **2001**, *5*, 29.
- 82 B. TIEKE, L. KRASEMANN, A. TOUTIANOUSH, *Macromol. Symp.* **2001**, *163*, 97.
- 83 F.V. ACKERN, L. KRASEMANN, B. TIEKE, *Thin Solid Films* **1998**, *327–329*, 762.
- 84 P. STROEVE, V. VASQUEZ, M.A.N. COELHO, J.F. RABOLT, *Thin Solid Films* **1996**, *284–285*, 708.
- 85 J. NEEL in *Introduction to Pervaporation in Pervaporation Membrane Separation Processes*, Ed.: R.Y.M. HUANG, Elsevier, Amsterdam, 1991, p. 42.
- 86 L. KRASEMANN, B. TIEKE, *J. Membr. Sci.* **1998**, *150*, 23.
- 87 M. LÖSCHE, J. SCHMITT, G. DECHER, W.G. BOUWMAN, K. KJAER, *Macromolecules* **1998**, *31*, 8893.
- 88 L. KRASEMANN, B. TIEKE, *Mater. Sci. Eng. C* **1999**, *8–9*, 513.
- 89 L. KRASEMANN, B. TIEKE, *Chem. Eng. Technol.* **2000**, *23*, 211.
- 90 L. KRASEMANN, A. TOUTIANOUSH, B. TIEKE, *J. Membr. Sci.* **2001**, *181*, 221.
- 91 A. TOUTIANOUSH, L. KRASEMANN, B. TIEKE, *Colloids Surf. A* **2002**, *198–200*, 881.
- 92 A. TOUTIANOUSH, B. TIEKE; in preparation.
- 93 S.S. SHIRATORI, M.F. RUBNER, *Macromolecules* **2000**, *33*, 4213.
- 94 M. URAIRI, T. TSURU, S. NAKAO, S. KIMURA, *J. Membr. Sci.* **1992**, *70*, 153.
- 95 T. TSURU, S. NAKAO, S. KIMURA, *J. Membr. Sci.* **1995**, *108*, 269.
- 96 L. KRASEMANN, B. TIEKE, *Langmuir* **2000**, *16*, 287.
- 97 A. TOUTIANOUSH, B. TIEKE in *Novel Methods to Study Interfacial Layers*, Eds.: D. MOEBIUS, R. MILLER, Elsevier, Amsterdam, **2001**, p. 416.
- 98 A. TOUTIANOUSH, B. TIEKE. *Mater. Sci. Eng. C* **2003**, accepted.

## 16

### Self-assembly and Characterization of Electro-optic Materials

R. CLAUS, Y.-X. WANG, L. ZHANG, and K. COOPER

#### Abstract

In the 1970s, studies of electro-optic (EO) materials were focused on inorganics including lithium niobate, and semiconductors such as cadmium sulfide, selenium, and tellurium. In 1982, the first electric field-poled second-order nonlinear optical (NLO) polymers were reported [1], and since then, intensive studies have led to the development of commercial electro-optic devices based on these materials, due to their intrinsic large optical nonlinearities, architectural flexibility and ease of fabrication [2]. Several novel methods for creating noncentrosymmetric materials incorporating organic molecules with large molecular susceptibilities have been developed over the past decade. These include Langmuir–Blodgett film [3–5] and covalent self-assembled monostructure [6–8] methods, and most of this work has concentrated on poled polymeric materials [9]. The polymer systems for poled materials include guest–host systems, in which a nonlinear chromophore is incorporated as a dissolved guest in the polymer host, side-chain polymers, main-chain polymers and cross-linked polymer systems. However, the fabrication process for such electric field-poled polymers, in which the field-induced polar ordering is temporarily frozen in by cooling the poled material below the glass transition temperature of the polymers, typically employs spin-coating techniques, which are not able to provide the precisely uniform and homogeneous films generally required by low-loss photonic waveguide devices. Furthermore, the NLO response of poled polymers undergoes a spontaneous decay over time because the system is not in an equilibrium state. Electrostatic self-assembly (ESA) materials overcome this limitation.

ESA films have recently been developed, and allow detailed structural control at the molecular level with ease of manufacturing [10–18]. The ESA method involves the alternate dipping of a charged substrate into aqueous solutions of oppositely charged ions at room temperature. For the synthetic EO materials, the ESA technique has been proven to provide a noncentrosymmetric arrangement of NLO chromophores to yield thin films using commercial ionic polymer dyes and other materials [19–21]. Results for these EO materials have demonstrated the linear growth of absorbance with the number of bilayers, and thus the homogeneous deposition of the EO materials with each successive layer.

This chapter considers the design, synthesis, structure and characterization of EO materials formed by ESA processing. The first section describes molecular precursors, their synthesis routes and structures. The following section describes the fabrication and characterization of different example materials.

## 16.1

### Nonlinear Optical Polymers

#### 16.1.1

##### Design, Synthesis and Characterization of Polydyes

In order to have finite second-order susceptibility, a polymer system must consist of chromophores, which are created through the combined noncentrosymmetries of molecules. The chromophores of organic molecules possess electron donor and acceptor groups attached to a  $\pi$ -conjugated system. Several chromophores (1–3) chosen for studies are shown in Fig. 16.1. These chromophores were designed to attach to polymers, and the designed polydyes are easy to synthesize. The other important consideration required by the ESA process is that the designed polymer must contain a functional group, which allows the molecules to be converted to water-soluble salts.

Polydye 1 can be made from the reaction of poly(methacryloyl chloride) with Disperse Red 1 in the presence of triethylamine as shown in Scheme 16.1. Dioxane was a suitable solvent because both reactants, including the polymer, are soluble in it. The  $T_g$  of this polydye, which was determined from a second heating scan of a differential scanning calorimetry (DSC) measurement, was 133 °C. The chemical shift of  $^1\text{H}$  NMR, and the FT-IR spectrum confirmed the structure of the side-chain of the obtained polymer.

One of the most frequently used synthetic methods for the synthesis of polyester is the reaction of equal amounts of diacid and diol in the presence of triphenylphosphine and diethyl azodicarboxylate (DEAD) [22]. Scheme 16.2 shows the polymerization of 5-hydroxyisophthalic acid with *N*-4-[(4-cyanophenylazo)phenyl]diethanolamine, which was obtained from the reaction of *p*-cyanophenyldiazonium

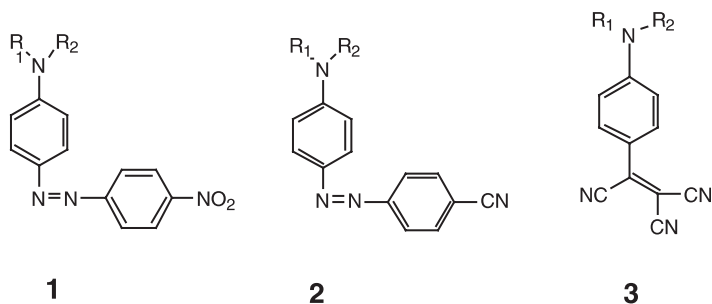
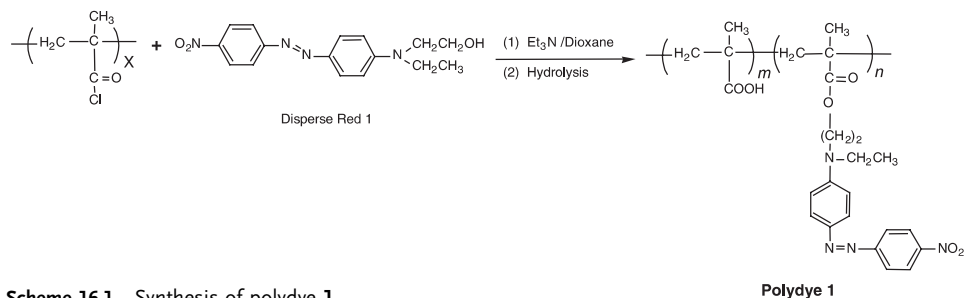
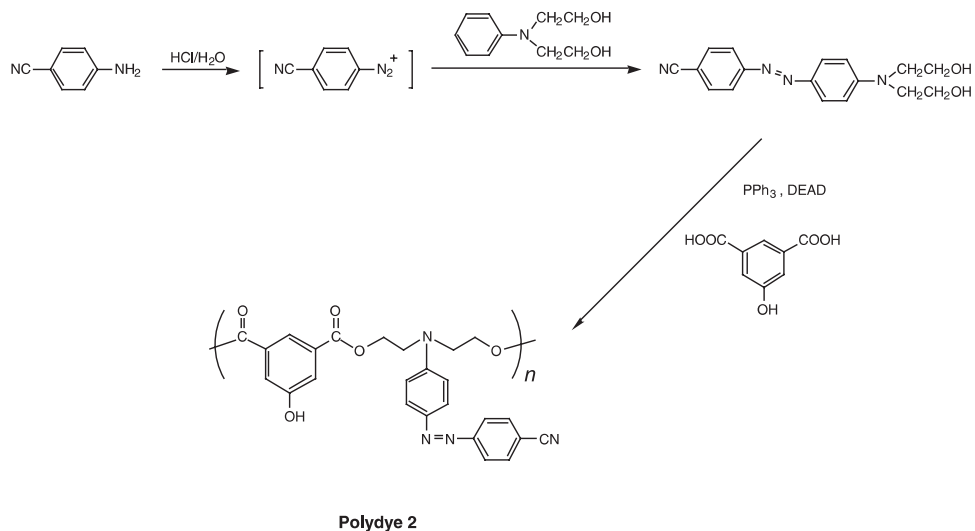


Fig. 16.1 Structures of chromophores.



Scheme 16.1 Synthesis of polydye 1

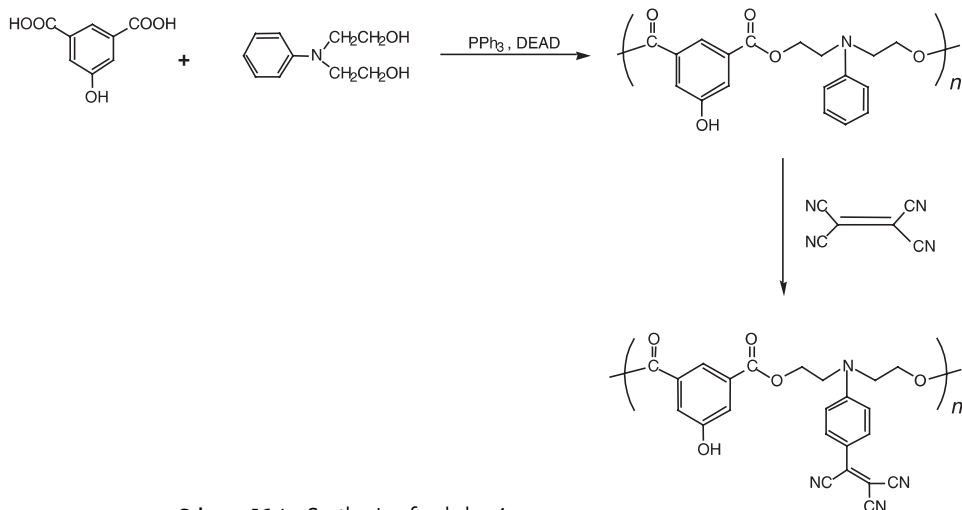
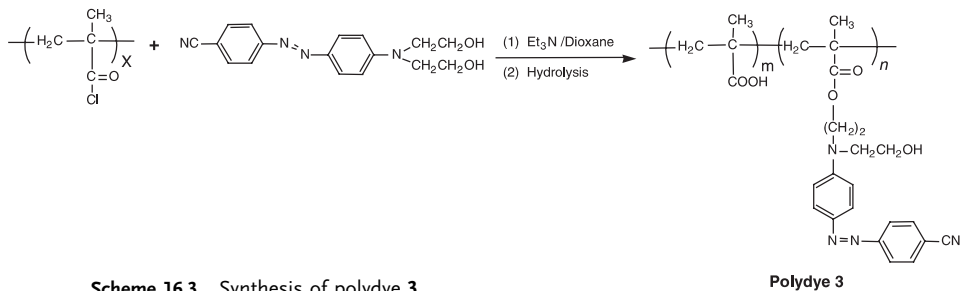


Scheme 16.2 Synthesis of polydye 2

with *N*-phenyldiethanolamine. Gel permeation chromatography (GPC) showed a weight-averaged molecular weight of 4380. The  $T_g$  of this polyester was 140 °C. The structure was also confirmed by  $^1\text{H}$  NMR and FT-IR spectroscopies.

Polydye 3 was synthesized from the reaction of poly(methacryloyl chloride) with *N*-4-[(4-cyanophenylazo)phenyl]diethanolamine using the same method as that used for polydye 1 (Scheme 16.3). The ratio ( $m/n$ ) could be also controlled by the addition ratio of Disperse Red 1 to polyacid chloride and the reaction time.

Polymerization of 5-hydroxyisophthalic acid with *N*-phenyldiethanolamine was carried out in the presence of triphenylphosphene and DEAD using the same procedure as that used for polydye 2. The obtained polyester then underwent tricyanovinylolation with tetracyanoethylene in DMF at 70 °C by a known method (Scheme 16.4) [23]. GPC measurement showed a number-averaged molecular weight of 25000. The structure was determined by  $^1\text{H}$  NMR and FT-IR spectra, which showed phenyl, hydroxy, cyano and carbonyl groups.



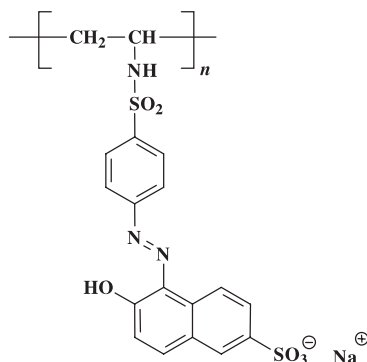
## 16.1.2

**ESA Fabrication of NLO Thin Films and Their Characterization**

Noncentrosymmetric thin films have been fabricated by ESA processing using commercial ionic polymer dyes, polydyes, such as those discussed above that have been designed and synthesized especially for  $\chi^{(2)}$  applications and other materials. Early EO thin films were made from commercial polymer dye Poly S-119 (Fig. 16.2), which consists of a poly(vinylamine) backbone with an ionic azo dye chromophore that serves as the polyanion for the ESA fabrication, while poly(allylamine hydrochloride) (PAH), which has no  $\chi^{(2)}$  response, was used for the polycation [19]. It has been found through measurements of UV-Vis absorbance and of film thickness as a function of immersion time that the formation of each monolayer is complete in less than 20 s of immersion in the polyelectrolyte. This allows the rapid build-up of self-assembled, multilayer EO films. The film is orange in color and exhibits exceptional homogeneity without scattering.



Fig. 16.2 Structure of Poly S-119.



In Fig. 16.3, the absorbance at 500 nm of several films is plotted versus the number of bilayers. The linear growth of absorbance with the number of deposited layers illustrates the homogeneous deposition of the polymer dye with each successive layer. The thickness, determined by ellipsometry, as a function of the number of deposited bilayers for Poly S-119 is shown in Fig. 16.4. Each bilayer is found to have a thickness of 1.2 nm.

Multi-layer thin films of synthetic polydyes were also self-assembled on glass substrates with poly(diallyldimethylammonium chloride) (PDDA) as the passive polycation layer [21]. Polydyes were converted to water-soluble sodium or ammonium salts before ESA fabrication. The films are grown monolayer by monolayer by first immersing an initially charged substrate into aqueous PDDA solution. This is followed by rinsing and then by immersion of the substrate into a solution of polydye salt. The dipping process can be repeated as many times as de-

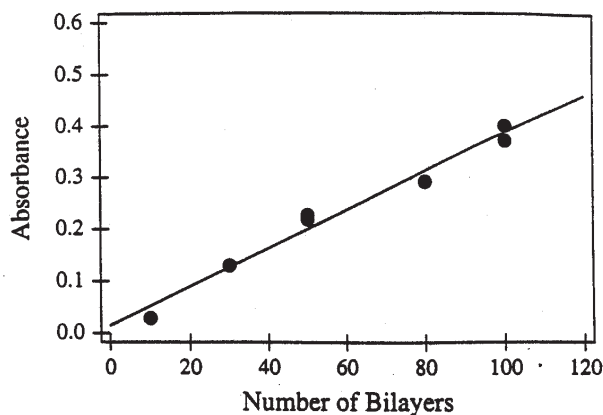


Fig. 16.3 Absorbance at 500 nm as a function of number of Poly S-119/PAH bilayers.

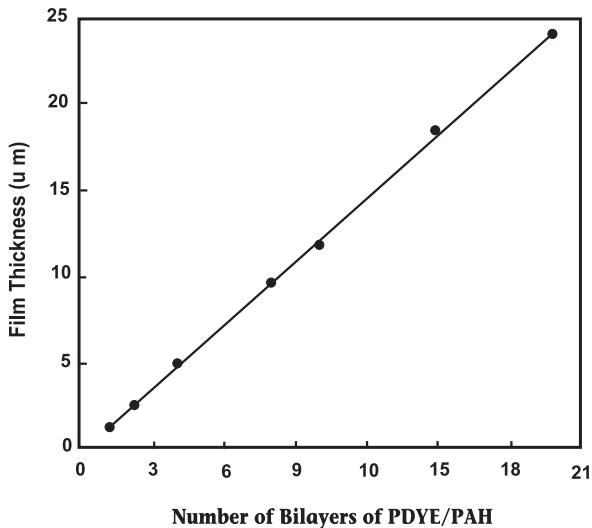


Fig. 16.4 Film thickness as a function of the number of Poly S-119/PAH multilayers.

sired. UV-Vis spectroscopy was used to monitor the ESA process, and to characterize of the NLO thin films. The absorbance peaks ( $\lambda_{\max}$ ) of polydyes 1–4 are at 470, 435, 445 and 365 nm, respectively. The ESA method provided films of excellent uniformity. As an example, the UV-Vis spectrum of 30 bilayers of PDDA/polydye 2 film (Fig. 16.5) exhibits a linear increase with the addition of bilayers, indicating that each bilayer contributes an equal amount of material to the thin-film growth [21]. In addition, the maximum differences between data collected at different locations across each film are, at most, a few percent, indicating excellent uniformity of the films. The ESA method therefore produces thin films that

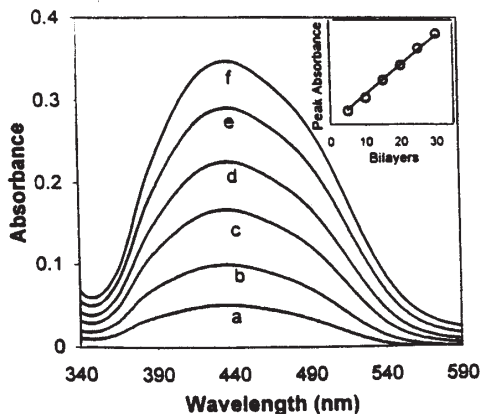


Fig. 16.5 UV-Vis spectra of polydye 2/PDDA ESA films: (a) 5, (b) 10, (c) 15, (d) 20, (e) 25, and (f) 30 bilayers. The inset shows the linear relationship between absorbance at 435 nm and the number of bilayers assembled.

are homogeneous through the film thickness as well as across the width and length of the film.

### 16.1.3

#### Nonlinear Optical Measurements

Second harmonic generation (SHG) experiments were performed by use of both the 1064 nm fundamental wavelength of a Q-switched Nd:YAG laser and the 1200 nm output from a broadband, BBO optical parametric oscillator (OPO) [19]. The OPO is pumped by the 355 nm third harmonic of the Nd:YAG and is continuously tunable from 400 to 2500 nm. The 504 nm OPO signal beam is removed from the 1200 nm idler beam using a 700 nm long pass filter. The incident intensity and polarization on the sample are controlled by a pair of Glan-Laser polarizing prisms. The incident fundamental intensity into the sample is measured using a beamsplitter and photodiode. The polymer sample was held at a 45° angle to the incident laser beam. A quartz crystal was used as a reference sample.

To determine the  $\chi^{(2)}$  of the polydye films, the SHG data for polydye thin films was fit to  $I_{2\omega} = A(I_{\omega})^2$ , where  $I_{2\omega}$  and  $I_{\omega}$  are the second harmonic and fundamental intensities, respectively [21]. The dependence of the second harmonic intensity on film thickness and  $\chi^{(2)}$  is given by

$$I_{2\omega} \propto (l_c \chi_{\text{eff}}^{(2)})^2 \sin^2 \left[ \frac{\pi l}{2l_c} \right], \quad (1)$$

where  $l$  is the sample thickness,  $l_c = \lambda / [4(n^{2\omega} - n^{\omega})]$  is the coherence length, and  $\chi_{\text{eff}}^{(2)}$  is the effective susceptibility determined by sample geometry and the nonzero components of the  $\chi^{(2)}$  tensor. In the limit that the sample thickness is much less than the coherence length, the second harmonic intensity is quadratic in the film thickness. Since the film studied here are in the  $l \ll l_c$  limit, the SHG intensity is expected to grow quadratically with the number of bilayers.

Fig. 16.6 illustrates the dependence of the SHG signal intensity as a function of the incident fundamental intensity for a single-sided, 68 bilayer Poly S-119/PAH film. The solid curve is a best fit to the data of the form  $I_{2\omega} = A(I_{\omega})^b$ . The fit yields a value of  $b = 2.02$ , in excellent agreement with the expected quadratic dependence on fundamental intensity.

When the ESA films are rotated to normal incidence, negligible SHG is observed. This is consistent with the expectation that the alignment of the chromophores occurs perpendicular to the substrate. Furthermore, when the sample is oriented at 45° to normal incidence and the polarization of the fundamental beam is varied, the SHG intensity is observed to vary smoothly from a maximum for horizontal, p-polarized light to a minimum for vertical, s-polarized light, again consistent with dipolar orientation perpendicular to the substrates. In Fig. 16.7,  $(I_{2\omega})^{1/2}$  is plotted versus the number of bilayers for several Poly S-119/PAH films. The data are seen to be in excellent agreement with the quadratic dependence.

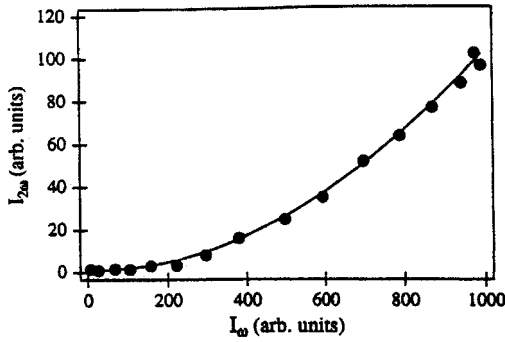


Fig. 16.6 Dependence of the second harmonic intensity at 600 nm on the fundamental intensity at 1200 nm for a single-side 68 bilayer Poly S-119/PAH ESA film.

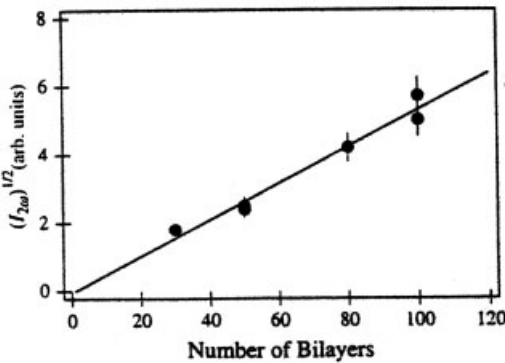


Fig. 16.7 Square root of the measured second harmonic intensity,  $(I_{2\omega})^{1/2}$ , as a function of the number of bilayers for Poly S-119/PAH films.

This demonstrates that the orientation of the chromophores is the same for each successive layer.

By comparison to the Maker fringe pattern generated by translation quartz, where across the fundamental beam the  $\chi^{(2)}$  value of the Poly S-119/PAH film is found to be 0.70 times the value of quartz, or  $1.34 \times 10^{-9}$  esu, these films exhibited no measured decay of  $\chi^{(2)}$  over a period of more than one year. Because the films *self-assemble* into the noncentrosymmetric, polar-ordered state, this thermodynamically stable state does not exhibit decay over time. This is in sharp contrast to the behavior of electro-optic poled polymers.

In order to investigate the thermal stability of ESA films, a 100 bilayer Poly S-119/PAH sample was heated to  $150^\circ\text{C}$  over the course of 3 h. The temperature was maintained at the intermediate values of  $50^\circ\text{C}$  and  $100^\circ\text{C}$  long enough to allow measurement of the second harmonic intensity. Fig. 16.8 shows data for 23, 50, 100, and  $150^\circ\text{C}$  as the sample was heated. The second harmonic intensity was observed to decrease monotonically as the temperature was raised. Once the temperature stabilized at  $150^\circ\text{C}$ , the sample was maintained at this temperature for 15 h. In Fig. 16.9, SHG data are shown for this initial time at  $150^\circ\text{C}$  as well as for 3.2, 5.6, and 15.3 h after the temperature had reached  $150^\circ\text{C}$ . Nearly identical curves for the SHG signal were observed throughout this time period. It is clear

Fig. 16.8 Second harmonic intensity as a function of incident fundamental intensity for Poly S-119/PAH film as the temperature is raised to 150°C.

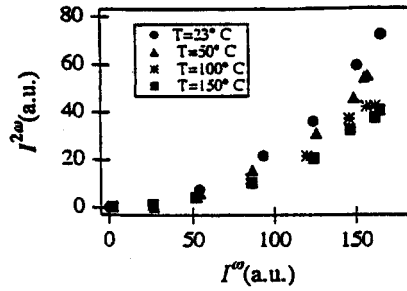
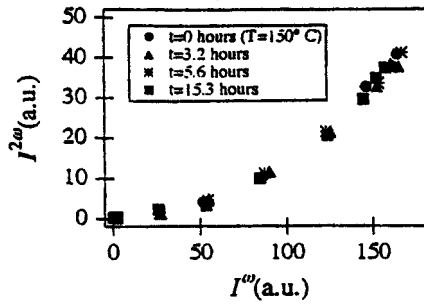


Fig. 16.9 Second harmonic intensity as a function of incident fundamental intensity for Poly S-119/PAH film as the temperature is maintained at 150°C.



that the  $\chi^{(2)}$  response of the sample exhibited exceptional stability at this elevated temperature for greater than 15 h.

Second harmonic generation experiments were carried out on the first two polymers we have designed and synthesized, using the 68 bilayer Poly S-119/PAH film as a standard reference material. Since the  $\chi^{(2)}$  of the PS-119/PAH film had been determined previously ( $0.56 \text{ pm V}^{-1}$ ), the  $\chi^{(2)}$  of the other ESA thin films could be rapidly determined by comparison to this reference. In this limit, the  $\chi^{(2)}$  value is determined by Eq. (2), where  $A$  is the coefficient of the fit to the second harmonic intensity as a function of fundamental intensity and  $l$  is the path length through the sample, i.e. the film thickness.

$$\chi^{(2)} = \chi_{\text{ref}}^{(2)} \sqrt{\frac{A}{A_{\text{ref}}}} \frac{l_{\text{ref}}}{l} \quad (2)$$

Figs. 16.10 and 16.11 illustrate the comparison of second harmonic intensity of polydye 1 and polydye 2 films with that for a Poly S-119/PAH film [21]. Since the thickness of the ESA films is much less than the second harmonic coherence length, the observed second harmonic intensity increases quadratically with the thickness of a given material. Although the second harmonic intensity of polydye 2 film in Fig. 16.11 is slightly less than that of the reference film, the Poly S-119 film is 30% thicker than the polydye 2 film. Equation (2) therefore results in a  $\chi^{(2)}$  value of  $0.62 \text{ pm V}^{-1}$ , a 10% increase over the Poly S-119 film. The polydye 1 film

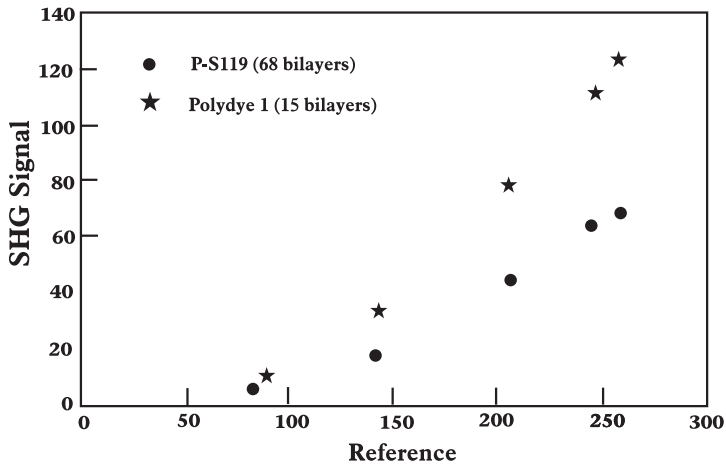


Fig. 16.10 Comparison of second harmonic intensities observed for a 15 bilayer polydye 1/PDDA film and a 68 bilayer Poly S-119/PAH film.

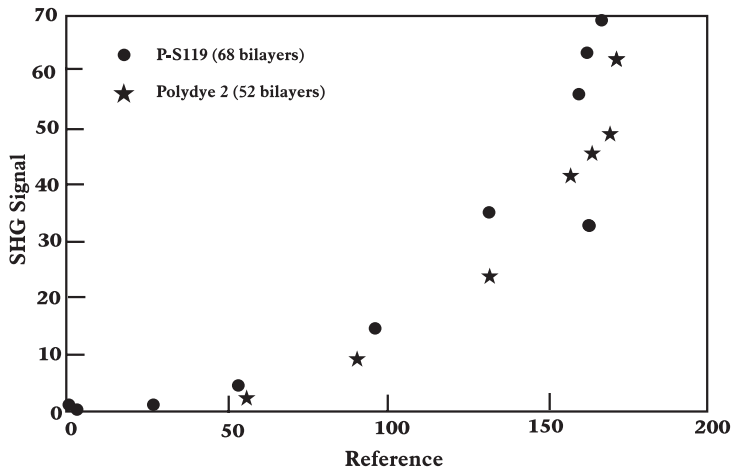


Fig. 16.11 Comparison of second harmonic intensities observed for a 52 bilayer polydye 2/PDDA film and a 68 bilayer Poly S-119/PAH film.

is much thinner than the reference film and yet exhibits a second harmonic intensity twice as large as the Poly S-119 film. The  $\chi^{(2)}$  of the polydye 1 film is thus found to be  $3.61 \text{ pm V}^{-1}$ , an increase of more than a factor of six over that of ESA films of commercially available NLO polymers.

## 16.2

## Electrostatic Self-assembly of CLD-1 Thin Films

EO polymers have been developed in part due to interest in these materials in high speed, low-drive-voltage modulators [24–25]. Traditional EO polymer modulators use a Mach–Zehnder interferometer architecture with only one arm modulated with a microstripline electrode [26]. The  $V_{\pi}$  of such a modulator can be expressed as

$$V_{\pi} = \lambda h / n^3 r_{33} L \Gamma, \quad (3)$$

where  $\lambda$  is the optical wavelength,  $h$  is the gap between electrodes,  $n$  is the index of refraction,  $r_{33}$  is the interaction length, and  $\Gamma$  is a modal overlap integral. The most effective approach for low  $V_{\pi}$  can be realized by the increase in the EO coefficient  $r_{33}$ . Dalton developed a series of EO polymers, including CLD-1 [27]. For this material, an EO coefficient over  $60 \text{ pm V}^{-1}$  has been demonstrated at 1318 nm. The structure of CLD-1 is shown in Fig. 16.12.

It should be noted that the fabrication of EO modulator devices involves the synthesis of multiple layers and regions of materials having different and controlled constitutive properties (permittivity, electrical conductivity). Subject to thickness properties, ESA processing may provide alternative routes to the formation of portions of the devices aside from the active waveguide material alone.

## 16.2.1

## Modification of CLD-1 and Fabrication of CLD-1 thin films

Dalton and coworkers have developed a CLD-1/poly(methylmethacrylate) guest–host system for fabrication of an optical intensity modulator [27]. In order to use this material for the ESA process, we have modified CLD-1 with sulfuric acid to form water-soluble sulfonated CLD-1. The aqueous solutions of sulfonated CLD-1 and PDDA were then used to ESA fabricate thin films on ITO-coated glass substrates. The layer by layer process was carried out at room temperature to form a 40 bilayer thin film. The thickness of the resulting film was 100 nm.

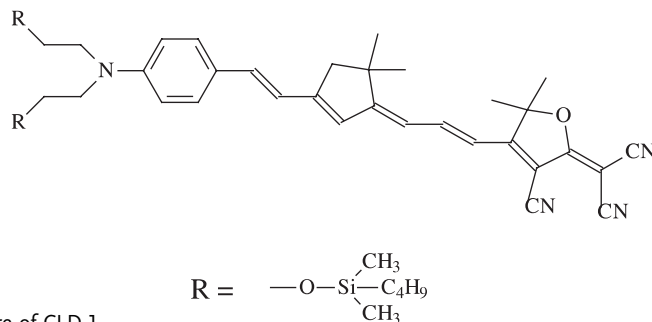


Fig. 16.12 The structure of CLD-1.

## 16.2.2

## Measurements of Electro-optic Properties

The electro-optic properties of the samples were measured by employing the Mach-Zehnder interferometric set-up shown in Fig. 16.13 [28–31]. Since the samples are very thin, a glass ring spacer of thickness 45  $\mu\text{m}$  with a central hole of di-

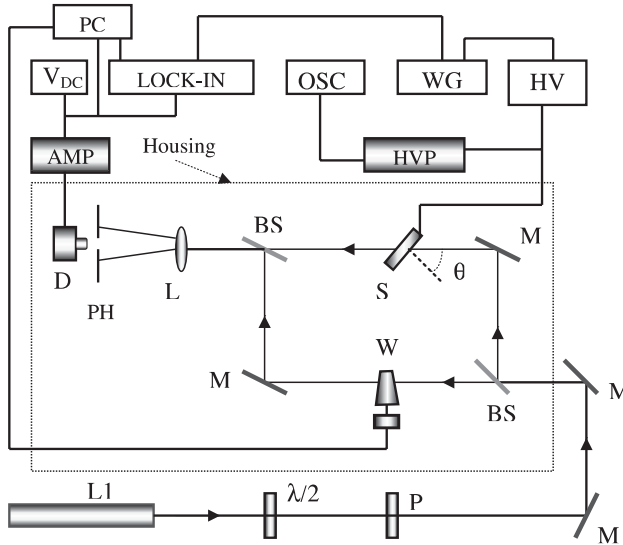


Fig. 16.13 Mach-Zehnder interferometric set-up for linear electro-optic effect measurements. L1, He-Ne laser;  $\lambda/2$ , half-wave plate at 632.8 nm; P, polarizer; S, sample; D, silicon photodetector; AMP, amplifier;  $V_{DC}$ , mul-

timer; HVP, high-voltage probe; LOCK-IN, lock-in amplifier; OSC, oscilloscope; WG, waveform generator; HV, high voltage amplifier; PC, computer; W, glass wedge; BSs, beamsplitters; Ms, mirrors; PH, pin hole; L, lens.

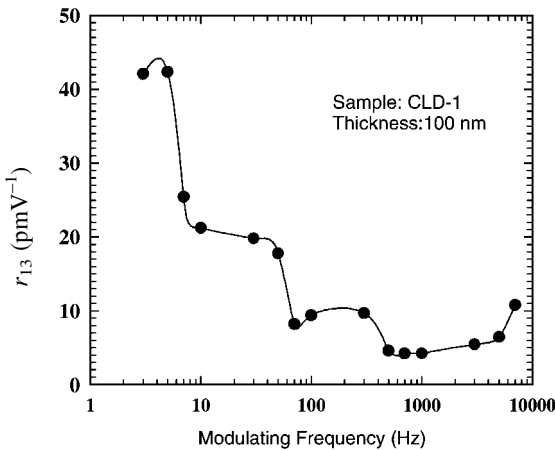
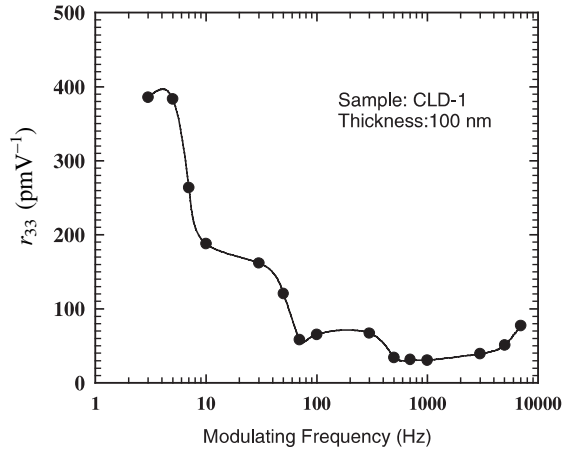


Fig. 16.14 Modulating frequency dependence of  $r_{13}$ .



Fig. 16.15 Modulating frequency dependence of  $r_{33}$ .



ameter 25 mm that allows the incident beam to impinge the sample directly, was placed between one ITO electrode and the film. A high voltage amplifier (Trek 610C) provided a sinusoidal waveform at a level of  $\sim 1 \text{ V } \mu\text{m}^{-1}$  as the modulating field. The magnitude of the AC modulating voltage applied to the sample was measured using a high voltage passive probe (Tektronix P6015) and an oscilloscope (Tektronix TDS 210). The employed laser intensity incident on the sample is  $220 \text{ mW cm}^{-2}$  at 632.8 nm. The modulation of the laser beam was detected by a silicon photodetector (UDT Pin 10) coupled with a transducer-amplifier (UDT Tramp), and measured using both a lock-in amplifier (Stanford Research System SRS850 DSP) and a dc multimeter (Hewlett Packard Digital 34401A). Data acquisition was performed with a PC. For each experimental data point, measurements were collected for 200 s and the average was taken. In this experiment, the response of each electronic device, namely the high voltage amplifier, the high voltage probe and the transducer amplifier was determined at each measured frequency to ensure a proper characterization of the electro-optic modulation of the samples. The highest measured modulating frequency, 10 kHz, was limited by the bandwidth of the high voltage amplifier supplying the modulating voltage.

To demonstrate the birefringence contribution to the overall electro-optic coefficients, we performed the electro-optic measurements over a broad range of modulating frequency ( $2\text{--}10^4$  Hz). The frequency dependences of the electro-optic coefficients  $r_{13}$  and  $r_{33}$  of the CLD-1 ESA film are presented in Figs. 16.14 and 16.15.

To compare with the ESA thin film of CLD-1, we also fabricated CLD-1/PMMA films by spin coating with a thickness of  $6 \mu\text{m}$ . The weight ratio of CLD-1 and PMMA is 1:32. The poling was performed at  $103^\circ\text{C}$  for 1 h at 120 V. The frequency dependences of the electro-optic coefficients  $r_{13}$  and  $r_{33}$  of CLD-1/PMMA poled film are shown in Figs. 16.16 and 16.17.

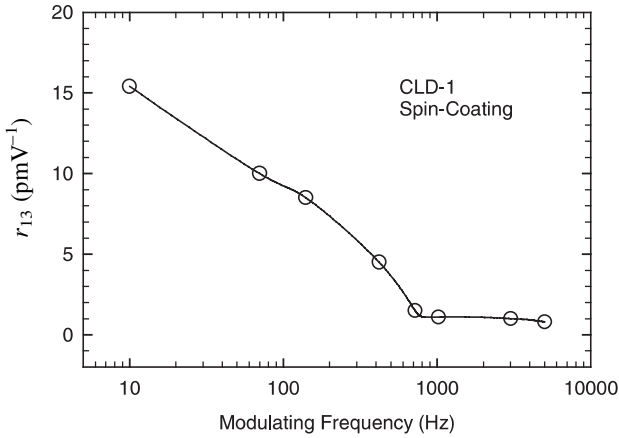


Fig. 16.16  $r_{13}$  of CLD-1/PMMA film.

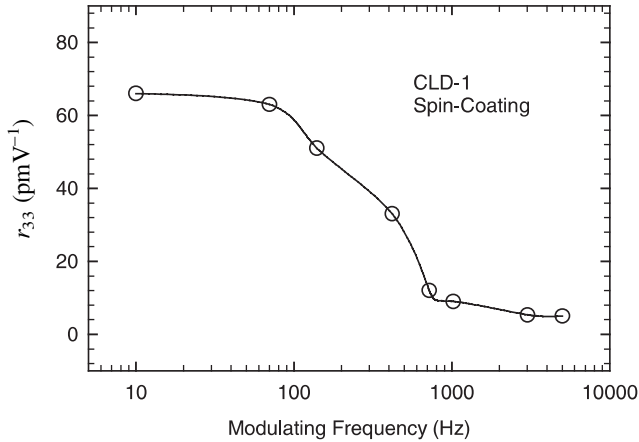


Fig. 16.17  $r_{33}$  of CLD-1/PMMA film.

### 16.3

#### Electrostatic Self-assembly of CdSe/PDDA Thin Films

Nanometer-scale materials promise to be important in the development of next-generation electronics and optoelectronic devices. II–VI and III–V semiconductor quantum dots such as CdSe [32, 33] and CdS [34] are particularly attractive because their optical emission and absorption are directly determined by their dimensions. Several groups have reported their synthesis [32, 34–36]. Incorporating such quantum dots into polymer films is of increasing interest because of their application in guided wave nonlinear optics and optical communication devices [27, 37–39]. We have used the ESA method for the creation of noncentrosym-

metric CdSe quantum dot-doped thin films with substantial second-order susceptibility. The advantages of this technique include simple, rapid, inexpensive production, long term and thermal stability of  $\chi^{(2)}$  [40], and the avoidance of a high electric poling field to produce even-order nonlinear optical properties.

### 16.3.1

#### Fabrication and characterization

CdSe quantum dots were modified with mercaptoacetic acid in methanol under nitrogen. The pH was adjusted to 10 by addition of tetramethylammonium hydroxide, and the reaction mixture was refluxed for 4 h. The mercaptoacetic acid-passivated CdSe quantum dots were purified by several cycles of precipitation with acetone followed by dissolution in methanol. Multilayer CdSe/PDDA films were fabricated on the ITO-coated glass substrates by the ESA process. An atomic force microscopy (AFM, DI Nanoscope IIIA) image of the film is shown in Fig. 16.18. One can see that the particle size of the CdSe quantum dots is about 2–3 nm, with a narrow size distribution.

The ESA process was monitored by UV–Vis spectroscopy and Fig. 16.19 shows the absorbance of a CdSe/PDDA 40 bilayer film versus the number of bilayers. The thickness was determined by ellipsometric measurements to be 150 nm. UV–Vis spectroscopy (Hitachi U-2001) was used to record the absorbance spectra of this sample. One can see that the peak absorption wavelength is approximately 580 nm.

To determine the concentration of CdSe in the thin film, XPS measurements were also performed by using a Perkin-Elmer 5400 spectrometer equipped with an X-ray Mg anode. Data were obtained with Mg- $K_{\alpha}$  radiation (1253.6 eV) at a power of 300 W. Survey scans were collected over the range 0–1100 eV. Close-up

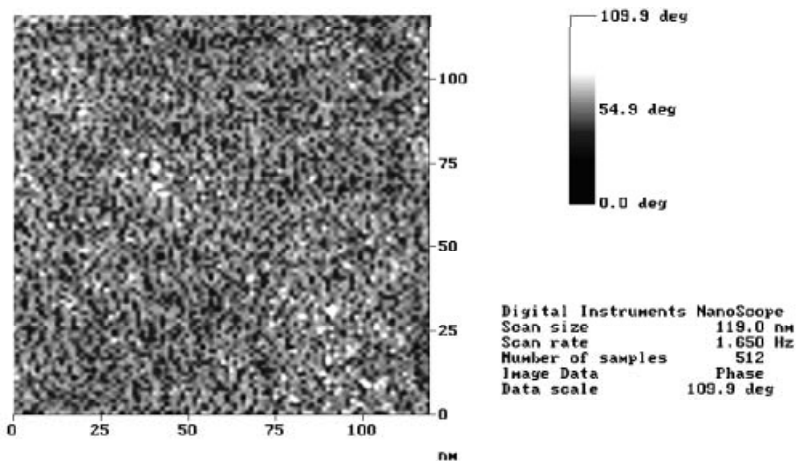


Fig. 16.18 AFM image of the CdSe/PDDA nanocomposite film.

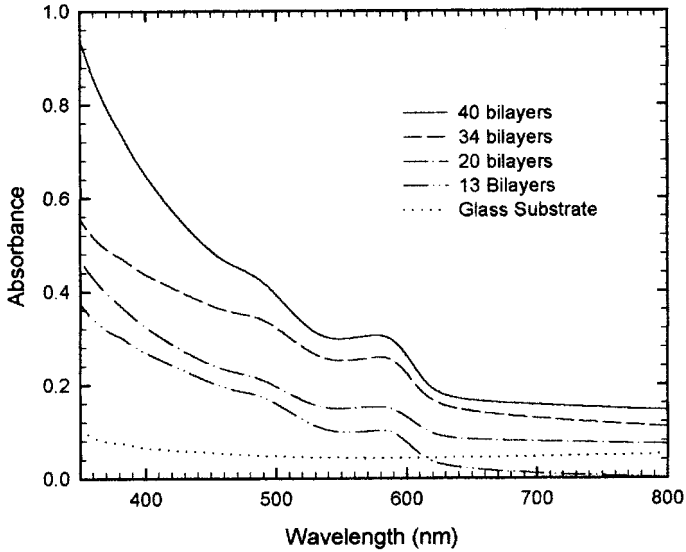


Fig. 16.19 UV-Vis spectra of the CdSe/PDDA ESA film.

scans were collected on the peaks of interest for the different elements with a 71.5 eV pass energy detection and a resolution of 1 eV. A base pressure of  $10^{-8}$  Torr was maintained during the experiments. From the XPS spectrum (Fig. 16.20), one can calculate that the concentration of CdSe quantum dots in the film is 2.14% (w/w).

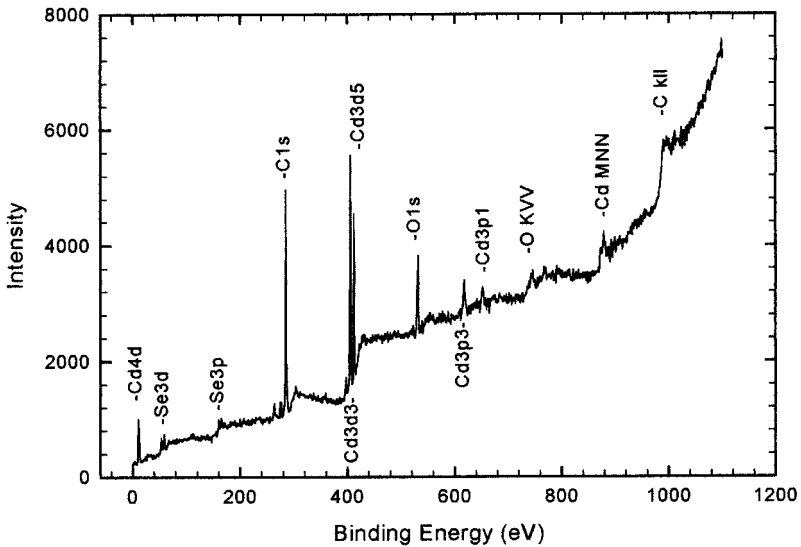


Fig. 16.20 XPS survey spectrum of the CdSe/PDDA film.

## 16.3.2

**Electro-optic Modulation Measurements**

The polymer films have a  $C_{\infty v}$  symmetric geometry. According to Kleinmann's symmetry rules [39,41],  $r_{113}$  and  $r_{333}$  (usually called  $r_{13}$  and  $r_{33}$ , respectively) are the only nonzero elements of the linear electro-optic tensor, and  $r_{1133}$  and  $r_{3333}$  are the only nonzero elements that describe the quadratic electro-optic effect. Two different techniques are usually used to investigate the electro-optic properties of thin film polymer materials. The first popular configuration is the ellipsometric technique [42, 43] utilizing a single laser beam, where the transmission amplitude modulation that results from beating the modulation of a wave polarized in the plane of incidence (p wave) against that of a wave polarized perpendicular to the plane of incidence (s wave) is detected. This measurement is relatively easy to perform, but allows only for determination of the difference  $r_{333}-r_{113}$ . In order to separate these two coefficients, one has to make an assumption concerning the relation between  $r_{333}$  and  $r_{113}$ . For a weak poling field condition in thin film polymers  $r_{333}/r_{113}=3$  [29, 42]. For our ESA-synthesized materials, a small correction to this ratio is required. The second conventional technique used in electro-optic property studies is based on Mach-Zehnder interferometry [28–30]. This technique, although tedious, allows a straightforward independent determination of the electro-optic coefficients  $r_{113}$  and  $r_{333}$ . Here, we use Mach-Zehnder interferometry to measure the linear electro-optic modulation and determine the ratio of the linear electro-optic coefficients  $r_{333}$  and  $r_{113}$ . Then, we use the simple ellipsometric technique to investigate the quadratic electro-optic modulation, and use the value of the coefficient ratio obtained by the Mach-Zehnder measurements to calculate the quadratic electro-optic coefficients  $r_{1133}$  and  $r_{3333}$  because it is difficult to derive the formulas to calculate them based on Mach-Zehnder data.

**16.3.2.1 Linear Electro-optic Modulation Measurement**

The electro-optic properties of the sample materials were measured by employing the conventional Mach-Zehnder interferometric set-up shown in Fig. 16.13 in Section 16.2. In addition, a polycarbonate housing enclosing the entire measurement system was used to reduce the influence of air fluctuations on the stability of the interferometer. The reference arm of the interferometer contains a glass wedge, which can be slowly translated by a stepper motor to produce a controllable phase shift between the two interfering optical beams. The electro-optic sample is mounted on a rotation stage and placed in the signal arm of the interferometer. When a modulating voltage is applied to the sample, a change in the refractive index, as well as a change in the path length due to the change in the refraction angle, occurs. The resulting phase modulation of the signal beam [28–30, 42–45] is

$$\Delta\Phi_{ac} = \frac{2\pi}{\lambda}(s\Delta n + n\Delta s), \quad (4)$$

where  $\lambda$  is the optical wavelength,  $n$  is the refractive index of the material, and  $s$  is the optical path length given by  $s=d/\cos a$ ; here,  $d$  is the thickness of the sample and  $a$  is the angle of refraction. This phase shift causes a modulation of the light intensity exiting the interferometer, and the relationship between the phase and intensity modulation can be expressed as

$$\Delta\Phi_{ac} = 2\sqrt{2} \frac{I_{ac,rms}}{I_{max} - I_{min}}, \quad (5)$$

where  $I_{ac,rms}$  is the modulated intensity due to the ac electric field, and  $I_{max}$  and  $I_{min}$  are the maximum and the minimum intensities associated with a  $\pi$  phase shift of the reference beam due to the wedge translation. For the case of s-polarized light obliquely illuminating the sample, a general formula for the  $r_{113}$  coefficient of the material can be determined from Eqs. (4) and (5) with the approximation that  $n_e \cong n_o = n$ ; it is given as

$$r_{113} = \frac{2\lambda}{\pi n V_{ac,rms}} \cdot \frac{I_{ac,rms}}{I_{max} - I_{min}} \cdot \frac{(1 - \sin^2 \theta/n^2)^{3/2}}{n^2 - 2 \sin^2 \theta}. \quad (6)$$

Here,  $V_{ac,rms}$  is the modulating voltage applied to the sample and  $\theta$  is the external angle of the incidence signal beam on the sample. For p-polarization of the laser beam, we obtain the expression relating to the coefficients  $r_{113}$  and  $r_{333}$  as

$$r_{333} \sin^2 a + r_{113} \cos^2 a = \frac{2\lambda}{\pi n V_{ac,rms}} \cdot \frac{I_{ac,rms}}{I_{max} - I_{min}} \cdot \frac{(1 - \sin^2 \theta/n^2)^{3/2}}{n^2 - 2 \sin^2 \theta}. \quad (7)$$

Therefore, by measuring the modulation for both light polarizations and from Eq. (6) and (7), one can obtain independent values for  $r_{113}$  and  $r_{333}$ .

The CdSe nanocluster/polymer thin film samples were sandwiched between two ITO-coated glass substrates. The samples were then sealed using UV-curable epoxy. Before making measurements, the samples were irradiated by a UV-light source for several hours to ensure that the epoxy fully cured and sealed firmly. A high voltage amplifier (Trek 610C) provided a sinusoidal drive waveform at a level of  $\sim 1 \text{ V } \mu\text{m}^{-1}$  as the modulating field. No external poling electric field was applied across the sample. Measurements were then performed using the same approach as used for the CLD-1 films described above.

Figs. 16.21 and 16.22 show the results obtained for  $r_{113}$  and  $r_{333}$ , respectively. Symbols and solid lines correspond to experimental measurements and fitted results, respectively. One can see that the maximum  $r_{333}$  at a modulating frequency of 30 Hz is  $560 \text{ pm V}^{-1}$  and both electro-optic coefficients  $r_{113}$  and  $r_{333}$  undergo a rapid decrease at frequencies less than around 100 Hz. At frequencies higher than 100 Hz, they continue to decrease slowly until reaching a diminished stable value. Reference [30] reports that CdSe quantum dots exhibit a large permanent dipole moment of  $25 \sim 47 \text{ D}$ . It is well-known that this moment can be rotated and oriented by the application of an external electric field [46, 47]. When a modulating

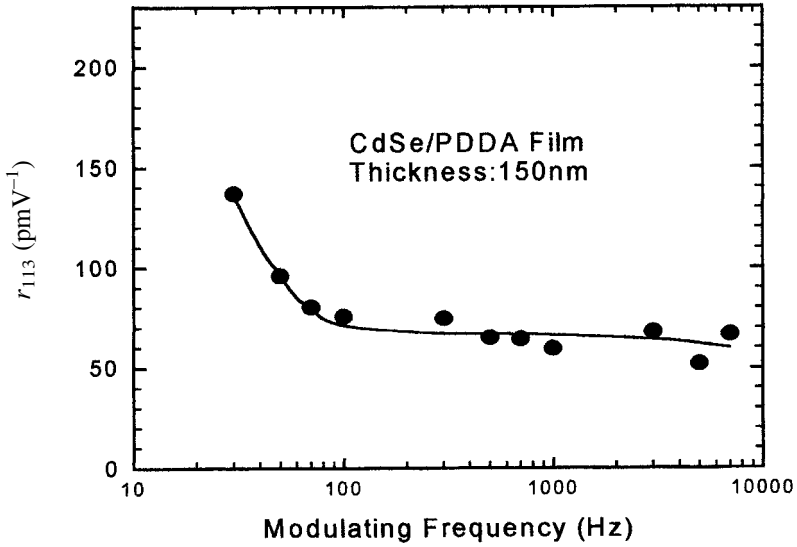


Fig. 16.21  $r_{113}$  as a function of modulating frequency measured using the Mach-Zehnder set-up. Symbols and solid line indicate the measured and fitted results, respectively.

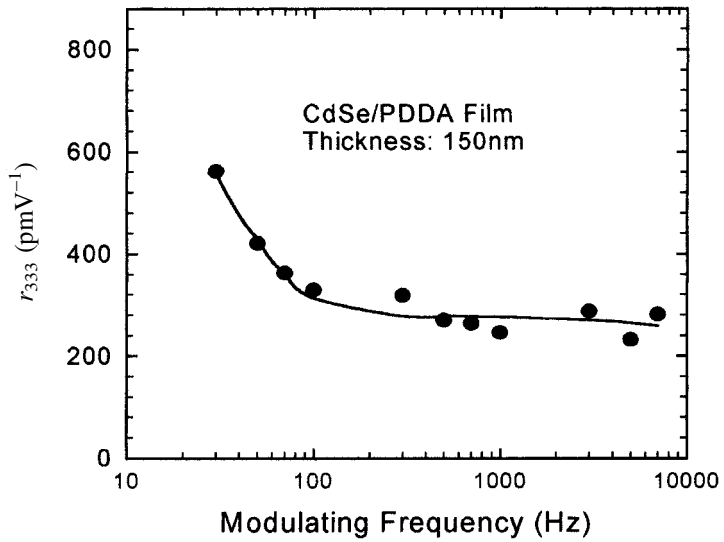


Fig. 16.22  $r_{333}$  as a function of modulating frequency measured using the Mach-Zehnder set-up. Symbols and solid line indicate the measured and fitted results, respectively.

voltage is applied across the sample, a modulating torque will be applied to the quantum dots. This results in an orientation distribution induced by the external electric field at lower frequencies, at which the quantum dots can respond. This orientation distribution of the permanent dipole moment can contribute to the electro-optic modulation. At higher modulating frequencies, because the quantum dots cannot follow the rapid modulation of the electric field to complete their rotation, the permanent dipole moment no longer has significant contribution to the electro-optic modulation.

To determine the typical frequency of orientation, let us review the tensor components of the molecular second-order susceptibility. In the one-dimensional case [47],

$$r_{113} \sim N\beta_{zzz}^*[(1/5)A_1 - (1/5)A_3], \quad (8)$$

and

$$r_{333} \sim N\beta_{zzz}^*[(3/5)A_1 + (2/5)A_3], \quad (9)$$

where  $N$  is the number density of quantum dots,  $A_1$  and  $A_3$  are order parameters of the Legendre polynomials, and  $\beta_{zzz}^*$  is the only nonvanishing, local-field-corrected second-order optical susceptibility of single quantum dots.

From Eqs. (8) and (9), one can see that the data in Fig. 16.21 and 16.22 indicate the frequency dependence behavior of  $\beta_{zzz}^*$ . To fit the experimental data in Fig. 16.21 and 16.22, let us write

$$\beta_{zzz}^* = a_0 + a_1 \exp(-f/f_{10}) + a_2 \exp(-f/f_{20}), \quad (10)$$

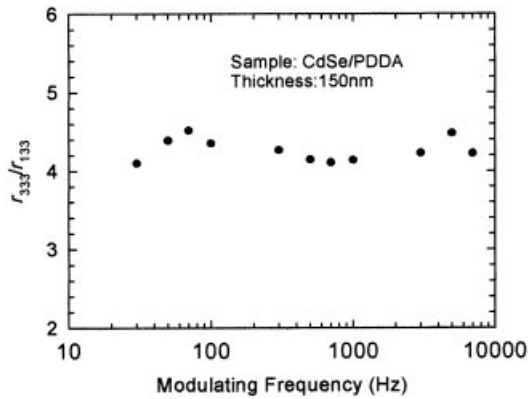
where the first term,  $a_0$ , represents the contribution of pure electron movement, the second term depicts the contribution from the permanent dipole moment orientation, and the third term arises from the induced dipole moment contribution. The terms  $a_0$ ,  $a_1$  and  $a_2$  are constants,  $f_{10}$  and  $f_{20}$  are two typical limiting frequencies for the permanent dipole and induced dipole moments, respectively, and  $f$  is the modulating frequency.

The solid lines in Fig. 16.21 and 16.22 show the fitted results. The two typical frequencies obtained are  $f_{10}=28.5$  Hz and  $f_{20}=5.8 \times 10^4$  Hz. From the value of  $f_{10}$ , one can see that a CdSe quantum dot needs  $1/2f_{10}=17.5$  ms to complete its physical orientation due to a rotation of its permanent dipole moment. Therefore, at lower frequencies ( $<100$  Hz), electro-optic modulation mainly stems from the orientation of the permanent dipole moment. At frequencies higher than 100 Hz, the electro-optic modulation mainly arises from the induced dipole moment orientation and pure electron movement.

Fig. 16.23 shows the ratio of  $r_{333}/r_{113}$  calculated from the measured data obtained with the Mach-Zehnder set-up. One can see that the ratio based on experimental measurement varies between 4.1 and 4.5 at different modulating frequencies.



**Fig. 16.23** Obtained ratios of  $r_{333}/r_{113}$  as a function of modulating frequency obtained using measured data from the Mach-Zehnder set-up. One can see that the ratio varies slightly with the modulating frequency.

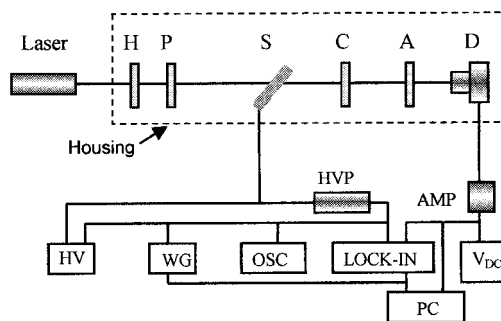


### 16.3.2.2 Quadratic Electro-optic Modulation

As we mentioned above, since it is difficult to derive concise equations to calculate  $r_{1133}$  and  $r_{3333}$  from the Mach-Zehnder configuration data, we employed the conventional ellipsometric set-up to investigate the quadratic electro-optic modulation. The experimental set-up is shown in Fig. 16.24.

In this configuration, the modulation of the refractive index of the sample by the externally applied AC electric field causes a phase retardation between the s and the p-polarized components of the incident beam. The input beam, polarized at  $45^\circ$  with respect to the plane of incidence (this results in equal amplitude components of the s and p polarizations), passes through the sample, propagates through the compensator and analyzer, and impinges onto a photodetector, which operates in the photovoltaic mode. The signal from the detector is amplified by the current/voltage transducer/amplifier (UDT Tramp), and measured using both a DC voltmeter (Hewlett Packard digital multimeter 34401A), and a lock-in amplifier (Stanford Research Systems SRS 850 DSP). This lock-in amplifier allows us to measure the modulated signal intensity either at the fundamental frequency (linear) or at second harmonic frequency (quadratic). The magnitude of the detected light intensity depends on the phase shift  $\varphi_{sp}$  between the s and the p components of the light signal, and can be expressed as

**Fig. 16.24** Ellipsometric set-up: H, half-wave plate at 632.8 nm; P, polarizer; S, sample; C, compensator; A, analyzer; D, silicon photodetector; AMP, amplifier;  $V_{DC}$ , voltmeter; HVP, high-voltage probe; LOCK-IN, lock-in amplifier; OSC, oscilloscope; WG, waveform generator; HV, high voltage amplifier; PC: computer.



$$I_d = I_m \sin^2 \left( \frac{\varphi_{sp}}{2} \right); \quad (11)$$

where  $I_d$  is the intensity arriving at the detector in our experimental set-up,  $I_m$  is the incident intensity, and  $\varphi_{sp}$  is the phase difference between the s and p polarizations after the beam passes through the sample, the compensator and the analyzer. At the midpoint  $I_c = I_m/2$  of the intensity distribution, the sinusoidal curve is in its most linear region. Applying a small AC field to the sample when operated in this region yields a modulation in the phase difference,  $\delta\varphi_{sp}$ , which results in a linear modulation of the transmitted intensity,  $I_{ac}$ . For such small modulation amplitude,  $I_{ac}$  (either for the fundamental or second harmonic frequencies) is related to  $\Delta\varphi_{sp}$  by the expression

$$I_{ac} = I_c \delta\varphi_{sp}. \quad (12)$$

For a single beam pass through the sample in this geometry, the phase difference between the s and the p polarizations is given by

$$\varphi_{sp} = \varphi_p - \varphi_s = \frac{2\pi d}{\lambda} \left( \frac{n_p}{\cos a_p} - \frac{n_s}{\cos a_s} \right), \quad (13)$$

where  $a_{p,s}$  are the angles of incidence inside the sample with respect to the sample surface normal for the s and p polarizations, respectively,  $d$  represents the thickness of the sample, and  $n_{p,s}$  are the refractive indices for the p and s polarization components, respectively. Since the applied field is perpendicular to the film plane,  $n_s = n_o$ , and  $n_p$  is related to  $n_o$  and  $n_e$  by the index ellipsoid

$$\frac{1}{n_p^2} = \frac{\sin^2 a_p}{n_e^2} + \frac{\cos^2 a_p}{n_o^2}. \quad (14)$$

The modulated phase difference  $\delta\varphi_{sp}$  is given by [29, 30, 43, 44]

$$\delta\varphi_{sp} = \frac{\partial\varphi_{sp}}{\partial n_o} \Delta n_o + \frac{\partial\varphi_{sp}}{\partial n_e} \Delta n_e. \quad (15)$$

If we take both linear and quadratic electro-optic modulations into account,  $\Delta n_o$  and  $\Delta n_e$  are related to the elements  $r_{113}$ ,  $r_{333}$ ,  $r_{1133}$ , and  $r_{3333}$  of the electro-optic tensor, by

$$\Delta n_o = \frac{1}{2} n_o^3 \left( r_{113} + r_{1133} \frac{V_{ac}}{d} \right) \frac{V_{ac}}{d}, \quad (16 a)$$

$$\Delta n_e = \frac{1}{2} n_e^3 \left( r_{333} + r_{3333} \frac{V_{ac}}{d} \right) \frac{V_{ac}}{d}, \quad (16 b)$$

where  $V_{ac}$  is modulating voltage. Evaluating the derivations with the approximation that  $n = n_o \approx n_e$ , Eq. (15) can be written

$$\Delta\varphi_{\text{sp}} = \frac{2\pi d}{\lambda} \cdot \frac{\sin^2 \theta (n^2 - 2 \sin^2 \theta)}{n(n^2 - \sin^2 \theta)^{3/2}} (\Delta n_e - \Delta n_o). \quad (17)$$

Let us write  $V_{\text{ac}}$  as

$$V_{\text{ac}} = V_{\text{AC}} \cos(\omega t), \quad (18)$$

where  $V_{\text{AC}}$  represents the amplitude of the modulating voltage,  $\omega$  is modulating radian frequency, and  $E = V_{\text{ac}}/d$  is modulating electric field across the sample. Substituting for  $V_{\text{ac}}$  with Eq. (18) in Eqs. (16), we have

$$\Delta n_e - \Delta n_o = \frac{1}{2} \left[ (r_{333} - r_{113}) \frac{V_{\text{AC}}}{d} \cos \omega t + \frac{r_{3333} - r_{1133}}{2} \frac{V_{\text{AC}}^2}{d^2} (1 + \cos 2\omega t) \right]. \quad (19)$$

Using Eq. (12) and separating the fundamental frequency and second harmonic frequency terms, we have

$$r_{333} - r_{113} = \frac{\lambda I_{\text{ac}}}{\pi V_{\text{ac}}^{\text{rms}} I_c} \cdot \frac{(n^2 - \sin^2 \theta)^{3/2}}{(n^2 - 2 \sin^2 \theta)} \cdot \frac{1}{n^2 \sin^2 \theta}, \quad (20)$$

for the linear electro-optic modulation in the ellipsometric configuration and

$$r_{3333} - r_{1133} = \frac{\lambda d I_{\text{ac}}^{2\omega}}{\pi (V_{\text{ac}}^{\text{rms}})^2 I_c} \cdot \frac{(n^2 - \sin^2 \theta)^{3/2}}{(n^2 - 2 \sin^2 \theta)} \cdot \frac{1}{n^2 \sin^2 \theta}, \quad (21)$$

for the quadratic electro-optic modulation in the same configuration. Here  $\theta$  is the external angle of incidence, and  $I_{\text{ac}}^{2\omega}$  is the intensity of the modulating signal at the second harmonic frequency, as we mentioned above, which can be measured by the lock-in amplifier.  $V_{\text{ac}}^{\text{rms}}$  can be measured using the oscilloscope and  $I_c$  can be measured by the multimeter. The difference  $r_{3333} - r_{1133}$  can be obtained according to Eq. (21). Then, using the ratio  $r_{3333}/r_{1133} = 4.3$ , we can separate the two electro-optic coefficients,  $r_{3333}$  and  $r_{1133}$ .

Figs. 16.25 and 16.26 show the measured results for  $r_{1133}$  and  $r_{3333}$ . The obtained maximum value of  $r_{3333}$  is  $176 \times 10^{-20} \text{ m}^2 \text{ V}^{-2}$  at a modulating frequency of 3 Hz. One can see that  $r_{3333}$  and  $r_{1133}$  have a similar frequency dependence to that of the linear electro-optic coefficients  $r_{333}$  and  $r_{113}$ . This indicates that the orientational distribution of the CdSe quantum dots contributes particularly to the quadratic electro-optic modulation.

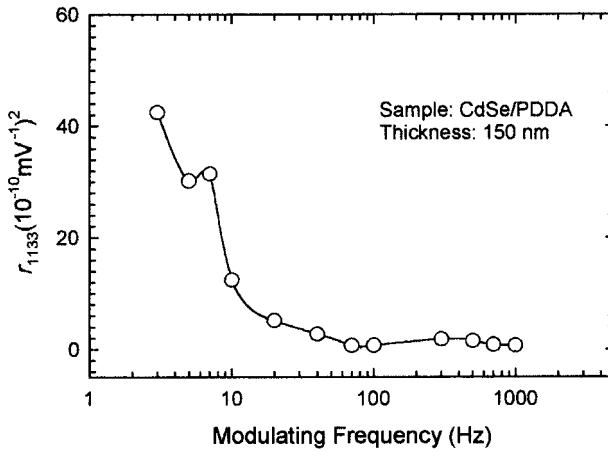


Fig. 16.25  $r_{1133}$  as a function of modulating frequency measured with the ellipsometric set-up.

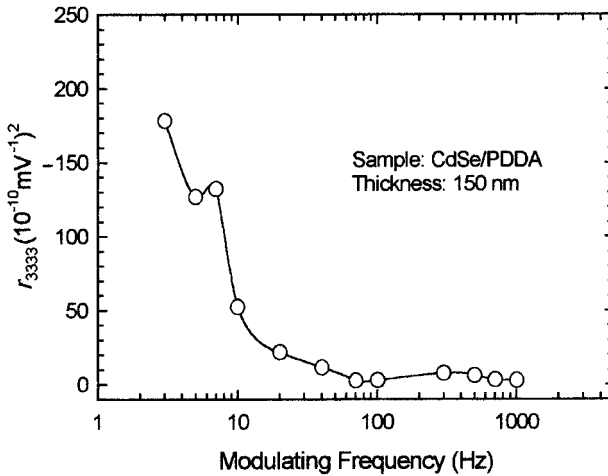


Fig. 16.26  $r_{3333}$  as a function of modulating frequency measured with the ellipsometric set-up.

#### 16.4 Summary

In summary, the ESA process can be applied to the fabrication of a variety of material structures including semiconductor materials and polymers that possess separate ionic and NLO-active groups. Accordingly, we have selected, designed and synthesized polydyes and nanoparticles optimized specifically for both compatibility with the ESA process and increased  $\chi^{(2)}$  values. The ESA-formed films

spontaneously assemble into a noncentrosymmetric structure with a substantial and stable  $\chi^{(2)}$  value, including a remarkably good high temperature stability. CdSe and CLD-1 thin films were fabricated and demonstrated to have electro-optical properties that can be interpreted in terms of simplified assumptions concerning molecular structure. The ESA technique represents an exciting new approach to the rapid, inexpensive production of optically active thin films for electro-optic applications.

### Acknowledgements

The Authors acknowledge the kind cooperation of Professor L. Dalton and his group for providing CLD-1 and Professor X. Peng, Dr. Y. Wang and their group for providing CdSe nanoclusters. This work was supported in part by Air Force contract F33615-00-C-5424. The authors thank J. Zetts, F.K. Hophins, J. Grote and R. Nelson for many useful discussions. R. Duncan and F. Zhang assisted with the EO measurements.

## 16.5

### References

- 1 G. MEREDITH, J. VANDUSEN, D. WILLIAMS, *Macromolecules*, **1982**, 15, 1385; A. Garito, K. Singer, *Laser Focus* **1982**, 80, 59.
- 2 G. A. LINDSAY, K. D. SINGER, *Polymers for Second-order Nonlinear Optics*, *ACS Symp. Ser.*, **1995**, 601.
- 3 O. A. AKTSIPETROV, N. N. AKHMEDIEV, E. D. MISHINA, V. R. NOVAK, *JETP Lett.*, **1983**, 37, 207.
- 4 I. R. GIRLIN, N. A. CADE, P. V. KELISKY, R. J. JONES, I. R. PETERSON, M. M. AHMAD, *J. Opt. Soc. Am. B*, **1987**, 4, 950.
- 5 G. L. ASHWELL, P. D. JACKSON, W. A. CROSSLAND, *Nature*, **1994**, 368, 438–440.
- 6 H. E. KATZ, G. SCHELLER, T. M. PUTVINSKI, M. L. SHILLING, W. L. WILSON, C. E. D. CHIDSEY, *Science*, **1991**, 254, 1485–1487.
- 7 S. YITZCHAIK, S. B. ROSCOE, S. K. KAKKAR, D. S. ALLAN, T. J. MARKS, Z. XU, T. ZHANG, W. LIN, G. K. WONG, *J. Phys. Chem.*, **1993**, 97, 6958.
- 8 W. LIN, S. YITZCHAIK, W. LIN, A. MALIK, M. K. DURBIN, A. G. RICHTER, G. K. WONG, P. DUTTA, T. J. MARKS, *Angew. Chem. Int. Ed. Engl.*, **1995**, 34, 1497–1499.
- 9 D. M. BURLAND, R. D. MILLER, C. A. WALSH, *Chem. Rev.*, **1994**, 94, 31–75.
- 10 G. DECHER, J. D. HONG, J. SCHMITT, *Thin Solid Films*, **1992**, 210/211, 831–835.
- 11 G. DECHER, Y. LVOV, J. SCHMITT, *Thin Solid Films*, **1994**, 244, 772–777.
- 12 Y. LIU, A. WANG, R. CLAU, *J. Phys. Chem. B*, **1997**, 101, 1385–1388.
- 13 A. ROSIDIAN, Y.-X. WANG, Y. LIU, R. CLAU, *Adv. Mater.*, **1998**, 10, 1087–1091.
- 14 Y. LIU, Y.-X. WANG, R. CLAU, *Chem. Phys. Lett.*, **1998**, 298, 315–319.
- 15 Y. LIU, Y.-X. WANG, H. LU, R. CLAU, *J. Phys. Chem. B*, **1999**, 103, 2035–2036.
- 16 Y. LIU, A. ROSIDIAN, K. LENEHAN, Y.-X. WANG, T. ZENG, *Smart Mater. Struct.* **1999**, 8, 100–105.
- 17 Y. LIU, R. CLAU, *J. Appl. Phys.*, **1999**, 85, 419–424.
- 18 Y.-X. WANG, W. SPILLMAN, JR., R. CLAU, *Proc. SPIE*, **2001**, 4265, 142–151.
- 19 J. R. HEFLIN, Y. LIU, C. FIGURA, D. MARCIU, R. CLAU, *Proc. SPIE*, **1997**, 3147, 10–19.
- 20 Y. LIU, Y.-X. WANG, W. ZHAO, R. CLAU, K. LENEHAN, R. HENEHAN, *Proc. SPIE*, **1998**, 3330, 75–79.

- 21 K. LENAHAN, Y.-X. WANG, Y. LIU, R. CLAUS, J. R. HEFLIN, D. MARCIU, C. FIGURA, *Adv. Mater.*, **1998**, *10*, 853–855.
- 22 N. NEMOTO, F. MIYATA, Y. NAGASE, J. ABE, M. HASEGAWA, Y. SHIRAI, *Macromolecules* **1996**, *29*, 2365–2371.
- 23 A. K.-Y. JEN, V. P. RAO, K. J. DROST, R. M. MININNI, J. T. KENNEY, E. S. BINKLEY, L. R. DALTON, *Proc. SPIE*, **1994**, *2285*, 49–57.
- 24 H. S. NALWA, S. MIYATA, eds., *Nonlinear Optics of Organic Materials and Polymers*, CRC Press, Boca Raton, FL, 1998.
- 25 D. L. WISE ET AL., eds., *Electrical and Optical Polymer Systems*, Marcel Dekker, New York, 1998.
- 26 H. LEE, W.-Y. HWANG, M.-C. OH, H. PARK, T. ZYUNG, *Appl. Phys. Lett.*, **1997**, *71*, 3779–3781.
- 27 Y. SHI, C. ZHANG, H. ZHANG, J. H. BECHTEL, L. R. DALTON, B. H. ROBINSON, W. H. STEIER, *Science*, **2000**, *288*, 119–122.
- 28 M. SIGELLE, R. HIERLE, *J. Appl. Phys.*, **1981**, *52*, 4199–4204.
- 29 K. D. SINGER, M. G. KUZYK, W. R. HOLLAND, J. E. SOHN, S. L. LALAMA, R. B. COMIZZOLI, H. E. KATZ, M. L. SCHILLING, *Appl. Phys. Lett.*, **1988**, *53*, 1800–1802.
- 30 B. SWEDEK, N. CHENG, Y. CUI, J. ZIEBA, J. WINIARZ, P. N. PRASAD, *J. Appl. Phys.*, **1997**, *82*, 5923–5930.
- 31 L. ZHANG, F. ZHANG, K. COOPER, Y. WANG, Y. LIU AND R. CLAUS, *Optics Commun.*, **2000**, *186*, 135–141.
- 32 A. P. ALIVISATOS, *J. Phys. Chem.*, **1996**, *100*, 13227–13238.
- 33 M. V. ARTEMYEV, U. WOGGON, *Appl. Phys. Lett.*, **2000**, *76*, 1353–1355.
- 34 J. G. WINIARZ, L. ZHANG, M. LAL, C. S. FRIEND, P. N. PRASAD, *J. Am. Chem. Soc.*, **1999**, *121*, 5287–5295.
- 35 C. B. MURRAY, D. J. NORRIS, M. G. BAWENDI, *J. Am. Chem. Soc.*, **1993**, *101*, 8706–8715.
- 36 B. O. DABBOUSI, J. R. VIEJO, F. V. MIKULEC, J. R. HEINE, H. MATTOUSSI, R. OBER, K. F. JENSEN, M. G. BAWENDI, *J. Phys. Chem. B*, **1997**, *101*, 9463–9457.
- 37 P. N. PRASAD, D. J. WILLIAMS, *Introduction to Nonlinear Optical Effects in Molecules and Polymers*, Wiley, New York, 1991, Ch. 11.
- 38 R. T. CHEN, D. ROBINSON, *Appl. Phys. Lett.*, **1992**, *60*, 1541–1543.
- 39 D. J. WILLIAMS, in *Nonlinear Optical Properties of Organic Molecules and Crystals*, D. S. Chemla, J. Zyss, eds., Academic Press, New York, 1987, Ch. II-7.
- 40 J. R. HEFLIN, C. FIGURA, D. MARCIU, Y. LIU, R. O. CLAUS, *Appl. Phys. Lett.*, **1999**, *74*, 495–497.
- 41 D. M. BURLAND, R. D. MILLER, C. A. WALSH, *Chem. Rev.*, **1994**, *94*, 31–75.
- 42 C. C. TENG, H. T. MAN, *Phys Appl. Lett.*, **1990**, *56*, 1734–1736.
- 43 S. B. KIPPELEN, K. MEERHOLZ, N. PEYGHAMBARIAN, *Appl. Opt.*, **1996**, *35*, 2346–2354.
- 44 J. S. SCHILDKRAUT, *Appl. Opt.*, **1990**, *29*, 2839–2841.
- 45 Y. SHUTO, M. AMANO, *J. Appl. Phys.*, **1995**, *77*, 4632–4638.
- 46 J. W. WU, *J. Opt. Soc. Am. B*, **1991**, *8*, 142–152.
- 47 M. G. KUZYK, J. E. SOHN, C. W. DIRK, *J. Opt. Soc. Am. B*, **1990**, *7*, 842–858

## 17

# Controlling the Ion-Permeability of Layered Polyelectrolyte Films and Membranes

MERLIN BRUENING

### Abstract

Multilayered polyelectrolyte films provide a versatile platform for the synthesis of ultrathin coatings and membranes with tunable ion-transport properties. Electrochemical studies show that ion transport through multilayered polyelectrolyte films varies with the number of layers in the film and the deposition conditions. Cross-linking of poly(acrylic acid)/poly(allylamine hydrochloride) films through heat-induced amidation results in especially blocking films, and these ultrathin coatings provide modest corrosion protection for aluminum. Deposition of films on porous alumina substrates results in ultrathin membranes that completely cover substrate pores without filling them, and such membranes allow rapid transport of monovalent ions, while largely rejecting multivalent species. Increasing the intrinsic charge in these membranes through methods such as templating with  $\text{Cu}^{2+}$  enhances membrane selectivity and suggests that Donnan exclusion is an important part of the selectivity mechanism. Transport can also depend greatly on the charge at the surface of the membrane, as changing this surface from a polyanion to a polycation sometimes results in large decreases in  $\text{Cl}^-/\text{SO}_4^{2-}$  selectivity. Variation of the surface structure through changes in constituent polyelectrolytes allows control over selectivity and yields  $\text{Cl}^-/\text{SO}_4^{2-}$  selectivities as high as 1000. The ability to tune the ion-permeability of layered polyelectrolyte films may allow their application in areas such as corrosion protection and water softening.

### 17.1

#### Introduction

Multilayered polyelectrolyte films [1] are attractive for applications in sensing [2–4], separations [5–7], controlled release [8], and surface protection [9] because of their ease of synthesis and versatility. However, the utility of polyelectrolyte films in these areas will depend directly on their permeability to ions and other species under relevant conditions. Permeability requirements will be specific to a particular application. For example, completely impermeable films will be ideal for surface protection, while films for separations and sensing applications should be se-

lectively permeable to specific species. This chapter focuses on studies of the ion-permeability of multilayered polyelectrolyte films (MPFs) and methods for controlling this permeability. By varying the deposition conditions, film composition, and/or the amount of cross-linking in MPFs, films can be highly permeable, selectively permeable, or nearly impermeable to ions.

Section 17.2 discusses electrochemical characterization of the permeability of MPFs. Studies in this area focus primarily on the movement of highly charged redox couples through MPFs and show that the permeability of these coatings depends upon the number of layers in the film, the deposition conditions, and the film composition. Notably, heat-induced amidation of poly(acrylic acid)/poly(allylamine hydrochloride) (PAA/PAH) films yields cross-linked coatings that are highly resistive to ion transport. These films provide modest corrosion protection for aluminum.

Section 17.3 discusses the use of MPFs as ion-selective membranes. Deposition of MPFs on porous supports results in ultrathin membranes that simultaneously exhibit high selectivity and allow a high flux of ions. As was the case in the electrochemical studies, the permeability of these membranes varies with the membrane composition, deposition conditions, and post-deposition reactions. Remarkably, films with thicknesses  $<40$  nm exhibit  $\text{Cl}^-/\text{SO}_4^{2-}$  transport selectivities as high as 1000. Section 17.4 presents some of our thoughts on modeling of transport through MPFs.

## 17.2

### Electrochemical Studies of the Permeability of MPFs

#### 17.2.1

##### As-deposited MPFs

The permeability of MPFs to redox-active species such as  $\text{Fe}(\text{CN})_6^{3-}$  or  $\text{Ru}(\text{NH}_3)_6^{3+}$  depends on many variables including the number of layers in the film, the deposition conditions, the surface charge, and the ionic strength. This section discusses each of these variables in turn.

Cyclic voltammetry experiments show that the first few layers of PAH/poly(styrene sulfonate) (PSS) are highly permeable to  $\text{Fe}(\text{CN})_6^{3-}$ ,  $\text{Fe}(\text{CN})_6^{4-}$ ,  $\text{Ru}(\text{NH}_3)_6^{3+}$ , and  $\text{Os}(\text{bipy})_3^{3+}$  [10–12]. Fig. 17.1 shows cyclic voltammograms of  $\text{Fe}(\text{CN})_6^{3-}$  at PAH/PSS-coated electrodes as a function of the number of bilayers in the film. (The term bilayer in this paper refers to a polycation/polyanion pair. In some sense the use of the term layer is a misnomer as polymer chains in these films are highly interpenetrating [1].) Only after deposition of three bilayers does the film drastically passivate the electrode [11]. Voltammograms of  $\text{Fe}(\text{CN})_6^{4-}$  at rotating disk electrodes coated with PSS/poly(diallyldimethylammonium chloride) (PDADMA) also show sharp decreases in currents after deposition of 3–4 polyelectrolyte bilayers [12]. Similarly, after adsorption of 3–4 bilayers of PAH/PSS on gold electrodes, impedance spectroscopy shows a sharp increase in resistance to



electron transfer between  $\text{Fe}(\text{CN})_6^{3-/4-}$ ,  $\text{Ru}(\text{NH}_3)_6^{3+/2+}$ , or  $\text{Os}(\text{bipy})_3^{3+/2+}$  and the electrode [10, 11]. All of these data are consistent with the fact that the first few bilayers on substrates generally have a different structure than later layers, which are deposited after the charge distribution of the polymer film is fully established [13, 14]. The first few layers may not fully cover the electrode or they may swell and thus be more permeable. After deposition of four or five bilayers, the blocking ability of MPFs increases slowly with adsorption of additional layers [12].

The permeability of PAH/PSS films is also a function of deposition conditions. In the results above, all of the films were prepared with a high concentration of salt ( $>0.2$  M) in at least one of the polyelectrolyte deposition solutions. To test whether the presence of supporting electrolyte in deposition solutions strongly affects the permeability of PAH/PSS films, we also prepared films in the absence of supporting electrolyte. Because supporting electrolyte greatly increases film thickness, we compared 20-bilayer PAH/PSS films prepared in the absence of salt with 4-bilayer films prepared in the presence of 0.5 M  $\text{MnCl}_2$  (PSS) or 0.5 M  $\text{NaBr}$  (PAH). Both films were about 15 nm thick. Electrodes coated with films prepared in the absence of salt gave a quasi-reversible  $\text{Fe}(\text{CN})_6^{3-}$  voltammogram with a peak current that was 80-fold larger than that obtained at electrodes coated with films prepared in the presence of salt [11]. These results show the ease with which one can control the permeability of MPFs simply by varying the amount of electrolyte in the deposition solutions. Presumably, salt present during deposition helps to screen charges on the polyelectrolyte and results in an intertwined structure with many loops and tails [15, 16]. This structure is evidently less permeable than that of films prepared in the absence of supporting electrolyte. Interestingly, PAH/PAA films were more permeable when prepared in the presence of salt. The structure of PAH/PAA films is complicated by a variety of factors, however, including deposition pH, ionic strength, and the pH of solutions to which the films are later exposed [17, 18]. PAH/PAA is likely more sensitive to these conditions than PAH/PSS because the polyanion is a weak acid.

Most of the charge in MPFs resides on the film surface because in the bulk of the film, charges on polycations are electrically compensated by charges on poly-

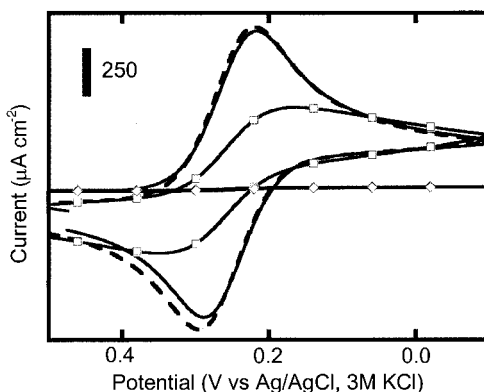


**Fig. 17.1** Cyclic voltammograms of  $\text{Fe}(\text{CN})_6^{3-}$  (5 mM in 0.5 M  $\text{Na}_2\text{SO}_4$ ) at a bare gold electrode (solid line) and similar electrodes coated with one (dashed line), two (squares), and three (diamonds) bilayers of PAH/PSS. Electrode area:  $0.1 \text{ cm}^2$ . Scan rate:  $100 \text{ mV s}^{-1}$ .

anions and vice versa [19, 20]. The charge at the film surface can affect permeability, however, as anions will be excluded from films with negatively charged surfaces and cations will be excluded from films terminated with polycations. Several recent studies have demonstrated this effect [12, 21, 22]. Lvov showed that voltammetric peak currents at electrodes coated with PDADMA/PSS films depend on the charge of the capping layer [21]. Currents decrease when the capping polyelectrolyte and the electroactive species have charges of the same sign and increase when these moieties have opposite charges. Superimposed on this effect, however, is the fact that currents decrease with the number of layers in the film. Oxidation of a neutral redox-active molecule, ferrocene dimethanol, showed little dependence on the charge at the film surface as would be expected. Willner and co-workers observed similar effects when using PAA/poly-L-lysine films [22].

One additional factor that affects transport of redox-active species through layered polyelectrolytes is the concentration of supporting electrolyte present during electrochemical measurements. Farhat and Schlenoff showed that limiting currents at rotating-disk electrodes coated with PDADMA/PSS films increased with the ionic strength of the electrochemical solution [12]. They suggested that this occurs because high concentrations of  $\text{Na}^+$  and  $\text{Cl}^-$  ions result in extrinsically charge-compensated sites in films, i.e. ions enter the film from solution and compensate the charges on polycations and polyanions, rather than having the oppositely charged polyelectrolytes electrically compensate each other. The presence of more ion-exchange sites would enhance the transport of  $\text{Fe}(\text{CN})_6^{4-}$  that occurs by hopping between these sites. Increasing ionic strength might also affect transport by decreasing Donnan exclusion [23] and/or swelling the film [24].

As this section shows, the permeability of MPFs to redox-active species depends on the deposition conditions, the surface charge, the number of layers in the film, and the ambient ionic strength. These variables complicate an understanding of the factors that govern permeability in MPFs, but they also offer a means to control the permeability of these films. This should allow tailoring of MPFs for specific applications. An additional means of tailoring film permeability involves post-deposition modification of MPFs as described in the next section.

### 17.2.2

#### **Cross-linked PAA/PAH Films**

Although the permeability of MPFs can be reduced to some extent by altering deposition conditions, even films with lower permeabilities are not sufficiently blocking for possible applications in the protection of surfaces from corrosion. This is probably due to the fact that MPFs are hydrophilic and swell in water [11, 24, 25]. In an effort to prepare layered polyelectrolyte films that are better suited for protection of substrates, we began exploring the possibility of cross-linking PAH/PAA films through heat-induced amidation as shown in Fig. 17.2 [26]. This reaction is analogous to that used in one method for synthesizing nylon, where heating of dicarboxylate/diammonium salts at  $215^\circ\text{C}$  results in polyamide forma-

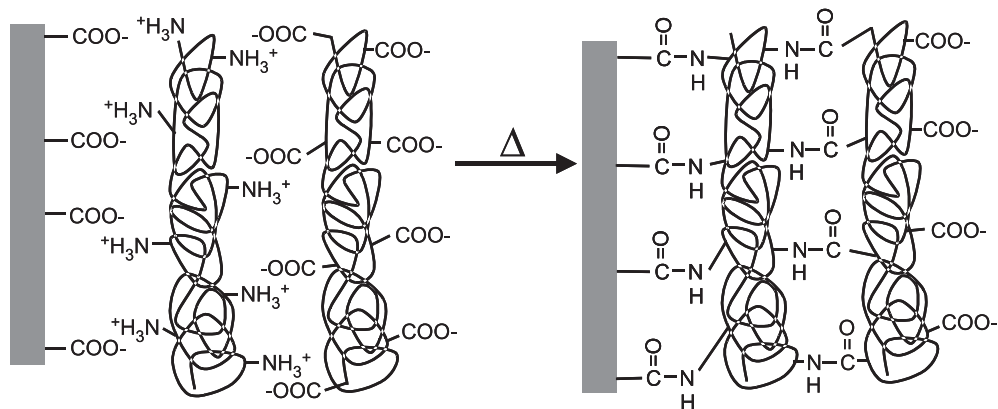


**Fig. 17.2** Schematic diagram of heat-induced cross-linking of PAH/PAA films via amidation. The intertwining of neighboring layers is not shown for figure clarity.

tion [27]. Amidation of PAH/PAA films allows construction of ultrathin (<50 nm thick) nylon-like films on a surface.

The reflectance FTIR spectra of PAH/PAA films shown in Fig. 17.3 demonstrate that the amidation reaction is temperature-dependent and proceeds in high yield at 215°C. The spectrum of an unheated PAH/PAA film is dominated by asymmetric and symmetric carboxylate stretches (1570 and 1400  $\text{cm}^{-1}$ , respectively) and a carbonyl peak (1710  $\text{cm}^{-1}$ ) due to residual  $-\text{COOH}$  groups. Because we performed film deposition at a pH of 4.5, not all carboxylate groups in the film are deprotonated, and some  $-\text{COOH}$  groups are present. After heating the film at 215°C for 2 h, amide peaks (1670 and 1540  $\text{cm}^{-1}$ ) appeared in the spec-

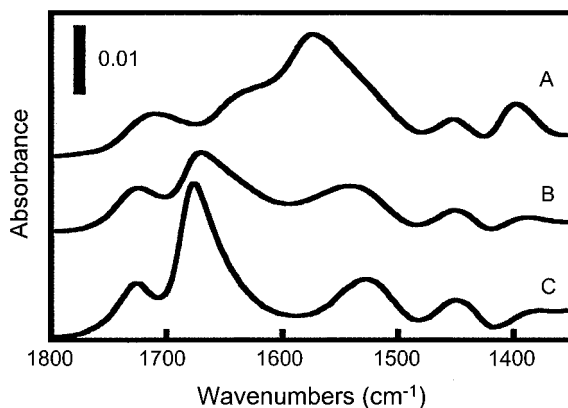


**Fig. 17.3** Reflectance FTIR spectra of nine-bilayer PAH/PAA films before heating (A) and after heating for 2 h at 130°C (B) or 215°C (C). Reproduced from ref. [26] by permission of the American Chemical Society.

trum, and the  $-\text{COO}^-$  peaks disappeared. This suggests that nearly all of the carboxylate/ammonium salts form amides. Heating at lower temperatures (e.g.,  $130^\circ\text{C}$ ) also results in some amide formation, but the reaction is not complete, as indicated by the appearance of smaller amide bands.

Cyclic voltammograms (CVs) at coated gold electrodes show that the permeability of PAA/PAA films to  $\text{Fe}(\text{CN})_6^{3-}$  decreases dramatically after cross-linking. After heating films at  $130^\circ\text{C}$ , the peak currents in the voltammograms decrease by two orders of magnitude. Heating at  $215^\circ\text{C}$  results in an additional decrease in peak current. In fact, capacitive currents dominate the CVs of highly cross-linked films. Electrochemical impedance spectroscopy confirms the large decrease in film permeability due to amidation. After heating at  $130^\circ\text{C}$ , resistance to charge transfer increases by about two orders of magnitude to  $10^4 \Omega \text{ cm}^2$ , and heating at  $215^\circ\text{C}$  results in another order of magnitude increase in this resistance [26].

Gold films are relatively immune to corrosion, so we prepared cross-linked PAA/PAH films on aluminum-coated Si wafers to investigate whether PAA/PAH coatings can protect a metal surface [9]. Because the oxidized aluminum surface carries a positive charge at pH values lower than 8 [28], PAA/PAH films can be deposited directly on the oxide of aluminum. Corrosion studies on aluminum are complicated, however, because the native oxide layer already provides a significant barrier to corrosion reactions.

Electrochemical impedance spectroscopy studies of aluminum electrodes in 0.5 M NaCl (adjusted to pH 3.0 with HCl) show that MPFs provide substantial protection for the oxide layer on the aluminum surface [9]. After immersion for 4 h in the 0.5 M NaCl solution, the oxide resistance of naked aluminum was  $0.07 \text{ M}\Omega \text{ cm}^2$ , while the same resistance for aluminum coated with a cross-linked 9-bilayer PAA/PAH film was  $70 \text{ M}\Omega \text{ cm}^2$ . The resistance due to just the cross-linked PAA/PAH coating was  $5 \text{ M}\Omega \text{ cm}^2$ . Thus, PAA/PAH films protect the aluminum oxide, and the oxide resistance is then the dominant feature in protecting the underlying aluminum.

Although cross-linked PAA/PAH provides a much higher film resistance than does unheated PAA/PAH, unheated PAA/PAH still provides significant protection for the oxide layer on aluminum. Even a monolayer of PAA can maintain oxide resistance at  $10 \text{ M}\Omega \text{ cm}^2$  after immersion for 4 h in 0.5 M NaCl at pH 3.0. We speculate that the charged PAA layer inhibits  $\text{Cl}^-$  adsorption and thus protects the oxide layer [29]. Even though unheated films provide little effective resistance to ion diffusion, they still protect the underlying oxide layer.

The high resistance of cross-linked PAA/PAH does suggest, though, that over long periods of time it may provide significantly better corrosion protection than would unheated films. However, even a film resistance of  $5 \text{ M}\Omega \text{ cm}^2$  is not likely to provide long-term corrosion protection. Practical corrosion-reduction coatings generally show resistances of at least  $10 \text{ M}\Omega \text{ cm}^2$  [30]. One must consider, however, that the cross-linked polyelectrolyte films we used had thicknesses as low as 10 nm. In mildly corrosive situations, an ultrathin anticorrosion coating such as cross-linked PAA/PAH may provide advantages in maintaining substrate properties such as heat transfer coefficients.

## 17.2.3

**Derivatized Polyelectrolyte Films**

Derivatization of polyelectrolytes prior to adsorption combined with post-deposition modifications provides another means to control the permeability of MPFs. Fig. 17.4 shows schematically our application of this strategy for modification of PAH/PAA films. Initially, we derivatized PAA through Fischer esterification and formed PAH/derivatized-PAA (d-PAA) films [31]. Partial esterification still leaves enough  $-\text{COO}^-$  groups to form MPFs, but allows dramatic modification of the wettability of PAH/d-PAA films. For example, PAH/d-PAA films prepared with PAA that was 60% esterified with butanol exhibited advancing water contact angles of  $101^\circ$ . Contact angles varied with both the degree of derivatization of PAA and the nature of the derivatizing group [31].

We hoped to use derivatization to introduce ion-exchange sites into PAH/d-PAA films through hydrolysis of the ester groups of d-PAA after film formation, but unfortunately, PAH/d-PAA films delaminate under the basic conditions needed for ester hydrolysis [11]. To avoid this problem, we cross-linked PAH/d-PAA films through heat-induced amidation and then hydrolyzed ester groups (Fig. 17.4). This results in cross-linked films with a high density of ion-exchange sites. Cyclic voltammetry of  $\text{Fe}(\text{CN})_6^{3-}$  and  $\text{Ru}(\text{NH}_3)_6^{3+}$  at gold electrodes coated with cross-linked, hydrolyzed PAH/d-PAA films shows selective reduction of  $\text{Ru}(\text{NH}_3)_6^{3+}$ . The positively charged redox-couple adsorbs in the film so the cyclic voltammograms are typical of thin film electrodes. In contrast,  $\text{Fe}(\text{CN})_6^{3-}$  is repelled by the film so little reduction of  $\text{Fe}(\text{CN})_6^{3-}$  occurs.

The  $-\text{COO}^-$  groups in cross-linked, hydrolyzed films are also capable of adsorbing multivalent metal cations, and thus the presence of  $\text{Ca}^{2+}$  has a large effect on  $\text{Ru}(\text{NH}_3)_6^{3+}$  reduction currents at these electrodes. Fig. 17.5 shows cyclic voltammograms of mM  $\text{Ru}(\text{NH}_3)_6^{3+}$  at a Au electrode coated with a cross-linked, hydrolyzed film as a function of  $\text{Ca}^{2+}$  concentration in solution. Decreases in current occur at  $\text{Ca}^{2+}$  concentrations as low as  $10^{-5}$  M in the presence of 0.1 M NaCl. Thus these films are possible candidates for sensors of divalent ions. However, the selectivity among different divalent ions does not appear to be very high [31].

The electrochemical studies described in this section demonstrate the versatility of MPFs in modifying the accessibility of an underlying electrode. Section 17.3 next discusses application of MPF versatility in preparing ion-separation membranes that exhibit both high flux and high selectivity.

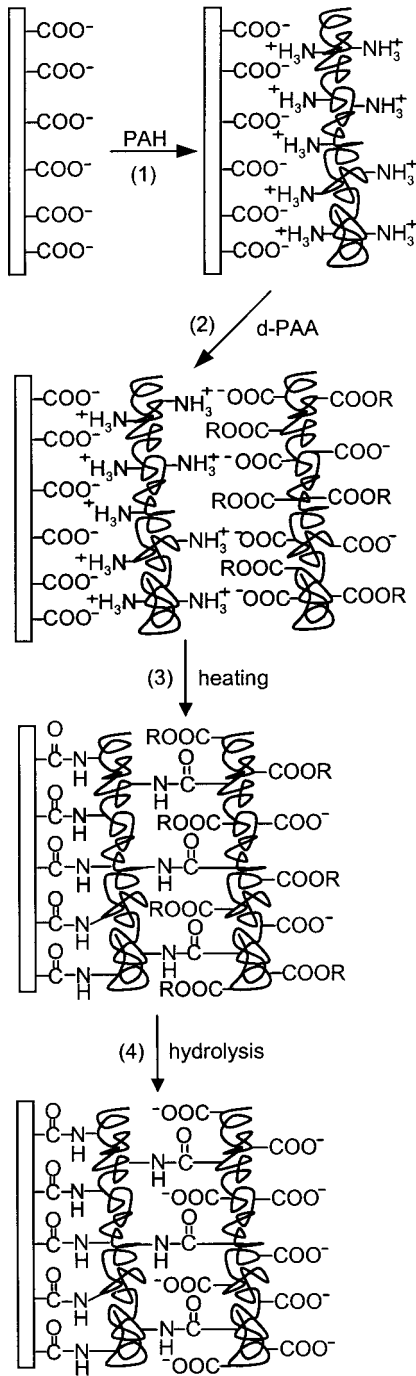
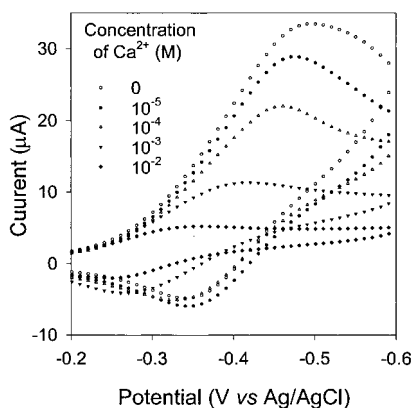


**Fig. 17.4** Synthesis (1 and 2), cross-linking (3), and hydrolysis (4) of PAH/d-PAA films. Repeating steps 1 and 2 yields multilayer films. Reproduced from ref. [31] by permission of the American Chemical Society.

**Fig. 17.5** Cyclic voltammograms of  $\text{Ru}(\text{NH}_3)_6^{3+}$  in 0.1 M NaCl containing different concentrations of  $\text{Ca}^{2+}$  (0 to  $10^{-2}$  M). The Au electrode was coated with six bilayers of cross-linked, hydrolyzed PAH/d-PAA. d-PAA stands for PAA that was 60% esterified with propanol. Electrode area:  $0.1 \text{ cm}^2$ . Scan rate:  $100 \text{ mV s}^{-1}$ . Reproduced from ref. [31] by permission of the American Chemical Society.



### 17.3 MPFs as Ion-Separation Membranes

#### 17.3.1 Membrane Formation

Although membrane separations are attractive because of their operational simplicity and low energy costs [32], full exploitation of the advantages of membrane-based separations will require membranes with higher fluxes and higher selectivities. MPFs are attractive candidates for ion-separation membranes because their minimal thickness should allow high flux, and their high surface charge density could result in Donnan exclusion of multivalent ions [6]. The first challenge in using MPFs as ultrathin ion-separation membranes is to show that these films are capable of covering a porous substrate without filling underlying pores. The highly porous support is needed to provide mechanical strength, while the MPF presents a discriminating high-flux skin layer. (A recent study showed that free-standing layered polyelectrolyte membranes can be prepared [33], but the mechanical weakness of those films will likely preclude their use in practical separations.) Although a number of groups investigated formation of MPFs on permeable supports [5, 6, 34–38], none of those studies demonstrated whether an ultrathin film can actually cover a porous support. We chose to work with MPFs on porous alumina because the regular structure of the alumina support facilitates field-emission scanning electron microscopy (FESEM) investigations of membrane structure [39].

Fig. 17.6 shows FESEM images (top views) of porous alumina supports before and after coating with 2, 4, and 5 bilayers of PAH/PSS. Although the initial bilayers of polyelectrolyte are not capable of covering the underlying pores, deposition of 5 bilayers appears to fully cover the  $0.02 \mu\text{m}$  diameter pores in the support. Below we show that these images correlate well with permeability data for these membranes.

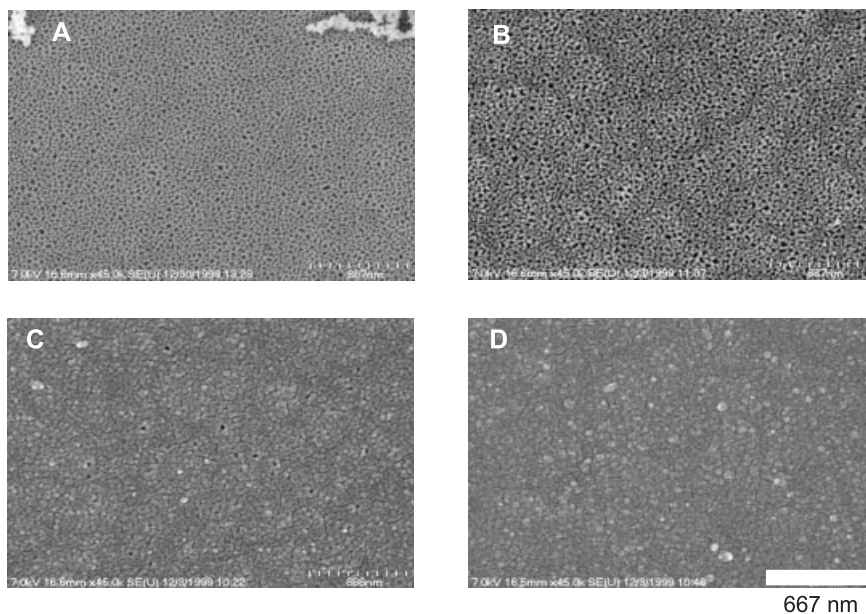


**Fig. 17.6** FESEM images (top view) of the filtrate side of porous alumina substrates before (A) and after coating with two (B), four (C), or five (D) PAH/PSS bilayers. Reproduced from ref. [7] by permission of the American Chemical Society.

To learn whether MPFs fill substrate pores, we prepared cross-sectional FESEM images of alumina substrates coated with 5 bilayers of PAH/PSS. The images, such as that shown in Fig. 17.7, clearly show that pores are unobstructed after deposition of the polyelectrolyte film. Although some polyelectrolyte may adsorb in the support during deposition of the first few bilayers, after coverage of the substrate, little or no polyelectrolyte deposition occurs within the pores. Surface coverage is facilitated by the fact that in this particular case, the alumina surface is a cake layer with  $0.02\ \mu\text{m}$  diameter pores, but the bulk of the alumina has pores with  $0.2\ \mu\text{m}$  diameters [7].

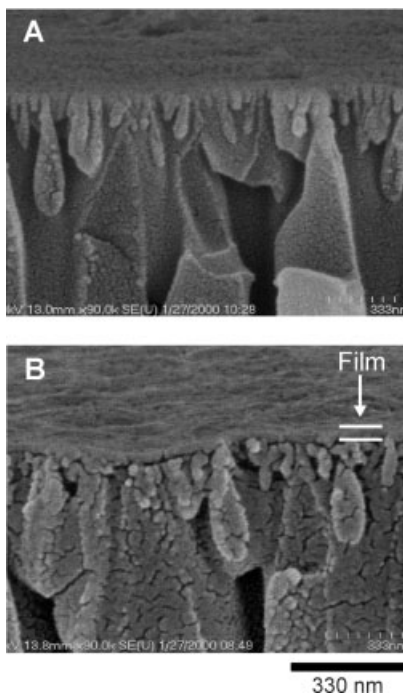
### 17.3.2

#### Permeability of PAH/PSS and PAH/PAA Membranes

To test the selectivity and permeability of multilayered polyelectrolyte membranes (MPMs), we perform diffusion dialysis experiments with a series of different salts. In these studies, we sandwich a membrane between a source phase that is  $0.1\ \text{F}$  in the salt of interest and a receiving phase that initially contains deionized water. By monitoring the increase in the conductivity of the receiving phase as a function of time, we can determine the flux of ions through the membrane. Vigorous stirring of both source and receiving phases minimizes concentration polarization.



**Fig. 17.7** Cross-sectional FESEM images of porous alumina substrates before (A) and after (B) coating with ten PAH/PSS bilayers. Film thickness is about 40 nm. Reproduced from ref. [7] by permission of the American Chemical Society.



Diffusion dialysis studies using PAH/PSS and PAH/PAA membranes show modest monovalent/divalent and substantial monovalent/trivalent anion-transport selectivities once the membrane has fully covered the substrate. (We define selectivity as the ratio of the fluxes of two different anions under the same anion-concentration driving force.) Fig. 17.8 shows how receiving phase conductivity varies as a function of time when using membranes containing 1–5 or 10 bilayers of

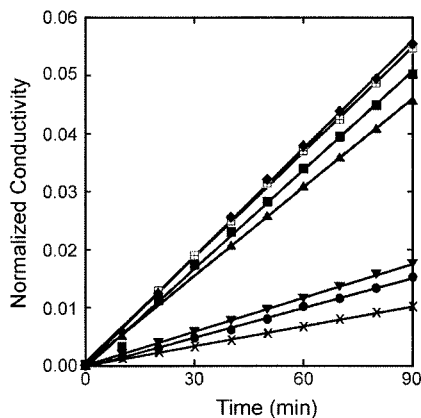


**Fig. 17.8** Plot of normalized receiving phase conductivity as a function of time when the source phase contained 0.1 F  $K_2SO_4$ . Representative data are shown for a bare porous alumina support (open squares) and for alumina coated with one (diamonds), two (squares), three (triangles), four (inverted triangles), five (circles), or ten (x) bilayers of PAH/PSS. Conductivity was normalized by dividing by the source-phase conductivity. Reproduced from ref. [7] by permission of the American Chemical Society.

PAH/PSS. Consistent with the FESEM images shown above, large reductions in  $\text{SO}_4^{2-}$  flux occur only after deposition of four bilayers. Additional bilayers do not greatly decrease flux.

Unlike  $\text{SO}_4^{2-}$ ,  $\text{Cl}^-$  flux is relatively unaffected by increasing the number of PAH/PSS bilayers in a membrane. Thus the  $\text{Cl}^-/\text{SO}_4^{2-}$  selectivity of these membranes reaches a limiting value of 4 to 7 after the deposition of 5 bilayers of PAH/PSS. Similar selectivity values obtain for PAH/PAA membranes. A previous study reported  $\text{Cl}^-/\text{SO}_4^{2-}$  selectivities of 17 and 45 for 5- and 60-bilayer PAH/PSS membranes, respectively [6]. Those membranes were deposited under somewhat different conditions and on a different (polymeric) support, and this may explain the differences in selectivity between the two systems. As will be seen below, small differences in deposition conditions or membrane composition can lead to large differences in selectivity.

Krasemann and Tieke suggested that the selectivity of MPMs is due in large part to Donnan exclusion [6]. Our experiments with  $\text{Fe}(\text{CN})_6^{3-}$  transport are consistent with this concept, as the flux of this trivalent anion is about 500 times less than that of  $\text{Cl}^-$ . Donnan exclusion predicts that ions with higher charges should be much more strongly excluded from the membrane [23]. If Donnan exclusion is indeed the major factor behind selectivity in layered MPMs, we would also expect that terminating the membrane with a polycation rather than a polyanion should result in a dramatic change in anion-transport selectivities. This is because, for most multilayered polyelectrolyte systems, the majority of the uncompensated charge in the film resides in its top layer [19]. For PAH/PSS, we find that changing the outer layer of the membrane from PSS to PAH results in a 2- to 3-fold decrease in  $\text{Cl}^-/\text{SO}_4^{2-}$  selectivity even though the membrane thickness increases slightly [7]. For membranes with even higher selectivities (see below),  $\text{Cl}^-/\text{SO}_4^{2-}$  selectivities decrease by up to two orders of magnitude upon changing the top layer of the film from a polyanion to a polycation.

In contrast,  $\text{Cl}^-/\text{Fe}(\text{CN})_6^{3-}$  selectivities are relatively unaffected by a change in the charge of the top layer of a PAH/PSS membrane [7]. Small  $\text{Fe}(\text{CN})_6^{3-}$  fluxes through MPMs must be due to mechanisms other than just Donnan exclusion by the top layer of the membrane. One possibility is that  $\text{Fe}(\text{CN})_6^{3-}$  adsorbs to the polyelectrolyte film, and the membrane becomes negatively charged, regardless of the sign of the surface charge [40]. Another possibility, suggested by Farhat and Schlenoff, is that the mechanism of transport of  $\text{Fe}(\text{CN})_6^{3-}$  through layered polyelectrolytes involves hopping between transient ion-exchange sites [12]. Because three anion exchange sites are required for each  $\text{Fe}(\text{CN})_6^{3-}$  ion, hopping through the membrane would be very slow if the concentration of these sites was low. A final reason for the low flux of  $\text{Fe}(\text{CN})_6^{3-}$  may be its large size and hydration energy relative to  $\text{Cl}^-$ . In any case, transport of  $\text{Fe}(\text{CN})_6^{3-}$  through PAH/PSS is much slower than transport of monovalent and divalent ions.

## 17.3.3

**Cross-linked PAA/PAH Membranes**

As mentioned in Section 17.2.2, cross-linking of PAH/PAA films dramatically reduces their permeability. Because a reduction in permeability may also result in an increase in selectivity due to reduced swelling of films, we began investigating ion transport through cross-linked PAA/PAH membranes [41, 42]. Anion flux through PAA/PAH membranes is a strong function of cross-linking temperature as shown in Tab. 17.1. Both  $\text{Cl}^-$  and  $\text{SO}_4^{2-}$  fluxes decrease with increasing cross-linking temperatures as might be expected due to reduced swelling. At low degrees of cross-linking (lower heating temperatures), however,  $\text{SO}_4^{2-}$  flux decreases more than  $\text{Cl}^-$  flux, resulting in increased  $\text{Cl}^-/\text{SO}_4^{2-}$  selectivities. Selectivities peak at a value of 20 for films cross-linked at  $115^\circ\text{C}$ . This is a 4-fold enhancement of selectivity relative to unheated films. Cross-linking of PAA/PAH membranes at temperatures greater than  $115^\circ\text{C}$  results in further decreases in the flux of both  $\text{Cl}^-$  and  $\text{SO}_4^{2-}$ , but  $\text{Cl}^-$  flux decreases faster than  $\text{SO}_4^{2-}$  flux, and selectivities decrease. Heat treatments at  $215^\circ\text{C}$  result in little flux of either ion.

To show that the surface of the membrane plays an important role in these selectivities, we capped films with a layer of PAH (5-bilayer PAA/PAH membranes) rather than PAA. The presence of the PAH capping layer on unheated films eliminates  $\text{Cl}^-/\text{SO}_4^{2-}$  selectivity as shown in Tab. 17.1. For films cross-linked at  $115^\circ\text{C}$ ,  $\text{Cl}^-/\text{SO}_4^{2-}$  selectivity decreases from 20 to 0.6 upon going from a 4.5-bilayer to a 5-

**Tab. 17.1** Anion fluxes ( $\text{mol cm}^{-2} \text{ s}^{-1}$ ) through bare porous alumina and alumina coated with PAA/PAH films that were partially cross-linked at different temperatures

Film Composition	$T/^\circ\text{C}^{\text{a}}$	$\text{Cl}^- \text{ flux}/10^{-8}$	$\text{SO}_4^{2-} \text{ flux}/10^{-8}$	$\text{Cl}^-/\text{SO}_4^{2-}^{\text{b}}$
Bare Membrane	–	$5.3 \pm 3\%$	$3.0 \pm 5\%$	$1.7 \pm 4\%$
Bare Membrane <sup>c)</sup>	400	$5.2 \pm 10\%$	$3.5 \pm 7\%$	$1.5 \pm 2\%$
4.5 PAA/PAH	–	$1.3 \pm 6\%$	$0.29 \pm 7\%$	$4.5 \pm 10\%$
4.5 PAA/PAH	105	$1.2 \pm 15\%$	$0.13 \pm 35\%$	$9.5 \pm 25\%$
4.5 PAA/PAH	110	$0.96 \pm 10\%$	$0.092 \pm 25\%$	$11 \pm 20\%$
4.5 PAA/PAH	115	$0.68 \pm 25\%$	$0.043 \pm 60\%$	$20 \pm 45\%$
4.5 PAA/PAH	130	$0.17 \pm 55\%$	$0.026 \pm 60\%$	$7 \pm 40\%$
4.5 PAA/PAH	215	$0.0041 \pm 25\%$	$0.0016 \pm 55\%$	$3.1 \pm 55\%$
5 PAA/PAH	–	$1.1 \pm 10\%$	$1.1 \pm 10\%$	$0.97 \pm 10\%$
5 PAA/PAH	115	$0.56 \pm 40\%$	$0.97 \pm 45\%$	$0.60 \pm 25\%$

a) Temperature at which membranes were heated for 2 h to partially cross-link films.

b)  $\text{Cl}^-/\text{SO}_4^{2-}$  ratios were calculated from the average of selectivities of different membranes and not from the average flux values. This results in a lower standard deviation and a slightly different average value.

c) For cross-linked PAA/PAH films, alumina was heated at  $400^\circ\text{C}$  prior to film deposition to remove the polymer support ring. These data are for bare alumina heated at  $400^\circ\text{C}$ .

Reproduced from Ref. [41] by permission of the American Chemical Society.

bilayer PAA/PAH membrane. These experiments clearly demonstrate that selectivity is a strong function of surface charge.

#### 17.3.4

##### Hybrid PSS/PAH + PAA/PAH Membranes

Although PAA/PAH films are attractive membrane materials because they can be modified by cross-linking, flux through these films (even before cross-linking) on porous alumina substrates is at least 3 times less than that through similar PSS/PAH membranes [41]. In an effort to increase fluxes and maintain the versatility of PAA/PAH, we began preparing hybrid films composed of 4.5 bilayers of PSS/PAH capped with 0.5–3 bilayers of PAA/PAH. The PSS/PAH layers allow full coverage of a porous support, and we hoped that the use of only a few bilayers of PAA/PAH would provide selectivity without greatly hampering flux. An unexpected benefit of these hybrid films is that they are 1–2 orders of magnitude more selective than pure PAA/PAH or PSS/PAH films [41].

Tab. 17.2 lists anion fluxes through PSS/PAH membranes and PSS/PAH membranes capped with 0.5–3 bilayers of PAA/PAH. The  $\text{Cl}^-$  flux through hybrid membranes shows an increase of 80–200% compared to pure 4.5-bilayer PAA/PAH membranes. Thus, the notion of increasing flux through preparation of hybrid films is feasible. In contrast,  $\text{SO}_4^{2-}$  flux through hybrid membranes is extremely low. The combination of low  $\text{SO}_4^{2-}$  flux and rapid  $\text{Cl}^-$  transport results in  $\text{Cl}^-/\text{SO}_4^{2-}$  selectivities of 70 and 120 for 4.5-bilayer PSS/PAH films capped with 1.5 and 2.5 bilayers of PAA/PAH, respectively. Thus, these films are up to ~30 times more selective than unheated pure PAA/PAH films.

The remarkable selectivity in hybrid PAA/PAH films implies that they have a significantly different structure than do pure PAA/PAH films. The FESEM images shown in Fig. 17.9 confirm that the topology of the surface of hybrid PSS/PAH + PAA/PAH films is quite different from that of pure PAA/PAH. Unfortunately, we do not yet know how to interpret these images. We speculate that the PAA/PAH surface in hybrid films is less strongly hydrated than in pure PAA/PAH films. Less hydration will result in higher charge density and hence more Donnan exclusion and higher monovalent/divalent anion-transport selectivity.

Rubner and coworkers showed that the pH at which PAA/PAH films are deposited has a dramatic effect on film thickness and structure [17, 18, 43]. With this in mind, we investigated what effect the deposition pH for the interfacial PAH layer (the layer at the boundary between PSS/PAH and PAA/PAH) would have on the selectivity of hybrid PSS/PAH + PAA/PAH membranes. Originally, we deposited the interfacial PAH layer at a pH of 2.3, while PAA/PAH capping layers were deposited at pH 4.5. Changing the deposition pH of the interfacial PAH layer to 4.5 resulted in a small selectivity increase for 4.5-bilayer PSS/PAH + 1.5-bilayer PAA/PAH films as shown in Tab. 17.2 (from 70 to 120). In the case of the 2.5-bilayer PAA/PAH capping film, selectivity did not change significantly when altering the deposition pH of the interfacial layer.

Tab. 17.2 Anion fluxes ( $\text{mol cm}^{-2} \text{s}^{-1}$ ) through pure PSS/PAH, hybrid PSS/PAH/PAA, and heated PSS/PAH/PAA films

Film Composition	T/C <sup>a)</sup>	Cl <sup>-</sup> flux/10 <sup>-8</sup>	SO <sub>4</sub> <sup>2-</sup> flux/10 <sup>-9</sup>	Fe(CN) <sub>6</sub> <sup>3-</sup> flux/10 <sup>-11</sup>	Cl <sup>-</sup> /SO <sub>4</sub> <sup>2-</sup> <sup>b)</sup>	Cl <sup>-</sup> /Fe(CN) <sub>6</sub> <sup>3-</sup> /10 <sup>3</sup> <sup>b)</sup>
4.5 PSS/PAH	-	4.3±8%	8.5±15%	5.7±70%	5.1±15%	1.0±65%
4.5 PSS/PAH	115	4.0±4%	4.0±15%	3.1±20%	10±15%	1.3±20%
5 PSS/PAH <sup>c)</sup>	-	3.5±9%	9.6±25%	8.1±95%	3.8±20%	0.76±70%
5 PSS/PAH + 1 Layer PAA	-	4.0±8%	1.6±4%	3.6±30%	25±5%	1.2±30%
5 PSS/PAH + 1 Layer PAA	115	3.4±4%	1.0±20%	2.6±120%	35±20%	4.7±120%
5 PSS/PAH + 1 Layer PAA <sup>d)</sup>	-	3.5±2%	1.4±50%	4.1±35%	30±55%	0.94±40%
5 PSS/PAH + 1 PAA/PAH	115	3.0±4%	7.7±15%	3.2±75%	4.0±10%	1.4±60%
5 PSS/PAH + 1.5 PAA/PAH	-	3.1±7%	0.47±25%	1.2±40%	70±20%	3.0±35%
5 PSS/PAH + 1.5 PAA/PAH	115	2.4±20%	0.18±65%	0.87±45%	160±30%	h3.8±70%
5 PSS/PAH + 1.5 PAA/PAH	120	1.7±20%	0.10±10%	1.24±10%	160±15%	1.4±30%
5 PSS/PAH + 1.5 PAA/PAH	215	0.14±35%	0.025±95%	1.2±50%	110±90%	0.16±60%
5 PSS/PAH + 1.5 PAA/PAH <sup>d)</sup>	-	2.8±10%	0.25±35%	1.2±30%	120±25%	2.5±30%
5 PSS/PAH + 1.5 PAA/PAH <sup>d)</sup>	115	2.6±10%	0.23±30%	1.7±20%	120±30%	1.5±20%
5 PSS/PAH + 2.5 PAA/PAH	-	2.3±15%	0.25±70%	1.2±50%	120±40%	2.1±30%
5 PSS/PAH + 2.5 PAA/PAH	115	1.5±30%	0.24±75%	0.46±115%	240±120%	13±100%
5 PSS/PAH + 2.5 PAA/PAH <sup>d)</sup>	-	2.4±10%	0.20±50%	0.83±20%	150±45%	3.0±25%
5 PSS/PAH + 3 PAA/PAH <sup>d)</sup>	-	3.0±15%	13±10%	5.7±10%	2.2±5%	0.52±20%

a) Temperature at which membranes were heated for 2 h to partially cross-link films.

b) Selectivity ratios were calculated from the average of selectivities of different membranes and not from the average flux values. This results in a lower standard deviation and a slightly different average value.

c) The top layer of PAH was deposited at a pH of 4.5 rather than 2.3.

d) The PAH layer between PSS and PAA was deposited at a pH of 4.5 rather than 2.3.

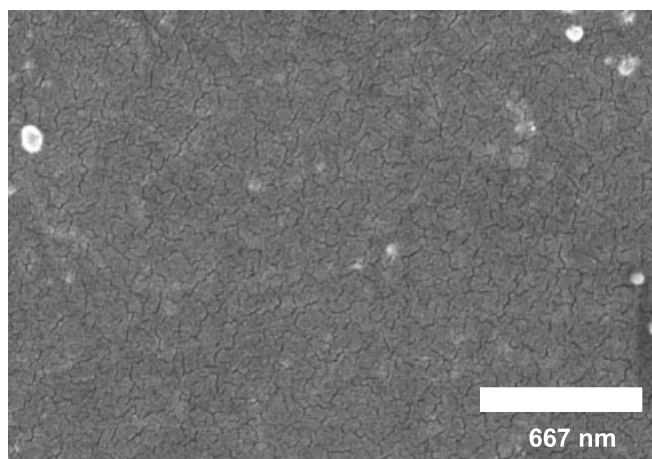
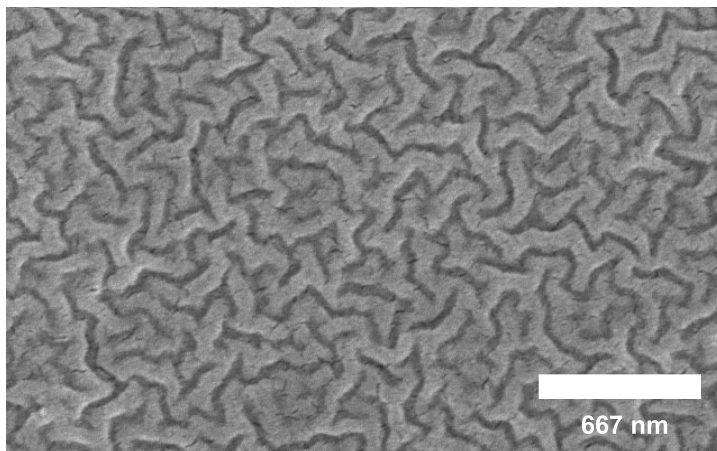


**Fig. 17.9** FESEM images (top view) of a 4.5-bilayer PAA/PAH film (top) and a 4.5-bilayer PSS/PAH + 1.5-bilayer PAA/PAH film (bottom). Both films were deposited on porous

alumina (0.02  $\mu\text{m}$  pore diameter) and heated at 115  $^{\circ}\text{C}$  for 2 h. Reproduced from ref. [41] by permission of the American Chemical Society.

The selectivity of hybrid membranes is due in large part to Donnan exclusion at the membrane surface. Capping a 4.5-bilayer PSS/PAH film with 3 bilayers of PAA/PAH rather than 2.5 bilayers decreases selectivity from 150 to 2.2. This remarkable difference almost certainly reflects the change in sign of the charge at the membrane surface.

Cross-linking of the PAA/PAH layers in hybrid films also results in increases in membrane selectivity in some cases. For films prepared with the interfacial PAH layer deposited at pH 2.3, cross-linking of 4.5-bilayer PSS/PAH + 1.5-bilayer PAA/PAH membranes increases  $\text{Cl}^-/\text{SO}_4^{2-}$  selectivity from 70 to 160. The change again

likely occurs because cross-linking of the surface layers results in a denser, highly charged surface that efficiently rejects divalent ions. For 4.5-bilayer PSS/PAH + 1.5-bilayer PAA/PAH films prepared with a PAH interfacial layer deposited at pH 4.5, cross-linking does not result in a significant increase in selectivity. These films are probably sufficiently dense that cross-linking does not result in increased Donnan exclusion.

### 17.3.5

#### Controlling the Charge Density in MPMs

The work discussed above showed that ion-transport selectivity is strongly dependent on the surface charge in the MPM. In an effort to further increase selectivity, we began exploring ways of inserting charged groups within the bulk of polyelectrolyte films such that there would be a net charge in the interior of the film and not just at the membrane surface [19, 20, 44, 45]. Section 17.2.3 presented one way of introducing extrinsically charge-compensated sites into MPFs, but the basic hydrolysis conditions in that procedure are incompatible with alumina supports. To overcome this challenge, we developed two new methods for introducing charged groups into MPFs. The first involves partial complexation of carboxylate groups with  $\text{Cu}^{2+}$  ions during membrane deposition. Subsequent removal of these ions after film formation results in cation-exchange sites. The second relies on partial derivatization of polyelectrolytes with photocleavable groups prior to film formation. Photocleavage after film formation to form  $-\text{COO}^-$  or  $-\text{NH}_3^+$  functionalities results in groups that must be extrinsically charge compensated. Below we discuss each of these methods in turn.

##### 17.3.5.1 Use of $\text{Cu}^{2+}$ complexes to imprint charged sites into PAA/PAH films [46]

The strategy for synthesis of these films is shown in Fig. 17.10. PAA is deposited from a pH 5.5 solution containing 0.04 M PAA (molarity is with respect to the repeating unit) and 0.005 M  $\text{CuCl}_2$ . This PAA/ $\text{Cu}^{2+}$  ratio and pH value result in about 25 % of the  $-\text{COO}^-$  groups of PAA being complexed by  $\text{Cu}^{2+}$  ions. The net charge on PAA, however, is still negative, and thus PAA-Cu/PAH films will still form. To prevent  $\text{Cu}^{2+}$  from being removed from the film during adsorption of polycationic layers, we also added 0.005 M  $\text{CuCl}_2$  to PAH solutions. Immersing PAA-Cu/PAH films in pH 3.5 water (pH adjusted with HCl) results in removal of the  $\text{Cu}^{2+}$ , and formation of cation-exchange sites. Cyclic voltammetry confirms the presence of  $\text{Cu}^{2+}$  in films and its removal at pH 3.5.

The presence of extrinsically charge-compensated  $-\text{COO}^-$  sites in the bulk of PAA/PAH membranes dramatically increases the selectivity of both cross-linked and unheated films. For unheated 10.5-bilayer PAA/PAH membranes,  $\text{Cl}^-/\text{SO}_4^{2-}$  selectivity increases from 13 to 55 when using  $\text{Cu}^{2+}$  as a templating ion [46,47]. In the case of films cross-linked at 130 °C prior to removal of  $\text{Cu}^{2+}$ , the selectivity increases from 26 to 600 when imprinting with  $\text{Cu}^{2+}$ . One question that arises is whether imprinting with  $\text{Cu}^{2+}$  increases selectivity due to an increase in surface

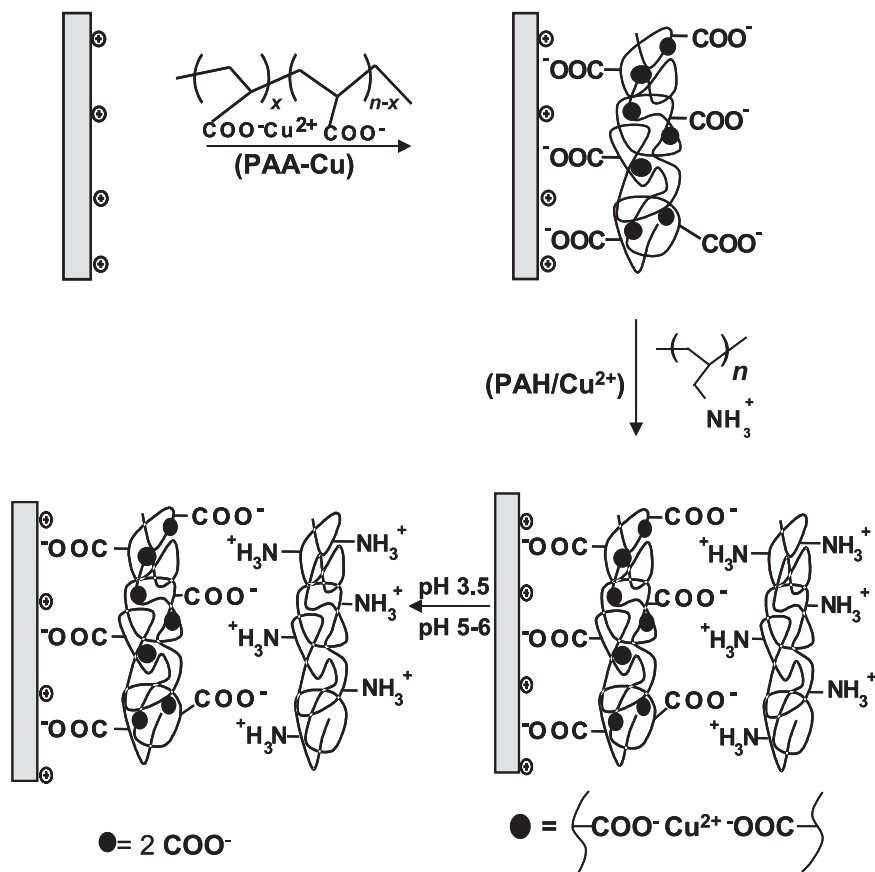


Fig. 17.10 Schematic diagram of imprinting of PAA/PAH films with  $\text{Cu}^{2+}$  to produce films containing cation-exchange sites. Repetition

of steps 1 and 2 yields multilayer films. The intertwining of neighboring layers is not shown for figure clarity.

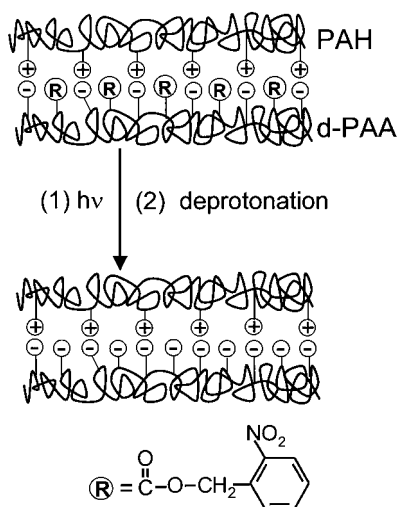
charge or whether charge in the bulk of the membrane also contributes to selectivity. To test this, we prepared cross-linked  $\text{Cu}^{2+}$ -templated films capped with PAH rather than PAA. The change in the sign of the surface charge decreased  $\text{Cl}^-/\text{SO}_4^{2-}$  selectivity by a factor of 10, but selectivity is still 2–3 times higher than for non- $\text{Cu}^{2+}$ -templated, cross-linked PAA/PAH films that are terminated with PAA. Thus charges both at the surface and in the bulk of these MPMs contribute to selectivity.

### 17.3.5.2 Control of Intrinsically Compensated Charge Through Derivatization and Photocleavage

To prepare PAA/PAH films with photocleavable groups, we partially reacted PAA with nitrobenzyl bromide [48]. Subsequent film formation on a porous support



**Fig. 17.11** Schematic diagram showing photolysis of a bilayer of a derivatized-PAA/PAH film and the formation of extrinsically charge-compensated  $\text{-COO}^-$  sites. The intertwining of neighboring layers is not shown for figure clarity.



followed by photolysis and deprotonation yields extrinsically compensated  $\text{-COO}^-$  sites in a membrane as shown in Fig. 17.11. As expected,  $\text{Cl}^-/\text{SO}_4^{2-}$  selectivities increased with the amount of charge (number of photocleavable groups) in the film. Selectivities increase from 10 for an underivatized 10.5 bilayer PAA/PAH membrane to 100, 145, and 165 for membranes prepared with 25, 50, and 63% esterified PAA, respectively [48].

### 17.3.6

#### Highly Selective Ultrathin Polyimide Membranes Formed from Layered Polyelectrolytes

The most anion-selective membranes that we have prepared consist of an ultrathin layer of polyimides deposited on a PSS/PAH film on porous alumina [49]. We form these polyimides using the scheme shown in Fig. 17.12. By depositing the poly(amic acid)/PAH film on PSS/PAH, we ensure full coverage of the alumina substrate, and heating of the film results in imidization of the poly(amic acid) [50–52]. We generally use heating temperatures of about  $165^\circ\text{C}$  so as to only partially imidize the film. Lower temperatures result in minimal imidization, while higher temperatures result in low fluxes. The appearance of imide peaks in the reflectance FTIR spectrum of heated films confirms partial imidization.

Under optimal preparation conditions, these polyimide membranes are extremely selective. The  $\text{Cl}^-/\text{SO}_4^{2-}$  selectivity of 4.5-bilayer PSS/PAH films coated with 2.5 bilayers of imidized poly(pyromellitic dianhydride–phenylenediamine) (PMDA–PDA)/PAH approaches 1000, and the  $\text{Na}^+/\text{Mg}^{2+}$  selectivity of these films can be as high as 200. Such high selectivities make these membranes especially attractive for applications such as water softening. Interestingly, these films yield both cation and anion selectivity. If selectivity were governed primarily by surface charge, we

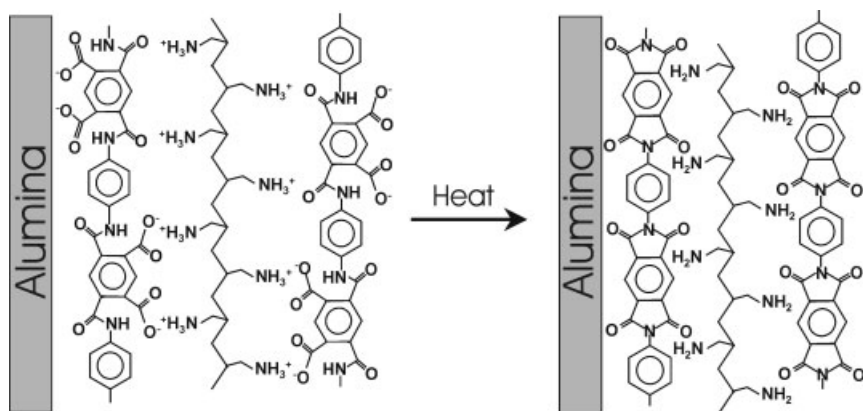


Fig. 17.12 Schematic diagram of the formation of a polyimide film by heating of a poly(amic acid)/PAH film.

would expect that polyanion-terminated surfaces would show substantial anion selectivity, but very little cation selectivity. Monovalent/divalent selectivity for both cations and anions is consistent with the results of Krasemann and Tieke with PAH/PSS membranes [6]. We suspect that the mechanism behind the selectivity of these membranes relies on differences in ion sizes and hydration energies.

### 17.3.7

#### Modeling of Selective Transport Through Layered Polyelectrolyte Membranes

To semiquantitatively understand the factors that govern the ion-transport selectivities of MPMs, we will need to utilize a model for transport through these systems. The most common starting point for modeling ion transport through membranes is Eq. (1), the Nernst–Planck equation [53].

$$J_i = -D_i \frac{dC_i}{dx} - \frac{z_i C_i D_i F}{RT} \frac{d\Phi}{dx} \quad (1)$$

This equation states that in the absence of convection, the flux,  $J$ , of ion  $i$  is the sum of diffusion and migration components. Diffusive flux is proportional to the concentration gradient  $dC_i/dx$ , while migration is proportional to the electrical potential gradient  $d\Phi/dx$  multiplied by the charge,  $z_i$ , and concentration,  $C_i$ , of the ion.  $D_i$  is the diffusion coefficient and  $F$ ,  $R$ , and  $T$  are Faraday's constant, the gas constant, and temperature, respectively.

The unique property of membranes containing fixed charge is that a Donnan potential

$$\frac{C_B^m}{C_B} = \left( \frac{|z_B| C_B}{|z_B| C_B^m + |z_X| C_X^m} \right)^{\frac{|z_B|}{|z_A|}} \quad (2)$$

develops at the interfaces between membrane and solution. Because of the fixed charges, mobile ions are not present in stoichiometric proportions in the membrane so a potential drop occurs at the membrane/solution interface. By neglecting activity coefficient variation between membrane and solution and assuming that the standard-state chemical potential is the same in the membrane and the solution, one can describe the partitioning of ions between membrane and solution using Eq. (2) [23]. In this equation  $z_X$ ,  $C_X$ ,  $z_B$ , and  $C_B$  are the charges and concentrations of the fixed ions and the excluded ions, respectively. The charge of the co-ion is  $z_A$  and the superscript  $m$  refers to the membrane phase. The Teorell–Meyer–Sievers (TMS) model of transport through ion-exchange membranes assumes Donnan equilibria at the two solution/membrane interfaces and uses the Nernst–Planck equation to calculate flux through the membrane [53, 54]. (Concentration polarization at the solution/membrane interface is assumed to be negligible.) To solve the Nernst–Planck equation, one often assumes electrical neutrality throughout the membrane (Eq. (3)), zero current (Eq. (4)), and constant flux through the membrane [23, 55, 56].

$$z_X C_X + \sum_i z_i C_i^m = 0 \quad (3)$$

$$\sum_i F z_i J_i = 0 \quad (4)$$

Adaptation of the TMS model to MPMs requires some knowledge of the charge distribution in these membranes. Krasemann and Tieke suggested that the charge distribution in PAH/PSS membranes consists of alternating positive and negative regions due to each polycation and polyanion layer [6]. They speculated that this distribution would result in selectivities that increased with the number of layers in the film. However, modeling by Lebedev et al. indicates that even if multiple polycation/polyanion interfaces are present, selectivity will not increase with the number of layers in the film [57]. Although multiply charged anions are excluded from polyanionic layers, their concentration is enhanced in polycationic layers due to the need to electrically compensate fixed cationic sites. After the initial bilayer, enhancement of anion concentration in polycationic layers effectively cancels the exclusion in polyanionic layers. A similar phenomenon will occur for cations.

Recent models of charge distribution in MPFs indicate complete intrinsic charge compensation in the bulk of the film and extrinsic charge present only at the film surface [1, 19, 20, 44]. These structural models would suggest that Donnan selectivity is controlled primarily by the membrane surface. To confirm this, we showed that changing the top layer of a membrane from a polyanion to a polycation greatly decreases (in some cases reverses)  $\text{Cl}^-/\text{SO}_4^{2-}$  selectivity as described in Section 17.3. Such results are consistent with a membrane structure that consists of a neutral bulk region and a charge distribution in the top layer(s) of the membrane [20, 58].

As an initial approximation, we simulated transport through membranes based on a uniform distribution of charge at the membrane surface [46, 48]. These simulations suggest that high  $\text{Cl}^-/\text{SO}_4^{2-}$  selectivities can be accounted for by Donnan exclusion only if there is also an order of magnitude difference in the diffusivities of  $\text{Cl}^-$  and  $\text{SO}_4^{2-}$ . As mentioned in Section 17.2, Schlenoff suggests that diffusivities may vary with ion charge due to hopping transport between transient ion-exchange sites in the bulk of the membrane [12].

Gaining a full understanding of transport through MPMs is challenging because of a lack of quantitative information about ion diffusivities and the charge distribution in the membrane. In the future, we plan to study the transport of neutral molecules through MPMs in order to avoid Donnan exclusion effects on selectivities. These studies will demonstrate, at least qualitatively, how much of a role size differences play in membrane selectivity.

## 17.4

### Conclusions

Control over the composition and chemistry of MPFs allows synthesis of films whose properties range from highly impermeable to highly selective. Although standard polyelectrolyte films are too permeable to reduce corrosion, heat-induced cross-linking of PAH/PAA increases film resistance by several orders of magnitude. Such films might prove useful under moderate corrosion conditions when an ultrathin film is advantageous.

As membranes, MPFs can allow highly selective transport of monovalent ions. Monovalent/divalent ion selectivities can be as high as 1000, and because MPMs are ultrathin, they also allow high fluxes. The reasons behind ion-transport selectivities are still under investigation, but Donnan exclusion at the surface of the membrane is a large factor in some cases. This is evident from the fact that changing the sign of the surface charge can have a dramatic effect on monovalent/divalent anion selectivity.

Because Donnan exclusion plays such an important role in determining selectivity, increases in fixed charge in a membrane enhance ion-transport selectivity. Insertion of ion-exchange sites into films by formation and removal of copper complexes or by hydrolysis of ester groups on constituent polymers results in order of magnitude increases in  $\text{Cl}^-/\text{SO}_4^{2-}$  selectivity. Deposition of hybrid membranes containing PAA/PAH or PMDA-PDA/PAH top-coatings on base layers of PSS/PAH also yields highly selective membranes, especially after post-deposition imidization.

In short, the versatility of alternating polyelectrolyte deposition coupled with post-deposition reactions allows the synthesis of a wide variety of films and membranes whose selectivity and permeability can be controlled. Use of this versatility will allow tailoring of membranes and coatings for specific applications such as corrosion prevention and water treatment.

## Acknowledgment

I thank the Department of Energy Office of Basic Energy Sciences, the National Science Foundation (CHE-9816108), the NSF-funded Center for Sensor Materials at Michigan State University, the Center for Fundamental Materials Research at Michigan State University, and the ACS Petroleum Research Fund for partial financial support of the different aspects of this work. This review presents the work of Anagi Balachandra, Jinhua Dai, Jeremy Harris, Daniel Sullivan, and Jacqueline Stair, and I very much appreciate their work and support in writing this chapter.

## 17.5

### References

- 1 G. DECHER, *Science* **1997**, *277*, 1232.
- 2 F. CARUSO, K. NIHKURA, D.N. FURLONG, Y. OKAHATA, *Langmuir* **1997**, *13*, 3427.
- 3 X. YANG, S. JOHNSON, J. SHI, T. HOLE-SINGER, B. SWANSON, *Sens. Actuators, B* **1997**, *45*, 87.
- 4 M.M. MONTREL, G.B. SUKHORUKOV, A.I. PETROV, L.I. SHABARCHINA, B.I. SUKHORUKOV, *Sens. Actuators, B* **1997**, *42*, 225.
- 5 L. KRAEMANN, A. TOUTIANOUSH, B. TIEKE, *J. Membr. Sci.* **2001**, *181*, 221.
- 6 L. KRAEMANN, B. TIEKE, *Langmuir* **2000**, *16*, 287.
- 7 J.J. HARRIS, J.L. STAIR, M.L. BRUENING, *Chem. Mater.* **2000**, *12*, 1941.
- 8 F. CARUSO, W. YANG, D. TRAU, R. RENNEBERG, *Langmuir* **2000**, *16*, 8932.
- 9 J. DAI, D.M. SULLIVAN, M.L. BRUENING, *Ind. Eng. Chem.* **2000**, *39*, 3528.
- 10 S. HAN, B. LINDHOLM-SETHSON, *Electrochim. Acta* **1999**, *45*, 845.
- 11 J.J. HARRIS, M.L. BRUENING, *Langmuir* **2000**, *16*, 2006.
- 12 T.R. FARHAT, J.B. SCHLENOFF, *Langmuir* **2001**, *17*, 1184.
- 13 G. DECHER, Y. LVOV, J. SCHMITT, *Thin Solid Films* **1994**, *244*, 772.
- 14 N.G. HOOGVEEN, M.A. COHEN STUART, G.J. FLEER, *Langmuir* **1996**, *12*, 3675.
- 15 H.G.M.V.D. STEEG, M.A.C. STUART, A.D. KEIZER, B.H. BIJSTERBOSCH, *Langmuir* **1992**, *8*, 2538.
- 16 V. SHUBIN, P. LINSE, *J. Phys. Chem.* **1995**, *99*, 1285.
- 17 J.D. MENDELSON, C.J. BARRETT, V. CHAN, A.J. PAL, A.M. MAYES, M.F. RUBNER, *Langmuir* **2000**, *16*, 5017.
- 18 S.S. SHIRATORI, M.F. RUBNER, *Macromolecules* **2000**, *33*, 4213.
- 19 J.B. SCHLENOFF, H. LY, M. LI, *J. Am. Chem. Soc.* **1998**, *120*, 7626.
- 20 J.B. SCHLENOFF, S.T. DUBAS, *Macromolecules* **2001**, *334*, 592.
- 21 Y. LVOV, in *Protein Architecture – Interfacing Molecular Assemblies and Immobilization Biotechnology* (Eds.: Y. LVOV, H. MÖHWALD), Marcel Dekker, New York, **2000**, pp. 135.
- 22 V. PARDO-YISSAR, E. KATZ, O. LIUBASHEVSKI, I. WILLNER, *Langmuir* **2001**, *17*, 1110.
- 23 J.M.M. PEETERS, J.P. BOOM, M.H.V. MULDER, H. STRATHMANN, *J. Membr. Sci.* **1998**, *145*, 199.
- 24 G.B. SUKHORUKOV, J. SCHMITT, G. DECHER, *Ber. Bunsen-Ges. Phys. Chem.* **1996**, *100*, 948.
- 25 M. LÖSCHE, J. SCHMITT, G. DECHER, W.G. BOUWMAN, K. KJAER, *Macromolecules* **1998**, *31*.
- 26 J.J. HARRIS, P.M. DEROSE, M.L. BRUENING, *J. Am. Chem. Soc.* **1999**, *121*, 1978.
- 27 H.R. ALLCOCK, F.W. LAMPE, *Contemporary Polymer Chemistry*, 2nd edn., Prentice Hall, Englewood Cliffs, NJ, **1990**.
- 28 E.A. BLUHM, E. BAUER, R.M. CHAMBERLIN, K.D. ABNEY, J.S. YOUNG, G.D. JARVINEN, *Langmuir* **1999**, *15*, 8668.

- 29 A. A. EI-AWADY, B. A. ABD-EL-NABEY, S. G. AZIZ, *J. Chem. Soc., Faraday Trans.* **1993**, *89*, 795.
- 30 J. R. SCULLY, S. T. HENSLEY, *Corrosion* **1994**, *50*, 705.
- 31 J. DAI, A. W. JENSEN, D. K. MOHANTY, J. ERNDT, M. L. BRUENING, *Langmuir* **2001**, *17*, 931.
- 32 P. H. ABELSON, *Science* **1989**, *244*, 1421.
- 33 S. T. DUBAS, T. R. FARHAT, J. B. SCHLENOFF, *J. Am. Chem. Soc.* **2001**, *123*, 5368.
- 34 P. STROEVE, V. VASQUEZ, M. A. N. COELHO, J. F. RABOLT, *Thin Solid Films* **1996**, *284–285*, 708.
- 35 J.-M. LEVÁSALMI, T. J. MCCARTHY, *Macromolecules* **1997**, *30*, 1752.
- 36 L. KRASEMANN, B. TIEKE, *J. Membr. Sci.* **1998**, *150*, 23.
- 37 L. KRASEMANN, B. TIEKE, *Mater. Sci. Eng. C* **1999**, *8–9*, 513.
- 38 J. MEIER-HAACK, W. LENK, D. LEHMANN, K. LUNKWITZ, *J. Membr. Sci.* **2001**, *184*, 233.
- 39 C. LIU, C. R. MARTIN, *Nature* **1991**, *352*, 50.
- 40 R. TAKAGI, M. NAKAGAKI, *J. Membr. Sci.* **1992**, *71*, 189.
- 41 J. L. STAIR, J. J. HARRIS, M. L. BRUENING, *Chem. Mater.* **2001**, *13*, 2641–2648.
- 42 Although in early studies we began alternating polyelectrolyte deposition on porous alumina with a polycation, alumina membranes are positively charged at low to moderate pH values, and thus in our more recent work we first adsorbed the polyanion.
- 43 D. YOO, S. S. SHIRATORI, M. F. RUBNER, *Macromolecules* **1998**, *31*, 4309.
- 44 S. T. DUBAS, J. B. SCHLENOFF, *Macromolecules* **1999**, *32*, 8153.
- 45 G. LADAM, P. SCHAAD, J. C. VOEGEL, P. SCHAAF, G. DECHER, F. CUISINER, *Langmuir* **2000**, *16*, 1249.
- 46 A. BALACHANDRA, M. L. BRUENING, *Macromolecules* **2002**, *35*, 3171.
- 47 The selectivities of the untemplated PAA/PAH membranes are slightly larger than those reported earlier in the chapter because films were deposited under different conditions.
- 48 J. DAI, J. I. LEE, M. L. BRUENING, *Macromolecules* **2002**, *35*, 3170.
- 49 D. M. SULLIVAN, M. L. BRUENING, *J. Am. Chem. Soc.* **2001**, *123*, 11805–11806.
- 50 J. W. BAUR, P. BESSON, S. A. O'CONNOR, M. F. RUBNER, *Mater. Res. Soc. Symp. Proc.* **1996**, *413*, 583.
- 51 Y. LIU, A. WANG, R. O. CLAUS, *Appl. Phys. Lett.* **1997**, *71*, 2265.
- 52 I. MORIGUCHI, Y. TERAOKA, S. KAGAWA, J. H. FENDLER, *Chem. Mater.* **1999**, *11*, 1603.
- 53 T. TEORELL, *Prog. Biophys.* **1953**, *3*, 305.
- 54 K. H. MEYER, J.-F. SIEVERS, *Helv. Chim. Acta* **1936**, *19*, 649.
- 55 M. D. AFONSO, M. N. DE PINHO, *J. Membr. Sci.* **2000**, *179*, 137.
- 56 W. R. BOWEN, H. MUKHTAR, *J. Membr. Sci.* **1996**, *112*, 263.
- 57 K. LEBEDEV, P. RAMÍREZ, S. MAFÉ, J. PELLICER, *Langmuir* **2000**, *16*, 9941.
- 58 R. V. KLITZING, H. MÖHWALD, *Langmuir* **1995**, *11*, 3554.

## Index

### **a**

absorbing chromophores 339  
accelerated deposition 212  
adhesion of particle 289  
adhesion of the metal 143  
adsorbed counter ions 398  
adsorption kinetics 10, 396  
adsorption kinetics polyelectrolytes 395  
advancing contact angle 145  
affinity of Li<sup>+</sup> cations to DNA 59  
AFM 274  
AFM measurements 192  
aggregates 336  
aggregation of protein 164  
alastic modulus 375  
albumin 167  
alignment of chromophore groups 187  
alignment of chromophores 467  
alignment of functional fragments 196  
alkylsiloxanes 219  
alternation in  $\zeta$ -potential 337  
alumination electrode interface 138  
aluminosilicate clays 229  
amidation reaction 491  
amidine functional group 292  
aminosilanization reagents 23  
amorphous protein aggregates 346  
amperometric sensor 309  
amphiphilic block copolymers 144, 148  
amphiphilic polymer 72, 387  
amphoteric exchangers 122  
analytical centrifugation 71  
analytical ultracentrifugation 61  
anchoring block 286  
angle reflectometry 10  
anion-transport selectivities 497  
anisotropic particles 224  
anisotropy 442  
anisotropy of nanoparticles 224

annealing 12  
annealing of defects 382  
antibacterial properties 3  
antifouling 3  
antigens 358  
antireflective coatings 3  
antistatic coatings 3  
area-selective binding 16  
artificial biochemical systems 171  
assembly of coated colloids 351  
assembly of colloidal particles 288  
assembly of colloids 208  
assembly of metal oxides and proteins 162  
assembly of particles 289  
assembly of weak polyelectrolyte multi-  
layers 134  
atomic force microscopy 10, 139, 219, 248,  
274, 341, 475  
attenuated total reflection 395  
attenuated total reflection Fourier transform  
infrared spectroscopy 10  
attractive electrostatic interactions 93  
attractive interactions 116  
attractive ionic interactions 275  
average water content 404  
azobenzene derivatives 428, 434

### **b**

back-to-back metal ion receptors 408  
bacteriorhodopsin 167  
barium ferrite nanocolloid 224  
barium ions 456  
barrier layer 26, 29  
barrier layer of montmorillonite 28  
basal spacing reflection 248  
bi-functional polymers 24  
bimacromolecular reaction 55  
binding of Na<sup>+</sup> counterions 69

- biocatalytic activities 356
- biocolloids 345, 348
- biocompatibility 3
- biofunctional coatings 343
- biofunctional fluorescent micro-  
particles 358
- biological applications 167
- biological cells 48
- bioreactors 171, 309
- biosensing 3
- biosensors 168, 309
- biospecific ligand binding 367
- biotechnological applications 356
- biotinylated poly(L-lysine) 15
- bipolar polyelectrolyte membranes 451
- bipolaron absorptions 295
- bipyridine ligands 408
- birefringence contribution 473
- Bjerrum length 89
- blending 99
- block and graft copolymers 285
- block copolymers 283
- block ionomer complexes 72
- bolaamphiphiles 429, 434
- bovine serum albumin 341
- Bragg peaks 20, 403
- Bragg reflections 180
- branched PDADMAC 401
- branched polyethyleneimine 278
- Brewster angle microscopic 247
- bridging between individual colloids 23
- building blocks, photo-active 301
- bulk polyelectrolyte complexes 187
- bulk polymer charge 109
  
- c**
- cadmium polynuclear complex 157
- calcination 352, 371
- Calcium Green 28
- capacitive currents 413, 492
- capillary zone electrophoretic separa-  
tions 117
- capping polyelectrolyte 490
- capsule elasticity 382
- capsule permeability 376f.
- capsules 126, 379
- carboxyfluorescein 387
- carboxylate stretches 491
- carboxylic acid functionalized monolayer  
surfaces 273
- cascade modification 309
- catalase crystals 356
- catalytic currents 315
- cationic compounds on metal oxide  
gels 157
- cationic semiconductor nanoparticles 259
- CdS clusters 219
- CdS semiconductor nanoparticles 254
- CdSe nanocluster/polymer thin film 478
- CdSe quantum dots 475
- CdSe/PDDA thin films 474
- CdTe nanocrystals 350
- cellulose acetate-coated glass 227
- centrifugation 335
- chain conformation 399
- chalcogenides 141
- characterization of coated colloids 333
- charge balance 99
- charge carrier 124
- charge density 134, 448
- charge distribution 489
- charge expulsion 113
- charge extrusion 113
- charge fluctuation 93
- charge overcompensation 11, , 399
- charge penetration length 129
- charge reversal 72
- charge storage 263
- charge transfer 442
- charge transfer band 442
- charge transfer complexes 218
- charged globular proteins 75
- charged nanoparticles 413
- charging characteristics 266
- charging hysteresis 262
- chemical gradients 386
- chemical reduction 253
- chemical sensing 3
- chemically modified electrodes 304, 324
- chemistry in capsules 389
- chitosane 366
- choice of assembly conditions 141
- chromophoric units 440
- chronopotentiometric curves 266
- chymotrypsin 346, 389
- chymotrypsin aggregates 346
- classical ion exchanger resins 121
- clay nanoplatelets 246
- clay-based systems 190
- cluster size 290
- coated catalase crystals 345
- coated colloids 331
  - characterization 333
  - preparation 333
- cobalt(II)-substituted POM compound 417
- coil conformation 434



- colloid particles 334, 337
  - colloid precipitation 349
  - colloidal biocatalysts 354
  - colloidal crystal templates 352
  - colloidal crystals 351f.
  - colloidal stability 334
  - colloidal templates 413
  - colloids 334
  - commercial applications 30
  - compaction of IPEC species upon specific binding 71
  - compartmentalization 26
  - compartmentalized film 26
  - compartmentalized multilayers 198
  - competitive ion pairing 101, 103
  - complementary coloring electrochromic device 295
  - complex microstructures 276
  - complex multilayer structures 276
  - complex stratified materials 225
  - complex systems 1
  - complex waveguides 3
  - composite particle diameter 340
  - compositionally graded heterostructures 138
  - compression modulus 384
  - concentration correlations 90
  - concentration gradient 377
  - concentration polarization 507
  - concentration profile 95
  - conducting polymer electrodes 287
  - conductive polyanion 315
  - conductive shells 376
  - confocal fluorescence image 173
  - confocal fluorescence microscopy 379
  - confocal microscopy 366, 372
  - conjugation length 434
  - constrained equilibrium 94
  - contact lenses 30, 100
  - continuum elastic theory 384
  - contrast gradients 25
  - controlled cluster size on multilayer templates 290
  - controlled release 378
  - controlling charge density 503
  - coordinative interactions 441, 457
  - copolymer adsorption 144
  - core decomposition 386
  - core destruction 369, 371
  - core dissolution 371
  - core materials 364
  - core removal 369, 378
  - core-shell materials 337
  - core-shell nanoparticles 210
  - corrosion 126
  - corrosion protection 3
  - corrosion studies 492
  - Coulomb interaction 89, 369
  - Coulombic repulsion 379
  - counter ions 101f., 411
  - covalently attached multilayer assemblies 318
  - critical salt concentration 108
  - crossed-linked interpolyelectrolyte complexes 74
  - crosslinked melamine formaldehyde 364
  - crosslinked membranes 499
  - crosslinked multilayer films 318
  - crosslinked PAA films 490
  - crosslinking 321, 375
  - crosslinking density 449
  - crystal-like arrangement 440
  - crystallization promoter 388
  - Cu<sup>2+</sup> complexes to imprint charged sites 503
  - cyclic radiovoltammograms 113
  - cyclic voltammetry 254, 315, 418, 488
  - cyclic voltammograms 306, 489, 492
  - cytochrome c 162
- d**
- damage to the particle surface 336
  - damping of Bragg peaks 82
  - day sheets 209
  - Debye length 401
  - Debye screening length 89
  - Debye-Hückel potential 89
  - decay rate  $l_{cp}$  116
  - decomposition 108
  - deconstruction of PEMUs 108
  - degree of conversion 48
  - degree of hydration 191
  - degree of selectivity 291
  - dendrimers 59
  - dependence of film thickness on ionic strength 400
  - depolymerization 369
  - deproteinizer 371
  - derivatization and photocleavage 504
  - derivatized polyelectrolyte films 493
  - deuterated layers 21
  - deuterated polymers 403
  - device efficiencies 138
  - dextran 349
  - diacetylene derivatives 429
  - diazonium groups 301
  - dielectric constant 100

- difference in free energies 58
- differential scanning calorimetry 462
- differential staining 179
- diffusion coefficient 120, 368, 377, 401 f.
- diffusion coefficient measurements 370
- diffusion collisions of polyelectrolyte coils 53
- diffusion dialysis 496
- dilute polyelectrolyte solution 89
- diphenyldiketopyrrolopyrrole derivatives 438
- dipolar orientation 467
- dipole-dipole interactions 231
- direct exchange of metal ions 412
- directed assembly 1
- Disperse Red 1 462
- disproportionation via interchange 67
- dissolution 387
- distance of interpenetration 182
- distance-dependent Förster energy transfer 2
- distribution of surface charge 113
- distribution of the concentration of chain segments 22
- DNA 59, 349
- Donnan equilibrium 386
- Donnan exclusion 121, 498, 502
- Donnan rejection 457
- donor-acceptor interactions 5
- donor-acceptor bonding 60
- drug crystals 377
- drug release rate 358
- drug removal 378
- dye precipitation 387
- dye probes 369
- dye-labeled polymers 356
  
- e**
- echinocyte cells 366
- echinocytes 348
- effect of irradiation 10
- effective dissociation constant 51
- efficient compartmentalization 259
- electrically compensated 489
- electroactive assemblies 441
- electroactive materials 301, 314
- electroactive properties 441
- electroactive species 304, 490
- electrocatalytic response 309
- electrochemical device 294
- electrochemical reduction of graphite oxide 254
- electrochemical response 427
- electrochemically isolated subunits 412
- electrochromic cell 295
- electrochromic devices 420, 444
- electrochromic response 420
- electrochromic thin films 294
- electrochromics 326
- electrode 305, 308
- electrode interfaces 138
- electrode, selectivity of the 308
- electroless metal deposition 288
- electroless plating 141, 287
- electroneutralization 102
- electron exchange interactions 231
- electronically active polymeric materials 137
- electronic applications 259
- electronic device 473
- electron self-exchange reactions 412
- electron transfer 488
- electro-optic coefficients 478
- electro-optic materials 461
- electro-optic modulation 473, 477
- electro-optic poled polymers 468
- electroosmotic flow 109, 117
- electrophoretic mobility 72
- electrostatic and secondary interactions 271
- electrostatic blobs 90
- electrostatic bonds 382
- electrostatic force 91
- electrostatic interactions 89, 218, 277, 334
- electrostatic neutralization 162
- electrostatic persistence length 90
- electrostatic pressure 93
- electrostatic repulsion 216, 221
- electrostatic repulsion of polyion charges 64
- elimination of charged groups 112
- ellipsometry 7, 10
- encapsulated biomaterial 355
- encapsulation of proteins 173
- energy densities 264
- energy transfer 401
- enhanced adhesion 291
- enhanced colloidal stability 343
- enhanced mechanical strength 228
- enhancement electroluminescence 29
- entropy 116
- entropy gains 116
- enzymatic activity 172, 354
- enzymatic catalysis 354
- enzyme cascades 367
- enzyme crystals 345
- enzyme engineering 310
- enzyme immobilization 310
- enzyme layer number 355
- enzyme multilayer film 310

- enzyme multilayer-coated particles 354  
 enzyme multilayers 354  
 enzyme particles 345, 355  
 enzyme reactors 354  
 enzyme-polyelectrolyte complexes 354  
 enzymes 309  
 enzyme-substrate reactions 343  
 EO modulator devices 471  
 equilibrated nonstoichiometric interpoly-  
   electrolyte complexes 61  
 equilibrium conversion in polyion  
   substitution reaction 57  
 equilibrium degree of swelling 74  
 equilibrium structure of polyion com-  
   plexes 22  
 equilibrium vs. nonequilibrium condi-  
   tions 117  
 erythrocytes 365, 388  
 ethylenediamine 412  
 excess surface charge reversal 128  
 exchange of counter ions 403  
 exchangeable cations 246  
 excimer absorption 414  
 excimer emission 414  
 excitonic luminescence 224  
 excluded volume interactions 89, 91  
 excluded volume theory 64  
 exfoliated clay platelets 210  
 exfoliated graphite oxide 190  
 exfoliated montmorillonite clay  
   platelets 228  
 exfoliated smectites 189  
 exfoliated transition metal oxides 188  
 external electric field 478  
 external quantum efficiencies 138  
 external salt cations 57  
 extrinsic charges 112f.  
 extrinsic charge compensation 103f.  
 extrinsic compensation 127, 129  
 extrinsically charge-compensated sites 503
- f**
- fast electron transfer 412  
 Fe<sub>2</sub>O<sub>3</sub> particles 388  
 Fe<sub>3</sub>O<sub>4</sub> nanoparticles 230  
 ferrocene dimethanol 490  
 field-effect transistor 168  
 field-emission scanning electron micro-  
   scopy 495  
 film microstructure 179  
 film/substrate roughness 216  
 filtration 336  
 Fischer esterification 493
- flat band potential 261  
 flexible elastic bodies 79  
 flexible macromolecules 209  
 flexible polyions 18  
 fluorescein 347  
 fluorescein particles 378  
 fluorescein-4-isothiocyanate 173  
 fluorescence emission band 414  
 fluorescence micrographs 16, 374  
 fluorescence optical micrograph 345  
 fluorescence recovery after  
   photobleaching 368  
 fluorescence spectroscopy 377  
 fluorescent microspheres 356  
 fluorescent particles 356  
 fluorescently labeled polyelectrolyte 335  
 fluorescing chromophores 339  
 fluorometric titration curves 70  
 flux 120  
 flux of ions through the membrane 496  
 force curves 279  
 formation and structure 395  
 Förster radius 402  
 forward bias 138  
 fraction of water immobilized 369  
 free acid groups 137  
 free energies of association 107  
 free energies of ionization 49  
 free energy 49  
 free energy change 101  
 free membranes 100  
 free-standing ultrathin films 227  
 Fresnel reflectivity 180  
 FTIR 320  
 FTIR absorption spectroscopy 123  
 fuel cell 100  
 fullerene C<sub>60</sub> 24  
 fullerene nanowires 221  
 fullerene-ferrocene dyads 221  
 fullerenes 25  
 fulleropyrrolidinium ion 221  
 functional amino surfaces 286  
 functional assemblies 326  
 functional groups at the surface 144  
 fundamental intensity 467
- g**
- gas permeation 446f.  
 Gaussian electrostatic blobs 89  
 globular species 59  
 glucoamylase 167, 172  
 gluconolactone 172  
 glucose oxidase 167, 306, 341

- gold electrodes 488
  - gold nanoparticles 316, 327, 344
  - gold nanoparticles/polymer hybrid 327
  - gold/platinum nanorods 210
  - Gouy-Chapman length 91
  - graded semiconductor films 231 f.
  - graft copolymers 283
  - grafting-from polyaddition reaction 441
  - graphite oxide 188
  - graphite oxide nanoplatelets 250
  - growth pattern 214
  - guest polyelectrolyte 51
- h**
- H-aggregated chromophores 434
  - half-conversion time 56
  - heat-induced amidation 490
  - hectorite 188
  - hectorite platelets 190
  - helix-coil transition 51
  - heterocoagulation of polymer 349
  - hexagonal close packing 157
  - hierarchically ordered monolith 352
  - high energy density power supply 263
  - high salt concentration limit 123
  - high-capacity carbonaceous materials 264
  - highly crystalline materials 77
  - highly swollen core 74
  - histone 166
  - hollow capsules 173, 353, 364, 378
  - hollow colloids 353
  - hollow shells 370
  - homogeneous deposition of polymer dye 465
  - hopping 124
  - horseradish peroxidase 341, 389
  - host polyelectrolyte 51
  - host-guest chemistry 415
  - hybrid assemblies 189
  - hybrid clay/polyelectrolyte multilayers 180
  - hybrid films 500
  - hybrid materials 282
  - hybrid membranes 500, 502
  - hybrid organic/inorganic compartmentalized multilayers 198
  - hybrid superlattices 196, 200
  - hybrid-structures 326
  - hydration 102
  - hydration forces 279
  - hydrodynamics 120
  - hydrogen bonding 50, 81, 277, 367
  - hydrogen bonding directed self-assembly 326
  - hydrogen bridging 5
  - hydrogen-bonded multilayers 148
  - hydrogen-bonding interactions 144
  - hydrophilic backbone 278
  - hydrophilic negatively charged particles 224
  - hydrophilic/hydrophobic balance 190
  - hydrophobic complexes 106
  - hydrophobic interactions 50, 54, 60, 218, 277
  - hydrophobic spacer 187
  - hydrophobic versus hydrophilic secondary interactions 277
  - hydrophobicity 102, 145
  - hydrophobicity index 129
  - hydrocalcite nanosheets 195
  - hyperswelling 107
- i**
- IgG coatings 342
  - imide conversion 171
  - immobilized antibodies 358
  - immunoassays 358
  - immunodiagnosics 357
  - immunoglobulin 341
  - immunoreagents 357
  - impedance spectroscopy 488
  - In<sub>2</sub>S<sub>3</sub> 224
  - increasing ionic strength 396
  - index of hydrophobicity 106
  - indium methoxyethoxide 162
  - induced dipole moment 480
  - industrial process 30
  - influence of core size 344
  - inking solution 285
  - ink-jet printing 141, 143, 148
  - inorganic colloid 364
  - inorganic cores 364
  - inorganic material epitaxially deposited 210
  - inorganic nanocomposites 141
  - inorganic nanoplatelets 188
  - inorganic shell 372
  - inorganic sintered films 383
  - inorganic templates 375
  - in-situ characterization 9
  - interaction energy 105
  - interaction of positive counterions 58
  - $\pi$ - $\pi$  interactions 413, 438
  - interchain screening 396
  - interchange reactions 52
  - interchange restriction 60
  - interfacial region 398
  - interfacial roughness 410, 418
  - interference 308

- interferometer 477
  - intermolecular interactions 208, 217
  - intermolecular organization 221
  - intermolecular rearrangements of polyions 53
  - intermolecular salt bonds 80
  - internal dynamics 368
  - internal rearrangements 52
  - internal roughness 182
  - internal structure 90, 181, 403
  - internally structured polyelectrolyte multilayers 177
  - interpenetration 112, 403
  - interpenetration of chains 210
  - interpenetration of linear polyions 75
  - interpolyelectrolyte complexes in external salt solutions 66
  - interpolyelectrolyte reactions 48
  - intramolecular rearrangements of polyions 53
  - intrinsic 103
  - intrinsic bulk compensation 109
  - intrinsic charge compensation 507
  - intrinsic compensation 104, 113, 127, 129
  - inverse opals 352
  - ion-assisted decomposition 129
  - ion breathing 107, 129
  - ion doping 124, 129
  - ion exchange 104
  - ion filtering 129
  - ion lubrication 129
  - ion pairing 102, 105,, 112
  - ion pairs 102
  - ion permeability 118
  - ion permeation 451
  - ion selective permeability 375
  - ion self-exchange 110
  - ion self-trapping 129
  - ion swelling 129
  - ion transport 118, 451
  - ion trapping 129
  - ionenes 185
  - ion-exchange 102, 141
  - ion-exchange sites 493
  - ionic conditions 222
  - ionic polymer dyes 464
  - ionic polypeptides 51
  - ionic shielding 274, 292
  - ionic strength 222, 400
  - ionic transport 119
  - ionically conductive films 296
  - ion-permeability 487
  - ion-separation membranes 495
  - IPEC aggregates 61
  - iron oxide nanoparticle shells 353
  - irreversibility 96, 118
  - $\gamma$ -irradiation of crystals 433
  - isoelectric point 224
  - isolated YIG islands 213
  - isotopic labeling 403
- j**
- J-aggregates 196
- k**
- Keggin type POM 417
  - Keplerate 415
  - Kiessig fringes 321, 404, 410
  - kinetic curves of polyion coupling 54
  - kinetics of adsorption 222
  - kinetics of macromolecular rearrangements 285
  - kinetics of polyelectrolyte coupling 52
  - kinetics of substitution reaction 60
  - kinetics of transfer 285
  - kinetic timescales of polymer transfer 284
- l**
- lactate dehydrogenase 346
  - lamellar phase 186
  - Langmuir-Blodgett technique 2
  - laponite-based hybrid films, structure 192
  - lateral domain expansion 215
  - lateral expansion mode 214
  - lateral resistivity of (PDDA/GO) 254
  - latex particles 344
  - layer interpenetration 25
  - layer order 226
  - layer profiles 21
  - layer thickness 321
  - layer-by-layer colloid templating 332
  - layered aluminosilicates 46
  - Levich equation 120
  - Li<sup>+</sup>-ion interaction into graphite 264
  - Li<sup>+</sup>-ion intercalation cathode 265
  - lifetime of the bound state 382
  - light emitting device 151
  - light emitting diodes 27
  - light emitting Ru(II) complex 138
  - light emitting thin film devices 137
  - light scattering 61
  - light-emission 151
  - linear charge density 55
  - linear growth behavior 23
  - linear PDADMAC 401
  - linear polyethyleneimine 278

- linear superstructures 221
  - linearly polarized light 437
  - lipid assembly 343
  - lipid-coated hollow polyelectrolyte shells 343
  - liquid cores 365
  - liquid crystalline ionomers 195
  - lithium anode 264
  - lithium batteries 263f.
  - lithium intercalation compound 268
  - local chain conformation 94
  - local charge fluctuations 401
  - long-distance Coulomb interaction 220
  - long-range electrostatic attraction 219
  - loop 396
  - loops and tails 489
  - loopy conformation 135
  - low-drive-voltage modulators 471
  - luminance levels 138
  - luminescence quenching 52
  - luminescence spectra 233
  - luminescent CdTe nanocrystals 232
  - luminescent dye multilayers 280
  - luminescent nanocrystals 350
  - lyotropic mesophase 184, 187
  - lysozyme 166, 75
- m**
- Mach-Zehnder interferometer 471
  - Mach-Zehnder interferometry 477
  - macroporous monolith 352
  - magnetic films 208
  - magnetic nanoparticles 354
  - magnetic phenomena 230
  - magnetic properties of nanoparticles 227
  - magnetic properties of stratified assemblies 229
  - magnetization curve 227
  - magnetization plots 231
  - magnetization reversal 231
  - Maker fringe pattern 468
  - maltose sensor 311
  - matrix for molecular imprinting 168
  - maximum surface density of nanoparticles 219
  - mean field calculation 91
  - mean field theory 91
  - mechanical behavior 80
  - mechanical properties of interpolyelectrolyte complexes 76
  - mechanism 101
  - mechanism of polyelectrolyte coupling 52
  - mediator 313
  - melamine formaldehyde 369
  - melamine resin 370
  - melamine resin particles 369
  - membrane currents 123
  - membrane filtration 336
  - membrane formation 495
  - membrane materials 500
  - membrane microstructure 447
  - membrane reactor 27
  - membrane selectivity 18, 508
  - membrane separations 126
  - membrane structure 495
  - membrane surface 507
  - membranes 118, 487
    - cross-linked 499
  - membranes of weak polyelectrolytes 80
  - mesomorphic organization 195
  - mesomorphic polyelectrolytes 196
  - mesomorphic polyions 195
  - mesoporous materials 351
  - mesoscale objects 291
  - metal alkoxides 156
  - metal cation binding 142
  - metal coated particle arrays 293
  - metal coordination 367
  - metal disulfide 188
  - metal nanoparticles 344, 356
  - metal patterns 143
  - metal phosphates 188
  - metal/insulator/metal 259
  - metallic silver particles 375
  - metallized shells 376
  - metallo-supramolecular coordination polyelectrolytes 408
  - metallo-supramolecular devices 405
  - methyl surface 278
  - Methylene Blue 148
  - Methylene Blue staining 148
  - mica sheets 229
  - microchannel flow control 3
  - micro-contact printing 15, 146, 148, 274
  - micro-contact printing techniques 143
  - microelectrophoresis 337, 341
  - microenvironmental effects 419
  - microfluidic systems 109
  - microfluidics 100, 117
  - microgravimetry 410
  - micro-patterns 151
  - microporous thin films 139
  - microstripline electrode 471
  - microstructure membrane 447
  - microwave absorber 367
  - mineral platelets 27

- mismatch 384
  - mixed valence hexacyanometalate salts 42
  - modeling of selective transport 506
  - modified colloidal particles 279
  - modified electrodes 418
  - modulating torque 480
  - molecular dyes 208
  - molecular dynamics 368
  - molecular organization 137
  - molecular orientation 437
  - molecular recognition 3, 168
  - molybdenum polyoxometalate clusters 417
  - monodisperse colloid spheres 351
  - monodisperse particles 338
  - monomer concentration profile 92
  - monovalent/divalent selectivity 506
  - Monte Carlo simulations 126
  - montmorillonite 188
  - morphological reorganizations 139
  - multi-bipolar membrane 451
  - multi-compartmentalized films 199
  - multi-element arrays 281
  - multifunctional materials 226
  - multilayer electrochemistry 113
  - multilayer formation 94
  - multilayer formation, theory 87
  - multilayer heterostructures 138
  - multilayer/solution interface 116
  - multimaterial films 24
  - multiple level heterostructures 282
  - multiple level patterning 284
  - multisite electrostatic bonding 51
  - multisite interaction 49
  - multivalent metal cations 493
  - myoglobin 166
- n**
- nanocolloids 207f.
  - nanocomposite core-shell particles 333
  - nancontainer 389
  - nanocrystallites 388
  - nano-filtration 169
  - nanometer scale organization 221
  - nanoparticles 207 f., 340
  - nanoparticle synthesis 141 f.
  - nanoplatelets 245
  - nanorainbows 231
  - nanoreactors 26, 141 f.
  - nanoscopic reaction spaces 27
  - nanotechnological devices 221
  - nanowires 259
  - negative selectivity 275
  - negatively charged gold colloids 23
  - negatively charged latex particles 173
  - Nernst-Planck equation 506
  - network structure 449
  - neutron reflectivity 400, 403 f.
  - neutron reflectivity scans 21
  - neutron reflectometry 180
  - nickel electroless plating 143
  - niobium butoxide 162
  - NLO thin films 464
  - NMR relaxation experiments 369
  - noble metals 141
  - noncentrosymmetric CdSe quantum dot-doped thin films 475
  - noncentrosymmetric thin films 464
  - nonelectrostatic interactions 23
  - nonequilibrium conditions 118
  - nonequilibrium state 53
  - nonflexible objects 23
  - nonionic interactions 218
  - nonlinear control of diffusion coefficient 124
  - nonlinear optical measurements 467
  - nonlinear optical polymers 462
  - nonsoluble stoichiometric complexes 76
  - nucleation sites 390
  - number of water molecules per polyelectrolyte 400
  - nylon-like films 491
- o**
- octahedral complexes 408
  - oligo-charged molecules 323
  - oligoethylene glycol resist 283
  - oligoethylene oxide 277
  - onion skins 100
  - onionskin PEMUs 108
  - open circuit voltage 265
  - oppositely charged hydrogels 74
  - optical communication devices 474
  - optical memory 420
  - optical parametric oscillator 467
  - optical properties 356
  - optical reflectometry 10
  - optical stop band 351
  - optical waveguide lightmode spectroscopy 10
  - optically functional materials 356
  - optimum pH 222
  - ordered arrays 351
  - ordered colloidal arrays 289
  - ordered macroporous monolith 353

- ordered microcrystals 433
- ordered stratified superlattice 198
- ordered structures in two and three dimensions 288
- organic clay-complexes 246
- organic colloid spheres 344
- organic dyes 156, 323
- organic zeolite membranes 457
- organic-inorganic hybrid materials 327
- organic-inorganic hybrid polymers 441
- orientation 196
- orientational distribution of CdSe quantum dots 483
- osmotic pressure 93, 345, 370, 373, 383
- osmotically active compounds 379
- osmotically induced stretching 370
- overcompensation 18, 128
- overcompensation charge 91, 95
- overshoot 397
- oxide layer on aluminium 492
- oxidized aluminium surface 492
- p**
- palladium 143
- parallel orientation 228
- paramagnetic quenching 401
- partial complexation of carboxylate groups 503
- partial desorption 216, 397
- partial esterification 493
- partial removal of YIG particles 216
- partially ordered films 184
- particle aggregation 223, 336
- particle density 219
- particle shape 224
- particle/polymer assemblies 291
- partitioning of ions 507
- patterned conducting films 288
- patterned multilayer film 147
- patterned polyelectrolyte multilayers 146
- patterned polymeric microstructures 274
- patterned surface 143
- patterning 15
- patterning approaches 141
- patterning of weak polyelectrolyte 145
- Patterson functions 180, 199
- PDMS stamp 285
- percolating microporous network 140
- perdeuterated PSS 20
- permanent dipole moment 480
- permanent pores 378
- permeability 126, 324, 368, 401, 488, 496
- permeability between sublayers 195
- permeability changes 379
- permeability control 376
- permeability of multilayers 413
- permeable coatings 415
- permeate 448
- permeation mechanisms 377
- permeation rate 451, 454
- permeation rates of gasses 447
- perovskites 188
- peroxidase 167
- persistence length 89, 382
- pervaporation 118
- pervaporation separation 447
- pH difference 386
- pH matrix 136
- pH sensitive fluorescent dye 398
- pH sensitive fluorescent probes 386
- pH sensitive molecules 134
- pH sensors 419
- phase separation 66
- phase shift  $\phi_{sp}$  481
- pH-controlled fabrication 133
- pH-driven spinodal decomposition 139
- phosphatidylcholine 73
- photoablation 15
- photoactive materials 318
- photobleaching 390
- photochemical process 428
- photocleavable groups 503
- photocleavage 504
- photocrosslinkable polyelectrolytes 194
- photocrosslinking 15, 152, 390
- photocurrent 221, 445
- photodegradation 255
- photodesorption 16
- photoelectrochemical behaviour 444
- photoelectrochemical measurements 254
- photoinduced sulfonic ester 320
- photoinitiator 375
- photoinitiator-labeled PAA copolymer 151
- photoisomerization 434
- photolithographic techniques 151
- photon coherence 182
- photonic crystal 375
- photonic devices 3
- photonic materials 351
- photoorientation 437
- photopatterning 15
- photopolymerization 429
- photoreaction 321, 375
- photoreactions in LBL 428
- photoreactive assemblies 428



- photoreactive diazo-resin 318  
 photoresponsive properties 445  
 photooxidation of water 254  
 phthalocyanines 305  
 phyllosilicates 188  
 pin-hole densities 138  
 plastic deformation 385  
 plastic surfaces 287  
 plasticity 385  
 plasticizer 79  
 Poisson-Boltzmann equation 91  
 polar-ordered state 468  
 pollutant photodestruction 256  
 poly(2-vinylpyridine) 209  
 poly(amic acid) 505  
 poly(amines) 66  
 poly(glutamic acid) 51  
 poly(lysine) 51  
 poly(metal tetrathiooxalates) 441  
 poly(phenylene vinylene) 112  
 poly(*p*-phenylene-vinylene) 28, 138  
 poly(sulfates) 66  
 poly(sulfonates) 66  
 poly(vinylamine) 464  
 polyaniline 139, 288, 326, 376  
 polycationic diazo-resins 324  
 polydiacetylene 429  
 polydimethylsiloxane stamp 274  
 polydyes 462  
 polyelectrolyte adsorption 72  
 polyelectrolyte complexes 47, 92, 99  
 polyelectrolyte coupling  
   – kinetics 52  
   – mechanism 52  
 polyelectrolyte interdiffusion 107  
 polyelectrolyte multilayers on  
   particles 335  
 polyelectrolyte protein complexation 50  
 polyelectrolyte templates 77  
 polyelectrolytes at interfaces 90  
 polyester 463  
 polyhydroxy compounds 156  
 polyimide membranes 505  
 polyion coupling reactions 50  
 polyion exchange reaction 52  
 polyion substitution reaction 52  
 polymer charge density 398  
 polymer charge extrusion 129  
 polymeric catalyst 386  
 polymeric counterions 435  
 polymer-inorganic particles 340  
 polymeric glasses 380  
 polymer-lipids 343  
 polymer molecular weight 135  
 polymer-on-polymer micro-contact  
   printing 146  
 polymer-on-polymer printing 146  
 polymer-on-polymer stamping 282  
 polymer-polymer interactions 101  
 polymer-proteins 341  
 polymer stamping 283  
 polymer stripping 118  
 polyoxometalate clusters 415  
 polystyrene latex colloids 279  
 polystyrene latex particles 292  
 polyviologen 113, 295  
 pore morphology 352  
 pores 370  
 porous alumina 495  
 porous hollow SiO<sub>2</sub> spheres 372  
 porous supporting membrane 446  
 porphyrins 305  
 positive vacancies 246  
 positively charged surfactant 292  
 ζ-potential 337, 398, 413  
 potentiometric copper (II) sensors 305  
 potentiometric titration 49  
 p-polarized light 467  
 PPV 138  
 precipitation and dissolution 387  
 preferential orientation 229, 437  
 preferred region of adsorption 291  
 preparation of coated colloids 333  
 prestructured ionene deposit 187  
 Preyssler-type heteropolytungstate 420  
 processing 100  
 proteases 346  
 protection of surfaces 490  
 protein aggregates 347  
 protein capsule 173  
 protein density 163  
 protein layers 342  
 protein multilayers 155, 341  
 protein precipitates 371  
 protein shell 173  
 protein/polyelectrolyte assembly 166  
 proteins as a structural material 367  
 proton distribution 398  
 proton exchange membranes 296  
 protonation cluster 419  
 Prussian blue 441f.  
 Prussian green 444  
 pyrene 347  
 pyrene stacks 414  
 pyrenyl tagged PMA\* 70  
 pyrenyl tags 53

**q**

quadratic electro-optic effect 477  
 quadratic electro-optic modulation 481, 483  
 quantum dots 474  
 quantum-size  $\text{TiO}_2$  particles 263  
 quartz crystal microbalance 10, 149, 157, 310, 355, 395, 415  
 quartz crystal microbalance measurements 212  
 quasi-equilibrium approach 96  
 quaternized ammonium groups 184  
 quenching mechanisms 401

**r**

radioactive labeling of counterions 16  
 radiolabeled 109  
 radiolabeled calcium 112  
 radiolabeled counterions 110  
 radiolabeled probes 114  
 Random Phase Approximation 90  
 rate constants of polyion exchange 55  
 reaction parameters 7  
 rearrangement of polymer chains 396  
 rearrangements 77  
 recharging of the particle surface 337  
 rectifying properties 259  
 red blood cells 365  
 redox process 306  
 redox-active molecule 490  
 redox-active polymer films 295  
 redox-active species 488  
 reduction by hydrogen 254  
 reduction of graphite oxide 253  
 reflectance FTIR spectra 491  
 refractive index 140  
 regularly packed strata 184  
 relaxation processes 380  
 relay-race transfer 74  
 reluctant exchange 105, 118f., 129  
 removal of excess polyelectrolyte 335  
 re-polymerization reaction 370  
 reproducibility 6  
 repulsive electrostatic interactions 89  
 response times for coloration 420  
 reversal of surface charge 109, 398  
 reverse bias 138  
 reversible swelling 404  
 reversible switching of the permeability 379  
 Rhodamine 401  
 rigid-rod-like structure 412  
 rod-like conformation 209  
 rod-like polynuclear structures 408  
 rotating disk electrode 119

roughness 398  
 rupture strength 385  
 ruthenium complex 259

**s**

salt concentration 7  
 SAXS diffraction 250  
 scaling argument 90  
 scanning force microscopy 430  
 scattering length density profiles 21  
 Schottky diode 259  
 screening length 91  
 screening surface counterions 91  
 second harmonic coherence length 469  
 second harmonic generation 10, 196, 467, 469  
 second harmonic intensities 467f., 470  
 second level of microstructures 284  
 second virial coefficient 65  
 secondary aggregation 347  
 secondary interactions 218, 271, 277  
 second-order non linear optical properties 196  
 second-order susceptibility 462  
 sedimentation 351  
 sedimentation mode 66  
 sedimentograms 66  
 selective adsorption 273, 282  
 selective adsorption of block copolymers 144  
 selective deposition 273f., 276  
 selective electroless metal plating 141  
 selective electroless plating 143, 293  
 selective ion binding 28  
 selective nickel deposition 294  
 selective permeability 375  
 selective plating of colloidal arrays 293  
 selective precipitation 387  
 selective reduction 493  
 selective surface binding 143  
 selective transportation 126, 427  
 selective uptake of metal ions 455  
 selectivity 125f., 308, 496, 499  
 selectivity function of surface charge 500  
 selectivity of particle adsorption 290  
 selectivity of the electrode 308  
 selectivity ratios 501  
 self-assembled electrodes 267  
 self-assembly 288  
 self-repulsive interactions 275  
 self-standing films 227  
 self-trapping 126  
 semiconductor films 208

- semiconductor quantum dots 231
- semidilute solution 90
- sensor applications 376, 458
- sensors 304
- separating membranes 446
- separation efficiency 449
- separation factor 448
- shear elastic modulus 384
- shell/core sharp boundary 75
- SHG intensity 467
- short range interactions 218
- short range repulsive interactions 96
- shrinking 381
- silver nanoparticles 142
- silver particles 255
- single chain conformations in the bulk 77
- single lines of particles 290
- single monolayer arrays 292
- single particle array 290
- single particle light scattering 337, 374
- slow aging 368
- small angle neutron scattering 77
- smart capsules 363
- smoothing 105
- smoothing of the surface 107
- snake cage exchangers 122
- sol-gel processes 352
- solid electrolyte 294
- solid planar substrates 393
- solid state electrochromic films 295
- solid/liquid interface 403
- solution-cast polyelectrolyte complex 447
- solution pH 135
- solution properties of polyelectrolytes 89
- solvation 102
- solvent etching 324
- specific energies 264
- specific interaction 59
- specific recognition 5
- spectral electrochemical properties 295
- specular reflectivity measurements 192
- spin coating 12
- spin flipping 231
- splitting of the S-O stretching modes 411
- s-polarized light 467
- spraying 12
- spreading of polymer charge 114
- stability 320, 325, 343
- stability against flocculation 365
- stability and mechanical properties 380
- stabilizer molecules 232
- stabilizer shell around CdS 220
- $\pi$ -stacking 415
- stamping of block copolymers 285
- stamping of ionic polymers 285
- steady-state diffusion-limited flux 120
- stereocomplex formation 5
- steric interactions 277
- sterically irregular polymer chains 77
- 1:1 stoichiometric complex 18
- stoichiometric IPECs 50
- stop-flow measurements 53
- stratification 228
- stratified arrangement 198
- stratified assemblies 225
- stratified binary hybrid organic/inorganic multilayers 188
- stratified binary organic multilayers 182
- stratified binary systems 182
- streaming potential 12, 398
- streptavidin 15
- stress-strain curves 80
- strongest water swollen films 79
- structural control 218
- structural factors 90, 217
- structural transformations 223
- structure of organic shell 219
- substantial extension of PMA coils 78
- substitution of contacts 58
- substitution reaction 59
- subtractive ink-jet printing 150
- sugar compounds 156
- superlattice 199, 403
- superlinear growth 24
- superparamagnetic behavior 231
- supporting electrolyte 490
- supramolecular assemblies 1
- supramolecular organization 414
- surface 109
- surface charge 452, 490
- surface charge density 136, 495
- surface charge reversal 100, 110
- surface-constrained complexation 187
- surface excess charge 114
- surface force microscopy 279
- surface forces measurements 10
- surface induced nucleation 3
- surface interactions 3, 397
- surface modification yttrium iron garnet 219
- surface overcompensation 116
- surface plasmon absorption band 344
- surface plasmon resonance 251
- surface plasmon resonance spectroscopy 395
- surface plasmon spectroscopy 10

- surface potential 11, 398
  - surface roughness 136, 138
  - surface sol-gel process 155f.
  - surface sorting 281, 291
  - swelling 100, 105, 127
  - swelling coefficient 106
  - swelling kinetics 369
  - swelling of film 12
  - switchable release 379
  - synthesis of nanoparticles 390
- t**
- tailored enzymatic yields 354
  - tails 396
  - TEM image 340
  - TEM micrographs 342
  - temperature dependence 382
  - temperature dependent structures 381
  - template assisted assembly 3
  - template molecule 168
  - templates 50
  - ternary solvent 321
  - terpyridine ligand 408
  - tetramethoxysilane 162
  - tetrathiooxalate 441
  - thermal stability 468
  - thermodynamic quality solvent 67
  - thick layers 136
  - thickness increment 116
  - three component array 281
  - three-dimensional macroporous materials 351
  - threshold concentration of salt for IPEC decomposition 71
  - titanium dioxide 257
  - titanium niobate sheets 222
  - titration curves of weak polyelectrolytes 49
  - topochemical reaction 431
  - total free energy change 58
  - total internal reflection fluorescence 395
  - trains 396
  - translational entropy 397
  - transmission electron microscopy 228, 339
  - transparent conducting polymer 287
  - transport 99
  - transport of ions 123
  - transport of small molecules 446
  - trapping of molecules 126
  - triethoxy silanes 282
  - turbidimetric titration curves 69
  - two component colloidal arrays 292
  - two component, laterally patterned polyelectrolyte multilayer films 280
- u**
- ultrathin polymer/metal oxide 161
  - uncompensated charge 498
  - unconstrained overcompensation 129
  - uniform nanoparticle coatings 341
  - unilamellar liquid liposomes 73
  - unimer complex species 61
  - uptake of water 411
  - urease 341
  - utilization of coated colloids 351
  - UV/Vis spectroscopy 7
- v**
- vertical disordering 192
  - visco-elastic behavior 82
  - viscosity 385
  - voltammograms 488
  - volume conductivity 254
- w**
- wall influence 385
  - wall materials 365
  - water contact angles 493
  - water diffusion 369
  - weak polyamine deposition 277
  - weakly swollen shell 74
  - well-ordered multilayers 200
  - wettability 493
  - wettable surface 145
  - wetting characteristics 286
- x**
- XPS 475
  - X-ray and neutron reflectivity 16
  - X-ray and neutron reflectometry 10
  - X-ray diffuse scattering 179
  - X-ray photoelectron spectroscopy 16, 157, 408
  - X-ray reflectivity 403
  - X-ray reflectometry 7, 20, 180, 418
- y**
- yeast cells 365
  - yttrium iron garnet 212
  - Young's modulus 384
- z**
- zeta potential measurements 11, 16
  - zeta potentials 220
  - Zimm diagram 61
  - zirconium butoxide 162
  - zirconium phosphate 210
  - zone model 16